

**Proceedings of the
18th Annual Symposium
Imaging Network Ontario
March 26 – 27, 2020
www.ImNO.ca/2020-Symposium**

Sponsoring Consortia

Biomedical Imaging Research Centre

Biomedical Computing Laboratory at Queen's University

Development of Novel Therapies for Bone and Joint Diseases

Heart Failure: Prevention through Early Detection Using New Imaging Methods

Imaging for Cardiovascular Device Intervention

Ontario Institute for Cancer Research Imaging Program

Ontario Network of Excellence for Translation of Hyperpolarized MRI Technologies



Table of Contents

Welcome Letter	5
Sponsoring Consortia	6
Development of Novel Therapies for Bone and Joint Diseases.....	6
Heart Failure: Prevention through Early Detection Using New Imaging Methods.....	6
Imaging for Cardiovascular Device Intervention (ICDI).....	6
Ontario Institute for Cancer Research Imaging Program.....	7
Ontario Network of Excellence for Translation of Hyperpolarized MRI Technologies.....	7
Biomedical Imaging Research Centre (BIRC).....	7
Queen’s University Imaging Group.....	8
Keynote Speakers	9
Bastiaan Driehuys.....	9
Michelle L. James.....	9
Jessica Burgner-Kahrs.....	10
Lisa Mielniczuk.....	10
Molly S. Shoichet.....	11
Scientific and Organizing Committees	12
Scientific Committee.....	12
Organizing Committee.....	12
Abstract Reviewers.....	12
Oral and Poster Judges.....	12
Program	13
Oral Presentation Abstracts	17
Session 1: Cellular and Molecular Imaging.....	18
Session 2: Lung Imaging.....	25
Session 3: Machine Learning in Cancer Imaging.....	32
Session 4: Image-Guided Interventions 1.....	39
Session 5: Image-Guided Interventions 2.....	46
Session 6: Neurology Imaging 1.....	52

Session 7: Musculoskeletal Imaging and Technology.....	58
Session 8: Cardiovascular and Vascular Imaging.....	65
Session 9: Instrumentation and Technology Development.....	72
Session 10: Neurology Imaging 2.....	78
Poster Presentation Abstracts	84
Session 1: Cellular and Molecular Imaging.....	85
Session 2: Lung Imaging.....	100
Session 3: Machine Learning in Cancer Imaging.....	107
Session 4: Machine Learning in Imaging.....	115
Session 5: Image-Guided Interventions.....	124
Session 6: Neurology Imaging.....	137
Session 7: Musculoskeletal Imaging and Technology.....	163
Session 8: Cardiovascular and Vascular Imaging.....	167
Session 9: Instrumentation and Technology Development.....	176
Imaging Network Ontario (ImNO) Code of Conduct	205

Welcome Letter

March 12, 2020

Dear ImNO 2020 Attendees:

Welcome to the Imaging Network Ontario (ImNO) 2020 Symposium. This year marks our 18th annual meeting and the first year that our conference will be fully virtual.

ImNO is an initiative created in response to a request by the Ontario Research Development Challenge Fund – now the Ontario Research Fund – for assistance in harmonizing its investments in imaging research. The establishment of ImNO provides a means of harnessing and focusing the intellectual and innovative capabilities at Ontario universities in partnerships with emerging and established medical imaging companies to create a strong and sustainable internationally competitive imaging industry based on scientific excellence in Ontario.

Since its' inception in 2003, the annual ImNO meeting has welcomed invited presentations from world-class scientists and proffered presentations from Ontario and across the county. This year, we are pleased to thank GE Healthcare, our corporate sponsor, and the following groups for supporting our conference:

- Biomedical Imaging Research Centre
- Development of Novel Therapies for Bone and Joint Diseases
- Heart Failure: Prevention through Early Detection Using New Imaging Methods
- Imaging for Cardiovascular Device Intervention
- Ontario Institute for Cancer Research Imaging Program; and
- Ontario Network of Excellence for Translation of Hyperpolarized MRI Technologies
- Biomedical Computing Laboratory at Queen's University

For the 2020 meeting, abstracts were reviewed by an average of 3 reviewers and 167 were accepted. The ImNO 2020 Scientific Committee then assembled the final program: 5 keynote speakers, 56 oral presentations and 111 poster presentations.

In closing, we would like to acknowledge the significant contributions made by the members of the Scientific and Organizing Committees, particularly over the last days as we transitioned to a virtual meeting. Together they have worked very hard to bring us a diverse program. We hope you enjoy this year's program and world-renowned keynote speakers.

Sincerely,

Amber Simpson
Chair, Scientific Committee, 2020 ImNO Symposium

Sponsoring Consortia

The Annual Meeting of Imaging Network Ontario (ImNO) promotes Canada's role as a leader in medical imaging innovation by cultivating synergy among consortia and partnerships between Ontario and other Canadian imaging entities.

The following consortia and programs supported the 2020 ImNO Symposium financially.

Development of Novel Therapies for Bone and Joint Diseases

Lead Researcher: Dr. David Holdsworth

Ontario Research Fund

Musculoskeletal disorders are the most common cause of severe long-term pain and physical disability, affecting hundreds of millions of people around the world. The economic burden is high; joint diseases cost the Ontario economy more than \$2 billion per year. To reduce this disease burden, this Ontario Research Fund Research Excellence program focuses on the "Development of Novel Therapies for Bone and Joint Diseases," including improved diagnostic imaging techniques and new approaches for image-guided therapy. A multidisciplinary team of imaging scientists, biomedical engineers, physical therapists, and orthopaedic surgeons work together on key research projects, including the development of new ways to post-process 3D MRI and CT data to guide surgery, dynamic imaging of moving joints (under load), and image-based design of "patient-specific" orthopaedic components.

Heart Failure: Prevention through Early Detection Using New Imaging Methods

Lead Researcher: Dr. Frank Prato

Ontario Research Fund

Consortium partners: Lawson Health Research Institute, Sunnybrook Research Institute and University of Ottawa Heart Institute. Ten percent of Ontarians over 60 have heart failure. One quarter will die within one year of diagnosis and almost all in ten years. Our LHRI/SRI/UOHI consortium is developing combined PET and MRI imaging methods for early diagnosis when treatment is still possible. The imaging methods developed are being commercialized and will benefit Ontario by improving the health of its citizens and creating new jobs.

Imaging for Cardiovascular Device Intervention

Lead Researcher: Dr. Graham Wright

Ontario Research Fund

Cardiovascular diseases have evolved from an acute killer to a chronic disease challenge. In recent years, there have been major advances in less invasive treatments, placing an emphasis on the development of imaging and tracking technologies. Focusing on electrophysiology, percutaneous procedures, and valve replacement, researchers at Sunnybrook and Robarts Research Institutes, working with local, national, and multinational diagnostic imaging and interventional device companies, are advancing the state-of-the-art in image acquisition and analysis with ultrasound, MRI, x-ray, and CT methods, including the design of visualization platforms and associated communication and control interfaces for interventional guidance, facilitating fusion and manipulation of prior and real-time imaging and device information. The ultimate goal is more effective utilization of imaging to improve outcomes for patients with chronic ischemia, complex arrhythmias, and heart failure related to structural heart diseases.

Ontario Institute for Cancer Research Imaging Program

Directors: Dr. Aaron Fenster and Dr. Martin Yaffe

Ontario Institute for Cancer Research

The OICR Imaging Program accelerates the translation of research into the development of new imaging innovations for earlier cancer detection, diagnosis and treatment through four major projects: probe development and commercialization, medical imaging instrumentation and software, pathology validation, and imaging for clinical trials. The Imaging Program facilitates improved screening and treatment options for cancer patients by streamlining advances in medical imaging through the complex pipeline from discovery to clinical translation and ultimately to clinical use.

Ontario Network of Excellence for Translation of Hyperpolarized MRI Technologies

Lead Researcher: Dr. Charles Cunningham

Ontario Research Fund

Ontario is home to five major research groups developing new forms of MRI based on Hyperpolarized (HP) contrast agents, with the aim of transforming patient care for conditions such as cancer, heart failure and lung disease. Just as an injection of dye prior to an x-ray exam can reveal important new information, the introduction of HP contrast agents, which are magnetized to be directly detectable in an MRI scan, can open up many new applications of MRI. Several HP agents have been developed in the past 20 years for MR imaging, and Ontario is uniquely positioned to take a leadership role in the development of the next generation of agents and technologies, with expertise and activity in all of the related technology development areas. The overall objective of this program is to integrate and develop this substantial expertise, creating an Ontario Network of Excellence, bringing these technologies forward to commercialization and, ultimately, application in the health system. Each of the related technologies is being developed in partnership with MRI hardware vendors and pharmaceutical companies for application in targeted disease areas.

There are five major centres of activity in HP-MRI in Ontario led by: Mitchell Albert in Thunder Bay, Andrea Kassner and Giles Santyr at the Hospital for Sick Children in Toronto, Charles Cunningham at Sunnybrook Health Sciences Centre in Toronto, Charles McKenzie, Grace Parraga and Timothy Scholl at the Robarts Research Institute in London, and Michael Noseworthy in Hamilton

Biomedical Imaging Research Centre

Director: Dr. Savita Dhanvantari

The Biomedical Imaging Research Centre (BIRC) is a Full Partnership Centre at Western University encompassing London-wide Imaging.

BIRC is focused on the discovery and development of innovative imaging techniques and instrumentation to improve the understanding, diagnosis, and treatment of human diseases. Under the umbrella of BIRC, biomedical imaging research in London is now a highly integrated program covering all major imaging modalities and biomedical applications, which include: Cardiovascular Imaging, Imaging in Neurosciences & Mental Health, Neonatology & Pediatric Imaging, Musculoskeletal Imaging, Imaging in Oncology, Respiratory Imaging, Image-guided Interventions, and Basic Imaging Science & Engineering.

BIRC represents biomedical imaging research across five key partners including two research institutes (Robarts Research Institute and Lawson Health Research Institute), two university departments (Department of Medical Imaging and School of Biomedical Engineering) and the Schulich School of Medicine & Dentistry.

Biomedical Computing Laboratory at Queen's University

Lead Researcher: Dr. Amber Simpson

The Biomedical Computing Laboratory at Queen's University is National Institutes of Health-funded lab that recently relocated to Ontario from the US. The lab is focused on developing novel computational analyses of routinely acquired diagnostic images such as CT and MRI as well as other relevant biomedical data. This highly integrated group works with hundreds of thousands of images to create biomarkers of cancer progression and survival for evaluation in phase I/II clinical trials. The group spans two faculties (Arts & Science & Health Sciences) and two departments (School of Computing & Department of Biomedical & Molecular Sciences).

Keynote Speakers

Thursday, March 26 at 8:40

Bastiaan Driehuys, PhD, Professor, Duke University

Dr. Driehuys is a professor of radiology at Duke University. His research focuses on the physics and applications of MRI using hyperpolarized ^{129}Xe gas. His team is focused on exploiting the unique properties of this technology for non-invasive 3D imaging of pulmonary function. Dr. Driehuys holds a B.A. in physics from Franklin & Marshall College (1990) and a Ph.D. in atomic physics from Princeton University (1995). Prior to his faculty role at Duke he held senior R&D positions at Amersham Health (now GE Healthcare). In addition to his academic role, he serves as chief scientific officer for Polarean Imaging, a company he founded to commercialize hyperpolarized ^{129}Xe MRI technology.



Thursday, March 26 at 13:00

Michelle L. James, PhD, Assistant Professor, Stanford University

Dr. James is an Assistant Professor in the Departments of Radiology and Neurology, within the Molecular Imaging Program at Stanford (MIPS). She received her BS in pharmacology and medicinal chemistry at the University of Sydney, where she also earned her PhD in radiochemistry and was awarded the University Medal. For the past fifteen years, Dr. James's research has focused on developing novel molecular imaging agents to improve the way we diagnose, treat, and understand devastating neurological diseases such as Alzheimer's and Multiple Sclerosis. As part of her work, Dr. James has multiple patented PET radiotracers for imaging brain diseases, four of which are currently being used in clinical studies at Stanford and around the world.



Thursday, March 26 at 15:20

Jessica Burgner-Kahrs, PhD, Associate Professor, University of Toronto

Dr. Burgner-Kahrs is Associate Professor of Computer Science as well as Mechanical & Industrial Engineering and the founding Director of the Continuum Robotics Laboratory at the University of Toronto. She holds a Diplom and doctoral degree in Computer Science from Karlsruhe Institute of Technology, Germany. Before moving to Toronto, Dr. Burgner-Kahrs hold appointments at Vanderbilt University, Nashville, USA and Leibniz University Hannover, Germany. Her research focus lies on continuum robotics and is driven by applications in minimally-invasive surgery. Dr. Burgner-Kahrs research was recognized by the Heinz Maier-Leibnitz Prize 2015 and the Engineering Science Prize in 2016 among others. She was entitled Germany's Young Researcher of the Year 2015 and nominated as a Young Global Leader from the World Economic Forum in 2019.



Friday, March 27 at 12:15

Lisa Mielniczuk, MD FRCPC, Professor, University of Ottawa Heart Institute

Dr. Mielniczuk is the Director of the Advanced Heart Diseases Program at the Ottawa Heart Institute. She is also cross-appointed to the Department of Cellular and Molecular Medicine. In 2019 Dr. Mielniczuk was appointed Vice-Chair of Patient Quality, Safety and Innovation for the Department of Medicine at the University of Ottawa. Her commitment to leadership and program development is evident in her multiple accomplishments at the Heart Institute, including being the co-Founder and Director of the Pulmonary Hypertension Program, developing a Rapid Intervention Clinic for HF patients, and a Regional HF program for the Ottawa/Champlain region. Provincially and Nationally, Dr. Mielniczuk is an active leader for the HF and Pulmonary Hypertension community, and currently sits as a member of the CorHealth Ontario Senior Leadership Council for Cardiac Disease, as well as serving as an expert panel member for Health Quality Ontario and CADTH.



Friday, March 27 at 14:30

Molly S. Shoichet, PhD, Professor, University of Toronto

Dr. Shoichet holds the Tier 1 Canada Research Chair in Tissue Engineering at the University of Toronto. Her research is focused on drug and cell delivery strategies in the central nervous system and 3D hydrogel culture systems to model cancer. Dr. Shoichet co-founded four spin-off companies, is actively engaged in translational research and science outreach. She is an Officer of the Order of Canada and holds the Order of Ontario. Dr. Shoichet is a University Professor – the highest distinction of the University of Toronto, which is held by less than 2% of the faculty. Dr. Shoichet received her SB from the Massachusetts Institute of Technology (1987) and her PhD from the University of Massachusetts, Amherst in Polymer Science and Engineering (1992).



Scientific and Organizing Committees

Chair: Amber Simpson

Scientific Committee

Robert deKemp	Ali Khan	Rebecca Thornhill
Savita Dhanvantari	David Holdsworth	Aaron Ward
Maria Drangova	Anne Martel	Cari Whyne
Aaron Fenster	Charles McKenzie	Graham Wright
Gabor Fichtinger	Tamie Poepping	Martin Yaffe

Organizing Committee

Johanne Langford	Jean Rookwood	Kitty Wong
Carol Richardson	Janette Wallace	

Abstract Reviewers

Nishard Abdeen	Pascal Fallavollita	M Louis Lauzon	Tim Scholl
Natasha Alves	Aaron Fenster	Chris Macgowan	Michael Seed
Corey Baron	Donna Goldhawk	James Mainprize	Amber Simpson
Stephen Breen	Roy Haast	Anne Martel	Navneet Singh
Tim Burkhart	Michael Hardisty	Naomi Matsuura	Jonathan Thiessen
Ian Cameron	Matthew Holden	Sarah Mattonen	Rebecca Thornhill
Elvis Chen	David W. Holdsworth	Charles McKenzie	Tamas Ungi
Derek Cool	Natasja Janssen	Elka Miller	Aaron Ward
Greg Cron	Michael Jurkiewicz	John Moore	Glenn Wells
Charles Cunningham	Ali R. Khan	Michael Noseworthy	Cari Whyne
Robert DeKemp	Miranda Kirby	Alexei Ouriadov	Eugene Wong
Savita Dhanvantari	Manuela Kunz	Terry Peters	Graham Wright
Mamadou Diop	Emily Lalone	Tamie Poepping	
Maria Drangova	Andras Lasso	Giles Santyr	

Oral and Poster Judges

Coordinator: Corey Baron

Natasha Alves-Kotzev	Uzair Hussain	Sarah Mattonen	Timothy Scholl
Amy Boyle	Miranda Kirby	Charles McKenzie	Ali Tavallaei
Elvis Chen	Andras Lasso	Alexei Ouriadov	Jonathan Thiessen
Donna Goldhawk	Christopher MacGowan	Tamie Poepping	Cari Whyne
Roy Haast	Paco Martinez	Normand Robert	Graham Wright
Michael Hardisty	Gabriel Mattatall	Giles Santyr	Yiming Xiao

Program

Thursday, March 26, 2020

8:30 – 8:40	Opening Remarks Amber Simpson, ImNO 2020 Scientific Committee Chair	Zoom Meeting Room 1
8:40 – 9:25	Keynote Session Chairs: Giles Santyr and Charles Cunningham Clinical Hyperpolarized ¹²⁹Xe MRI: past, present, and future Bastiaan Driehuys, Duke University	Zoom Meeting Room 1
9:25 – 10:25	Poster Session	
	Zoom Meeting Room 1	Zoom Meeting Room 2
	1 - Cellular and Molecular Imaging Chairs: Michelle James and Veronica Dubois	2 - Lung Imaging Chairs: Bastiaan Driehuys and Lauren Smith
10:25 – 10:39	1-1 Whole-body Detection of Metastasizing Cancer Cells in Preclinical Animal Models Nivin N Nyström, Robarts Research Institute	2-1 Comparison of Automated to Manual Histology Quantitation of Regional Lung Tissue and Blood Fractions in a Rat Model of Rili Jordan D Fliss, Hospital for Sick Children
10:39 – 10:53	1-2 Trimodal cell tracking in vivo: Combining iron- and fluorine-based MRI with MPI to monitor the delivery of mesenchymal stem cells and the ensuing inflammation Olivia C Sehl, Robarts Research Institute	2-2 Computed Tomography Airway Tree Tortuosity Features Predict Functional Small Airway Disease in Chronic Obstructive Pulmonary Disease Daniel Genkin, Ryerson University
10:53 – 11:07	1-3 Evaluating survivin-driven tumour-activatable minicircles for prostate cancer theranostics TianDuo Wang, Robarts Research Institute	2-3 Relationships between Computed Tomography Texture Features and Visual Scoring of Emphysema in Chronic Obstructive Pulmonary Disease Wai Tai Lui, Ryerson University
11:07 – 11:21	1-4 Evaluation of two ¹¹C-labeled cyclooxygenase-1 (COX-1) and COX-2 radioligands for PET imaging of ovarian, breast, and pancreatic cancer xenograft mouse models Amanda Boyle, Centre for Addiction and Mental Health	2-4 Comparison of PREFUL and Hyperpolarized Xenon gas MRI Ventilation Distributions in Pediatric Cystic Fibrosis Lung Disease Samal Munidasa, Hospital for Sick Children
11:21 – 11:35	1-5 Prostate specific membrane antigen positron emission tomography for the identification of intra-prostatic tumors: investigating targeting guidelines for focal therapy and guided biopsy Ryan M Alfano, Western University	2-5 Identifying Functional Information Determinants in Thoracic Computed Tomography Images Using Machine Learning Maksym Sharma, Robarts Research Institute
11:35 – 11:49	1-6 Developing Magnetic Resonance Reporter Gene imaging: Co-localization and Interaction of Magnetotactic Bacteria Genes mamI and mamL Qin Sun, Lawson Health Research Institute	2-6 Supervised shallow learning of ¹²⁹-Xe MRI texture features to predict response to Anti-IL-5 biologic therapy in severe asthma Marrissa McIntosh, Robarts Research Institute

Thursday, March 26, 2020

11:49 – 13:00	Break	
13:00 – 13:45	Keynote Session	Zoom Meeting Room 1
	Chairs: Maged Goubran and Rebecca Sullivan	
	Tracking immune activation and invasion in neurological diseases using PET	
	Michelle James, Stanford University	
	Zoom Meeting Room 1	Zoom Meeting Room 2
	3 - Machine Learning in Cancer Imaging	4 - Image-Guided Interventions 1
	Chairs: Chetan Srinidhi and Amoon Jamzad	Chairs: Ali Khan and Natasja Janssen
13:45 – 13:59	3-1 A Deep Learning-based Method for Generalized Prostate Segmentation in 3D Ultrasound Nathan Orlando, Robarts Research Institute	4-1 Evaluation of a mixed-reality first person point of view needle navigation system Leah Groves, Robarts Research Institute
13:59 – 14:13	3-2 Tissue component segmentation and cancer detection on digitized prostatectomy slides using convolutional neural networks Laurie Huang, Baines Imaging	4-2 Proteus: An Open Source Software Platform for Modulated Therapy with MRgHIFU Ben Keunen, Hospital for Sick Children
14:13 – 14:27	3-3 Prediction of tumour mutational burden of squamous cell carcinoma using histopathology images of surgical specimens Salma Dammak, Western University	4-3 A mechatronic needle-tracking system for image-guided breast biopsy using positron emission mammography and ultrasound Claire K Park, Robarts Research Institute
14:27 – 14:41	3-4 Visualization of Clinically Significant Prostate Cancer Using Multi-stream U-Nets Alireza Sedghi, Queen's University	4-4 Reinforcement learning approach for video-based task recognition in central venous catheterization Rebecca Hisey, Queen's University
14:41 – 14:55	3-5 Computer Aided Detection and Evaluation of Renal Masses in Computed Tomography Images Using Deep Learning Methods Fatemeh Zabihollahy, Carleton University	4-5 Development of a Surgical Simulator for Spinal Decompression Procedures using Virtual Reality Yukun Zhang, Sunnybrook Research Institute
14:55 – 15:09	3-6 Masking Risk Predictor for Screening Mammography using a Convolutional Neural Network Theo S Cleland, Sunnybrook Research Institute	4-6 Localizing high-dose-rate interstitial gynecologic brachytherapy needles intraoperatively using automatic segmentation approaches Jessica R Rodgers, Robarts Research Institute
15:09 – 15:20	Break	
15:20 – 16:05	Keynote Session	Zoom Meeting Room 1
	Chairs: Amber Simpson and Jessica Rodgers	
	Through the Keyhole - Soft and Continuum Robots for Surgical Applications	
	Jessica Burgner-Kahrs, University of Toronto	

Friday, March 27, 2020

Zoom Meeting Room 1

5 - Image-Guided Interventions 2

Chairs: Elvis Chen and Ryan Alfano

- 8:30 – 8:44 **5-1 A Novel Approach for Guiding Catheter-Based Interventions**
James J Zhou, Sunnybrook Health Sciences Centre
- 8:44 – 8:58 **5-2 Automated surgical video annotation on open-source data collection platform**
Jacob R Laframboise, Queen's University
- 8:58 – 9:12 **5-3 Symmetric Autoencoder for Tissue Classification of Mass Spectrometry IKnife Data**
Alice ML Santilli, Queen's University
- 9:12 – 9:26 **5-4 Validation of a Projector-Based Navigation System for Bedside Surgical Procedures**
Colton A Barr, Queen's University
- 9:26 – 9:40 **5-5 Respiratory Motion Estimates for Catheter Tracking with Undersampled 3D Image-Based Navigators**
Jaykumar Patel, University of Toronto

9:40 – 10:40

Poster Session

Zoom Meeting Room 1

7 - Musculoskeletal Imaging and Technology

Chairs: Adam Waspe and Daniel Lorusso

- 10:40 – 10:54 **7-1 Validation of 3D Ultrasound for Bedside Monitoring of Osteoarthritis-Induced Synovium Inflammation and Cartilage Degradation**
Sam Papernick, Robarts Research Institute
- 10:54 – 11:08 **7-2 Four-Dimensional Computed Tomography to Measure Distal-radial and Radio-carpal Joint Congruency Following Wrist Fracture**
Puneet Ranota, Western University
- 11:08 – 11:22 **7-3 Sparse-view cone-beam CT reconstruction for assessing migration in knee arthroplasty: a phantom study**
Rudy Baronette, Robarts Research Institute
- 11:22 – 11:36 **7-4 MR-Guided Focused Ultrasound-Induced Blood-Spinal Cord Barrier Opening Facilitates a Localized Increased Uptake of Trastuzumab into Leptomeningeal Metastases**
Paige Smith, University of Toronto
- 11:36 – 11:50 **7-5 Diffusion Tensor Tractography of Tendons as a Tool for Assessing MRgFUS Ablation**
William Chu Kwan, Hospital for Sick Children
- 11:50 – 12:04 **7-6 MRI characterization of a novel porous 3D printed metal scaffold**
Gregory Hong, Robarts Research Institute

Zoom Meeting Room 2

6 - Neurology Imaging 1

Chairs: Corey Baron and Roy Haast

- 6-1 Translocator Protein in Post-traumatic Stress Disorder: Preliminary findings using the [18F]FEPPA PET radioligand**
Sarah Watling, Centre for Addiction and Mental Health
- 6-2 Can Brain Activity Predict Manual Dexterity Improvement after Surgery in Cervical Myelopathy?**
Alicia Cronin, Western University
- 6-3 In Vitro Characterization of novel PET Radiotracers for the "Glycogen Synthase Kinase-3 Hypothesis of Alzheimer's Disease"**
Ashley C Knight, Centre for Addiction and Mental Health
- 6-4 Longitudinal MRI and TSPO-PET: Alzheimer's Disease Interacts with Subcortical Stroke through Inflammation**
Nassir U.N. Al-Khishman, Western University
- 6-5 Are Cognitive Deficits in Parkinson's Disease Associated with Dopaminergic Dysfunction: A Graph Theory Analysis**
Alexander Mihaescu, Centre for Addiction and Mental Health

Zoom Meeting Room 2

8 - Cardiovascular and Vascular Imaging

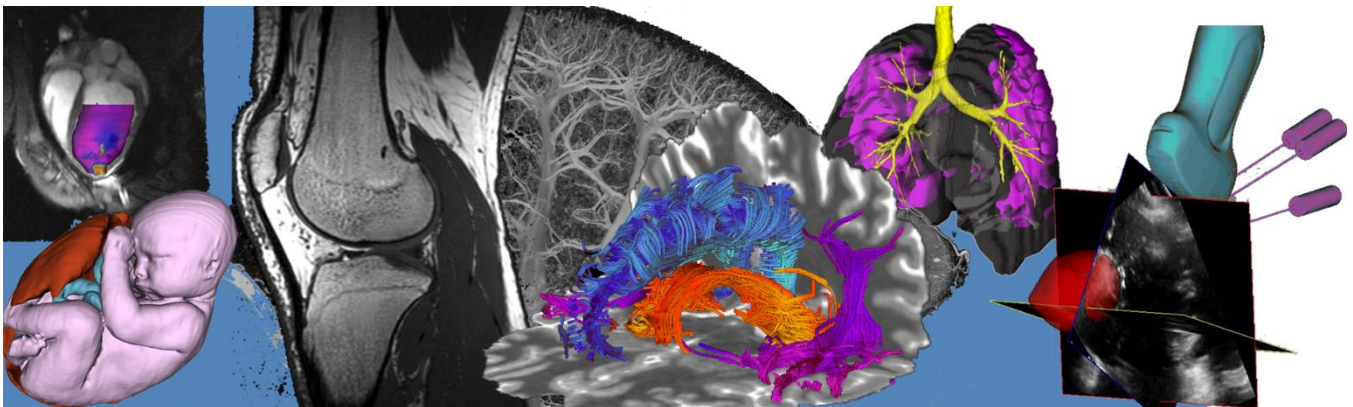
Chairs: Lisa Mielniczuk and Jill Weyers

- 8-1 Non-Invasive MRI Engraftment Localization Of Stem Cell-Derived Cardiomyocyte Therapy**
Moses P Cook, Univeristy of Toronto
- 8-2 Optimizing vasodilator dose to induce hyperemic stress during myocardial perfusion assessment in a porcine model**
Jill Weyers, Sunnybrook Research Institute
- 8-3 Correlation of high-resolution 3D MR-derived gray zone with VT cycle length in a swine model of chronic infarction**
Terenz R Escartin, Sunnybrook Research Institute
- 8-4 Multi-view 3D echocardiography volume compounding for mitral valve procedure planning**
Patrick Carnahan, Robarts Research Institute
- 8-5 A Novel PET Tracer Enables Imaging of the Cardiac Growth Hormone Secretagogue Receptor in a Large Animal Model of Heart Failure**
Rebecca Sullivan, Lawson Health Research Institute
- 8-6 Low-dose CT Perfusion by Sparse Projections in Acute Ischemic Stroke**
Kevin J Chung, Western University

Friday, March 27, 2020

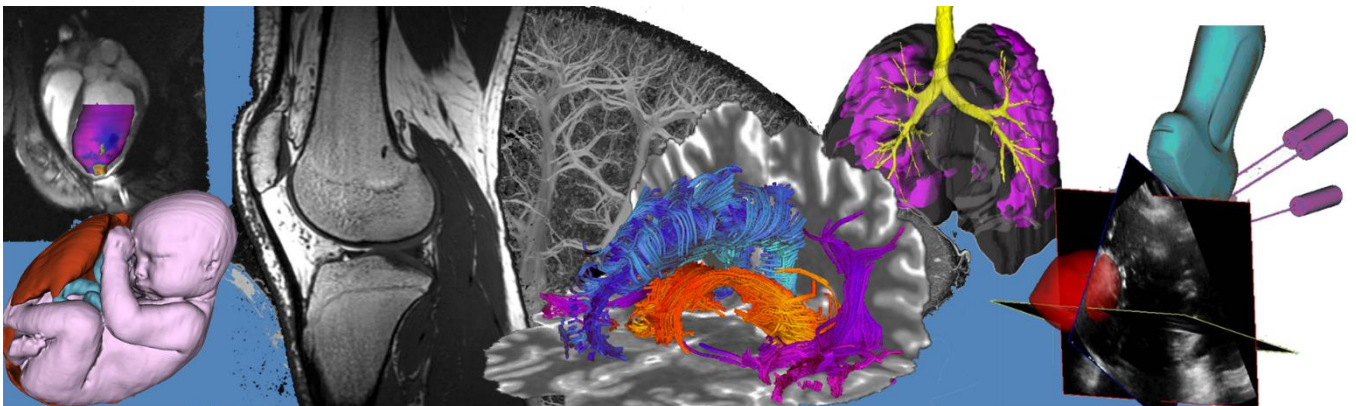
12:04 – 12:15	Break	
12:15 – 13:00	Keynote Session Zoom Meeting Room 1	
	Chairs: Rob DeKemp and Nilesh Ghugre	
	Right Ventricular Adaptation to pressure overload. The Role of Metabolism and Neurohormonal Activation	
	Lisa Mielniczuk, University of Ottawa	
	Zoom Meeting Room 1	Zoom Meeting Room 2
	9 - Instrumentation and Technology Development	10 - Neurology Imaging 2
	Chairs: Ali Tavallaei and Tamie Poepping	Chairs: Sarah Mattonen and Salma Dammak
13:00 – 13:14	9-1 The Effects of Elasticity and Scattering on Tissue Characterization Using Ultrasound Time Series Justin Gerolami, Queen's University	10-1 Exponential Analysis for Magnetic Resonance Relaxation Spectrum using Artificial Neural Networks Tristhal Parasram, University of Windsor
13:14 – 13:28	9-2 Tuning an RF Birdcage Coil by Varying the Shield Radius Kieffer J Davieau, Western University	10-2 Simulation of Spectral Modification for Suppressing CSF in Oscillating Gradient Diffusion MRI Kevin B Borsos, Robarts Research Institute
13:28 – 13:42	9-3 Integration of a Real-Time Field Monitoring System for Artifact Correction in Diffusion MRI Paul I Dubovan, Western University	10-3 Characterization of orientation dispersion's effect on DTI using a 3D printed axon-mimetic phantom Tristan K Kuehn, Robarts Research Institute
13:42 – 13:56	9-4 An Optimised Diffusion MRI Technique to Study White Matter Integrity Nico J J Arezza, Robarts Research Institute	10-4 Beyond the Diffusion Tensor: Validation of Advanced Approaches for Microstructural Diffusion MRI Naila M Rahman, Robarts Research Institute
13:56 – 14:10	9-5 Microstructural characterization and Visualization a 3D printed phantom using diffusion MRI and microscopy Farah N Mushtaha, Robarts Research Institute	10-5 Neuritic Architecture Relates to Functional Brain Activity Christin Schifani, Centre for Addiction and Mental Health
14:10 – 14:30	Break	
14:30 – 15:15	Keynote Session Zoom Meeting Room 1	
	Chairs: Amber Simpson and Heather Young	
	Making Change: Engineering the Future of Medicine	
	Molly Shoichet, University of Toronto	
15:15 – 16:00	Awards and Closing Remarks Zoom Meeting Room 1	

Oral Presentation Abstracts (in order of the talks)



Oral Presentation Abstracts

Session 1: Cellular and Molecular Imaging



Whole-body Detection of Metastasizing Cancer Cells in Preclinical Animal Models

Nivin N. Nyström^{1,2}, Timothy J. Scholl^{1,2,3}, John A. Ronald^{1,2,4}

1. Department of Medical Biophysics, University of Western Ontario; 2. Medical Imaging Laboratories, Robarts Research Institute; 3. Ontario Institute for Cancer Research; 4. Lawson Health Research Institute.

Introduction. Metastasis accounts for >90% of cancer-related mortalities.¹ However, a major analysis recently uncovered that over 75% of studies in oncology that employ preclinical animal models focus only on the primary tumour and do not extend whatsoever to the study of metastasis.² Specifically, Gengenbacher *et al* state that preclinical evaluation of metastasis is challenging. We need better tools to dynamically track metastases *in vivo* to improve our understanding of the metastatic process and advance our abilities to test therapies targeting metastatic disease. For this purpose, we developed an MRI reporter gene based on *Organic anion-transporting polypeptide 1b3* (*Oatp1b3*), a protein capable of taking up the paramagnetic contrast agent Gd-EOB-DTPA.³ The objective of this study was to assess the feasibility of this genetically-encoded reporter for whole-body tracking of cancer cells in preclinical animals using a spontaneous metastasis model of triple negative breast cancer.⁴

Methods. MDA-MB-231 cells were first engineered with integrating lentivirus to express *luciferase* for bioluminescent imaging (BLI). A subset of these was additionally engineered to express *Oatp1b3* for MRI. 3×10^5 *luciferase* control cells or *luciferase/Oatp1b3* cells were implanted into the left-bearing 4th mammary fat pad of female nod scid gamma mice (n=7). BLI and T_1 -weighted images at 3 Tesla, before and 5-hours post 1 mmol/kg Gd-EOB-DTPA, were acquired 30 days after implantation of the primary tumour. Regions of interest were manually segmented, and one-way analysis of variance was used to determine statistical significance.

Results. Macro-metastatic lesions (>1mm³) of mice burdened with *luciferase/Oatp1b3* primary tumours (n=7) exhibited significantly increased signal intensity on post-contrast images (4926±1159 a.u.) relative to pre-contrast images (617.5±140.8 a.u.), and to lesions of mice burdened with control *luciferase* primary tumours (n=3) pre- (840.1±122.2 a.u.) and post-contrast (1058±198.0 a.u.) (p<0.0001). Micro-metastases (<1mm³) within lungs of mice burdened with *luciferase/Oatp1b3* primary tumours were also observed on MRI, suggesting that small numbers of cells could be detected with *Oatp1b3*. Contrast enhancement 5-hours post-administration of 1-mmol/kg Gd-EOB-DTPA was additionally observed by the gallbladder, urinary bladder, and more diffusely, within the intestines and jugular veins of some animals. A new cohort of animals was imaged longitudinally for detection of early-stage metastasis. Metastasis at the ipsilateral axillary lymph node was detected (n=4) in mice approximately 10-days post-implantation of the primary tumours, with significantly increased signal intensity (2903±616.6 a.u.) relative to surrounding muscle tissue (1123±110.4 a.u.). Imaging again at 20-days post-implantation revealed growth of tumours at the initial axillary lymph node metastasis as well as subsequent lymph node metastases at other loci, including the contralateral axillary and ipsilateral brachial lymph nodes.

Conclusions. BLI provides whole-body information on locations of engineered cells, but smaller tumours can go undetected due to light scattering from larger lesions. *Oatp1b3*-MRI mitigates these limitations for tracking metastatic disease. We show that *Oatp1b3* can track the metastatic process at both early (single lymph node) and late stages once the cancer has spread to multiple lymph nodes and other organs *e.g.* lungs. Importantly, MR reporter gene development has largely focused on iron-based negative contrast, which already exists within animal models in critical regions such as the lungs. With its positive contrast mechanism however, *Oatp1b3* overcomes this problem and paves the path towards molecular imaging of reporter gene-expressing cells on MRI with combined high resolution, sensitivity and 3D spatial information with surrounding anatomical context.

References. [1] Lambert *et al.* *Cell* 2017; 168(4): 670-91. [2] Gengenbacher *et al.* *Nature Reviews Cancer* 2017; 17(12): 751-65. [3] Patrick *et al.* *PNAS* 2014; 111(1): 415-20. [4] Iorns *et al.* *PLoS One.* 2012; 7(10): e47995.

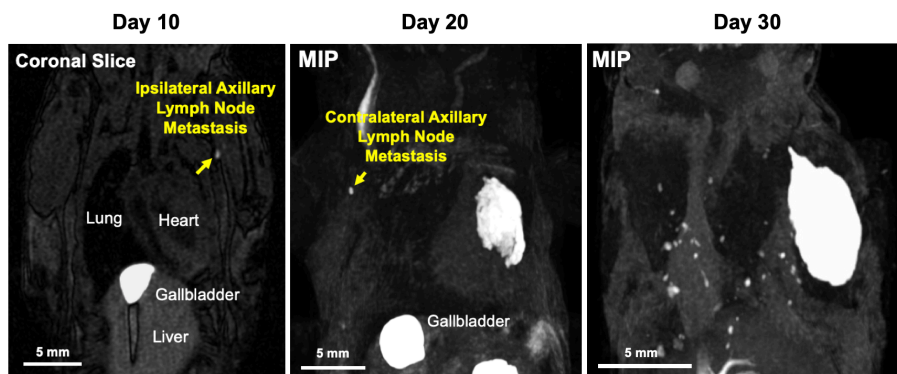


Figure. Representative T_1 -weighted images of metastasizing cancer cells in mice on: (A) Day 10, where an ipsilateral axillary lymph node metastasis was detected; (B) Day 20, where a subsequent contralateral axillary lymph node metastasis was detected; and (C) micro-metastases in the lungs were detected. MIP, maximal intensity projection. Scale bar, 5 mm.

Trimodal cell tracking *in vivo*: Combining iron- and fluorine-based MRI with MPI to monitor the delivery of mesenchymal stem cells and the ensuing inflammation

Olivia C. Sehl^{1,2}, Ashley V. Makela³, Amanda M. Hamilton¹, Paula J. Foster^{1,2}

¹ Imaging Research Laboratories, Robarts Research Institute, Canada

² Department of Medical Biophysics, University of Western Ontario, Canada

³ The Institute for Quantitative Health Science and Engineering, Michigan State University, USA

Introduction Mesenchymal stem cells (MSCs) have shown promising results as a cellular therapeutic¹⁻³. MSCs are capable of restoring and regenerating damaged tissues since they are multipotent cells. Additionally, MSCs can modulate inflammation and promote local vascularization and cell growth by secreting cytokines and tropic factors^{1,2}. Unfortunately, this therapeutic potential is limited by stem cell death, which begins soon after administration. Apoptotic stem cells release cytokines to attract macrophages to the implant site and can ultimately trigger stem cell rejection. Fundamental questions regarding the fate of MSCs after transplantation remain unanswered. Our goal is to implement a trimodal imaging technique to quantitatively monitor the fate of transplanted MSCs and the ensuing macrophage infiltrate *in vivo*. In this study we explored the ability to label, detect, and quantify two cell types (MSCs and macrophages) simultaneously using iron-based ¹H MRI, fluorine-19 (¹⁹F) MRI, and magnetic particle imaging (MPI) cell tracking. MPI is an emerging technology which directly detects the presence of iron oxides within labeled cells and has the potential to overcome limitations of both iron-based MRI cell tracking (specificity and quantification) and ¹⁹F MRI cell tracking (sensitivity)⁴.

Methods *Animal Model.* 1×10^6 MSCs were labeled with iron oxide nanoparticles (Fe, ferumoxytol) then implanted within the hind limb muscle of C57B1/6 mice (n = 10). Controls received unlabeled MSCs (n = 5). Subsequently, a perfluorocarbon agent was administered intravenously for uptake by phagocytic macrophages *in situ*. *Image Acquisition.* 24 hours later, both ¹H and ¹⁹F images were acquired on a 3 Tesla clinical MRI (MR750, GE) using a dual tuned surface coil and a balanced steady state free precession (bSSFP) sequence (day 1)⁵. MPI images were acquired on the MomentumTM scanner (Magnetic Insight) in 3D isotropic mode. Imaging was repeated on day 12 to investigate temporal changes in iron-associated signal voids, ¹⁹F signal, and MPI signal. *Histology.* Following the last imaging session, mice were sacrificed, and muscle tissue was sectioned and stained with H&E, Perl's Prussian blue (to label iron), and F4/80 (to identify macrophages).

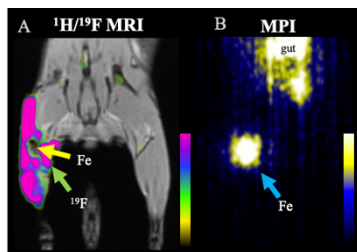


Fig 1. (A) ¹H/¹⁹F MRI overlay reveals iron-labeled MSCs (Fe) and surrounding ¹⁹F-labeled macrophages. (B) MPI images detect iron-labeled MSCs (Fe) and iron within the mouse gut.

Results Iron-labeled MSCs were detected by ¹H MRI and MPI on both day 1 and 12. Perfluorocarbon-labeled macrophages were detected by ¹⁹F MRI on day 1 and 12. Representative day 1 images are shown in **fig 1**. The measured volume of signal loss (in ¹H MRI) and MPI signal declined over 12 days (both $p < 0.01$), which is consistent with the death and clearance of iron-labeled MSCs. ¹⁹F signal persisted over 12 days, suggesting the continuous infiltration of perfluorocarbon-labeled macrophages. Since MPI and ¹⁹F MRI signal are directly quantitative, we estimated that there were 6.2×10^5 MSCs on day 1 and 2.0×10^5 on day 12 ($p < 0.01$), and 7.4×10^7 macrophages present at the site of MSC implantation on day 1 and 6.9×10^7 cells on day 12 (no significant difference). Macrophage infiltrate to the same region as iron-labeled MSCs was confirmed in histology.

Conclusions We have demonstrated that iron-based ¹H MRI, ¹⁹F MRI, and MPI can be used together to noninvasively monitor the fate of two cell populations (MSCs and macrophages) in live mice. This is the first time that these 3 modalities are combined to monitor cell populations *in vivo*. This is also the first study to demonstrate the ability to image macrophage infiltration using ¹⁹F on a clinical MRI. The bSSFP sequence and surface RF coil play a major role in our ability to detect and track ¹⁹F positive cells at 3T⁵. These cellular imaging techniques could be used to monitor MSC delivery and engraftment over time and quantify the infiltration of macrophages at transplant sites, to identify MSC rejection.

[1] Le Blanc K. & Ringdén O. *Biol Blood Marrow Transplant* **11**(5); 321-34 (2005). [2] Samsonraj R.M. *et al. Stem Cell Transl Med* **6**(12), 2173-85 (2017). [3] Gaudet J. *et al. Magn Reson Med.* **78**(2), 713-720 (2017). [4] Bulte J.W.M. & Daldrup-Link H.E. *Radiology* **289**:604-15 (2018). [5] Makela A.V. & Foster P.J. *Magn Reson Mater Physics Biol Med.* **32**, 123-132 (2019).

Evaluating survivin-driven tumour-activatable minicircles for prostate cancer theranostics

TianDuo Wang^{1,2}, Yuanxin Chen¹, John. A. Ronald^{1,2,3}

1. Robarts Research Institute – Imaging; 2. Department of Medical Biophysics, University of Western Ontario;
3. Lawson Health Research Institute, London, ON, Canada.

INTRODUCTION: Gene vectors co-expressing reporter genes and therapeutic genes are an emerging platform for developing concurrent cancer diagnostic and therapeutic technologies, also known as theranostics. Thus far, however, these strategies have been limited by specificity, delivery efficiency, and safety. To prevent effects in normal tissues, groups have used tumour-specific promoters such as the survivin promoter (pSurv) to specifically drive the expression of genes of interest in cancer cells. In prostate cancer (PCa), pSurv activity has been correlated to Gleason grade and cancer aggressiveness¹. Our group recently used pSurv to mediate the expression of blood reporters encoded on non-viral gene vectors called minicircles (MCs), plasmid derivatives stripped of prokaryotic components, creating clinically-friendly and relatively efficient gene transfer agents². We have called these new vectors tumour-activatable minicircles (TA-MC)³. In this work, we continued to develop this technology by building two novel TA-MCs. First, **diagnostic** TA-MCs expressing *Gaussia luciferase* (GLuc), a sensitive reporter protein detectable in urine⁴, allowing for non-invasive urinary detection of PCa presence and aggressiveness. Second, **therapeutic** TA-MCs encoding a fusion enzyme called cytosine deaminase uracil phosphoribosyl transferase (CD-UPRT) which activates the prodrug 5-fluorocytosine (5-FC) for cancer therapy⁵. Our objective in this study was to evaluate these diagnostic and therapeutic TA-MCs in a mouse model of PCa.

METHODS: We constructed parental plasmids (PPs) expressing pSurv-GLuc (Fig 1A) or pSurv-CD-UPRT (Fig 1C). TA-MCs were then made from PPs using a described production system⁶. Orthotopic tumours were established in nude mice by injecting one million PC3MLN4 or LNCaP PCa cells into the right dorsal prostate. These PCa cells were engineered to express firefly luciferase (Fluc), allowing for bioluminescence imaging (BLI) to track tumour growth. Once tumours reached $\sim 100\text{mm}^3$, mice received intratumoural injections with either diagnostic or therapeutic TA-MCs complexed with a polyethylenimine transfection agent. Urine samples were collected from mice receiving diagnostic TA-MCs, and GLuc activity was quantified using a commercial kit. For mice receiving therapeutic TA-MCs, PC3MLN4 tumour burden was assessed via BLI and compared to sham mice that received saline instead of TA-MCs. Daily intraperitoneal 5-FC injections were administered to all mice.

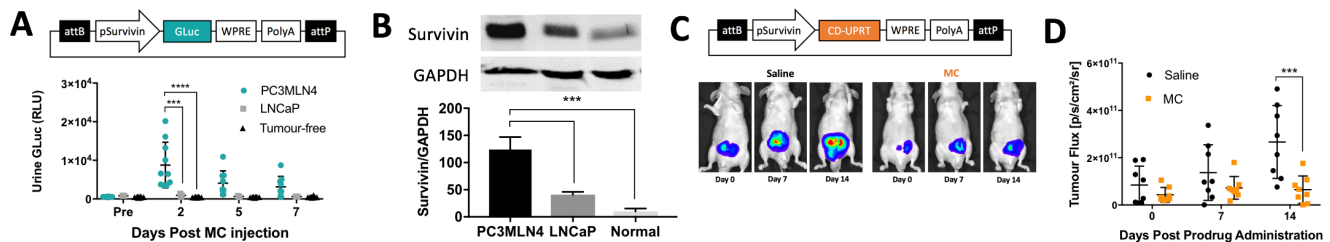


Figure 1. (A) Urine GLuc activity on day 2 post-TA-MC injection (n=10). (B) Western blot of cellular survivin levels (n=3). (C) Bioluminescence images and (D) signal from mice with PC3MLN4 tumours post-TA-MC injection and with 5-FC administration until endpoint at 14 days (n=8). Data are presented as mean \pm SD. ***, $p < 0.005$, ****, $p < 0.0001$.

RESULTS: Near-zero GLuc activity in urine was detected in all mice prior to diagnostic TA-MC injection (Fig 1A). Two days after TA-MC-injection, mice with aggressive PC3MLN4 tumours exhibited significantly higher GLuc than mice with non-aggressive LNCaP tumours and tumour-free mice ($p < 0.01$; Fig. 1A). GLuc activity correlated well with survivin expression (Fig. 1B). Compared to sham (saline), mice treated with therapeutic TA-MCs showed significantly attenuated tumour growth (lower BLI signal) at endpoint ($p < 0.01$; Fig. 1C and D).

CONCLUSIONS: Our work describes the first cancer-inducible TA-MC systems encoding urinary biomarkers and therapeutic genes. Diagnostic TA-MCs allowed for specific identification of mice with aggressive tumours using a simple urine exam for GLuc activity. Thus far, therapeutic TA-MCs have shown promise in attenuating growth of aggressive PCa tumours and future work will focus on evaluating the effects of MC dose on treatment efficacy. Used sequentially or together, these TA-MCs form the basis for a convenient and clinically-friendly theranostic system for improved early detection and treatment of aggressive PCa.

REFERENCES: [1] Shariat S. et al., *Cancer*, 2004, 100(4):751–757. [2] Chen Z. et al., *Mol Ther*, 2003, 8(3):495–500. [3] Ronald J. et al., *PNAS*, 2015, 112(10):3068–3073. [4] Tannous B. et al., *Mol Ther*, 2005, 11(5):435–443. [5] Koyama F. et al., *Nat Am*, 2000, 7(7):1015–1022. [6] Kay M. et al., *Nat Biotechnol*, 2010, 28(12):1287–1289.

Evaluation of two ^{11}C -labeled cyclooxygenase-1 (COX-1) and COX-2 radioligands for PET imaging of ovarian, breast, and pancreatic cancer xenograft mouse models.

Amanda J. Boyle¹, Junchao Tong¹, Victor W. Pike³, Robert B. Innis³, and Neil Vasdev^{1,2,*}.

¹Azrieli Centre for Neuro-Radiochemistry, Centre for Addiction and Mental Health, Toronto, Canada. Department of Psychiatry, University of Toronto, Canada. ³Molecular Imaging Branch, National Institute of Mental Health, Maryland, USA.

*neil.vasdev@utoronto.ca

Introduction: The role of putative inflammatory biomarkers cyclooxygenase-1 (COX-1) and COX-2 in cancer progression and prognosis is evident, yet mechanistic insight remains unclear. The COX-1 isoform is constitutively active throughout the body, while COX-2 is induced in response to inflammatory stimuli. The aim of this study is to evaluate two radioligands for positron emission tomography (PET) imaging, [^{11}C]PS13 and [^{11}C]MC1, which target COX-1 and COX-2, respectively, in xenograft mouse models of ovarian, breast, and pancreatic cancers.

Methods: Radiosyntheses of [^{11}C]PS13 and [^{11}C]MC1 were performed as previously described[1] and the tracers were evaluated in a panel of xenograft mouse models prepared from ovarian, breast, and pancreatic cancer cell lines, OVCAR3, MDA-MB-231, and PANC-1, inoculated subcutaneously (s.c.) on the right flank of ICRscid mice. Evaluation of [^{11}C]PS13 and [^{11}C]MC1 was performed by dynamic PET imaging and biodistribution studies.

Results: OVCAR3 xenografts were well visualized with [^{11}C]PS13 (**Fig. 1**; 0-60 min average image). Time-activity curves (TACs) revealed steady tumour radioactivity accumulation that plateaued from 40-60 min with an average uptake of 2.94 ± 1.30 %ID/g (40-60 min), and was significantly reduced by pre-treatment with the known COX-1 inhibitor, ketoprofen, to 1.64 ± 0.56 %ID/g ($p=0.032$), and was significantly higher than muscle tissue, 1.09 ± 0.16 %ID/g ($p=0.0006$). *In vivo* PET imaging analysis results were validated by biodistribution studies. TACs revealed steady tumour radioactivity accumulation with no washout over 60 min. MDA-MB-231 xenografts were not visualized by PET imaging with [^{11}C]PS13 or [^{11}C]MC1 despite reported overexpression of COX-1 and COX-2[2]. PANC-1 xenografts were not visualized by [^{11}C]MC1 despite reported high expression of COX-2[3].

Conclusions: The potent and specific COX-1 radioligand, [^{11}C]PS13 has a favourable radiobiological profile for studying the role of COX-1 in cancer *in vivo*. Further studies for the assessment of [^{11}C]PS13, though not [^{11}C]MC1, as a tool for diagnosis and prognosis of ovarian cancer and response to treatment are warranted.

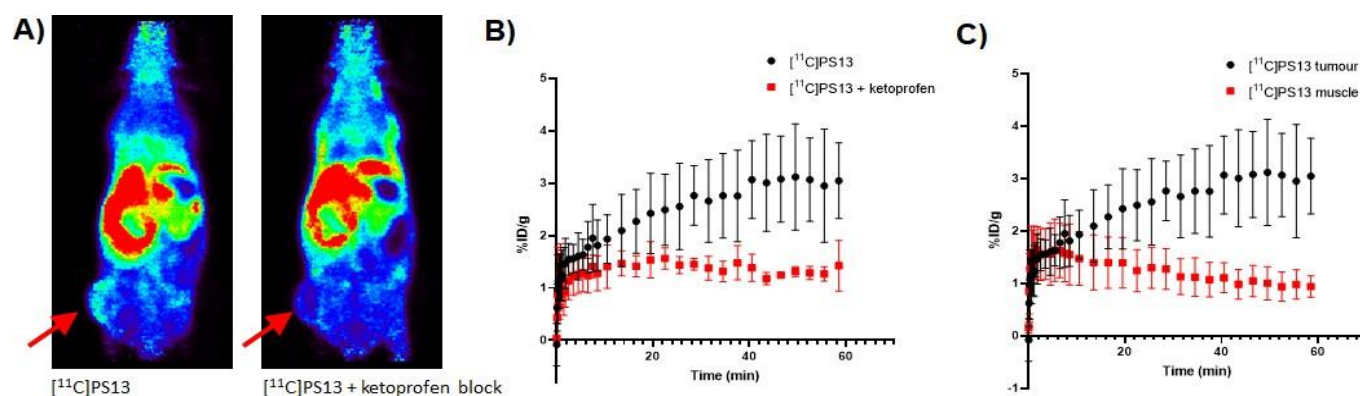


Fig. 1. PET imaging of [^{11}C]PS13 in OVCAR3 s.c. xenografts. **A)** PET imaging of [^{11}C]PS13 and [^{11}C]PS13 blocked with 67 mg/kg ketoprofen. Red arrows indicate OVCAR3 xenografts. **B)** TACs of [^{11}C]PS13 in OVCAR3 s.c. tumours with and without ketoprofen blockade. **C)** TACs of [^{11}C]PS13 in s.c. OVCAR3 tumours compared to muscle tissue.

References:

[1] Kim MJ, *et al.* Evaluation of two potent and selective PET radioligands to image COX-1 and COX-2 in rhesus monkeys. *J Nucl Med* 2018;59:1907-12. [2] Liu XH and Rose DP. Differential expression and regulation of cyclooxygenase-1 and -2 in two human breast cancer cell lines. *Cancer Res* 1996;56:5125-7. [3] Li S, *et al.* Anti-tumor effect and mechanism of cyclooxygenase-2 inhibitor through matrix metalloproteinase 14 pathway in PANC-1 cells. *Int J Clin Exp Pathol* 2015;8:1737-42.

Prostate specific membrane antigen positron emission tomography for the identification of intra-prostatic tumors: investigating targeting guidelines for focal therapy and guided biopsy

R. Alfano^{1,2,7}, G. Bauman^{2,6}, J. Thiessen^{2,7}, I. Rachinsky⁷, W. Pavlosky⁷, J. Butler⁷, M. Moussa⁴, J. A. Gomez⁴, M. Gaed^{3,4}, S. Pautler^{5,6}, J. L. Chin^{5,6}, A. D. Ward^{1,2,6,7}

1. Baines Imaging Research Laboratory, 2. Department of Medical Biophysics, 3. Robarts Research Institute, Department of 4. Pathology and Laboratory Medicine, 5. Surgery, 6. Oncology, 7. Lawson Health Research Institute

Introduction: Prostate specific membrane antigen positron emission tomography (PSMA PET) has shown good concordance with histology in involved sextants, but there is a need, addressed in this study, to investigate the ability of PSMA PET to delineate dominant intraprostatic lesion (DIL) boundaries for guided biopsy and focal therapy planning.

Methods: Using a prostatectomy cohort of 12 patients, we registered whole-mount mid-gland histology sections to in-vivo PSMA PET imaging. PET volumes were thresholded from 1–100% max standard uptake value (SUV_{max}) in 1% intervals. At each interval, we applied a margin of 0–30 voxels at one voxel increments, for a total of 3,000 segmentations for each patient. Example segmentations on the 2D oblique plane are demonstrated in Figure 1. We calculated sensitivity and specificity on the 2D oblique histologic planes that intersect with the 3D segmentation for each patient. We determined the percent threshold and margin combination that satisfied the following criteria: $\geq 95\%$ sensitivity with maximal specificity (supporting focal therapy) and $\geq 95\%$ specificity with maximal sensitivity (supporting guided biopsy).

Results: Figure 2 shows histologic cancer sensitivity (left) and specificity (right) as a function of SUV threshold and expansion margin. A threshold of 67% SUV_{max} with an 8.4 mm margin (white circle) achieved a (mean \pm std.) sensitivity of $95.0 \pm 7.8\%$ and specificity of $76.4 \pm 14.7\%$. A threshold of 81% SUV_{max} with a 5.1 mm margin (white diamond) achieved sensitivity of $65.1 \pm 28.4\%$ and specificity of $95.1 \pm 5.2\%$.

Conclusion: This study used accurate co-registration of PSMA PET/MRI and surgical histology to determine SUV thresholds and margin expansions having high sensitivity, supporting focal therapy, and high specificity, supporting guided biopsy. These parameters can be used in a larger validation study supporting clinical translation.

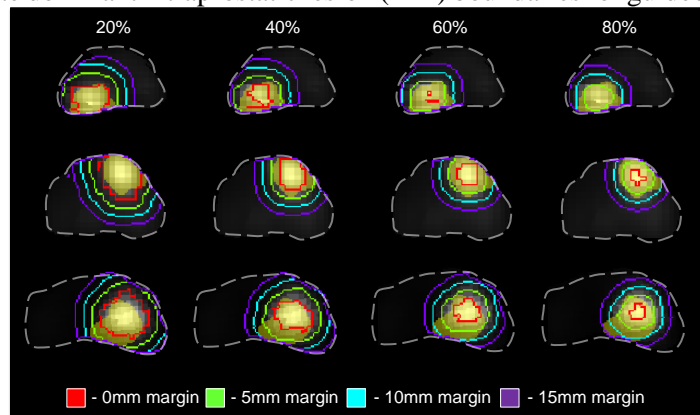


Figure 2: Example threshold and margin expansion segmentations. Each row corresponds to a 2D oblique histologic plane for three different patients. Each column represents a different threshold percentage of SUV_{max} within the prostate. Beneath the segmentation in yellow is the underlying histology of the DIL for that specific patient. Gray voxels in the background represent the underlying SUV corrected PET signal for the representative 2D oblique histologic plane.

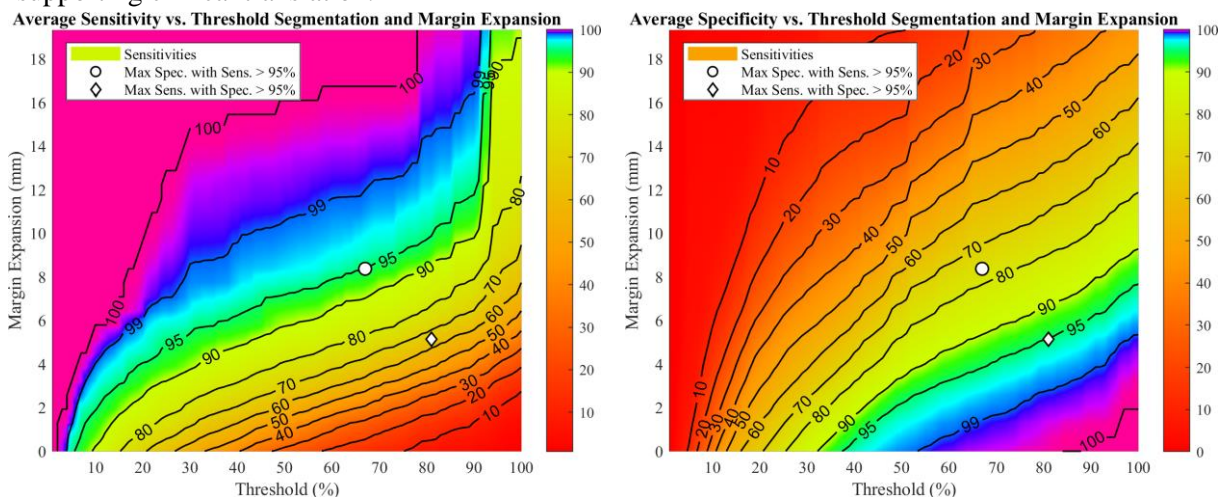


Figure 1: Contour plots of average sensitivity (left) and average specificity (right) for segmentations on SUV corrected PET calculated on each oblique slice of co-registered histology for each patient.

Developing Magnetic Resonance Reporter Gene imaging: Co-localization and Interaction of Magnetotactic Bacteria Genes *mamI* and *mamL*

Q. Sun^{1,2,3}, C. Fradin⁴, L. Yu⁵, R.T. Thompson^{1,2}, F.S. Prato^{1,2,3}, D.E. Goldhawk^{1,2,3}

¹Imaging Program, Lawson Health Research Institute, ²Medical Biophysics & ³Collaborative Graduate Program in Molecular Imaging, Western University, London, Canada; ⁴Physics & Astronomy, McMaster University, Hamilton, Canada; ⁵Biomedical Engineering, McMaster University, Hamilton, Canada

Introduction: With its superb spatial and temporal resolution, magnetic resonance imaging (MRI) has great potential to track cellular activities that define early stages of disease [1]. To improve molecular imaging techniques, we are developing MRI reporter gene expression based on the magnetosome. In magnetotactic bacteria (MTB), magnetosome formation allows cells to concentrate and compartmentalize iron biominerals in membrane-enclosed vesicles [2]. Biosynthesis of magnetosome-like nanoparticles provides an endogenous magnetic resonance (MR) contrast agent under genetic control (Fig. 1). This patent-protected technology [3,4] enables MRI reporter gene expression of cellular activity and provides long-term molecular imaging throughout the cell's life cycle.

Hypothesis: In mammalian cells, MamI and MamL co-localize on an intracellular membrane and interact to initiate formation of a rudimentary magnetosome-like nanoparticle.

Methods: MTB genes *mamI* and *mamL* were cloned from *M. magneticum* sp. AMB-1 genomic DNA by PCR and inserted into fluorescent vectors (pEGFP and ptdTomato, respectively) to create Mam fusion proteins. GFP-MamI and Tomato-MamL were stably expressed in human MDA-MB-435 melanoma cells, alone and in combination, using antibiotic selection and fluorescence-activated cell sorting (FACS). Protein expression was verified by immunoblot. Subcellular location and co-localization of fusion proteins were examined with confocal microscopy (Nikon A1R). Diffusion coefficient and apparent radius of fusion proteins were measured by fluorescence correlation spectroscopy (FCS, Evotec Insight Confocal Instrument) in cell-free samples. Analyses of Variance (ANOVA) and post hoc tests were performed in GraphPad Prism 8.

Results: Confocal microscopy of GFP-MamI and Tomato-MamL demonstrated fluorescence co-localization and protein-protein interactions [5]. FCS data (Table 1) indicated a significant decrease in diffusion coefficient when GFP-MamI is co-expressed with Tomato-MamL compared to expression of GFP or GFP-MamI alone. This was consistent with a significant increase in apparent radius of co-expressed GFP-MamI/Tomato-MamL particles compared to GFP or GFP-MamI alone. The same trend was obtained when examining red fluorescence.

Table 1. FCS parameters in MDA-MB-435 cell lysates.

	GFP	GFP-MamI	GFP-MamI/ Tomato-MamL	Tomato	Tomato-MamL	Tomato-MamL/ GFP-MamI
Diffusion coefficient ($\mu\text{m}^2/\text{s}$) [*]	108 ± 4% [†]	90 ± 3% [‡]	43.2 ± 50% ^{†,‡}	51.4 ± 60%	49.2 ± 3%	40.1 ± 9%
Apparent radius (nm) [*]	1.7 ± 4% [§]	2.1 ± 3% [¶]	4.4 ± 50% ^{§,¶}	3.7 ± 60%	3.8 ± 3%	4.7 ± 9%

^{*}Data are the mean +/- standard deviation, expressed as a percentage (n = 5). ^{†,‡}p < 0.001 ^{§,¶}p < 0.05

Conclusions: MTB fusion proteins of MamI and MamL co-localize in a mammalian cell expression system. Future work includes co-expressing iron-handling MTB proteins MamB and MamE with MamI and MamL to develop a rudimentary magnetosome-like particle which will be evaluated for co-localization, protein interactions, and for its effects on the MR signal and cellular iron content.

References: [1] Goldhawk *et al* (2017) Design and Applications of Nanoparticles in Biomedical Imaging, pp 187-203 [2] Uebe & Schuler (2016) Nat Rev Microbiol 14:621 [3] Goldhawk *et al* (2019) European Patent #3110952 [4] Prato *et al* (2017) USPTO Patent #US 9,556,238 B2; MMI [5] Sun *et al* (2019) Imaging Network of Ontario

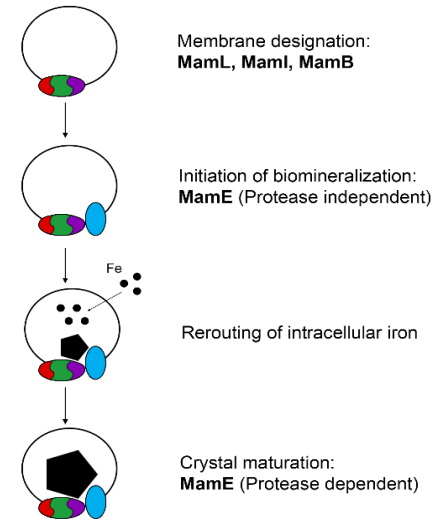
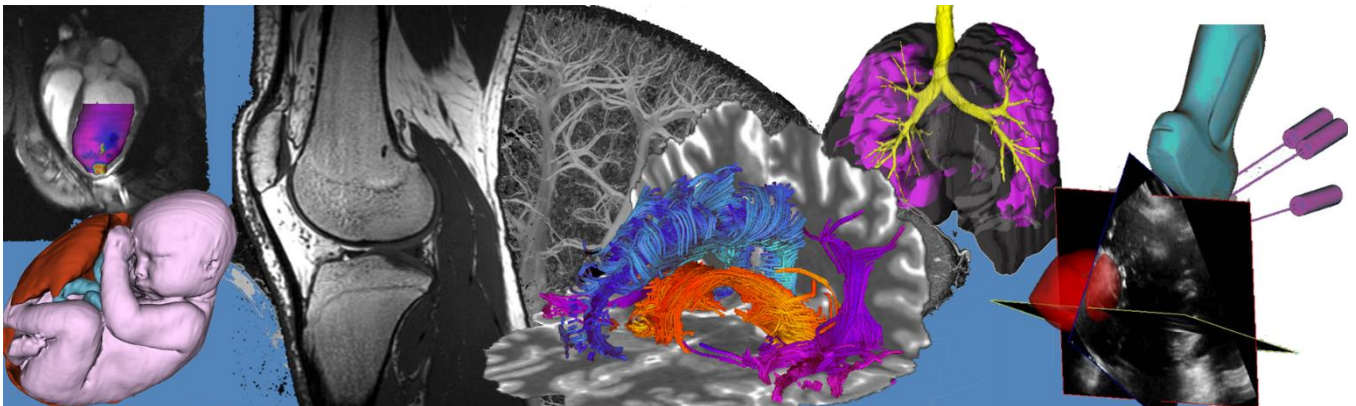


Fig. 1. Modelling roles of essential magnetosome proteins in step-wise formation of the magnetosome. MamL (red), MamI (green), and MamB (purple) assemble at the membrane and designate site for magnetosome formation. MamE (blue) initiates iron biomineralization; intracellular iron is rerouted to the magnetosome compartment; and the iron biomineral grows.

Oral Presentation Abstracts

Session 2: Lung Imaging



COMPARISON OF AUTOMATED TO MANUAL HISTOLOGY QUANTITATION OF REGIONAL LUNG TISSUE AND BLOOD FRACTIONS IN A RAT MODEL OF RILI

J. D. Fliss^{1,2}, B. Zanette¹, E. Stirrat¹, S. Sadanand^{1,3}, A. Lindenmaier^{1,2}, D. Li¹, G. Santyr^{1,2}

¹Translational Medicine Program, Hospital for Sick Children, Toronto, Ontario, Canada

²Department of Medical Biophysics, University of Toronto, Toronto, Ontario, Canada

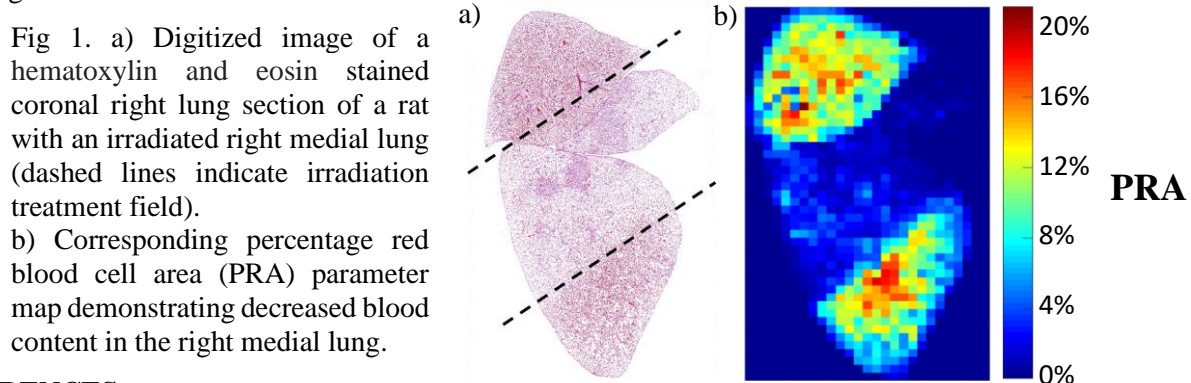
³Department of Biomedical Physics, Ryerson University, Toronto, Ontario, Canada

INTRODUCTION: Early detection of lung diseases, such as radiation induced lung injury (RILI) and bronchopulmonary dysplasia (BPD), is crucial for effective treatment and preventing severe and permanent damage. Non-invasive imaging methods that assess the structure and function of the lungs, such as Hyperpolarized (HP) ^{129}Xe magnetic resonance imaging (MRI), can potentially provide new biomarkers based on detecting the exchange of ^{129}Xe gas with the tissue and red blood cell (RBC) compartments in the lung. For example, changes in regional air-capillary barrier thickness (δ) and hematocrit (HCT) from ^{129}Xe MRI in a rat model of RILI has been shown to correlate with regional changes in lung septal wall thickness and RBC content respectively¹. However, standard histology validation methods are manual, and therefore laborious, time consuming, prone to observer bias, and limited by inadequate sampling. The purpose of the project was to modify a custom automated histological analysis program, known as quantitative-automated whole slide morphometry (AWSM-Q)², and compare to a traditional manual histological approach in a rat model of RILI.

METHODS: Previous whole-slide histological data (fig.1a) from a RILI rat model involving irradiation of the right medial lung³ (n=6) and controls (n=6) were tiled into smaller images for processing using Panoramic Viewer (3DHISTECH) and selected by automated tile sampling to generate a training set for k-means clustering based image segmentation. The whole slides were then segmented and used to calculate percentage tissue area (PTA) and percentage RBC area (PRA) on a tile-wise basis, using the number of tissue and RBC pixels per tile. Histological parameter maps were then generated (fig.1b). Average PTA and PRA values from a selected region of interest (ROI) approximately encompassing the medial lung were then compared to a traditional manual method³. The effect of several different AWSM-Q segmentation and sampling approaches was also investigated.

RESULTS: The histological parameter maps demonstrated regional changes consistent with the RILI model pathology and allowed for qualitative comparison. Average ROI PTA and PRA measurements using all AWSM-Q approaches agreed with values from the manual method (i.e. $r > 0.93$) and preserved the strong Pearson correlation of PRA with hematocrit from ^{129}Xe MRI of both left and right lungs (i.e. $r = 0.74$ and $r = 0.89$ respectively).

CONCLUSIONS: The excellent agreement between AWSM-Q and manual measurements of PTA and PRA supports the use of AWSM-Q as a tool for future analysis of regional blood/tissue distribution in rat models of lung injury, including RILI. AWSM-Q removes observer bias and labour and potentially allows for rapid, regional and robust comparison with MRI. AWSM-Q also generates maps of other parameters, such as mean linear intercept and percentage air area, and may allow regional assessment and quantitation of subtly presented pathologies like BPD.



REFERENCES:

1. Zanette et al, *Advances in Radiation Oncology* (2017) 2(3), 475-484
2. Lindenmaier et al, (ATS 2019)
3. Zanette et al, *Medical Physics* (2018), 45(2), 803–816

Computed Tomography Airway Tree Tortuosity Features Predict Functional Small Airway Disease in Chronic Obstructive Pulmonary Disease

Daniel Genkin,¹ Xavier Bauza,² Danesh Aslam,¹ Jason Bartlett,² Harvey Coxson PhD,³ Wan C. Tan MD,³ James C. Hogg MD, PhD,³ Sri Krishnan PhD¹ and Miranda Kirby PhD²

¹Department of Electrical, Computer, and Biomedical Engineering, Faculty of Engineering and Architectural Science, Ryerson University; ²Department of Physics, Faculty of Science, Ryerson University; ³Center for Heart, Lung Innovation, University of British Columbia.

Introduction: Chronic Obstructive Pulmonary Disease (COPD) will be the third leading cause of death worldwide by 2020. Despite high mortality rates of COPD, diagnosis occurs late in the disease course after a large portion of the small airways have already been destroyed. Current methods to quantify small airway disease (SAD) use the Disease Probability Measure (DPM) approach that registers computed tomography (CT) images acquired at full-inspiration and full-expiration. However, acquiring two CT images increases radiation dose to patients, and may pose technical challenges. In contrast, a 3D airway tree segmentation can be generated using a single full-inspiration CT image and provide quantitative airway measurements. One such measurement that has not been extensively studied is airway tree tortuosity. The objective of this study was to determine if CT airway tortuosity measures can be developed and are independently associated with DPM SAD.

Methods: The CanCOLD Cohort study was used to analyze the extracted morphometric measurements from participants between 45-90 years of age identified by random digit dialing from the general population. All participants performed CT imaging and spirometry. Participants were classified as never-smokers, current or former smokers with normal spirometry (at risk), GOLD I and GOLD II+ COPD according to GOLD criteria. CT full-inspiration and full-expiration images were registered using deformable image registration, and all voxels were classified as normal, emphysema or SAD. Established morphometric measurements such as Pi10 (hypothetical wall thickness of an airway with 10mm internal perimeter), TAC (number of observable airway segments), WT (airway wall thickness), LA (lumen area), and WA% (wall area/total bronchial area) were generated. An algorithm to measure airway tree tortuosity was developed and termed Deviation Tortuosity (DT). DT was subcategorized into maximum (DTm) and average (DTa) and defined as the max or average distance between an airway segment to the absolute straight path between the segment's branch points. The DT's for five airway segments (RB1, RB4, RB10, LB1, LB10) were generated, normalized to the arc length of the segment, and averaged to obtain a whole lung measure. A multivariable linear regression model was generated using "The REG Procedure" (least square estimates) through SAS 9.4 to determine the association between CT airway tree tortuosity (DTm and DTa) measures with DPM SAD, adjusting for conventional CT airway measures (Pi10, TAC, WT, WA%, LA).

Results: A total of 551 participants were included in the study: n=29 never-smokers, n=166 at risk, n=181 GOLD I and n=175 GOLD II+. The GOLD I participants were slightly but significantly older and had lower BMI than GOLD II+ participants and had significantly more male participants than never-smokers ($p<0.05$); there were no other significant differences between the groups. A multivariable linear regression model for DPM SAD showed a significant association with DTm ($r^2=0.08$; $\beta=0.10$; $p=0.02$), after adjusting for established CT morphometry measurements. In a multivariable linear regression model for DPM SAD with DTa, there were also significant associations found for DTa ($r^2=0.08$; $\beta=0.09$; $p=0.047$).

Conclusions: We demonstrated that CT airway tree tortuosity measurements are significantly and independently associated with small airway disease measurements in COPD. This data supports the notion that morphometric measurements generated from 3D airway tree segmentation can provide relevant information associated with small airway disease. Future work will be to investigate the association between CT airway tree tortuosity and DPM SAD regionally in the lobe and along sub-lobar paths. Machine learning will be used to predict DPM SAD using various CT airway tree feature morphometry features, including CT airway tree tortuosity.

Relationships between Computed Tomography Texture Features and Visual Scoring of Emphysema in Chronic Obstructive Pulmonary Disease

V. Lui,¹ R. Au,³ M. Koo,³ W.C. Tan MD,² J.C. Hogg MD, PhD,² H.O. Coxson PhD² and M. Kirby PhD³
 1. Department of Computer Science, Ryerson University; 2. Centre for Heart Lung Innovation, University of British Columbia; 3. Department of Physics, Ryerson University.

Introduction: Emphysema severity in chronic obstructive pulmonary disease (COPD) patients can be assessed using computed tomography (CT) qualitatively by radiologist scoring and quantitatively using histogram-based density thresholding. While CT density thresholding quantifies the percentage of lung voxels with emphysema, studies suggest that qualitative CT might capture other information relevant to disease, such as clustering of emphysema and spatial distribution.¹⁻³ Therefore, novel quantitative imaging measures that quantify “texture”, such as gray level co-occurrence matrix (GLCM) and fractal dimensions (FD), might provide further information in characterizing emphysema. We hypothesized that CT texture features can be developed for evaluating COPD and may provide information complementary to qualitative visual assessment. The objective of this study was to determine if CT texture features are independently associated with objective measures of emphysema severity, independent of qualitative scoring and standard CT emphysema measurements.

Method: Participants from the Canadian Cohort Obstructive Lung Disease (CanCOLD) study were evaluated.⁴ Participants included never-smoker, current or former smokers with normal lung function (at risk), GOLD I (mild) COPD and GOLD II+ (moderate/severe) COPD, according to GOLD criteria. Diffusion capacity of the lung for carbon monoxide (DL_{CO}) is sensitive to emphysema destruction and was therefore used as an objective measure of emphysema severity. CT images were visually scored by a trained radiologist as a binary variable, with emphysema presence as none (0)/visible (1). Standard quantitative CT measures included the low attenuation areas of the lung below -950HU (LAA₉₅₀). GLCM were generated and 23 texture features were extracted. A total of 10 FD first order statistics were also derived via the *boxcount* method using 16x16x16 window increments with *Blockproc3D*. Features selection was performed via *generalized orthogonal matching pursuit algorithm* (gOMP). Multivariable regression models of the extracted features were used to determine the association between visual scoring, standard CT emphysema measurements (LAA₉₅₀) and CT texture with DL_{CO}, adjusting for potential confounding variables (age, sex, BMI, pack-years, and smoking status).

Results: A total of 1187 participants were evaluated: n=258 never-smokers, n=255 at-risk, n=411 GOLD I COPD and n=263 GOLD II+ COPD. As shown in Table 1, multivariable linear regression models for DL_{CO} that included CT texture features explained a greater proportion of the variance ($r^2=0.62$) than visual score ($r^2=0.47$) or LAA₉₅₀ ($r^2=0.47$) alone. In a linear multivariable regression model for DL_{CO} that included all measures, CT texture, LAA₉₅₀ and visual score as predictors, CT texture features ($p<0.0001$) and visual score ($p=0.01$) were significant and independent predictors, but not LAA₉₅₀.

Table 1. Linear regression model for DL_{CO}

Model: DL _{CO}	Adjusted R ²	95% CI
Covariates: Age, sex, BMI, pack-years, smoking status	0.47	(0.42, 0.50)
+ visual score	0.47	(0.43, 0.51)
+ LAA ₉₅₀	0.47	(0.43, 0.51)
+ CT texture measurements	0.62	(0.58, 0.66)
+ visual score, LAA ₉₅₀	0.48	(0.44, 0.52)
+ visual score, LAA ₉₅₀ , CT texture measurements	0.62	(0.58, 0.66)

Conclusion: These findings demonstrate that CT visual emphysema score and CT texture features provide independent and complementary information related to pulmonary function in COPD when both are in the same regression model, but texture features outperforms visual score when used alone or when combined with QCT. CT texture analysis is therefore a promising new method for characterizing emphysema. Further investigation is warranted to determine the association between CT texture features with emphysema subtypes, and its use in longitudinal studies of emphysema progression.

References:

1. Kirby, M. et al. (2017). Am J Respir Crit Care Med., 195(1).
2. Kim, S. S, et al. (2013). Radiology, 266(2).
3. Gietema, H.A. et al. (2011). Acad Radiol. 18(6):661-71.
4. Bourbeau, J. et al. (2014). COPD, 11:2, 125-132.

Comparison of PREFUL and Hyperpolarized Xenon gas MRI Ventilation Distributions in Pediatric Cystic Fibrosis Lung Disease

Samal Munidasa¹, Marcus Couch¹, Jonathan Rayment³, Felix Ratjen⁴, Giles Santyr¹

¹Translational Medicine Program, The Hospital for Sick Children, Toronto, ON, Canada.

²Division of Respiratory Medicine, British Columbia Children's Hospital, Vancouver, BC, Canada

³Division of Respiratory Medicine, The Hospital for Sick Children, Toronto, ON, Canada

Introduction. Cystic Fibrosis (CF) is a chronic disease that causes a buildup of sticky mucus within the major airways, leading to bacterial infection and inflammation. Repeated infections known as pulmonary exacerbations (PEX) lead to irreversible airway damage (i.e. bronchiectasis) and progressive decline in pulmonary function [1]. Current pulmonary function tests (PFTs) are not sensitive enough to detect CF lung disease at an early stage and do not distinguish regional ventilation heterogeneities. Hyperpolarized (HP) ¹²⁹Xe MRI (Xe-MRI) has been shown to be more sensitive to early CF lung disease compared to PFTs and captures ventilation improvements in CF patients receiving intravenous antibiotic treatment for PEX [2]. However, HP gas MRI requires the inhalation and breath-hold of a gas contrast agent which can be challenging to administer in young and/or very sick subjects. Thus, free-breathing proton MRI techniques, such as phase resolved functional lung (PREFUL) MRI, may be more attractive for mapping of pulmonary function in children with CF [3]. PREFUL functional ventilation (FV) maps have been used for the assessment of PEX in pediatric CF patients using K-means clustering analysis [4]. However, anchored linear binning (LB) analysis [5], which can reveal higher-order ventilation distribution differences has yet to be applied to PREFUL.

Methods. The work was carried out using an REB-approved protocol at the Hospital for Sick Children (clinicaltrials.gov: NCT02740868). 7 healthy, 4 stable CF, and 10 physician-diagnosed PEX CF subjects (8-18 years old) were recruited. The PEX subjects were imaged before and two weeks after intravenous antibiotic treatment. PREFUL data was not available for both visits in 2 of the 10 PEX subjects for technical reasons. PREFUL and Xe-MRI was conducted on a 3T MRI scanner as previously described [4] and images were processed using MATLAB. K-means ventilation defect percentage (VDP_{Kmeans}) and ventilation defect region (VDR) as well as low, normal, and high ventilation regions (LVR, NVR, and HVR) were determined from Xe-MRI and PREFUL MRI ventilation signal histograms using the LB approach proposed by He et al [5]. Significant differences were determined using a one-way ANOVA with Tukey-Kramer post-hoc test.

Results. All PREFUL and Xe-MRI parameters (except HVR) could differentiate healthy from PEX subjects (pre-treatment). Xe-MRI, but not PREFUL

MRI, could differentiate healthy from stable CF subjects. A statistically significant drop can be seen in PREFUL VDP_{Kmeans} and VDR ($p=0.028$; $p=0.033$, respectively) after antibiotic treatment of PEX subjects.

Discussion and Conclusion. The LB method applied to PREFUL and Xe-MRI ventilation distributions was able to highlight differences in low to high ventilation regions. PREFUL LVR, was the only parameter that could differentiate stable CF and PEX (pre- & post-treatment), and this may be useful in future for prognosticating an exacerbation in a stable CF child. Compared to a previous study [6], Xe-MRI was less sensitive to the effect of antibiotic treatment on PEX subjects, likely since only a subset of the PEX CF subjects underwent both PREFUL and Xe-MRI, resulting in a decrease in statistical power. Since PREFUL MRI is expected to capture both ventilation and lung mechanics while Xe-MRI is expected to capture only the former, this comparison will provide physiological insight into the mechanisms that lead to ventilation defects in CF. PREFUL may be useful as an easier and inexpensive alternative or addition to Xe-MRI for measuring ventilation distributions in pediatric CF lung disease.

References. 1. Cutting GR. *Nat Rev Genet.* (2015) 16(1): 45-56 2.G. Santyr, et al. *Acad. Radiol.* (2018) 1-12 3. Voskrebenezv A et al. *Magn Reson Med.* (2018) 79(4):2306-2314 4. Couch M.J. et al. *ISMRM.* (2019) Montreal, 11-16 May (0006) 5. M. He et al. *Acad. Radiol.* (2016) 23: 1521-1531 6. Rayment J. et al. *Eur Respir J.* (2019) 53: 1802188

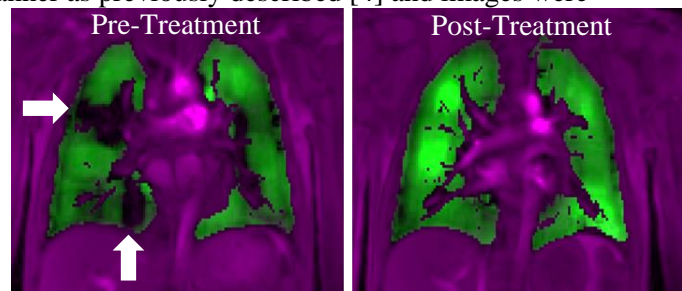


Figure 1. FV map (green) & proton image (purple) of a representative PEX CF subject pre- & post-antibiotic treatment. White arrows indicate areas of low FV.

Identifying Functional Information Determinants in Thoracic Computed Tomography Images Using Machine Learning

Maksym Sharma,^{1,2} Andrew Westcott,^{1,2} Jonathan L MacNeil,^{1,3} David G McCormack⁴ and Grace Parraga¹⁻⁴

¹Robarts Research Institute, ²Department of Medical Biophysics, ³School of Biomedical Engineering,

⁴Department of Medicine, Western University, London, Canada

INTRODUCTION: Hyperpolarized gas magnetic resonance imaging (MRI) provides a way to measure global and regional pulmonary ventilation and perfusion but this approach is not widely available. In contrast, x-ray computed tomography (CT) is the most commonly used medical imaging modality for lung disease,¹ although it is complex to extract functional information from chest CT. MRI apparent diffusion coefficient (ADC) measurements are sensitive to early or mild disease, such that participants with abnormal MRI ADC often present without CT evidence of lung disease.² To better understand these discrepant MRI and CT results, we aimed to develop novel texture analysis tools with machine-learning to facilitate the identification of functional information determinants in CT images. We hypothesized that machine-learning and CT texture analysis used in tandem would identify hidden CT features that explain differences between ex-smokers with normal and abnormal MRI ADC.

METHODS: Ex-smokers with no spirometry evidence of COPD provided informed consent to approved protocol (NCT02279329) and underwent spirometry, ³He MRI and thoracic CT as previously described.³ Participants were dichotomized based on a DL_{CO} threshold of $\geq 75\%$ _{pred} into normal and abnormal subgroups.² CT parameters used for training the algorithm were extracted from novel cluster volume matrices, which are 3-dimensional extensions of gray-level run-length, gap-length, zone-size and co-occurrence matrices,⁴ based on density levels and 3-dimensionally connected volumes. Wald forward selection logistic regression was used to select CT features significantly contributing to the accuracy of the models and selected features were then compared with well established MRI ADC measurements. Selected models included support vector machines, decision trees, logistic regression and nearest neighbour classifiers. Performance of models was evaluated using area-under-the-curve (AUC), sensitivity and specificity values.

RESULTS: As shown in Figure 1, 65 ex-smokers were evaluated (Normal: $n=41$, Abnormal: $n=24$) with no significant difference in pulmonary function, RA₉₅₀ or HU₁₅ between groups. Long run emphasis (LRE) and run percentage (RP) strongly contributed to the accuracy of all models and significantly correlated with MRI ADC measurements having $r = 0.48$, $p < 0.001$ and $r = -0.46$, $p < 0.001$ respectively. Quadratic-SVM model achieved the highest classification accuracy of 79.8%.

CONCLUSIONS: We identified novel CT texture features that explained ex-smokers with normal or abnormal DL_{CO}. Such features also explain abnormal MRI-ADC in patients with normal CT and bridge the gap between modalities, generating functional information from CT. High LRE and low RP represent more homogeneous CT textures indicating potential subclinical abnormalities. Ex-smokers with normal spirometry may be misclassified due to insufficient CT information, but machine learning can identify CT abnormalities related to MRI findings.

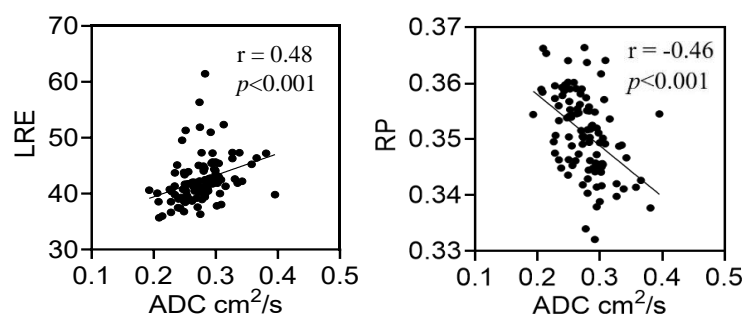
REFERENCES:

- 1) Dammann, F *et al. Dtsch Arztebl Int* (2014).
- 2) Kirby, M *et al. Thorax* (2013).
- 3) Parraga, G *et al. Invest Radiol* (2007).
- 4) Depeursinge, A *et al. Acad Press* (2017).

Figure 1: Demographics, pulmonary-function, best model and feature comparison results in ex-smoker subgroups.

Ex-smokers : ($n=65$)	DL _{CO} $\geq 75\%$ _{pred} ($n=41$)	DL _{CO} $< 75\%$ _{pred} ($n=24$)	P-value	
Age	67 (9)	71 (9)	0.18	
Sex Female (%)	12 (29)	14 (58)	0.02	
FEV ₁ % _{pred}	103 (16)	94 (18)	0.05	
DL _{CO}	91 (12)	56 (13)	<0.001	
6MWD	438 (66)	363 (94)	0.001	
RA ₉₅₀ %	1.2 (1.1)	1.1 (1.0)	0.7	
ADC cm ² /s	0.26 (0.03)	0.30 (0.04)	<0.001	
Feature 1 - LRE	42 (3)	48 (6)	0.001	
Feature 2 - RP	0.345 (0.009)	0.333 (0.012)	0.02	
Classifier	AUC	Sensitivity	Specificity	Accuracy
Quadratic SVM	0.77	85.7 %	76.5 %	79.8 %

FEV₁ = Forced Expiratory Volume in 1 second; 6MWD = Six-minute walk distance; DL_{CO} = Diffusing Capacity of Lungs for Carbon Monoxide; RA₉₅₀ = Relative Area < -950HU; **LRE** = Long run emphasis and **RP** = Run percentage.



Supervised shallow learning of ^{129}Xe MRI texture features to predict response to Anti-IL-5 biologic therapy in severe asthma

Marrissa J McIntosh,^{1,2} Rachel L Eddy,^{1,2} Danielle Knipping,¹ Tamas Lindenmaier,¹ David G McCormack³, Christopher Liciskai³, Cory Yamashita,³ and Grace Parraga¹⁻³

¹Robarts Research Institute, ²Department of Medical Biophysics, ³Division of Respiriology, Department of Medicine, Western University, London, Canada

INTRODUCTION: Hyperpolarized ^{129}Xe magnetic resonance imaging (MRI) provides a way to spatially locate and quantify inhaled gas abnormalities through the measurement of ventilation defect percent (VDP) which is directly related to airway wall inflammation¹ and sputum eosinophilia in patients with severe asthma.² Currently-used segmentation tools binarize ventilated versus non-ventilated lung tissue and assuming all ventilated regions contribute equally to global lung function. Signal intensity differences can be quantified using gray-level run length matrices (GLRLM)³. Texture features, such as short run emphasis (SRE) and low gray-level run emphasis (LGRE) can be extracted from GLRLM to describe ventilation heterogeneity. We hypothesized that VDP and texture features would significantly distinguish responders from non-responders with severe eosinophilic asthma prior to treatment with benralizumab, a biologic therapy that has been shown to reduce exacerbations, steroid use and improve quality of life (QOL) in patients with severe asthma.⁴ Therefore, the objective of this work was to extract texture features from ^{129}Xe MRI prior to therapy and use a shallow learning approach to identify features that predict response to benralizumab therapy using asthma control improvements as the gold standard.

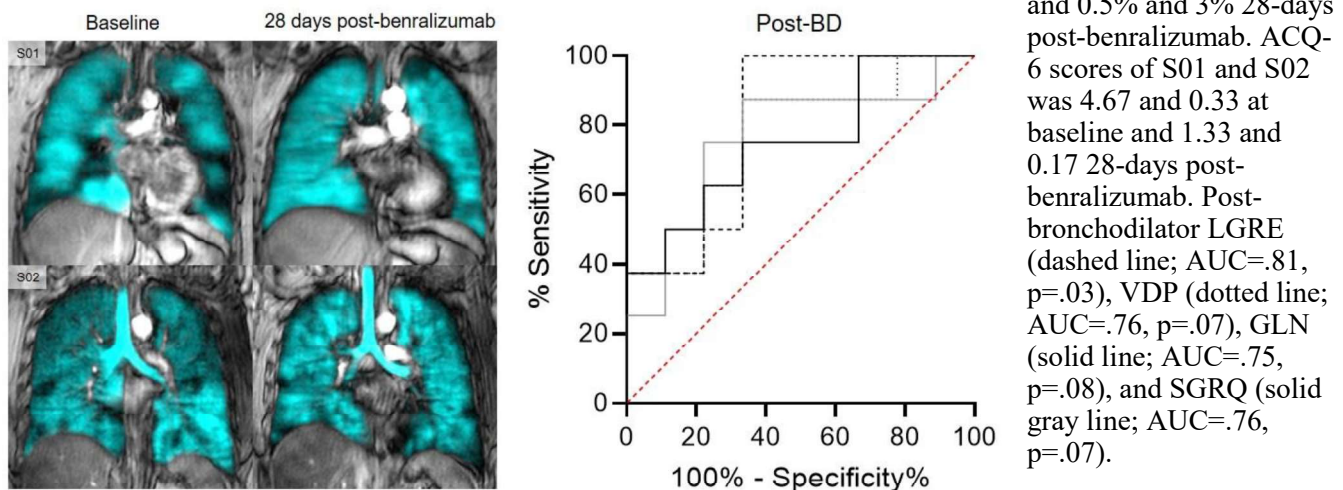
METHODS: Participants with severe eosinophilic asthma (n=17) provided written informed consent and performed ^{129}Xe MRI and pulmonary function tests at baseline and 28-days post-benralizumab. Anatomical ^1H and hyperpolarized ^{129}Xe images were segmented to measure VDP⁵ and the GLRLM^{3,6} was calculated pre- and post-salbutamol before benralizumab was administered. 11 second-order texture features, including SRE and LGRE⁶ were extracted from the GLRLM. Participants who reported an ACQ-6 improvement \geq minimal clinically-important-difference 28-days post-benralizumab were stratified as benralizumab responders.⁷ Receiver operator characteristic (ROC) curves were generated pre-and post-bronchodilator for pulmonary function tests, VDP, GLRLM texture features, and the St. George's Respiratory Questionnaire (SGRQ) using GraphPad Prism 8.0.2.

RESULTS: As shown in Figure 1, post-bronchodilator baseline MRI LGRE (AUC=.81, p=.03) was significantly predictive, whereas post-bronchodilator baseline VDP (AUC=.76, p=.07), gray level non-uniformity (AUC=.75, p=.08), and SGRQ (AUC=.76, p=.07) trended towards significance. Oscillometry, pulmonary function tests and lung clearance index values, were not significant predictors of benralizumab response.

CONCLUSION: Post-bronchodilator baseline MRI features and VDP are potential predictors of improved asthma control in response to biologic therapy in severe asthma. This is important and clinically relevant because of the high cost of biologic therapy and the inability to predict patients who will respond prior to therapy initiation.

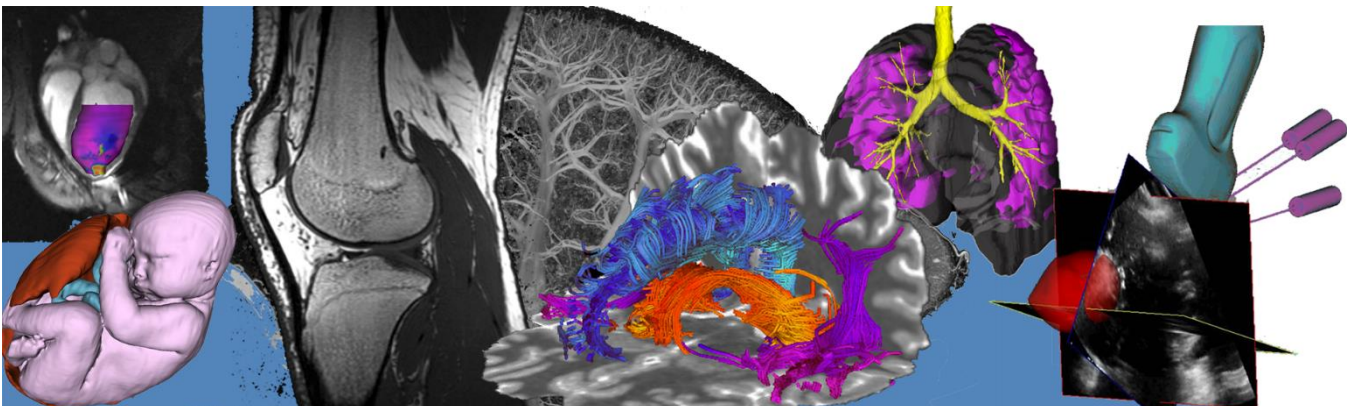
REFERENCES: 1. Svenningsen, S. et al. *Thorax* (2014). 2. Svenningsen, S. et al. *AJRCCM* (2018). 3. Haralick, R.M. et al. *Ieee Transactions on Systems Man and Cybernetics* (1973). 4. Skolnik, N.S. & Carnahan, S.P. *CurrMedResOp* (2019). 5. Kirby, M. et al. *AcadRadiol* (2012). 6. Zha, N. et al. *AcadRadiol* (2016). 7. FitzGerald, J.M. et al. *Lancet* (2016).

Figure 1: Qualitative results of responders (S01) vs. non-responders (S02) pre- and 28-days post-benralizumab and ROC curves for response predictors. At baseline, VDP of S01 and S02 was 11% and 3% and 0.5% and 3% 28-days post-benralizumab. ACQ-6 scores of S01 and S02 was 4.67 and 0.33 at baseline and 1.33 and 0.17 28-days post-benralizumab. Post-bronchodilator LGRE (dashed line; AUC=.81, p=.03), VDP (dotted line; AUC=.76, p=.07), GLN (solid line; AUC=.75, p=.08), and SGRQ (solid gray line; AUC=.76, p=.07).



Oral Presentation Abstracts

Session 3: Machine Learning in Cancer Imaging



A Deep Learning-based Method for Generalized Prostate Segmentation in 3D Ultrasound

Nathan Orlando^{1,2} and Derek J Gillies^{1,2}, Igor Gyacskov², Cesare Romagnoli³, David D'Souza^{4,5}, Aaron Fenster^{1,4}

¹Department of Medical Biophysics, ²Robarts Research Institute, ³Department of Medical Imaging, ⁴Department of Oncology, Western University; ⁵London Health Sciences Centre; London, Ontario, Canada

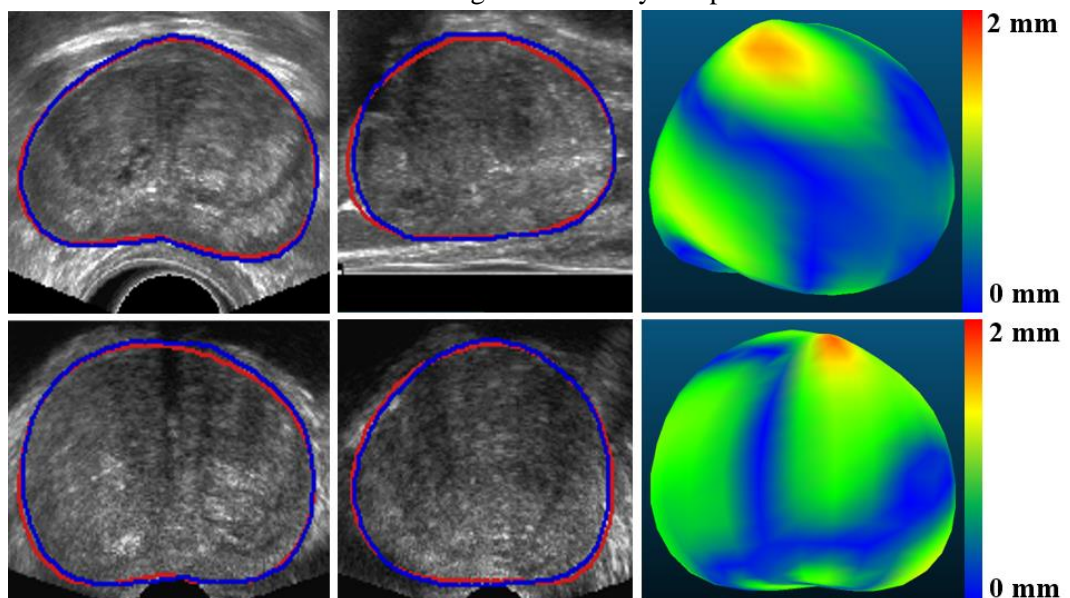
Introduction: Three-dimensional (3D) transrectal ultrasound (TRUS) imaging has been shown to benefit needle-based procedures for diagnosing and treating prostate cancer (i.e., biopsy and brachytherapy); however, these images require the physician to manually segment the prostate, which is time-consuming and difficult, often occurring while the patient is under sedation or anesthesia. Deep learning-based automatic prostate segmentation algorithms for 3D TRUS images have been previously discussed,^{1,2} but are limited by their use of cross-validation study designs and 3D TRUS images acquired from a single ultrasound system with the same acquisition geometry. To address this limitation and provide a more robust and generalizable segmentation method, we propose a new deep learning-based approach which was trained and evaluated using a clinically diverse dataset.

Methods: Our training dataset consisted of 206 3D TRUS patient images acquired from two different procedures (biopsy and brachytherapy), two acquisition geometries (end-fire and side-fire), and four transducers used with 3 different ultrasound systems. The 3D images were resliced at random planes resulting in a dataset of 6,773 2D TRUS images used to train a U-net, which was modified by adding 50% dropouts at every block in the expansion section of the network to increase regularization and prevent overfitting. Our proposed 3D segmentation method involved deep-learning predictions on 2D radial slices, followed by reconstruction into a 3D surface. Our method was evaluated using 20 end-fire and 20 side-fire 3D TRUS images unseen by the network. An extended selection of error metrics was computed, including Dice similarity coefficient (DSC), recall, precision, volume percent differences (VPD), mean surface distance (MSD), and Hausdorff distance (HD), to assess segmentation accuracy.

Results: On the overall test dataset of 40 3D TRUS images, our proposed method performed with a median [quartile 1, quartile 3] absolute DSC, recall, precision, VPD, MSD, and HD of 94.1 [92.6, 94.9] %, 96.0 [93.1, 98.5] %, 93.2 [88.8, 95.4] %, 5.78 [2.49, 11.50] %, 0.89 [0.73, 1.09] mm, and 2.89 [2.37, 4.35] mm, respectively. Compared to previously published deep learning-based algorithms,^{1,2} our proposed method improved performance on nearly all metrics. Full 3D segmentation time was <0.7 s per 3D TRUS image, which is sufficiently short for intraoperative implementation, and an improvement compared to previously published methods.

Conclusions: We present a deep learning-based automatic prostate segmentation algorithm for 3D TRUS images. In contrast with previously published work, our algorithm was trained and tested on a clinically diverse dataset of 3D TRUS images from different procedures, acquisition geometries, and ultrasound systems, with varied voxel dimensions and image quality, resulting in a more robust and generalizable method. This method has the potential to improve clinical workflow and decrease procedure time for needle-based prostate cancer procedures. Future work includes a prospective multi-center clinical trial to assess generalizability and practical clinical translation.

Fig 1: Side-fire (top row) and end-fire (bottom row) 3D TRUS prostate segmentation results comparing manual (red) and our proposed algorithm (blue). The left and middle columns show segmentations in the sagittal and axial plane, respectively, while the right column shows the reconstructed 3D surface and colour map displaying distance between the algorithmic and manual surfaces.



References: [1] Ghavami et al. J Med Imaging 6(1), 2018. [2] Lei et al. Med Phys 46(7), 2019.

Tissue component segmentation and cancer detection on digitized prostatectomy slides using convolutional neural networks

L.Huang^{1,2,6}, W.Han^{1,2,6}, J.A.Gomez³, M.Moussa³, S.E.Pautler⁴, J.L.Chin⁴, G.S.Bauman^{2,5,6}, and A.D.Ward^{1,2,5,6}

¹Baines Imaging Laboratory, London Regional Cancer Program, ²Depts. of Medical Biophysics, ³Pathology and Laboratory Medicine, ⁴Surgery, ⁵Oncology, Western University, ⁶Lawson Health Research Institute, London, Ontario

Introduction:

Prostate cancer (PCa) is the third most frequently-diagnosed cancer globally. It is assessed via tissue examination by a pathologist, but this is labour-intensive. Deep learning approaches may alleviate the pathologist's burden by automating cancer detection. However, the potential future role of deep learning in the clinical process is not well understood. In this work, we applied deep learning to the problems of (1) segmenting tissue components from histology slides, and (2) determining the locations of cancer on the slides based on the tissue components.

Methods:

From 68 patients enrolled in our Image Guidance for Prostate Cancer (IGPC) trial, we obtained 286 whole slide images of whole-mount, mid-gland radical prostatectomy tissue sections, stained with haematoxylin and eosin. We scanned the slides at $0.5 \mu\text{m}$ / pixel and downsampled to $2 \mu\text{m}$ / pixel. We then digitally cut them into 240 by 240 pixel regions of interest (ROIs), resulting in ~ 1.2 million ROIs. We also obtained 114 digitally restitched psuedo-whole mount slide scans across 18 patients from The Cancer Imaging Archive (TCIA) [5].

We previously developed a tissue component mapping (TCM) approach that labels pixels as nucleus, lumen, or other [2]. It uses adaptive thresholding tailored for nucleus segmentation, and an empirically determined global threshold for lumen segmentation. A CNN could avoid the need for such handcrafted algorithms and could be more easily extended to segment additional tissue components, potentially yielding improved cancer detection and grading. In this preliminary work, we used the TCMs generated by our previous method to train a CNN, yielding a larger number of training TCMs than could be manually produced.

We trained a U-Net [6] to produce TCMs from histological images and validated against a subset of ROIs for which TCMs were generated manually by thresholding the blue and green channels to segment the nuclei and luminal regions, respectively. We then used transfer learning to train AlexNet [4], VGG16 [7] and Xception [1] for cancer vs. non-cancer predictions based on the TCMs and pathologists' annotations as the truth labels. We trained the models for 10 epochs, a balanced database of cancer and non-cancer samples, binary cross entropy as the loss function and Adam as the optimizer [3]. We used leave-one-patient-out cross validation as an exhaustive method of determining training-validation split separation.

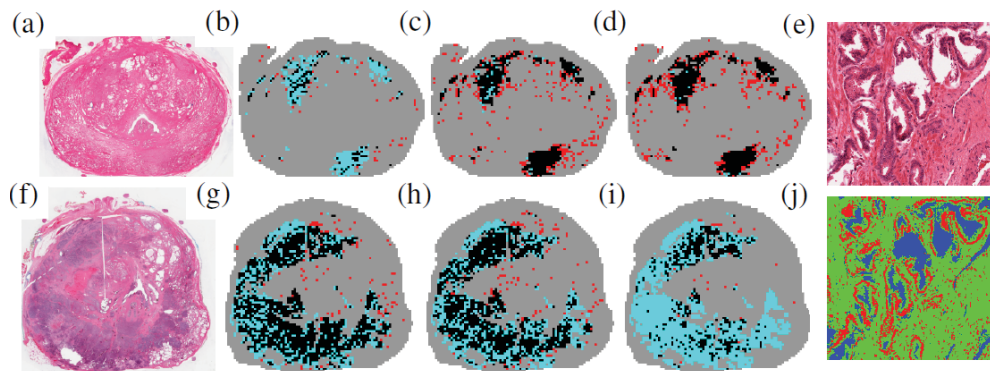
Results:

The U-Net segmentations performed similarly on both data sets. The areas under the receiver operating characteristic curves (AUCs) for the nuclei maps were 0.98 ± 0.06 and 0.99 ± 0.03 for the IGPC and TCIA data sets, respectively. The AUCs for the lumen maps were 0.99 ± 0.02 and 0.99 ± 0.02 for the IGPC and TCIA data sets, respectively. The cancer detection AUCs for the IGPC data set were 0.98 ± 0.02 for AlexNet, 0.98 ± 0.02 for VGG16 and 0.99 ± 0.02 for Xception. Error metrics were calculated on a per ROI basis for each patient. Sample cancer detection maps are shown in Fig. 1.

Conclusions:

The U-Net was able to segment lumen and nuclei on multi-center histology data with similar mean AUCs. AlexNet, VGG16, and Xception yielded similar AUCs, but individual slide results indicate that further investigation is needed to understand their differences in performance, in order to optimize a model to support cancer detection in the digital pathology workflow.

Figure 1: (a,f) whole mount histology slides; (b-d), (g-i) corresponding cancer maps (black: true positive, grey: true negative, blue: false negative, red: false positive). (b,g) generated by AlexNet; (c,h) VGG16; (d,i) Xception. (e,j) ROI and corresponding TCM, (red: nucleus, blue: lumen, green: other).



References:

[1] F. Chollet. *CVPR*, 2017. [2] W. Han and et al. *SPIE Medical Imaging*, 25:1097–1105, 2018. [3] D. P. Kingma and et al. *ICLR*, 2015. [4] A. Krizhevsky and et al. *NIPS*, 25:1097–1105, 2012. [5] A. Madabhushi and M. Feldman. *TCIA*, 2016. [6] O. Ronneberger and et al. *MICCAI*, pages 234–241, 2015. [7] K. Simonyan and A. Zisserman. *ICLR*, 2015.

Prediction of tumour mutational burden of squamous cell carcinoma using histopathology images of surgical specimens

Salma Dammak¹, Matthew Cecchini⁴, Katherina Baranova⁵, David Palma¹⁻³, Keith Kwan⁴, Aaron D. Ward¹⁻³
 Western University: ¹School of Biomedical Engineering, ²Department of Medical Biophysics, ³Department of Oncology, ⁴Department of Pathology and Laboratory Medicine, ⁵Schulich School of Medicine & Dentistry

Introduction: Immunotherapy is a novel anti-cancer treatment that shows significant improvements in outcomes for lung cancer patients. However, this treatment has the potential for substantial side effects in a minority of patients, and many lung cancer patients do not benefit from it. Programmed-death ligand-1 expression in tumour cells is currently the main biomarker used to identify those who might benefit but it is not very accurate. Tumour mutational burden (TMB) is a promising alternative, with lung cancers having more than 10 mutations/megabase being more likely to respond to immunotherapy. However, the cost, \$1,000, and time, about a month, it takes to obtain TMB results makes it difficult to implement in the clinic, so a way to estimate it quickly and cheaply would be highly useful.

Several studies in digital histopathology have shown that some genetic information can be successfully estimated from standard-of-care hematoxylin and eosin (H&E)-stained slides containing the cancer tissue obtained during resections or biopsies.¹ H&E slides are routinely obtained in the clinic and using scanned slides as the only input to a system predicting TMB would be highly translatable to clinical practice. Based on this, we hypothesize that TMB can be predicted in lung squamous cell carcinoma from histopathology slides of tissue from the surgical resection of the tumours.

Methods: To test this hypothesis, we obtained digitized histopathology slides of resected lung squamous cell tumours from 20 patients through the National Cancer Institute's Genomic Data Commons (TCGA). The slides were all formalin-fixed, paraffin-embedded and stained using H&E. All were processed at Christiana Healthcare (Newark, Delaware, United States). Since this is a preliminary study involving a novel and challenging research objective, we limited our analysis to a single institution to minimize noise from variability in tissue processing and imaging. We also obtained the ground truth label of whether TMB is more than 10 mutations/megabase from the TCGA. To predict this label, we performed transfer learning using AlexNet² in MATLAB R2019a (The MathWorks Inc., Natick, MA, USA).

AlexNet is a neural network that has been shown to perform well in transfer learning scenarios. We maintained the same structure and mainly retrained the last six layers but allowed for some training in the previous layers as well. We split patients with a 3:1 split for training and validation and optimized for cross-entropy using the stochastic optimization algorithm Adam, used ReLU as the activation function. The only pre-processing we performed was splitting each slide into images that are 1108 pixels \times 1108 pixels in size, which we resized down to 227 \times 227 pixels using the bilinear transform to make them conform to the input size of AlexNet. We measured the area under the receiver operator characteristic curve (AUC), error rate, false negative rate (FNR) and false positive rate (FPR) for the network for both the training and validation sets.

Table 1: Error metrics

Error metric	Training	Validation
AUC	0.90	0.80
Error Rate	18%	24%
FNR	15%	26%
FRR	20%	22%

Results: The error metrics for both training and validation are in Table 1. Transfer learning from AlexNet was successful, as evidenced by the training AUC being well above chance, and all other metrics being well below 50%. The validation set results were similar, giving us confidence in the generalizability of model developed in training. Training took less than an hour and testing took less than a minute per patient on a graphics processing unit (NVIDIA GTX1080).

Conclusions: This preliminary study (n = 20) shows that predicting TMB from digitized standard-of-care hematoxylin and eosin-stained histopathology slides of squamous cell carcinoma tumour resection tissue is possible using transfer learning with Alexnet. These findings are promising for pursuing further work in this direction. However, more data are needed to achieve better performance and data from more centres should be included to obtain a more robust system. With future work developing such a system and external validation, the system can act as an alternative to traditional genetic sequencing for patients with lung squamous cell carcinoma which will make it easier and quicker for physicians to determine whether patients should be given immunotherapy. This will more effectively give access to immunotherapy drugs to those who need them and help spare those who do not need them the toxicities associated with immunotherapy.

[1] N. Coudray, P. S. Ocampo, T. Sakellaropoulos *et al.*, Nature medicine, 1 (2018).

[2] A. Krizhevsky, I. Sutskever, and G. E. Hinton, 1097-1105.

Visualization of Clinically Significant Prostate Cancer Using Multi-stream U-Nets

Alireza Sedghi¹, Alireza Mehrtash², Amoon Jamzad¹, Amel Amalou³, Jin Tae Kwak⁴, Baris Turkbey³, Peter Choyke³, Peter Pinto³, Bradford Wood³, Sheng Xu³, Purang Abolmaesumi², and Parvin Mousavi¹

¹Queen’s University, Kingston, ON, CA, ²The University of British Columbia, Vancouver, BC, CA, ³The National Institutes of Health Research Center, Baltimore, MD, USA, ⁴Sejong University, Seoul, KR

Introduction: Prostate Cancer (PCa) is the most frequent non-cutaneous cancer diagnosed in men. The current standard of care for PCa diagnosis is the histopathology analysis of the biopsied specimen under transrectal ultrasound guidance. Recently, multi-parametric MRI (MP-MRI) and Ultrasound fusion biopsy techniques have been more widely used in clinical centres, promising better targeting of cancer lesions. Although fusion of the coordinate spaces of MP-MRI and Ultrasound has shown to improve PCa diagnosis [1], the quantitative integration of information represented by each modality has not been investigated widely. Temporal Enhance Ultrasound (TeUS) is a new paradigm based on analysing the Ultrasound time series data. In this paper, we demonstrate a feasibility study of information fusion from MP-MRI and TeUS for better prediction of PCa.

Methods: Our cohort include 145 biopsy cores from 107 patients who underwent prostate MP-MRI Ultrasound fusion biopsy at National Institutes of Health. We use ADC sequences from the MP-MRI data acquired by a $3T$ MR scanner (Achieva-TX, Philips), for analysis and model training.

Prior to firing of the biopsy gun, 100 frames of Ultrasound were acquired by an endocavity curvilinear probe with central frequency of 6.6 MHz. MP-MRI data is pre-processed by cropping the centre of the images and normalizing intensities to $[0, 1]$ range, followed by resizing to 256×256 . For TeUS, we compute the Discrete Fourier Transform of the TeUS signals. Previous studies have shown that the frequency content of TeUS is associated with tissue-specific information. U-Nets have shown promising results in segmentation literature; however, they need per-pixel labeling which is not available for biopsy data. To accommodate this, we consider a region of interest in shape of a circle with radius of 3 mm centered at biopsy location and assign biopsy-proven label to it. We study two main information fusion techniques: (1) *Late-fusion*: We use two separate U-nets for MP-MRI and TeUS images and we get the average of each prediction to predict the label. (2) *Intermediate-fusion*: A multi-stream U-net is utilized which includes separate encoder and decoders with shared weights in the bottleneck.

Results: Area Under the Curve (AUC) of 0.69 is achieved for MP-MRI, and 0.66 for TeUS training on each modality alone. Our *late-fusion* method results in an improved AUC of 0.70 and our *intermediate-fusion* approach yields a significantly higher AUC of 0.79.

Conclusion: The fusion of information between MP-MRI and TeUS results in a better classifier than each alone. Specifically, *intermediate fusion* with shared representations yield best results.

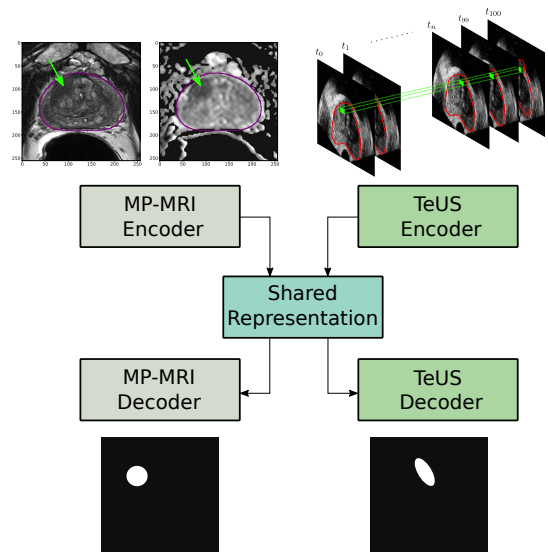


Figure 1: Multi-stream U-net for information fusion of MP-MRI and Ultrasound

References

- [1] Ahmed, Hashim U., et al. "Diagnostic accuracy of multi-parametric MRI and TRUS biopsy in prostate cancer (PROMIS): a paired validating confirmatory study." *The Lancet* 389.10071 (2017): 815-822.

Computer Aided Detection and Evaluation of Renal Masses in Computed Tomography Images Using Deep Learning Methods

Zabihollahy Fatemeh¹, Schieda Nicola², Krishna Satheesh³, Ukwatta Eranga⁴

¹Department of Systems and Computer Engineering, Carleton University, Ottawa, ON, Canada

²Department of Radiology, University of Ottawa, Ottawa, ON, Canada

³Department of Medical Imaging, University of Toronto, Toronto, ON, Canada

⁴School of Engineering, University of Guelph, Guelph, ON, Canada

Objective: Accurate localization of renal masses is a fundamental step for the potential classification of benign versus malignant renal masses. In this study, we describe a novel, fully automated methodology for accurate detection and segmentation of renal masses from contrast-enhanced computed tomography (CECT) images. Additionally, we present a deep learning-based algorithm to diagnose benign renal cyst versus solid renal masses.

Materials and Methods: We first segmented the boundaries of the kidneys on the CECT images using a convolutional neural network (CNN)-based method. We then developed a homogenous U-Net-based ensemble learning model to identify and delineate renal masses within automatically pre-segmented kidney boundaries. Moreover, we used a decision fusion of the CNN-based model to differentiate renal cell carcinoma (RCC) from benign renal masses that have been identified on CECT images by radiologists. Our dataset comprised CECT scans in 315 patients with benign and malignant kidney tumors including renal cell carcinoma (clear cell, papillary, chromophobe), oncocytomas, and fat poor renal angiomyolipoma (fpAML). Images were annotated and labelled by a fellowship-trained genitourinary radiologist with 13 years of experience in renal CT working in conjunction with a research assistant experienced in the analysis and segmentation of CT images.

Results: The algorithm for kidney boundary segmentation reported a Dice similarity coefficient (DSC) of $94.3\% \pm 3.8\%$ (mean \pm SD) using 290 test images consisting of 41363 slices. Using our method, renal masses were detected in 280 test cases, which corresponds to 96.6% sensitivity at the patient level. Our proposed ensemble method for renal mass localization yielded sensitivity, specificity, and DSC of 89.62%, 79.5%, and $85.6\% \pm 8.4\%$ on the test dataset, respectively. As shown in Figure 1, our method not only detected the renal masses with a high degree of accuracy but also accurately segmented its boundary compared to manual segmentation.

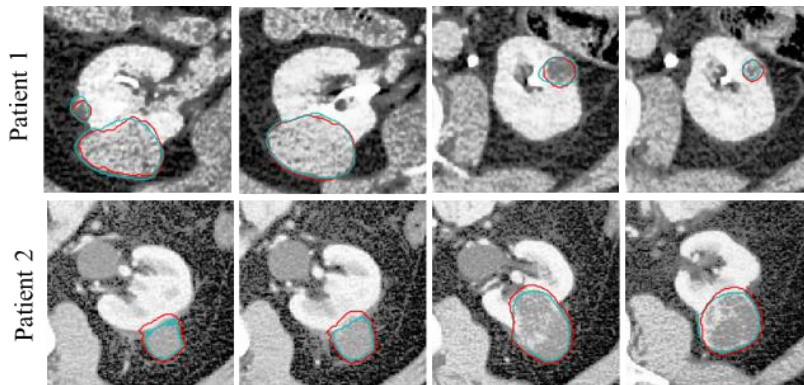


Figure 1. Example results from localized renal masses on CECT images in two patients. In columns 1 to 4, 2D slices enclosing renal masses compiled over kidneys are shown. In all images, the renal masses contours computed from algorithm-generated and manual segmentations are shown in red and cyan, respectively.

For differentiation of RCC versus benign solid masses, the semi-automated majority voting-based CNN algorithm reported accuracy, precision, and recall of 83.8%, 89.1%, and 91.7% using 160 test cases, respectively. Fully automated pipeline yielded accuracy, precision, and recall of 76.9%, 85.3%, and 87.2% on the same test cases, respectively.

Conclusion: We describe a deep-learning-based method for fully automated renal mass detection and segmentation using CECT images. The results demonstrate the usefulness of our technique for this application, which is clinically important as renal mass localization is a pre-step for fully automated diagnosis of benign versus malignant disease. The results for distinguishing RCC from benign renal masses indicate that a semi-automated majority voting CNN-based methodology enabled accurate classification of RCC from benign neoplasms among solid renal masses on CECT.

Masking Risk Predictor for Screening Mammography using a Convolutional Neural Network

Theo Cleland, James G Mainprize, Olivier Alonzo-Proulx, Jennifer A Harvey, Martin J Yaffe
Sunnybrook Research Institute Toronto, ON, Canada
University of Virginia Health System, Charlottesville, VA, USA

Introduction: Masking in mammography is caused by surrounding and overlying dense tissue hiding lesions resulting in reduced screening sensitivity in the dense breast. We use a VGG16 convolutional neural network (CNN) and demonstrate a) its ability to predict masking risk in a case-case study of non screen-detected (masked) and screen-detected cancers and b) assess its efficiency in a simulated stratified screening program where women at high risk of masking could potentially be directed to supplemental screening.

Methods: This case-case study was conducted on a population of 224 cancer cases (461 mammograms) categorized as either a screen-detected (SD) cancer, cancer detected at a scheduled screening examination, or non screen-detected (NSD) cancer, detected via other means up to 2 years after a negative screen. A subset of NSD cancers ('interval cancers') found up to 1 year after a negative screen was also identified. We compare the effectiveness of 3 masking risk predictors: CNN, volumetric breast density (VBD) and BI-RADS density in discriminating between NSD and SD cancers. The CNN was a pre-trained VGG16/ImageNet model, fine-tuned to distinguish between mammograms associated with NSD and SD cases in a seven cross-fold validated approach. Folding was performed at the patient level. The receiver operating characteristic area under the curve (ROC-AUC) was used to assess each predictor. Next, we tested the efficiency of each model by simulating a supplemental screening program to select masked mammograms (associated with NSD subjects) against the normal population assuming 100,000 disease-free women and 60 interval cases. We assess the concordance statistic (c-statistic) of each model and the screening cost (SC), which is defined as the number of women needed to undergo supplemental screening to find one additional interval cancer.

Results: The ROC-AUCs (95% CI in brackets) for BI-RADS, VBD and CNN in distinguishing NSD from SD cancers are: 0.64 [0.56-0.70], 0.70 [0.63-0.78] and 0.75 [0.66-0.82]. Differences in AUC were statistically significant only between CNN and BI-RADS. On the 1 year subset, CNN's ROC-AUC increased to 0.82 [0.74-0.90]. CNN and VBD were each statistically different than BI-RADS only. In the simulated screening program, the models respectively had a c-statistic of 0.63 [0.56-0.69], 0.66 [0.57-0.74] and 0.75 [0.66-0.82]. At an operating point that captures 63% of masked cancers, BI-RADS stratification would require 42,645 extra screens or SC=1117. At the same operating point, VBD would require SC=1051 and the CNN would have SC=641.

Conclusion: The CNN has been shown to outperform BI-RADS and VBD in identifying high masking risk subjects. It may be an effective stratifier for use in a supplemental screening program.

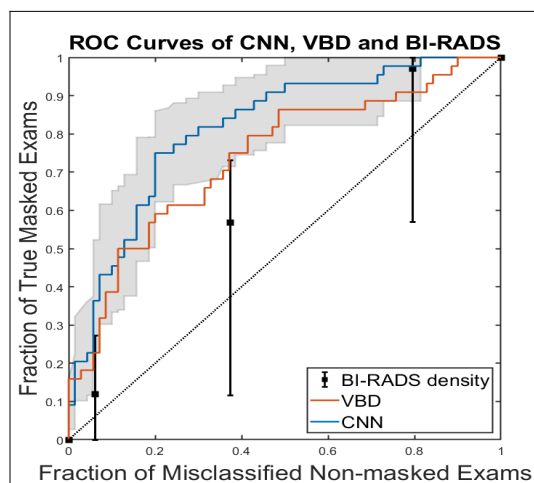


Figure 1: ROC curve for distinguishing between SD and NSD cases. Shaded region and error bars give 95% CIs for CNN.

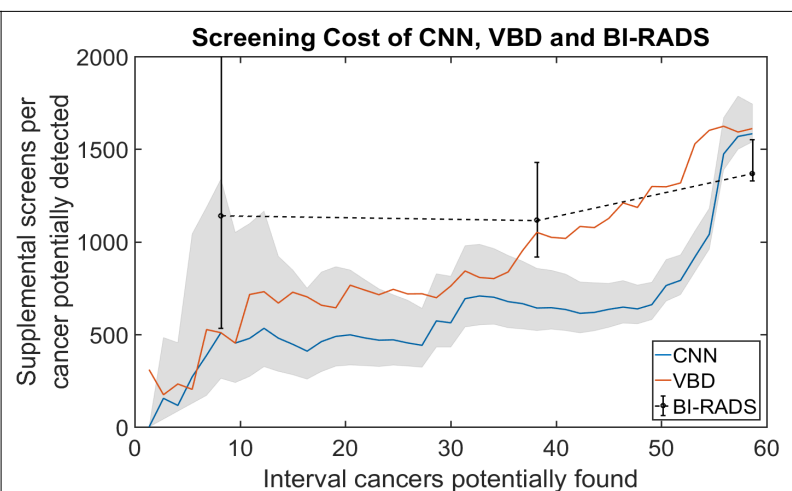
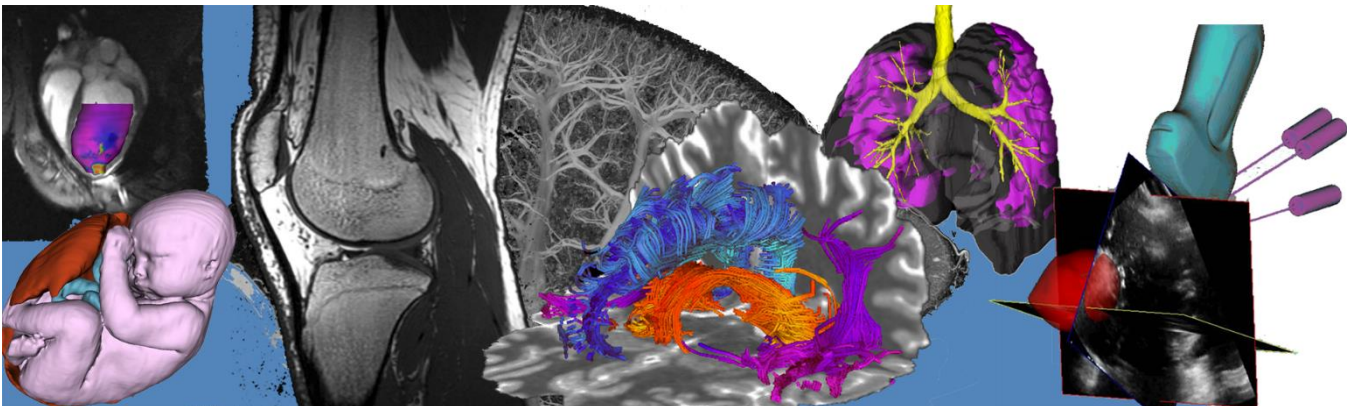


Figure 2: Screening cost of CNN, VBD and BI-RADS. 95% confidence interval for CNN denoted by shaded region and BI-RADS denoted with bars.

Oral Presentation Abstracts

Session 4: Image-Guided Interventions 1



Evaluation of a mixed-reality first person point of view needle navigation system

Leah Groves¹, Natalie Li², Terry Peters^{1,2,3}, Elvis Chen^{1,2,3}

¹School of Biomedical Engineering, Western University, Canada

²Medical Biophysics, Western University, Canada

³Robarts Research Institute, Canada

Introduction: Five Million central venous catheterizations (CVCs) are performed annually in the United States. The most common insertion site is the internal jugular vein (IJV), which is situated close to the carotid artery (CA). The gold standard is a blind insertion that relies on anatomical landmarks and palpitation. Ultrasound-(US)-guided CVC has been shown to reduce complications. However, even with US-guidance rates of CA puncture can be up to 7.8% in US-guided trainees. One potential factor in the frequency of complications during US-guided CVC is the disparity between the clinician's visual and motor fields. We hypothesize that aligning the visual and motor fields will improve targeting accuracy in the needle insertion required for CVC.

Methods: A PVA-C phantom that mimics the appearance of the IJV and CA under US was developed. A screen-based surgical navigation system was developed by calibrating an US probe such that the US image was registered to a magnetic tracker's coordinate system. This allows for the US image and tracked tools to be visualized in a common coordinate system. A co-calibration apparatus was used to register the tracker's coordinate system, with the HTC VIVE Pro head-mounted display's (HMD) coordinate system. This allows for the tracked tools and US image to be visualized within the HMD in a common coordinate system directly in the user's field of view. Thirty-three clinical practitioners, all trained on US-guided CVC, were recruited for this study. Each participant was brief on and given time to train on the two systems and the US-only approach on the training vessel set in the phantom. Each user performed one needle insertion for each system (HMD, screen and US-only) on the experimental vessel set in a randomized counter-balanced order. All tracking and imaging data was recorded. From the recorded data, each insertion was assigned as successful or unsuccessful. A successful insertion was defined as the final needle position within the vessel lumen on the first attempt. The distance from the final needle tip position to the closest point on the vessel wall was calculated.

Results:

Number of successful insertions

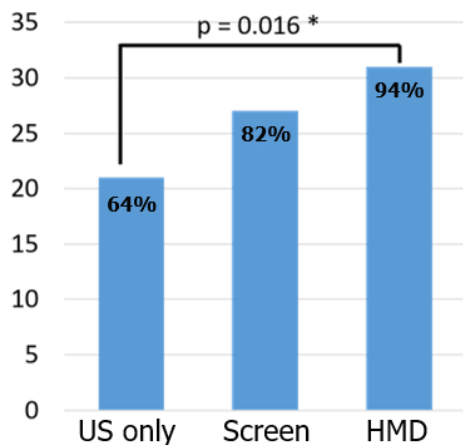


Fig 1. Number of successful insertions by modality

Distance from final needle tip position to vessel wall

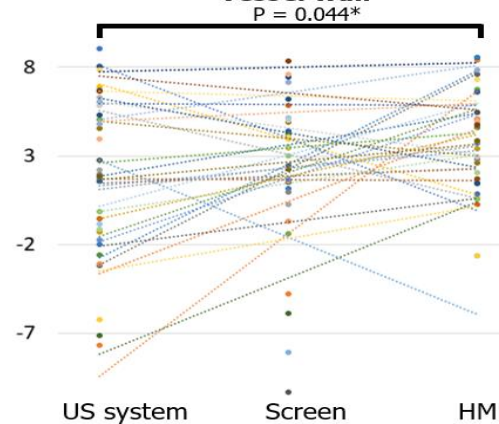


Fig 2. Distance from the final needle tip position to the closest point on the vessel wall by modality. Each colour represents a user.

Conclusions: To conclude, the use of a HMD to align the visual and motor fields improved needle navigation. The HMD system had a success rate of 94% compared to 64% for the US-only method. Furthermore, clinicians were able to more consistently target the center of the vessel, with an average distance from the final needle tip position to the center wall of 3.8 mm for the HMD system compared to 2.2 mm for the US-only system. This indicates the importance of coherent visual and motor fields, promoting the continued pursuit of HMD surgical navigation research.

Proteus: An Open Source Software Platform for Modulated Therapy with MRgHIFU

Ben Keunen¹, Maryam Siddiqui², Chris Krasnichuk³, Claire Wunker^{4,5}, Karolina Piorkowska¹, Yael Babichev⁴, Warren Foltz^{5,6}, Adam C. Waspe^{1,5}, Rebecca Gladly^{4,5}, J. Ted Gerstle^{1,7}, Samuel Pichardo²
¹Hospital for Sick Children, ²University of Calgary, ³Lakehead University, ⁴Mount Sinai Hospital, ⁵University of Toronto, ⁶University Health Network, ⁷Memorial Sloan Kettering Cancer

Introduction: Magnetic Resonance-guided High Intensity Focused Ultrasound (MRgHIFU) can be used to administer non-invasive thermal ablation, cavitation and mild hyperthermia, while also modulating and monitoring the energy delivery through a collection of software libraries known as Proteus. This open source software developed by multiple institutions contains core functionalities while allowing a modular design to tailor the program for each form of HIFU therapy and platform. This allows Proteus to be used with different MRI vendors (Bruker, Siemens, GE, and Philips), while also using multiple HIFU systems (Profound Medical, IGT, and FUS Instruments) with the various HIFU applications: blood brain barrier disruption, hyperthermia, thermal ablation, and cavitation. Our objective for Proteus is to develop a software platform that can be used on any system to monitor and modulate HIFU therapy. This study demonstrates the Proteus software for controlling HIFU thermal therapy for mild hyperthermia on the Bruker 7T MRI+IGT small animal HIFU system. There are parallel studies being performed at the University of Calgary using the same software platform with similar hardware on a GE MRI to study MRgHIFU-based hyperthermia.

Methods: Proteus was used to perform a proportional–integral–derivative (PID) controlled closed-loop hyperthermia study using a Bruker 7T MRI + IGT small animal HIFU located at the Spatio-Temporal Targeting and Amplification of Radiation Response (STTARR) facility. Proteus includes a module to obtain MRI real-time data from the Bruker scanner to produce thermal maps used for the monitoring of the procedure, including magnetic field drift correction from a region of interest (ROI) in a thermally isolated drift tube or from fibre-optic temperature probes. First, thermal experiments were performed with gel and tissue phantoms to ensure that Proteus properly controlled the system for both ablation and hyperthermia treatments. Second, hyperthermia was performed *in vivo* in an immune-competent mouse model of pediatric rhabdomyosarcoma (RMS).

Results: Mice (n=30) were treated with 10 or 20 minutes of mild hyperthermia on the Bruker MRI system with real-time monitoring of the heating. Our feedback control system consistently maintained a temperature of $40.5^{\circ}\text{C} \pm 3^{\circ}\text{C}$ within an intra-tumoral ROI encompassing the HIFU focal spot. As well fiber optic probes in the rectum verified the internal temperature and ensured that hyperthermia remained localized. The probes showed an average temperature of $35.5^{\circ}\text{C} \pm 1.8^{\circ}\text{C}$. The acoustic power was displayed and logged as it was modulated by the controller during treatment. There is also the ability to view graphs of the temperatures within ROIs. Using the data collected during the treatment, correlations were observed between peaks in the temperature graph and peaks in the acoustic power graph. As well it can be seen that there are points where the transducer is receiving minimal power (< 1W), yet the ROI temperature remains consistent showing how once the temperature is reached it can be maintained through minimal amounts of acoustic power.

Conclusion: Proteus is the culmination of collaboration between different pre-clinical research centers that normally would not be able to translate methodologies due to differing hardware infrastructure. Now, these centers can work together to develop techniques of monitoring and controlling HIFU devices for thermal therapy. Proteus is vendor agnostic software that enables cross-platform techniques in real-time monitoring and control of non-invasive MRgHIFU.

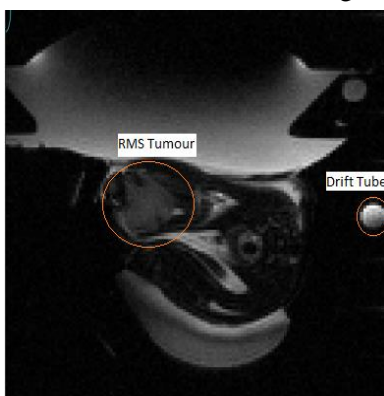


Figure 1: T2-weighted image showing RMS tumor

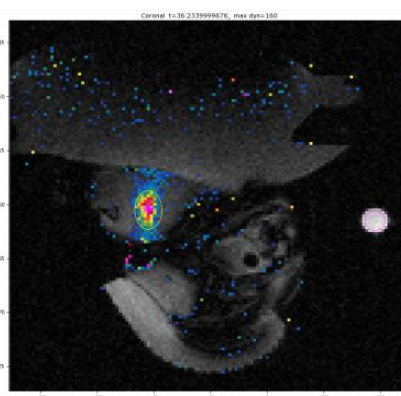


Figure 2: T1-weighted GRE image with temperature overlay

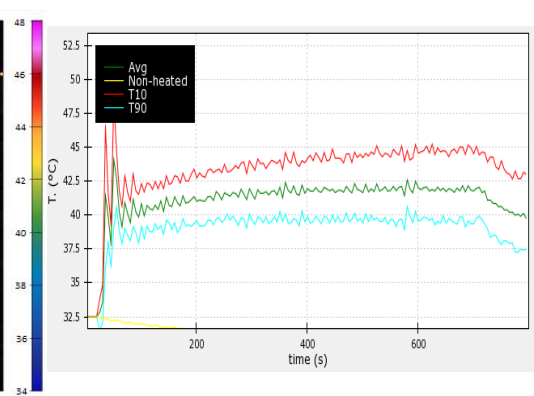


Figure 3: Temperature chart corresponding to treatment

A mechatronic needle-tracking system for image-guided breast biopsy using positron emission mammography and ultrasound

Claire K. Park^{1,2*}, Jeffrey Bax², Lori Gardi², Aaron Fenster^{1,2}

¹Department of Medical Biophysics, Western University, London, Ontario, Canada

²Center for Medical Imaging Technology, Robarts Research Institute, London, Ontario, Canada

Introduction: Image-guided biopsy is crucial for diagnosis and treatment planning for women with breast cancer. Positron emission mammography (PEM) is an emerging breast-specific functional imaging method, demonstrating high sensitivity and diagnostic accuracy compared to conventional breast imaging modalities [1]. PEM shows potential for improved tumour detection for image-guided breast biopsy, but anatomical reference and visualization for needle guidance is not available. These limitations can be overcome by combining PEM with an ultrasound (US) guided method to improve image-guided biopsy. The aim of this work is to develop a mechatronic needle-tracking system for combined PEM and US-guided breast biopsy. This paper reports on the development, calibration and needle-tracking validation for image-guided biopsy.

Methods: A mechatronic needle-tracking system was designed and fabricated to operate with an advanced PEM system (Radialis Medical, Thunder Bay, Ontario) and conventional US imaging system. The mechatronic system features a manually manipulated, multi-jointed robotic arm and a counterbalanced support, with the ability to access the breast between PEM detector plates. These components contain angle sensing encoders for 3D needle-tracking and electromechanical breaks for locking the system during biopsy. The end-effector is a biopsy device with an integrated US transducer and biopsy gun, which we previously designed and validated [2]. The postfire configuration needle and two degrees-of-freedom for US-guidance are focused on a remote-center-of-motion (RCM). This allows for targeting and needle guidance to be fixed on a PEM detected lesion. Forward kinematics were implemented to the mechatronic system and custom software modules were developed to track and display 3D position and orientation of the biopsy device and RCM (Fig. 1A). The coordinate space of the mechatronic system was registered to a simulated PEM detector plate using landmark-based registration [3] and fiducial divots in known locations (Fig. 1B). Guiding the needle to calibration fiducials registered the coordinate systems and determination of the Fiducial Registration Error (FRE). Validation was performed with testing fiducials, positioned at various locations on the detector plate. Accuracy was quantified as the Target Registration Error (TRE) and 3D Principal Component Analysis (PCA) assessed directional bias in each axis within 95% prediction intervals.

Results: Registration of the mechatronic system to the PEM detector plate resulted in an FRE of 0.23 ± 0.20 mm (N=8) and validation performed resulted in a TRE of 0.87 ± 0.43 mm (N=72). Within 95% confidence intervals, targeting accuracy is within 2mm in each axis. Prediction ellipsoids centered on the mean error, such that any future observation is expected to have 95% probability of sampling within the 3D volume was determined.

Conclusion: A mechatronic needle-tracking system for PEM and US-guided breast biopsy was developed. Successful calibration and needle-tracking validation with simulated PEM detector plates demonstrates feasibility for implementation with the advanced PEM system. Current work evaluates mechatronic system accuracy to target and perform mock biopsy on simulated lesions using tissue-mimicking breast phantoms.

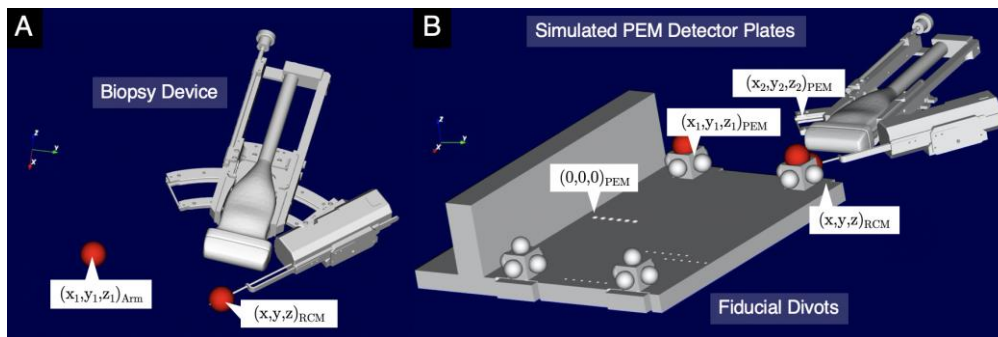


Fig. 1: Adapted screen capture images of custom guidance software user-interface. **A.** The software displays the real-time 3D position and orientation of the biopsy device for needle-tracking and guidance about its RCM, coincident to the postfire biopsy needle, for alignment with the PEM

detected lesion. **B.** Mechatronic guidance arm coordinate space registered to simulated PEM detector plates, using rigid landmark-based registration and select fiducial divots in known 3D coordinate locations.

[1] A. Chudgar, et al. (2016) PET Clinics. 12(1):39-51. [2] C. Park, et al. (2019) Med. Phys. 46(6) AAPM. An. Meeting Program. [3] J. Fitzpatrick, et al. (1998) IEEE Trans. Med. Imaging 17(5):694-702.

Reinforcement learning approach for video-based task recognition in central venous catheterization

Rebecca Hisey¹, Brian Chen², Tamas Ungi¹, Daenis Camire³, Jason Erb³, Daniel Howes³, Gabor Fichtinger¹

¹Laboratory for Percutaneous Surgery, School of Computing, Queen's University, Kingston, Canada

²Medical Informatics Laboratory, School of Computing, Queen's University, Kingston, Canada

³Department of Critical Care Medicine, Queen's University, Kingston, Canada

Introduction: Central venous catheterization (CVC) involves inserting a catheter into a major vein such as the internal jugular. This essential skill is taught during residency for many medical specialties such as critical care. The workflow for this procedure is long. By recognizing the task that is being done, we can provide feedback about workflow compliance that will help novices learn the procedure. Here, we present a method for recognizing CVC tasks from a video using a combination of convolutional neural networks (CNN) and reinforcement learning.

Methods: In our initial attempts to recognize the tasks in CVC, we recognize tasks solely based on the tool that is identified using a CNN with a soft-max output layer. For this approach, we use the output of the same CNN and use it to train a policy for predicting the most likely task. We model this problem as a search for the optimal path through a grid. An optimal path is the path that yields the highest reward. Each row of the grid represents one of the eight tasks that we are recognizing, and each column represents a single frame of the video (Fig. 1). To generate a policy, we begin by using the CNN to classify all frames in 4 videos of medical residents performing CVC. In addition to classifying all frames with a CNN, we also manually label each frame based on the task that is being done. Since each tool corresponds one-to-one with a task in the procedure, we define our reward scheme by using the CNN's confidence that each tool is being used and add an additional bonus of +2 for the tool that corresponds to the task label (Fig. 2). Next, for each video in the training set, we use Q-learning to train a policy to find the optimal path based on our reward scheme. We allow the system to train for 100 000 episodes, or until it converges to the optimal reward.

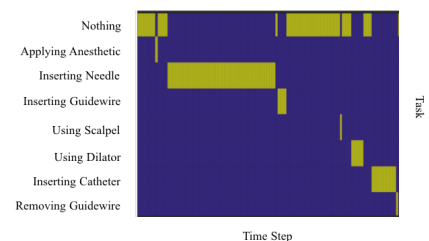


Figure 1. Example of an optimal path for a single video.

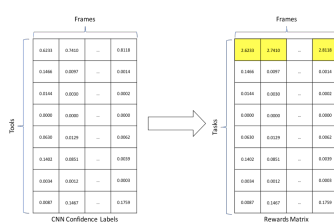


Figure 2. Generation of reward matrix.

To use the policy for prediction, we classify each frame in the test video and find its nearest neighbor in the training set. The nearest neighbor is found by comparing the output of the CNN along with the time at which it occurs in the video. The system then uses the policy that was generated in training to select the task that has the highest expected reward. For this work, we perform a leave-one-video-out cross validation whereby we use 4 videos to train the policy, and test on the remaining video. This process is repeated for all 5 videos and we report the average accuracy. The videos are of second year residents performing CVC on a venous access phantom. The videos focus only on the resident's hands and the tool in use.

Results: The average accuracy across all cross-validation folds was 85%. As can be seen from the example Figure 3, the path found by our system closely resembles the optimal path shown in Figure 1. In contrast, the path found using the CNN alone, is much more prone to errors and only achieves 56% accuracy on average.

Conclusions: Our approach using CNNs and reinforcement learning clearly outperforms the CNN alone. This is due to the fact that the reinforcement learning approach takes temporal information into account. This allows it to still correctly predict the task even when the CNN recognizes the wrong tool based on which task is likely being performed at that time in the procedure. Further work will be done to evaluate the applicability of this work to real-time task detection.

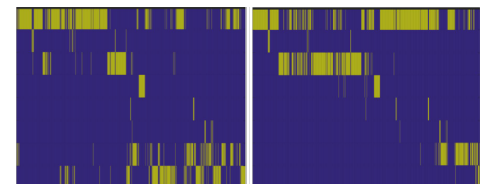


Figure 3. Predicted Paths using CNN alone (Left) and CNN & Q-Learning (Right).

Acknowledgements: This work was funded, in part, by NIH/NIBIB and NIH/NIGMS (via grant 1R01EB021396-01A1), by CANARIE's Research Software Program, and is supported as a Collaborative Health Research Project (CHRP #127797) by the Natural Sciences and Engineering Research Council of Canada (NSERC) and the Canadian Institutes of Health Research (CIHR). R. Hisey is supported by the Ontario Graduate Scholarship. G. Fichtinger is supported as a Canada Research Chair.

Development of a Surgical Simulator for Spinal Decompression Procedures using Virtual Reality

Y Zhang¹; T Chen², MD FRCSC; M Hardisty¹, PhD; E Crawford², MD MSc; J Finkelstein², MD MSc FRCSC
¹Sunnybrook Research Institute, Sunnybrook Health Sciences Center, Toronto, Ontario, Canada
²Division of Spine Surgery, Sunnybrook Health Sciences Center, Toronto, Ontario, Canada

Introduction

Spinal decompression (SD), is a surgical procedure for treatment of spinal stenosis that involves resection of tissue compressing the neural elements. SD surgery requires appropriate planning and strategies depending on the specific situation. Given the potential for neural complications, there exists significant barriers to residents and fellows obtaining adequate surgical experience. Virtual surgical teaching tools present a possible method to promote experiential learning of this procedure, however, current existing technology do not simulate the many challenges of SD surgery. The aim of this work was to develop a SD-specific open-source 3D virtual simulator as a teaching tool to improve surgical training.

Methods

A SD simulator was built using 3D Slicer; an open-source software platform for medical image visualization and processing. Two components comprise the simulator, 1) a tool for semi-automated building of patient specific geometry from medical imaging (Magnetic Resonance Imaging (MRI) and Computed Tomography (CT)), 2) a module for interaction with the geometries and simulation of the procedure. The procedural steps include import of patient-specific imaging, image fusion, bone threshold-based segmentation, soft tissue segmentation, surgical planning, surgical field simulation, simulation of SD procedures and neural element decompression. Bone and soft tissue resecting tools were developed by manually customizing 3D models (Kerrison Punch, Burr, etc.). SD simulation was enabled through bone ligamentum flavum, and intervertebral disc resection at the site of compression. Neural element decompression was simulated by interpolation of the undeformed anatomy above and below the site of compression. Users can interact with the patient geometry and perform procedures with a virtual reality (SlicerVR) headset or visualized on a computer screen, as shown in Figure 1. Standard hand-held controllers were integrated through button-state tracking (OpenVR API), allowing for control of the scene and use of tools for surgery.

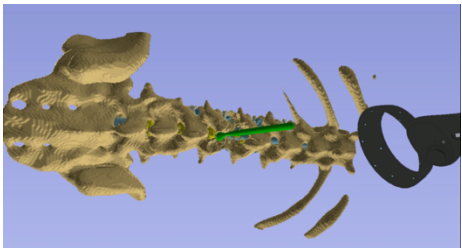


Figure 1: Virtual reality view of segmentation model and burr tool during SD surgical simulation

Orthopaedic and neurosurgical trainees (n=15) were prospectively enrolled in a trial of the simulator's utility. Participants were evaluated through questionnaires on their understanding of the anatomy and pathology specific to spinal stenosis before and after using the simulator.

Results

93% of participants found the SD simulator useful in understanding and learning the pathology of spinal stenosis, 80% found it useful in learning how to perform SD surgery. Post-surgery questionnaire scores saw an improvement in anatomical knowledge of 2.9% to 11.7% with a greater effect for more junior trainees.

Simulation quality in terms of spinal geometry and tool modeling were acknowledged by senior surgeons while addition of drilling sounds (with pitching changing with bone density) for guiding burr holes¹ and diversified instrument selection were suggested. User testing revealed technical limitations when interacting with the model, specifically slow virtual reality display updates when performing continuous resection.

Conclusion

The decompression surgical simulator shows potential as a useful educational tool for spinal stenosis pathology and surgical procedures, especially for trainees with little experience. Future development of the simulation technology will include, simulating drilling sounds, quicker visual updates by multithreading, further automation of patient specific modelling, and creation of machine learning analysis of results to provide feedback to trainees. Virtual reality simulations can play a vital role in medical training and be influential as surgical curriculums become competency-based.

Acknowledgements: Feldberg Chair for Spinal Research

References

1. Praamsma M, Carnahan H, Backstein D, Veillette CJ, Gonzalez D, Dubrowski A. Drilling sounds are used by surgeons and intermediate residents, but not novice orthopedic trainees, to guide drilling motions. *Can J Surg.* 2008;51(6):442-446.

Localizing high-dose-rate interstitial gynecologic brachytherapy needles intraoperatively using automatic segmentation approaches

Jessica R. Rodgers^{1,2}, Derek J. Gillies^{2,3}, W. Thomas Hrinivich⁴, Igor Gyackov², Kathleen Surry⁵, Aaron Fenster^{1,2}
¹School of Biomedical Engineering, ²Robarts Research Institute, ³Dept. of Medical Biophysics, Western University, London, Canada; ⁴Johns Hopkins Hospital, Baltimore, USA; ⁵London Regional Cancer Program, London, Canada

Introduction: During high-dose-rate interstitial brachytherapy (ISBT) of gynecologic malignancies, multiple needles (typically ~14) must be inserted into the tumor and surrounding tissues, allowing a radioactive source to be positioned via these needles. Precise placement is necessary to provide optimal treatment and avoid nearby organs-at-risk (OARs), such as the bladder and rectum. We previously proposed a 360° three-dimensional (3D) transvaginal ultrasound (TVUS) system to visualize OARs and needles. A key limitation to intraoperative clinical translation of 3D TVUS is the difficulty in manually localizing needles quickly, which may be mitigated with the implementation of automatic needle segmentation to ease and expedite localization. Our aim was to implement two algorithms to aid in localizing ISBT needles in two different clinical imaging scenarios that are common during this procedure. To our knowledge, this is the first use of automatic needle segmentation in ISBT TVUS images.

Methods: Two-dimensional (2D) TVUS allows clinicians to immediately adjust needle trajectories, mitigating deflection and avoiding OARs. Segmentation was implemented using a U-Net architecture with a modified dropout rate, trained on a dataset of 262 2D ultrasound images from procedures using needle-like applicators, including prostate and gynecologic ISBT, liver ablation, and kidney ablation and biopsy. The training/validation set (80%) included 34 gynecologic ISBT images, while 18 were maintained as unseen testing data. Supplementing 2D views, 3D TVUS allows needle implants to be assessed in a broader context, including OAR volumes and relative needle positions, which is critical for appropriate dosimetry. Due to the limited number of 3D images available, convolutional neural network approaches were not appropriate and thus segmentation was implemented by leveraging the randomized 3D Hough transform. This was tested on two images, containing a total of 18 needles, as a proof-of-concept. Both algorithms may be limited by the assumption of linear needles, though no noticeable curvature occurred within the TVUS field-of-view and therefore these methods were considered appropriate for this task.

The success of the segmentation algorithms was assessed by comparing the algorithmically segmented needles to manual segmentations, calculating the Euclidean distance between the needle positions and the angular differences between the trajectories. The Dice-coefficient was also computed to evaluate the 2D segmentations.

Results: In the 2D approach, the median [first quartile, third quartile] position and angular differences were 0.27 [0.20, 0.68] mm and 0.50 [0.27, 1.16] °, respectively, between manually and algorithmically segmented needles, requiring ~50 ms per segmentation. The median Dice-coefficient was 91.2 [78.0, 92.7]. In the 3D segmentation, all needles were localized, requiring ~30 s per patient. The median position and angular differences were 1.04 [0.77, 1.32] mm and 0.73 [0.58, 1.78] °, respectively, when compared to manual segmentations. Both approaches were robust even in complex cases, containing air, shadowing, or reverberation artefacts, as shown in Fig. 1.

Conclusions: Intraoperative automatic needle segmentation in gynecologic ISBT has the potential to improve needle implant quality, allowing positions to be immediately assessed and refined, and provides the potential for 3D TVUS to be used for treatment planning. Future studies will investigate the clinical treatment impact of these segmentations with a larger patient cohort and optimization of the 2D approach for real-time segmentation of live needle insertions.

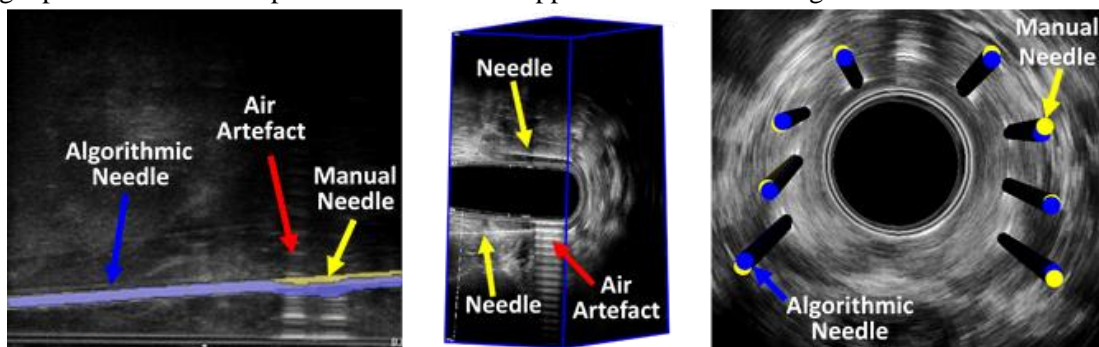
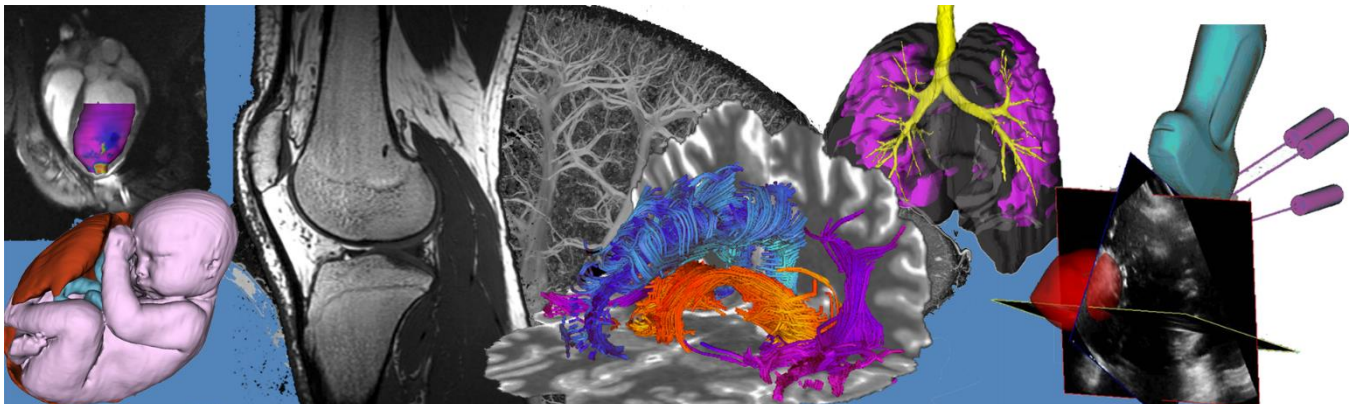


Figure 1: (a) 2D TVUS image with a manually and algorithmically segmented needle. (b) Example 3D TVUS image and (c) corresponding manual and algorithmic needle segmentation models overlaid on an axial slice.

Oral Presentation Abstracts

Session 5: Image-Guided Interventions 2



A Novel Approach for Guiding Catheter-Based Interventions

James J. Zhou^{1,2}, Alykhan Sewani^{1,2}, Trisha L. Roy¹, Andrew D. Dueck¹, Brandon Van Asseldonk¹, Graham A. Wright¹, M. Ali Tavallaei^{1,2}

¹Sunnybrook Health Sciences Centre, ²Ryerson University

Background: Many catheter-based procedures have high technical failure rates (e.g. >20%) [1]-[3] and high complication rates (30%) [4]-[6]. This is partially due to the difficulty in remote catheter navigation from outside the body and the mechanical engagement of the flexible device with the anatomy along its path. Furthermore, these procedures are guided by 2D projection x-ray which has limited contrast and does not allow the operator to see the position of the device relative to the anatomy in 3D. These limitations motivated us to develop a catheter (CathPilot) with a completely novel steering concept with the goal of mitigating these problems. The objective of this study is an initial performance assessment of the CathPilot for catheter steering and navigation in arterial phantom models.

Methods: The CathPilot uses a cable-driven expandable structure to localize steering input, thus eliminating the effect of mechanical engagement along its length with the anatomy. The expandable frame located at the distal end can be deployed to act as a rigid leverage point for the cables to localize the steering effect (Fig. 1). The change in cable lengths are measured and used to estimate the real-time position of the device relative to the frame and present it on a graphical user interface (GUI). Three aspects of the device were tested: targeting accuracy, applicable force range, and navigation workspace. To test targeting accuracy, 3D-printed targets, 10 mm in diameter with randomly positioned 1.0 mm diameter holes, were placed in an arterial phantom as targets. Four operators, blinded to the targets, attempted to enter the holes with a conventional guidewire vs. the CathPilot. The navigation times were recorded. To determine the applicable force range, the amount of force that can be delivered through a guidewire supported by a non-steerable conventional catheter, a steerable conventional catheter, and the CathPilot were compared. To assess the navigation workspace, aluminum foil was mounted to the arterial phantom, and operators were given 5 minutes to trace as much area as possible with the guidewire tip and assistance of each of the three catheters.

Results: When users failed to hit the targets with the non-steerable catheter, they were successful using the CathPilot in less than 5 minutes. The CathPilot covered the greatest surface area and allowed the user to navigate to any position (Fig. 2). Finally, the CathPilot yielded the greatest applied forces, averaging 0.429N compared to 0.109N and 0.118N for the conventional non-steerable and steerable catheters, respectively (Table).

Conclusions: Initial assessments of the CathPilot demonstrated significant improvement in navigation accuracy and increased the range of applicable forces. The novel concept demonstrates great potential in helping overcome the limitations in device steering, pushability, and visualization for various cardiovascular interventions.

References: [1] Bradbury et al., *J Vasc Surg*, 2010. [2] Hsu et al., *J Am Heart Assoc*, 2013. [3] Al-Hijji et al., *Am Heart J*, 2016. [4] Daye et al., *Cardiovascular Diagnosis and Therapy*, 2018. [5] Gupta et al., *Circ Arrhythmia Electrophysiol*, 2013. [6] Brilakis et al., *JACC Cardiovasc Interv*, 2015.

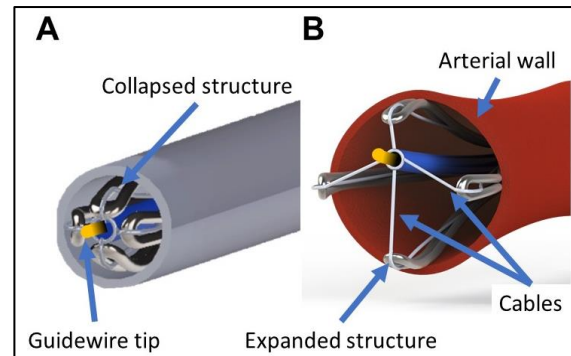


Fig. 1. A. CathPilot in collapsed state to allow advancement of the catheter through the body. B. CathPilot with the expandable structure engaged to localize steering input; the change in cable lengths is used to calculate the real-time position of the catheter for a GUI.

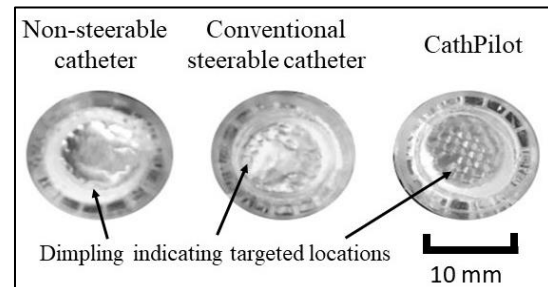


Fig. 2. The non-steering catheter was only able to target the periphery; the CathPilot was able to cover more area than the conventional catheters and navigate to any position.

Table of applicable forces

Catheter Type	Non-Steerable Catheter	Conventional Steerable Catheter	CathPilot
Applicable Force: Mean \pm S.D. (N)	0.109 \pm 0.08	0.118 \pm 0.08	0.429 \pm 0.16

Automated surgical video annotation on open-source data collection platform

Jacob Laframboise¹, Tamas Ungi¹, Kyle Sunderland¹, Boris Zevin², Gabor Fichtinger¹

¹Laboratory for Percutaneous Surgery, School of Computing, Queen's University, Kingston, Canada

²Department of Surgery, Queen's University, Kingston, Canada

INTRODUCTION: Surgical video annotation is of particular use for surgical training, such as in detection of workflow steps and to generate data for machine learning. Deep learning is a powerful tool for video annotation but requires efficient management of a large quantity of data. We propose the open source 3D Slicer / PLUS Toolkit[1] platform to collect and synchronize tracking, video, and other data streams to support deep learning based video processing. To demonstrate this platform, we use it to collect training data and deploy real-time annotation to label which tool is interacting with which tissue in an inguinal hernia repair surgery.

METHODS: A life-like model from Imperial College¹ is used for surgery simulation. PLUS Toolkit collects optical tracking data from the OptiTrack Duo on tools with 3D printed markers, and RGB video from an overhead Microsoft HD webcam. Each class of data is saved in 3D Slicer as a Sequence to handle labelling. They are exported by Jupyter notebooks with 3D Slicer integration. The Optical tracking determines the tool in use, and a convolutional neural network is used to classify the tissue being touched by the tool. The CNN takes in RGB images of size 128 by 128 in batches of 32 and is comprised of 5 units. Each unit contains two 2D convolutional



Figure 1. Automatic video annotation in 3D Slicer. The CNN model is correctly predicting that tool 2 (scissors) is touching external obliques.

layers with 16 filters in the first unit, doubling each unit, ReLU activation, and a MaxPooling layer of size (2,2). The CNN is finished with a dense layer of 256 nodes, and a final dense layer of 5 nodes with SoftMax activation. We collected four datasets and trained our model for 30 epochs using gradient descent with categorical cross entropy on the first, third, and fourth datasets, totaling 96,189 images. Our CNN model was tested on the second dataset comprised of 32,359 images. The full source code can be found on GitHub².

RESULTS: The platform enabled collection of 128,548 labelled images in just four 30-minute recording sessions. The platform collected high quality data, with ground-truth human accuracy of 98.5%. Our CNN model reached a classification accuracy of 98.8% on the training frames, and 98.0% on the testing video frames. The CNN model was deployed in a custom 3D Slicer module to annotate real-time video at 30fps.

CONCLUSION: The 3D Slicer / PLUS Toolkit platform facilitates rapid collection of high-quality datasets for surgical video processing, and enables deployment of real-time video processing models on multimodal data with a high degree of accuracy. This platform is well-suited to collecting training data for image processing algorithms in surgical contexts, as data can be collected in a minimal amount of expensive OR time. This work motivates further use of the 3D Slicer platform in medical deep learning applications, especially surgical video annotation.

ACKNOWLEDGEMENTS: G. Fichtinger is supported as a Canada Research Chair. This work was funded, in part, by NIH/NIBIB and NIH/NIGMS (via grant 1R01EB021396-01A1 - Slicer+PLUS: Point-of-Care Ultrasound) and by CANARIE's Research Software Program. Financial support was received from SEAMO.

REFERENCES:

- [1] T. Ungi, A. Lasso, C. Pinter, A. Rankin, T. Heffter, and G. Fichtinger, "PLUS: Open-Source Toolkit for Ultrasound-Guided Intervention Systems," *IEEE Trans. Biomed. Eng.*, 2014.

¹ <http://www.imperial.ac.uk/>

² <https://github.com/SlicerIGT/aigt/tree/master/HerniaAnnotation>

Symmetric Autoencoder for Tissue Classification of Mass Spectrometry iKnife Data.

*Alice M.L. Santilli¹, *Amoon Jamzad¹, Natasja N.Y. Janssen¹, Martin Kaufmann², Laura Connolly¹, Kaitlin Vanderbeck³, Ami Wang³, Doug McKay⁴, John F. Rudan⁴, Gabor Fichtinger¹, Parvin Mousavi¹.

¹School of Computing, Queen's University, Canada, ² Department of Medicine, Queen's University, Canada, ³ Department of Pathology, Queen's University, Canada, ⁴Department of Surgery, Queen's University, Canada

*These authors have contributed equally to this work

Introduction: The Intelligent Knife, iKnife by Waters Corp., is a new intraoperative tool that has the capability of addressing the challenge of detecting cancerous resection margins during specimen excision. The iKnife utilizes Rapid Evaporative Ionization Mass Spectrometry (REIMS), a mass spectrometry approach for analyzing phospholipids. It can provide feedback on the chemical profile of the tissue being analysed in only a few seconds. Previously, REIMS has been used on limited cases of fresh ex-vivo human specimens containing breast, colorectal and other cancer types, for tissue characterization using linear discriminant approaches in a black box fashion [1,2]. However, during real-time resection, the cautery tip may pass through mixed tissue and the mass spectral data collected may be noisy. We propose using a deep learning framework to build a tissue characterization model for the iKnife with Basal Cell Carcinoma (BCC). Autoencoders have been successful in mass spectrometry applications as they enable the representation of data in a concise format as latent variables (encoding) while making it possible to reconstruct the main data (decoding) from this representation [3].

Methods: Figure 1 depicts an overview of the data collection, preprocessing and analysis workflow. Forty-two specimens were excised from 35 patients, a total number of 190 burn spectra were recorded, including 127 normal and 63 BCC which were then augmented to form the dataset for learning a model. Each scan contained 8000 values between 100 and 900 mass charge ratios (m/z). With non-overlapping windows of size 10 (stride of 10), the max peak was chosen, reducing each scan from 8000 to 800

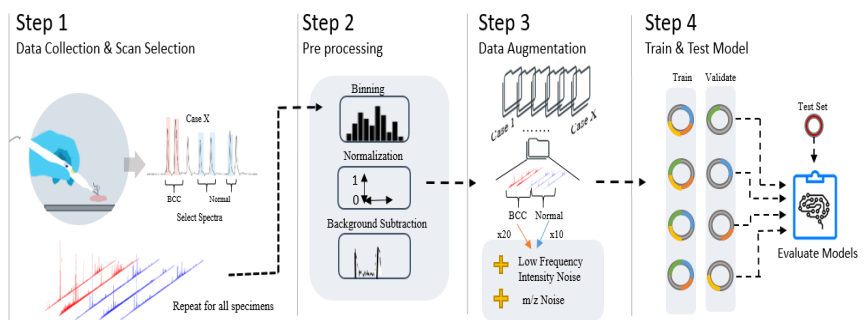


Fig. 1: Overview of the methodology: Scans of ex vivo BCC burns from specimen are labeled and selected. The spectra are preprocessed and normalized prior to analysis. Data is augmented and balanced, followed by training and evaluation of deep models.

values. We used a symmetrical autoencoder structure with 5 layers including the input layer. The dimension of the encoded data in latent space was chosen to be 100 neurons. Each layer of the autoencoder was followed by a ReLU activation function and L2 regularization. The autoencoder/classifier structure was trained simultaneously using the Adam optimization function. To evaluate the models, we stratified the data to training and test sets; in the training set the data was further divided for 4-fold cross validation. We assure that the balance and separation of the data was consistent across folds for different classes.

Results: Having trained and validated 4 different models through cross validation, the classification performance of these models were evaluated on the test data. We achieved an average (standard deviation) accuracy of 96.62% (1.35%), sensitivity of 100.00% (0.00%), and specificity of 95.00% (2.00%) for BCC/normal burn classification. We used T-distributed Stochastic Neighbor Embedding (t-SNE) to represent our high dimensional data [4]. In Figure 2, we can clearly see the contribution of the data encoding in separability of BCC and normal spectra.

Conclusion: Our network demonstrates high accuracy for the classification of BCC vs. normal iKnife burn profiles.

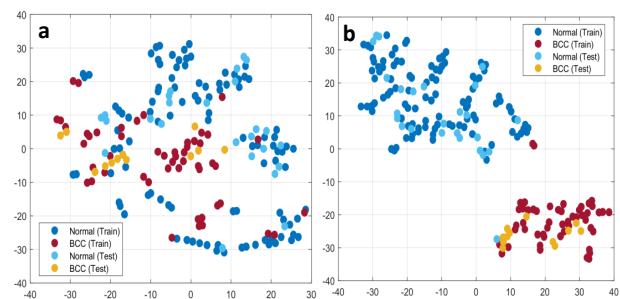


Fig. 2: (A) t-SNE representation of the scan space. All of the input data with no augmentation represented in two dimensions. (B) t-SNE representation of the latent space. All of the input data reduced by the network at the latent space represented in two dimensions.

References : [1] RE St.John. Breast Cancer Research,19:1-14, 2017. [2] DL Phelps, British Journal of Cancer, 118:1349-1358, 2018. [3] SA Thomas, IEEE SSCI, 1-7, 2016. [4] LVD Maaten, J. of Machine Learning Research, 9:2579-2605, 2008.

Validation of a Projector-Based Navigation System for Bedside Surgical Procedures

Colton Barr¹, Andras Lasso¹, Mark Asselin¹, Steve Pieper², Faith C. Robertson³, William B. Gormley³, Gabor Fichtinger^{1,4}

¹Laboratory for Percutaneous Surgery, School of Computing, Queen's University, Kingston, Canada ²Isomics, Inc., Cambridge, MA, USA ³Department of Neurosurgery, Brigham and Women's Hospital, Harvard Medical School, Boston, Massachusetts, USA ⁴Department of Surgery, School of Medicine, Queen's University, Kingston, Canada

INTRODUCTION: There is a subset of critical surgical interventions that are performed at the bedside with minimal technological assistance. One such procedure is ventriculostomy, which involves the insertion of a catheter through the skull and brain into a fluid filled ventricle. This procedure is typically an emergent one, performed freehand at the bedside using anatomical landmarks to select an entry point. A recent study simulating ventriculostomy predicted cortical vessel injury in up to 20% of catheter insertions, however it was also found that there was at least one vessel free zone in all subjects that would mitigate vessel damage [1]. The purpose of this study was to develop a low cost, portable image guidance system capable of automatic patient registration, optical marker tracking and insertion point visualization directly on the patient's anatomy.

METHODS: We used an RGB-Depth (RGB-D) camera calibrated to a consumer grade optical projector to project navigation information directly in the surgical field. We selected the Intel RealSense D435 RGB-D camera and the AAXA Pico M6 projector since both products are readily available at a low price point. The RGB-D camera enabled us to perform depth-based patient registration without requiring the use of a tracked pointer. Optical marker tracking was accomplished using the ArUco marker library, with real-time transforms streamed using the PLUS Toolkit. The software to perform patient registration and target point projection was written as an extension in 3D Slicer (www.slicer.org). The core components of the system were tested separately to quantify their individual accuracy. Optical marker tracking and camera-projector calibration was tested by projecting points onto a modified ArUco marker and measuring the distance of the points from the marker's corners. Depth-based registration was evaluating by comparing it to the gold standard fiducial registration approach using a pointer tracked by a commercial optical navigation system. Finally, point projection onto the target anatomy was tested by selecting a point on a 3D model of the manikin in 3D Slicer and projecting the corresponding point onto the manikin. The distance of the projected point from the true point location was measured using the gold standard navigation system.

RESULTS: The 8 cm ArUco marker was captured at 5 distances from the system and in 10 distinct orientations. The average absolute distance of the projected points from their targets was 5.3 mm (SD 2.9 mm). The average distance of the point cloud from the manikin model following depth-based registration was 1.83 mm (SD 0.15 mm), while the average fiducial registration error using the commercial system was 2.47 mm (SD 0.63 mm). The average distance between the projected point on the manikin and the actual point as selected in 3D Slicer was 4.01 mm (SD 1.51 mm) over 3 trials of 20 points each. The results from Trial 2 are shown in Figure 1.

CONCLUSIONS: The accuracy of depth-based registration and point projection using the camera-projector system highlights the potential of this system in navigating bedside surgical interventions. Future work will focus on minimizing point projection error through refining registration and system calibration techniques.

ACKNOWLEDGEMENTS: Colton Barr was supported by an NSERC USRA. G. Fichtinger is supported as a Canada Research Chair. Work funded, in part, by NIH/NIBIB and NIH/NIGMS (via grant 1R01EB021396-01A1 - Slicer+PLUS: Point-of-Care Ultrasound) and by CANARIE's Research Software Program.

REFERENCES:

[1] Robertson, F. C., Adb-El-Barr, M. M., Mukundan, S. and Gormley, W. B., "Ventriculostomy-associated hemorrhage: a risk assessment by radiographic simulation," *J. Neurosurg.* 127(1), 532-536 (2017).

Projected Target Locations and Distance of Projected Points from Targets

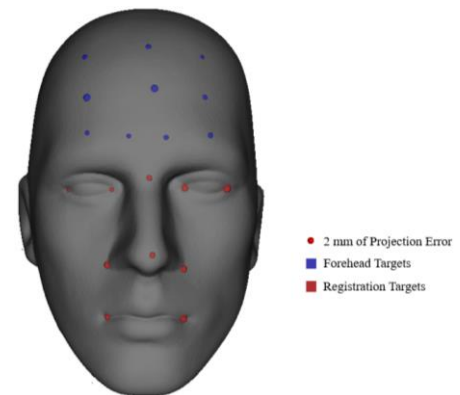


Fig. 1. Manikin model displaying target point positions selected in 3D Slicer. Projection error measured is proportional to target size.

Respiratory Motion Estimates for Catheter Tracking with Undersampled 3D Image-Based Navigators

Authors: Jaykumar Patel[†], Saqeeb Hassan[†], Nii Okai Addy^{*}, and Graham Wright[†]

Institutional Affiliations: Sunnybrook Research Institute ([†]), HeartVista (^{*})

Introduction: Cardiac Magnetic Resonance Imaging (MRI) can be used to assist *in vivo* catheter ablation procedures that treat cardiac arrhythmias. Interventional cardiac MRI procedures improve the success rate of treating arrhythmias of $\sim 2.5 \text{ mm}^1$ in size, due to its ability to provide excellent soft tissue contrast which allows enhanced visualization of the scarred tissues from prior heart attacks. A major challenge associated with this technique involves the respiratory motion of the heart which causes misalignment of the catheter position relative to the heart wall. In an attempt to solve motion misalignment, previous research quantified respiratory motion using multiscale registration from 3D roadmaps and real-time (RT) 2D MR images using datasets acquired prior to catheter ablation treatments. These preclinical studies yielded in-plane accuracy of 4.0 mm^2 . Due to poor coverage and low through-plane resolution, current techniques often mischaracterize the respiratory-induced heart motion in through-plane direction. Thus volumetric approaches are proposed for motion characterization. Recent work has examined the use of image-based navigators (iNAV) with cone-shaped k-space trajectories acquired every heartbeat to track the 3D non-rigid motion³. 3D cone trajectories are able to sample k-space more efficiently than Cartesian trajectories and are more robust to motion due to low order k-space oversampling³. In this work, I demonstrate the feasibility of highly undersampled 6mm isotropic resolution 3D cone iNAVs to characterize the per-heartbeat respiratory motion.

Methods: To characterize the respiratory motion during a free-breathing scan, a 3D cone acquisition was designed to acquire with 176 ms temporal and 6 mm isotropic resolution images on a GE 1.5T MRI scanner with a $28 \times 28 \times 14 \text{ cm}^3$ FOV, TE=5ms and total scan time of 135 heartbeats, cardiac gated from a healthy volunteer. The resulting undersampled 3D cones were reconstructed with the Berkeley Advanced reconstruction toolbox (BART) with parallel imaging compressed sensing reconstruction ℓ_1 -ESPIRiT at an acceleration factor (AF) of 6. Parallel imaging was used to take advantage of the multi-coil data which allows reconstruction with reduced data and compressed sensing allowed the removal of aliasing artifacts from undersampled imaging. The processing time for each iNAV was 30s, using ℓ_1 -ESPIRiT computed with an 8 GB Nvidia 1070 Ti GPU. The reconstruction time for each undersampled 3D iNAV was 10 sec with most of the time being used to prepare the data and compute the coil sensitivity. Afterwards, the iNAVs were rigidly registered to the reference 3D iNAV using the image registration tool Elastix.

Results: An example of a 6 mm isotropic spatial resolution 3D iNAV (fully sampled and undersampled) is shown in Figure 1 and the respiratory motion of the heart in all three directions (A/P, L/R, S/I) is shown in Figure 2. The measurements are normalized by subtracting the mean displacement in all directions. The undersampled cardiac images retained enough structural features to sufficiently extract the respiratory motion. Figure 2 shows the periodic respiratory motion every 4-5 heartbeats with the largest range of motion, 10mm, observed in the S/I direction. The motion ranges around 7mm in the L/R and A/P directions.

Conclusion: The undersampled 3D cone trajectory MR images can be acquired every heartbeat and reconstructed using parallel imaging and compressed sensing with BART. The respiratory motion of the heart can be estimated every heartbeat using undersampled 6mm 3D cone trajectory iNAV, demonstrating the feasibility to perform motion correction which can be used to correct the misalignment of the catheter. The motion accuracy and robustness will be tested *in vitro* phantom and *in vivo*.

References: [1] Tanner et al. Cardiovasc Electr , 21, 2010. [2] Xu R. et al. IEEE, 62(12):2899–2910, 2015. [3] Nii A. et al. Magn Reson Med. 2017;77(5)

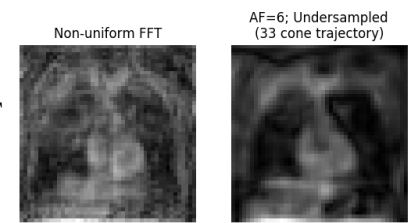


Figure 1: 3D cone trajectory reconstruction of the heart (Coronal Slice)

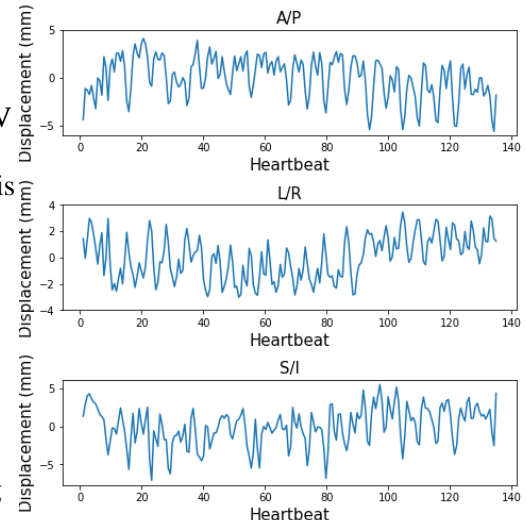
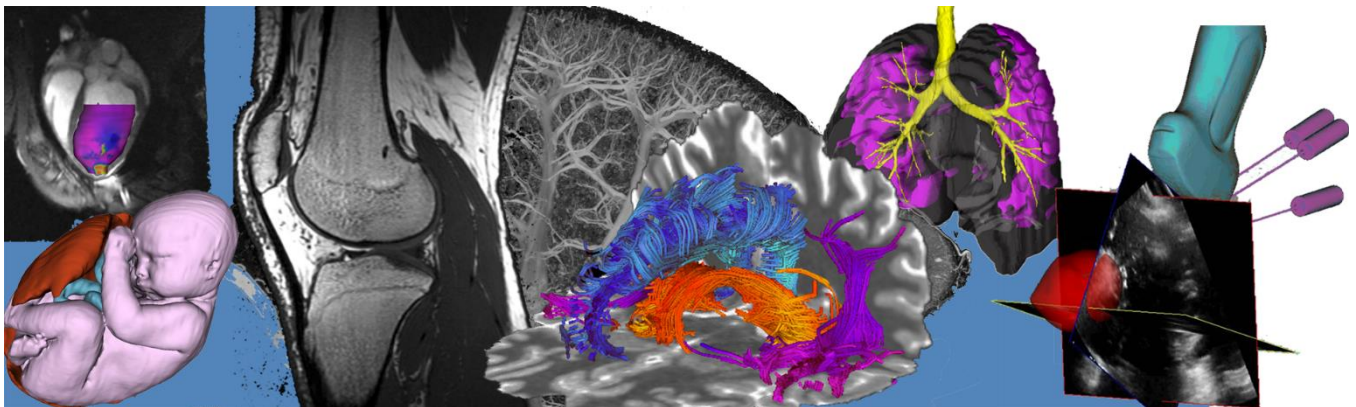


Figure 2: Respiratory motion from rigid registration of the undersampled 3D iNav.

Oral Presentation Abstracts

Session 6: Neurology Imaging 1



Translocator Protein in Post-traumatic Stress Disorder: Preliminary findings using the [¹⁸F]FEPPA PET radioligand

Sarah Watling MSc^{1,6}, Talwinder Gill MSc^{1,6}, Erin Gaudette^{1,6}, Junchao Tong PhD^{1,3-4}, Tina McCluskey MSc^{1,3}, Jeffrey Meyer MD PhD^{1,3-6}, Jerry Warsh MD^{1,3-6}, Ruth A. Lanius MD PhD¹⁰, Rakesh Jetly MD¹¹, Don J. Richardson MD^{9,10}, Sylvain Houle MD PhD^{1,3-4}, Stephen Kish PhD^{1,3-6}, Michael Hutchison⁷, Neil Vasdev^{1-4,6}, Shawn G. Rhind PhD^{6,8}, Isabelle Boileau PhD^{1,3-4,6}

¹Research Imaging Centre, ²Azrieli Centre for Neuro-Radiochemistry, and ³Campbell Mental Health Research Institute, Centre for Addiction and Mental Health, Toronto, Ontario, Canada

⁴Department of Psychiatry, ⁵Pharmacology and Toxicology, ⁶Institute of Medical Sciences and ⁷Faculty of Kinesiology and Physical Education, University of Toronto, Toronto, Ontario, Canada

⁸Defense Research and Development Canada, Toronto Research Centre, Toronto, Ontario, Canada

⁹Parkwood Operational Stress Injury Clinic, London, Ontario, Canada

¹⁰Department of Psychiatry, University of Western Ontario, London, Ontario, Canada

¹¹Department of National Defence, Canadian Forces Health Services, Ottawa, Canada.

Introduction: Post-traumatic stress disorder (PTSD) is a psychiatric condition developed in response to experiencing or witnessing a traumatic event. Microglia cells have been implicated in psychiatric disorders such as depression and in preclinical models of PTSD. However, there is no *in vivo* evidence supporting a role of these central immune cells in humans with PTSD. Therefore, the purpose of this study was to utilize positron emission tomography (PET) of translocator protein (TSPO) probe [¹⁸F]FEPPA (an imaging biomarker of microglia activation), to investigate microglia status in living humans with PTSD.

Methods: TSPO binding ([¹⁸F]FEPPA total distribution volume V_T) was measured with PET and arterial blood sampling in 10 participants who fulfilled DSM-IV criteria for PTSD (mean age 39 years, 50% male) and 53 healthy trauma-unexposed controls (HC; mean age 29 years, 47% male). A magnetic resonance image was acquired for delineation of brain regions of interest (ROIs) by co-registration with the dynamic PET image. Repeated measures analysis of variance (RM-ANOVA) was employed to evaluate group differences (PTSD vs HC) in V_T amongst 9 cortical and subcortical ROIs, controlling for the TSPO genetic polymorphism rs6971 that influences [¹⁸F]FEPPA binding (low binder was excluded).

Results: A marginally significant Group * ROI interaction ($F_{(3.02,181.03)} = 2.51, p = 0.06$) was observed across 9 ROIs although the overall group difference in FEPPA V_T between PTSD and HC was not significant ($F_{(1,60)} = 1.56, p = 0.22$). *Post hoc* analyses revealed that the difference reached significance in the anterior cingulate cortex (p -uncorrected = 0.044; +22%). [¹⁸F]FEPPA binding was not associated with measures of symptom severity in PTSD.

Conclusion: Our preliminary findings suggest a trend toward increased TSPO binding in PTSD, in particular within the anterior cingulate cortex, an area commonly implicated in mood disorders and of reported microglial activation in major depression. Further research with a larger sample size is warranted to improve statistical power and appropriately characterize and account for potentially confounding factors such as co-morbid depression and history of head trauma.

Can Brain Activity Predict Manual Dexterity Improvement after Surgery in Cervical Myelopathy?

Alicia Cronin*, BSc,^{1,2} Sarah Detombe, PhD³, Pat Doyle-Pettypiece, RN³, Sukhvinder Kalsi-Ryan, PhD⁴, Mark Speechley, PhD⁵, Neil Duggal, MD, MSc, FRCS(C),^{1,3} and Robert Bartha, PhD^{1,2}

¹Department of Medical Biophysics; ²Centre for Functional and Metabolic Mapping, Robarts Research Institute, The University of Western Ontario; ³Department of Clinical Neurological Sciences, University Hospital, London Health Sciences Centre; ⁴Department of Physical Therapy, University of Toronto, Toronto, ON, Canada; and ⁵Department of Epidemiology and Biostatistics, The University of Western Ontario, London, ON, Canada

Introduction: Cervical spondylotic myelopathy (CSM) is a degenerative disease of the spine that causes compression of the spinal cord and altered brain activity patterns related to task performance. CSM patients experience a variety of symptoms that reduce quality of life, including gait and bowel/bladder dysfunction, and disturbances in overall hand function/dexterity, which are particularly debilitating. CSM is potentially reversible following surgery, with 35% of patients improving.¹ However, it is currently unclear whether changes in manual dexterity are attributable to spinal compression or the result of cortical reorganization. The objective of the current study is to determine whether changes in manual dexterity in CSM patients following spinal decompression surgery are associated with changes in brain activation measured by functional magnetic resonance imaging (fMRI).

Methods: 12 patients (10 men, mean age (\pm SD) 65 ± 11.9 years, 12 right-handed) with a clinical history of CSM and dexterity issues were scanned on a 3.0 Tesla Siemens Prisma Fit MRI scanner, prior to and six weeks after spinal decompression surgery. The motor pathway was activated during functional imaging using a block paradigm task, where subjects were instructed to perform a controlled finger-to-thumb motion using a button box, alternating between a 30 second rest period and a 30 second task period, for a total scan time of 5 minutes and 30 seconds. Group averages were created using cluster-based thresholding ($Z > 3.1$, corrected $p = 0.001$) and volume of activation (VOA) and % BOLD signal were determined using region of interest analysis. The mean difference in the parameters over the two time points were compared using a paired t-test ($p < 0.05$). All patients also completed the Graded Redefined Assessment of Strength, Sensation and Prehension, or GRASSP; an objective validated dexterity measure of functional improvement in CSM patients. GRASSP was measured at both time-points and the change in the GRASSP measurements were compared with both the change in VOA and change in % BOLD signal by linear regression.

Results: Following decompression surgery, there was a significant increase ($p = 0.02$) in the VOA of the contralateral supplementary motor area (SMA) when patients were performing the task with their right hand, as shown in the group average maps in Figure 1. In the contralateral primary somatosensory cortex (S1), a decrease in BOLD signal is approaching significance ($p = 0.051$). These preliminary results also suggest that patients with a less severe decrease in % BOLD signal (in the S1) have a clinically significant improvement in manual hand dexterity (GRASSP score, $r = 0.52$), although this association was not statistically significant ($p = 0.10$).

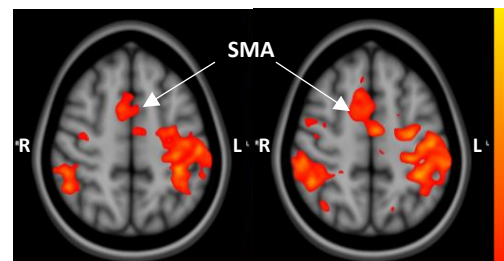


Figure 1: Group average maps ($n = 12$), when patients are tapping with right hand (Left: baseline, Right: 6-week post-op)

Conclusion: This interim analysis shows a significant increase in VOA of the contralateral SMA after surgery in CSM patients potentially due to neuronal recruitment to assist in functional recovery. The demonstration of neuronal recruitment in the motor regions is consistent with previous studies in CSM patients.² Patient recruitment is currently ongoing to increase the statistical power of this study to detect a statistically significant association between % BOLD signal in the S1 and improved manual hand dexterity score, which would add to our understanding of the important role of this brain region in the recovery of manual function following surgery.

References: [1] Bernhardt *et al.*, 1993; [2] Duggal *et al.*, 2010

***In Vitro* Characterization of novel PET Radiotracers for the “Glycogen Synthase Kinase-3 Hypothesis of Alzheimer’s Disease”**

Ashley Knight^a, Cassis Varlow^a and Neil Vasdev^{a,*}

^aAzrieli Centre for Neuro-Radiochemistry, Brain Health Imaging Centre, Centre for Addiction and Mental Health & Institute of Medical Science
and/or Department of Psychiatry, University of Toronto

*neil.vasdev@utoronto.ca

Introduction: Glycogen synthase kinase 3 (GSK-3) dysregulation has been implicated in the pathogenesis of several mental health illnesses. Recently, a “GSK-3 Hypothesis of Alzheimer’s disease” has been proposed¹. Our laboratory was the first to develop PET imaging agents for imaging GSK-3 *in vivo* with positron emission tomography (PET)² and led to our development and preclinical PET neuroimaging of [¹¹C]PF-04802367; [¹¹C]PF-367), the first selective and brain-penetrant GSK-3 inhibitor³. We recently reported the next-generation and initial *in vitro* and *in vivo* characterization of PF-367 derivatives, through rigorous medicinal chemistry studies in collaboration with big pharma⁴. PET studies in non-human primates using one of our new generation ligands, [¹¹C]OCM-44, displayed significantly higher brain exposure with SUV_{peak} of 2.0-2.5 in contrast to the 1.0 SUV uptake of [¹¹C]PF-367. The present studies set out to further characterize [³H]PF-367 and our novel lead [¹¹C]OCM-44 *in vitro* in control and post-mortem tissues from human patients with Alzheimer’s disease (AD) and related dementias and to establish the criteria for first-in-human translation of this radiopharmaceutical.

Methods: Herein, [³H]PF-367 and [¹¹C]OCM-44 specificity was evaluated in brain tissue sections of a Tg2576 mouse model of Alzheimer’s disease compared to aged controls, and human tissue using *in vitro* autoradiography and homogenate binding. Thin section [³H]PF-367 and [¹¹C]OCM-44 autoradiography in gray matter of brain tissue revealed high, ubiquitous total GSK-3 binding. Target density estimates were compared between groups by using a single saturating concentration of the radioligands. Specific binding was experimentally determined for [³H]PF-367 and [¹¹C]OCM-44 in healthy control human post-mortem tissue sections.

Results: Specificity of both radioligands was shown through competition with structurally dissimilar compounds showing true specificity. In addition, a 17-fold increase in [³H]PF-367 specific binding was observed in cortex of Tg2576 Alzheimer’s disease (AD) mice compared to aged wild-type control animals indicating an increase in this model under pathological conditions, while initial *ex vivo* analysis showed a modest decrease of 1.1-fold compared to baseline and 1.4-fold decrease in the same model using [¹¹C]OCM-44 compared to age-matched controls. Preliminary saturation studies with [¹¹C]OCM-44 have revealed a 1.6-fold decrease in GSK-3 density in the cortex of post-mortem AD tissues compared to controls.

Conclusions: We have demonstrated the specificity of PF-367 and OCM-44, providing evidence of potential use for these radiotracers in AD diagnosis and drug development. Clinical translation with our lead radiotracers for GSK-3 are planned. Our newest lead molecules with GSK-3 β isoform selectivity are also being explored and will be presented.

References:

1. Hooper, C.; Killick, R.; Lovestone, S. The GSK3 Hypothesis of Alzheimer’s Disease. *Journal of Neurochemistry* **2007**, *104*(6), 1433–1439.
2. Vasdev N, Garcia A, Stableford WT, Young AB, Meyer JH, Houle S, Wilson AA. *Bioorg Med Chem Lett.* **2005**;15:5270–5273.
3. Liang, S. H.; Chen, J. M. & Vasdev, N. [with Pfizer et al], Discovery of a Highly Selective Glycogen Synthase Kinase-3 Inhibitor (PF-04802367) That Modulates Tau Phosphorylation in the Brain: Translation for PET Neuroimaging. *Angewandte Chemie* **2016**, *128*(33), 9753–9757. VIP Article.
4. Bernard-Gauthier, V.; Mossine, A. V.; Knight, A. & Vasdev, N [with Pfizer, Biogen and Eisai Pharmaceuticals, et al.] Structural Basis for Achieving GSK-3 β Inhibition with High Potency, Selectivity, and Brain Exposure for Positron Emission Tomography Imaging and Drug Discovery. *Journal of Medicinal Chemistry* **2019**, *62*(21), 9600–9617 (Cover Article).

Longitudinal MRI and TSPO-PET: Alzheimer's Disease interacts with Subcortical Stroke through inflammation

Al-Khishman N.^{1,3}, Roseborough A.², Fox M.S.³, Qi Q.^{1,3}, Levit A.², Hachinski V.⁴, Whitehead S.N.², and Thiessen J.D.^{1,3}

¹Medical Biophysics and ²Anatomy & Cell Biology, University of Western Ontario

³Lawson Health Research Institute, ⁴Clinical Neurological Sciences, University Campus

Introduction: Subcortical stroke and Alzheimer's Disease (AD) often coexist and exacerbate one another cognitively, and we suspect they interact through inflammation. Independently, subcortical stroke and AD increase inflammatory microglia and astrocytes, both of which may be dichotomized into phenotypes that are anti-inflammatory or proinflammatory. We previously used immunohistochemistry to show that (i) proinflammatory microglia are increased in white matter (WM) remote to the injury site if rat subcortical stroke is comorbid with prodromal AD and (ii) that in prodromal AD rats, similar postmortem WM inflammation correlated with cognitive decline. To predict cognitive decline, there is a need to quantify inflammation longitudinally. This is possible using positron emission tomography (PET) of a translocator protein (TSPO) that is upregulated in astrocytes and microglia during inflammation. In this study, we hypothesized that TSPO-PET can be used to quantify post subcortical-stroke spatiotemporal inflammatory differences between rats overexpressing a pathogenetic amyloid precursor protein variant (Tg) and their wildtype counterparts (Wt).

Methods: To model subcortical stroke, the right dorsal striatum was injected with the vasoconstrictor endothelin-1 or saline to yield four male 9-14 month old Fischer 344 rat groups; Tg-stroke (n=5), Wt-stroke (n=5), Tg-saline (n=5), Wt-saline (n=3). We imaged at baseline then post-stroke by 7-days and 28-days. To quantify inflammation, imaging included 33.1 ± 4.6 MBq [¹⁸F]FEPPA PET (Siemens Inveon). Immediately after PET, rats were transferred on the animal bed to a 3T MRI for T₂-weighted images (Siemens Biograph mMR) with a dedicated rat brain RF coil (Cubresa). All images were coregistered to the 7-days T₂-weighted MRI, which was used to delineate the infarct, frontal cortex, white matter along the corpus collosum, and to calculate uptake ratios (UR) the cerebellum. UR was analyzed with age as a covariate in a 4-way ANCOVA within time and region and between genotype and procedure (SPSS 25). To phenotype the inflammatory response, these rats and additional 7-day rats were sacrificed for immunohistochemistry of TSPO, astrocytes using GFAP, and proinflammatory microglia using iNOS and OX6. Immunohistochemistry analysis is underway (ImageJ 1.52a).

Results: In the infarct, [¹⁸F]FEPPA UR was elevated in the stroke groups at 7-days (figure 1). By 28-days, there was a larger drop in Tg-stroke (1.25 ± 0.44 UR) than Wt-stroke (1.77 ± 0.34 UR) as detected in a time-Tg/Wt interaction ($F_{(1,21)}=9.64$, $p<.01$). WM [¹⁸F]FEPPA UR changes were negligible, and this was confirmed by TSPO immunohistochemistry. At 28-days, iNOS agreed with [¹⁸F]FEPPA; cells were only positive in the infarct of Tg-stroke (173 ± 92 cells/mm²) and Wt-stroke (222 ± 232 cells/mm²). Contrarily to TSPO and iNOS, a preliminary analysis of OX6 showed remote WM inflammation at 28-days.

Conclusion: In this study, we were the first to use TSPO-PET to show that subcortical stroke comorbidity with prodromal AD decreases infarct inflammation at 28-days. This suggests a reduction of proinflammatory microglia as seen using immunohistochemistry of iNOS. Preliminary results indicate that unlike TSPO and iNOS, OX6 shows remote WM inflammation. Overall, this study suggests that a whole-brain spatiotemporal quantification of inflammation requires the development of *in vivo* protocols that can quantify multiple inflammatory markers and that inflammation is disrupted in the comorbidity of subcortical stroke with prodromal AD.

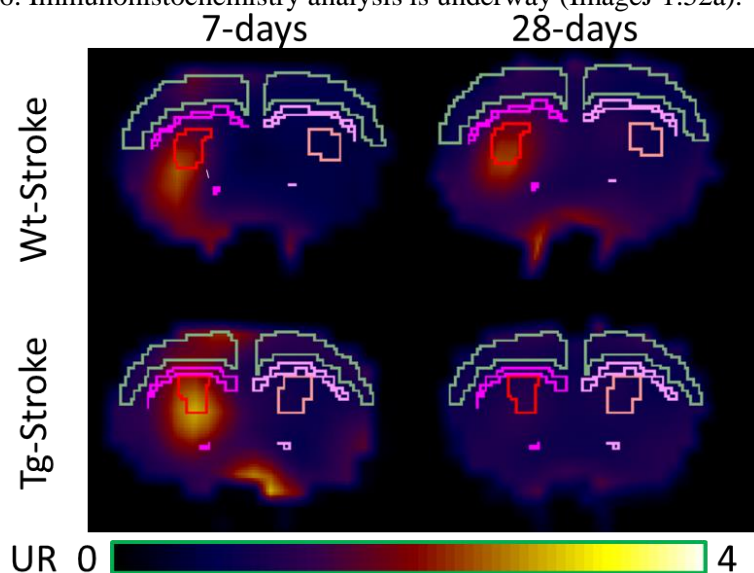


Figure 1. [¹⁸F]FEPPA PET maps of uptake ratio (UR) to the cerebellum. ROIs show ipsilateral (dark) and contralateral (bright) infarct (red), WM (purple), and frontal cortex (green).

Are Cognitive Deficits in Parkinson's Disease Associated with Dopaminergic Dysfunction: A Graph Theory Analysis

Alexander Mihaescu^{1,2,3}, Jinhee Kim^{1,2}, Sang Soo Cho^{1,2}, Maria Diez-Cirarda^{1,2,3}, Mikael Valli^{1,2,3}, Yuko Koshimori¹ & Antonio P. Strafella^{1,2,3,4}

1. Research Imaging Centre, Campbell Family Mental Health Research Institute, Centre for Addiction and Mental Health, University of Toronto, Ontario, Canada.
2. Division of Brain, Imaging and Behaviour – Systems Neuroscience, Krembil Research Institute, UHN, University of Toronto, Ontario, Canada.
3. Institute of Medical Science, University of Toronto, Ontario, Canada.
4. Morton and Gloria Shulman Movement Disorder Unit & E.J. Safra Parkinson Disease Program, Neurology Division, Dept. of Medicine, Toronto Western Hospital, UHN, University of Toronto, Ontario, Canada.

Disclosures: All authors declare none.

Introduction: Cognitive decline in PD is a common sequela of the disorder, occurring in up to 60% of PD patients. Previous research found that there is a gradual loss of D2R in the cortex of PD patients as parkinsonism advances. Brain network analysis using graph theory methods is a new way of investigating the whole-brain communication patterns between different brain regions. This project investigates the network connectivity patterns that occur in the dopamine D2 receptors (D2R) network in Parkinson's disease (PD) patients with mild cognitive impairment (PD-MCI) and normal cognition (PD-NC) using graph theory analysis methodology.

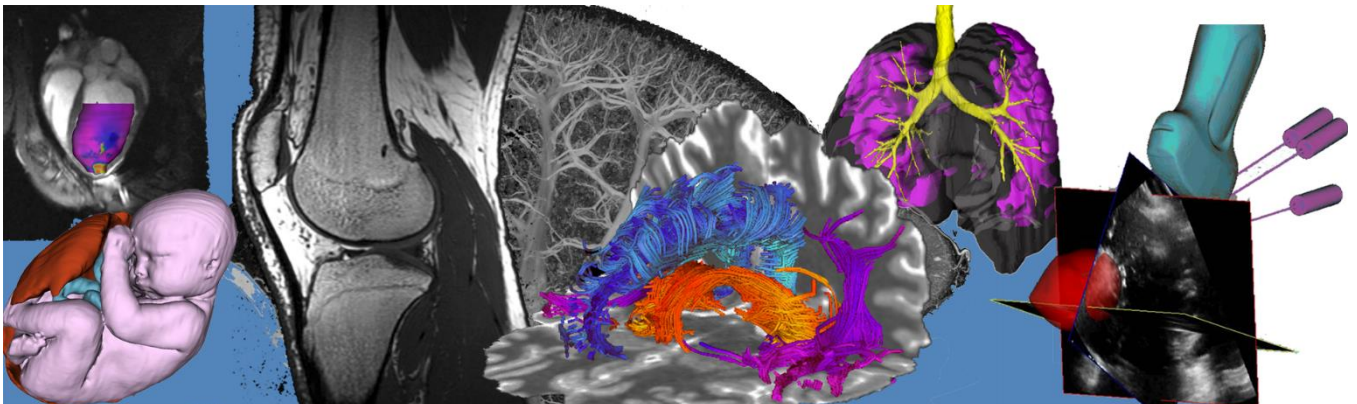
Methods: 43 participants (healthy control=13, PD-NC=13, PD-MCI=17) underwent 90 minute PET scans with the radioligand [¹¹C]FLB 457, which binds with high affinity to D2 receptors in the cortex. PET scans were acquired using a high-resolution PET/CT Siemens Biograph HiRez XVI PET scanner. An MRI scan for co-registration was also acquired using a 3.0 T GE Discovery MR750 MRI system. Imaging data was processed using both ROMI, an inhouse image processing software, and PMOD v4.005 PET analysis software package to calculate the partial volume error corrected binding potentials for each region of interest (ROI) in the AAL atlas. Graph theory analysis was performed using the Graph Theory Analysis Toolbox for MATLAB.

Results: Two brain networks were examined: the dorsal dopamine network with nigrostriatal dopamine projections comprised of 16 bilateral ROIs, and the mesolimbic dopamine network with ventral tegmental area projections comprised of 28 bilateral ROI. The dorsal dopamine brain network was found to be more efficient in PD-NC patients compared to PD-MCI patients, with reduced small-worldness and clustering ($p < 0.05$). The mesolimbic dopamine network had reduced network efficiency in PD-NC compared to healthy controls, but no differences were found between the PD groups ($p < 0.05$).

Conclusions: Dopaminergic dysregulation in PD results in less efficient brain network architecture in PD-MCI patients compared to PD-NC.

Oral Presentation Abstracts

Session 7: Musculoskeletal Imaging and Technology



Validation of 3D ultrasound for bedside monitoring of osteoarthritis-induced synovium inflammation and cartilage degradation

Sam Papernick,^{1,2} Robert Dima,³ Derek J Gillies,^{1,2} Tom Appleton,^{3,4,5} and Aaron Fenster^{1,2,6}

¹Department of Medical Biophysics, ²Robarts Research Institute, ³Department of Health and Rehabilitation Science, ⁴Department of Physiology and Pharmacology, ⁵Department of Medicine, ⁶Department of Biomedical Engineering; Western University, London, Ontario, Canada;

Introduction: Osteoarthritis is the most common chronic disease in Canada, affecting 21% of the population, and is described as an abnormal remodeling of joint tissues caused by a host of inflammatory agents. Conventional x-ray radiography and magnetic resonance imaging (MRI) are widely accepted modalities for clinically assessing OA and its response to therapy; however, x-ray radiographs are unable to quantitatively assess synovium inflammation due to a lack of soft tissue sensitivity. While MRI shows adequate soft tissue sensitivity for detecting inflammation, scanning is expensive, associated with long acquisition times, and is inaccessible to many mobility-impaired patients. There is currently a gap in clinical care where patients are placed on waitlists for several weeks before they receive an MRI scan and can begin OA treatment. There is a need for an imaging modality that can overcome the limitations associated with x-ray and MRI, while providing physicians with volume measurements of the synovium and articular cartilage while in the clinic or at the patient's bedside. We propose the use of three-dimensional ultrasound (3D US) for providing physicians with high quality synovium and cartilage volume measurements without the aforementioned limitations. Our lab has previously validated the linear and volumetric measurement capabilities of a handheld 3D US acquisition device on wire and agar phantoms. The 3D US device acquires images by linearly translating a two-dimensional (2D) US transducer over a fixed distance, and produces reconstructed 3D images after 15 seconds of scanning. This work investigates the validation of our handheld 3D US device with MRI for assessing knee tissues of healthy and diseased patients.

Methods: For this work, 25 healthy volunteers had both knees scanned using our 3D US device, along with a 3T MRI system. US scans were acquired on a Canon Aplio i800 machine with a 14L5 linear transducer (10 MHz). The 3D US images of the articular cartilage were acquired with maximum knee flexion, and images of the synovium were acquired with 15° knee flexion. The MRI and 3D US images were manually segmented in 3D Slicer to produce 3D tissue models for each volunteer (Fig. 1a, 1b). Segmentations were completed by 2 users and repeated at a separate time point to assess interrater and intrarater reliability. Intraclass correlation coefficient (ICC) estimates were calculated based on a mean-rating ($k = 2$), consistency, 2-way random-effects model. ICC estimates less than 0.5 indicated poor reliability, between 0.5 and 0.75 indicated moderate reliability, between 0.75 and 0.9 indicated good reliability, and > 0.9 indicated excellent reliability.

Results: The 3D US scans were able to visualize suprapatellar effusion synovitis and articular cartilage degradation, both of which are clinically relevant for assessing and monitoring OA development and response to treatment. ICC estimates were 0.89 for the synovium segmentations and 0.99 for the articular cartilage segmentations.

Conclusions: Our handheld 3D US acquisition device was able to visualize clinically relevant anatomy needed for monitoring OA progression and response to treatment. Initial reliability assessments indicate good reliability for synovium and excellent reliability for cartilage segmentations from 3D US images. Improvements on the reliability of synovium segmentations may be necessary for future clinical implementation. Future work will focus on comparing the volumes of the tissue models produced between MRI and 3D US. Test/retest reliability of segmentations will also be assessed in future work. 3D US may enable a physician to directly observe the state of OA, monitor its development over time, and its response to treatment without the limitations associated with x-ray and MRI.

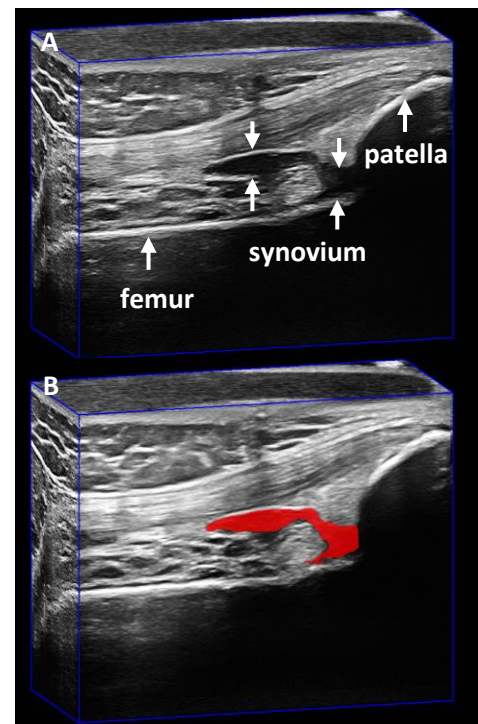


Figure 1: Cross section of a suprapatellar 3D US acquisition of a knee displaying relevant anatomical structures and mild effusion synovitis (A), with a manual segmentation of a slice in the 3D image (B).

Four-Dimensional Computed Tomography to Measure Distal-radial and Radio-carpal Joint Congruency Following Wrist Fracture

Puneet Ranota^{1,2,3}, Ting-Yim Lee^{4,5,6}, Nina Suh^{6,7,8}, Emily Lalone^{1,2,3,6,8}

¹School of Biomedical Engineering, ²Department of Mechanical and Materials Engineering, ³Faculty of Engineering, ⁴Medical Biophysics, ⁵Robarts Research Institute, ⁶Lawson Health Research Institute,

⁷Roth|McFarlane Hand and Upper Limb Center, ⁸Department of Surgery, Western University, London, Ontario

INTRODUCTION:

The wrist consists of articulating structures that allow for complex motions while maintaining stability. Previous studies examining carpal contact mechanics have been limited by their ability to capture dynamic data (3D reconstructions + time). Four-dimensional Computed Tomography (4DCT) captures joint motion and can be used to measure 3D joint space which is known to be affected by wrist osteoarthritis. A previous study investigated only the distal radioulnar joint (DRUJ) joint space in patients with wrist fractures, but the impact of the fracture on the surrounding joint mechanics was not examined. The purpose of this study was to employ a 4DCT approach and examine the joint congruency at the DRUJ and radiocarpal joints following a wrist fracture.

METHODS:

A participant with a distal radius fracture was recruited. Radiographs were used to measure Radial Inclination (RI), Dorsal Angulation (DA) and Ulnar Variance (UV). The GE Revolution 4DCT Scanner was used to scan the wrist for 8 seconds in a pronation-supination motion (25 frames) at a radiation dose less than standard CT (0.2 Gy). The 3D reconstructions of the radius, ulna, scaphoid and lunate were created using static and dynamic scans. A surface-based registration algorithm (ICP) was used to match the kinematic bone surfaces with the static bone surfaces. An inter-bone distance algorithm was used to analyze the contact areas for each joint.

RESULTS:

The 8-month follow-up radiographs (RI: 18.6°, DA: 23.4°, and UV: 7 mm) indicated unacceptable radiographic alignment according to ASSH standards (RI <15°, DA >10° and UV ≥3 mm). The changes in joint congruency through pronation at the radiocarpal and distal radioulnar joints are shown in Table 1. Overall, joint congruency surface area, as shown in the proximity maps in Figure 1, increased in the radiolunate joint (figure 1a), and decreased in the radioscapoid joint (figure 1b) and in the distal radioulnar joint through pronation (figure 1c).

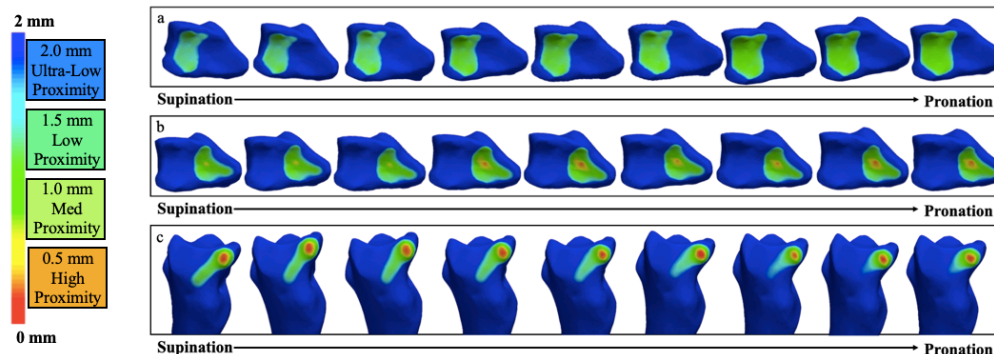
CONCLUSION:

Preliminary results suggest that as the wrist moved from supination to pronation, there was less cartilage contacts at the radioscapoid and distal radioulnar joints, but more cartilage contact at the radiolunate joint. Early results show changes in contact area in the radiocarpal and distal radioulnar joints which has implications in increasing our understanding of altered joint contact mechanics and its association with osteoarthritis development.

Joint	Frame Number (approx. 1 frame/second)								
	1	4	7	10	13	16	19	22	25
Radiolunate	29.6%	30.0%	30.5%	32.5%	32.9%	32.9%	35.0%	34.8%	36.1%
Radioscapoid	27.1%	26.6%	26.7%	28.1%	27.4%	26.3%	25.5%	25.6%	24.9%
Distal Radioulnar	33.7%	32.2%	32.0%	32.3%	31.3%	30.9%	27.3%	23.1%	23.6%

Table 1. Changes in contact areas (with inter-bone distance= 2.0 mm) for each joint. The contact areas of the lunate, scaphoid and ulna on the radius through pronation were compared to static contact surface areas.

Figure 1. Joint congruency maps for each joint during wrist pronation-supination motion. A color-bar (0-2 mm: red-blue) corresponds to high (red), medium (yellow-green), low (green-blue) and ultra-low (blue) proximity. Figure 1a. Radiolunate Joint. Figure 1b. Radioscapoid Joint. Figure 1c. Distal Radioulnar Joint.



Sparse-view cone-beam CT reconstruction for assessing migration in knee arthroplasty: a phantom studyRudolphe J Baronette^{1,2,3}, Santiago Cobos^{1,2,3}, Steven I Pollmann², Xunhua Yuan²,Matthew G Teeter^{1,3,4,5}, David W Holdsworth^{1,2,3,4}¹Western Bone and Joint Institute²Imaging Research Laboratories, Robarts Research InstituteDepts. of Medical Biophysics³ and Surgery,⁴ Western University⁵Lawson Health Research Institute, London ON, Canada

Introduction: Radiostereometric analysis (RSA) utilizes two x-ray projections to accurately determine the locations of a sparse distribution of marker beads in implant migration studies. Recent advances in cone-beam CT (CBCT) have accentuated reconstruction from few views using iteration and prior knowledge.^{1,2} The purpose of this study was to explore the concept that conventional RSA imaging, traditionally performed with two geometrically calibrated x-ray detectors, is a subset of sparse-view cone-beam CT (CBCT) reconstruction. In both CBCT and RSA, the x-ray acquisition geometry is precisely calibrated, allowing a mathematical reconstruction technique to “backproject” the rays along known geometric paths. In this study, we demonstrate that conventional RSA, performed with a direct digital x-ray detector is a subset of CBCT reconstruction.

Methods: Image acquisitions were performed using a ceiling-mounted x-ray system (Proteus XR/a, GE Medical Systems, 90 kVp, 1 mAs), using a flat-panel detector (DRX-3543, Carestream Health) that has a 2560 x 3072 image matrix over a nominal 35 x 43 cm field of view with a 0.139 mm pixel pitch. Using anatomical bone models instrumented with 0.8 mm tantalum beads, 217 projection views were acquired at 1° increments. A total of five (n = 5) translations were applied to the tibia, with inter-segment translations between 0 and 2.0 mm in all three axes using a three-axis stage with 1 μm precision. Intrinsic x-ray camera geometric parameters were determined from a geometric calibration cage. Marker bead locations are derived from two views using conventional RSA analysis, and from 2, 3, 5, 10, and 217 projection images, using CBCT reconstruction and customized analysis software. Resulting CBCT image volumes were reconstructed at an isotropic voxel size of 0.11 mm. A repeated measures one-way ANOVA was used for statistical analysis.

Results: Overall, the average error of CBCT-derived measurements was lower when compared to the average error of RSA-derived measurements (p=0.418). RSA-derived measurements showed an average error of 41 μm. In contrast, the average error CBCT-derived measurements reconstructed from 2, 3, 5, 10, and 217 views were 66.5 μm, 20.7 μm, 24.0 μm, 29.1 μm, and 23.0 μm, respectively.

Conclusion: In this study, we demonstrated that conventional RSA is a subset of the general class of CBCT reconstruction. CBCT-derived measurements, using three or more views, were comparable to the average error in RSA-derived measurements. Recent developments in CBCT will be advantageous during the development of new RSA techniques to improve performance through additional view angles, iterative reconstruction, and deep learning reconstruction algorithms. The use of direct digital detectors may allow low-dose cone-beam CT techniques to supplant dedicated RSA, in some applications.

References: 1. Cao, Q., et al. (2016). *Phys Med Biol* 61(20):7263-7281. 2. Gajny, L., et al. (2019). *Eur Spine J* 28(4):658-664.

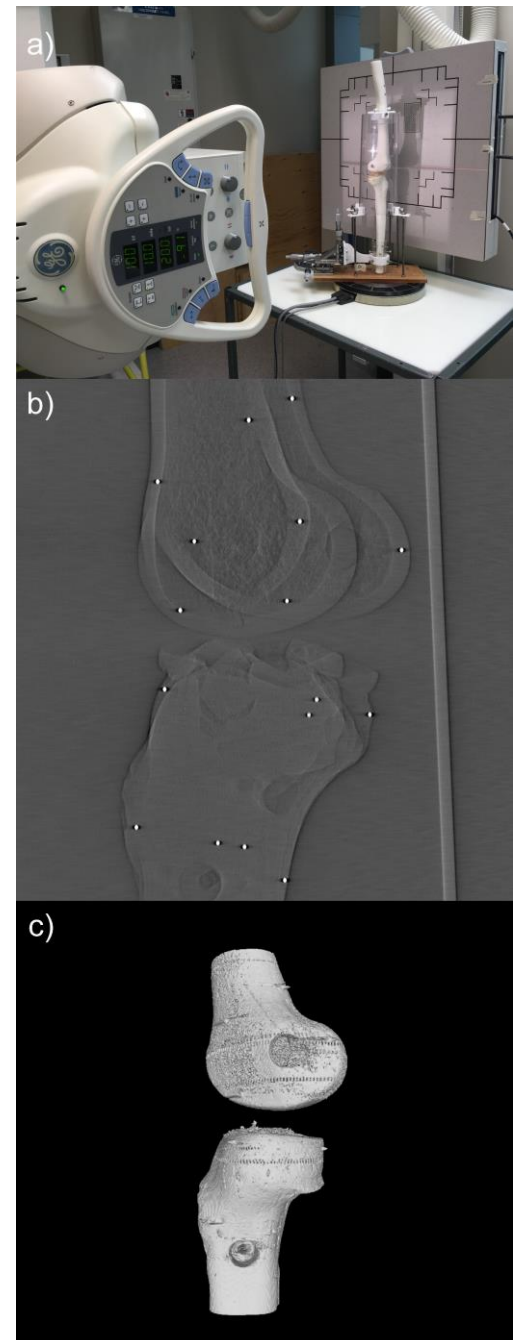


Fig. 1: (a) photo of the CBCT setup used to generate image volumes; (b) marker beads reconstructed from two views; and (c) isosurface generated from 217 view reconstruction.

MR-Guided Focused Ultrasound-Induced Blood-Spinal Cord Barrier Opening Facilitates a Localized Increased Uptake of Trastuzumab into Leptomeningeal Metastases

Paige Smith^{1,2}, Natalia Ogrodnik¹, Janani Satkunarahaj¹, Meaghan O'Reilly^{1,2}

1 Physical Sciences, Sunnybrook Research Institute; 2 Medical Biophysics, University of Toronto

INTRODUCTION Due to a lack of effective treatment options, leptomeningeal metastases (LM) are often considered a terminal diagnosis, affecting ~10% of patients with solid tumors [1]. Systemically delivered chemotherapeutics have limited effectiveness in treating tumors situated in the spinal cord because of the presence of the blood-spinal cord barrier (BSCB) which is functionally and morphologically similar to the blood-brain barrier (BBB) [2]. Tight junctions between non-fenestrated endothelial cells, astrocytes, pericytes and the basal lamina limit active and passive transport of molecules from the bloodstream into the tissue [3]. This prevents nearly all large molecules (>500 Da) from accumulating in therapeutically relevant quantities [4]. Under MRI guidance, focused ultrasound (FUS) in combination with circulating microbubbles has been used to temporarily open the BBB and increase the concentration of trastuzumab (148 kDa) in sonicated regions of the brain compared to un-sonicated regions [5]. The purpose of this study is to apply a similar treatment approach as was used in the brain to deliver trastuzumab to tumor masses in a rat model of spinal cord LM and to quantify the concentration of the drug both inside and outside of the sonicated region. Additionally, the time-course of clearance of free drug in the tissue will be evaluated.

METHODS Three athymic rats underwent a laminectomy at L4 and a catheter was inserted into the subarachnoid space and directed 2 cm cephalad. 10 days post-surgery, HER2+ human breast cancer cells (MDA-MB-231-H2N) suspended in Matrigel were injected via the catheter. Tumors were confirmed on contrast-enhanced T1w MRI at 7T one-week post-cell implantation and were treated using FUS 2 weeks post-cell implantation. Gadolinium (0.1 mg/kg), trastuzumab (0.38 mL/kg) and Definity microbubbles (0.02 mL/kg) were injected intravenously immediately before FUS treatment with a spherically-focused single-element PZT transducer (F#0.8, 580 kHz, 10 ms burst at 1 Hz for two minutes). BSCB opening was confirmed using T1w MRI and Evans blue dye was injected intravenously to locate the sonicated region after removal of the spinal cord. The rats were transcardially perfused with saline followed by 10% neutral buffered formalin two hours post-treatment. 5µm sagittal sliced sections of the spinal cord were stained with Hematoxylin and Eosin (H&E) and an anti-human IgG antibody. A separate cohort of healthy rats (N=12) were treated with FUS in a similar manner as above at 2 separate locations in the spinal cord. The rats were transcardially perfused either 2 hours- (N=3), 24 hours- (N=3), 48 hours- (N=3) or 7 days- (N=3) post FUS with saline. 4 mm sections of sonicated tissue (N=2/rat) and 4 mm sections of un-sonicated tissue (N=2/rat) were removed and homogenized. The tissue lysate was used in the Abcam IgG Human SimpleStep ELISA® Kit (Catalog No.ab195215) to measure the trastuzumab concentration.

RESULTS FUS-induced BSCB opening was achieved in all rats as confirmed on MRI. Increased IgG signal was seen on histology in the sonicated regions of the tumors relative to the un-sonicated regions of the tumors and relative to the healthy tissue in both the sonicated and un-sonicated regions. The highest concentration of trastuzumab was observed in the sonicated sections 2 hours-post FUS (1.77 mg/g tissue) with a mean increase above the later time points (0.41 mg/g tissue @ 24 hours, 0.24 mg/g tissue @ 48 hours, and 0.19 mg/g tissue) and a mean increase above the un-sonicated sections 2 hours-post FUS (0.16 mg/g tissue).

CONCLUSIONS MR guided FUS can be used to temporarily open the BSCB in a localized manner. This process allows systemically circulating large molecules such as trastuzumab to exit the bloodstream and enter the tissue in quantities higher than when the BSCB is closed. When both tumor and healthy tissue were sonicated, increased trastuzumab was detected within the tumors. The free drug appears to be cleared by 24 hours post-treatment. This work will be useful in future longitudinal studies on treating LM with FUS in combination with trastuzumab.

REFERENCES

- [1] S. Taillibert & M. Chamberlain, *Handb Clin Neurol* **149**, 2018.
- [2] N. R. Saunders *et al.*, *F1000Research* **5**, 2016.
- [3] V. Bartanusz *et al.*, *Ann Neurol* **70**(2), 2011.
- [4] W. M. Pardridge, *NeuroRx* **2**(1), 2005.
- [5] M. Kinoshita *et al.*, *PNAS* **103**(31), 2006.

Diffusion Tensor Tractography of Tendons as a Tool for Assessing MRgFUS Ablation

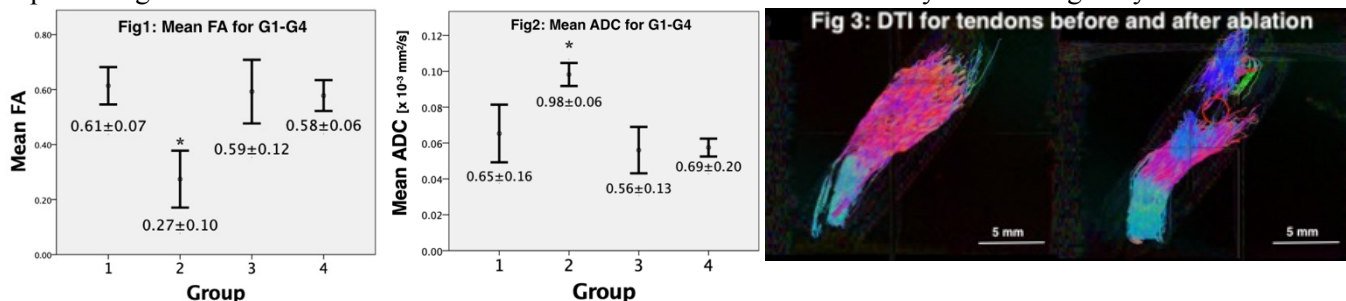
William Chu Kwan¹, Warren Foltz², Ben Keunen¹, Matt Walker², Karolina Piorkowska¹, Adam Waspe¹, James Drake¹ ¹CIGITI, Hospital for Sick Kids. ²University Health Network.

Introduction. Non-invasive ablation of tendons using Magnetic Resonance-guided Focused Ultrasound (MRgFUS) is a viable application that could precisely disrupt a tendon transcutaneously. Promising tools for monitoring ablation in tendons are Diffusion Tensor Magnetic Resonance Imaging (DTI) and tractography. They provide a quantitative, directional, and visual assessment of tendon tract integrity, superior to changes visualised in T1-weighted imaging. Given that tendon fascicles are organized into tracts, fractional anisotropy (FA) and apparent diffusion coefficient (ADC) could quantify changes following ablation, and tractography could visually demonstrate tendon architecture changes and disrupted fascicle directionality. This study aims to evaluate diffusivity parameters and tractography as tools to assess tendons before and after MRgFUS ablation treatments.

Methods. *Ex-vivo* porcine flexor tendons (n=4) were dissected, degassed, and embedded in 2% agar at the magic angle of 55° relative to B₀ to maximize tendon T₂. Pre- and post-ablation imaging were acquired in a Bruker BioSpin 7T MRI with a 7.2 cm inner diameter RF transmit coil and anatomically shaped rat brain receiver coil. Ablation was performed with a custom high-field small animal HIFU system (IGT, France), at a frequency of 2.5 MHz at 8 W for 30 seconds, reaching central temperatures greater than 60°C for more than 20 seconds based on real-time MR thermometry achieving ablative thermal dosages. DTI was performed using a 3D spin-echo segmented EPI technique (4 segments, TR=1200 ms, TE=26 ms, δ/Δ=3.5/10 ms, NEX=1, 1 b0 image, 12 diffusion directions with Jones sampling scheme with b=400 s/mm², 160x160x60 matrix over 32x 32x24 mm FOV for 200x200x400 μm spatial resolution, 250 kHz effective bandwidth, 62 min acquisition). Diffusion tractography was constructed using DiffusionToolkit 0.6.4.1 and TrackVis 0.6.1. Tracking used a tensorline propagation algorithm, and an angle threshold of 35°. Treatment volume segmentation was manually performed using MIPAV 9.0.0. Statistical analysis compared the FA and ADC averages pre- and post- ablation in the tendons within (n=4) and distal (n=4) to the ablated volume (AV). Thus, this study compared 4 groups: pre-ablation within AV (G1), post-ablation within AV (G2), pre-ablation distal to AV (G3), post-ablation distal to AV (G4). A one-way ANOVA and student's *t*-test determined differences within and between groups. Statistical significance was set at p<0.05.

Results. Within the AV, FA and ADC values for pre-ablated, compared to post-ablated tendons, were found to be significantly different; FA pre-ablation = 0.61±0.07 and post-ablation = 0.27±0.10 (p<0.005), ADC pre-ablation = 0.65±0.16x10⁻³ mm²/s, and post-ablation = 0.98±0.06 (p<0.05). In tendons distal to the AV, there was no significant difference found in either FA or ADC when comparing pre- and- post ablation; FA pre-ablation = 0.59±0.12 and post-ablation = 0.58±0.06, ADC pre-ablation=0.56±0.13 and post-ablation=0.69±0.20 (both p>0.05). Also, there was no significant difference in FA and ADC within groups (p>0.05) (Fig1, Fig2). With tractography, visual tendon tract disruption at the level of MRgFUS treatment was confirmed in all tendons (Fig3).

Conclusions. This is the first study that investigated changes in diffusivity parameters and tendon tractography following MRgFUS ablation. The decrease in FA and increase in ADC within the treatment volume following MRgFUS ablation were consistent with changes in anisotropy after disruption of tendon fascicles and loss of microstructural integrity. No statistical differences were observed in either FA or ADC in tendons pre-ablation within the AV, and distal to the AV pre- and post-ablation indicating there were no tendon structural changes in these regions. Additionally, diffusion tractography visually demonstrated the discontinuation of tendon fascicles at the level of ablation. Clinically, DTI and tractography could assess tendon integrity pre- and post-MRgFUS ablation in surgically treated conditions such as musculotendinous contracture in spinal cord injury or cerebral palsy, idiopathic toe walking, and Achilles tendon lengthening for diabetic foot. DTI and tractography are a promising evaluation tool for non-invasive treatments of conditions currently treated surgically.



MRI characterization of a novel porous 3D printed metal scaffold

Gregory Hong, Tina Khazaei, Santiago Cobos, Maria Drangova, David W Holdsworth
Robarts Research Institute, Western Bone and Joint Institute, Department of Medical Biophysics, Western University, London, Ontario, Canada

Introduction: The demand for hip and knee replacements continue to rise in Canada with a 17% increase in the number of arthroplasties performed over the past 5 years. Unfortunately, 9700 (7%) of these surgeries were for implant revisions, which are more complex than primary surgeries and result in longer recovery time and higher procedure costs. Infection is the most common reason for early revision (within 5 years of primary surgery) of both hip and knee replacements for arthritis.¹ The gold standard treatment of periprosthetic infection is to implant temporary antibiotic impregnated cement spacers in a 2-stage revision. This has the obvious downside of requiring two surgeries, with the associated cost and potentially problematic bone loss. We aim to address this concern with a 3D printed porous metal (titanium) scaffold with favorable mechanical properties that can be filled with antibiotics and deployed as a permanent cementless replacement for the failed solid implant. These porous scaffolds have another benefit: the decreased overall density of the high magnetic susceptibility metal will decrease the susceptibility related metal artifacts, leading directly to better monitoring of the infection and potentially allowing for *in-vivo* tracking of the antibiotic's elution through quantitative imaging of contrast agent. To accomplish this, we need to better understand the MR properties of porous metal scaffolds; thus our objective is to characterize the signal loss and magnetic susceptibility of titanium scaffolds of varying porosities.

Methods: To measure the effect of varying porosity on MRI, 5 gyroid-based scaffolds were designed by repeating a 6-mm³ gyroid unit cell and varying its wall thickness between 0.2 mm – 0.8 mm to achieve nominal porosities between 90% and 60%, respectively. The resulting scaffold is truncated to conform to a cylinder with 17 mm diameter and 40 mm length and 3D printed in titanium (Ti-6Al-4V, $\chi = 182 \text{ ppm}$)² along with a matching solid cylinder. The fabricated porosity is derived through the mass of the scaffolds and measured density of the printed titanium.

Imaging: The cylinders are placed in a previously presented fiducial phantom³ that establishes a co-registration between scan and simulation. B_0 field maps were calculated from the difference in phase accumulation between two gradient-echo scans at 3T (8-channel head coil; 256x128x128; 1 mm isotropic; TE = 3, 3.5 ms; TR = 15 ms)

Analysis: Signal-void volume was measured through thresholding the early echo magnitude image. An estimation of the scaffold's effective susceptibility was achieved by comparing the scanned field maps against simulated field maps of a cylinder assigned susceptibility values ranging from water to titanium (-9 to 182 ppm²).

Results: Figure 1 shows the decreasing artifact with increasing scaffold porosity. Figure 2 shows the relationship between the scaffold's fabricated porosity and both signal-void volume (number of low signal voxels) and effective susceptibility. The susceptibility estimates give a highly correlated linear relationship with a 100% porosity value of $\chi = -9.9 \text{ ppm}$, similar to the expected value of pure water ($\chi = -9.06 \text{ ppm}^2$).

Conclusions: We have shown that artifact size and effective susceptibility are strongly correlated with porosity. The reduced artifact around porous implants is promising for MR imaging as lowering effective densities reduces the artifact size to within millimeters of the scaffold, which clearly shows potential for imaging around implants made using this scaffold and likely will allow us to use quantitative imaging techniques to map gadolinium deposition for tracking elution of antibiotic.

1. Canadian Institute for Health Information. Hip and Knee Replacements in Canada, 2017–2018: CJRR Annual Report. Ottawa, ON: CIHI; 2019.
2. Schenck, J. F. Med. Phys. 23, 815-850, doi:10.1118/1.597854 (1996).
3. Hong G., *et al.* Validation of simulated vs. experimentally acquired B_0 field maps surrounding metal. In: *Proceedings of the 2019 IMNO Symposium*; 2019

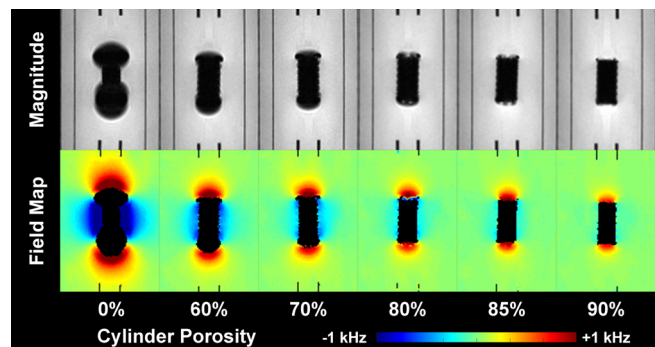


Figure 1: Central slice of MR images of the 6 cylinders (top) and corresponding measured field map (bottom)

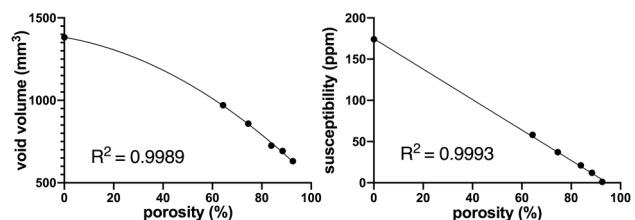
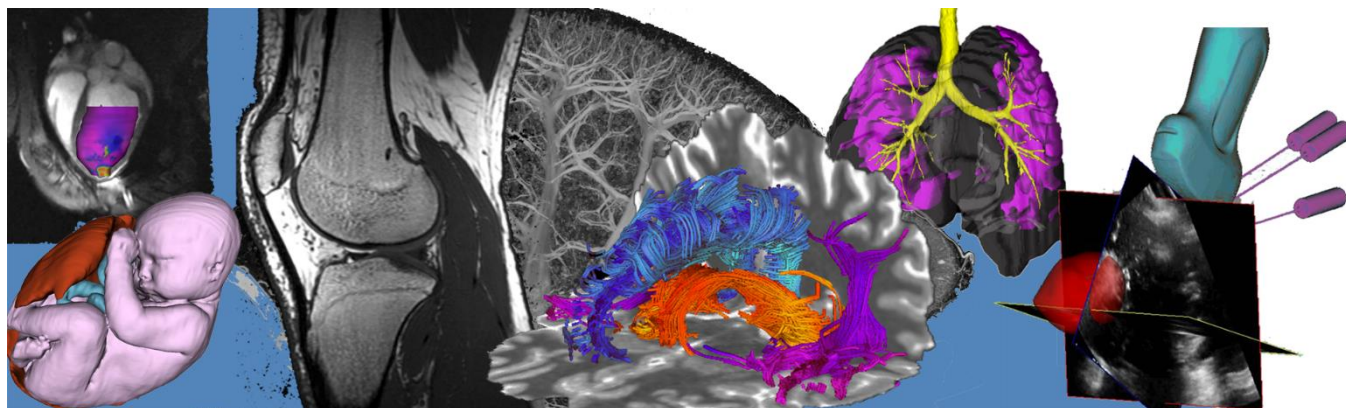


Figure 2: Measured signal-void volume and estimated susceptibility of scaffolds of varying porosity.

Oral Presentation Abstracts

Session 8: Cardiovascular and Vascular Imaging



Non-Invasive MRI Engraftment Localization Of Stem Cell-Derived Cardiomyocyte Therapy

Moses Cook BSc¹; Jill Weyers PhD³; Rocco Romagnuolo PhD^{2,4}; Beiping Qiang PhD^{2,4}; Jennifer Barry VT³; Xiuling Qi MD PhD³; Graham A. Wright PhD^{1,3}; Michael A. Laflamme MD PhD^{2,4}; Nilesh R. Ghugre PhD^{1,3}

(1) Department of Medical Biophysics - University of Toronto; (2) McEwen Centre for Regenerative Medicine, University Health Network; (3) Schulich Heart Research Program, Sunnybrook Research Institute; (4) Toronto General Hospital Research Institute, University Health Network, Toronto, ON, Canada

Introduction: Myocardial infarction (MI or a heart attack) remains the most common cause of heart failure worldwide. The ischemic injury often results in extensive loss of cardiomyocytes that are replaced by non-functional scar tissue. New cell-based technologies utilizing human pluripotent stem cell-derived cardiomyocytes (hPSC-CMs) present a novel method to repair the scar and restore the heart's contractility. Such approaches aim to achieve an increase in new viable cells within the dead scar region. However, the mechanisms of host-graft integration and efficacy of therapy need to be established prior to translation into humans. To this end, the objective of our study was to utilize regional strain deformation and high-resolution Late Gadolinium Enhanced (LGE) Cardiovascular Magnetic Resonance (CMR) to characterize the graft in an in vivo porcine model of MI.

Methods: Images were acquired on a 3T whole body MRI scanner. Yorkshire pigs were either treated with cells (N=2) or vehicle/control (N=2) at week 3 post-MI and then imaged up to 4 weeks post transplantation. hPSC-CMs were delivered surgically into the infarct territory via a lateral thoracotomy procedure. Cine SSFP imaging was utilized to assess global and regional cardiac function as well as strain deformation using tissue tracking (Circle CVI42). Strain deformation was chosen as it may give quantitative evidence of improved cardiac contractility in 2 orthogonal directions. Following administration of gadolinium contrast agent, free breathing navigator-gated high-resolution LGE imaging was conducted (TI = 350ms, matrix size = 224 x 224, resolution = 1x1x3 mm). LGE has the capability of highlighting the area of infarction in-vivo, as well as the possibility of graft localization as healthy myocardium does not uptake gadolinium, thus appearing dark on LGE images.

Results: We saw spatial correlation of graft localization between 3 LGE and histological ground truth observations. A representative section of LGE and histology were reoriented using landmarks as shown in Figure 1. Infarcts were predominantly apical and anteroseptal. Cells were delivered in this region, hence strain assessment was performed in segment 13 of the AHA model. In this segment at 4 weeks post transplantation, the two vehicle-injected animals recorded impaired peak radial strain (-4.2% and -3.6%) and peak circumferential strain (4.8% and 4.6%). In contrast, the two cell-treated animals demonstrated an increase in both radial (11.4% and 9.3%) and circumferential strain (-7.9% and -7.1%) in this graft associated region. Segment 7 contains the engraftment as encircled in Figure 2.

Conclusion: This study showcases the feasibility of using high-resolution LGE CMR to localize cellular grafts in vivo following regenerative therapy. Strain deformation could distinguish alterations in regional contractile function between cell treated and untreated groups, and demonstrated good correspondence and improved performance in both radial and circumferential strain within segment 13. In contrast, the vehicle-injected animal demonstrated a loss of both radial and circumferential strain functionality. Establishing a comprehensive CMR imaging platform can help determine the underlying mechanisms of cell therapy in MI and potentially aid translation of new therapies to the ever-increasing MI-related heart failure population.

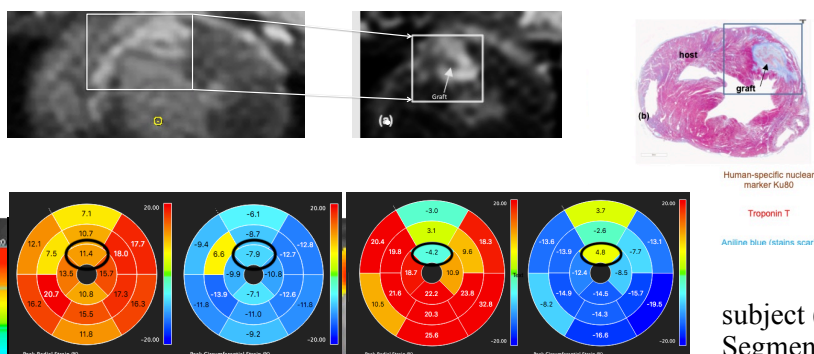


Figure 1a) and b): LGE image of left ventricle depicting bright scar (left), hPSC-CM engraftment with dark signal intensity (middle), and representative histological slices confirming graft location (right).

Figure 2: Polar plots of radial and circumferential peak strain of vehicle injected (right) and a hPSC-CM treated subject (left) in the AHA 17 segment model. Segment 13 contains the infarction.

Optimizing vasodilator dose to induce hyperemic stress during myocardial perfusion assessment in a porcine model

Jill J Weyers¹, Ahsan Javed², Jennifer Barry¹, Melissa Larsen¹, Graham A. Wright^{1,3,4}, Krishna Nayak², Nilesh R. Ghugre^{1,3,4}

¹ Physical Sciences Platform, Sunnybrook Research Institute, Toronto, ON; ² Ming Hsieh Department of Electrical Engineering, University of Southern California, Los Angeles, CA; ³ Schulich Heart Research Program, Sunnybrook Health Sciences Centre, Toronto, ON; ⁴ Department of Medical Biophysics, University of Toronto, Toronto, ON.

Introduction: Comparison of rest and stress blood flow is a key component of multiple cardiovascular magnetic resonance (CMR) techniques, including blood-oxygen-level-dependent (BOLD) imaging and other direct tests of coronary function, where diseased areas are evidenced by reduced myocardial perfusion ratio (MPR).

“Stress” for these techniques is usually a hyperemic state induced by pharmacological systemic vasodilation. Two commonly used vasodilators for both clinical and preclinical work are the adenosine receptor agonists adenosine and dipyridamole. However, when evaluating CMR techniques in large animal models, these vasodilators have been applied over a wide range of doses. As such, the optimal dose to induce maximal hyperemic response is unclear. Thus, our objective was to establish the optimal stress dosing scheme in the highly relevant porcine model, using BOLD imaging to assess vasodilator function.

Methods: Healthy Yorkshire pigs (n=12) of varying age, weight, and gender were injected with dipyridamole or various doses of adenosine during several rounds of rest and stress. Dipyridamole was given at the “standard” dose of 0.56 mg/kg, injected slowly over 4 minutes. Adenosine was given at the standard human dose (0.14 mg/kg/min) and increased to a 2X, 3X, and 4X dose. Myocardial BOLD imaging (via rest/stress ratio of T2 relaxation values) was employed to detect in vivo tissue perfusion changes. Blood pressure (BP) and heart rate (HR) were also monitored, and fluorescent microspheres were injected to confirm perfusion levels. After sacrifice, heart tissue was processed to quantify microsphere perfusion values.

Results: Dipyridamole induced the most consistent vasodilation, but its effect persisted for over an hour, well beyond its expected half-life of 25 minutes. Thus, further tests were not possible after Dipyridamole injection. While Aminophylline, an adenosine receptor antagonist, was able to reverse the effects of Dipyridamole to reset to resting conditions, its 8-hour half-life precluded further stress induction after its administration. The 1X and 2X doses of adenosine showed minimal changes in BP, HR, and MPR. However, both the 3X and 4X doses induced noticeable decreases in all three metrics (Fig 1). The 4X dose was most consistent, causing an immediate $31.5 \pm 2.5\%$ drop in BP and a $14.7 \pm 13.0\%$ change in T2 times across multiple pigs (average $T2_{rest} = 37.6 \pm 3.2$ ms and $T2_{stress} = 41.6 \pm 5.0$ ms, Fig 1).

Conclusions: Dipyridamole, while excellent at inducing hyperemic stress, is not appropriate for studies requiring repeated rounds of rest/stress or a fast reset to rest conditions. Lower doses of adenosine showed minimal hyperemic responses, while higher doses led to more noticeable effects. A dose of 4X the standard human dose was the most consistent and reliable across multiple pigs. Overall, a 4X dose of adenosine provides the best option for inducing vasodilation in repeated rounds of rest/stress during porcine preclinical studies where determination of MPR values via CMR is critical.

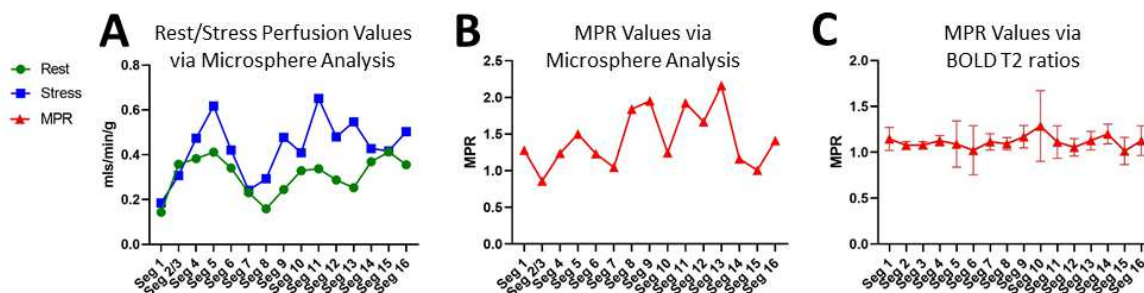


Figure 1: Perfusion values within AHA segments of the heart wall during a 4X dose of adenosine. A,B) Example of perfusion values obtained via microspheres from one pig (A) or MPR values from the same pig (B). C) Calculation of MPR via BOLD T2 rest/stress ratios (n=4).

Correlation of high-resolution 3D MR-derived gray zone with VT cycle length in a swine model of chronic infarctionTerenz Escartin^{1,2}, Sheldon Singh^{1,3}, Philippa Krahn^{1,2}, Jen Barry¹, John Quinto^{1,2}, Peter Lin^{1,2}, Matthew Ng^{1,2}, Venkat Ramanan¹, Melissa Larsen¹, Yue C Yu², Xiuling Qi², Graham Wright^{1,2}, Mihaela Pop^{1,2}¹Sunnybrook Research Institute, Toronto, ²Dept. of Medical Biophysics and ³Dept. of Cardiology, Univ. of Toronto, Canada

INTRODUCTION: Scar-related ventricular tachycardia (VT) is a major cause of death [1]. The VT substrate (a mixture of viable myocytes and collagen fibrils) facilitates electrical waves to traverse dense scars and loop around those with a VT cycle length (i.e., peak-to-peak ECG measurement of the heart rate during VT) depending on the infarct size. Thus, accurate localization of the substrate/scar is critical for arrhythmia diagnosis [2]. CMR can identify VT substrate in late gadolinium enhanced (LGE) images as a ‘grey zone’ (GZ) of intermediate SI between healthy tissue and scar; however, the clinical spatial resolution is limited to ~8mm slice thickness [3]. Here we aim to use high-resolution CMR methods to identify VT substrate in a swine model of chronic infarction, and to correlate the amount of MR-derived infarcted tissue (histologically validated) with the VT cycle length (VTCL) measured in x-ray guided electrophysiology studies.

METHODS: Myocardial infarction was created in n=6 swine using a 90min occlusion-reperfusion method, as in [4]. After ~5 weeks, the pigs underwent CMR (1.4mm isotropic resolution) on a 3T GE scanner, using conventional 3D LGE methods (TR=3.7ms, TE=1.6ms, optimized TI=225ms). A standard SI threshold of 5SD [3] was used to classify GZ/scar pixels. In a subset of 5 pigs we also tested a fully-sampled version of our 3D multi-contrast late enhancement (MCLE) method [5], where 10 MCLE phases/cardiac cycle were acquired per volume and used to derive GZ/scar pixels from T1*-SS (steady state) maps using a fuzzy-logic algorithm [6]. All pigs underwent an x-ray guided electro-anatomical voltage mapping (EAVM) of the left ventricle (LV) and VT inducibility test mimicking the clinical diagnostic tests. For analysis, VTCL was correlated with the MR-derived (GZ+scar) volume calculated relative to the total LV volume. Select tissue slices were histologically stained with collagen-sensitive stain to facilitate the correspondence of fibrotic areas to MR-derived GZ/scar.

RESULTS: Fig. 1 shows examples of LGE and MCLE images at the same level through a pig heart, along with resulting segmentation of tissue into: healthy myocardium, GZ, and scar. The pattern and location of MR-derived GZ/scar zones matched very well the features of histologically-defined fibrosis in the peri-infarct, collagenous areas and the viable sub-endocardial layer, as well as bipolar voltages with low amplitude in electro-anatomical voltage map, EAVM (Fig 2). There was a strong correlation ($R^2 > 0.8$) between the amount of MR-derived infarcted tissue and VTCL, suggesting that a smaller amount of MR-derived (GZ+scar) is a predictor of fast VT.

CONCLUSION: We successfully demonstrated that 3D LGE and MCLE images acquired at 1.4mm isotropic resolution can detect GZ/scar in scar-related VT cases. Future work will focus on translating these 3D MR methods into clinical MR scans to accurately identify the VT substrate and to help plan the RF ablation therapy.

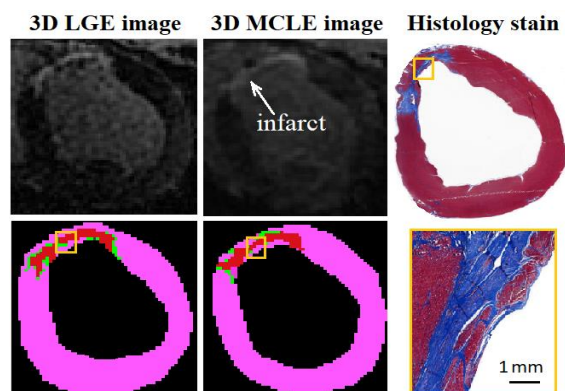


Fig 1. Example of LGE and MCLE images; associated pixel-wise tissue maps (pink=healthy myocardium, green=GZ, red=scar); and corresponding histological slide (collagen/fibrosis in blue).

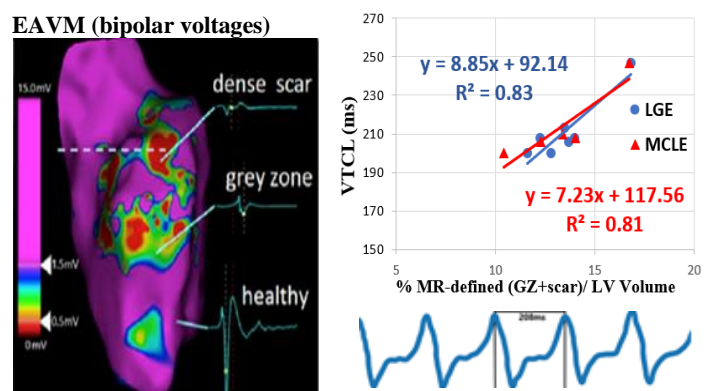


Fig 2. Example of x-ray guided EAVM (dashed line corresponds to the level of short-axis MR images in Fig 1), along with the plot of VT cycle length vs %(GZ+scar)/LV derived by MRI and example of VT waves obtained during the VT inducibility test.

References: [1] J Roy et al; *The Lancet*; 2012; 380, 1520-29; [2] Ranjan R et al; *Circ Arrhythmia and EP*, 2011; 279-86; [3] Gao P et al; *Circ Imaging*, 2012; (5), 448–56; [4] Pop M et al; *Physics Med Biol*, 2013; 58 (15), 5009-28; [5] Zhang L et al; *Magnetic Resonance in Medicine*, 2018; 79 (6), 3018-31; 6.) Detsky et al; *IEEE Trans Med Img*, 2009; 28 (10), 1606-14.

Multi-view 3D echocardiography volume compounding for mitral valve procedure planning

Patrick Carnahan^{1,2}, John Moore¹, Daniel Bainbridge³, Elvis C.S. Chen^{1,2,4}, and Terry M. Peters^{1,2,4}

¹Imaging, Robarts Research Institute, London, CA,

²School of Biomedical Engineering, ³Department of Anesthesiology, London Health Sciences Centre, ⁴Department of Medical Biophysics Western University, London, CA

Introduction: Current standard of care diagnostic imaging for mitral valve procedures primarily consists of transesophageal echocardiography (TEE) as it provides a clear view of the mitral valve leaflets and surrounding tissue.^{1,2} However, TEE has limitations in signal dropout and artefacts, particularly for structures lying below the valve such as chordae tendineae. As a result, multiple image acquisitions from multiple position along the esophagus must be made and viewed separately to observe all relevant structures. We propose a trackerless, volume compounding system to fuse mid-esophageal and transgastric 3D volumes to create a single ultrasound volume containing the mitral valve and sub-valvular structures with a high level of detail. This will enable the measurement of chordae length, which is required for procedures involving the implantation of artificial chordae.

Methods: Images are acquired during standard pre-operative imaging sessions using Philips Epiq TEE probes. One or more mid-esophageal volumes and four or more transgastric volumes with a high degree of overlap are acquired with ECG gating. These volumes are then rigidly registered with a semi-simultaneous group wise registration method³ using the end-diastolic phase of the cardiac cycle. Following rigid alignment, for each frame in the image sequences, non-rigid registration is performed to account for slight variation in cardiac phase. Then, each voxel in every volume is weighted according to a combination of distance from the image probe and a basic feature detector using Gaussian blurring and thresholding. The volumes are then resampled onto a common grid, and voxel-wise weighted averaging is used to generate the final output volume.

Results: We validated this image compounding approach on two excised porcine mitral valve units, a custom silicone phantom, and on two patient data sets acquired from University Hospital with REB approval. The porcine valves and silicone phantom were imaged according to our clinical acquisition procedure. The porcine valves were also stained with iodine and imaged with a CT scanner to provide ground truth data. The ultrasound images were then compounded using the described approach. The resulting compounded volumes were registered to the CT volumes to enable direct comparison for both the porcine models and phantom. The compounded volumes visually replicate the structures visible in the ground truth CT scan, and chordae measurements have an error of 0.6 ± 0.5 mm between modalities. Results of ultrasound compounding on patient data sets are shown in Figure 1. Visual inspection shows clear delineation of the mitral valve leaflets, chordae tendineae, and papillary muscles.

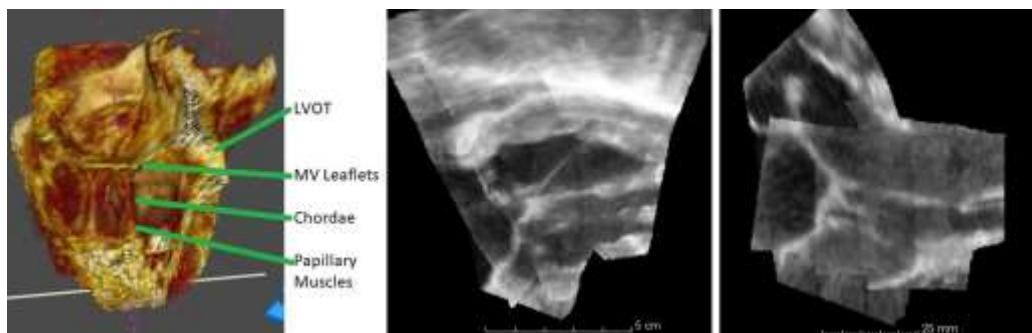


Figure 1: Visualizations of compounded TEE data from five different TEE volumes. Left, a volume rendered view. Middle, a commissure-commissure slice. Right, an AP slice.

Conclusions: We have described a workflow for capturing a series of images using a TEE probe during standard diagnostic imaging that can then be registered and compounded together. These compounded volumes capture the sub-valvular structures of interest for cardiac procedure planning. Capturing the necessary additional volumes can be done with only an additional ten minutes to the current standard of care diagnostic images. This method is able to provide clinicians with a single volume that captures the mitral valve and the sub-valvular structures, which will enhance the mitral valve procedure planning process.

References: 1. Shah, P. M, *Journal of Cardiology* 56, 125–133 (2010). 2. Linden, A *et al.*, *The Thoracic and Cardiovascular Surgeon* 65, S213–S216 (2017). 3. Wachinger, C. *et al.*, *Medical Image Computing and Computer-Assisted Intervention – MICCAI 2007* 327–335 (2007).

A Novel PET Tracer Enables Imaging of the Cardiac Growth Hormone Secretagogue Receptor in a Large Animal Model of Heart Failure

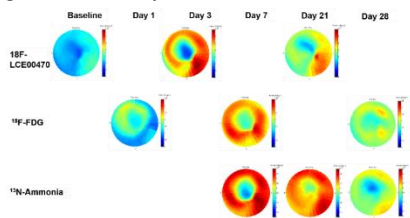
Rebecca Sullivan¹, Lihai Yu², Jinqiang Hou², Justin Hicks^{5,7}, Jane Sykes³, John Butler⁴, Heather Biernaski⁴, Leonard Luyt^{2,5,6}, Frank Prato^{5,7}, Jonathan D. Thiessen^{5,7}, Rohan Dharmakumar⁸, Gerald Wisenberg^{5,7}, and Savita Dhanvantari^{1,5,7,9}

1. Pathology and Laboratory Medicine, Western University; 2. Chemistry, Western University; 3. Thames Valley Veterinary Services, Lawson Health Research Institute; 4. Radiology Department, Lawson Health Research Institute; 5. Imaging Program, Lawson Health Research Institute; 6. Department of Oncology, London Regional Cancer Program; 7. Medical Biophysics, Western University; 8. Cedars-Sinai, Los Angeles, California, USA; 9. Metabolism and Diabetes, Lawson Health Research Institute.

Introduction: Cardiac imaging technologies, including echocardiography and magnetic resonance imaging (MRI), enable the non-invasive detection of changes in heart function that may indicate disease progression. These modalities detect changes in structure, anatomy and function, and thus there is a critical need for detection of biochemical and molecular changes that precede these gross structural changes. Development of imaging agents that target molecular changes, combined with hybrid imaging technology, is a powerful means to address this need. There is evidence that cardiac growth hormone secretagogue receptor (GHSR) could be a potential molecular imaging target. An array of imaging agents are being characterized for detection of myocardial GHSR by positron emission tomography (PET) and with one of these novel agents, termed ¹⁸F-LCE00470, we used hybrid PET and MRI (PET/MRI) to detect and quantify changes in regional distribution of myocardial GHSR in a canine model of myocardial infarction (MI).

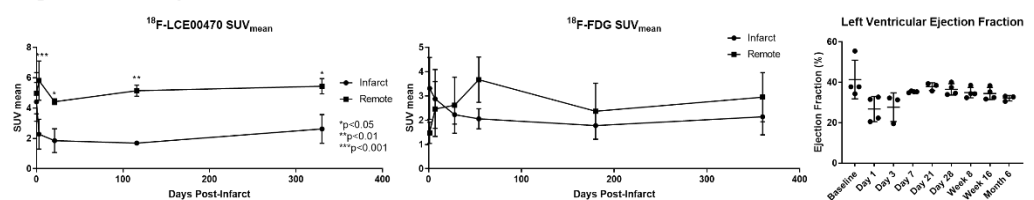
Methods: Female hounds (11-12 months) were used in this study. An MI was generated by a 2-hour occlusion of the left descending coronary artery, followed by reperfusion. Dogs (n=4) were imaged with a combination of PET tracers at specific timepoints: ¹⁸F-LCE00470 for GHSR (baseline, days 3, 21, 4 months post infarct); ¹⁸F-FDG for inflammation (days 1, 7, 28, 6 months post infarct); and ¹³N-ammonia for perfusion (days 7, 21, 28, 4 and 6 months post infarct). At these time points, there are marked regional changes in inflammation and perfusion. Dogs were scanned with simultaneous PET/MRI, as follows: dogs were injected with 100-150 MBq of one of the above tracers, immediately followed by a 1-hour (¹⁸F-LCE00470 and ¹⁸F-FDG) or 30 min (¹³N-ammonia) dynamic PET scan. MRI included: 3D T1-weighted images and short-axis, 2D T1 maps spanning the left ventricle (LV) before and after gadolinium contrast to quantify fibrosis and perfusion defects, short-axis T2 maps (reflecting edema) before contrast, and short-axis cine images (heart function). FlowQuant software (Ottawa Heart) was used to generate polar maps representing a 3D version of the entire LV myocardium. These polar maps were used to determine regional changes in tracer uptake at each timepoint. 3D Slicer was used to quantify the standardized uptake value (SUV) in specific regions of interest for each tracer. Heart function data was analyzed using CircleCV142.

Figure 1. Polar Maps of n=1 Canine Left Ventricle



Results: FlowQuant analysis initially showed differences in patterns of regional distribution between tracers at all timepoints post-MI, indicating that uptake of ¹⁸F-LCE00470 does not simply reflect changes in cardiac perfusion or inflammation. For ¹⁸F-LCE00470 the SUV_{mean} was significantly higher in the remote non-infarcted tissue compared to the infarct at all time points (p<0.05) post-MI while the ¹⁸F-FDG SUV_{mean} was not significantly elevated in any area at any time point post-MI. These

Figure 2. SUV Analysis for ¹⁸F-LCE00470 and ¹⁸F-FDG, and Heart Function Data



changes in ¹⁸F-LCE00470 were seen prior to any functional changes in the heart as determined by global LV ejection fraction.

Conclusions: We used a novel small molecule PET tracer, ¹⁸F-LCE00470, to detect changes in regional distribution of GHSR post-MI in canine heart. We have shown differences in patterns of regional uptake compared to known tracers of perfusion and inflammation while there are no observable functional changes seen in MRI. The next steps are to analyze this data using compartmental modeling to better understand the function of this tracer and to longitudinally compare tracer distribution to scar formation. This tracer is expected to be elevated in areas of cardiac damage tracking GHSR pathophysiology. This tool can be applied to other cardiac diseases and will ultimately help improve knowledge of molecular changes in the heart prior to conventional imaging methods used for heart failure.

Low-dose CT Perfusion by Sparse Projections in Acute Ischemic Stroke

Kevin J. Chung,¹ Bijoy K. Menon,² Ting-Yim Lee^{1,3}

¹Department of Medical Biophysics, University of Western Ontario, London, Ontario, Canada

²Department of Clinical Neurosciences, University of Calgary, Calgary, Alberta, Canada

³Lawson Health Research Institute and Robarts Research Institute, London, Ontario, Canada

Introduction: Computed tomography perfusion (CTP) efficiently provides valuable hemodynamic information for triage of acute ischemic stroke patients at the expense of additional radiation exposure from consecutive CT acquisitions. Low-dose CTP is therefore highly desirable but is often attempted by iterative reconstruction or deep learning techniques that are computationally intensive. We aimed to demonstrate that filtered back-projection (FBP) image reconstruction with sparse projections can reduce radiation dose without impacting clinical utility.

Methods: Six CTP studies originally acquired with 984 projections were selected from the PProve-IT clinical database. For each axial source CTP slice, a sinogram was synthesized using a Radon transform with 984, 492, 328, 246, and 164 projections. An FBP was applied to reconstruct the sparse-view source images and were used to generate perfusion maps using a delay-insensitive deconvolution algorithm with arterial and venous time density curves located on the original full-view source CTP images. The resulting T_{\max} and cerebral blood flow (CBF) perfusion maps were evaluated for their ability to identify ischemic penumbra and infarct core volumes using the Pearson coefficient and Bland-Altman analysis. In addition, sparse-view perfusion maps were assessed for fidelity to full-view maps using structural similarity (SSIM), peak signal-to-noise ratio (PSNR), and normalized root mean squared error (NRMSE).

Results: As shown in the Table, penumbra and infarct core volume correlation and agreement decreased as the number of projections became sparse. Image fidelity metrics also followed a similar trend. Sample CBF and T_{\max} maps are illustrated for each number of projections in the Figure.

Conclusions: Our analysis indicates that the number of projections in a CTP acquisition can be reduced to 328 while maintaining image fidelity and volume accuracy for the penumbra and infarct core. Further evaluation must be conducted to determine whether the observed difference of < 4.0 ml in infarct volume is clinically significant.

Table. Penumbra and ischemic core volume correlation and agreement for sparse-view CT perfusion

Tissue Class	Metric	Number of Projections				
		984	492	328	246	164
Penumbra	Pearson Coefficient	0.999 (p<0.001)	0.999 (p<0.001)	0.994 (p<0.001)	0.837 (p<0.05)	0.147 (p=0.781)
	Mean Difference (ml)	1.4	0.3	3.2	28.3	84.9
	Limits of Agreement (ml)	-15.9 – 18.7	-16.8 – 17.4	-16.5 – 22.9	-60.5 – 117.1	-177.8 – 347.7
Ischemic Core	Pearson Coefficient	0.998 (p<0.001)	0.985 (p<0.001)	0.986 (p<0.001)	0.945 (p<0.005)	0.946 (p<0.005)
	Mean Difference (ml)	-0.3	-2.0	-2.5	-4.0	-6.7
	Limits of Agreement (ml)	-1.7 – 1.0	-5.2 – 1.2	-5.6 – 0.7	-10.2 – 2.2	-15.7 – 2.4

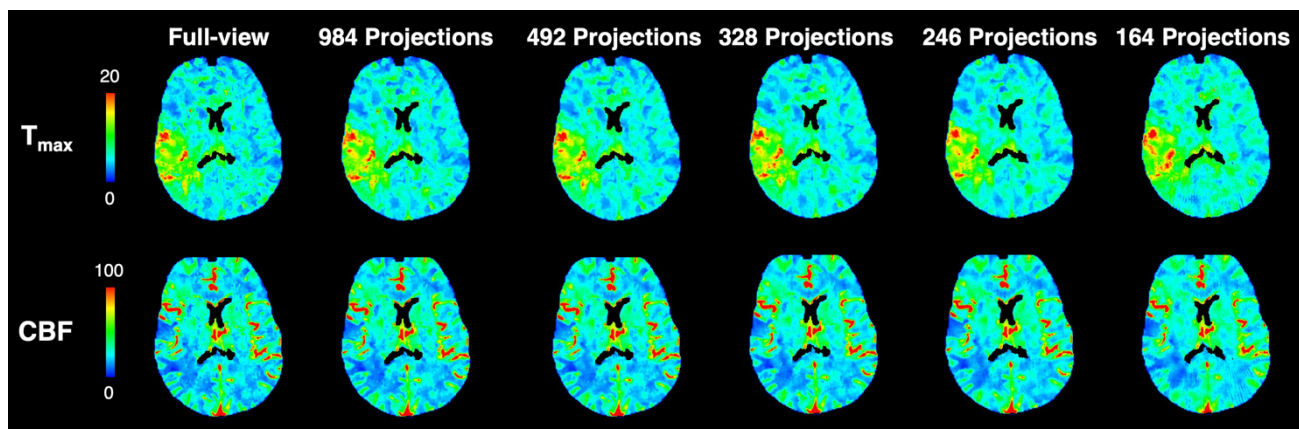
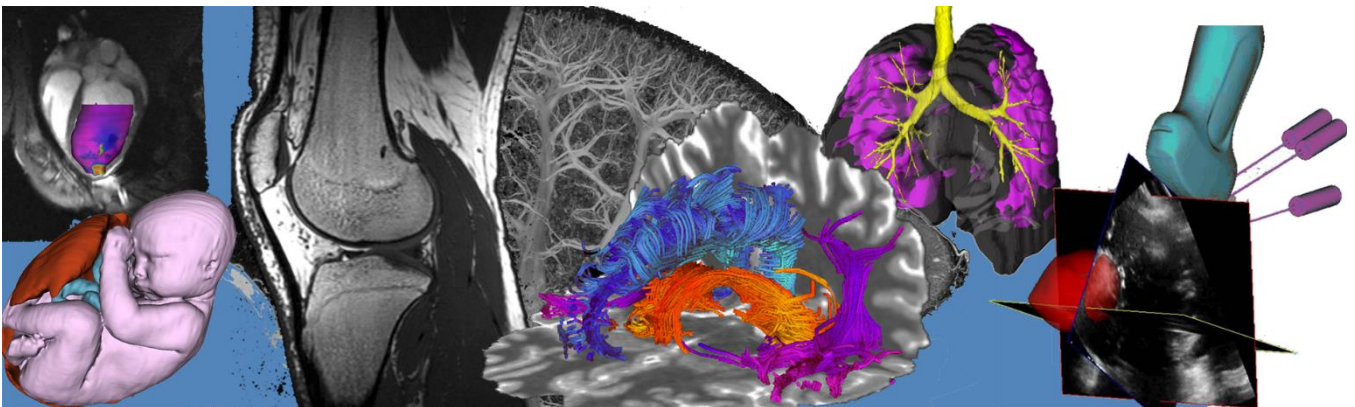


Figure. Qualitative examples of T_{\max} and cerebral blood flow (CBF) perfusion maps using full-view, 984, 492, 328, 246, and 164-projection source computed tomography perfusion images

Oral Presentation Abstracts

Session 9: Instrumentation and Technology Development



The Effects of Elasticity and Scattering on Tissue Characterization Using Ultrasound Time Series

Justin Gerolami¹, Amoon Jamzad¹, Si Jia Li^{1,2}, Parvin Mousavi¹

¹Queen's University School of Computing, ²University of Washington

Introduction

Conventional B-mode ultrasound imaging lacks the soft tissue contrast to differentiate tissue types. To address this, our group proposed Temporal Enhanced Ultrasound (TeUS), a method based on the analysis of time series extracted from ultrasound data¹. We have previously utilized machine and deep learning approaches to interpret TeUS sequences for cancer detection². The model for TeUS is a convolution between a point spread function and a scattering function. The tissue-correlated information in TeUS is due to the minor tissue motions (intrinsic or induced) that changes the scattering function³. However, these movements are difficult to control which makes the clinical translation of the method challenging. In this study, we explore the feasibility of generating the same effect through the manipulation of imaging system point by changing the focal depth in a time-dependent manner during data acquisition.



Figure 1. Temporal-enhanced ultrasound acquisition setup. The clamp holds the transducer in place on the phantom surface.

Methods

Three phantoms were designed to mimic tissues with different elasticity and scattering sizes. For each phantom, 2 planes of TeUS were acquired (Fig 1) in the form of in-phase-quadrature readouts. The focal point was set to an initial depth and was changed in small sinusoidal steps for each frame. Each TeUS series consist of 200 samples. After preprocessing and feature extraction using Discrete Fourier Transform, a region of interest of 67 axial and 63 lateral samples was chosen (Fig 2). The first 4 frequency peaks as main features were used as input to a Quadratic Discriminant Analysis classifier. The classifier was trained using the first plane and tested using the second plane. Classifications between phantoms with different elasticity, different scattering, and different elasticity and scattering were performed.

Results

The classification accuracy for phantoms with different elasticity was 54%; different scattering was 81%; and different elasticity and scattering was 83%. These results are consistent with the properties of TeUS – we expect to differentiate between tissues when there are differences in scattering, whereas elasticity is more associated with real mechanical interaction with the tissue.

Conclusion

This work provides an alternative method for TeUS that does not require physical motion of tissue. We believe that with proper tuning of TeUS acquisition parameters and setup, future *in-vivo* studies for cancer detection can be explored.

References

1. F. Imani et al., "Computer-aided Prostate Cancer Detection Using Ultrasound RF Time Series: In vivo Feasibility Study.", *IEEE Trans. Med. Imaging*, vol. PP, no. 99, p. 1, 2015.
2. S. Azizi et al., "Detection and grading of prostate cancer using temporal enhanced ultrasound" *IJCARS*, 12, no. 6, pp. 1293-1305, Aug. 2017
3. S. Li et al. "Temporal enhanced ultrasound and shear wave elastography for tissue classification in cancer interventions: an experimental evaluation", *Proceedings of SPIE Vol. 10951, 109510V* (2019)

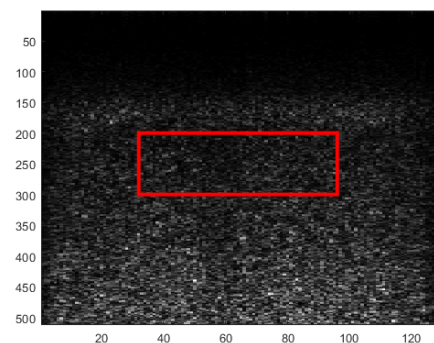


Figure 2. A B-mode image showing the region of interest that was selected.

Tuning an RF Birdcage Coil by Varying the Shield Radius

Kieffer J. Davieau^{1,2}, James E. Pardy², Colin J. Metrow², Blaine A. Chronik^{1,2}

¹Department of Medical Biophysics, Western University, London, Ontario, Canada.

²The xMR Labs, Department of Physics and Astronomy, Western University, London, Ontario, Canada.

INTRODUCTION: Since their introduction by Hayes in 1985, the birdcage design has been widely used in clinical MRIs as transmit and receive (Tx/Rx) coils due to their high RF (B_1) field homogeneity and signal-to-noise ratio¹. This came at the expense of having to tune and match the coil to a desired resonant frequency. In practice, these coils are tuned and matched using variable capacitors positioned along the end rings for a high-pass design, resulting in a less homogenous B_1 field along the transverse and longitudinal plane². Previous research has found that moving the shortened shield longitudinally along the coil acts as a viable method for tuning at the cost of field inhomogeneities^{3,4,5}. Ideally, reducing the need for variable capacitors while maintaining a full shield would result in a more homogenous B_1 field along the transverse and longitudinal plane, and result in reduced manufacturing costs. In this study, we investigate variable shield radius as a novel method for tuning and matching the RF coil. This is possible due to the change in self and mutual inductances of the coil by altering the shield radius. This has the potential to be used as a viable method for tuning and matching a coil, while maintaining a highly homogenous B_1 field at potentially lower cost.

METHODS: The design of the coil used in this study was based upon the geometry of other commercially available head coils at 1.5T. A high-pass birdcage configuration was chosen due to their clinical presence as a result of lower E-fields near the imaging region. The coil was designed in Advanced Design System (ADS, Keysight Technologies) to have 16 rungs with a length of 38.4 cm and a diameter of 14.5 cm. BirdcageBuilder (CNMRR Software, Penn State) was used to calculate the capacitance needed. Given the physical parameters and the desired resonant frequency of 63.85 MHz, this software analytically calculates the capacitance required for resonance using a lumped circuit element method. Using a lumped circuit model in ADS, the capacitor values calculated from BirdcageBuilder were added to the ADS schematic. This schematic was simulated in ADS using an EM cosimulator to determine the location of the resonance peaks, and later tuned and matched to provide proper matching and isolation. Once a resonant peak was noticed on the S-parameters, the shield radius was altered in the ADS layout to observe the effects on the S-parameters.

RESULTS: As shown in Fig. 1 (a), the resonant frequency can be seen to increase or decrease with a change in shield radius. The values for shield radii were chosen to show the change in resonant frequency. Fig. 1 (b) and (c) show that changing the shield radius had similar effects as using a variable tuning capacitor, as a result of the changing mutual inductances.

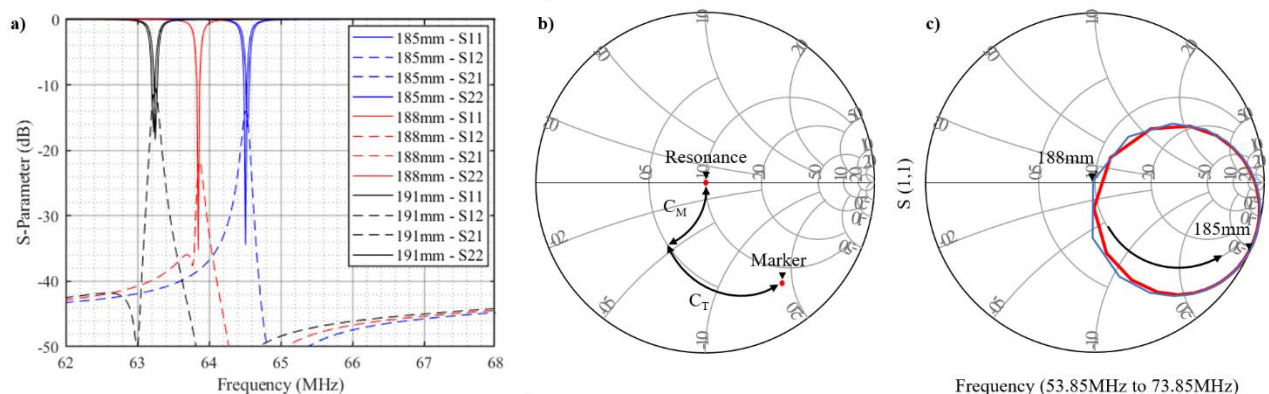


Figure 1. The effects on S-parameters of for variable shield radii of 185 mm, 188 mm, and 191 mm (a); Smith charts showing effects of tuning/matching capacitors (b) in comparison with effects of variable shield radii (c).

CONCLUSION: The results of this study show that the shield radius does have a similar effect on the S-parameters as a variable tuning capacitor. This offers a novel method for tuning an RF coil which may serve to reduce manufacturing costs and provide on-the-fly variable tuning for multi-nuclear imaging applications⁶.

REFERENCES: [1] Hayes CE, Edelstein WA, Schenck JF, Mueller AM, Eash M: *J Magn Reson.* 1985;63:622-628. [2] Jin J, Shen G, Perkins T: *J Magn Reson.* 1994;32(3):418-422. [3] Dardzinski BJ, Li S, Collins CM, Williams GD, Smith MB: *J Magn Reson.* 1998;38(131):32-38. [4] Hayes CE: *NMR Biomed.* 2009;22(9):908-918. [5] Jin J, Magin RL, Shen G, Perkins T: *IEEE Trans Biomed Eng.* 1995;42(8):840-843. [6] Fox MS, Gaudet JM, Foster PJ. *Magn Reson Insights.* 2016;8(Suppl 1):53-67.

Integration of a Real-Time Field Monitoring System for Artifact Correction in Diffusion MRI

Paul I. Dubovan^{1,2}, and Corey A. Baron^{1,2}

¹Department of Medical Biophysics, Schulich School of Medicine & Dentistry, Western University

²Centre for Functional and Metabolic Mapping, Robarts Research Institute, London, Ontario, Canada

Introduction: Diffusion-weighted imaging (DWI) sensitizes MRI images to the differences in water diffusion. Despite the advantages, the technique contributes to image artifacts due to eddy currents induced by the strong and rapidly switching gradients needed for diffusion encoding¹. One of the most effective techniques that correct for these distortions involves the application of a newly commercialized concurrent field monitoring system². With the rise of more demanding diffusion pulse sequences such as the Oscillating Gradient Spin Echo (OGSE)³ sequence over traditional Pulsed Gradient Spin Echo (PGSE), attention to proper correction methods is necessary moving forward to acquire reliable data. With the aid of a field monitoring system, this study aimed to show the degree of distortion of these diffusion sequences by characterizing their k-space trajectory deviations.

Methods: A clip-on camera field monitoring system, consisting of sixteen ¹⁹F-NMR field probes designed and manufactured by Skope was used to concurrently acquire dynamic NMR data while scanning a saline solution phantom (Fig. 1). Following the acquisition, vendor provided software was used to compute the k-coefficients from the NMR phase data using a spherical harmonic basis. Scanning was carried out using a Siemens MAGNETOM 7T MRI Plus scanner. Using an echo-planar imaging (EPI) pulse sequence, 17 different diffusion gradient directions were applied, with 16 of these directions encompassing either PGSE or OGSE, using a b-value of 750 s/mm². No diffusion weighting was applied for the remaining dynamic (b = 0). OGSE frequency was set to 40 Hz and was selected based on the optimized results reported by Arbabi et al.⁴ Remaining parameters

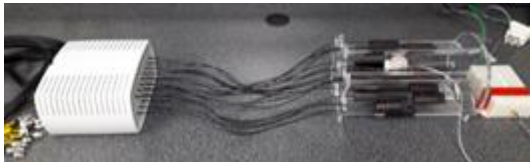


Fig. 1: Illustration showing the sixteen-field probe assembly surrounding the ball phantom, along with the connections made to the RF front end.

were TE/TR = 124.0/2000 ms, 2 mm isotropic resolution, FOV 224x224 mm², and ~1 min scan time. Field probe data was collected and visualized on the system software. The difference in k-space coefficients for the x, y, and z real-valued linear spherical harmonics were taken between PGSE data and b = 0 data and repeated for OGSE data. Resulting differences were compared to characterize the degree of deviation between methods.

Results: Both diffusion acquisition methods showed apparent differences relative to the b = 0 baseline trajectory (Figs. 2a and 2b), confirming eddy current effects. Larger variation and overall deviation were observed for the OGSE pulse sequence across the entire sampling period. This is further explored in Fig. 2c, which shows a larger shift in the EPI k-space trajectory for the OGSE sequence.

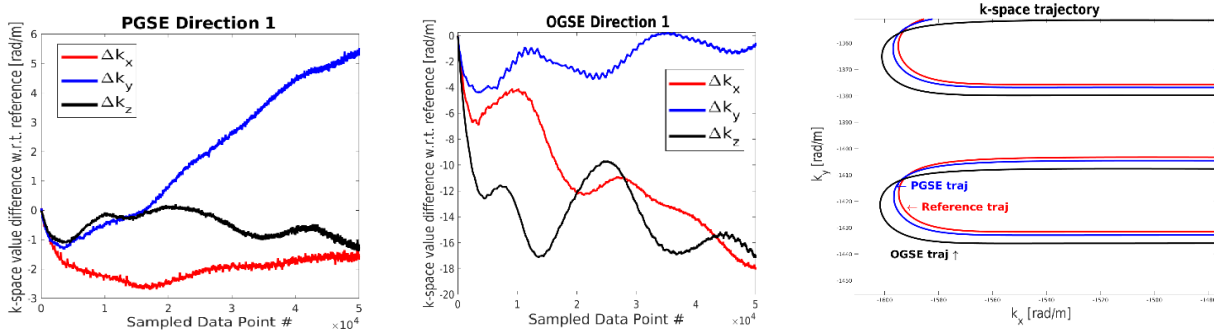


Fig. 2: Plots showing the difference in k-space coefficient values relative to b = 0 values, for (a) PGSE and (b) OGSE sequences respectively (along one diffusion direction). Similar results were observed along the other diffusion directions tested. (c) Zoom-in of EPI sequence k-space trajectory for the three acquisition methods: PGSE, OGSE, and b=0.

Conclusions: The data acquired by the system successfully showed how the deviation in k-space coefficients increases with more demanding diffusion pulse sequences. Future studies will aim to investigate acquisitions using spiral trajectories and focus on developing correction models to improve data reliability.

References: ¹Irfanoglu M et al. *Magn Reson Med* 81 (2019). ²Vannesjo S et al. *Magn Reson Med* 76 (2016). ³Baron C et al. *Magn Reson Med* 72 (2014). ⁴Arbabi A et al. *Magn Reson Med* 00 (2019).

An Optimised Diffusion MRI Technique to Study White Matter Integrity

Nico J. J. Arezza^{1,2} and Corey A. Baron^{1,2}

¹Department of Medical Biophysics, Schulich School of Medicine and Dentistry, Western University, London, ON, Canada,

²Centre for Functional and Metabolic Mapping, Robarts Research Institute, Western University, London, ON, Canada

Introduction: Water diffusion anisotropy is an indirect measure of neuron integrity, and reduced anisotropy in white matter (WM) is observed in diseases like dementia [1] and multiple sclerosis [2]. Microscopic anisotropy (μA) and its normalized counterpart, microscopic fractional anisotropy (μFA), can measure diffusion anisotropy independent of neuron fiber orientation, potentially providing improved specificity to changes in neuron structure over standard anisotropy metrics [3]. Here, we demonstrate an optimised $\mu A/\mu FA$ diffusion MRI (dMRI) protocol at 3T that can acquire high-SNR full-brain coverage in 4 minutes.

Methods: μA is computed via [4] $\mu A^2 = \ln(S_{lin}/S_{iso})/b^2$ where S_{lin} and S_{iso} are the averages of the linear and isotropic signals, respectively, and b is the b -value, a dMRI parameter that determines the amount of diffusion weighting. To develop an optimised sequence, the signal-to-noise ratio (SNR) of μA^2 was estimated using standard error propagation and data was collected from four healthy volunteers (2 male, 2 female), abiding by ethics board guidelines, on a 3T MRI system (80 mT/m strength and 200 T/m/s slew rate). 6 linear and 6 isotropic encodings were acquired at b -values from 0 to 3500 s/mm² in increments of 500 s/mm² with TE/TR=125/8700 ms, FOV=192x192 mm², 2 mm isotropic in-plane resolution, 45 slices (2 mm), rate 2 GRAPPA, 2 averages, 29 min scan time. Signal data used in the optimization was measured in a WM region-of-interest (ROI) and WM T2 was assumed to be 80 ms [5]. Note that the SNR of μFA is proportional to the SNR of μA^2 . To test an optimized protocol, two volunteers were scanned (6 averages at $b=0$ s/mm² 6 isotropic at $b=1000$ s/mm², and 6 linear and 12 isotropic encodings at $b=2200$ s/mm²) with TE/TR=102/7400 ms and a scan time of 4 min. μFA was derived to be $\mu FA = \sqrt{1.5\mu A^2/(\mu A^2+0.2MD^2)}$ where MD is the mean diffusivity.

Results: Error propagation theory revealed that μA^2 SNR is maximized when b -value is ~ 2000 s/mm² and the ratio of isotropic to linear scans is ~ 1.5 -2 (Fig.1). Sample μFA images from the volunteers are shown in Fig. 2.

Fig. 1. μA^2 SNR as a function of b -value and ratio of isotropic to linear diffusion-weighted encodings.

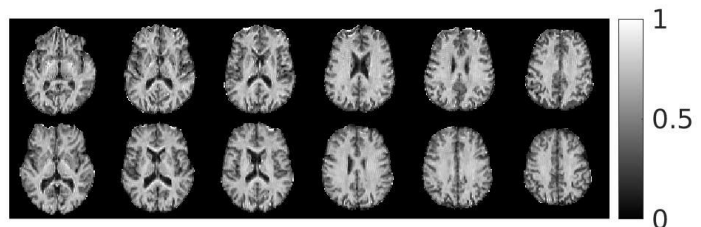
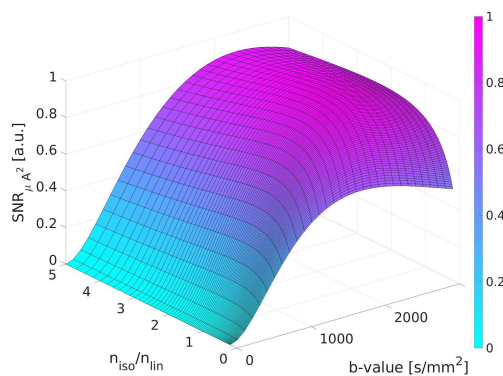


Fig. 2. μFA images acquired using an optimized 4-minute protocol. Axial slices were acquired from volunteer 1 (top row) and volunteer 2 (bottom row), respectively. Note that μFA is normalized between 0 and 1.

Conclusions: The optimised protocol produced high-quality μFA images with full-brain coverage in only 4 min, demonstrating the clinical feasibility of the technique. In previous works, we used a 1:1 ratio of isotropic to linear scans to acquire $\mu A/\mu FA$ images;

however, implementing the optimal ratio of isotropic to linear scans will allow us to increase SNR without increasing scan time. In future projects, we will use an optimised μFA protocol to study WM integrity in neurodegenerative disorders.

References: [1] E. Englund *et al. J. Neurol.*, 2004. [2] M. Rovaris *et al. Neurology*, 2005. [3] N. Shemesh *et al. Magn. Reson. Med.*, 2016. [4] A. Ianus *et al. Magn. Reson. Med.*, 2017. [5] S. Lasic *et al. Frontiers in Physics*, 2014.

Acknowledgements: Canada First Research Excellence Fund to BrainsCAN, Ontario Graduate Scholarships, Queen Elizabeth II Scholarship in Science and Technology, NSERC

Microstructural characterization and Visualization a 3D printed phantom using diffusion MRI and microscopyFarah N. Mushtaha¹, Tristan K. Kuehn¹, Omar El-Deeb², Amanda Moehring², Ali R. Khan¹, Corey A. Baron¹^[1]Robarts Research Institute, Western University, London, Canada^[2]Department of Biology, Western University, London, Canada

Introduction. Diffusion MRI (dMRI) is a promising technique to quantify histological features of the brain at a micrometre scale¹. However, there is no “ground truth” to validate it. We investigate a novel phantom produced using fused deposition modeling (FDM) 3D printing with a dual-component material that consists of an elastomeric polymer and polyvinyl alcohol (PVA)². When immersed in water the PVA dissolves, leaving behind small pores that can mimic diffusion characteristics of axons (Fig.1). In this study, we characterize Diffusion Kurtosis Imaging (DKI) parameters in dMRI phantoms, assess their reproducibility, and visualize the phantom's microstructure with microscopy.

Methods. 4 identical phantoms were created by printing 11 mm radius cylinders with 100 μm thick layers of parallel lines to mimic linear fibers. The phantoms were immersed in water for 168 hrs and stacked in a test tube with distilled water for imaging. Diffusion MRI was implemented at 9.4 T using 120 directions at $b=2000 \text{ s/mm}^2$, and 60 directions at $b=1000$, TE/TR=37/2500 ms, FOV=200x200 mm^2 , 0.7 mm isotropic in-plane resolution, 4 axial slices (3 mm, one per phantom), and scan time 8.5 min per scan. DiPy³ was used to compute DKI-derived metrics (axial kurtosis, AK; radial kurtosis, RK; Mean kurtosis, MK; axial diffusivity, AD; radial diffusivity, RD; Mean diffusivity, MD; fractional anisotropy, FA).

To visualize the pores, a 35x15x25 mm^3 phantom block was printed using identical print parameters. The block was immersed in water for 10 hrs then sliced into 50 μm slices. Rhodamine Beta fluorescent dye was used to stain the elastomer part of the phantoms. Confocal microscopy was performed using a Leica SP5 laser system and a 40X oil immersion objective lens.

Results. The phantoms showed AK close to zero and a RK ~ 1.1 (Table.1). The coefficient of variation across different phantoms of the same parameters was less than 15% in all of the obtained DKI-Parameters. Confocal microscopy images revealed two types of pores; larger pores on the order of 70 μm caused by the 3D printing pattern and smaller pores on the order of 2-30 μm caused by the PVA dissolving away (Fig.2).

Conclusion. AK and RK values reveal negligible restriction of water movement along the axial directions of the porous structure and relatively high restriction in the radial direction. The low coefficient of variation across the different DKI parameters suggests that these phantoms could be used for quantitative analysis. Microscopy images confirm pores as small as 2 μm wide that could mimic the axons in white matter.

Acknowledgements. This work was supported by the Canada First Research Excellence Fund, Brain Canada, and Discovery Grants from the Natural Sciences and Engineering Research Council (NSERC).

References. [1] Alexander D.C, *et al.* *NMR in Biomedicine*. 2017;e3841. doi:10.1002/nbm.3841. [2] Abu-Sardana S.O, *et*

al. *Proc. SPIE*. 10573, 2018. [3] Garyfallidis, *et al.* *Frontiers in neuroinformatics*. 2014. doi.org/10.3389/fninf.2014.00008.

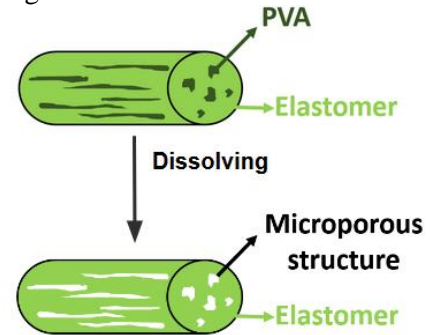


Figure1. Illustration of PORO-LAY before and after immersing it in water.

Metric	Mean Value	Coefficient of variation (%)
AD (mm^2/s)	0.00213	3.19
RD (mm^2/s)	0.00101	13.20
MD (mm^2/s)	0.00138	8.78
FA	0.46220	5.24
AK	0.07335	10.10
RK	1.13332	6.31
MK	0.52469	1.86

Table 1. Mean dMRI values from a nominal phantoms and the coefficient of variation.

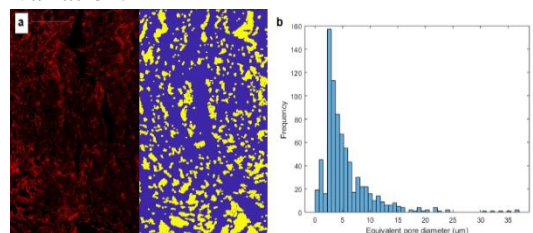
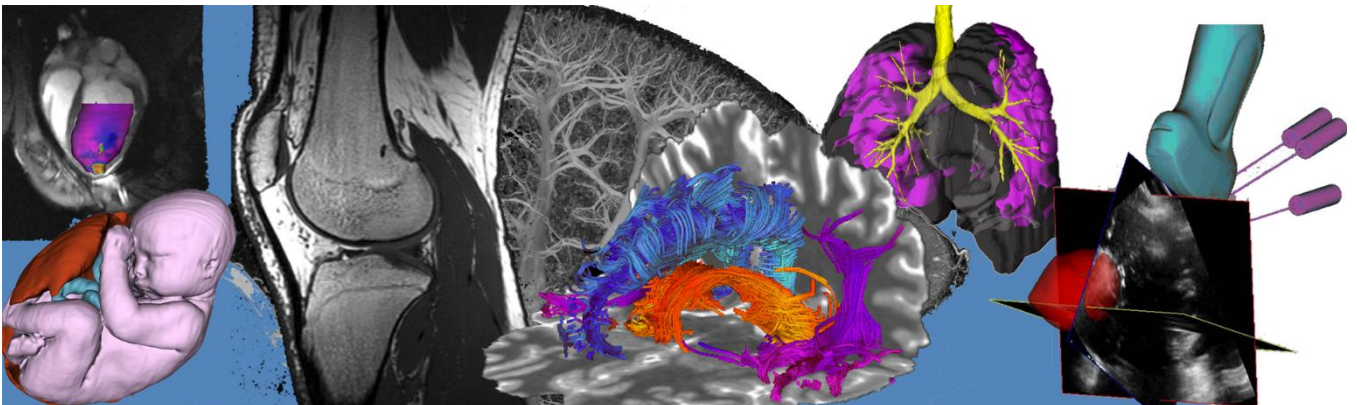


Figure 2. a) Fluorescent microscopy image before (left) and after (right) performing pore segmentation. b) Histogram of equivalent diameter of pores obtained from segmentation and their frequency. Other microscopy slides looked qualitatively

Oral Presentation Abstracts

Session 10: Neurology Imaging 2



Exponential Analysis for Magnetic Resonance Relaxation Spectrum using Artificial Neural Networks

Tristhal Parasram¹, Rebecca Daoud¹, Dan Xiao¹

¹Physics Department, University of Windsor, ON, Canada

Introduction: Quantitative analysis of MR relaxation times could reveal molecular scale information, and has significance in the study of brain, spinal cord, articular cartilage, and cancer discrimination. Multi-compartment model, with a continuous relaxation spectrum, requires exponential analysis which is an intrinsically ill-posed problem. The traditional inverse Laplace transform (ILT) employs a nonnegative constraint and a user defined regularization parameter for spectrum smoothness. In this work, artificial neural networks (ANNs) have been trained to generate the T_2 distribution spectra. The performance was evaluated across a large parameter range. In addition to superior computation speed, higher accuracy was achieved compared to the traditional method.

Methods: Keras and NumPy were employed to create the networks, with an array of the decay signal values as input and spectrum amplitude as output. The network was trained on 400 000 simulated multiple spin echo decay signals, with 512 equally spaced (echo spacing ES) points. The loss function was the sum of mean squared errors of the T_2 spectrum and the T_2 decay signal compared to the ideal decay and a factor to punish negative values. Rician noise was added to the scaled decay signals. Two Gaussian functions with random widths, positions and relative heights on a logarithmic scale were added, which results in both one and two peak spectra in the training data.

Results and Discussion: The minimum T_2 value that could be potentially detected was ES, i.e. defined by the first 3 points on the decay curve. The maximum T_2 value was the echo train duration, i.e. the signal had decayed at least by a factor of e^{-1} at the end of the acquisition window. These defined the dynamic range of simulation spectra.

The accuracy of two-peak T_2 spectrum analysis depends on the peak width, peak positions and area ratio. To investigate the network performance, spectra with varying peak width, varying area ratio and fixed peak positions (at 20 ES and 200 ES) were tested, and the error maps are shown in Fig. 1. Spectra with fixed peak width (0.3), fixed area ratio (50:50), and varying peak positions were tested, as shown in Fig. 2. The results were compared with ILT, which produced higher errors. The transition boundaries, in both figures, highlighted the resolution limit, higher for ANN than ILT. This is the intrinsic limit in exponential analysis, agreeing with theoretical results in the literature.

Dynamic spectra of phantom experiments are shown in Figure 3. Both the positions and areas of the two peaks changed with time, as CuSO_4 migrated into the Agar gel. The two peaks merged into one after 4 hours, and the peak width became narrower afterwards as the relaxation rates within the sample became more homogeneous. ANN generated dynamic T_2 spectra with a smoother transition than ILT.

Conclusion: We demonstrated the effectiveness of ANN for analyzing continuous T_2 distribution. The performance was evaluated across a large parameter space and was superior compared to the traditional ILT method. The technique can be easily extended to higher dimensional relaxation correlation analysis and/or incorporating spatial encoding.

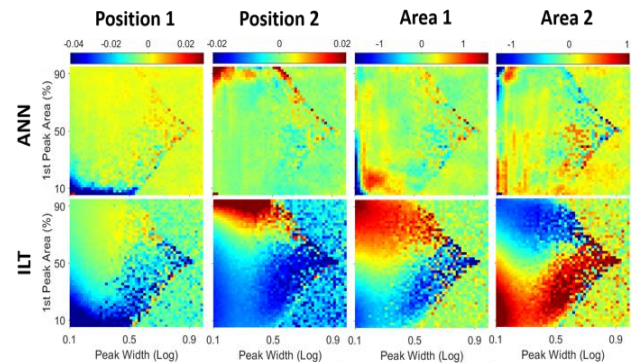


Figure 1. Error maps of simulated two-peak T_2 distribution from ANN (1st row) and ILT (2nd row), with SNR 2000. In the sections to the right of the distinct boundaries, only one peak was detected.

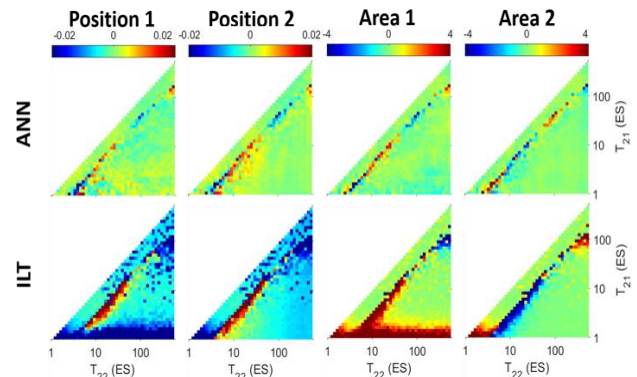


Figure 2. Error maps of simulated two-peak T_2 distribution with varying peak positions. In the diagonal sections to the left of the distinct boundaries, only one peak was detected.

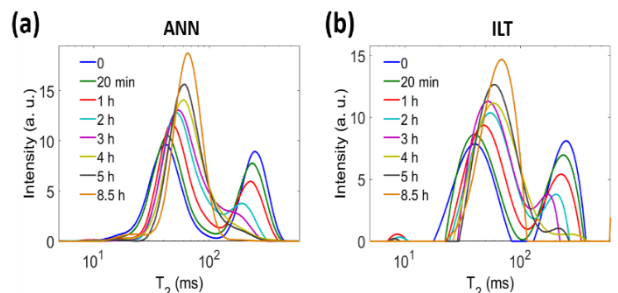


Figure 3. CPMG measurements on a phantom consisting of an Agar gel ($T_2 \approx 250$ ms) in contact with doped CuSO_4 solution ($T_2 \approx 40$ ms). T_2 distributions acquired with (a) ANN showed a smoother transition than with (b) ILT.

Simulation of Spectral Modification for Suppressing CSF in Oscillating Gradient Diffusion MRI

KB Borsos^{1,2}, CA Baron^{1,2,3}

¹Department of Medical Biophysics, Western University, London Ontario, ²Centre for Functional and Metabolic Mapping, Western University, London Ontario, ³Robarts Research Institute, London Ontario

Introduction: Oscillating gradient spin-echo (OGSE) sequences are rapidly emerging as a novel technique for diffusion MRI neuroimaging. The variable frequency of gradient oscillation enables the probing of shorter diffusion times, thereby providing unique microstructural information about the brain [1]. However like all diffusion imaging methods, OGSE also suffers from cerebrospinal fluid (CSF) partial volume contamination. Due to its high diffusivity, even small amounts of CSF in a voxel can obstruct the underlying tissue, severely bias diffusion metrics and introduce Gibbs ringing artifacts [2]. Existing techniques for CSF suppression such as fluid-attenuated inversion recovery (FLAIR) have reduced signal to noise and require elongated scan times. Hence, our goal was to design and simulate the effectiveness of using a spectrally modified OGSE sequence in conjunction with a pulse gradient spin-echo (PGSE) sequence for the purpose of mitigating CSF in the context of diffusion dispersion MRI.

Methods: A standard OGSE sequence at 38 Hz was modified by reducing the duration of the initial gradient lobe to introduce a zero-frequency spectral component. This waveform was further optimized to encode a net b-value of 1000 s/mm^2 . To remove the CSF contribution a PGSE sequence of equal b-value was also required. Using a dual-compartment voxel model and a recently determined power law diffusion dispersion model [3], the signal intensities for both waveforms were simulated for varying partial volume fractions of CSF. The apparent diffusion coefficient (ADC) was extracted from the total signal and the difference in ADCs between the modified OGSE and PGSE sequence (ΔD) was evaluated to monitor CSF invariability. For comparison this method was repeated with an unmodified 38 Hz OGSE and PGSE waveform with b-values of 600 s/mm^2 – equal to the b-value associated with the non-zero spectral component of the modified waveform.

Results: The modified and unmodified OGSE in addition to the PGSE waveforms along with their associated spectral densities are shown in Figure 1. The presence of a zero and non-zero frequency component characterizes the modified pulse. The ΔD values are shown with increasing fractional volume of CSF in Figure 2. The modified and unmodified waveforms produce ΔD estimates within 10% error (relative to their initial values), at 53% and 31% CSF volume respectively. The difference between the ΔD values for the two methods at 0% CSF volume is attributed to the broadening of spectral components.

Conclusions: Our results indicate that the ADC difference calculated using a modified OGSE sequence is considerably less susceptible to changes in CSF partial volume when compared to a normal OGSE sequence. It should be noted that as the net b-value is increased kurtosis effects may introduce additional error however, these effects are likely negligible for the chosen b-value of 1000 s/mm^2 . Consequently, this study demonstrates the potential for modified OGSE sequences to be used in conjunction with PGSE for effective CSF suppressed diffusion dispersion mapping.

References: [1] Baron & Beaulieu. *MRM*, 2014; 72: 726-736, [2] Pierpaoli *et al.* *ISMRM* (Kyoto, May 2004) 1215, [3] Arbabi *et al.* *MRM*, 2019; 00: 1–12

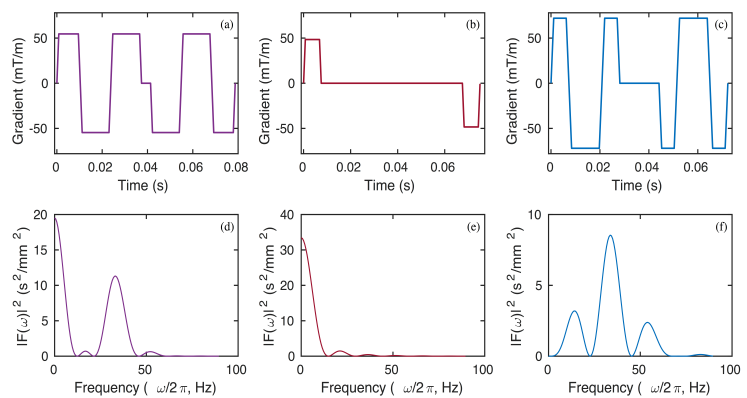


Figure 1: Gradient waveforms of the (a) modified OGSE, (b) PGSE and (c) unmodified OGSE sequences with their respective spectral densities below (d, e, f).

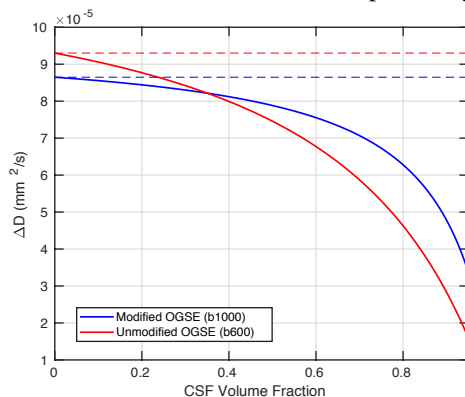


Figure 2: Difference in ADC values (ΔD) between a modified OGSE and PGSE sequence and a normal OGSE and PGSE sequence for varying partial volume fractions of CSF.

Characterization of orientation dispersion's effect on DTI using a 3D printed axon-mimetic phantom

Tristan K. Kuehn, Farah N. Mushtaha, Corey A. Baron, Ali R. Khan

Robarts Research Institute, Western University, London, Canada

Introduction: Diffusion MRI (dMRI) representations of brain microstructure are affected by the orientation and structure of axonal fibres.¹ The effect of orientation is difficult to validate in vivo because there is no widely accepted imaging modality that generates a ground truth of axonal orientation. To provide a sample with a ground truth orientation, we propose a phantom produced using fused deposition modeling with a composite material (Poro-Lay) made of an elastomer and polyvinyl alcohol (PVA). The PVA dissolves in water, leaving anisotropic pores that mimic diffusion characteristics of axons.² Here, we use the phantom to investigate the effect of complex fibre orientations on diffusion tensor imaging (DTI) metrics.³

Methods: Four cylindrical phantoms (radius 11 mm) were 3D printed with 100 μm layers of Poro-Lay. One phantom each was printed with a straight, crossing, bending, kissing, and fanning pattern. The phantoms were immersed in water for 8 days then imaged in a test tube with distilled water. Diffusion MRI was implemented at 9.4 T using 0, 60 and 120 directions at $b=0, 1000, \text{ and } 2000 \text{ s/mm}^2$, respectively.

Ground truth maps of arc radius or crossing angle were constructed for the appropriate phantoms based on their schematics, then a rigid registration was performed to align the ground truths to the phantom images. Diffusion imaging in Python (DIPY)⁴ was used to compute a diffusion tensor imaging (DTI) representation of each phantom. A quadratic regression was performed relating mean diffusivity (MD) and fractional anisotropy (FA) to the ground truth values for each voxel.

Results: MD and FA both showed weak relationships with arc radius in the bending phantom. Both trended toward the distribution seen in the straight phantom with increasing arc radius.

FA showed a significant decrease with increasing crossing angle, from 0.6 to 0.4. MD was insensitive to crossing angle.

Conclusions: These 3D printed phantoms provide a ground truth of fibre curvature and dispersion for real scan data, which would be difficult to achieve with any previously reported technique. They were manufactured in ten minutes of print time per phantom at a cost of \$0.50 per phantom.

FA's strong relationship with crossing angle means that it is difficult to differentiate between microstructural and orientational effects on FA. MD is insensitive to the effect of crossing fibres, so MD may be a robust indicator of microstructural change.

Acknowledgements: This work was supported by the Canada First Research Excellence Fund, Brain Canada, and NSERC Discovery Grants.

References: [1] Alexander AL et al. *Magnetic Resonance in Medicine*. 2001;45(5):770-780. [2] Abu-Sardana SO et al. In: *Proc. SPIE 10573*. International Society for Optics and Photonics; 2018. [3] Basser PJ et al. *Biophysical Journal*. 1994;66(1):259-267 [4] Garyfallidis et al. *Front Neuroinform*. 2014;8.

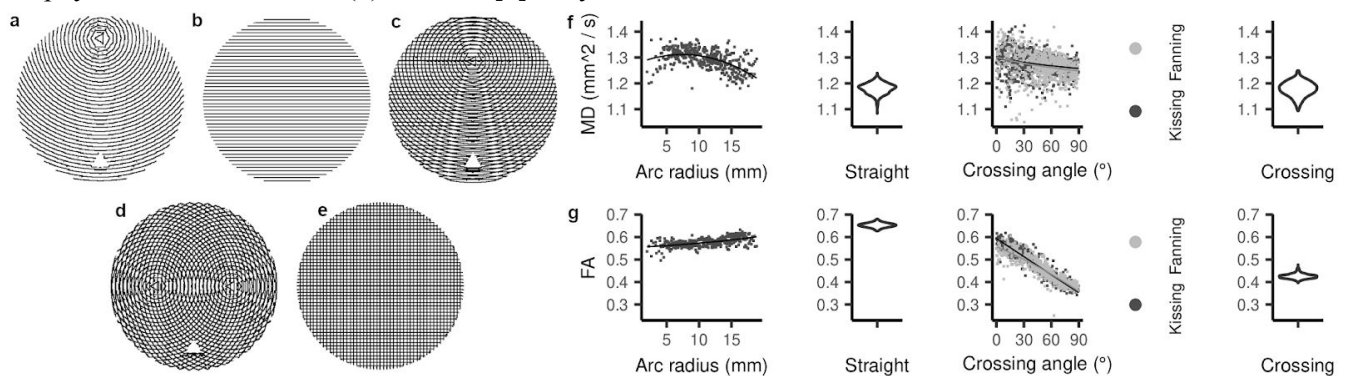


Figure 1: a-e: Schematics for the bending, straight, kissing, fanning, and crossing phantoms, in that order. f-g: For MD and FA, a scatter plot of the metric vs. arc radius in the bending phantom, a violin plot of the metric in the straight phantom, scatter plots of the metric vs. crossing angle in the kissing and fanning phantoms, and a violin plot of the metric in the crossing phantom. Violin plots depict the probability density of the metric values in each phantom.

Beyond the Diffusion Tensor: Validation of Advanced Approaches for Microstructural Diffusion MRI

Naila Rahman, Farah N. Mushtaha, Tristan K. Kuehn, Nico J. J. Arezza, Ali R. Khan, Arthur Brown, Corey A. Baron

Robarts Research Institute, Western University, London, Canada

Introduction: Microstructural diffusion MRI (dMRI) enables *in vivo* longitudinal tracking of quantitative parameters sensitive to brain microstructural changes related to pathophysiology. Multiple dMRI scans sensitive to cell microstructure in complementary ways can potentially enable microstructural modelling of cellular changes in pathology. For example: (1) Structural disorder can be probed via oscillating gradient spin-echo (OGSE) dMRI [1]; (2) Axonal spatial distribution via high b-value dMRI [2]; and (3) Cell shape via microscopic fractional anisotropy (μ FA) dMRI [3]. Here, OGSE, high b-value ($b=10,000\text{s/mm}^2$), and μ FA scan protocols were validated in a 3D printed phantom with various fiber crossing angles [4] and the μ FA protocol was successfully applied in a mouse.

Methods: Imaging was performed at 9.4T with a 1 T/m gradient insert. For all phantom scans, 2 axial slices (3mm, one per phantom) were acquired with $\text{FOV}=40\times 40\text{mm}^2$, $\text{TR}=1\text{ s}$, and 0.4 mm isotropic in-plane resolution. The OGSE sequence was implemented with $b=1000\text{s/mm}^2$, $\text{TE}=58\text{ms}$, 6 directions and OGSE frequencies of 0, 67, 100, and 133 Hz. The high b-value protocol was acquired at short (18ms) and long (52ms) diffusion times, with $\text{TE}=90\text{ms}$ and 15 directions. The temporal diffusion ratio (TDR) [2], a contrast specific to signal decay at different diffusion times, was calculated for each phantom. The μ FA protocol was implemented using a single diffusion encoding (SDE) scheme [5] with 15 linear and isotropic encodings at $b=2200\text{s/mm}^2$ and 6 linear and isotropic encodings at $b=1000\text{s/mm}^2$. Abiding by ethics board guidelines, the μ FA protocol was implemented on a SOX9 healthy female mouse, with $\text{TE/TR}=37/1000\text{ms}$, $\text{FOV}=19.2\times 14.4\text{mm}^2$, 0.2 mm isotropic in-plane resolution, 0.75mm slice thickness, 20 axial slices, and 10-minute total scan time. Post-processing included PCA denoising [6]. The DTI metrics fractional anisotropy (FA) and apparent diffusion coefficient (ADC) were calculated using MRtrix3 [7].

Results: Fig. 1a shows a steep increase of ADC at lower frequencies and a more gradual increase of ADC at higher frequencies, which is expected behaviour for hindered diffusion. The TDR did not change with respect to fiber crossing angle (Fig. 1b) and a positive TDR is a signature of diffusion restriction. FA values were lower than μ FA values (Fig. 1c), which validated the μ FA protocol, as μ FA is independent of fiber orientation dispersion [3]. FA and μ FA maps from a healthy mouse brain (Fig. 2) indicate that μ FA may be more sensitive to neurites in the grey matter, as many parts of the FA map are hypointense, likely due to crossing neuron fibers.

Conclusions: In this work, OGSE, high b-value, and μ FA scan protocols were validated in a 3D printed phantom and the μ FA protocol was implemented in a mouse. The preliminary results reveal the potential of TDR as a contrast for white matter characterization, the sensitivity of μ FA maps to microstructure compared to conventional FA maps, and a strong ADC dependence on frequency. Evidence of a linear dependence of ADC on the square root of frequency in healthy human white matter was shown for the first time by Arbabi et al. [8] and in future studies, this relationship will be explored in animal models to probe tissue microstructure in various pathologies.

References: [1] Schachter, M et al. *J Magn Reson* 147 (2000). [2] Dell'Acqua, F et al. *Proc Int Soc Magn Reson Med* 26 (2019). [3] Shemesh, N et al. *Magn Reson Med* 75 (2016). [4] Abu-Sardanah, S et al. *Proc. SPIE* 10573 (2018). [5] Arezza, N et al. *Proc Int Soc Magn Reson Med* 80 (2018). [6] Veraart, J et al. *Neuroimage* 142 (2016). [7] Tournier, JD et al. *Neuroimage* 202 (2019). [8] Arbabi, A et al. *Magn Reson Med* October (2019).

Acknowledgements: New Frontiers in Research Fund, NSERC CGS-M

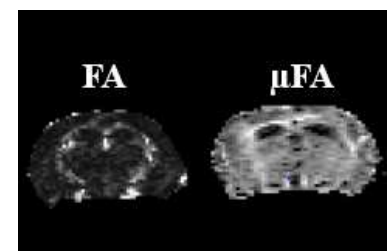
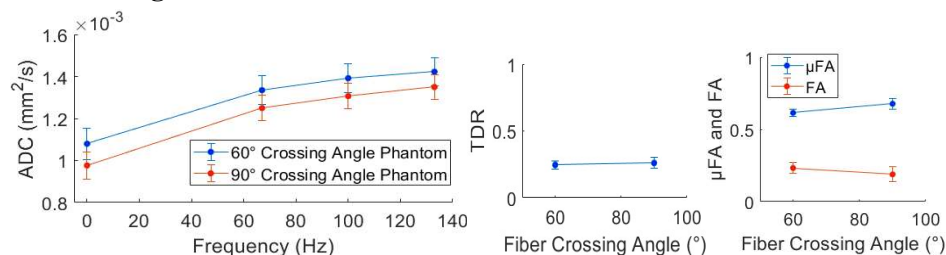


Fig. 1. a) ADC dependence on frequency. b) Relationship of TDR with fiber crossing angle. c) Relationship of μ FA and FA with fiber crossing angles. All error bars indicate standard deviation in the ROI.

Fig. 2. FA and μ FA maps from a healthy mouse brain.

Neuritic Architecture Relates to Functional Brain Activity

Christin Schifani^{1,2}, **Colin Hawco**^{1,2,3}, **Arash Nazeri**⁴, **Aristotle N. Voineskos**^{1,3}

¹ Campbell Family Mental Health Research Institute, Centre for Addiction and Mental Health, Toronto, Canada

² Temerty Centre for Therapeutic Brain Intervention and Campbell Family Research Institute, Centre for Addiction and Mental Health, Toronto, Canada

³ Department of Psychiatry, Faculty of Medicine, University of Toronto, Toronto, Canada

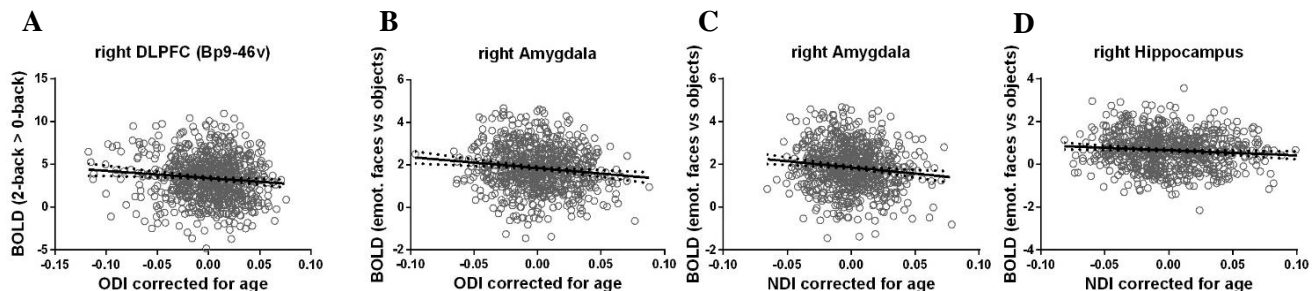
⁴ Mallinckrodt Institute of Radiology, Washington University School of Medicine, Saint Louis, MO, USA

Introduction: Impairment in working memory and emotion processing are features of psychiatric disorders and are linked to alterations in functional brain activity. Although cognitive deficits are thought to be driven by synaptic/neuritic alterations, there is limited *in vivo* evidence. Recent studies confirmed neuritic architecture alterations *in vivo* in schizophrenia using Neuritic Orientation Dispersion and Density Imaging (NODDI). To identify biological mechanisms underlying brain activity, we characterized relationships between neuritic architecture, BOLD (Blood-Oxygen-Level-Dependent) activation and cognition using human *in vivo* imaging.

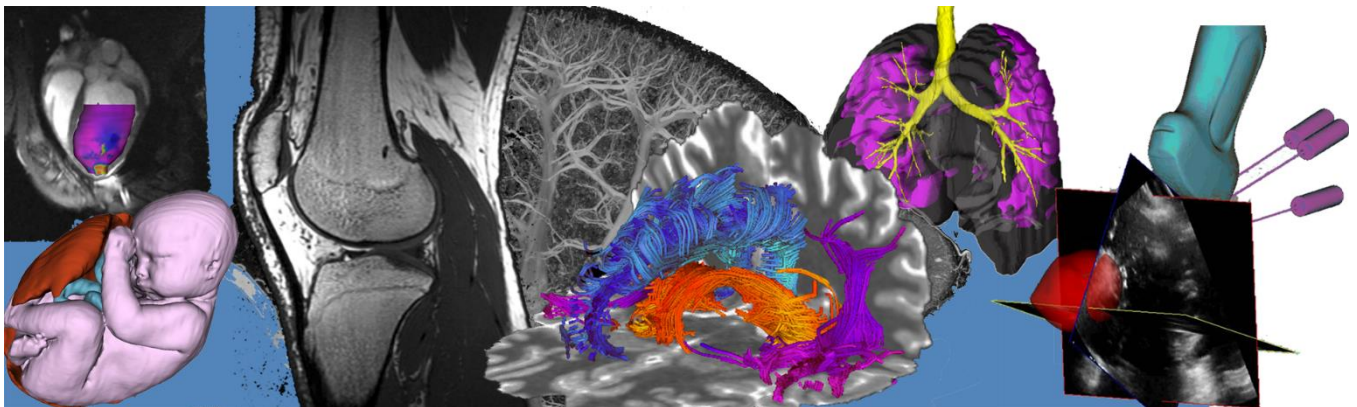
Methods: We used publicly-available human connectome project imaging data from 763 healthy volunteers. Brain activity was estimated using functional MRI BOLD signal contrast of an N-back working memory task (2-back>0-back) in the dorsolateral prefrontal cortex (DLPFC) and emotion processing task (faces>objects) in amygdala and hippocampus. Neuritic architecture was estimated using diffusion-weighted NODDI providing neuritic orientation dispersion (ODI) and density (NDI) indices per region of interest. Associations were assessed using linear correlation analysis. Mediation between neuritic architecture and task accuracy by BOLD activation was explored using bootstrapping (1000x).

Results: Preliminary analysis revealed associations between task-induced BOLD activation and neuritic architecture in the right hemisphere. Lower working memory task-induced BOLD signal was related to higher ODI in DLPFC (**A**; $r=-0.10$; Bonferroni-corrected $p=0.016$). We observed a reliable partial mediation of BOLD on ODI-to-N-back-task-accuracy relationship (52%; $\beta=-12.6\pm 4.3$; 95%CI [-21.2,-4.47]). Lower emotion processing task-induced BOLD signal was related to higher ODI (**B**; $r=-0.130$; Bonferroni-corrected $p=0.0028$) and NDI (**C**; $r=-0.127$; Bonferroni-corrected $p=0.0038$) in amygdala, and NDI in hippocampus (**D**; $r=-0.095$; Bonferroni-corrected $p=0.070$). We observed reliable partial mediations of BOLD on NDI/ODI-to-emotion-processing-task-accuracy relationships in hippocampus (NDI-to-task-accuracy: 33%; $\beta=-1.09\pm 0.49$; 95%CI [-2.14,-0.26]) and amygdala (NDI-to-task-accuracy: 31%; $\beta=-1.4\pm 0.85$; 95%CI [-3.34,-0.14]; ODI-to-task-accuracy: 18%; $\beta=-1.1\pm 0.68$; 95%CI [-2.62,-0.077]).

Conclusions: We provide first direct evidence linking neuritic architecture and BOLD activation across tasks. This may suggest that changes in neuritic architecture account for some variability in functional activity. Our next step is to examine these relationships in a schizophrenia sample.

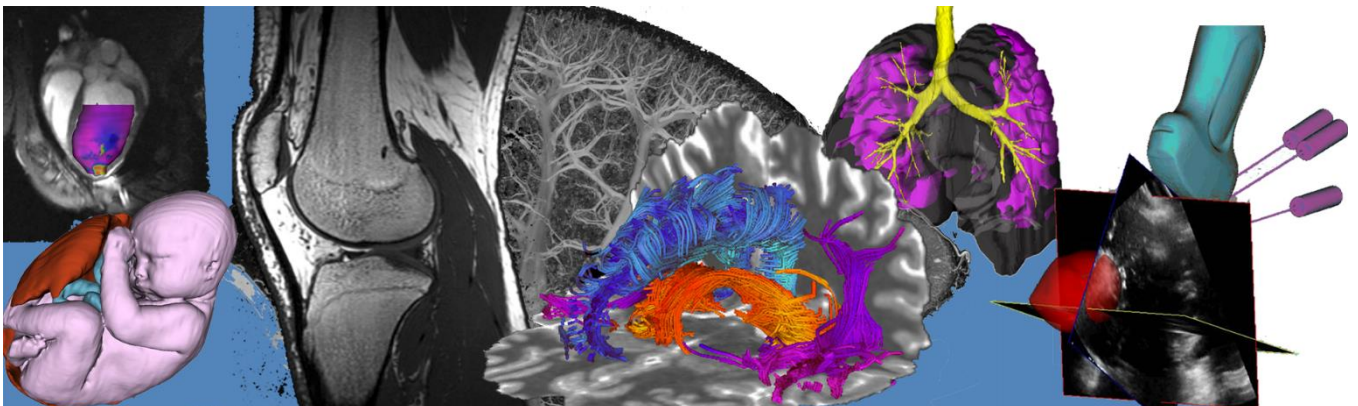


Poster Presentation Abstracts



Poster Presentation Abstracts

Session 1: Cellular and Molecular Imaging



Vascular Disruption in Subcutaneous Mouse Cancer Models Using Ultrasound Activated Agents

Yu-Jack Shen¹, Sean F McGrath^{2*}, Yamato Motooka³, Yun Xiang⁴, Yiran Zou¹, Nicholas Bernards³, Alexander Gregor³, Kazuhiro Yasufuku³ and Naomi Matsuura^{1,2,4}.

¹Department of Material Science and Engineering, University of Toronto

²Institute of Biomaterials and Biomedical Engineering, University of Toronto

³Division of Thoracic Surgery, Toronto General Hospital, University Health Network, Toronto

⁴Department of Medical Imaging, University of Toronto

*Presenting Author

Introduction: Ultrasound-active agents (e.g. microbubbles or nanodroplets) combined with high-intensity focused ultrasound are used for vascular disruption therapy (VDT) and have proven to inhibit tumor growth. [1, 2, 3]. Vaporizing and cavitating decafluorobutane (DFB) nanodroplets by exposure to ultrasound energy generates microjets and shockwaves that damage tumour vasculature [3, 5]. Conventional ultrasound (applied from outside of the body) cannot penetrate through lung tissue due to the tissue-air interfaces in the alveoli [4]. However, endobronchial ultrasound (EBUS) systems enable access to the deep lung. Combining EBUS with ultrasound-active agents could present a novel VDT-based treatment for lung tumours. This project focusses on the development of ultrasound-active agents and their application with EBUS for lung cancer treatment.

Methods: Microbubbles, composed of 1,2-dipalmitoyl-sn-glycero-3-phosphatidylcholine and 1,2-dipalmitoyl-sn-glycero-3-phosphate (sodium salt) in cyclooctane and 1,2-dipalmitoyl-sn-glycero-3-phosphatidylethanolamine-N-[methoxy(polyethylene glycol)-5000] and DFB, were first synthesized in-house. Next, the emulsion was condensed in -20°C isopropyl alcohol for approximately 10 seconds. The size distribution was analyzed by diluting the nanodroplet solution in physiological temperature (37°C) Isoton II electrolyte (Beckman Coulter, USA), and measuring size distributions with a Multisizer 4e Coulter counter (Beckman Coulter, USA). *In vivo* experiments were conducted using AE17-OVA murine mesothelioma subcutaneous tumours in the right flank of C57BL/6 mice (n=1). Intravenous injection of 150 µL of DFB nanodroplets was followed by 5MHz, approximate mechanical index 1.2 EBUS exposure (EU-ME-2 PREMIER ultrasound processor with BF-UC-180F EBUS bronchoscope (Olympus, Japan)). The effects on the vasculature were examined by comparing tumour blood perfusion using contrast-enhanced ultrasound with microbubbles before and after EBUS exposure.

Results: Nanodroplet size distribution following incubation in Isoton is shown in Figure 1 (left), at various time points. The stability the nanodroplet distribution was plotted (Figure 1 right), with 68% of the nanodroplets remaining after 5 hours. *In vivo*, the perfusion of the tumour pre- and post-treatment measured using contrast-enhanced ultrasound and microbubbles showed that the normalized peak intensity pre-treatment is significantly greater than post treatment (Figure 2). The tumour microbubble perfusion profile is shown versus time in Figure 2 left, and the peak intensity is shown in Figure 2 right.

Conclusion: Long lasting, EBUS-active DFB nanodroplets were synthesized with good stability. *In vivo*, local ultrasound treatment with the EBUS platform combined with DFB nanodroplets reduced tumour perfusion in mouse models. The long-term effects of VDT using this EBUS-DFB nanodroplet platform will be evaluated in future work.

References: [1] C. Gridelli et al, *Oncologist*, vol. 14, no. 6, pp. 612 – 620, 2009. [2] J. Wang et al, *International journal of cancer*, vol. 137, pp. 2478 – 2491, 2015 [3] Y. Ho, C. Yeh, *Acta Biomaterialia*, vol. 49, pp. 472 – 485, 2017 [4] C.F. Dietrich, *Endoscopic Ultrasound*, vol. 6, no. 1, pp. 43 – 48, 2017 [5] Y. Zhou, *Journal of Therapeutic Ultrasound*, vol. 3, no. 20, 2015

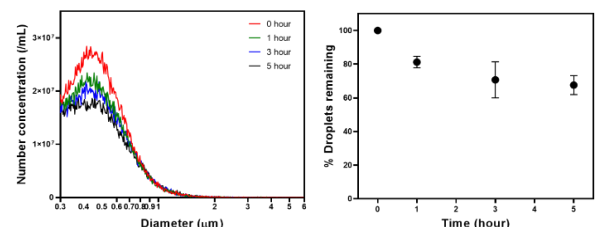


Figure 1: Size distribution (left) and normalized concentration (right) of diluted DFB nanodroplets decay in physiological temperature.

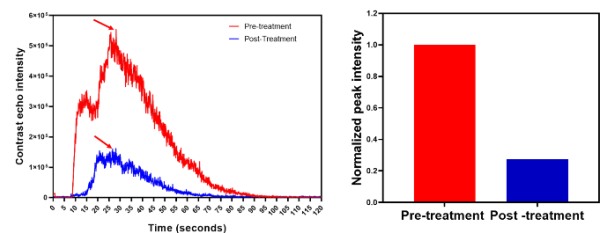


Figure 2: Tumour microbubble perfusion profile pre and post nanodroplet treatment (left). Quantification of blood flow reduction with bolus injection peak intensity processing (right).

Docetaxel-loaded nanobubbles for combined focused ultrasound-induced antivascular therapy and targeted drug delivery of breast cancer

Yun Xiang^{1,2}, Yiran Zou^{3*}, Carly Pellow^{4,5,6}, David Goertz^{4,5}, and Naomi Matsuura^{1,2,3}

¹Institute of Biomaterials and Biomedical Engineering, ²Department of Medical Imaging, ³Department of Material Science and Engineering, and ⁴Department of Medical Biophysics, University of Toronto, Ontario, Canada.

⁵Sunnybrook Research Institute, Toronto, Ontario, Canada.

⁶Princess Margaret Cancer Center, University Health Network, Toronto, Ontario, Canada.

*Presenting author

Introduction. Breast cancer is the leading cause of cancer death for women worldwide [1]. Docetaxel (DTX, commercially known as Taxotere®) plays an essential role in breast cancer therapy but exhibits suboptimal pharmacokinetic profiles, leading to limited drug accumulation in cancerous tissues [2]. As a result, multiple lengthy infusions are required, which can provoke systemic toxicity and debilitating side effects. Studies have shown that the co-injection of Taxotere® with lipid-stabilized microbubbles results in synergistic, profound antitumour efficacy in preclinical models after focused ultrasound (FUS)-induced microbubble cavitation [3]. Although treatment efficacy is improved, systemic injections of toxic free DTX are still required. In this study, DTX-loaded, acoustically active nanobubbles (NB) are introduced. Upon FUS exposure, these DTX-NBs can cavitate to damage tumour vasculature (i.e., antivascular effect) while delivering high dosage of DTX (due to its high surface area to volume ratio) on tumour site for improved therapeutic outcomes.

Methods. DTX was first localized in a precursor oil-in-water droplet emulsion stabilized by phospholipids including 1,2-dipalmitoyl-sn-glycero-3-phosphocholine, 1,2-dipalmitoyl-sn-glycero-3-phosphate, and 1,2-dipalmitoyl-sn-glycero-3-phosphoethanolamine-N-[methoxy(polyethylene glycol)-5000]. After purification, droplets were lyophilized to form hollow lipid shells that can then form a bubble suspension via gas exchange and reconstitution. Bubble size distributions were characterized using Multisizer 4e, and DTX loading was quantified using a UPLC system. The bioavailability of DTX-NBs was assessed *in vitro* on EMT-6 cell viability using MTT assay (n=18). The *in vivo* capability of DTX-NBs to induce antivascular effect upon FUS exposure (1 MHz, 1.65 MPa) was examined utilizing the CT26 xenograft tumour model on Balb/c mice (n=3). Pre-established sonication schemes with an in-house FUS setup was employed for DTX-NB cavitation [3]. Microbubbles were injected and allowed to circulate for 3 mins before and immediately after the treatment to observe the change in blood perfusion using a clinical ultrasound scanner (EPIQ 7G, Philips). MATLAB was used to draw a region of interest (ROI) in tumour center (figure 1-C) and extract per frame pixel intensity for blood flow reduction assessment.

Results. 106±19 µg of DTX has loaded onto ~10¹⁰ bubbles with a mode diameter of ~240 nm per ~0.45 µL of gas (n>6). At a clinically relevant dose of ~50-100 µL fluorocarbon gas/kg, a DTX dosage of ~10-20 mg/kg can be achieved, comparable to FDA-approved clinical dosage. At 200 nM, the cytotoxicity of DTX-NBs after cavitation was equivalent to that of Taxotere® (*p<0.001), as shown in figure 1-A, demonstrating the bioavailability of released drugs after FUS. *In vivo* perfusion studies showed a significant blood flow reduction (**p<0.05) in tumour center after FUS treatment, as shown in Figure 1-B, indicating successful vascular disruption due to NB cavitation.

Conclusions. This study introduces novel acoustically responsive NBs, at high DTX loading concentration equivalent to clinical doses. *In vitro* and *in vivo* characterization of these DTX-NBs demonstrated the successful release of bioavailable DTX and antivascular efficacy with FUS. The next steps, including *in vivo* DTX bio-distribution and survival studies, will be conducted in the future.

References. [1] F. Bray et al., *CA. Cancer J. Clin.*, vol. 68, pp. 394-424, 2018. [2] L. Feng et al., *Cancer lett.*, vol. 334, no. 2, pp. 157-175, 2013. [3] D. E. Goertz et al., *PLoS One*, vol. 7, no. 12, 2012.

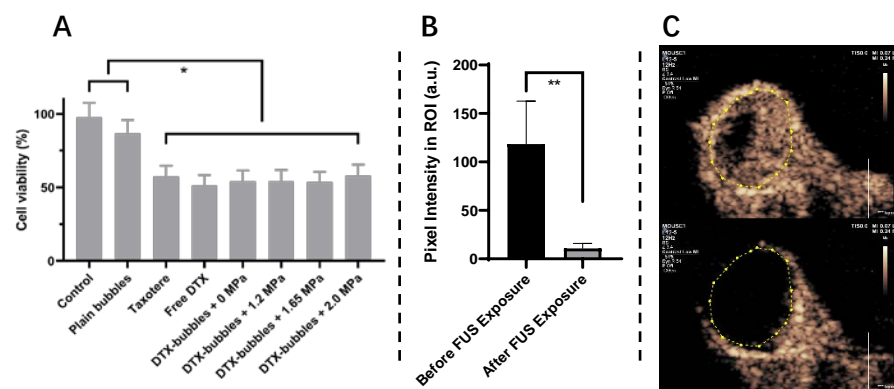


Figure 1. (A) *In vitro* bioavailability assessment comparing plain NBs, Taxotere and DTX-NBs with FUS exposure, (B) *in vivo* perfusion assessment on ROI intensity at peak frames, and (C) examples of ultrasound images showing circulating microbubbles with ROI delineating tumour center before (top) and after (bottom) FUS treatment.

Detecting the depletion of liver, splenic, and tumor-associated macrophages with fluorine-19 MRI at 3 Tesla

Olivia C. Sehl^{1,2}, Amanda M. Hamilton¹, Paula J. Foster^{1,2}

¹ Imaging Research Laboratories, Robarts Research Institute, Canada

² Department of Medical Biophysics, University of Western Ontario, Canada

Introduction Tumor promotion and progression are dependent on processes provided by cells in the tumor microenvironment^{1,2}. The most abundant and influential cells are tumor-associated macrophages (TAMs). TAMs are associated with tumor growth, progression, and metastatic potential, by promoting tumoral angiogenesis, immunosuppression, and invasion. TAMs can also modulate the efficacy of anti-cancer therapies through similar processes². As such, many therapeutic approaches consider TAMs as an additional target. A meta-analysis of clinical data indicated that in over 80% of breast cancer cases, there exists a strong correlation between TAM infiltration and poor patient prognosis. Despite this strong evidence, there are limited approaches to investigate the role of TAMs *in vivo*. We aim to (1) image and quantify TAMs using fluorine-19 (¹⁹F) MRI cell tracking and (2) detect changes in ¹⁹F signal and monitor tumor response following macrophage depletion. Our overall hypothesis is that *in vivo* ¹⁹F-based MRI cell tracking can be used to evaluate the density and distribution of macrophages in tumors and associated metastases. Additionally, systemic administration of a macrophage depleting drug, clodronate³, will result in detectable changes in tumoral ¹⁹F signal.

Methods *Animal Model.* 3×10^5 4T1 breast cancer cells were implanted to the mammary fat pad of 11 BALB/c mice. 5, 10, and 15 days later, 6 of these mice received 1 mg clodronate by intravenous injection. Clodronate will be taken up by phagocytic macrophages of the reticuloendothelial system and result in cell apoptosis³. Control mice (n=5) received no clodronate. On day 16, each mouse was administered 200 μ L perfluorocarbon agent (VS-1000H DM Red, CelSense Inc.), intravenously. This agent is taken up by phagocytic macrophages *in situ* and is detected by ¹⁹F MRI. *Image Acquisition.* 24 hours later, both ¹H and ¹⁹F images were acquired on a 3 Tesla clinical MRI using a dual tuned surface coil and a balanced steady state free precession (bSSFP) sequence⁴. Regions of ¹⁹F signal were delineated, assessed for changes in spatial distribution, and quantified by comparison to ¹⁹F signal in reference tubes. *Endpoint Verification.* Following the last MRI exam, mice were sacrificed, and their livers, spleens, and tumors were excised. F4/80 immunostaining and fluorescence microscopy was conducted on these organs to identify macrophage populations and confirm the localization of the perfluorocarbon agent (red).

Results ¹⁹F signal in the liver and spleen was significantly reduced (by 65%, $p < 0.05$) with clodronate treatment, indicating macrophage depletion (seen in **fig 1**). Mice that were administered clodronate developed smaller tumors (24%, $p < 0.01$) and less ¹⁹F signal was detected in these tumors (26%, $p < 0.05$). These findings are visually intuitive in 3D renderings. Using our previous measurement of PFC-macrophage loading by NMR⁴, we estimate there are 9.81×10^7 TAMs in control mice and 7.31×10^7 TAMs in mice treated with clodronate. In both MRI and histology, the perfluorocarbon agent and TAMs were identified predominately at the tumor periphery.

Conclusions ¹⁹F MRI cell tracking can be used to evaluate the density and distribution of macrophages in the liver, spleen, and tumor, using a clinical (3T) MRI. ¹⁹F signal (TAM burden) may provide a better indicator of future tumor growth, aggressiveness, and risk of metastasis, than traditional measurements of tumor size. ¹⁹F MRI is sensitive to changes in macrophage number and may be a useful strategy to monitor traditional and TAM-targeting cancer therapies. To the best of our knowledge this is the second study demonstrating the ability to track cells in mice using ¹⁹F at 3T. By implementing ¹⁹F cell tracking on a 3T clinical MRI, we are moving towards translation of this technique⁴. We hope that this approach can be used to provide a measure of the macrophage content in primary tumors and metastases to study various tumor models and novel cancer treatments.

[1] Makela, A. V & Foster, P. J. *Magn Reson Med* **80**, 1138–1147 (2018). [2] De Palma, M. & Lewis, C. E. *Cancer Cell* **23**, 277–286 (2013). [3] Zeisberger, S. M. *et al. Br J Cancer* **95**, 272–281 (2006). [4] Makela, A. V. & Foster, P. J. *Magn Reson Mater Physics Biol Med.* (2018).

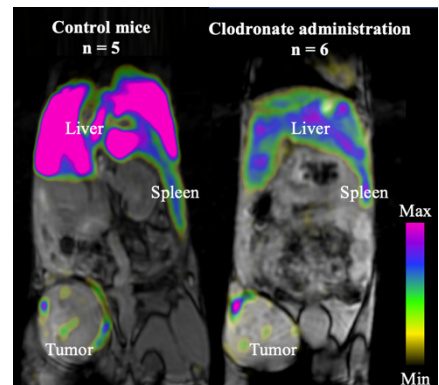


Fig 1. ¹⁹F overlay to anatomical ¹H MRI reveals the distribution of macrophages in the liver, spleen and tumor. ¹⁹F signal is reduced in mice administered clodronate.

Quantitative spatial analysis of single cells in the tumour microenvironment using digital immunofluorescence protein multiplexing

Alison M Cheung¹, Dan Wang¹, Kela Liu¹, Simone Stone², Ben X. Wang², Fiona Ginty³, Anne Martel¹, Pam Ohashi² & Martin J. Yaffe¹

¹Biomarker Imaging Research Lab, Sunnybrook Research Institute, Toronto, ON

²Princess Margaret Cancer Centre, Toronto, ON

³Biosciences, General Electric Research (GER), Niskayuna, NY

Background: Immune checkpoint-inhibitor therapy attempts to harness the cells of the immune system to target cancer. The expression of checkpoint inhibitor molecules (PD1/PDL-1) on immune cell subsets, such as CD4⁺ or CD8⁺ tumour-infiltrating lymphocytes (TILs) or CD68⁺ tumour-associated macrophages, could strongly influence the patient's response to immunotherapeutic treatment. Protein marker imaging with single-cell analysis allows us to identify and quantify each immune subset as well as spatial relationships between subsets. **Methods:** The expressions of T cell markers CD3, CD4 and CD8, macrophage marker CD68, immune checkpoint proteins PD-1 and PD-L1, together with proliferative marker (KI67) and cancer-specific marker PCK (pan-Cytokeratin) were studied on single 4µm sections of formalin-fixed, paraffin-embedded (FFPE) of ovarian cancers using *in situ* immunofluorescence protein marker multiplexing system (MxIF, Cell DIVE™ GE Healthcare, Issaquah WA) (Fig. 1). Co-expression patterns of markers on single cells were studied using the t-distributed stochastic neighbor embedding (t-SNE) dimensionality reduction method. Densities of immune subsets were quantified using thresholding with levels defined by comparing positive and negative control tissues. Spatial relationship was evaluated by quantifying the most common neighboring cell type with co-occurrence matrices. **Results:** Significant variations in the densities of immune infiltrates as well as the expressions of the immune checkpoint molecules were observed from six ovarian cancer cases studied. The percentage of PD-1⁺ CD4⁺ T-helper lymphocytes or PD-1⁺ CD8⁺ T-cytotoxic lymphocytes ranged from as low as 2% to as high as 46%. PDL-1 expressing cancer cells ranged from 11.5% to 33%. Spatial analysis suggests that PD-1 expressing lymphocytes tend to be in close proximity to PDL-1⁺ cancer cells (Fig. 2). **Conclusions:** Our work demonstrates the application of MxIF in quantitative imaging analysis of the immune repertoire and in assessing their heterogeneous spatial distributions in tumours. Our next step is to study a cohort of pre- and post-treatment specimens with outcome data to examine how immune subset densities could predict response to checkpoint inhibition therapy.

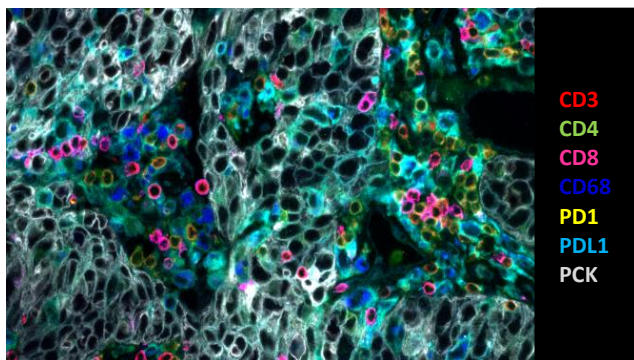


Figure 1: MxIF staining of immune cell subsets. Representative composite image showing the simultaneous staining of multiple immune protein markers on an ovarian cancer tissue section

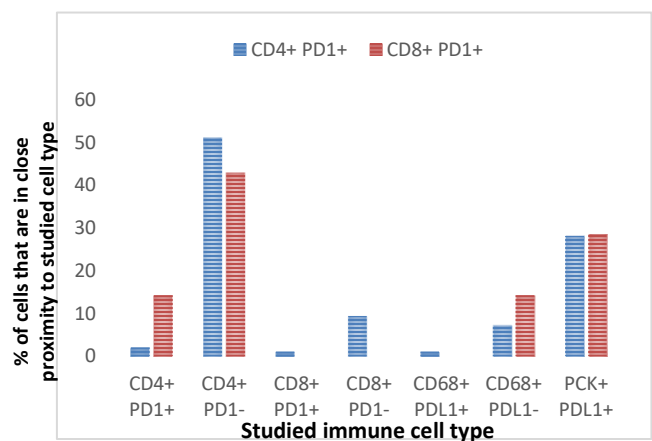


Figure 2: Spatial analysis of immune subsets in one ovarian cancer specimen. The most common neighboring immune cell type (x-axis) of CD4+ PD1+ T cell (blue bar) or of CD8+ PD1+ T cell (red bar) are presented as a %. In this case, both CD4+ PD1+ and CD8+ PD1+ cell types were mostly located next to CD4+ PD1- immune cells or PCK+ PDL1+ cancer cells.

Non-destructive Quantification of Small Molecules Diffusion using Micro-CT

Tina Khazaei,^{1,2,3} Chris J.D Norley,² Steven I. Pollmann,² Hristo N. Nikolov,² and David W. Holdsworth,^{1,2,3,4}
¹Department of Medical Biophysics, ²Robarts Research Institute, ³Western Bone and Joint Institute,
⁴Department of Surgery, Western University, London, Ontario, Canada

Introduction: Optimization and characterization of small-molecule diffusion is important in the development of novel drug-delivery systems for medical therapy. For example, the delivery of local antibiotics is an important component of therapy for infection near orthopedic implants; however, the exact local elution kinetics of antibiotics from carriers is not yet fully understood. In this study, our objective is to validate a novel micro-computed tomography (micro-CT) imaging technique to track diffusion of a small-molecule drug surrogate. This approach is relevant to applications of novel drug-delivery and release systems for local-treatment.

Method(s): In this work we characterized diffusion of the contrast agent drug surrogate through an agar-based tissue-equivalent phantom. A radio-opaque contrast agent (Iohexol; MW 821 Da) was chosen as a small-molecule surrogate for commonly used antibiotics (*e.g.* Vancomycin; MW 1449 Da). A two-part phantom was fabricated in a custom-made container. The central core (diameter = 1.7cm, length = 4.0cm) was loaded with 30 mg ml⁻¹ of Iohexol contrast agent. The outer annulus (diameter = 7.0cm, length = 5.0cm) was filled with pure agar. Agar was prepared by manually mixing 300 ml of deionized water with 10.5 g agar powder (Sigma-Aldrich, A9799). The product was cooked in a microwave for 5 minutes; impurities were skimmed from the surface and heating continued for two additional minutes to obtain a final product with no visible imperfections. The inner cylinder was fabricated in a standardized fashion by casting in an inert silicon elastomer mold. Agar was mixed in the ratio of 8.17 ml of agar to 0.91 ml Iohexol (Omnipaque 300 mg ml⁻¹) and injected into the mold; the phantom was then kept undisturbed for 30 minutes. The Iohexol-loaded agar cylinder was then placed into the container and cast with a peripheral annulus of pure agar, resulting in an intact two-part phantom.

Image acquisition was performed with a pre-clinical micro-CT system (GE eXplore SpeCZT; 90 KVP, 40 mA, 16ms exposure and 900 views). A 5-minute short-scan protocol was used; scans were repeated at regular intervals for up to 76.0 hours. Projections were then reconstructed, corrected for beam hardening and scaled in Hounsfield units.

Results: Custom 3D volumes of interest were selected in axial CT slices to measure signal intensity (Fig. 1). Diametric line profiles were plotted across axial slices at varying time points, representing diffusion from an Iohexol-loaded core to agar at the periphery. Images of the sample volume were acquired as early as 75 minutes after fabrication. The maximum Iohexol concentration (30 mg ml⁻¹) corresponds to 1380 ±24 Hounsfield units, and image noise observed in the periphery of the phantom was ±15 HU. The diffusion distance at each time point was measured by image thresholding to a constant value of 300 HU. The diffusion coefficient was derived by analysis of early-phase 2D (*i.e.* radial) diffusion distance over the first 12 hours. The derived diffusion coefficient was $2.30 \times 10^{-10} \text{ m}^2 \text{ s}^{-1}$, which compares well with literature values of $2.5 \times 10^{-10} \text{ m}^2 \text{ s}^{-1}$.

Conclusions: We report that non-invasive micro-CT imaging can be used to measure small-molecule diffusion in a tissue-equivalent phantom. We will take advantage of this technique to measure elution kinetics in new novel hybrid structures for local drug delivery, which includes current bone-substitute antibiotic carriers within a 3D-printed Ti-based highly porous scaffold.

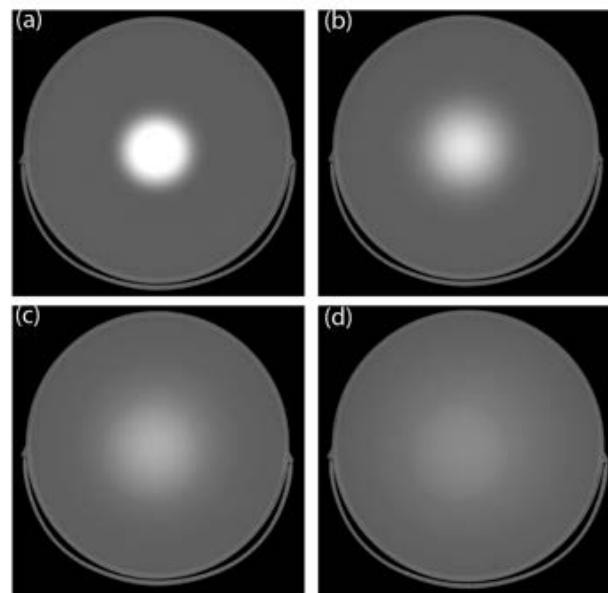


Fig. 1: 3D CT images represent Iohexol concentration and diffusion over time. (a) 1 hour, (b) 12 hours, (c) 30 hours, and (d) 76 hours after phantom fabrication.

Development of molecular imaging tools for monitoring the fate of T cell cancer immunotherapiesVeronica P Dubois^{1,2}, John J Kelly², Paula Foster^{1,2}, John Ronald^{1,2,3}

1. The Department of Medical Biophysics, Western University, London, Ontario 2. Robarts Research Institute, London, Ontario 3. Lawson Health Research Institute, London, Ontario

Introduction: Chimeric antigen receptor T (CAR-T) cell therapy is an emerging cancer treatment in which a patient's own T cells are isolated and engineered to express a CAR. CAR engineering redirects the T cells to bind to a specific protein expressed by cancer cells and induce cancer cell death. CAR-T cells targeting the B cell antigen CD19 have shown promising results in patients with hematological malignancies with up to 70% of patients responding to treatment¹. Despite this success, CAR-T cell therapies can cause severe off-target toxicities and not all patients respond to this treatment (up to 30%). Currently, CAR-T cell monitoring is limited to blood tests that are invasive and one-dimensional as they only provide information on the total number of circulating CAR-T cells and lack any information about biodistribution, particularly at tumour sites². An imaging tool for tracking CAR-T cells could provide important patient-specific data on CAR-T cell fate to inform on potential success or failure of treatment as well as off-target toxicities. Fluorine-19 magnetic resonance imaging (¹⁹F MRI) allows for the detection of ¹⁹F perfluorocarbon (¹⁹F PFC) labeled cells non-invasively to provide information on cell location(s) and number(s). Our end goal is to track the fate of ¹⁹F PFC-labeled CD19-targeted CAR-T cells in a mouse model of B cell leukemia using ¹⁹F MRI.

Methods: T cells were engineered to co-express a CD19-targeted CAR and green fluorescent protein (GFP). Engineered cells were evaluated with flow cytometry, expanded, and then labeled with 5 mg/ml ¹⁹F PFC overnight. Next, CAR-T cells were co-cultured with firefly luciferase-expressing CD19+ human B cell leukemia cells (NALM6) and bioluminescence imaging was performed to evaluate cancer cell cytotoxicity. Pilot experiments were performed in naïve nod-scid-gamma (NSG) mice (n=2) that received an intravenous injection of 3-5 million ¹⁹F PFC labeled CAR-T cells. ¹⁹F MRI was performed on a 3T clinical scanner using a dual tuned surface coil and balanced steady state free precession (bSSFP) sequence day 1 and day 6 post CAR-T cell injection. MRI images were analyzed to evaluate CAR-T cell location and relative number.

Results: Flow cytometry revealed that engineered T cells populations were 75-99% GFP/CAR positive. *In vitro* luminescence cytotoxicity assays confirmed that ¹⁹F PFC labeled CAR-T cells significantly decrease leukemia cell viability compared to naïve T cells (p<0.05). Day 1 following ¹⁹F PFC labeled CAR-T cell injection, ¹⁹F signal was detected in the abdomen of both mice with an average signal of 1.28×10^{18} ¹⁹F spins. By Day 6, the ¹⁹F signal was still visible in the abdomen but the signal had decreased to 3.6×10^{17} ¹⁹F spins.

Conclusions: We have shown that ¹⁹F MRI is able to detect signal one and six days post injection of ¹⁹F PFC labeled CAR-T cells. Current work is focused on extensive characterization of ¹⁹F PFC labeled CAR-T cytotoxicity *in vitro* before tracking these cells in a mouse model of B cell leukemia using ¹⁹F MRI. If successful, these imaging tools may be useful for the evaluation of CAR-T cell therapies in patients and may have broad applications for tracking emerging CAR-T cell formulations directed towards solid tumour antigens.

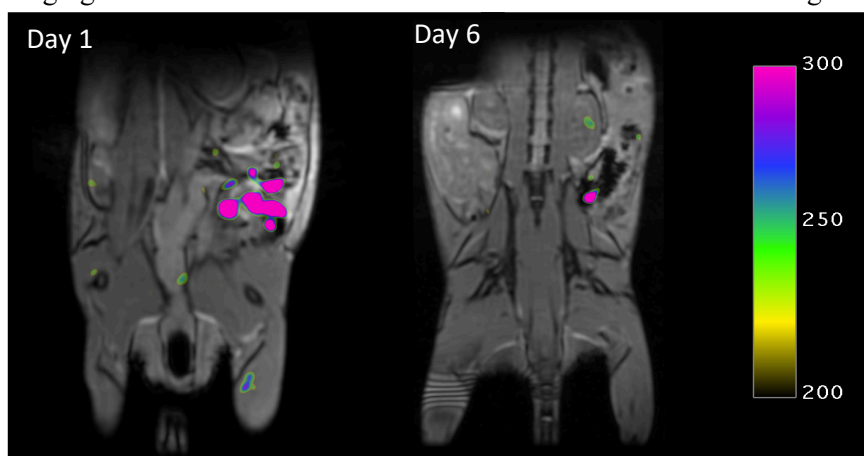


Figure 1: ¹⁹F MRI of ¹⁹F PFC labeled CAR-T cells injected intravenously into a nod-scid-gamma mouse imaged on day 1 and day 6 post-injection.

References: [1] Maude SL, Frey N, Shaw PA et al. Chimeric antigen receptor T cells for sustained remissions in leukemia. *N Engl J Med.* 2014;371:1507-1517., [2] Porter DL, Levine BL, Kalos M et al. Chimeric antigen receptor-modified T cells in chronic lymphoid leukemia. *N Engl J Med.* 2011;365:725-733.

Development of a Human-Based Dual PET/MR Reporter Gene System for Cell Tracking

Authors: Shalaby, N.¹, Nystrom, N.¹, Kelly, J.¹, Martinez, F.¹, Dhanvantari, S.^{1,2,4}, Hicks, J.^{1,2,3,4}, Fox, M.^{2,4}, Thiessen, J.^{1,2,3}, Scholl, T.¹, Ronald, J.^{1,2}

¹Department of Medical Biophysics, Schulich School of Medicine and Dentistry, Western University, ²Lawson Health Research Institute, ³Lawson Cyclotron and Radiochemistry Facility, ⁴Saint Joseph's Health Care

Introduction: Although various molecular imaging tools and labelling techniques have been developed for preclinical and clinical cell-tracking, there is a need for safer, more sensitive and reliable methods to track available cell therapies. Multi-modal imaging is a common technique which combines the benefits of more than one imaging tool to non-invasively determine cell viability, functionality, biodistribution and persistence of transplanted therapeutic cells. For this work, we are investigating the benefits of a dual PET and MRI reporter gene system that is safe, sensitive and allows for optimization of cell-tracking information from both modalities. This reporter gene system uses human-derived genes in combination with clinically approved imaging contrast agents to provide quantifiable, sensitive information as well as longitudinal monitoring. **Methods:** 231 triple negative breast cancer cells were dual-engineered to express human-derived Organic Anion Transporter Polypeptide 1B3 (OATP1B3) which can uptake the MRI contrast agent Gd-EOB-DTPA, and Sodium Iodide Symporter (NIS), also a human-derived gene for uptake of the PET tracer, ¹⁸F-tetrafluoroborate (¹⁸F-TFB). In addition, we have incorporated a zsGreen fluorescence reporter gene for cell characterization purposes. Flow cytometry and Western blots were performed to determine transduction efficiency and the presence of the reporter proteins. To test the transporters uptake ability for their respective agents, we incubated non-engineered, as well as NIS-OATP1B3-zsG cells with a 1.6 mmol dose of Primovist. Cells pellets were embedded in a 1% agarose phantom followed by scanning with a 3T MR scanner. An analogous experiment was performed with ¹⁸F-TFB, measuring cell uptake activity using a gamma counter. **Results:** Flow cytometry revealed no fluorescence in the non-engineered cells, and a 93% transduction efficiency in the PET/MRI reporter gene expressing cells (Fig. 1A). Western blots confirmed the presence of both transporters in the NIS-OATP1B3 expressing cells (Fig. 1B). Our functional tests with MRI showed over a 44% increase in spin lattice relaxivity in *T*₁-weighted images of OATP1B3-expressing cells corresponding to higher Gd-EOB-DTPA uptake than in non-OATP1B3 expressing cells (Fig. 1D). We also noted over a 45-fold increase in ¹⁸F-TFB tracer uptake in NIS-expressing cells as opposed to non-engineered cells (Fig. 1E), validating the functionality of both transporters. **Conclusion:** We have developed a human-derived PET and MRI reporter gene system for potential cell tracking. This system combines quantifiable and sensitive information retrieved from PET with the feasibility and longitudinal tracking abilities of MRI in a safe system that uses human-derived genes and thus poses high translation potential for cell-tracking purposes.

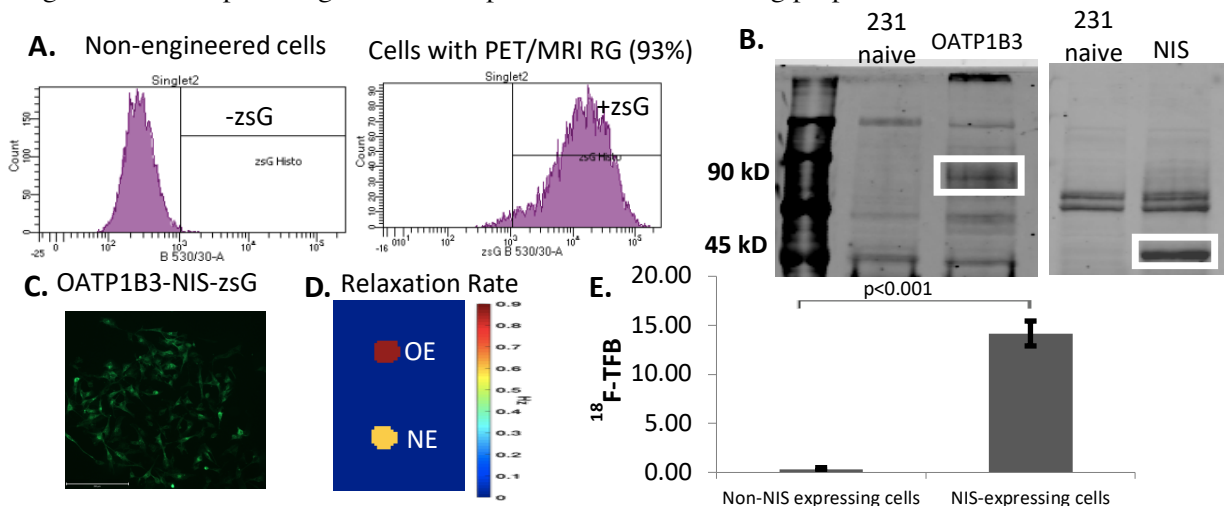


Fig.1: Flow cytometry (A) showing the absence of zsG in non-engineered cells and zsG in the transduced cells, with 93% transduction efficiency. Western blots (B) showed clear bands in OATP1B3 and NIS expressing cells and no corresponding bands for the control cells. Fluorescence microscopy also indicated zsG cells in the transduced cells (C). Relaxivity map (D) showing higher Primovist uptake in OATP1B3-expressing (OE) cells in comparison to Non-engineered (NE) cells. (E) shows the significant increase (n=12) in ¹⁸F-TFB uptake in NIS-expressing cells in comparison to non-NIS expressing cells.

Development of Aldehyde-Sensing Probes for Early Biomarkers of Disease and Injury Using PET and Fluorescence Microscopy

Alexia Kirby^{a,c}, Mojmír Suchý^{b,c}, Adam Shuhendler^{a,b,c}

^aDepartment of Biology, University of Ottawa, Ottawa, ON, Canada

^bDepartment of Chemistry & Biomolecular Sciences, University of Ottawa, Ottawa, ON, Canada

^cUniversity of Ottawa Heart Institute, Ottawa, ON, Canada

Introduction: An increase in endogenous aldehyde production often underlies the early stages of many pathologies, including cardiovascular disease, cancer, and mild traumatic brain injury. This increase of structurally diverse aldehydes in tissues can lead to propagation of the pathology and determines the fate of the cell or tissue, which emphasizes the importance of total aldehydic load. While aldehydes are an attractive biomarker for the early molecular events leading to disease, their *in vivo* and *in vitro* detection by imaging has not yet been fully realized. We have recently developed a new anthranilic-acid based scaffold capable of rapid and catalyst-free reaction with aldehydes. With this scaffold, we developed and validated an aldehyde-targeted radiotracer ($[^{18}\text{F}]\text{NA}_3\text{BF}_3$), allowing for whole body, *in vivo* imaging of aldehydes by positron emission tomography (PET). We use this tool to investigate total aldehyde production in various disease and injury models. We also created a fluorogenic probe, 5-MeO-*N*-aminoanthranilate, which can be used for detection of aldehydic load *via* live cell microscopy.

Methods: To assess the ability of $[^{18}\text{F}]\text{NA}_3\text{BF}_3$ to bind aldehydes *in vivo*, two studies were carried out in mice. (1) The first involved injecting mice with an exogenous, localized source of aldehydes. Aldehyde-bearing microparticles (AldMP), pre-blocked AldMPs, or saline alone was injected subcutaneously above the shoulders of mice, providing known “aldehyde-rich” (+AldMP) and “aldehyde-poor” (-AldMP) regions. The mice then received $[^{18}\text{F}]\text{NA}_3\text{BF}_3$ by intravenous injection, followed by dynamic PET. (2) The second *in vivo* validation study was performed in a mouse model of sepsis. Bacterial cell wall lipopolysaccharide (LPS) is known to induce oxidative stress in the liver and kidneys. The mice received either saline or 5 mg/kg LPS *i.v.* 2 hours prior to PET imaging with $[^{18}\text{F}]\text{NA}_3\text{BF}_3$ to investigate whole-body aldehyde production during systemic inflammation. The ability of our aldehyde-sensing fluorophore to bind to aldehydes in cells was assessed using a cell model of oxidative stress. HEK293 cells were treated with either diethyl maleate (DEM) to increase oxidation, Vitamin E as an antioxidant, both to attenuate the oxidative stress, or vehicle control, followed by confocal microscopy to evaluate fluorescence.

Results: $[^{18}\text{F}]\text{NA}_3\text{BF}_3$ was able to detect both exogenous and endogenous aldehydes *in vivo*. Radiotracer uptake was observed in the shoulder bearing AldMP, as well as in the kidneys, liver, and circulation 60 minutes after AldMP injection. Following the induction of sepsis, a significant increase in $[^{18}\text{F}]\text{NA}_3\text{BF}_3$ uptake was observed in the liver, renal cortex and medulla, as well as cervical and inguinal lymph nodes, suggesting aldehydes are produced in these organs during the inflammatory cascade. In mice that received saline, $[^{18}\text{F}]\text{NA}_3\text{BF}_3$ uptake was observed in the gallbladder, proximal GI tract, renal pelvis, and bladder, suggesting both renal and GI tract elimination. The fluorophore detected an increase of aldehydes following DEM treatment, a decrease in aldehydes with Vitamin E, and an attenuation of aldehyde production with antioxidant pre-treatment.

Conclusions: These probes give us the ability to map aldehyde production and movement *in vivo* with PET and in live cells with fluorescence microscopy and may help us better understand the cellular outcomes of electrophilic stress. Together, these probes may be used to interrogate the chemical biology of aldehydic load relevant to a variety of diseases.

Derivation of Monoclonal Antibodies Targeting GvpA, the major structural protein of Gas Vesicles: A New Set of Tool for Detecting and Imaging Gas Vesicles

Ann Fernando^{1,2} and Jean Gariépy*^{1,2,3}

¹ Department of Pharmaceutical Sciences, University of Toronto, Toronto, Ontario, Canada

² Sunnybrook Research Institute, Toronto, Ontario, Canada

³ Department of Medical Biophysics, University of Toronto, Toronto, Ontario, Canada

Introduction: Gas Vesicles (GVs) are proteinaceous nanoparticles that are naturally expressed by various strains of buoyant, photosynthetic microbes to aid in their stratification within aqueous environments (Walsby 1994). GV's have recently emerged as a new class of contrast agent for ultrasound and magnetic resonance imaging due to their hollow air-filled core (Shapiro 2014). Furthermore, they are particularly attractive because they can be modified at the level of their protein subunits to display new epitopes or therapeutic peptides (Sremac and Stuart 2008, Balakrishnan et al. 2016). Despite their unique properties, the study of GV's and their re-purposing as pharmaceuticals have been limited by a lack of versatile tools and agents to specifically guide them to disease sites and to detect them in the context of *in vitro* and *in vivo* experiments. Indeed, there has been great challenge in characterizing and modifying gas vesicles due to their nature of residing at the air-water interface. As a result of these issues, we have developed monoclonal antibodies (mAbs) targeting the dominant surface protein on *Halobacterium sp*GVs, namely gvpA.

Methods: mAbs were generated by vaccinating mice with a 26-residue long synthetic peptide corresponding to the solvent-accessible C-terminal domain of gvp A (Strunk et al. 2011). Surface plasmon resonance (SPR) and enzyme-linked immunosorbent assay (ELISA) were used to characterize their *in vitro* binding affinity to GV's. Purified antibodies were subsequently modified with 10 nm gold nanoparticles and incubated with native GV's to assess their binding using transmission electron microscopy (TEM).

Results: Monoclonal antibodies recognize native GV's ($K_d = 0.62$ nM) and a gvpA fusion protein ($K_d = 0.22$ nM) with high binding affinity as measured by ELISA and SPR. Furthermore, antibodies modified with 10nm gold nanoparticles associated readily with floating native GV's giving rise to a distinctive pink-colored layer. The number of gold nanoparticles bound per GV was determined by TEM to be on average 18 ± 13 .

Conclusions: We have developed monoclonal antibodies which bind and recognize the surface of GV's and specifically, the structural gvpA protein subunit which represent the main building block of each gas vesicle. The antibodies were found to bind native GV's with high binding affinity and were amenable to chemical modification to incorporate gold nanoparticles for tracking GV's. These mAbs represent versatile tools that can be readily modified with imaging and cytotoxic agents to generate targeted, long-circulating GV's. As such, my future work will focus on using modified gvpA-specific mAbs to develop families of tumor-targeted GV's as theranostic agents.

References:

Balakrishnan A, DasSarma P, Bhattacharjee O, Kim JM, DasSarma S, et al (2016). Halobacterial nano vesicles displaying murine bactericidal permeability-increasing protein rescue mice from lethal endotoxic shock. *Sci Rep*, 6: 33679.

Shapiro MG, Goodwill PW, Neogy A, Yin M, Foster FS, et al. (2014) Biogenic gas nanostructures as ultrasonic molecular reporters. *Nat. Nanotechnol.* 9:311–316.

Sremac M and Stuart ES. (2008) Recombinant gas vesicles from *Halobacterium sp.* displaying SIV peptides demonstrate biotechnology potential as a pathogen peptide delivery vehicle. *BMC Biotechnol* 8: 9

Strunk T, Hamacher K, Hoffgaard F, Engelhardt H, Zillig MD et al. (2011) Structural model of the gas vesicle protein GvpA and analysis of GvpA mutants *in vivo*. *Mol Micro* 81:56-68.

Walsby A (1994) Gas vesicles. *Microbiol. Rev.* 58:94–144.

Selective Imaging of Matrix Metalloproteinase-13 to Detect Extracellular Matrix Remodelling in Atherosclerotic Lesions

Ariel Buchler^{1,2}, Maxime Munch, PhD^{1,2}, Gedaliah Farber^{1,2}, Benjamin H. Rotstein, PhD^{1,2}

¹University of Ottawa, Ottawa, ON, Canada, ²University of Ottawa Heart Institute, Ottawa, ON, Canada.

Introduction: Dysregulation of extracellular matrix remodelling by matrix metalloproteinases (MMPs) in vasculature is associated with atherosclerotic plaque vulnerability. Specifically, MMP-13 predominantly exhibits collagenolysis in atheromatous plaques and reduces smooth muscle cell accumulation, contributing directly to plaque destabilization by degradation of the fibrous cap. Knockout of MMP-13 in mice abolishes lesion activity, while selective inhibition increases local collagen content, suggesting that MMP-13 provokes plaque instability and represents an *in vivo* biomarker of high-risk lesions. Nevertheless, current MMP-targeted nuclear medicine agents such as [¹⁸F]BR-351 possess broad spectrum activity. The objective of this study was to evaluate the feasibility for imaging plaque vulnerability in animal models of atherosclerosis with selective MMP-targeted PET radiotracers. A comparative analysis between [¹⁸F]BR-351 and the selective MMP-13 candidate, herein entitled [¹⁸F]FMBP, was performed.

Methods: Initial validation was performed by *in vitro* autoradiography. *ApoE*^{-/-} or age-matched C57Bl/6 (control) en face aortae were incubated with 45 kBq high molar activity [¹⁸F]FMBP or [¹⁸F]BR-351 in the presence and absence of 2 μ M non-radioactive standard (FMBP or BR-351), and imaged on a super-resolution phosphor screen (n = 6). *Ex vivo* biodistributions were further evaluated in mice pre-administered with FMBP/BR-351 (5 mg/kg, IP) or equivalently dosed vehicle, by measuring radioactivity in selected organs (t = 30 min, n = 4 per group). Corresponding en face aortae were additionally imaged by autoradiography. Histological analysis has been performed with Oil Red O (lipids), Mac-2 (macrophages), and MMP-13 to illustrate regional concordance and correlation to autoradiographic tracer uptake.

Results: [¹⁸F]FMBP and [¹⁸F]BR-351 were routinely obtained by automated radiosynthesis in decay-corrected yields between 20-30%, radiochemical purities of >99%, and molar activities between 37-74 GBq/ μ mol (t = 60-90 min). *In vitro* autoradiography revealed that [¹⁸F]FMBP exhibits 1.8-fold greater aortic lesion activity density in *ApoE*^{-/-} models, reducible by 23% upon blocking in atherosclerotic tissue (unoptimized). *Ex vivo* biodistribution studies illustrated that both tracers primarily exhibit hepatic, intestinal, and renal uptake in *ApoE*^{-/-} mice. Low tracer accumulation was observed in non-excretory organs with only minor changes between strains and conditions. While *ex vivo* autoradiography revealed >2.5-fold higher aortic lesion activity density in *ApoE*^{-/-} models, [¹⁸F]FMBP exhibited 2.2-fold greater aortic lesion uptake in comparison to [¹⁸F]BR-351. Pharmacological dosing with corresponding non-radioactive standards reduced [¹⁸F]FMBP uptake by 63% to baseline levels, but did not significantly reduce [¹⁸F]BR-351 uptake. Both tracers further demonstrated regional concordance and correlation with Oil Red O stainings ($R^2 > 0.72$).

Conclusions: *In vitro* autoradiography can be employed to assess tracer performance and provide justification for comprehensive *in vivo* evaluations. [¹⁸F]FMBP and [¹⁸F]BR-351 predominantly undergo hepatobiliary excretion and renal clearance. Limited expression of MMP-13 was observed in non-pathologically implicated organs. While [¹⁸F]FMBP and [¹⁸F]BR-351 localized with atherosclerotic plaques *ex vivo*, [¹⁸F]BR-351 did not exhibit measurable specific binding. Moreover, [¹⁸F]FMBP possessed superior lesion sensitivity and correlation with extent of plaque accumulation. Altogether, [¹⁸F]FMBP, a selective PET radiotracer for MMP-13, has proven superior for the detection of ECM remodelling in atherosclerosis.

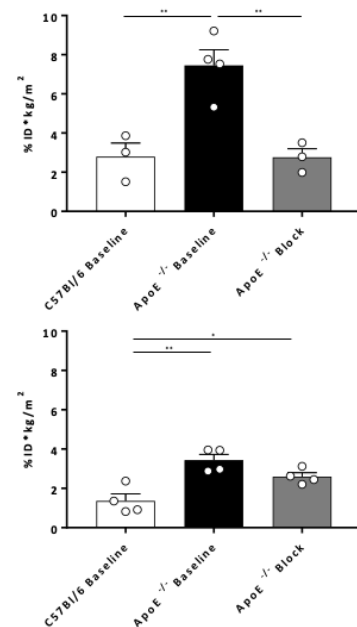


Figure 1. [¹⁸F]FMBP (top) and [¹⁸F]BR-351 (bottom) Aortic Lesion Uptake

Comparing detection limits of Magnetic Particle Imaging (MPI) to Magnetic Resonance Imaging (MRI) using super paramagnetic iron oxide nanoparticles in a breast cancer metastasis model

Kierstin P Melo^{1,2}, Ashley V Makela³, Amanda M Hamilton¹, and Paula J Foster^{1,2}

¹Imaging Research Laboratories, Robarts Research Institute, London ON

²Department of Medical Biophysics, University of Western Ontario, London ON

³Institute for Quantitative Health Science and Engineering (IQ), Michigan State University, East Lansing, MI, USA

Introduction: Magnetic particle imaging (MPI) is a new imaging modality that sensitively and specifically detects superparamagnetic iron oxide nanoparticles (SPIONs) within the body. Our lab has been developing cellular magnetic resonance imaging (MRI) tools for well over a decade using both SPIONs and fluorine-19 (¹⁹F)-based contrast agents for numerous important applications, including tracking of immune and stem cells used for cellular therapies. We have shown that SPION-based MRI cell tracking has very high sensitivity, but low specificity. Contrastingly, our work has demonstrated that ¹⁹F-MRI cell tracking has high specificity, but low sensitivity. SPION-MPI cell tracking could overcome the challenges of MRI-based cell tracking allowing for both high sensitivity and high specificity cell detection. This study is the first to demonstrate that micron sized iron oxide particles (MPIO) can be used for quantitative MPI of iron-labeled cancer cells in the mouse brain.

Methods: Human breast cancer cells (231BR) were labeled with micron-sized iron oxide nanoparticles (MPIO), Immune compromised mice (NSG) were injected with either 2.5×10^5 or 5.0×10^5 cells. MPIO-labeled cells were administered intracardially using ultrasound guidance. MRI was performed in vivo the same day at 3T using a balanced steady state free precession (bSSFP) sequence. After imaging, the mice were euthanized, and brains were fixed and removed for MPI scans. MPI was performed on a Momentum™ scanner. MRI images were used to quantify the percentage of black pixels which represent the black voids created by iron labeled cells. MPI images were used to quantify the amount of MPI signal which is related linearly to the amount of iron. In a second experiment, NSG mice were also injected with 5×10^4 4T1BR cells, a murine breast cancer cell line, labelled with either MPIO or the SPION ferucarbotran (Vivotrax) which is currently the gold standard SPION for MPI. MRI and MPI was performed in vivo.

Results: Figure 1 shows representative MRI and MPI images. Signal voids due to MPIO-labeled cells can be detected in the in vivo brain MRI of mice injected with either 2.5×10^5 or 5.0×10^5 cells (Figure 1A,B). Ex vivo MPI also showed signal in the brain from iron, which is visible as a hot spot (Figure 1C,D). More black pixels were measured in the brain MRI of mice receiving an injection of 5.0×10^5 cells. This agreed with MPI data which showed that there is less iron in the brains of mice injected with 2.5×10^5 cells compared to those injected with 5.0×10^5 cells. In the second experiment, in vivo MRI was able to detect signal voids in the brains of mice injected with 5.0×10^4 cells which were labeled with either Vivotrax or MPIO (Figure 2A,C), although voids were fainter in Vivotrax labeled cells. In vivo MPI signal was only detectable in mice injected with MPIO-labeled cells (Figure 2B).

Conclusions: This is the first example of the use of MPIO for cell tracking with MPI. The major advantage of MPI is the ability to quantify iron content and estimate the number of iron labeled cells. With an intracardiac cell injection approximately 15% of the injected cells are expected to arrest in the brain vasculature. For our lowest cell injection of 5.0×10^4 cells this is ~7500 cells. Next steps include increasing sensitivity for MPI by testing different MPI tailored iron nanoparticles.

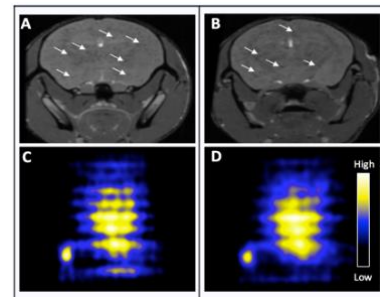


Figure 1: (A) MRI of mouse with 2.5×10^5 cells (B) MRI of mouse with 5.0×10^5 iron labeled 231BR cells. (C) MPI of mouse with 2.5×10^5 cells (D) MPI of mouse with 5.0×10^5 iron labeled 231BR cells

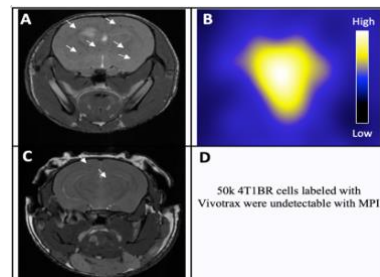


Figure 2: (A) Comparing percentage of black pixels in mice brains with 5×10^4 MPIO labeled 4T1BR cells using MRI (B) to MPI signal of the same mouse (C) MRI of mouse brain injected with 5×10^4 Vivotrax labeled 4T1BR cells (D) no signal detected when same brain was scanned with MPI

Exploring Surface Ligand Chemistry to Optimize *in vivo* Cell Tracking in Magnetic Particle ImagingNicholas D. Calvert^{a,b}, Mojmír Suchý^{a,b}, Paula J. Foster^{d,e}, Adam Shuhendler^{a,b,c}^aDepartment of Chemistry & Biomolecular Sciences, University of Ottawa, Ottawa ON, Canada^bUniversity of Ottawa Heart Institute, Ottawa ON, Canada^cDepartment of Biology, University of Ottawa, Ottawa ON, Canada^dDepartment of Medical Biophysics, Shulich School of Medicine & Dentistry, The University of Western Ontario, London, ON, Canada^eImaging Research Laboratories, Robarts Research Institute, London, ON

Introduction: Magnetic particle imaging (MPI) is an emerging imaging modality which can sensitively and specifically detect magnetic nanoparticle contrast agents, providing quantitative and tomographic data with spatial resolution of 1 mm. The most common particle type evaluated is superparamagnetic iron oxide nanoparticles (SPIONs). An important application of MPI is *in vivo* cell tracking. Promoting and enhancing cellular uptake of SPIONs for tracking cells in living systems is accomplished through a variety of methods, the most popular being surface coating and functionalization. Common functional groups are often cationic in nature, and while these have a high binding efficiency to the outer leaflet of the mammalian cell membrane, they are often toxic. Zwitterionic ligands (net neutral molecules) have much greater cell uptake potential without a loss of cell viability, however zwitterions have not been rationally explored as ligands for SPION cell loading. These biomimetic ligands may allow for a more universal approach to designing the ideal MPI contrast agent.

Methods: Commercially available SPIONs with nanoflower morphology (Synomag[®]-D, COOH-terminated dextran coat, 50 nm; Micromod GmbH) were functionalized through carbodiimide chemistry to generate two unique SPIONs with biomimetic- zwitterionic functional groups: L-cysteine (Cys) and D,L-homocysteine (HCys). The unfunctionalized SPIONs were used as a third, control tracer. SPIONs were characterized by DLS, TGA, and TEM to confirm surface functionalization and identify changes in particle physicochemical properties. SPION uptake was rationally evaluated in a human triple negative breast cancer cell line, MDA-MB-231, by varying particle concentrations and incubation times by light microscopy through Prussian Blue/Nuclear-Fast Red cellular staining, and inductively coupled plasma optical emission spectrometry. MPI measurements are being performed using the newly acquired Momentum MPI system installed in the Robarts Research Institute at Western University, the only pre-clinical system in Canada as of February 2020.

Results: Functionalized particles had a larger hydrodynamic size (44.9 ± 0.19 nm for COOH versus 144.5 ± 28.9 nm and 68.8 ± 1.6 nm for Cys and HCys, respective) and zeta potential (-46.0 ± 1.9

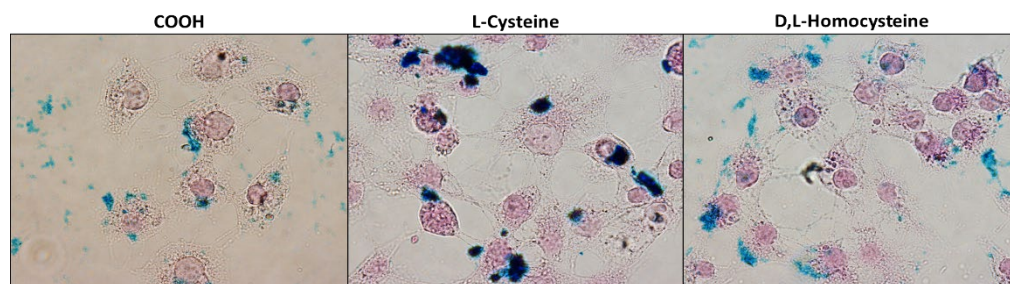


Figure 1. Particle uptake in MDA-MB-231 cells.

mV for COOH versus -27.3 ± 1.2 mV and -29.1 ± 0.1 mV for Cys and HCys, respectively), indicating successful functionalization and excellent solubility. Optimal particle uptake was shown to occur at an incubation time of 4 h with a particle concentration of 10 or 20 $\mu\text{g/mL}$. Ultimately, 10 $\mu\text{g/mL}$ has been chosen as a working concentration as it showed both the highest iron loading and most efficient uptake. Overall, surface functionalization did not significantly affect cell labelling efficiency ($83 \pm 12\%$ for COOH versus $70 \pm 18\%$ and $60 \pm 27\%$ for Cys and HCys, respectively), but Cys or HCys-functionalized particles demonstrated an increased median intensity after histological staining, indicative of an increase in the amount of particle uptake in the cell for both formulations compared to the commercial particles at the optimal concentration of 10 $\mu\text{g/mL}$ and incubation time of 4 h.

Conclusion: With MPI being an emerging imaging modality in its early stages of broad adoption, contrast agent optimization is limited but holds important promise for the future of this new imaging modality. The combinatorial effects of the nanoflower SPION morphology and the biomimetic zwitterionic ligands may lead to the development of a novel SPION with extensive, rapid, and efficient cellular uptake.

Real-time microscopic imaging of endothelial cell responses to laminar and disturbed fluid flow

Lorusso, D.¹, Soon, K.², Sacoransky, E.², Nikolov, H.N.¹, deBruyn, J.R.², Pickering, J.G.^{3,4}, Dixon, S.J.⁵, Holdsworth, D.W.^{1,6,7}, Poepping, T.L.²

¹Imaging Research Laboratories, Robarts Research Institute; Departments of ²Physics and Astronomy; ³Biochemistry; ⁴Medicine; ⁵Physiology and Pharmacology; ⁶Medical Biophysics; ⁷Surgery Schulich School of Medicine and Dentistry, The Bone and Joint Institute, The University of Western Ontario, London, CANADA

Introduction: Blood flow dynamics play a critical role in health and disease of the human vasculature. Endothelial cells (ECs) lining these vessels are mechanosensitive and are able to discern between unidirectional laminar flow and multi-directional disturbed flow – a pathological stimulus that is associated with the initiation and progression of atherosclerosis. The immediate mechanotransductive response of ECs exposed to disturbed flow is not well understood. Here, a microfluidic device is presented that is able to generate laminar and disturbed flow regimens at physiologically relevant wall shear magnitudes, and is also compatible with real-time live-cell imaging. The device was used to observe immediate responses of ECs to disturbed flow.

Methods: The custom-designed device was fabricated from polydimethylsiloxane using a replica molding technique (Fig 1 a). Flow within the channels was evaluated experimentally using micro-particle image velocimetry. Human umbilical vein endothelial cells were seeded within the channels, loaded with a calcium-sensitive fluorescent probe, and changes in the concentration of cytosolic free calcium elicited by laminar and disturbed flow were monitored.

Results: Repeatable and physiologically relevant levels of uni- and multi-directional wall shear stress (0-5 Pa) were generated (Fig 1 b). Human aortic and human umbilical vein endothelial cells (HAEC and HUVEC) were found to be viable during our experiment, and intracellular calcium could be imaged and monitored over time (Fig 2). Cells appeared to be more sensitive to disturbed flow, as well as elicit more sustained calcium responses over time when compared to uni-directional laminar flow.

Conclusions: This device will enable further studies into the understanding of the responses of ECs to flow dynamics and their relevance to vascular health and disease.

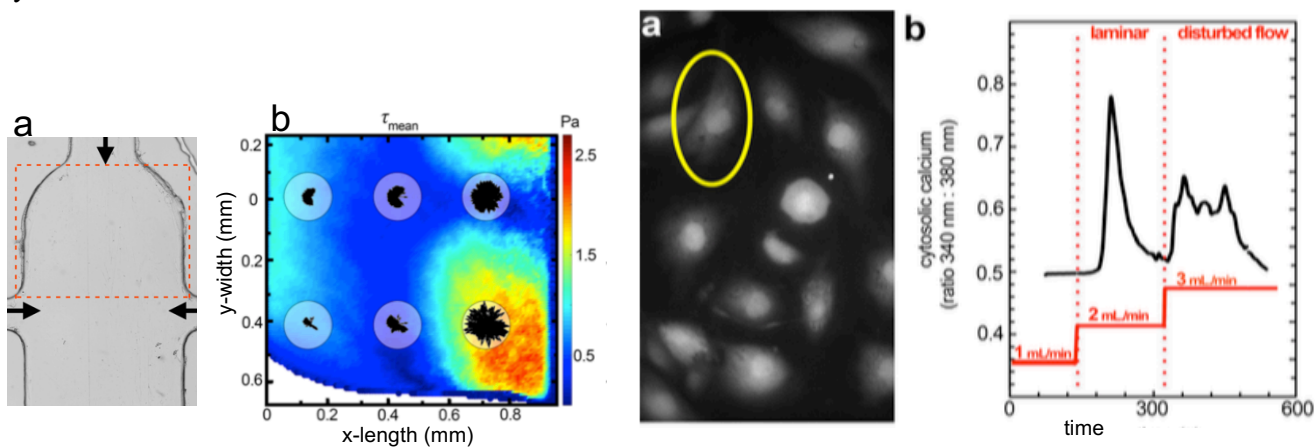


FIG. 1 a) A micrograph of the custom-built microfluidic device. Arrows indicate the flow inlets to the disturbed flow chamber. b) 2D colour-encoded maps of wall shear stress metrics derived from micro-PIV during disturbed flow in the microfluidic device. Map of magnitude of the mean vector, $|\tau_{\text{mean}}|$, with direction quiver plots overlaid, where compass radii is equal to ~ 10 Pa. Vector quiver plot reveals a high degree of multi-directional flow, dependent upon position within the channel, ranging from bi-directional fluctuations to nearly uniform directional changes.

FIG. 2 Cytosolic free calcium imaging in HAECs during disturbed flow. a) Representative field of fura-2-loaded cells. HAECs were seeded within the microfluidic device and allowed to adhere. b) Monitoring of cytosolic free calcium in response to flow stimuli. Background flow was applied through both the side inlets. When flow was increased, a sharp calcium transient was observed. When flow rate was further increased, creating disturbed flow, a muted but temporally sustained transient was observed.

Dictionary Learning for Automated Cell Tracking

Mark Armstrong¹, Cornelius Faber², Dan Xiao¹

¹Physics Department, University of Windsor, ON, Canada

²Institute for Clinical Radiology, University of Muenster, Muenster, Germany

Introduction: Magnetic Resonance Imaging (MRI) is a powerful imaging modality with excellent soft tissue contrast. The contrast of an MRI image can be influenced using contrast agents, such as iron nanoparticles, to highlight certain features. Cells can be labeled with contrast agent to create a signal void, allowing individual cells to be imaged. This is a valuable tool for the studies of inflammatory diseases and metastasis of cancer in the animal model. Counting cells manually is cumbersome, motivating an automated technique. A method of automated signal void detection is tested with simulated signal voids on a human brain image.

Methods: Dictionary learning was performed with the K-SVD algorithm. Each dictionary consisted of a set of “atoms”, representing features in the image. The 1st set of atoms were trained on a human brain image. Simulated signal voids and noise were added to the brain image, to form the “original” image to be processed, as shown in Fig 1a. The signal voids were added by scaling pixels in a 3 by 3 region, with the contrast of the void defined as the inverse of the scale factor for the center pixel. This image was projected onto the 1st set of atoms with orthogonal matching pursuit. The “fit” image, Fig 1b, was obtained by reconstruction with only the largest coefficient for each image patch. This fitted image was subtracted from the original to create a residual, Fig 1c. The residual image was used to train the 2nd set of atoms. A 3rd set of atoms were created based on a simulated image with only random void features. The residual image was fit using the combination of the 2nd and 3rd atom sets. The coefficients of the 2nd set atoms were zeroed to extract the void features, as shown in Fig 1d. Thresholding was performed on this image to identify the signal void locations, in Fig 1e.

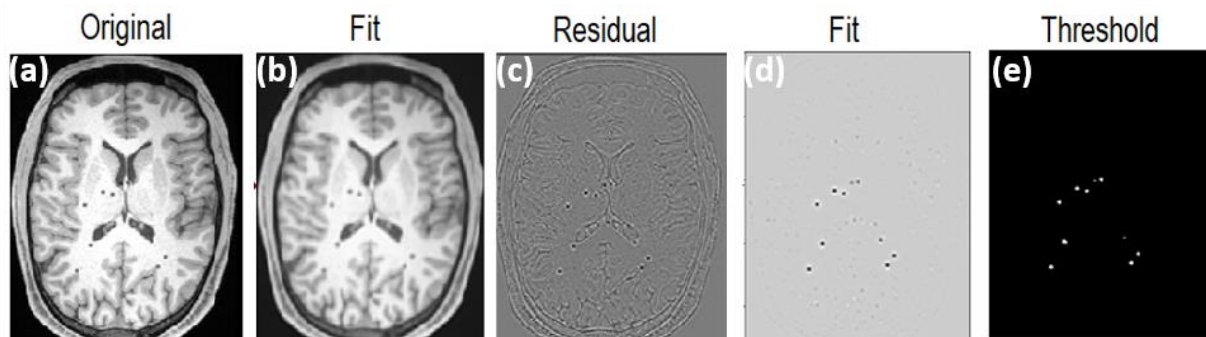


Figure 1. Demonstration of the separation method. The residual (c) was the original (a) subtracting the one-atom fitted image (b). (d) was reconstructed with only the atoms representing the void features, with coefficients obtained from (c). (d) was thresholded to locate the void features in (e).

Results: The method was tested on simulated images, with 10 voids and various contrasts and SNR. The procedures of feature extraction are shown in Fig. 1. The number of voids successfully determined at various contrasts and SNRs is shown in Fig 2.

Conclusion: With sufficient contrast and SNR, the algorithm was able to extract the signal voids in simulated images with complex features. The method will be applied to process the images acquired in cell tracking MRI experiments, to release the burden of manual counting. The high sparsity in dictionary domain will be exploited to enable k -space under-sampling, accelerating image acquisition and improving the temporal resolution.

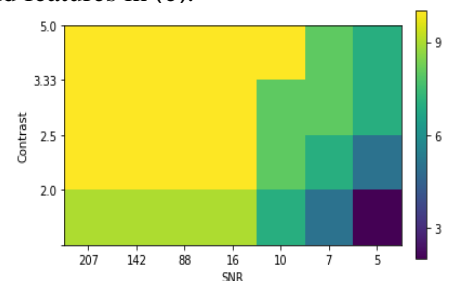
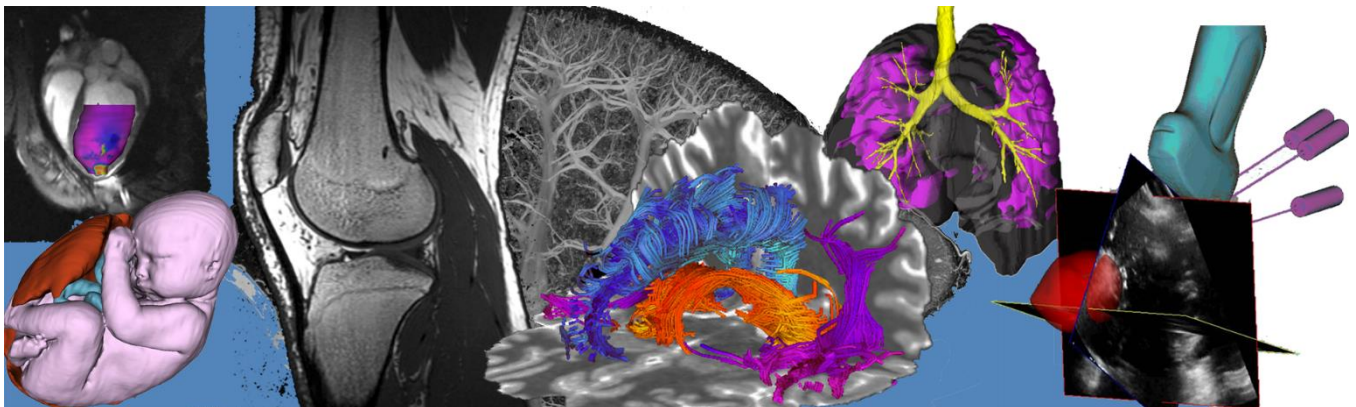


Figure 2. The number of voids successfully extracted, from simulated images with 10 voids and various contrasts and SNR.

Poster Presentation Abstracts

Session 2: Lung Imaging



Spatial Dependence of Computed Tomography Disease Features in COPD Quantified using Join Count Statistics

Sukhraj Virdee BSc,¹ Wan C. Tan MD,² James C. Hogg MD, PhD,² Harvey O. Coxson PhD,² and Miranda Kirby PhD^{1,2}

¹Department of Physics, Ryerson University; ²Center for Heart Lung Innovation, St. Paul's Hospital..

Rationale: Chronic obstructive pulmonary disease (COPD) is a lung disease characterized by chronic airflow obstruction that is caused by emphysema and/or small airways disease. Recent advances in computed tomography (CT) image analysis allow for emphysema and functional small airway disease (fSAD) to be quantified. Although studies have established emphysema and fSAD as imaging biomarkers of COPD, the spatial distributions of emphysema and fSAD within the lung, and their relative influence on lung function, are still poorly understood. We propose that a modified Geostatistical method known as Join Counts [1], which address the degree of clustering and dispersion, will provide additional information related to COPD severity. Here, our objective was to apply Join Count's to CT disease features and investigate the relationship with lung function in COPD participants from the Canadian Cohort Obstructive Lung Disease (CanCOLD) study [2].

Methods: Spirometry and CT images from the CanCOLD study were obtained. Spirometry measurements included the forced volume expiratory volume in 1 sec (FEV₁), forced vital capacity (FVC), and FEV₁/FVC [2]. All participants were categorized as according to the Global initiative for Obstructive Lung Disease (GOLD) criteria: current or ex-smokers with normal lung function (at risk), GOLD I (mild COPD) and GOLD II+ (moderate/severe COPD). CT imaging was performed at full-inspiration and full expiration. The inspiration/expiration CT images were registered (the target registration error was approximately 1–2 voxels) [3], and each voxel was classified as normal, emphysema or fSAD (VIDA Diagnostics, Inc, Coralville, IA, USA) [4]. The classified CT images were converted to binary maps, and two binary maps were created for emphysema only voxels (Emph) and fSAD only voxels (fSAD). For each binary map, a join (or edge) between two voxels counted as a single count if both voxels had an identical value, and then normalized by dividing the Join Count for each measurement of interest by the total number of Join Counts within the CT image. An analysis of variance (ANOVA) with Tukey post hoc test was used to determine differences between groups. A Pearson correlation was used to determine the relationship between the Join Count measurements with measures of lung function.

Results: A total of 500 participants were evaluated. Of these n=141 were at risk, n=209 mild COPD, and n=150 moderate/severe COPD. There was no significant differences between at risk, mild and moderate/severe COPD groups for age or sex. As shown in Table 1, Emph Join Count and fSAD join count measurements were significantly greater in moderate/severe COPD than at risk and mild COPD groups. In addition, Emph Join Count measurements were significantly different between mild COPD and moderate/severe COPD. There were significant correlations for FEV₁/FVC with Emph (r=0.46, p<0.0001) and fSAD (r=0.23, p<0.0001).

Table 1: Demographic and Imaging Measurements

Parameter (±SD unless specified)	At-Risk (n=141)	GOLD I (n=209)	GOLD II+ (n=150)
Age, yrs	66 (9)	66 (10)	65 (9)
F Sex, n (%)	63 (45)	80 (38)	68 (45)†
Pack-years, yrs	21 (16)	18 (23)	26 (25) ‡
BMI, kg/m ²	28 (5)	26 (4) †	28 (6) ‡
Emph Join Count	0.012 (0.026)	0.034 (0.044) †	0.039 (0.065) †‡
fSAD Join Count	0.282 (0.166)	0.317 (0.145)	0.367 (0.150) †‡

†Significantly different from At-Risk; ‡Significantly different from GOLD I

Conclusions: The Join Count measurements from CT images significantly differentiated COPD groups based on disease severity, and were significantly correlated with lung function measurements. This finding suggests that as COPD severity increases, there is increased clustering of emphysema and fSAD in the lung. Further analysis of Join Count measurements in comparison to other established CT measurements is required to better understand the potential role of Join Counts for investigating COPD disease severity and progression.

References: 1. A. Cliff, J. Ord, *Spatial processes: Model and Applications* (Pion, 1981); 2. J. Bourbeau *et al.*, *COPD: Journal of Chronic Obstructive Pulmonary Disease*. 11, 125–132 (2014); 3. Yin Y, Raffy P, Sieren JP, *et al.*, *Am J Respir Crit Care Med* 2014;189:A4332; 4. M. Kirby *et al.*, *Respiration*. 94, 336–345 (2017).

Emphysema Measurements in Alpha-1 Antitrypsin Deficiency using ^3He and ^{129}Xe MRIElise Woodward¹, Matthew S. Fox^{1,2}, David G. McCormack⁵, Grace Parraga^{3,5} and Alexei Ouriadov^{1,2}¹Department of Physics and Astronomy; ²Lawson Health Research Institute;³Robarts Research Institute; ⁴Department of Medical Biophysics;⁵Division of Respiriology, Department of Medicine,
The University of Western Ontario, London, Canada.

RATIONALE: Many patients experience emphysema relating to COPD and Alpha-1 Antitrypsin Deficiency (AATD). There are limited biomarkers capable of accurately sensing emphysema in order to study changes and developments of emphysema related diseases. Unlike conventional methods that are invasive and/or dangerously radiative, hyperpolarized ^3He & ^{129}Xe gas MRI^{1,2} offers a direct acinar duct measurement tool. This tool allows the direct measurements of acinar duct geometry as well as diffusion estimates. Over a 4 year period, we measured changes in apparent diffusion coefficient (ADC) and morphometry estimates. We hypothesize that emphysemas progression will be evident in relationship to changes in ADC/morphometry estimates. These estimates are sensitive to emphysema progression and offer disease progression detection in patients where CT evidence is either not detected or not acquired.

METHODS: All subjects provided written informed consent to an ethics board approved protocol and underwent two visits, four years apart that included PFTs (CT, spirometry, plethysmography, DL_{CO}) and MRI including anatomical ^1H , ^3He (2014) and ^{129}Xe (2018) diffusion-weighted and static-ventilation imaging. MRI was performed at 3.0T as previously described.³ 3D ^3He & ^{129}Xe MRI-based ADC and lung morphometry maps were generated using the stretched-exponential-method⁴ which was extended and adapted for both ^3He & ^{129}Xe to provide clinically-relevant biomarkers of emphysema.² CT relative area of the lung with attenuation $\leq -950\text{HU}$ (RA₉₅₀) was measured using the custom built software. Since ^{129}Xe and ^3He share a linear relationship³, we were able to directly compare ^{129}Xe ADC estimates with ^3He estimates. We then converted ^{129}Xe estimates to values comparable to ^3He , in order to compare slice by slice.

RESULTS: Six AATD patients (58 \pm 5yr) were evaluated at baseline as well as 4 years later. Figure-1 shows CT,³ He & ^{129}Xe MRI ADC, mean-linear-intercept (L_m) maps and ADC and L_m values for both gases in all participants. CT low attenuating areas reflected moderate to severe emphysema (RA₉₅₀=8%, 14% and 31%) in 2014 but CT was not acquired in 2018. Mean ADC^{Xe} estimates were used to calculate ADC^{He} values utilizing linear-regression (ADC^{Xe} = 0.11*(ADC^{He}) + 0.03)³. Mean ADC²⁰¹⁴ estimates were not significantly different from corresponding mean ADC²⁰¹⁸ estimates (0.46cm²s⁻¹ vs 0.44cm²s⁻¹; p>.80).

DISCUSSION: In the six AATD patients, increased ADC estimates confirmed emphysema progression. In all patients, increases in ADC values proved significant, and longitudinal changes in ADC estimates can be confirmed as a novel biomarker. As for AATD-2 patient, regions at visit-1 with abnormally high ADC^{He} and L_m^{He} values were not ventilated at the visit-2 with the result being apparently improved ADC^{Xe} and L_m^{Xe} values.

CONCLUSIONS: ^3He & ^{129}Xe MRI-based ADC and morphometry maps, can measure regional emphysema progression and can be considered before CT to minimize negative side effects. However, as ventilation worsens over time, ADC and L_m values require normalization to ventilation volume.⁶

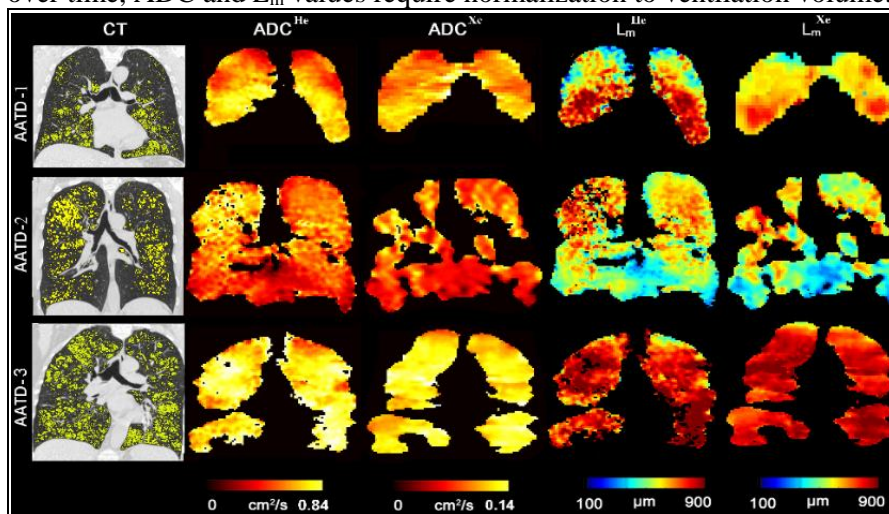


Figure 1. Representative CT and ^3He and ^{129}Xe MRI maps for three AATD subjects: AATD-1- top panel, AATD-2 - middle panel and AATD-3 - bottom panel.

References

1. Yablonskiy DA et al J Appl Physiol (2009).
2. Ouriadov A et al MRM (2019).
3. Kirby M et al Radiol (2012).
4. Abascal JFPJ et al ArXiv (2017).
5. Ouriadov A et al MRM (2017).
6. Westcott A et al JMRI (2018).

Acknowledgments

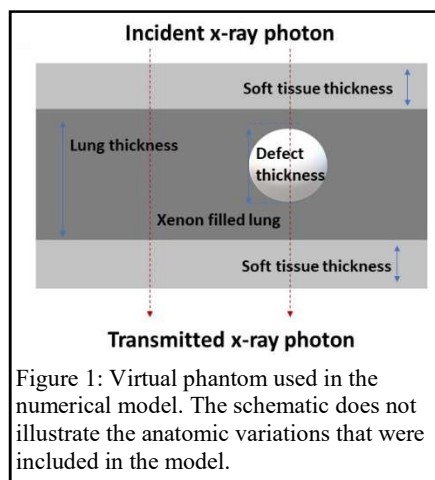
A. Ouriadov was funded in part by the Alpha-1 Foundation.

Theoretical feasibility of xenon-enhanced dual energy x-ray radiography for functional imaging of respiratory disease

Fateen Basharat¹ and Jesse Tanguay¹

¹Department of Physics, Ryerson University, Ontario, Canada

Introduction: Chronic obstructive pulmonary disease (COPD) affects ~2.5 million Canadians. Respiratory exacerbations associated with COPD may result in hospitalization and are a substantial burden to the Canadian health care system. Functional imaging of COPD using advanced, hyperpolarized magnetic resonance imaging (MRI) methods can predict COPD exacerbations. However, MRI-based methods are expensive, not widely available, and are primarily used as research tools. Dual-energy xenon-enhanced computed tomography enables assessment of pulmonary ventilation, but results in high radiation doses (i.e. > 7 mSv). We propose a two-dimensional (2D) xenon-enhanced dual-energy (XeDE) approach for functional imaging of COPD. This approach would be a low-dose, low-cost alternative to MRI and CT-based approaches. The purpose of this work was to investigate the image quality of XeDE using a theoretical model. To this end, we used signal detection theory to model theoretically the detectability of ventilation defects associated with COPD in 2D XeDE images.



Methods: We used the detectability index of a human observer as a figure of merit to investigate the image quality of 2D XeDE imaging. This figure of merit relies on Fourier-based descriptions of image signal, image noise, and the imaging task, in addition to the efficiency a human observer. Our model of image noise accounted for quantum noise, electronic noise, and anatomic noise, the latter of which accounts for variations in soft-tissue structures in 2D XeDE images. We modelled spherical ventilation defects empty of xenon in uniformly-ventilated lung, as shown in Fig. 1. Our model of quantum noise and defect contrast accounted for patient scatter and assumed an ideal energy-integrating x-ray detector. We calculated the detectability index for the defect present vs. defect absent classification task for spherical defects of varying diameter in adults, patient entrance exposures of 18 mR to 90 mR (approximate effective radiation doses of 0.02-0.10 mSv), low-energy tube voltages ranging 50 kV to 70 kV, and a high-energy tube voltage of 140 kV with 1.1 mm of

Cu filtration. In all cases we assumed a Xe/air concentration of 0.75. We used a detectability threshold of 2 to identify whether a defect was detectable or not.

Results: Defect contrast and defect detectability decreased as the energy of the low-energy beam increased. The optimal combination of tube voltages was found to be 50/140 kV. For this combination of tube voltages, the smallest detectable defect was ~4 cm in diameter for a patient exposure of 18 mR. Increasing the exposure to 90 mR reduced the smallest detectable defect to 2.4 cm. Poor defect detectability was due primarily to the combination of low contrast ($<10\%$) and anatomic noise. Anatomic noise reduces detectability by ~90% relative to quantum-noise-limited conditions (including scatter) and is due to superimposition of soft-tissue and Xe-enhanced structures.

Conclusion: Our analysis shows that small-defect conspicuity is severely limited by overlying anatomic clutter and low contrast. For a 90 mR exposure, the 2D XeDE approach proposed here may enable visualization of defects as small as 2.4 cm in diameter. Given that overlying anatomic clutter is the primary cause of reduced detectability, a tomosynthesis approach, which would reduce anatomic clutter, may improve visualization of ventilation defects. Future work will focus on experimental verification of the results presented here and investigation of xenon-enhanced tomosynthesis for functional imaging of respiratory disease.

Key words: **lung imaging**, x-ray imaging, dual-energy x-ray imaging, functional imaging, COPD

Convolutional Neural Network ^1H MRI Lung Segmentation for Hyperpolarized Gas Imaging

Alexander M Matheson^{1,2}, Rachel L Eddy^{1,2}, Jonathan MacNeil^{1,3}, Marrissa J McIntosh^{1,2} and Grace Parraga¹⁻³
¹Robarts Research Institute, ²Department of Medical Biophysics, ³School of Biomedical Engineering, Western University, London, Canada, Western University London, Canada

INTRODUCTION: Hyperpolarized gas MRI (^3He and ^{129}Xe) has allowed characterization of lung function through ventilation defect percent (VDP) measurements, defined as the ratio of defect volume to lung volume. Volume-matched ^1H MRI are acquired alongside hyperpolarized MRI to segment the thoracic cavity for VDP. Prior methods for thoracic segmentation have relied on semi-automated methods;^{1,2} a truly automatic method is desirable for repeatability, multi-site studies, and clinical deployment. Recently, convolutional neural networks (CNN) have shown promise in providing precise, fast and fully automated segmentations in medical imaging. The objective of this work was to train a dense v-net CNN³ and validate segmentations using Dice similarity coefficients (DSC) and receiver operating characteristics (ROCs).

METHODS: Data were retrospectively pooled from previous imaging studies. Healthy participants, ex-smoker participants with and without chronic obstructive pulmonary disease (COPD), and participants with asthma underwent thoracic ^1H MRI. 3D convolutional networks perform poorly on anisotropic voxels, therefore the 442 volumes were divided into slices yielding 6792 data sets. Axis-swapping augmented the data to 27168 sets. Ground-truth labeling was performed by 4 trained imaging scientists with 0.5-4 years (mean=2yrs) experience. A dense v-net architecture was adapted from the NiftyNet platform,⁴ and implemented on a workstation GPU. Network learning was driven by a combination Dice and cross-entropy loss function.⁵ The model was validated using 5-fold cross validation ($n_{\text{training}}=314$, $n_{\text{validation}}=45$, $n_{\text{testing}}=90$).

RESULTS: Model testing occurred in approximately 0.08s/volume when executed via GPU. Figure 1 shows example segmentations from the 1st-fold testing step. CNN segmentations tended to slightly over-estimate lung volume, bleed into the diaphragm on occasion, and were relatively insensitive to pulmonary arteries. Quantitative analyses showed exceptional segmentation overlap (average DSC=0.96, DSC=0.95 for right and left lungs) with high sensitivity/specificity (average AUC=0.997). Segmentation effectiveness was slice dependent (DSC_{slice-1}=0.73 for both, DSC_{slice-15}=0.46, 0.66 respectively) with central slices in better agreement with ground truth (DSC_{slice-8}=0.97 for both).

DISCUSSION: CNN performance allowed fully-automated left and right lung segmentation in a fraction of the time required for current semi-automated methods. Data were skewed towards diseased states, however this matches the intended application of the network. Model results experienced occasional imperfections around pulmonary arteries: adding manual labels for arteries during training may improve performance in future. Reduced performance at the most anterior and posterior slices occurred due to a combination of partial volume effects and difficulty when the anterior mediastinum was thin – readers labeled this as a continuous region. The impact of reduced anterior and posterior performance is minimal since current analyses tend to focus on center-slice defects. By adding hyperpolarized gas images in future, information about the presence or absence of gas may improve partial-volume segmentation.

CONCLUSIONS: A dense v-net was implemented that successfully and accurately segmented left and right lungs in proton MRI. Quantitative DSC and ROC analyses indicated results matched semi-automated ground truths. The NiftyNet platform allows simple distribution of a trained model and dependencies,⁴ which may permit multi-site implementation in future.

REFERENCES: 1. Kirby, M. *et al. Acad Radiol* (2012). 2. Guo, F. *et al. Med Image Anal* (2015). 3. Gibson, E. *et al. IEEE Trans Med Imaging* (2018). 4. Gibson, E. *et al. Comput Methods Programs Biomed* (2018). 5. Isensee, F. *et al. arXiv e-prints* (2018).

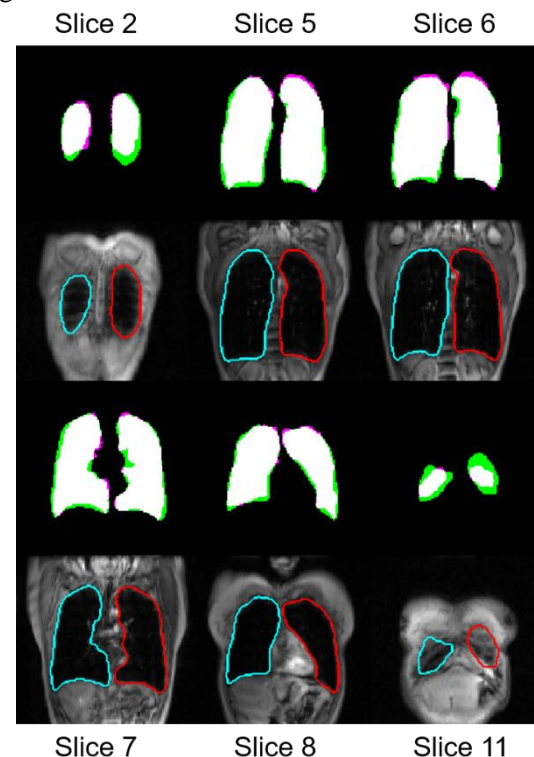


Figure 1. Top: prediction/ground truth comparison (black=true negative; white=true positive; green=false positive; pink=false negative), bottom: CNN segmentations for right (blue) and left (red) lungs.

Computed Tomography Radiomics Imaging Measurements in Chronic Obstructive Pulmonary DiseaseRyan Au BSc¹, Victor Lui², Meghan Koo BSc¹, Miranda Kirby PhD¹¹Department of Physics, Ryerson University, Toronto Canada²Department of Computer Science, Ryerson University, Toronto Canada

Introduction: Chronic Obstructive Pulmonary Disease (COPD) is a progressive lung disease that causes destruction of the airways and lung tissue (i.e. emphysema), and eventually leads to permanent airflow obstruction. Computed tomography (CT) imaging enables lung disease visualization and quantification, however current measurements focus on structural features, such as segmentation of the volume of lung with emphysema. There are no studies that interrogate the spatial relationships between image voxels that may have signal intensity information relevant to disease pathogenesis. Radiomics is an emerging imaging method that extracts a large number of features that quantify the spatial relationships between voxels. We hypothesize that an image analysis pipeline for extracting CT radiomics features can be developed, and measurements will be significantly correlated with lung function in COPD.

Methods: Spirometry and CT images were obtained from the Canadian Cohort of Obstructive Lung Disease (CanCOLD) study. Spirometry measurements included the forced expiratory volume in one second (FEV₁) and forced vital capacity (FVC). Participants were classified into two categories: participants with and without COPD, where COPD was defined as the FEV₁/FVC ratio less than 0.70. A CT radiomics feature analysis pipeline was developed for calculating second-order (grey level co-occurrence matrix (GLCM)) statistics; a total of 19 image features were measured using the pipeline. The image analysis pipeline consisted of segmentation of the whole lungs followed by Hounsfield unit (HU) thresholding between -1000 HU and 0 HU before calculation of the GLCM features. An unpaired t-test was used for comparing age, sex, BMI, and all 19 radiomics features between no COPD and COPD groups. Pearson correlation coefficients were used to determine association between lung function and radiomics features with strength defined as: weak; $r = 0.1 - 0.3$ ($-0.1 - -0.3$), moderate; $r = 0.3 - 0.7$ ($-0.3 - -0.7$), and strong; $r = 0.7 - 1.0$ ($-0.7 - -1.0$). A multivariate regression model with LASSO was performed to select radiomics features as potential predictors of lung function.

Results: The participants were classified into two groups: no COPD (n=53) and COPD (n=43). There were no significant differences between the groups in terms of age, sex, and BMI. 15/19 radiomics features were significantly different between the no COPD and COPD groups ($p < 0.02$). Table 1 shows the Pearson correlation coefficients for FEV₁/FVC with radiomics features. Overall, 15/19 radiomics features were significantly correlated with FEV₁/FVC; the same 15 features that differentiated the no COPD/COPD groups. Autocorrelation, sum of squares: variance, sum variance, sum average, and sum entropy features showed moderate correlation with lung function ($p < 0.003$). Of the 15 significant features, ten radiomics features indicated with * in Table 1 were selected by LASSO as predictors of lung function.

Conclusion: CT radiomics features can be extracted from CT images. CT radiomics features were shown to significantly differentiate participants with and without COPD and were significantly correlated with lung function. Therefore, our findings will motivate future studies to further investigate CT radiomics features as a potential imaging biomarker of COPD in longitudinal studies assessing disease progression.

Table 1: The Pearson Correlation between CT Radiomics Features and Lung Function.

Radiomics Features	FEV ₁ /FVC	
	Pearson's r	p-value
*Autocorrelation	-0.47	<0.001
*Sum of Squares: Variance	-0.47	<0.001
*Sum Variance	-0.47	<0.001
*Sum Average	-0.46	<0.001
*Sum Entropy	0.30	0.003
*Entropy	0.29	0.004
Inverse Difference Moment Normalized	-0.28	0.007
*Contrast	0.27	0.007
*Difference Variance	0.27	0.007
Inverse Difference Normalized	-0.27	0.009
*Dissimilarity	0.27	0.009
*Difference Entropy	0.26	0.01
Energy	-0.23	0.03
Maximum Probability	-0.21	0.04
Homogeneity	-0.20	0.05
Correlation	-0.09	0.4
Cluster Shade	-0.04	0.7
Information Measure of Correlation	0.04	0.7
Cluster Prominence	-0.03	0.8

Machine Learning for Predicting COPD Hospitalization using Quantitative CT Imaging

Amir Moslemi MSc,¹ Wan C. Tan MD,² James C. Hogg MD, PhD,² Harvey O. Coxson PhD²
and Miranda Kirby PhD^{1,2}

¹Department of Physics, Ryerson University, Toronto, ON, Canada; ²Centre for Heart Lung Innovation, University of British Columbia, Vancouver, BC, Canada.

Introduction: One of the most life threatening outcomes in patients with chronic obstructive pulmonary disease (COPD) is exacerbations that required hospitalization. Predicting COPD patients at increased risk of hospitalization is therefore an important goal of improving COPD management. Computed tomography (CT) imaging allows for quantification of numerous features in the lung that characterize the underlying pathologies in COPD, namely emphysema and airway disease. Machine learning is a powerful tool to make decisions and predictions based on large amounts of disparate data. The objective of this study was to predict subsequent hospitalization in COPD using machine learning techniques that include demographic, conventional lung function and CT imaging features.

Methods: Participants from the Canadian Cohort of Obstructive Lung Disease (CanCOLD) study were evaluated. In all participants, demographic information, spirometry and CT imaging was collected at the initial visit. The demographic information included: age, sex, BMI and smoking history. Spirometry was performed for measurements of forced expiratory volume in 1s (FEV₁) and forced expiratory vital capacity (FVC); all participants categorized into four groups based on GOLD criteria: never-smokers, current or former smokers with normal lung function (at risk), GOLD I (mild) COPD and GOLD II+ (moderate) COPD. All CT images were analyzed using VIDA vision software (VIDA Diagnostics Inc., Coralville IA, USA). A total of 48 CT imaging features were investigated, including several well-established CT emphysema measurements: the low attenuation area below -950 HU (LAA₉₅₀), 15th percentile lung density (PD15), low attenuation cluster (LAC) slope, and LAC total hole count. Hospitalizations were defined as any COPD hospitalization in the 12 months since their initial CanCOLD visit (binary variable). All features were first standardized, and features with greater than 3 times the standard deviation were considered outliers and removed. Feature selection was then performed using a chi-2 test. COPD hospitalization was predicted by using five different machine learning classification algorithms: logistic regression, Naïve Bayes, random forest, Adaboost, multi layer perceptron (MLP) and support vector machine (SVM). Enhanced Fuzzy Twin SVM (FTWSVM) was also applied, and parameter tuning was performed using Grid Search Cross validation (GSCV) and Particle Swarm optimization (PSO). Tuned parameters were selected by PSO. All 1247 participants were included in training and testing. The performance of the classification algorithm was determined by calculating the accuracy and F-measure.

Results: A total of 1247 CanCOLD participants were investigated: n=436 never-smokers, n=365 at risk, n=349 GOLD I and n=266 GOLD II+ COPD. Of the 1247 participants investigated, 114/1247 (9.1%) experienced hospitalization in the 12 months following their initial visit. The optimal four features selected were: age, GOLD severity group, LAA₉₅₀ and LAA₉₅₀ total hole count. As shown in Table 1, COPD hospitalization could be predicted from select demographic, spirometry and imaging measurements, and the best performing approach was enhanced FTWSVM (accuracy=95.1% accuracy, F-measure 81.3%).

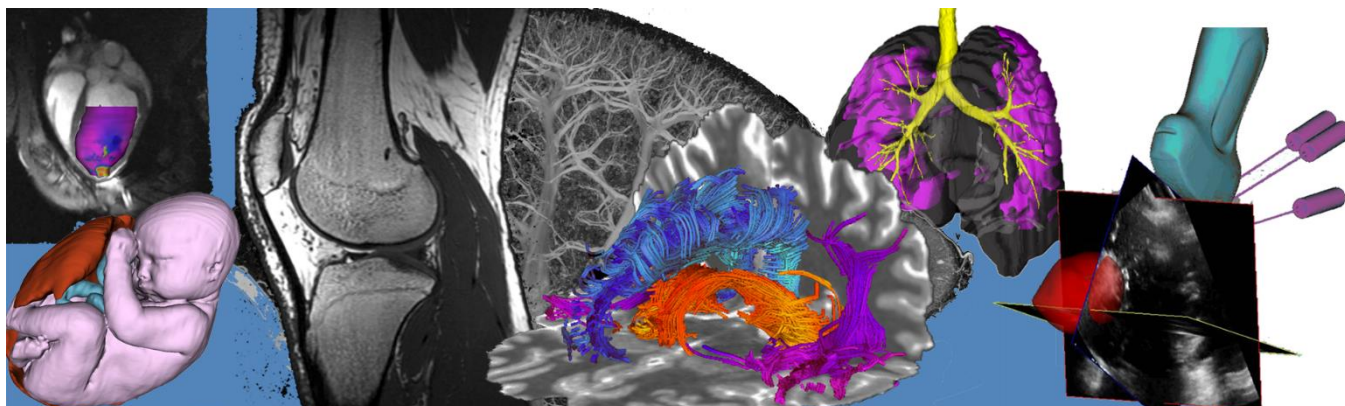
Table 1. Performance of Classification Techniques

	F-measure %	Accuracy %
Naïve Bayes	9	82.8
Logistic Regression	33.3	82.8
MLP	0	83.4
Random Forest	43.4	85.6
Adaboost	26.5	84.7
SVM	80	94.5
EFTWSVM	81.3	95.1

Conclusions: The results show that age, GOLD severity group, CT LAA₉₅₀ and LAC total hole count image features were able to predict hospitalization, and EFTWSVM was the best performing machine learning approach in comparison with SVM and other classifiers. Among imaging features investigated, features reflecting emphysema severity and distribution throughout the lung were the most important features for predicting hospitalization.

Poster Presentation Abstracts

Session 3: Machine Learning in Cancer Imaging



Fully Automated Segmentation of Prostate Zonal Anatomy on T2-weighted (T2W) and Apparent Diffusion Coefficient (ADC) Map MR Images and Localization of Prostate Peripheral Zone Tumors on ADC Map MR Image Using a U-Net-based Method

Zabihollahy Fatemeh¹, Schieda Nicola², Krishna Satheesh³, Ukwatta Eranga⁴

¹Department of Systems and Computer Engineering, Carleton University, Ottawa, ON, Canada

²Department of Radiology, University of Ottawa, Ottawa, ON, Canada

³Department of Medical Imaging, University of Toronto, Toronto, ON, Canada

⁴School of Engineering, University of Guelph, Guelph, ON, Canada

Introduction: Accurate detection and localization of prostate cancer (PCa) in men undergoing prostate MRI is a fundamental step for future targeted prostate biopsies and treatment planning. Accurate regional segmentation of the prostate boundaries on MR images is a fundamental requirement before automated prostate cancer diagnosis can be achieved. In this study, we first, describe a novel methodology to segment prostate whole gland (WG), central gland (CG), and peripheral zone (PZ), where $PZ+CG=WG$, from T2W and ADC map prostate MR images. Moreover, automated localization of PCa in the PZ on ADC map MR images using an ensemble U-Net-based model is described.

Methods: We designed two similar models each made up of two cascaded U-Nets to delineate the WG, CG, and PZ from T2W and ADC map MR images, separately. Then an ensemble U-Net-based model was developed to automatically localize PCa in the PZ on ADC map MR images. We used a dataset consisted of 225 patients (combining 153 and 72 patients with and without clinically significant prostate cancer) imaged with multi-parametric MRI at 3 Tesla. The ground truth was established by manual delineation of the prostate and prostate PZ tumors on T2W and ADC maps by four dedicated radiologists using MRI-radical prostatectomy maps as a reference standard, where each Radiologist segmented a subset of the data. We used sensitivity and specificity to assess the performance of our proposed method for PCa detection in the PZ from the ADC map MR images. To compute those values, a confusion matrix for each patient in the test dataset was created slice-wise. Having TP, FN, FP, and TN, the sensitivity and specificity could be calculated for each patient in the test set.

Results: Our proposed model for prostate zonal segmentation from T2W was trained and tested using 1154 and 1587 slices of 100 and 125 patients respectively. Figure 1 illustrates segmentation results for different image types in two patients. Table 1 shows a summary of the results of our method.

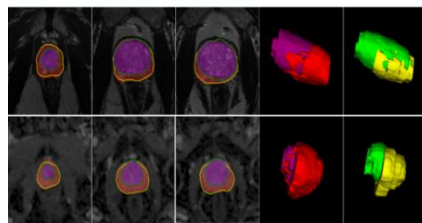


Figure 1. From top to bottom, example results from segmented prostate WG, CG, and PZ using T2W and ADC map MR images in two patients. On the source two-dimensional images, the U-net-based method segmentation of the prostate CG and PZ for three slices presented from apex to base (left to right) extracted from magnetic resonance imaging are shown in purple and red, respectively, and the contours computed from the expert manual are displayed in green and yellow. The fourth and fifth picture elements depict a three-dimensional surface rendering of algorithm-generated and expert manual segmentation of prostate zones, respectively.

TABLE 1. Summary of results of our proposed technique for prostate zonal

MR Image	Segmented Region	DSC (%)				
		Mean	SD	Median	25 th quartile	75 th quartile
T2W	WG	92.96	7.77	95.33	92.35	95.11
	CG	91.07	8.91	93.75	90.84	93.95
	PZ	86.22	3.72	86.78	84.48	89.00
ADC map	WG	89.71	8.89	92.09	86.35	92.74
	CG	86.33	10.69	89.89	83.51	90.59
	PZ	83.30	9.56	86.10	82.43	87.99

Our developed algorithm for fully automated localization of PCa on ADC map MR images yielded DSC, sensitivity, and specificity of $86.72\% \pm 9.93\%$, $85.76\% \pm 23.33\%$, and $76.44\% \pm 23.70\%$, respectively (mean \pm standard deviation) on 80 test cases consisting of 41 and 39 instances from patients with and without clinically significant tumors including 660 extracted 2D slices. AUC was reported as 0.779.

Conclusion: We describe a method for automated prostate zonal segmentation using ADC map and T2W MR images independent of prostate size and presence or absence of tumor. Additionally, we presented an ensemble learning-based model for fully automated PCa localization in the PZ from ADC map MR images. Our results are important in terms of clinical perspective as fully automated methods for ADC map images, which are considered as one of the most important sequences for prostate cancer detection in the PZ and CG, have not been reported previously. Future studies may evaluate the incremental yield of combined sequences for fully automated tumor detection.

Using natural language processing to predict splenomegaly from >100,000 structured radiology reports

Batch, K¹, Lupton, K¹, Sun, S³, Gangai, N⁴, Cho, J⁴, Gazit, L⁴, Nguyen, H⁴, Zulkernine, F¹, Do, RK⁴, Simpson, AL^{1,2}.

¹School of Computing, ²Department of Biomedical and Molecular Sciences, Queen's University

³McGill University Health Center

⁴Department of Radiology, Memorial Sloan Kettering Cancer Center

Introduction

This research aims to detect splenomegaly (increased spleen size) over time from structured radiology reports as a proof-of-principle for analyzing large volumes of CT images with weak labels. Splenomegaly is a result of chemotherapy treatment and is associated with increased risk of complications in cancer surgery among other poor outcomes for patients. We will demonstrate that natural language processing (NLP) can generate weak labels for semi-supervised classification of 105,042 CT scans based on information extracted from the associated structured reports, predicting the occurrence of splenomegaly as patients undergo chemotherapy treatment.

Methods

In an IRB approved, retrospective study, all CT chest/abdomen/pelvis reports (July 2009 to April 2019) from Memorial Sloan Kettering Cancer Center adhering to a standardized departmental structured template were included. The SPLEEN subsection was extracted and those with default 'unremarkable' text were excluded from training. For patients with colorectal cancers (CRC), hepatobiliary cancers (HB), leukemia, Hodgkin's lymphoma (HL) and non-HL (NHL), 1920 of 105,042 reports were annotated as: positive or negative/uncertain for splenomegaly by a radiologist to serve as ground truth. Model training was performed on 1536 reports and model accuracy was tested on 384 reports. The prediction model was applied to the remaining reports to calculate frequencies of splenomegaly within each of the cancer types. The implemented prediction model made decisions by analyzing unique word frequencies and importance levels using a term-frequency inverse-document frequency (TF-IDF) algorithm. Data produced by the TF-IDF algorithm was passed through a logistic regression where the target value was whether or not splenomegaly was present in a given instance.

Results

Splenomegaly was present in 42% of the annotated reports. After training, the splenomegaly classifier achieved 94% overall accuracy, 94.6% precision (positive predictive value), 94% recall (sensitivity), and 94.2% F1 score. Applied to the unannotated reports – those whose ground truth is unknown – the predicted frequency of splenomegaly was for CRC patients 8.7% (5275/60462), HB: 17.7% (2210/12506), leukemia: 31.5% (1684/5340), HL: 6.1% (390/6386) and NHL 9.2% (1866/20348). Total splenomegaly presence across all diseases was 24%, which compared similarly to expected totals determined via consultation with a team of radiologists.

Conclusions

NLP can predict splenomegaly from structured radiology reports after training from a limited sample of annotated text reports. This demonstrates a promising approach for analyzing large-scale imaging data, where ground truth is impossible to annotate directly due to the time required by humans for annotation. Our future work will apply this approach to mapping and predicting metastatic spread across the entire population of cancer patients and multiple cancer types.

Transfer Learning for Prostate Cancer Diagnosis

Andrew Grebenisan^a, Alireza Sedghi^a, Alexandre Menard^b, Jason Izard^c, Robert Siemens^c, Parvin Mousavi^a

^aMedical Informatics Laboratory, Queen's University, Kingston, ON, Canada

^bRadiology Department, Kingston General Hospital, Kingston, ON, Canada

^cUrology Department, Kingston General Hospital, Kingston, ON, Canada

Introduction

Deep learning has shown promise in medical imaging in the last few years, with advances such as a neural net that classifies breast cancer better than human specialists¹. However, many clinical centers do not possess the quantities of data required to develop locally accurate deep learning models, and 83% of them still use 1.5 T machines rather than 3.0 T. We propose a deep learning framework that takes advantage of publicly available 3.0 T MP-MRI data and then is fine tuned to data from a small 1.5 T dataset. We achieve AUC of up to 0.76 on the extraneous dataset and provide visualization of the most informative image regions.

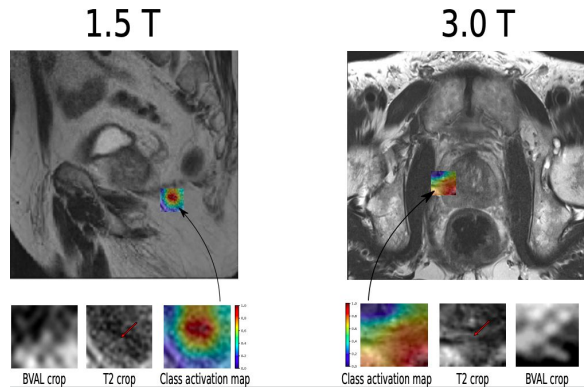


Fig 1: Visualizations produced by CAM-CNN on a 1.5 T slice as well as a 3.0 T slice

Methods

With the ProstateX dataset², we resample all images to $0.5 \times 0.5 \times 3 \text{mm}^3$ using cosine windowed sinc interpolation and crop 20 patches of size $32 \times 32 \times 3$ around the biopsy locations provided. Each one of these patches is derived from images that are, prior to cropping, randomly rotated and translated. We train a convolutional neural net that has a global average pooling penultimate layer and use the class activation map algorithm to generate visualizations that display the most important regions in the image. For the KGH dataset, the data is pre-processed identically to the ProstateX domain. For fine tuning, only the last linear layer is fine-tuned on the training set.

Results

We achieved an AUC of 0.86 on the ProstateX grand challenge, and a maximum 0.76 AUC after repurposing the CAM-CNN to the KGH dataset. In Fig 1 is an image of the neural network creating an activation map for patches from the 1.5 T and 3.0 T domain, overlaid onto their original images.

Conclusions

Without the use of transfer learning, models developed solely on locally available datasets from small hospitals cannot learn. In this work, a deep learning framework is established that allows for the classification of PCa for 1.5 T images from clinical centers that do not have abundant supplies of data.

References

1. S. M. McKinney, M. Sieniek, V. Godbole, J. Godwin, N. Antapova, H. Ashrafian, T. Back, M. Chesus, G. C. Corrado, A. Drazi, *et al*, "International evaluation of an ai system for breast cancer screening." *Nature* **577**(7788), pp. 89-94, 2020.
2. G. Litjens, O. Debtas, J. Barentsz, N. Karssemeijer, and H. Huisman, "Prostatex challenge data." TCIA, 2017.
3. G. Litjens, O. Debtas, J. Barentsz, N. Karssemeijer, and H. Huisman, "Computer-aided detection of prostate cancer in mri," *IEEE transactions on medical imaging* **33**(5), pp. 1083-1092, 2014.

Radiomic and genomic heterogeneity as predictors of acquired resistance to targeted therapy in metastatic CRC

Malaika Ngugama^{1,2}, Rami Srouji³, Caitlin McIntyre³, Qingling Duan^{1,2}, Jaclyn F. Hechtman⁴, Rona Yaeger⁵, Jennifer S. Golia Pernicka⁶, and Amber L. Simpson^{1,2}

¹School of Computing, ²Department of Biomedical and Molecular Sciences, Queen's University

³Departments of Surgery, ⁴Pathology, ⁵Medicine, and ⁶Radiology, Memorial Sloan Kettering Cancer Center

Introduction

Colorectal cancer (CRC) is the third most common cancer and a leading cause of cancer mortality worldwide. Recent advances in the molecular understanding of CRC has led to matched targeted therapies for subsets of patients. While these treatments can lead to rapid response, their therapeutic effect is limited by the development of resistance. A significant contributor to this resistance is tumor heterogeneity where patients have multiple genomic alterations that emerge during targeted therapy. We investigate the relationship between CT imaging (radiomics) and genomic data garnered from a patient who exhibited an excellent response to BRAF targeted therapy and then progressed and rapidly declined. Multiple tumor sites collected at autopsy were sampled and sequenced to correlate with radiographic imaging.

Methods

We collected the primary colon tumor and metastases present in the liver, portacaval space, umbilicus, and left and right lung. A single biopsy acquired from pre-treatment, as well as multiple autopsy samples post-treatment, were extracted and underwent next generation sequencing. Additionally, radiomic analysis was undertaken in CT scans over multiple time points; 6, 12, 18, and 24 weeks. CT images were manually segmented by a radiologist. Feature extraction occurred, identifying radiomic features from each region of interest. Analysis regarding feature selection will occur in order to identify specific biomarkers within both the genomic and radiomic data, which can be used to determine possible features of therapeutic resistant present in the patient. The radiomic data will undergo z-score normalization, and a tumor heterogeneity index will be created for each tumor using the average z-score value of each standardized feature. Unsupervised hierarchical clustering will be performed on the features to identify intrinsic imaging phenotypes (low, medium, or high heterogeneity). Similarly, each tumor will be assigned a genomic phenotype based on mutational load and copy number extracted from the sequenced genomic data.

Results

Our expected results will identify changes in heterogeneity in radiomic features and genomic alterations across multiple samples in the patient. Preliminary findings show multiple fusion events present in numerous post-treatment tumors, with a greater frequency of mutational alterations in some tumors compared with others – thus suggesting a difference in heterogeneity levels. For example, the liver sample extracted post-treatment shows 9 mutational alterations (including a deleterious in frame fusion of the BRAF gene), while the colon sample undergoes only 3 translocation mutations.

Conclusions

Rapid resistance to targeted therapies in CRC has been attributed to tumor heterogeneity and pre-existent resistant clones. No methodology is currently available to assess tumor heterogeneity in real-time to guide treatment. We expect that tumors analyzed from a single patient treated with selective targeted agents for BRAF mutated metastatic CRC will exhibit unique imaging and genomic patterns, allowing us to correlate radiomic features with genomic alterations. Preliminary analysis shows a difference in alteration frequency between tumors, suggesting differing heterogeneity levels among tumors. Our ultimate aim is to use radiographic imaging to identify tumor heterogeneity to inform the application of targeted therapies in CRC.

Automatic paraspinal muscles segmentation in patients with lumbar pathology with deep convolutional neural network

Wenyao Xia¹, Maryse Fortin^{2,3}, Joshua Ahn⁴, Hassan Rivaz^{3,5}, Michele C. Battie⁶, Terry Peters¹, Yiming Xiao¹

¹Robarts Research Institute, Western University, London, Canada

²Health Kinesiology & Applied Physiology, Concordia University, Montreal, Canada

³PERFORM Centre, Concordia University, Montreal, Canada

⁴Department of Kinesiology, Western University, London, Canada

⁵Electrical and Computer Engineering, Concordia University, Montreal, Canada

⁶School of Physical Therapy and Western's Bone and Joint Institute, Western University, London, Canada

Introduction: Recent evidence suggests an association between low back pain (LBP) and changes in lumbar paraspinal muscle morphology and composition (i.e., fatty infiltration). Quantitative measurements of muscle cross-sectional areas (CSAs) from MRI scans are commonly used to examine the relationship between paraspinal muscle characters and different LBP conditions. However, the manual segmentation required is time-consuming, laborious, and can be inconsistent. To date, no automatic MRI segmentation algorithms exist for patient data, which is likely due to the complex paraspinal muscle anatomy and high variability in muscle composition among the patient population.

Methods: We employed deep convolutional neural networks to automatically perform the segmentation from T2-weighted MRI axial slices at the L4-L5 and L5-S1 spinal levels. In this proposed architecture, we combine the classic U-Net, conditional random fields as the recurrent neural network (CRF-RNN), and multi-data training with a gradient magnitude map to achieve highly accurate multi-class segmentation.

Results: We use the Dice coefficient, sensitivity (recall), positive predictive value (PPV), and mean boundary distance (MBD) to quantitatively assess the segmentation performance of our trained neural networks. For all target muscles, we obtain an average Dice of 93.8%, recall of 93.9%, PPV of 94.2%, and an overall MBD of 1.00 mm. In comparison, the U-Net baseline has an average Dice of 92.4%, recall of 92.7%, PPV of 93.0%, and an overall MBD of 1.93 mm.

Conclusion: Our results demonstrate that adding gradient magnitude images as additional training sets can significantly improve the segmentation accuracy, especially in terms of MBD, without increasing network complexity, and adding CRF-RNN can reduce issues of island labels. In addition, leveraging the automatic segmentation results, the muscle morphometric analysis demonstrates that female sex and aging is correlated with increased fatty infiltration in multifidus and erector spinae muscles ($p < 0.05$) among patients with lumbar pathologies.

Domain Adapted Breast Tissue Segmentation in Magnetic Resonance Imaging

Grey Kuling^a, Belinda Curpen^b, and Anne L. Martel^{a,c}

^aMedical Biophysics, University of Toronto, Toronto, ON, Canada

^bDept of Medical Imaging, Sunnybrook Health Sciences Centre, Toronto, ON, Canada

^cPhysical Sciences, Sunnybrook Research Institute, Toronto, ON, Canada

Introduction: For women of high risk (> 25% lifetime risk) for developing Breast cancer (BCa), combination screening of mammography and magnetic resonance imaging (MRI) is recommended due to the increased sensitivity compared to mammography alone^[1]. Risk stratification is determined by risk assessment models, however adding additional radiological features may improve AUC^[2], prompting investigations of deep learning methods^[3] to create continuous measures of tissue features in breast MRI. To validate these features for risk assessment requires large scale epidemiological studies across health centers; therefore, it is essential, to have a robust, fully automated segmentation method. This presents a unique challenge of imaging domain adaptation when many different MRI protocols are used or are unknown to the model. We present a breast segmentation pipeline that uses multiple UNet^[4] segmentation models trained on different image domains and then uses Monte-Carlo Dropout (MCD)^[5] to measure each model's uncertainty, allowing us to select the most appropriate output.

Method: We performed the experiment using 58 patient scans split into train(68%)/validation(17%)/test(15%) sets. The trained models utilize 2D T1w images with and without fat suppression (FS and WOFS) of the breast acquired in the sagittal plane. The breast volume was found using a model developed by Fashandi et al.^[6]. Fibroglandular tissue (FGT) ground truth was estimated using thresholding, k-means clustering and manual editing. 3 2D-UNets were trained; one 1 channel UNet trained on mixed modalities (UNet-MM), and two 1 channel UNets trained on FS and WOFS images separately (1ChFS and 1ChWOFS). We used the generalized dice similarity coefficient (DSC) as the loss function^[7]. Domain adaption was applied during training by using techniques developed by Hesse et al.^[8]. During testing, when the image domain is unknown, the dropout layers of the 1ChFS-UNet and 1ChWOFS-UNet are turned on during prediction to create a Gaussian process that can then give a standard deviation (St.Dev) for each pixel in the segmentation mask.^[11] Uncertainty is then measured by taking the sum of squared St.Dev of the pixels. For a given scan volume, the quarter of slices with the largest amount of tissue are taken to a vote.

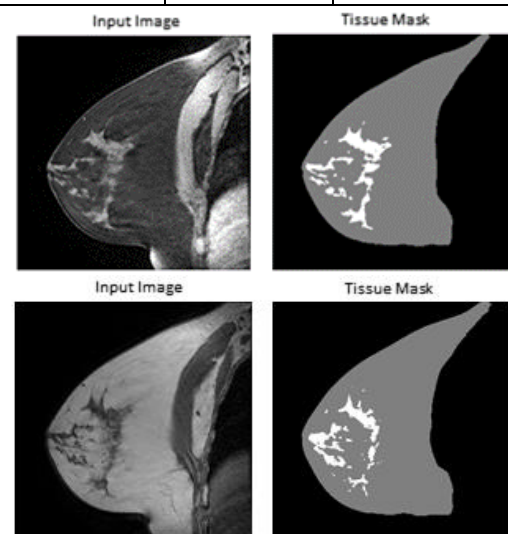
Each slice's vote is decided by the lower uncertainty measurement of each UNet. The UNet with the most votes is taken as the most appropriate output for the entire volume. This is the proposed UNet-MCD.

Results: For the test set, we evaluated the DSC using the UNet-MM and UNet-MCD, for the 3D volume of a whole breast. For the UNet-MCD, the correct UNet was used on the FS images and WOFS images 100% of the time during testing. These results are visualized in Figure 1.

Conclusion: We have presented a novel and robust means of choosing a segmentation output from multiple models trained on different modalities when an exam modality in question is unknown. This can be used as an automated tool to evaluate breast tissue features in MRI.

References: [1] Kriege, M. et al., N.E. J of Med 351(5), 427–437 (2004). [2] Quante, A. et al., Br Ca Res 14(6), R144 (2012). [3] Dalmis, M. U. et al., Med phys 44(2), 533–546 (2017). [4] Ronneberger, O. et al., in [Int Conf on MICCAI], 234–241, Springer (2015). [5] Gal, Y. et al., in [ICML], 1050–1059 (2016). [6] Fashandi, H. et al., Med. Phys 46(3), 1230–1244 (2019). [7] Sudre, C. e. a., in [DL in Med.Imag.Anal], 240–248, Springer (2017). [8] Hesse, L. et al., arXiv: 1909.02642 (2019).

<u>Model</u>	<u>Fat Tissue</u> <u>Ave. DSC</u> <u>± St.Dev</u>	<u>FGT Tissue</u> <u>Ave. DSC ±</u> <u>St.Dev</u>
UNet-MM	0.93±0.04	0.70±0.18
UNet-MCD	0.95±0.04	0.78±0.15



Automatic cancer subtype grading on digital histopathology images of radical prostatectomy specimensWenchao Han^{1,2,5}, M. R. Downes⁶, T. H. van der Kwast⁷, J. L. Chin^{3,4}, S. E. Pautler^{3,4}, and A. D. Ward^{1,2,4,5}¹Baines Imaging Research Laboratory, London Regional Cancer Program, Depts. of ²Medical Biophysics, ³Surgery, ⁴Oncology, Western University; ⁵Lawson Health Research Institute, London; ⁶Dept. of Laboratory Medicine and Pathology, University of Toronto, ⁷Dept. of Pathology, University Health Network, Toronto, Ontario, Canada

Introduction: Automatic cancer subtype grading of radical prostatectomy (RP) specimens can support clinical studies exploring the prognostic indications of the subtypes, and potentially benefits patient risk management and treatment planning. Many published methods have demonstrated the potential for computer-assisted detection and grading of prostate cancer (PCa) on digital histopathology images. However, there is no study in the literature demonstrating the use of an automated tool for PCa subtype grading. In this work, our objective is to develop and validate a system which grades cancerous regions of interest (ROIs) according to eight common subtypes.

Methods: 92 mid-gland whole-slide-images (WSIs) were obtained from 25 radical prostatectomy patients. The surgically removed prostates were sectioned at $4\mu\text{m}$, stained with hematoxylin and eosin (H&E) and scanned at $20\times$ ($0.5\mu\text{m}/\text{pixel}$). Each of the RP sections was reviewed cooperatively by two pathologists. Gleason Grade 3 (G3) was divided into desmoplastic, sparse, intermediate, and packed G3; G4 was separated into 1) large cribriform, 2) small fused glands, 3) poorly formed glands. Each WSI was separated into a set of square $480\times 480\mu\text{m}$ ROIs. ROIs containing more than 50% cancerous tissue were used in our experiment and a subtype label was assigned to each ROI according to the manual pathology annotations. We used pre-trained AlexNet to perform supervised machine learning for each experiment classifying: (1) sparse G3, (2) intermediate G3, (3) packed G3, (4) desmoplastic G3, (5) large cribriform G4, (6) small fused G4, (7) poorly formed G4, (8) benign intervening vs. negative samples (i.e. all the samples which were not defined as positive in the experiment) respectively. We performed leave-one-WSI-out cross-validation (CV) validating against the subtype labels. We calculated the area under the receiver operating characteristic curve (AUC). We also calculated the error rate, the false positive rate (FPR) and the false negative rate (FNR) using the closest operating point to top left corner of the receiver operating characteristic (ROC) curve.

Results: Table 1 shows the error metrics for cancer subtype grading, classifying each ROI either as the given subtype in the row, or not the subtype in the given row. The system yielded AUCs larger than 0.7 for all the subtypes except for packed G3. The subtypes of desmoplastic G3, small fused G4, poorly formed G4, and benign intervening have AUCs larger than 0.8. Figure 1 shows the system's output for a selected case, which contains confounding cancer regions of packed G3 and small fused G4. We found that generally the eight predicted label maps correctly mapped out most of the positive and negative regions. The major errors happened in the regions of packed G3, which were missed by the system and falsely labeled as small fused G4 and intermediate G3 (see the regions indicated by the yellow and blue arrows in Figure 1 (b), (c), and (f)).

Conclusion: In general, our experiments demonstrated promising results for this novel and challenging problem, using binary classification. Some subtypes are more challenging to detect, requiring further engineering efforts in future work.

	Error Rate	FNR	FPR	AUC
Sparse G3	26.8%	29.9%	26.2%	0.78
Intermediate G3	36.0%	32.0%	38.3%	0.70
Packed G3	50.2%	34.0%	51.5%	0.58
Desmoplastic G3	22.0%	26.8%	21.8%	0.82
Large cribriform G4	23.7%	33.8%	23.4%	0.74
Small fused G4	23.1%	28.6%	21.5%	0.82
Poorly formed G4	23.8%	18.4%	24.4%	0.86
Benign intervening	26.6%	20.9%	26.7%	0.82

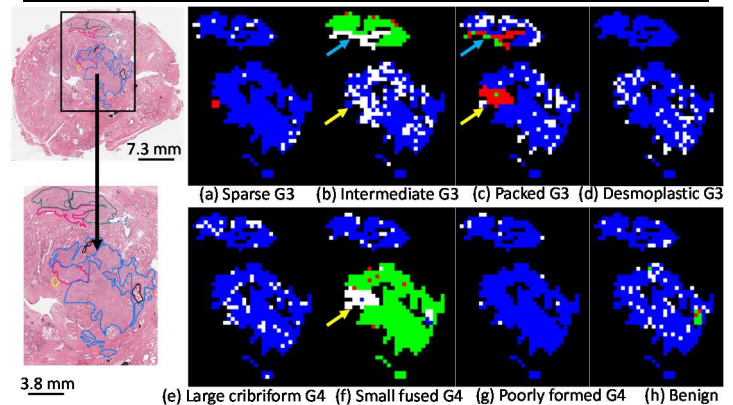
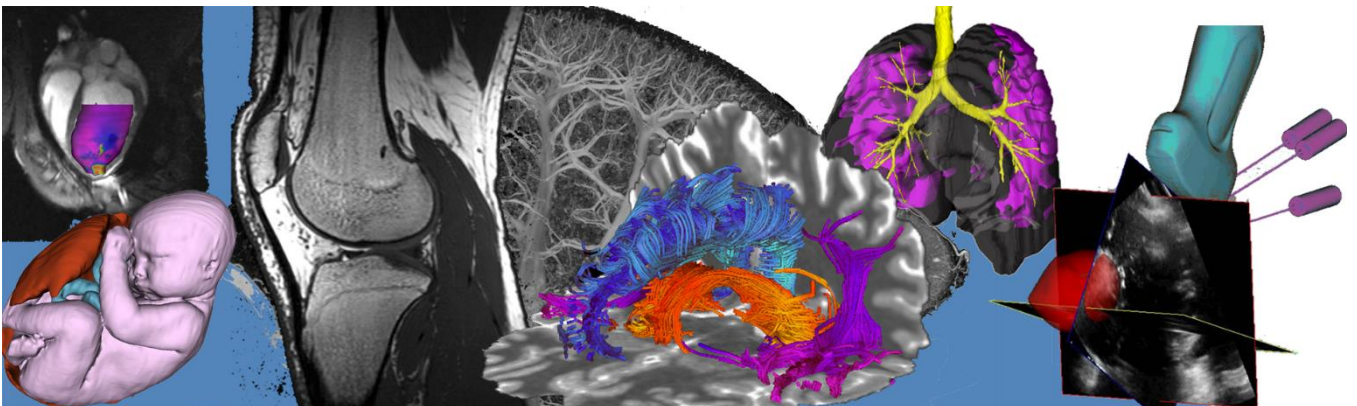


Figure 1: Label maps from an example WSI for PCa sub-grading. Left column: WSI with the region shown below zoomed in from the black box. (a) – (h) are label maps after validating system predicted results against manual annotation. Map annotations: Blue = true negative, Green = true positive, Red = false negative, white = false positive. Pathologist's annotations: Pink = Packed G3, blue = small fused G4, green = Intermediate G3, brown = Benign intervening. Yellow arrows indicate the false negative regions. Blue arrows indicate the false positive regions.

Poster Presentation Abstracts

Session 4: Machine Learning In Imaging



Classification of primary cancer and surrounding tissue in breast cancer xenograft models

Laura Connolly, Amoon Jamzad, Martin Kaufmann, Rachel Rubino, Alireza Sedghi,
Tamas Ungi, Mark Asselin, Scott Yam, John Rudan, Christopher Nicol, Gabor Fichtinger,
Parvin Mousavi

1. Queen's University, Kingston, Ontario

INTRODUCTION: The intelligent knife (iKnife) is a tool used for mass spectrometry that is designed for intraoperative tissue diagnosis and recognition [1]. Previous studies suggest that there is value in developing a robust machine learning algorithm for this device that can accurately distinguish cancerous from healthy tissue for a variety of different cancer types. This technology can improve margin decisions during tumor resections by offering real-time feedback without any interruptions to surgical workflow. In this paper, we demonstrate the feasibility of using the iKnife for data collection and classification of primary cancer from its surrounding tissues in xenograft mice models by implementing a framework that incorporates deep learning.

METHODS: Two cohorts (n=6) of human breast cancer xenografts were used for this analysis. These mice were orthotopically injected in the mammary fat pad with MDA-MB-231 breast cancer cells. The first cohort was sacrificed 4 weeks after the cell line was injected and the second cohort was sacrificed after 6 weeks. In the 6 week cohort, multiple macro-metastasis were noted in each organ, whereas metastasis in the 4 week cohort required more microscopic assessments. The iKnife was used to sample tissue from various regions including the primary tumor, lung, liver, intraperitoneal membrane and the spleen. In total, our training set consists of 145 samples from the 6 week cohort and our testing set consists of 125 samples from the 4 week cohort. This data was preprocessed and augmented to train a deep learning network for classification. The framework we developed consists of a neural network with two branches: an autoencoder for dimension reduction and a fully connected network for prediction (Figure 1) [2]. This structure was chosen so that the decisions made at each layer of the neural network are chemically intuitive and can be used to understand classification outliers. Our network was compared to traditional linear analysis, principal component analysis (PCA), to validate this new structure.

RESULTS: Our classifier and PCA were both used to predict the classes for each sample in the test set. We achieved an accuracy of 96.8% with the neural network and 96% with PCA. The confusion matrix in Figure 1 better describes how our non-linear network performed.

CONCLUSIONS: Our results indicate that our network performs comparably with linear analysis techniques. We can also conclude that tissue classification of primary tumor and surrounding tissue at various stages of cancer progression is possible with the use of the iKnife and machine learning.

ACKNOWLEDGEMENTS: Laura Connolly was supported by NSERC URSA. G. Fichtinger is supported as a Canada Research Chair. This work was funded, in part, by CANARIE's Research Software Program.

REFERENCES:

- [1] J. Balog *et al.*, "Intraoperative tissue identification using rapid evaporative ionization mass spectrometry," *Sci. Transl. Med.*, 2013.
- [2] S. A. Thomas *et al.*, "Dimensionality reduction of mass spectrometry imaging data using autoencoders," in *2016 IEEE Symposium Series on Computational Intelligence (SSCI)*, 2016, pp. 1–7.

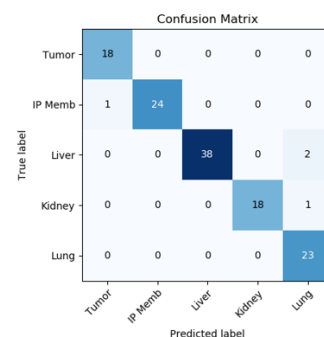


Figure 1: Confusion matrix – nonlinear network (96.8% accuracy)

Volumetric vs. Conventional 4-dimensional CT in Non-Small Cell Lung Cancer Patients

Heather M Young^{1,2,3}, Ting-Yim Lee^{2,3}, and Stewart Gaede^{1,2}

¹Department of Physics and Engineering, London Regional Cancer Program, ²Department of Medical Biophysics, University of Western Ontario, ³Robarts Research Institute, University of Western Ontario

Introduction: Conventional 4-dimensional computed tomography (4D-CT) images are acquired using a narrow axial field-of-view (aFOV), and are susceptible to respiratory motion artefacts. The objective of this work is to assess four-dimensional computed tomography (4D-CT) artefact reduction using a volumetric CT (vCT) scanner in a phantom and in patients with non-small cell lung cancer.

Methods: 4D-CT images of a Quasar Respiratory Motion Phantom (Modus Medical Devices, London Canada) with a moving insert containing four polystyrene spheres (5-30mm diameter) were acquired on a GE Revolution 256-slice vCT scanner, and a clinical 16-slice Philips Brilliance Big Bore CT simulator. 4D-CT images of three patients with non-small cell lung cancer were acquired on the same two scanners. vCT was acquired using the following parameters; cine mode, 0.28s/revolution, 160mm aFOV, 120 kV, 100 mA (for 10 s), and 10 mA (for 45 s). Clinical 4D-CT simulations were acquired using helical mode, 0.5s/revolution, 24 mm aFOV, 120 kV, 97 mA, and pitch adjusted for respiratory rate. The phantom was imaged under four breathing conditions: 1) sinusoidal, 2) incomplete sampling (IS), 3) baseline drift (BD), and 4) irregular amplitude (IA), and phantom images acquired at 10 mA were recombined to increase the signal-to-noise ratio (SNR). Phantom motion was measured and compared to the known motion using Pearson correlation. Each image acquired using vCT was compared to the corresponding image acquired using conventional 4D-CT and qualitatively assessed for motion artefacts.

Results: In the vCT images, phantom motion was strongly correlated to the known motion trace (sinusoidal: $r=0.998$, $p<.0001$; BD: $r=0.9972$, $p<.0001$; IA: $r=0.9974$, $p<.0001$). In the images acquired at 10 mA, SNR improved from 5.8 to 12.8 after recombination, which was higher than the clinical 4D-CT acquisition (SNR=8.8). The 10mA scans also delivered lower imaging dose (CTDIvol=29.5mGy) than the 100mA scans (CTDIvol=64.6mGy). Motion artefacts were clearly visible in the clinical images of both the phantom and lung cancer patients, but no artefacts were present in images from the vCT scanner.

Conclusion: 4D-CT acquired using the vCT scanner eliminates visible respiratory motion artefacts commonly present in conventional 4D-CT, and accurately captures tumour respiratory motion.

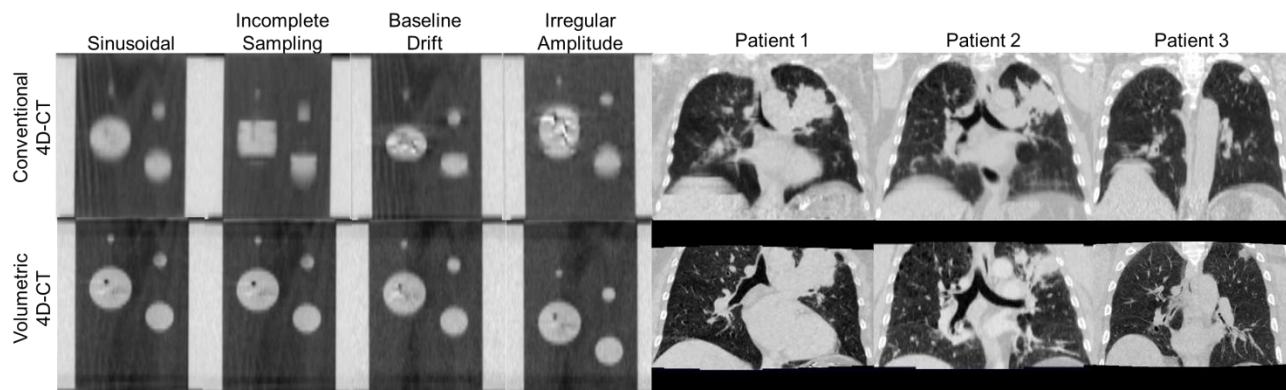


Figure 1. Clinical 4D-CT (top row) and volumetric 4D-CT (bottom row) of the Quasar respiratory motion phantom (left) and of three patients with non-small cell lung cancer (right). Motion artefacts are clearly visible in all of the clinical images, but are not present in the v4D-CT scans.

Cancer Cell Detection with Raman Spectroscopy: A Multidisciplinary Workflow

Amoon Jamzad¹, Rachel Rubino², Christine Orr³, Dalila Villalobos³, Sonal Varma³, Gabor Fichtinger¹, John Rudan⁴, Christopher Nicol^{2,3}, Scott Yam⁵, and Parvin Mousavi¹

1. School of Computing, Queen's University, Kingston, Canada,
2. Cancer Research Institute, Queen's University, Kingston, Canada,
3. Department of Pathology & Molecular Medicine, Queen's University, Kingston, Canada,
4. Department of Surgery, Queen's University, Kingston, Canada,
5. Department of Electrical & Computer Engineering, Queen's University, Kingston, Canada.

INTRODUCTION: Raman spectroscopy is a non-invasive label-free optical technique that can reveal the biochemical fingerprints of molecular bonds in materials and tissues. Vibrational spectroscopic techniques such as Raman have attracted a large attention in cancer research during the past years, especially in surgical interventions [1]. Quantitative evaluation of resected tumours and site of the resection during cancer surgery plays an important role in decreasing cancer recurrence rates. Raman paired with proper acquisition and analysis scheme, can differentiate molecular signature of cancer with high specificity and may potentially be used as an intra-operative guidance tool for margin assessment. In this preliminary study, we show the feasibility of the introduced cancer cell detection workflow post-operatively, using human breast cancer xenograft mouse model.

METHODS: Two adjacent slices were cut from formalin-fixed paraffin-embedded tissue block; one fixed on a Raman compatible substrate while the other fixed on microscope slide, and both went through standard de-waxing and re-hydration process. The glass slide got hematoxylin and eosin stained, scanned, and annotated by a trained pathologist. Spatio-spectral Raman data were acquired from the other slide with excitation wavelength of 785 nm and spatial resolution of 200 μm controlled by a mechanical stage. The Raman spectra were pre-processed [2], linearly compressed through principle component analysis, and clustered using hierarchical algorithm, resulting in a pseudo-color image. This image was then registered to the color-processed digital scan of the stained slide to be comparable with pathology annotations (Figure 1).

RESULTS: Based on the preliminary results, the label image generated from the proposed Raman spectra analysis matched to the gold standard annotation by pathologist with 81.79% spatial overlay, considering intersection over union measure. This shows the feasibility of proposed framework for cancer cell differentiation using Raman spectroscopy.

CONCLUSIONS: The intra-operative detection of cancer cells in real time is very beneficial for margin assessment during surgery. By proper optimization of parameters, the proposed model in this study can be used as a point-base sampling tool where the probe is held by hand, which makes the translation of the workflow to surgical interventions more practical. Addressing the challenges such as time/noise trade-off is our future plan to adopt the proposed workflow to intra-operative cases where there is proper line of sight and accessibility for surgeon to evaluate the margins.

REFERENCES:

- [1] Auner, G.W., Koya, S.K., Huang, C. et al. Applications of Raman spectroscopy in cancer diagnosis. *Cancer Metastasis Rev* 37, 691–717 (2018).
- [2] Zhang, Z.M., Chen, S., Liang, Y.Z. Baseline correction using adaptive iteratively reweighted penalized least squares. *Analyst* 135, 1138–46 (2010).

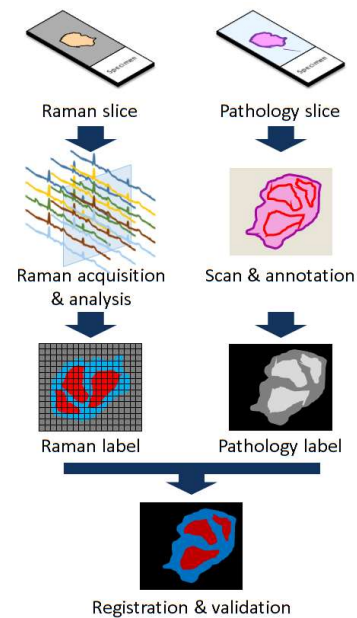


Figure 1. Schematic of the proposed framework for cancer detection using Raman

Descriptive Electrospray Ionization Mass Spectrometry Imaging (DESI-MSI) in the Application of Cancer Identification in Prostate

Jenny Wang¹, Nicole Morse¹, Tamara Jamaspishvili¹, Martin Kaufmann², Kevin Ren³, Alireza Sedghi⁴, Amoon Jamzad⁴, Parvin Mousavi⁴, David Berman^{1,3,5}

1. Department of Pathology & Molecular Medicine, Queen's University
2. Department of Biomedical and Molecular Sciences, Queen's University
3. Kingston General Hospital
4. School of Computing, Queen's University
5. Cancer Research Institute, Queen's University

Introduction: Early stage prostate cancer is often treated with Radical Prostatectomy (RP), where positive margins are associated with higher recurrent rates and adjuvant treatments. Precise detection of residual cancer cells is important to maintain a clean margin. For this purpose, we propose to develop a data analysis pipeline which can reliably differentiate between benign and cancer prostate cells. The imaging modality of our choice is Descriptive Electrospray Ionization Mass Spectrometry Imaging (DESI-MSI). It is a type of imaging modality that can capture mass spectrometry signature of metabolites and map these signatures over spatial coordinates to create a 2D representation of tissue in real time.

Method: Fresh frozen prostates were collected from RP at Kingston General Hospital [1]. Biopsy cores were extracted from each prostate and sections were cut for DESI-MSI analysis. After DESI-MSI analysis, each section was stained and analyzed by a trained pathologist for histopathology annotation. Single-pixel regions of interest (ROIs) were selected from each section using an in-house script. Data modelling and classification were performed on these ROIs through feature selection and machine learning algorithms. Methods used in model training include principal component analysis – linear discriminant analysis (PCA-LDA), decision tree, autoencoder and support vector machine (SVM).

Results: Around 2000 ROIs were collected from each biopsy core and used for classification model. Of the models tested, PCA-LDA was able to predict cancer at 88% accuracy between two labels (benign/cancer), and at 78% accuracy between four labels (benign/cancer/pre-cancer/stroma). Decision tree model was able to predict cancer at 94% accuracy between benign and cancer.

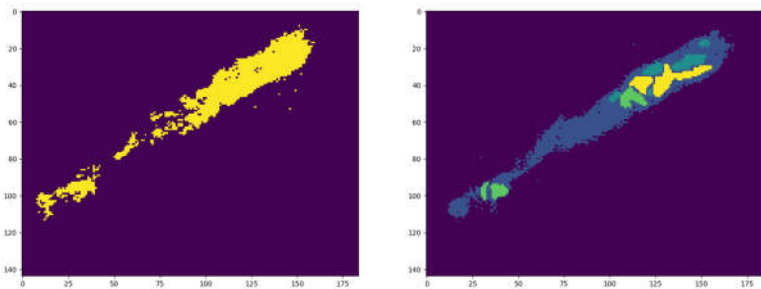


Figure 1 DESI-MSI image (left) and pathology mask (right), used for ROI extraction.

Conclusion: This analysis pipeline was able to accurately predict cancer ROIs from a number of different labels. Future work includes model optimization using more sophisticated algorithms such as autoencoder and SVM, and introduction of more detailed classification labels, such as low grade and high grade prostate cancers, or cancers with different genomic instabilities. The long-term goal is to provide a robust data analysis workflow common to mass spectrometry imaging data from any type of sub categories.

References: [1] Morse, N., Jamaspishvili, T., Simon, D. et al. Reliable identification of prostate cancer using mass spectrometry metabolomic imaging in needle core biopsies. *Lab Invest* 99, 1561–1571 (2019)

Investigating the role of immune environments and quantitative imaging phenotypes in pancreatic cancer

Mary Anne Panoyan^{1,2}, Caitlin A. McIntyre³, Jayasree Chakraborty³, Maura Koszalka³, Jared Bassman³, Yuting Chou³, Mithat Gonen⁴, Tricia Cottrell⁵, Richard K. G. Do⁶, Alice Wei³, Vinod P. Balachandran³, Qingling Duan^{1,2}, and Amber L. Simpson^{1,2}

¹School of Computing, ²Department of Biomedical and Molecular Sciences and ⁵Pathology, Queen's University
³Departments of Surgery, ⁴Biostatistics, and ⁶Radiology, Memorial Sloan Kettering Cancer Center

Introduction: Pancreatic ductal adenocarcinoma (PDAC) is an aggressive uniformly lethal cancer^{1,2}. There are limited prognostic and predictive biomarkers for PDAC patients¹. High-throughput analysis of CT scans (radiomics) is a non-invasive tool to quantitatively analyze images. Previous data shows CT images can be used to accurately predict survival in patients with PDAC³. The unique environment in which PDAC develops has shown immune privilege, where enhanced intratumoral adaptive immunity is associated with improved survival¹. We sought to build a CT radiomics model to predict immune infiltration that would enable optimized selection of patients for immunotherapy based on routine CT scans.

Methods: Sixty-four PDAC patients from Memorial Sloan Kettering Cancer Center (MSK) were included in our analysis. A tissue microarray (TMA) was constructed with tumor arranged in triplicate from short-term (>3 months and <1 year) and long-term survivors (>3 years). Multiplexed immunohistochemistry was performed for intratumoral mature dendritic cells (DC-LAMP⁺), regulatory T cells (CD3⁺FoxP3⁺), CD8⁺ T cells, (CD3⁺CD8⁺), activated cytolytic CD8⁺ T cells (CD3⁺CD8⁺GrB⁺), and macrophages (CD68⁺). The highest value or the “hot spot” of the triplicates was chosen for analysis. The pancreatic tumor in the portal venous phase on preoperative CT was manually delineated, and 254 radiomic features were extracted and analyzed for significance. Using multivariate linear regression analysis radiomic features can be correlated with immune infiltrate to predict immune phenotypes. This can be achieved through supervised machine learning methods to accurately classify radiomic features and immune infiltrate phenotypes.

Results: In preliminary analysis, twenty-two patients were included in a multivariate linear regression of radiomic and immune infiltration, feature selection resulted in 17 significant radiomic features and five regression models were then constructed using the significant radiomic features to predict intratumoral immune infiltration. strong associations were found between imaging phenotypes and dendritic cells (R²=0.83, 95% CI 0.761-0.906, p<0.001) and activated cytolytic T cells (R²=0.85, 95% CI 0.811-0.89, p=0.07), however the correlation was weaker (R²<0.7) for the other three cell types. Analysis in the larger cohort of patients will validate these results.

Conclusion: The preliminary study shows promise in predicting dendritic cells, and cytolytic T cells. As current biomarkers for PDAC are tissue based. this novel approach is unique as it may provide an easily applicable and non-invasive imaging tool to select patients with enhanced intratumoral adaptive immunity for immunotherapy, based on CT scans.

References:

1. Ino Y, Yamazaki-Itoh R, Shimada K, Iwasaki M, Kosuge T, Kanai Y, et al. Immune cell infiltration as an indicator of the immune microenvironment of pancreatic cancer. *Br J Cancer*. Nature Publishing Group; 2013;108(4):914–23.
2. Balachandran VP, Łuksza M, Zhao JN, Makarov V, Moral JA, Remark R, et al. Identification of unique neoantigen qualities in long-term survivors of pancreatic cancer. *Nature*. Nature Publishing Group; 2017;551(7681):512–6.
3. Chakraborty J, Langdon-Embry L, Cunanan KM, Escalon JG, Allen PJ, Lowery MA, et al. Preliminary study of tumor heterogeneity predicts two year survival in pancreatic cancer patients. *PLoS One*. 2017; 12(12):e0188022.

Micro-Finite Element Modeling of Osteoblastic Vertebral Metastasis Fractures

Authors: Allison Clement¹, Michael Hardisty¹, Cari Whyne¹⁻³

¹Sunnybrook Research Institute, Toronto, Canada ²Institute of Biomedical and Biomaterials Engineering, University of Toronto, Canada ³Department of Surgery, University of Toronto, Canada

Introduction: The negative consequences of fracture in the metastatic spine motivates improved understanding of bone quality and fracture risk. Computational models can evaluate effects of changes in structural and material properties due to the presence of pathology or intervention. This work aimed to develop and validate voxel-based micro-finite element (μ FE) models of vertebrae with osteoblastic involvement that can predict fracture initiation and propagation.

Methods: A preclinical of osteoblastic metastatic lesions in the spine was created via intracardiac injection of ZR-75-1 breast cancer cells into athymic rats. Motion segments, T13-L1 and L1-L3, were excised 4-months post inoculation. Displacement-controlled axial and bending loads were applied to the metastatically involved motion segments with sequential μ CT imaging ($34\ \mu\text{m}$) to capture progression of failure.

Specimen specific μ FE models ($n=2$) were created from unloaded μ CT images using an in-house voxel-based meshing algorithm. Displacement boundary conditions were created using surface-based registration. Damage mechanics were incorporated using cohesive elements to model damage within predefined regions of interest. Healthy and metastatic bone material property assignment was implemented via spine specific thresholding and manual segmentation of osteoblastic tissue.

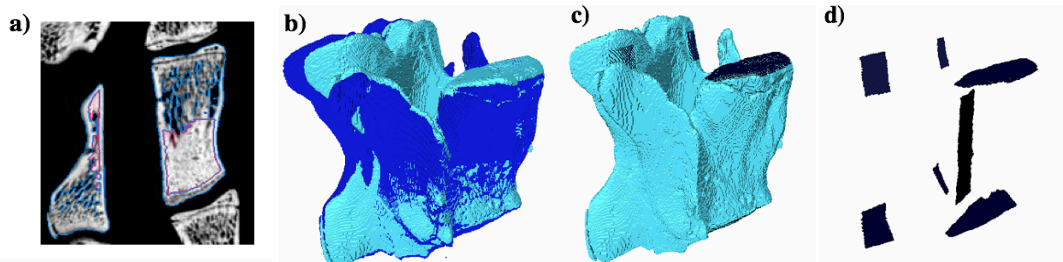


Figure 1: μ FE model construction a) μ CT image ($34\mu\text{m}$) with manual segmentation of vertebrae, b) unloaded (light blue) and loaded (dark blue) surface registered with affine registration, c) unloaded scan with loading surfaces (in darker colour), d) loading surfaces from image (c) for application of boundary conditions (facet joints, endplates, and rod).

Results: Failed elements were seen at anatomical sites consistent with experimental observation, with one model predicting failure in the pedicle and the second at the endplate. However, the μ FE models predicted less displacement at the fracture sites than seen experimentally. Changes in crack propagation direction at the growth-plate was not captured, as the growth plate was not specifically included in the μ FE models.

Conclusion: The specimen specific voxel-based μ FE models including cohesive zone-based damage mechanics were able to accurately predict the location of damage in preclinical vertebrae with osteoblastic lesions. The assumed damage mechanics parameters and material property definitions of the osteoblastic tissue and the absence of growth-plate specific material properties may have limited the ability to predict the extent of the damage propagation and displacement. Identifying fracture initiation and propagation in osteoblastic vertebrae with μ FE modeling may ultimately be useful in guiding therapeutic interventions.

Using deep learning to simulate kidney ultrasound images

Grace Pigeau, Lydia Elbatarny, Victoria Wu, Abigael Schonewille,
Gabor Fichtinger, Tamas Ungi

Laboratory for Percutaneous Surgery, School of Computing, Queen's University, Kingston, Canada

INTRODUCTION: Ultrasound (US) has become an indispensable alternative to X-ray fluoroscopy for percutaneous kidney interventions. Ultrasound-guidance provides equivalent accuracy in needle placement, but with a shorter total operation time and less complications compared to fluoroscopy [1]. Ultrasound is also safer and more accessible than X-ray. However, the efficacy of US as a guidance method for clinical interventions relies heavily on the examiner's experience. Simulation-based medical training can shorten the learning curve for ultrasound-guided interventions. However, simulation tools which serve as an alternative to real patients are limited by a lack of available medical images. Synthetic US images offer a potential solution but are difficult to generate realistically due to the complexity of acoustic artifacts that contribute to a real US image. Recent developments in deep neural networks, especially generative adversarial networks (GANs), may help overcome this difficulty. GANs have proven practical to simulate complex images and have been reported to simulate acoustic artifacts beyond the capabilities of conventional methods [2]. We propose to use and evaluate a GAN for simulating kidney US images from segmentations.

METHODS: To achieve our goal, kidney ultrasounds were collected from 9 healthy volunteers. Relevant anatomy was segmented to create anatomical label-maps using the 3D Slicer open source software package. A GAN was then trained to generate US images from these label-maps. The network used is the pix2pix conditional GAN which was developed for image-to-image translation [2]. Finally, a two-part survey of 4 participants with sonography experience (3 radiologists, 1 medical student) was conducted to assess the realism of the generated images. The first part of the survey consisted of 50 kidney US images; half of which were real while the other half were simulated. Participants were asked to label each of the 50 US images as either real or simulated. In the second part of the survey, the participants were presented with ten simulated images not included in the first part

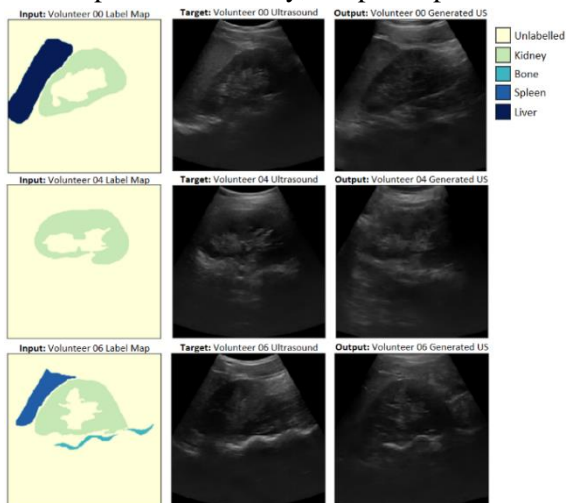


Figure 1. Sample input, target, and simulated.

of the survey. The participants were told that these images were simulated and asked to evaluate the realism of different aspects of the images as well as determine how many contained distinguishable kidney anatomy.

RESULTS: The average number of correctly identified images was 28 of 50 (56%). On a scale of 1-5, where 5 is indistinguishable from real US, the generated images received an average score of 3.75 for realistic anatomy and 4.0 for realistic ultrasound effects.

CONCLUSIONS: We evaluated the realism of kidney ultrasound images generated using adversarial networks. Generative adversarial networks appear to be a promising method of simulating realistic ultrasound images from cross-sectional anatomical label-maps.

Acknowledgements: G. Pigeau was supported by an NSERC USRA. G. Fichtinger is supported as a Canada Research Chair. This work was funded, in part, by NIH/NIBIB and NIH/NIGMS (via grant 1R01EB021396-01A1 - Slicer+PLUS: Point-of-Care Ultrasound) and by CANARIE's Research Software Program.

REFERENCES:

- [1] M. Agarwal, M. S. Agrawal, A. Jaiswal, D. Kumar, H. Yadav, and P. Lavania. "Safety and efficacy of ultrasonography as an adjunct to fluoroscopy for renal access in percutaneous nephrolithotomy (PCNL)," *BJU International*, vol. 108, no. 8, pp. 1346-1349, 2011.
- [2] P. Isola, J. Y. Zhu, T. Zhou, and A. A. Efros. "Image-to-image translation with conditional adversarial networks," *Proceedings - 30th IEEE Conference on Computer Vision and Pattern Recognition*, vol. 2017-January, pp. 5967-5976, 2017.

Implementation of density-adapted 3D projection-reconstruction MRI sequence for sodium imaging of small animals at 3 Tesla

Xin Yue Wang¹, Alireza Akbari¹, Francisco M. Martínez-Santesteban², Timothy J. Scholl^{1,2,3}

¹Department of Medical Biophysics, Western University, London, Ontario ²Robarts Research Institute, Western University, London, Ontario ³Ontario Institute for Cancer Research, Toronto, Ontario

Introduction: Tissue sodium concentration (TSC) is a sensitive indicator of disease. Changes in tissue sodium distribution are implicated in many diseases¹. In cancer, aerobic glycolysis causes sodium to accumulate in tumour cells². These molecular changes mean sodium imaging could potentially improve characterization of tumour response to treatment. Sodium has previously been imaged preclinically with magnetic resonance imaging (MRI) at high field strengths³. Since sodium has limited *in vivo* concentration, low gyromagnetic ratio, and quadrupolar relaxation ($T_1=10-40\text{ms}$, $T_{2,\text{fast}}=1-5\text{ms}$, $T_{2,\text{slow}}=15-30\text{ms}$), adequate signal-to-noise ratio (SNR) is difficult to achieve¹. The density-adapted three-dimensional projection-reconstruction (DA3DPR) sequence has been demonstrated to achieve improved sodium SNR compared to cartesian imaging sequences, and without extreme hardware requirements⁴. We aim to implement the DA3DPR sequence for preclinical sodium MRI of rat glioblastoma at 3T. Improved sodium imaging adapted for preclinical studies at 3T lends significance to translation of sodium imaging for clinical use.

Methods: DA3DPR imaging was optimized on a GE Discovery MR750 3.0T MRI. Performance was evaluated at 1-mm and 3-mm isotropic resolution ($TE=0.5\text{ ms}$, $TR=100\text{ ms}$, $T_{\text{aq}}=8\text{ ms}$, flip angle (FA)= 90° , gradient slew rate= 20 mT/m , isotropic FOV= 80 mm). Sodium imaging was performed using a curved transmit/receive butterfly radiofrequency (RF) surface coil. A phantom of 50-mmol/L sodium (physiological sodium concentration) and 1% agarose was imaged to determine the coil sensitivity profile. Imaging at 3-mm resolution was further evaluated in an animal model. Stereotactic surgery was performed to implant 1×10^6 C6 cells into the right hemisphere of a Wistar rat brain. Seven days following implantation, rats were imaged with DA3DPR sodium MRI (NEX = 10, total acquisition time = 12 mins) and 3D T_2 -weighted MRI (CUBE) every 3 days until experimental endpoint. Images were co-registered manually using 3D-Slicer and manual segmentation of the tumour and healthy brain were performed using ITK-SNAP.

Results: Phantom imaging at 3-mm isotropic resolution revealed that it was possible to detect physiological levels of sodium throughout a volume the size of a rat head with an SNR greater than 30 within a total scan time of 12 minutes. Sodium MRI of a rat glioblastoma (Figure 1) reveals a significant increase in TSC within the tumour compared to healthy brain region beginning 14 days after implantation.

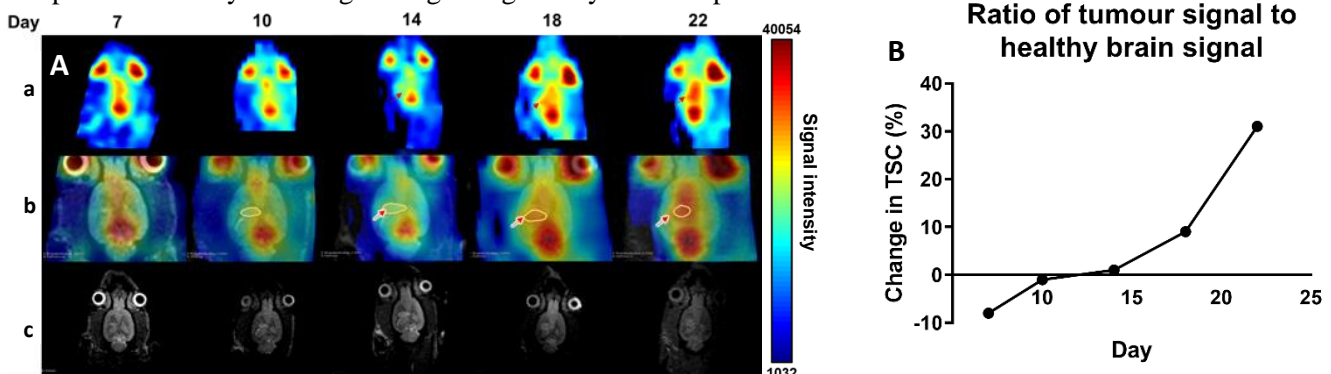


Figure 1. A) Longitudinal sodium (a) and proton (c) images of the head of an untreated animal and a magnified overlay image, (b) combined from (a) and (c). Arrows show sodium accumulation in tumorous region **B)** Percent change in sodium signal over time in tumour region compared to contralateral healthy brain region ($n=1$).

Conclusions: We have successfully implemented a DA3DPR sequence for sodium imaging with a 3-mm isotropic resolution at 3T for preclinical imaging research. Our implementation can visualize regional changes in sodium with enough SNR (> 30) for assessment of brain tumours. In the future, we intend to measure longitudinal changes in TSC in the tumour in response to chemo- and radiotherapies. Additionally, we will examine changes compared to reference markers of varying concentrations.

References: [1] Madelin, G., et al., Prog Nucl Magn Reson Spectrosc. 2014, 79:14-47 [2] Vander Heiden, M.G. et al., Science. 2009, 324(5930):1029-1033 [3] Schepkin, V.D., et al., Magn Reson Med. 2005, 53(1):85-92 [4] Nagel, A.M., et al., Magn Reson Med. 2009, 62(6): 1565-1573

Poster Presentation Abstracts

Session 5: Image-Guided Interventions

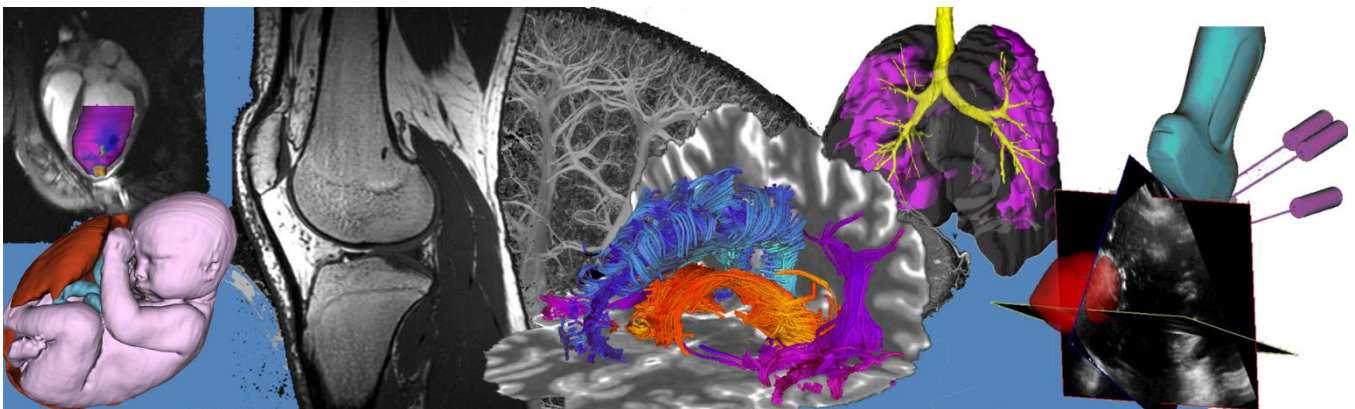


Image-Guided Fluorescence Tomography: Assessment in Pre-Clinical Models of Oral Cancer Surgery

Ashley Gilbank,¹ Jacqueline A. Fleisig,¹ Donovan Eu,²
Brian C. Wilson,^{1,3,4} David A. Jaffray,^{1,3-5} Jonathan C. Irish¹⁻³ and Michael J. Daly¹

¹TECHNA Institute, University Health Network, Toronto ON

²Department of Otolaryngology – Head & Neck Surgery, University of Toronto

³Ontario Cancer Institute, Princess Margaret Cancer Centre, Toronto ON

⁴Department of Medical Biophysics, University of Toronto

⁵MD Anderson Cancer Center, Houston TX

Introduction: Current intraoperative methods to assess tumor invasion depth in mucosal oral cancer provide limited real-time information. The advent of targeted fluorescence contrast agents for head and neck cancer is a promising innovation, but surgical imaging systems typically provide only two-dimensional views. Here, we investigate the use of an image-guided fluorescence tomography (igFT) system for 3D imaging in tissue-simulating oral cancer phantoms.

Methods: Non-contact diffuse optical tomography was implemented using finite-element software (NIRFAST), with the addition of geometric data from intraoperative cone-beam CT imaging and stereoscopic optical navigation. Tissue phantoms used gelatin for the background (5% for fat, 10% for muscle) and 2% agar for palpable, tumor-like inclusions infiltrating from the surface (an “iceberg” model). Standard agents were used for absorption (hemoglobin), scattering (Intralipid), fluorescence (indocyanine green), and CT contrast (iohexol). Experiments characterize fluorescence tomography performance across a range of tumor invasion depths, fluorescent tumor-to-background ratios, and inclusion shapes.

Results: Initial simulation and phantom results demonstrate that igFT can recover the inclusion depth with an accuracy of <1mm over a range of clinically relevant depths (2-6 mm). Figure 1(a) shows representative results of fluorescence reconstruction in a simulated tonsil tumour. Tumor “depth maps” [(b),(c)] are fused with navigated endoscopic video with accuracy <0.6 mm. Surgical models are under development for a range of head and neck sites including tongue, buccal, tonsil, and oropharynx.

Conclusions: This work presents preliminary results using an image-guided fluorescence tomography system in models simulating infiltrative oral cancer. Further streamlining of the acquisition hardware and computational software is necessary to facilitate clinical studies, which are essential to assess the potential benefits of this technology for surgical guidance.

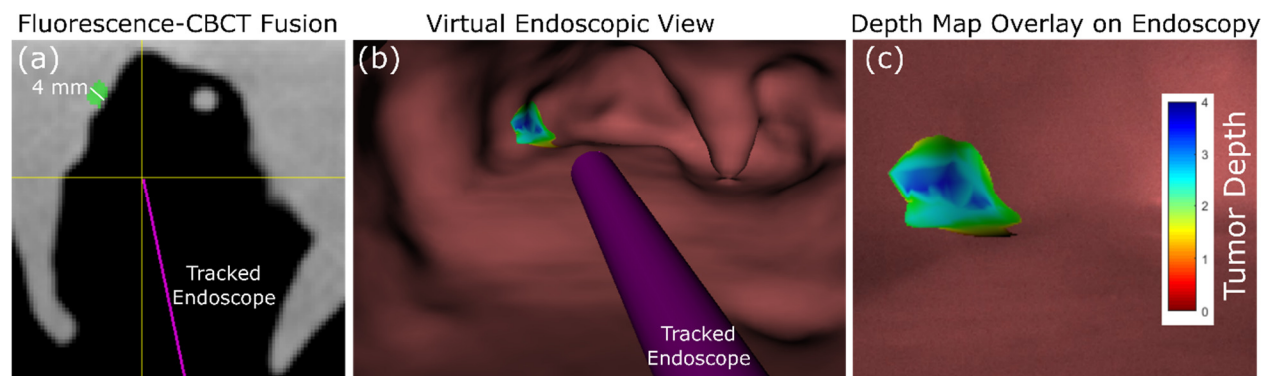


Figure. (a) Representative fluorescence reconstruction of a simulated tonsil tumor, superimposed on cone-beam CT. (b) Volumetric information is converted to a surface map that shows the maximum fluorescence depth below the surface. (c) A navigated endoscope enables superposition of the depth map on the endoscopic video.

Navigated skin cancer surgery with real-time tissue characterization

Natasja N.Y. Janssen¹, Martin Kaufmann², Alice Santilli¹, Amoon Jamzad¹, Kaitlin Vanderbeck³, Kevin Yi Mi Ren³, Tamas Ungi¹, Parvin Mousavi¹, John F. Rudan², Doug McKay², Ami Wang³, Gabor Fichtinger¹

¹ School of Computing, ² Department of Surgery, ³ Department of Pathology, Queen's University, Kingston (Ontario), Canada

Introduction: Basal Cell Carcinoma (BCC) is the most common type of skin cancer worldwide. Incomplete tumor removal during the first surgery requires a second operation, leading to significant healthcare costs, impaired cosmetic outcome and patient distress. There is a clinical need for intraoperative evaluation of the resected tissue, providing direct feedback about the presence of any remaining tumor tissue in the patient. This study evaluates the clinical feasibility and accuracy of a novel surgical navigation system for skin cancer resection, based on real-time navigated mass spectrometry tissue analysis.

Methods: Rapid Evaporative Ionization Mass Spectrometry (REIMS) enables direct tissue characterization by analysis of cell-specific molecules present within surgical smoke, produced during standard electrocautery tissue resection. A tissue characterization model was built by acquiring REIMS spectra of BCC, healthy skin, and fat from *ex vivo* skin cancer specimens. This model was used for intraoperative tissue characterization during navigated skin cancer surgery. Surgical navigation was enabled by optical tracking (OptiTrack Duo, Fig. 1A) and real-time visualization of the cautery with respect to a previously contoured optimal resection volume (Fig. 1B, yellow). Standard skin cancer resection was performed, but the surgical smoke was aspirated into a mass spectrometer and directly analyzed with REIMS. Immediate feedback was provided by annotating classified BCC at the real-time position of the cautery (Fig. 1B, red dot), representing remaining tumor tissue. Primary endpoints were safety and feasibility of the navigation system, as well as the tissue classification accuracy for both *ex vivo* and intraoperative surgery.

Results: A total of 54 fresh excision specimens were used to build the *ex vivo* tissue characterization model of BCC, normal skin, and fat, which had an average accuracy of 92%. This model was used for intraoperative tissue classifications during 5 navigated skin cancer surgeries, without breach of sterility. Position data of the cautery could be tracked throughout the entire procedure in 3 patients. Total procedure time for the 3 tracked surgeries, including prior delineation of the optimal resection volume, was 2.0 ± 0.4 min. Use of the *ex vivo* model in the intraoperative cases resulted in an average tissue classification accuracy of $< 50\%$.

Conclusions: REIMS-Navigated skin cancer surgery has the potential to detect remaining tumor tissue intraoperatively, and guide the surgeon towards complete tumor resection. Future work will focus on a larger prospective study and improving diagnostic accuracy of the BCC characterization model.

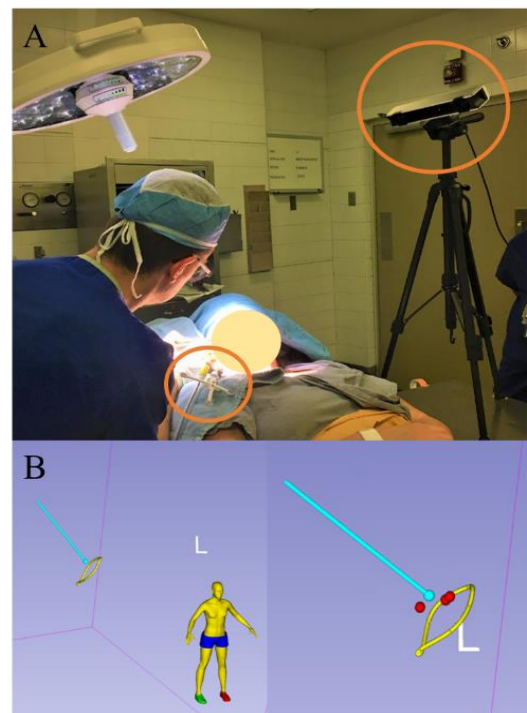


Fig. 1. A: The surgical knife was tracked using optical navigation (encircled in orange). **B:** REIMS-characterized BCC tissue was represented with red spheres, with respect to the pre-defined resection volume (yellow) and the real-time cautery position (blue).

Using computer vision sensing technologies for anterior cruciate ligament injury screening.Benjamin Dourthe¹, Megan Brenkel^{1,2}, David Wasserstein^{1,3}, Karl Zabjek³, Tyson Beach³, Tyler Saumur³, Steven Mark Hirsch³, Cari Whyne^{1,3}, Michael Hardisty^{1,3}¹Sunnybrook Health Sciences Centre, ²University of Ottawa, ³University of Toronto*benjamin.dourthe@gmail.com*

INTRODUCTION: Anterior cruciate ligament (ACL) injuries represent a significant burden on the healthcare system with 100,000-250,000 cases reported each year in the United States alone¹. Reports have shown that most ACL injuries result from noncontact mechanisms occurring during sports requiring cutting and jumping movements². Neuromuscular training programs have been shown to decrease incidence however low compliance rates have limited their effectiveness. A screening tool that is able to identify specific individuals at highest risk of ACL injury could inform targets for injury prevention and may increase compliance by motivating individuals who are identified to actively engage in prevention measures. ACL injury risk and return to sport readiness has been associated with features of the biomechanics of knee control, including increased knee abduction angle and/or reduced hip and knee flexion angles during a drop vertical jump (DVJ) and hop test performance³⁻⁶. Unfortunately, current methods to assess biomechanical features are onerous, lengthy (~1-2hrs) and use costly lab-installed marker-based multi-camera systems (i.e. Vicon, Optitrack) requiring expert users, available only in large centers. These protocols are not feasible for routine use in the field or clinic. To address this issue, this investigation compared a low-cost portable marker-less computer-vision based technology (Microsoft Kinect V2) to an established multi-camera marker-based Vicon system in terms of utility for ACL injury risk assessment.

METHODS: Twenty-five young (17-23yo) varsity athletes performed a series of DVJ and single-legged hop (SLH) tests, during which the kinematics of their lower extremities (hips and knees) was simultaneously recorded by a multi-camera Vicon system and a 3D Microsoft Kinect camera. Vicon data were processed in Visual 3D, where hips and knees flexion and abduction angles were calculated using an (y-x-z) Cardan angle sequence (y: medio-lateral, x: antero-posterior, z: vertical). Kinect data were processed using the Injury Fortune Teller (IFT) 2.0, a custom-built software that quantifies biomechanical features based on the kinematic data from the 3D camera, it calculates knee angles by projecting into estimates of physiologic planes of interest (coronal or sagittal). The 3D trajectories of hip, knee and ankle joint centers, as well as the evolution of hip and knee angles were compared in the time domain using dynamic time wrapping. Intra-class correlation coefficients (ICC) (two-way, mean, consistency) was used to assess agreement between Vicon and Kinect based calculations of peak joint angles and performance variables (maximal distance and time to reach 2.5 meters during SLH tests).

RESULTS: Good to excellent agreement was found between Kinect and Vicon for peak hip (ICC = 0.73, $p < 0.0001$) and knee (ICC = 0.93, $p < 0.0001$) flexion angles, as well as for maximal distance during SLH test (ICC = 0.97, $p < 0.0001$). The time series resulting from the calculation of hip and knee joint angles showed poor to moderate agreement between technologies ($0.26 < R^2 < 0.45$). Moderate agreement was found between Kinect and Vicon when comparing hip and knee joint centers trajectories along the antero-posterior and medio-lateral directions ($0.49 < R^2 < 0.61$). Poor agreement was found for the ankle joint centers trajectories ($0.26 < R^2 < 0.41$), the peak knee abduction angle (ICC ~ 0, $p > 0.5$) and the time to reach 2.5 meters during SLH test (ICC = 0.40, $p < 0.05$). Kinect slightly under-estimated the hip and knee flexion angles, and slightly over-estimated the knee abduction angle.

CONCLUSIONS: Kinect based estimates of peak hip and knee flexion angles during standardized tasks were sufficiently accurate, which is a critical feature for the development of a portable ACL injury screening tool. The poor agreement in knee abduction angle calculations can be explained by two factors: 1) the Kinect only tracks joint centres, not allowing for direct calculation of local 3D transformations, therefore requiring surrogate approaches to estimate local joint orientation; 2) the abduction angles are low magnitude and depend on the ankle joint, which has poor tracking agreement between the Vicon and Kinect. Future work will focus on machine learning based enhancement of abduction angle estimation, potentially enabling the design of a cost-effective, portable and accessible system to assess ACL injury risk in young athletes.

REFERENCES: ¹Hewett et al., *J. Orthop. Res.* (2016) ²Griffin et al., *J. Am. Acad. Orthop. Surg.* (2001) ³Hewett et al., *Am. J. Sports. Med.* (2005) ⁴Leppänen et al., *Orthop. J. Sports. Med.* (2017) ⁵Markolf et al., *J. Orthop. Res.* (1995) ⁶Blackburn et al., *Clin. Biomech.* (2008)

ACKNOWLEDGEMENTS: NSERC, OCE, Curv Labs, SRI Summer Studentship Award

Assessment of usability of real-time needle tracking with a virtual reality display

Saleh Choueib¹, Ciara McGarry¹, Melanie Jaeger², Tamas Ungi¹, Natasja Janssen¹,
Gabor Fichtinger¹, Lindsey Patterson²

Laboratory for Percutaneous Surgery, School of Computing, Queen's University, Kingston, Canada
Department of Anesthesiology and Perioperative Medicine, School of Medicine, Queen's University,
Kingston, Canada

INTRODUCTION: Lumbar puncture (LP) is a procedure in which a needle is inserted typically between the L3 and L4 vertebrae. This procedure requires a high level of precision in order to successfully puncture spinal canal, which can be difficult for inexperienced physicians. Current techniques, such as the hand palpation technique, rely on physician's ability to visualize the anatomy by distinguishing anatomical landmarks by touch. Furthermore, new students are taught LP skills through the apprenticeship method, in which they execute the procedure on a live patient under the supervision of an experienced physician. This method of teaching is disadvantageous and potentially harmful to the patient. To address this issue, training simulators for LP skills have become more widely used. These simulators typically consist of a human torso model and a spine model insert. However, both the simulators and the apprenticeship method of training lack visual feedback and skill metrics. Our aim is to integrate virtual reality (VR), a technology that immerses users in a virtual and intractable environment, into the LP training workflow. By doing this, we can provide both metrics and visual feedback. **METHODS:** The complete system consists of the following: 1. a VR-capable laptop; 2. an Ascension EM tracker; 3. Commercially available VR headset; 4. Lumbar puncture trainer with soft tissue insert; 5. 3D Slicer and PLUS toolkit software [1]. Using 3D Slicer in conjunction with the SlicerIGT [1] and PLUS toolkit extensions, we can translate tracked data into 3D Slicer to be visualized into a 3D environment. The needle's positional data will be tracked using the 3D trackSTAR (Northern Digital Inc., Waterloo, ON, Canada), which uses an electromagnetic (EM) field to triangulate the position of the EM sensor embedded in the needle. We will track the needle relative to the spine model insert in the LP training simulator. The whole procedure can be recorded for playback within 3D Slicer. Using this complete system, we aim to assess the feasibility of this system to teach translatable LP skills. To assess our system and the effect of using VR, we randomly split a group of medical school students into control and test groups. Each group completed 3 insertions sequentially. The test group was asked to review the playback of their insertions in virtual reality before the next insertion; while the control group reviewed the final position of the needle (relative to the spine model) on a computer monitor. After completion of the three insertions, participants completed a System

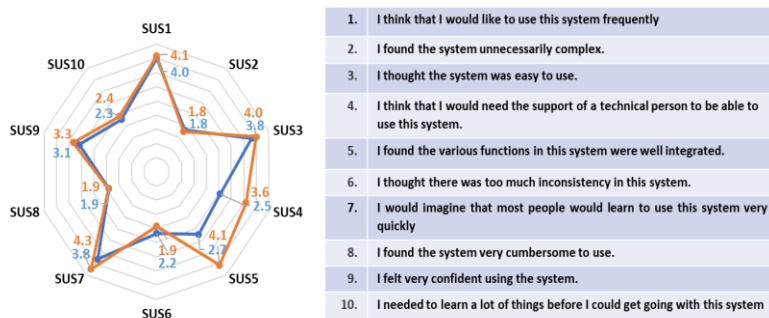


Figure 1: The mean scores (1 to 5) for the 10 System Usability Survey, where 5 is strongly agree and 1 is strongly disagree. Orange values represent VR group, blue values represent Control group

Usability Survey.

RESULTS: The mean normalized System Usability Survey score from the twenty-three medical school participants was 68.7, responses for each question can be seen in Figure 3. The normalized average score was 70.4 in the VR group vs. 66.8 in the Control group, indicating a favorable trend towards VR. The individual scores of each question indicate that the visual feedback provided by the system is favorable amongst trainees. **CONCLUSION:** We developed a workflow for LP trainers which added

visual feedback, both via VR and on a conventional monitor. The system increased confidence levels of medical students learning LP. **ACKNOWLEDGMENTS:** This work was funded by the Southeastern Ontario Academic Medical Association (SEAMO), Educational Innovation and Research Fund. Gabor Fichtinger is supported as a Canada Research Chair in Computer-Integrated Surgery. This work was funded, in part, by NIH/NIBIB and NIH/NIGMS (via grant 1R01EB021396-01A1). **REFERENCES:** [1] Ungi T, et al. Open-source platforms for navigated image-guided interventions. *Med Image Anal.* Oct;33:181-6, 2006

Deriving blood flow directions from neurosurgical videos using deep learning and dynamic linear modelsR. Vassallo*^{1,2}, A.J. McLeod⁴, S.P. Lownie³, H. Fukuda⁵, H. Kasuya⁶, B.W.Y. Lo⁷, T. Peters^{1,2}, Y. Xiao¹

¹Robarts Research Institute, ²School of Biomedical Engineering, ³Department of Clinical Neurological Sciences, Western University, London, Canada; ⁴Intuitive Surgical, Sunnyvale, USA; ⁵Department of Neurosurgery, Kochi University Hospital, Kochi, Japan; ⁶Department of Neurosurgery, Tokyo Women's Medical University Medical Centre East, Tokyo, Japan; ⁷Department of Neurosurgery and Neurointensive Care, Lenox Hill Hospital, New York City, USA

Introduction: Neurovascular surgery involves the repair of diseased blood vessels associated with the brain and spine. This includes arteriovenous malformations (AVM) resection, aneurysm repair, and carotid endarterectomy (CEA), among others. Surgical microscopes are routinely used across neurosurgery in general, providing convenient access to videos of surgical sites. In this type of surgery, it is crucial to correctly identify the direction of blood flow in vessels feeding and draining the diseased region. However, it is virtually impossible to differentiate these with visual inspection alone [1]. The misjudgment may contribute to over 7% of AVM surgeries having complications that result in permanent neurological deficits or death [2]. Current standard practice highlights blood flow by injecting fluorescent dye observable through special surgical microscopes, but this fails to provide continuous hemodynamic updates and further complicates the surgical workflow. Additionally, this injected dye adds cost and may have adverse effects on patients' health (e.g., allergic reaction). Other solutions using imaging (e.g., ultrasound or surgical augmented-reality) have been proposed, but may risk rupturing fragile vessels or suffer from inaccurate real-time vessel identification. Therefore, a new contactless and robust method with minimal workflow interruption is desired.

Methods: For preliminary validation, 5-10 second videos were obtained retrospectively from 3 types of neurovascular surgeries: AVM resection, aneurysm repair, and carotid endarterectomy. The operating surgeon in each case documented which direction the blood was flowing in specific vessels, creating the ground truths. These videos underwent deep-learning-based motion attenuation [3] with a pre-trained model to mitigate physiological motions, and dynamic linear modelling (DLM) was used to find the periodic changes in the vessel due to blood flow [4]. The phase of this cyclic component at various locations along the vessel is used to find the direction of blood flow (blood flows along the direction of decreasing phase). Then, an arrow indicating the flow direction is automatically overlaid onto the video frame. The operating surgeon of each case determined ground truth direction.

Results: In all cases considered in this preliminary validation, the direction found in this preliminary validation matched the ground truth. Our results are shown in **Fig. 1**.

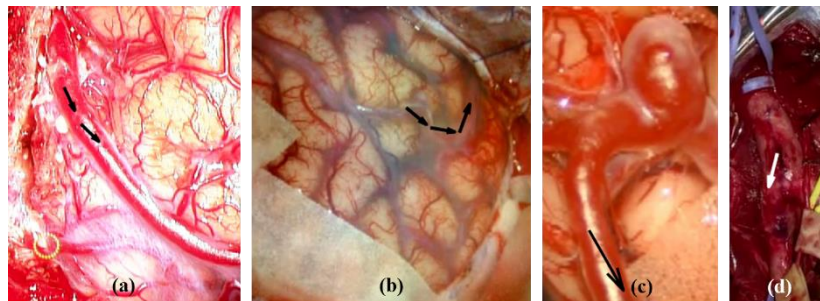


Figure 1: Annotated views of the correct blood flow directions found using our technique in retrospective analysis of: (a,b) AVM resection cases, (c) aneurysm repair, and (d) carotid endarterectomy (CEA)

Conclusions: Our preliminary results suggest that the proposed workflow can be used to identify the direction of flow in blood vessels during neurovascular surgery, without the limitations that are inherent to existing solutions. Namely, it is a contactless method that can provide intraoperative hemodynamic information to clinicians without the need for any extraneous contrast agents or additional imaging tools. This may lead to a safer and more informed surgical practice. Future studies with more clinical cases, simulation, and animal models will be employed to further validate this technique. We also plan to make this technique more resilient in the face of specular highlights, as we currently cannot determine flow direction in the presence of these saturated pixels (such as in **Fig. 1(a)**).

References: [1] R.F. Spetzler, *et al.*, *Comprehensive Management of Arteriovenous Malformations of the Brain and Spine*, 2015; [2] J. van Beijnum *et al.*, "Treatment of Brain Arteriovenous Malformations: A Systematic Review and Meta-analysis," *JAMA*, 2011; [3] T.-H. Oh *et al.*, "Learning-based Video Motion Magnification" presented at ECCV 2018; [4] A.J. McLeod, *et al.*, "Analysis of Periodicity in Video Sequences Through Dynamic Linear Modeling," presented at MICCAI 2017

Augmented reality simulator for ultrasound-guided percutaneous renal access

Yanyu Mu^{1,2}, David Hocking³, Zhan Tao (Peter) Wang⁴, Gregory J. Garvin³, Roy Eagleson^{1,5}, Terry M. Peters^{1,2}

¹School of Biomedical Engineering, Western University

²Robarts Research Institute

³Department of Medical Imaging, Western University

⁴Division of Urology, Western University

⁵Department of Electrical and Computer Engineering, Western University

Introduction: Traditional training for percutaneous renal access (PCA) relies on apprenticeship, which raises concerns about patient safety, limited training opportunities, and inconsistent quality of feedback. In this study, we proposed the development of a novel augmented reality (AR) simulator for ultrasound (US)-guided PCA and evaluated its validity and efficacy as a teaching tool.

Methods: Our simulator allows the user to practice PCA on a silicone phantom using a tracked needle and US probe emulator under the guidance of simulated US on a tablet screen (Fig 1). 24 Expert and 6 novice participants were recruited to evaluate the efficacy of our AR simulator. During evaluation, participants were asked to insert a needle to the center of the posterior calyx of the lower pole, under the simulated US guidance. Each needle access trajectory was recorded by the application then compared to the predefined optimal trajectory. In addition, 7 evaluation metrics were recorded for accessing user performance including: final distance to target, total path length, total time, overall adaptive distance, needle shaft visualization time, needle tip visualization time, and inside collecting system or not.

Results: Experts highly rated the realism and usefulness of our simulator on questionnaires, reflected by the average face validity score of 4.39 out of 5 and content validity score of 4.53 out of 5 on a Likert scale. Comparisons with a Mann-Whitney U test revealed significant differences ($p < 0.05$) in performances between the experts and novices on 6 out of 7 evaluation metrics, demonstrating strong construct validity. Furthermore, a paired T-test indicated significant performance improvements ($p < 0.05$) of the novices in both objective and subjective evaluation measurements after training with our simulator.

Conclusion: The AR simulator developed by our group for US-guided PCA demonstrated strong face, content, and construct validity indicating its effectiveness as a novel training tool.

Keywords Augmented reality, Percutaneous renal access, Training simulator, Ultrasound-guided needle insertion

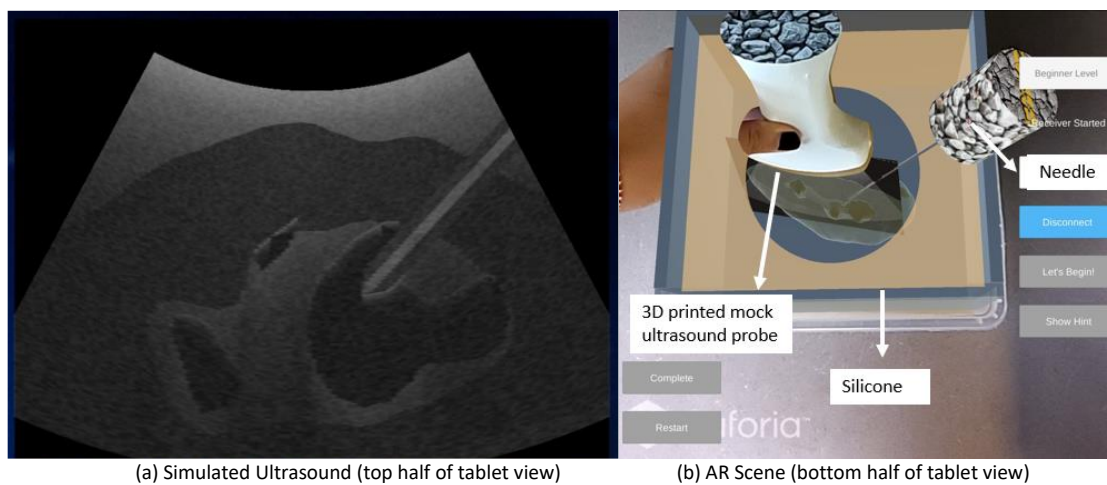
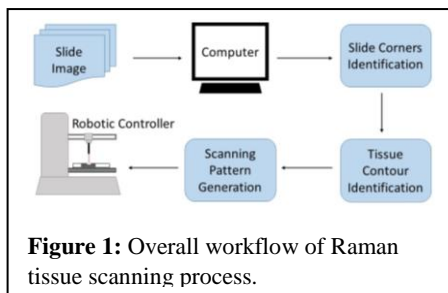


Fig. 1: AR visualization and system hardware

Using a biophotonic probe for robotic tissue scanning

Lauren Yates, Laura Connolly, Amoon Jamzad, Mark Asselin, Rachel Rubino, Scott Yam, Tamas Ungi, Andras Lasso, Christopher Nicol, Parvin Mousavi, Gabor Fichtinger
Queen's University, Kingston, Canada

INTRODUCTION: Raman Spectroscopy is a non-destructive method of optical analysis that offers promise for cancer diagnosis and imaging. Raman Spectroscopy uses a laser to detect the inelastic scattering of photons and resulting frequency shifts upon incident with a sample. Since these frequency shifts are unique for each molecular band, Raman spectra are chemical-specific [2]. By detecting the differences in Raman photon frequencies using a non-destructive laser, Raman Spectroscopy has the potential to be used for real time intraoperative margin assessment via noninvasive, high-speed tissue classification [2]. There is currently no documented database of Raman spectra of malignant tissue specimens for reference. In order for Raman Spectroscopy to be used in real-time tissue classification, a sophisticated machine learning algorithm is required to assist in the analysis. Training a machine learning algorithm will require a reliable and efficient automated scanning system to gather large quantities of data from numerous training cases. Collecting Raman spectra data takes approximately 1 second per point [3], meaning that conducting exhaustive scanning on one piece of tissue may take hours. We have developed an automated tissue scanning pattern method to improve the efficiency of a workflow designed for Raman spectra data collection on tissue samples (figure 1). The scanning pattern method works in conjunction with a mechanically controlled biophotonic tissue probe [1] to reduce the amount of non-tissue area scanned on a slide, thus reducing the time required for data collection.



METHODS: A camera mounted to a robotic controller modified by Connolly et al. [1] was used to take an image of a tissue slide. The corners of the tissue slides within the sample image were identified, and the size of the slide was calculated. The image was cropped to fit the size of the slide and the image was manipulated to identify the tissue contour. A grid set to fit around the size of the tissue was calculated and a grid scanning pattern was generated. A masked image of the tissue contour was used to create a scanning pattern containing only the tissue. The tissue scanning pattern points were transformed to the robot controller coordinate system and used for robotic tissue scanning. We validated the pattern by using

two different formalin-fixed paraffin-preserved pork liver tissue samples prepped for Raman spectroscopy. The tissue was scanned using the generated scanning pattern and compared to the effectiveness of a region of interest grid scan at the same resolution. The area coverage of the grid scanning pattern was compared to a convex hull area calculation of the tissue samples.

RESULTS: The average scanning time for the tissue scanning pattern and region of interest scanning was 1 minute and 46 seconds, and 6 minutes and 44 seconds respectively. The tissue scanning pattern reduced scanning time by 4 minutes and 58 seconds. The generated tissue scanning pattern had an average tissue area coverage of 96.83%, due to the holes in the tissue samples that the convex hull did not account for.

CONCLUSIONS: This scanning system reduced the amount of time spent collecting samples while covering the tissue area. This method makes our data collection workflow more efficient for optical tissue data collection.

ACKNOWLEDGEMENTS: L. Yates was supported by an Undergraduate Student Research Award from the Natural Sciences and Engineering Research Council of Canada (NSERC). G. Fichtinger is supported as a Canada Research Chair. This work was funded, in part, by NIH/NIBIB and NIH/NIGMS (via grant 1R01EB021396-01A1 – Slicer+PLUS: Point-of-Care Ultrasound) and by CANARIE's Research Software Program.

REFERENCES:

- [1] L. Connolly, T. Ungi, A. Lasso, T. Vaughn, M. Asselin, P. Mousavi, S. Yam, G. Fichtinger, "Mechanically controlled spectroscopic imaging for tissue classification," Proc. SPIE 10951, *Medical Imaging 2019: Image-Guided Procedures, Robotic Interventions, and Modeling*, pp. 109512E, 2019.
- [2] A. S. Haka, K. E. Shafer-Peltier, M. Fitzmaurice, J. Crowe, R. R. Dasari, and M. S. Feld, "Diagnosing breast cancer by using Raman spectroscopy," *PNAS*, 102(35), pp. 12371-12376, 2005.
- [3] J. T. Motz, S. J. Gandhi, O. R. Scepanovic, A. S. Haka, J. R. Kramer Jr., R. R. Dasari, M. S. Feld, "Real-time Raman system for *in vivo* disease diagnosis," *J. Biomed. Opt.*, 10(30), pp. 031113, 2007.

Creation and evaluation of virtual nephrolithotomy training models

Catherine O. Wu^{1,2}, Kyle Sunderland¹, Mihail Filippov², Ben Sainsbury², Gabor Fichtinger¹, Tamas Ungi¹

¹Laboratory for Percutaneous Surgery, School of Computing, Queen's University, Kingston, Canada,

²Marion Surgical, Toronto, Canada

INTRODUCTION: Percutaneous nephrolithotomy is the most common surgical treatment used to remove large renal stones. This type of endoscopic procedure requires considerable training for surgical skills and experience due to the complications that may arise from an inaccurate puncture into major renal vessels [1]. Although traditional physician-student relationships are the foundation of residency programs, recently, virtual reality (VR) surgical simulators have gained considerable interest [2].

Our study proposes a workflow to transform abdominal CT scans into low polygon 3D models that can provide haptic feedback and visualization for surgical simulation. To evaluate the workflow, we integrate the models into the K181 PCNL and Kidney Access Array by Marion Surgical¹ and measure the validity of the models through feedback from urological surgeons.

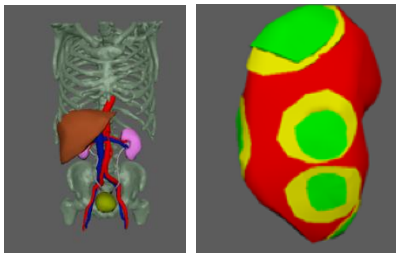


Figure 1: *Left.* Low polygon models of necessary abdominal organs and bones. *Right.* Needle entry zones displayed as the kidney surface.

METHODS: We segmented patient abdominal CTs into major organs and bones using the Segment Editor module of 3D Slicer [3]. Autodesk Maya modelling softwareⁱⁱ was used to produce low polygon models from the segmentations, using both automatic and manual decimation methods. We then created scoring metric models representing safe, warning, and danger zones for needle entry (Figure 1). The models were integrated into the system with haptic feedback and the simulator was tested by two urological surgeons (Figure 2).

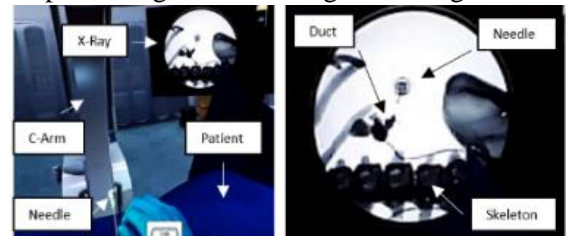


Figure 2: *Left.* Virtual surgical environment. *Right.* Close-up on fluoroscopy X-Ray.

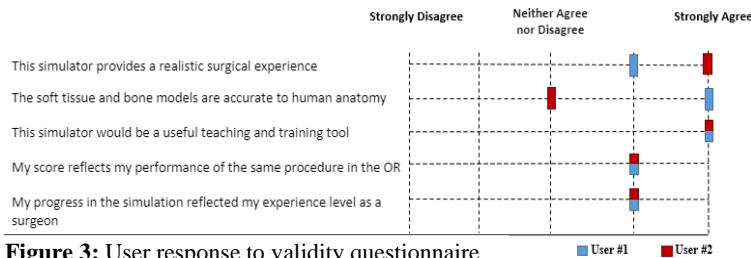


Figure 3: User response to validity questionnaire

strongly agree (Figure 3). They rated that the simulator was a level 3 and above in visual realism, and level 4 and above for training usability, identification of surgical experience and reflection of operating room performance.

CONCLUSION: The integration of the models into the simulator and the results of the questionnaire demonstrated the creation of an effective workflow for generating virtual models from patient data using 3D Slicer.

ACKNOWLEDGEMENTS: G. Fichtinger is supported as a Canada Research Chair. This work was funded, in part, by NIH/NIBIB and NIH/NIGMS (via grant 1R01EB021396-01A1 - Slicer+PLUS: Point-of-Care Ultrasound) and by CANARIE's Research Software Program.

REFERENCES:

- [1] Srivastava A, et al. "Vascular complications after percutaneous nephrolithotomy: are there any predictive factors?" *Urology* 66(1), 38-40 (2005).
- [2] Seymour NE, et al. Virtual reality training improves operating room performance: results of a randomized, double-blinded study. *Ann Surg* 236(4), 458-463 (2002).
- [3] Fedorov A, et al. 3D Slicer as an Image Computing Platform for the Quantitative Imaging Network. *Magn Reson Imaging*. 30(9), 1323-1341 (2012).

ⁱ <https://www.marionsurgical.com/>

ⁱⁱ <https://www.autodesk.ca/en/products/maya>

RF magnetic fields Interaction with the intracranial pressure sensor in a 64 MHz head-only RF coil

Saghar Batebi, Kieffer J Davieau, William B Handler, and Blaine Alexander Chronik

The xMR Labs, Physics and Astronomy, Western University, London, ON, Canada, Department of Medical Biophysics, Western University, London, ON, Canada

INTRODUCTION

The presence of implantable medical devices in patients exposed to magnetic resonance imaging RF radiation raises concerns related to MRI safety issues. Numerical simulation is an essential tool for complex situations with many different configurations as it allows the worst-case scenario to be determined in silico[1]. In this study, we evaluated a simplified intracranial pressure sensor. We performed the simulations in 1.5 T head-only RF coil to evaluate the Peak spatial-average specific absorption rate (PsSAR which is maximum average specific absorption rate within a constant-mass cubes) of 0.1 g mass to find the worst case.

METHOD

The RF coil was modeled as a circularly polarized shielded head-only 64 MHz cylindrical RF coil, with 16 equally spaced rungs, radius of 145 mm, and length of 384 mm. The diameter of shield was 400 mm with a length of 500 mm. The current in the rungs was set such that B1 in the center volume of the coil would be 1 μ T when no device was present. We conducted the simulations with an anatomical head model from the Virtual Population member Duke which consists in an anatomically realistic 3D model of human body based on MRI data[2]. The device was simply modeled as a 0.75 mm diameter that had a total fixed length of 200 mm with the length of 10 mm, 65 and 120 mm within the brain while the remainder of the device implanted under the skin, outside the skull, with 40 mm extruding out of the skin. The conductive wires of the implants were modeled as perfect electrical conductors and the insulation was modeled as an insulator (insulation thickness of 0.5 mm, exposed end of 2 mm, $\epsilon_r = 3$ and $\sigma = 0$ S/m). Materials regarding Duke model are automatically inserted, and the properties of the tissues adjusted to the selected frequency.

RESULTS

Figure 1A Spatial Average SAR over 0.1 g of tissue for different length of the lead along YZ slice at the location of the wire. Figure 1B shows 0.1 g PsSAR of tissue at three different regions(tip of the wire in the brain, wire location under the skin, and the wire bend location). As expected, the heating is highest when the amount of the wire within the brain is minimized.

CONCLUSION

In this study, the PsSAR for intracranial pressure sensor in different configurations in human body model was numerically evaluated, to find the “worst case” scenario at 64 MHz MRI in Sim4Life platform. For the devices simulated in this study, it is found that the heating is highest when the amount of the device within the brain is minimized. This study shows that modeling of the ICP implant path has a huge impact on the SAR induced at the tissue surrounding the implant. Expansion of this study to other wire configurations and also to 128 MHz head-only RF coils is also an avenue for future work.

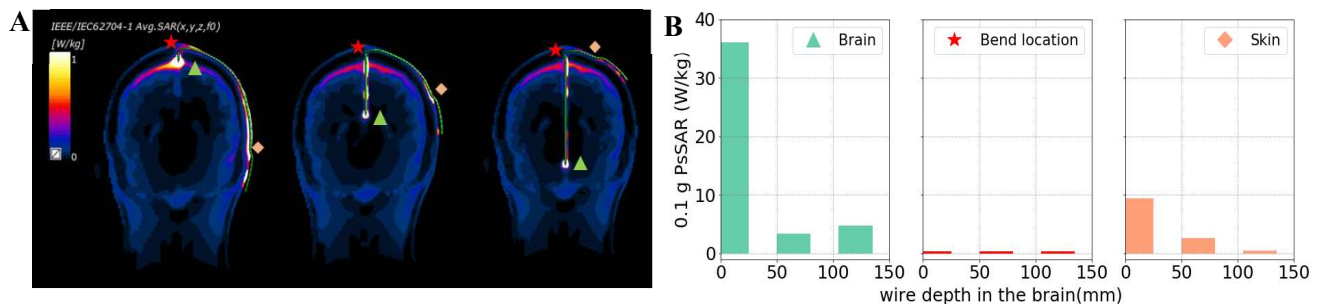


Figure 1. A: 0.1 g PsSAR along YZ slice. B: 0.1 g PsSAR at the tip of the wire in the brain, wire bend location and under the skin.

REFERENCES

- [1] J. Kabil, L. Belguerras, S. Trattinig, C. Pasquier, J. Felblinger, and A. Missoffe, “A Review of Numerical Simulation and Analytical Modeling for Medical Devices Safety in MRI,” *Yearb. Med. Inform.*, no. 1, pp. 152–158, Nov. 2016.
- [2] “OVERVIEW » IT’IS Foundation.” [Online]. Available: <https://itis.swiss/virtual-population/virtual-population/overview/>.

Image-guidance Accuracy of a 3D Ultrasound System for Interventional Liver Cancer TherapiesDerek J Gillies^{1,2}, Jeffery Bax², Kevin Barker², Lori Gardi², David Tessier², Nirmal Kakani³, Aaron Fenster^{1,2}¹Department of Medical Biophysics, ²Robarts Research Institute, Western University, London, Ontario, Canada;³Department of Radiology, Manchester Royal Infirmary, Manchester, UK;

Introduction: Minimally invasive focal ablation of liver cancer is an alternative technique to conventional methods for early-stage tumours. Sufficient therapy relies on the accurate placement of ablation applicators at their intended target locations but reported local cancer recurrence rates show this is not always achieved.¹ These minimally invasive techniques typically use CT images for planning and two-dimensional (2D) ultrasound (US) for intraoperative image-guidance of applicator insertion(s), but work into CT and MRI guidance have been proposed to improve verification of applicator placements.² To avoid limiting issues like cost, clinical workflow, and additional ionizing radiation, we have previously presented on a novel intraoperative three-dimensional (3D) US imaging and guidance system to improve therapy applicator placement accuracy. This work will present a mock image-guidance phantom procedure to assess expected clinical targeting errors.

Methods: A three-motor mover was designed to provide geometrically adjustable linear, tilt, and combined hybrid geometries for 3D US acquisition that was repeatable with consistent image spacing. This mover was supported by a counterbalanced mechanically encoded tracking system mounted to a cart to increase usability and portability. A custom 3D-printed applicator guide was manufactured to attach to a C5-1 US probe (iU22, Philips) and enabled a guided insertion workflow. Fabrication of a tissue mimicking agar phantom with embedded agar and tungsten spheres provided a homogeneous imaging volume to ease applicator visualization with US and visible structures for image registration with CT. The mock image-guidance procedure consisted of: 3D US image acquisition (tilt $n=7$, hybrid $n=8$), digital target selection, motorized image plane navigation, applicator insertion, 3D US image acquisition for verification, and cone-beam CT acquisition (O-arm, Medtronic) for an external image validation. Evaluation of applicator placement accuracy was performed by performing fiducial registration between the verification 3D US and the CT image, followed by manual selection of the visible applicator tip in both modalities. Error was assessed by computing Euclidean distances for 3D US and CT tip location agreement, 3D US tip to target distance, and CT tip to target distance.

Results: Mean \pm SD fiducial registration error between 3D US and CT was evaluated to be 1.02 ± 0.33 mm. Overall 3D US and CT tip location agreement, 3D US tip to target distance, and CT tip to target distance was 1.32 ± 0.69 mm, 4.44 ± 3.08 mm, 4.04 ± 2.79 mm, respectively, showing good agreement and placement accuracy.

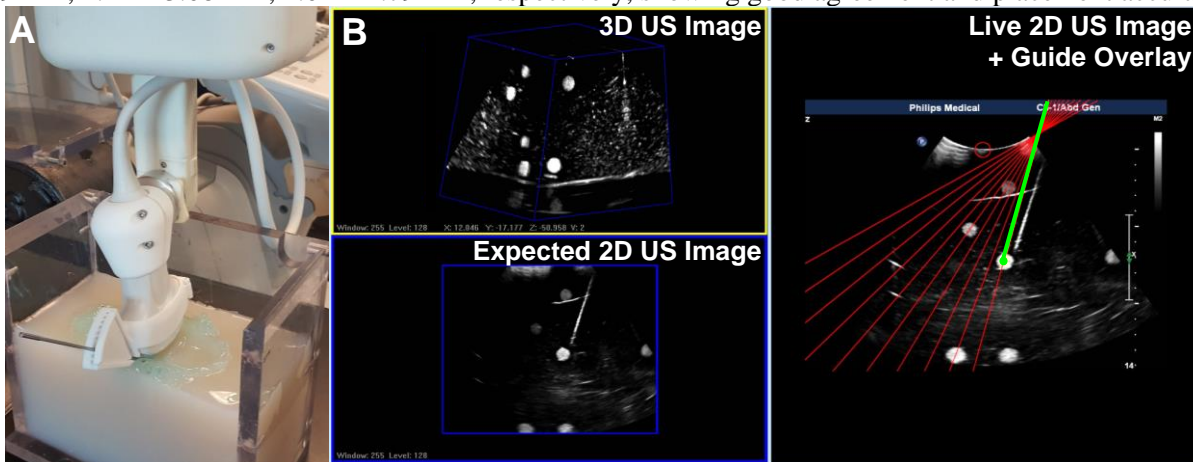


Figure 1. (A) Experiment set-up with 3D-printed applicator guide, mechanical 3D US system, and phantom. (B) Image-guidance software to perform a targeted applicator insertion (green) using an applicator guide (red).

Conclusions: A mock phantom procedure was performed to demonstrate the overall targeting accuracy of our system to place applicators at embedded targets and evaluate the expected accuracy during clinical focal liver tumour ablation. Since the range of liver tumors diameters that are candidates for RF and microwave ablation are 3-5 cm, and typically a 5-10 mm ablation margin is used, we believe that our system's targeting accuracy is sufficient for clinical use. Future work is focused on performing a similar image-guidance experiment using a manual approach with the mechanically encoded tracking system and a clinical trial for applicator verification.

References: [1] Wong et al., *J. Clin. Oncol.* (2010); [2] Decadt et al., *Lancet. Oncol.* (2004);

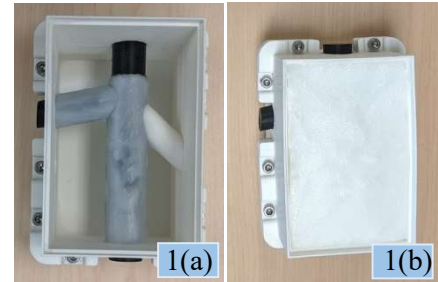
Fluoro-free, Ultrasound-based Navigation System for Cardiac Interventions

Hareem Nisar, John Moore, Terry Peters, and Elvis Chen
VASST Lab, Robarts Research Institute, Western University

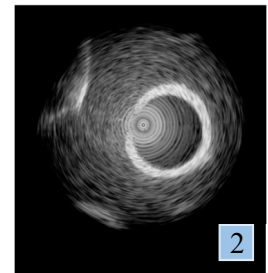
Introduction: Image-guided systems (IGS) have shown to improve the outcomes of percutaneous cardiac interventions by compensating for the absence of a direct line of sight with the anatomy and the tools. These interventions include two steps: 1) Navigation of tools through the vasculature and into the heart and 2) Positioning of tools at the target site to deliver therapy. Current standards include repeated fluoroscopy for navigation, and ultrasound, either transesophageal or intracardiac echocardiography (ICE), for positioning. X-ray navigation exposes the patient and staff to harmful radiation. Complex venous structures with bifurcations can further complicate navigation by introducing the risk of puncturing the veins.

ICE is often used to guide minimally invasive cardiac procedures by advancing the probe through the same vascular path as the guidewires and tools. Recently introduced Conavi Foresight™ ICE system generates unique, forward-looking, 2.5D conical ultrasound images. We aim to reduce fluoroscopy by introducing tracked guidewires and tracked Foresight™ ultrasound to facilitate the navigation and manipulation of the tools through the vasculature. In this preliminary phantom study, we will use a tracked Foresight™ ICE probe to generate a vascular roadmap to be used for tool navigation.

Method: Tracking of Conavi Foresight ICE is achieved by placing NDI Aurora electromagnetic tracking sensors on the probe, followed by calibration procedures. A realistic, hollow, and walled PVA phantom is prepared to simulate human inferior vena-cava in terms of shape and size. First, a heavily speckled PVA-gel is injected into a 1.5mm vessel wall plastic-mould which undergoes two freeze-thaw cycles. PVA vessel is then placed in a box mould (Fig 1a) with PVA-gel (with 0.05% w/w talc to introduce backscatter) on the outside to mimic surrounding soft tissue. The entire assembly is subjected to two more freeze-thaw cycles (Fig 1b). The phantom is imaged using the tracked ultrasound probe. Since the data is acquired using a frame-grabber, the 2.5D cone is recorded as a circular 2D projection. An additional step is required to convert the 2D images back to their correct 3D coordinates based on the imaging angle displayed on the console. We use temporal median filtering to remove background artefacts inherent to the ICE probe. We will use active contours to segment the lumen boundary, followed by the generation of the 3D vascular model by employing the tracking information from the sensor. For validation, the ultrasound generated model will be compared to the CT scan of the phantom.



Results: Preliminary phantom images (Fig 2) look promising and visually similar to those of an animal vasculature acquired using Foresight™ ICE. Temporal filtering adequately removes the background noise generated by the probe with a constraint that the window-level is kept constant. Lumen segmentation via active contours is under-way. As seen in the ICE image, some part of the vessel wall does not appear on the image and will have to be estimated; however, accuracy requirements are less strict for navigation.



Conclusion: The proposed surgical workflow introduces minimal changes to the existing methods while significantly reducing the use of fluoroscopy during navigation. An ultrasound-based roadmap, to be followed by a tracked guidewire, will potentially reduce the cognitive load of interventional cardiologists, decrease radiation exposure and improve on the safety of minimally invasive procedures.

Using multiple frame input U-net for automated segmentation of spinal ultrasound images

Victoria Wu, Tamas Ungi, Kyle Sunderland, Grace Pigeau, Abigail Schonewille,
Gabor Fichtinger

Laboratory for Percutaneous Surgery, School of Computing, Queen's University, Kingston, Canada

INTRODUCTION: Scoliosis, an excessive curvature of the spine, is diagnosed in approximately 2-3% of the population, mostly in children. One common method to reduce the need for vertebral fusion surgery is bracing of the spine. Effective bracing requires early referral, which is prevented due to the lack of a safe and affordable instrument for spinal curvature measurement. Currently, x-rays are used, but this exposes young children to harmful levels of radiation. Spinal ultrasound is a viable alternative to X-ray [1], but manual annotation of images is difficult. We propose using deep learning through a U-net neural network to generate automatic segmentations of the spine. We develop a variation of the U-net that takes consecutive images per individual input, as an enhancement over using single input images. This is based on the user looking back on previous ultrasound images to acquire general information about the anatomy.

METHODS: Data was collected from nine healthy volunteers, using tracked ultrasound. Images were manually segmented using the open source software 3D Slicer (www.slicer.org). In total, seven of the scans were used for training data, and the additional two scans were used for testing data. To accommodate for consecutive input images, the ultrasound images were exported along with previous images stacked to serve as input for a modified U-net. All the images were converted into numpy arrays for network input. Five separate series of numpy arrays were created based on the exported images, containing one to four preceding images, giving arrays that contained two to five channels in total. Resulting output segmentations were evaluated based on the percentage of true negative and true positive pixel predictions.

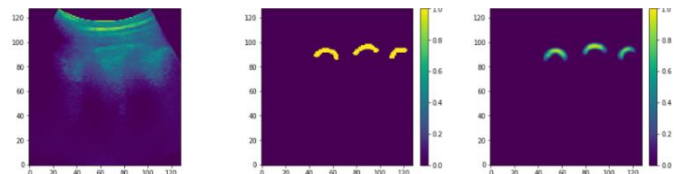


Figure 1: *Left.* Ultrasound image. *Middle.* Input segmentation. *Right.* Generated prediction

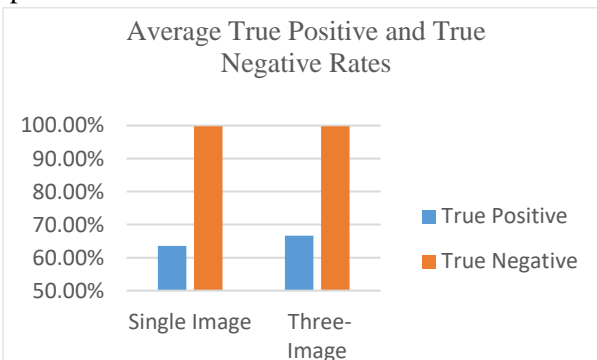


Figure 2: Comparison of average true positive (blue) and true negative (orange) rates between single image (left) and three-image input (right)

RESULTS: After comparing the single to five-image input arrays, the three-image input had the best performance in terms of true positive value. The single input and three-input images were then further tested. The single image input neural network had a true negative rate of 99.79%, and a true positive rate of 63.56%. The three-image input neural network had a true negative rate of 99.75%, and a true positive rate of 66.64%.

CONCLUSION: The three-image input network outperformed the single input network in terms of the true positive rate by 3.08%. This is a marginal improvement, suggesting that the capabilities of this methodology of examining consecutive images is limited. However, despite

the modest improvement, segmentations generated from the single input and three-input networks are both quite accurate, suggesting that U-net is a viable architecture for spine ultrasound segmentation.

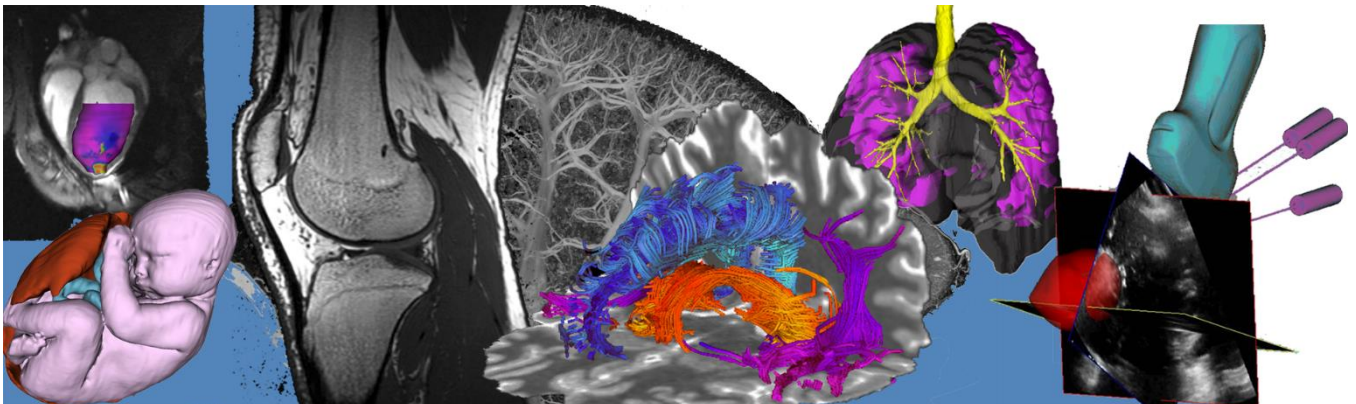
ACKNOWLEDGEMENTS: V. Wu is supported by CIHR Undergraduate Summer Studentship Award. G. Fichtinger is supported as a Canada Research Chair. This work was funded, in part, by NIH/NIBIB and NIH/NIGMS (via grant 1R01EB021396-01A1 - Slicer+PLUS: Point-of-Care Ultrasound) and by CANARIE's Research Software Program.

REFERENCES:

[1] Ungi T, King F, Kempston M, Keri Z, Lasso A, Mousavi P, Rudan J, Borschneck DP, Fichtinger G. "Spinal curvature measurement by tracked ultrasound snapshots," *Ultrasound Med Biol* 40(2), 447-54 (2014).

Poster Presentation Abstracts

Session 6: Neurology Imaging



A machine learning approach to detect early-stage Parkinson's disease

Dimuthu Hemachandra¹², Penny MacDonald³⁴, Ali R. Khan¹²

¹ School of Biomedical Engineering, University of Western Ontario, London, ON, N6A5C1, Canada

² Robarts Research Institute, University of Western Ontario, London, ON, N6A5B7, Canada

³ Brain and Mind Institute, University of Western Ontario, London, ON, N6A5B7, Canada

⁴ Department of Clinical Neurological Sciences, University of Western Ontario, London, ON, N6A5A5, Canada

Introduction:

Parkinson's disease (PD) is a progressive neurodegenerative disorder with motor and non-motor symptoms, affecting one in 50 people aged over 65, in industrialized countries such as Canada. PD has no cure or disease-modifying therapies due to the lack of diagnostic biomarkers. Recent advancements in neuroimaging techniques such as magnetic resonance imaging (MRI) have shown promise as biomarkers using both functional and structural brain data, however, most studies have had a small sample size and lack test-retest reliability, limiting their role in clinical diagnosis or staging of PD. Machine learning approaches to distinguish patients with PD from healthy controls have demonstrated high accuracy (over 90%), however, these studies were mostly limited to PD patients with more severe or late-stage PD, where the distinction is already obvious. It is of greater importance to develop a model that can distinguish PD patients at the earlier stages of disease as there can be a greater chance of impacting disease evolution and enacting potential disease-modifying therapies. To address this problem, we parcellated the striatum, the most affected brain region in PD, into sub-regions where the disease is likely to first affect patients. These parcellated sub-regions then were used to extract sensitive measures/features from MRI data, to be used in machine learning techniques to identify patients with PD at their early stages. By analyzing the importance of each feature within the classifier, we can localize the abnormalities that can lead us to potential biomarkers.

Methods:

3T Diffusion and T1 weighted (DW T1W) MRI data of 100 subjects with Parkinson's disease and 52 healthy control subjects were obtained from the Parkinson's Progression Markers Initiative (PPMI) database. For this analysis, we used only the baseline data and no PD or healthy subjects included in the analysis were treated with dopaminergic therapy. Probabilistic tractography was used to parcellate striatum into 14 sub-regions according to its connectivity to the cortex. Within these 14 regions, fiber integrity measures of fractional anisotropy (FA) and mean diffusivity (MD) were calculated and the connectivity, surface area and volume of these 14 sub-regions were also calculated. Diffeomorphic shape registration was used to compute striatal surface displacements relative to a canonical surface and averaged for each sub-region. A random forest classifier was trained with 80% of the data using the above information as features to distinguish PD subjects from healthy controls. The trained model was tested on the remaining 20% of the data. An independent dataset of 20 PD and 20 healthy controls (acquired as part of an ongoing local study) was also used as a separate validation data set. Moreover, the total UPDRS (Unified Parkinson's Disease Rating Scale) score which is an index of the severity of the disease progress was used to separate early PD patients from the database. Patients with a UPDRS score of 10 or less, have being categorized as early PD (n=26) and trained another RF classifier to distinguish early PD patients from health controls. Receiver operating characteristic (ROC) curves were used to evaluate the accuracies of the models.

Results:

The features extracted from the parcellated striatal sub-regions were able to distinguish Parkinson's patients from the healthy controls with over 94% accuracy. The classification accuracy with the validation data set was over 86%. The classification of early PD from health controls shows an accuracy over 90%. ROC curves revealed that the surface displacement and surface area features have the highest test accuracies in classifying the two groups.

Conclusions:

We were able to train a classifier using structural and anatomical data of the brain as features to distinguish early Parkinson's patients from healthy controls with over 90% accuracy. Surface displacement and surface area features show high performance in classifying the two groups, implying that, it can be a potential candidate for a reliable biomarker for Parkinson's disease.

Uncertainty estimation of automated white matter hyperintensity segmentation using a Bayesian 3D UNet

Mojiri Forooshani P¹, Ntiri E E¹, Holmes M¹, Adamo S¹, Ramirez J¹, Gao F¹, Ozzoude M¹, Scott C¹, Dowlatshahi D², Lawrence-Dewar JM³, Kwan D⁴, Marras C⁵, Lang T⁵, Bartha R⁶, Strother S⁷, Tardif J-C⁸, Symons S⁹, Masellis M¹⁰, Swartz R¹⁰, Moody A⁹, Black SE*^{1,10}, Goubran M*^{1,11}

¹Sunnybrook Research Institute; ²University of Ottawa; ³Thunder Bay Regional Health Sciences Center; ⁴York University; ⁵Toronto Western Hospital; ⁶Robarts Research Institute; ⁷Rotman Research Institute; ⁸Montreal Heart Institute; ⁹Department of Medical Imaging, University of Toronto; ¹⁰Department of Medicine (Neurology division), University of Toronto; ¹¹Department of Medical Biophysics, University of Toronto

Introduction: White matter hyperintensities (WMH) of presumed vascular origin are frequently observed on structural neuroimaging of elderly populations and are associated with cognitive decline and increased risk of dementia [1]. While many automated algorithms for WMH segmentation exist, they commonly produce suboptimal results in populations with vascular lesions or brain atrophy or require parameter tuning and are computationally expensive. In addition, the vast majority of algorithms do not generate an estimate of the segmentation confidence or quality. Here we propose a Bayesian 3D Convolutional Neural Network (CNN) that automatically segments WMH and estimates uncertainty of the segmentation output (**Fig. 1**).

Methods: Subjects with carotid stenosis from the Canadian Atherosclerosis Imaging Network (CAIN) and Cerebrovascular disease (CVD) +/- cognitive impairment patients from the Ontario Neurodegenerative Disease Research Initiative (ONDRI) multi-site studies were recruited (N=432). We implemented a 3D UNet [2] using Monte Carlo (MC) dropout [3] to improve segmentation accuracy and estimate the model uncertainty. At test-time, the average over MC samples is used as the final prediction and epistemic (model) uncertainty is then measured [4]. Our networks were validated against two state-of-the-art techniques: 1) BIANCA from the FSL suite [5] and 2) a winning model (UDundee) from the MICCAI WMH challenge [6], on a separate test set (N=159), including subjects from a third unseen study not part of the training dataset (MITNEC, N=53).

Results: Our Baseline (non-Bayesian) and Bayesian networks had the highest Dice coefficient similarity on the test set including MITNEC (0.84±0.1) by a significant margin and lowest Hausdorff distance (4.3±5.8mm) across tested methods (**Table 1**). The Dice similarity and Hausdorff distance on the previously unseen MITNEC study only were 0.89±0.05 and 2.31±2.33mm respectively. Our network was also the fastest among techniques, segmenting the WMH in less than a minute.

Conclusions: We present, HyperMapper, a robust and fast Bayesian CNN for accurate segmentation of WMH and estimation of model uncertainty for quality control. Future work will assess test-retest reliability and longitudinal progression of WMH.

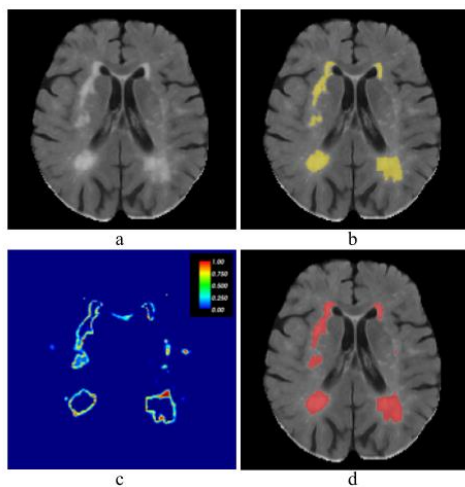


Fig 1. a) FLAIR, b) ground truth, c) model uncertainty, and d) our Bayesian model prediction.

References: [1] Debette, S. 2010. BMJ. [2] Goubran, M., et al. 2019. HBM. [3] Gal, Y. 2016. ICML. [4] Wang, G., et al. 2019. Neurocomputing. [5] Griffanti, L. 2016. Neuroimage. [6] Li, H. 2018. Neuroimage.

Table 1. Evaluation of WMH segmentation of different method: Dice coefficient (DSC), hausdorff distance (modified as 95th percentile) (H95), average volume difference (AVD%), sensitivity (Recall) and F-1 score for individual lesions.

Method	DSC (max=1)	H95 (mm) (min=0)	AVD (%) (min=0)	Recall (max=1)	F-1 (max=1)
BIANCA	0.60 (±0.22)	29.73 (±17.06)	108.54 (±215.73)	0.80 (±0.17)	0.20 (±0.15)
UDundee	0.53 (±0.23)	34.13 (±20.96)	39.58 (±42.06)	0.59 (±0.23)	0.44 (±0.17)
HyperMapper	0.84 (±0.09)	4.36 (±5.88)	16.09 (±13.90)	0.62 (±0.17)	0.69 (±0.12)

Fatty Acid Amide Hydrolase and Threat Related Amygdala Activity: A Combined Positron Emission Tomography and Magnetic Resonance Imaging Study

Duncan GJ Green^{1,7}, Jinhee Kim⁵, Stephen J Kish²⁻⁷, Rachel F Tyndale^{3,5-6}, Matthew N Hill⁸, Antonio P Strafella^{3-5,9}, Junchao Tong^{2,4}, Tina McCluskey^{2,4}, Duncan J. Westwood¹, Sylvain Houle^{3-5,7}, Nancy J. Lobaugh^{3,4,7,10}, Isabelle Boileau^{1,3-5,7}.

1) Addiction Imaging Research Group, **2)** Human Brain Lab, **3)** Campbell Family Mental Health Research Institute and **4)** Research Imaging Centre, Centre for Addiction and Mental Health, 250 College Street, Toronto, ON, Canada; **5)** Departments of Psychiatry, **6)** Pharmacology & Toxicology, **7)** Institute of Medical Sciences, University of Toronto, Toronto, Canada, **8)** Hotchkiss Brain Institute and Mathison Centre for Mental Health Research and Education, Departments of Cell Biology and Anatomy & Psychiatry, University of Calgary, Calgary, Canada **9)** Morton and Gloria Shulman Movement Disorder Unit and E.J. Safra Parkinson Disease Program, Toronto Western Hospital, UHN, University of Toronto **10)** Division of Neurology, Faculty of Medicine, University of Toronto

Introduction: Fatty acid amide hydrolase (FAAH) is the major catabolic enzyme for the endocannabinoid anandamide. A functional single nucleotide polymorphism (SNP) (rs324420, 385C/A) in FAAH has been linked with decreased self-reported anxiety during stress exposure and decreased amygdala responses to facial cues signaling threat. The goal of the current study was to test the hypothesis that FAAH levels measured in vivo in brain would correlate with amygdala reactivity to pictures of angry facial expressions.

Methods: 28 healthy subjects (mean age: 31, 16 females, 12 males) completed Positron Emission Tomography imaging with the FAAH probe [C-11]CURB as well as an fMRI session during exposure to angry facial expressions. Using a bilateral amygdala mask, we performed the correlation analysis between individual [C-11]CURB binding, a reliable measure of FAAH levels, and amygdala neuronal response to angry facial stimuli.

Results: BOLD signaling in bilateral amygdala was positively correlated with amygdala [C-11]CURB binding ($p < 0.05$, $t = 3.38$). We did not find that the BOLD signal was significantly different amongst FAAH SNP variants ($p > 0.05$). The relationship between BOLD and [C-11]CURB binding was stronger in females than in males.

Conclusion: Extending the literature linking genetic variability in FAAH (C385A) with amygdala response to threat, here we report that direct measurement of FAAH in brain correlates with amygdala reactivity to threat. Results from this preliminary study which needs to be replicated suggest that therapies aimed at lowering FAAH (e.g. by FAAH inhibitors) may modulate heightened amygdala response in disorders such as posttraumatic stress disorder.

Graph-based Representation of 3D Brain Volume for Alzheimer's Disease Analysis

Kauê T.N. Duarte,^{1,2} David G. Gobbi,^{2,3} Richard Frayne,^{2,4} Marco A.G. de Carvalho¹

¹ Computing Visual Laboratory, School of Technology, University of Campinas, Campinas, SP, Brazil

² Calgary Image Processing and Analysis Centre, Foothills Medical Centre, Calgary, AB, Canada

³ Radiology and Clinical Neurosciences, Hotchkiss Brain Institute, University of Calgary, Calgary, AB, Canada

⁴ Seaman Family MR Research Centre, Foothills Medical Centre, Calgary, AB, Canada

Introduction: Alzheimer's disease (AD) is a prevalent type of neurodegenerative disease in which both the function and structure of the brain are compromised. In functional imaging, mathematical graphs are a commonly used method for modeling and analysis. On the other hand, using graphs to understand structural imaging change is more challenging [1]; however, this approach potentially could find new patterns that are not apparent in more conventional spatial domain analyses. The distance between graphs across subjects is a measure of brain dissimilarity with smaller values corresponding to similar subjects. This study is focused on representing brain volume images as graphs in order to determine if it is possible to use these representations to infer diseased from non-diseased subjects.

Materials and Methods: This study was performed using T1-weighted magnetic resonance (MR) images from the Alzheimer's Disease Neuroimaging Initiative (ADNI) dataset. A set of 25 subjects, 5 from each ADNI-defined class (CN=control, EMCI=early MCI, MCI=mild cognitive impairment, LMCI=late MCI, and AD), was used to test the proposed processing pipeline. The approach was composed of five steps (Figure 1): 1) *Data Acquisition*: Volumetric MP-RAGE and IR-SPGR scans were selected from the ADNI dataset. 2) *Brain Segmentation*: Freesurfer software was used to segment the brain and parcellate it into 108 labelled, structural regions. 3) *Graph Representation*: A sparse-weighted graph was constructed for each image where the graph nodes represent the labelled anatomical regions and the edges were the relationships between adjacent regions calculated based on a voxel connectivity metric. 4) *Similarity Matrix Generation*: All graphs were compared pairwise to generate the similarity matrix. Graph distance was based on the number of edges and their weights. 5) *Graph-based Image Retrieval*: Finally, the similarity matrix was processed using a ranking algorithm that assists and, sometimes, recalculates the similarities among the graphs. To the best of our knowledge in the medical field, there is no published image retrieval approach that uses graph distance similarities. Here we report on the first four steps.

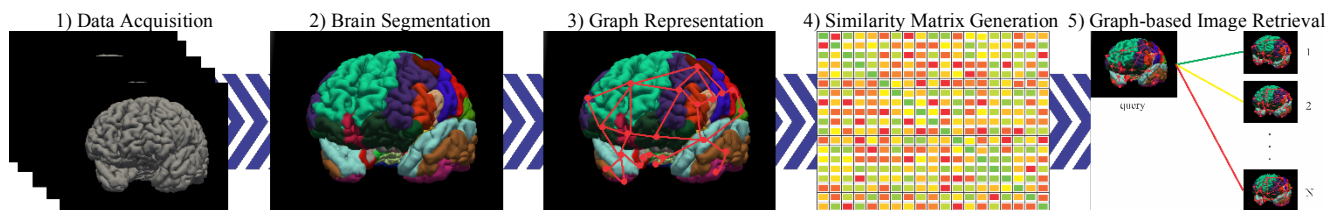


Figure 1: Pipeline of the proposed graph-based structural analysis approach.

Results: The graph representation of the brain was computed for the 25 subjects; each graph recorded the number of voxel transitions between regions. Figure 2 shows the similarity matrix obtained using the Pearson correlation. When comparing graphs from different classes, the correlation should be minimized. However, for this preliminary set of subjects, there was high inter-class correlation except for the AD and MCI groups.

Conclusions: Graphs represent medical images in a novel domain and potentially can play an important role in understanding connections between structural brain regions. Determination of ADNI classes in the spatial domain is challenging due to similarities among early stages of AD, but may be easier using graphs. This initial assessment illustrates the key concepts of graph representation. The next steps are to refine the graph generation and to apply a graph-based image retrieval approach to identify images that are most similar to an input image. Implementation of texture and shape descriptors can also assist in this approach.

Acknowledgements: Data used in preparation of this work were obtained from the Alzheimer's Disease Neuroimaging Initiative (ADNI) database (adni.loni.ucla.edu). As such, the investigators within the ADNI contributed to the design and implementation of ADNI and/or provided data but did not participate in analysis or writing of this report. The authors also thank CAPES (Brazil) and the CFI (Canada) for research support.

Reference: [1] Mijalkov M, Kakaei E, Pereira JB, Westman E, Volpe G, for the Alzheimer's Disease Neuroimaging Initiative. BRAPH: A graph theory software for the analysis of brain connectivity. *PLoS ONE* 2017; **12**: e0178798.

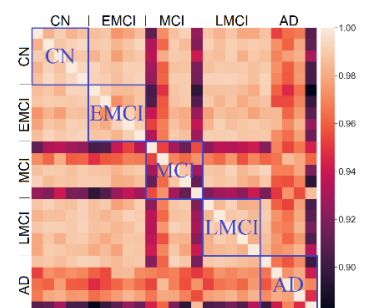


Figure 2: Similarity matrix Pearson correlation of the subjects. Each blue box represents the correlation among graphs of the same class.

Diffusion Kurtosis Imaging Goodness of Fit and Estimated Parameter Precision at Varying Gradient Strength in High Spatial Resolution 3T MRI

Loxlan W. Kasa^{a, b}, Terry Peters^{a, b, c, d}, Roy AM Haast^a, Ali R. Khan^{a, b, c}

^aRobarts Research Institute, London, Ontario, Canada, ^bSchool of Biomedical Engineering, Western University, London, Ontario, Canada, ^cDepartment of Medical Biophysics, Western University, London, Ontario, Canada, ^dDepartments of Medical Imaging, Western University, London, Ontario, Canada

Introduction: Diffusion tensor imaging (DTI) assumes unrestricted water diffusion in the brain, characterized by a Gaussian distribution. However, *in vivo*, DTI may be suboptimal when diffusion becomes non-Gaussian due to the complex intracellular and extracellular environment. Instead, diffusion kurtosis imaging (DKI), an extension to DTI, aims to provide a more comprehensive characterization of water diffusion properties^[1] but requires larger b-values and/or stronger gradients. The use of higher b-values reduces the signal-to-noise ratio and repeatability of the calculated parameters^[2]. Here, we explored the goodness of fit and precision of the DKI-derived metrics based on the number of b-values used in a test-retest scenario.

Methods: Test-retest diffusion-weighted imaging (DWI) data from 44 subjects were obtained from the Human Connectome Project (HCP) 3T MRI dataset. DWI acquisition parameters included TR/TE=5520/89.5 ms, and nominal isotropic voxel size=1.25 mm. A total of 288 images were acquired in each DWI dataset including 18 baseline images $b=5$ s/mm² and diffusion-weighted (DW) images at $b=(1000, 2000, 3000)$ s/mm². The acquired data were processed following HCP's 'minimum processing pipeline'^[3]. Two subsets of data were generated from the original three shells dataset. The second dataset included b-values=(1000, 2000) s/mm², while a third dataset included b-values=(1000, 3000) s/mm². Three separate fitting procedures were conducted, to minimize variability, each subject's DKI maps were co-registered and transformed to a custom build template. For white matter (WM) region-based analyses the JHU-ICBM-labels atlas was registered to the template. In addition, for grey matter (GM) analyses of the individual lobes, we mapped all the individual subject's co-registered maps onto the 'fsaverage' surface space using FreeSurfer's 'mri_vol2surf' function, sampling hereby between pial and WM-GM boundaries. Finally, we calculated the voxel- and vertex-wise within-subject coefficient of variation (CoV), a ratio of the standard deviation to the mean (across test-retest timepoints), to evaluate the precision of the parametric maps. In addition, to check for DKI fitting quality, we calculated the residuals, which is the difference of the modeled and measured signal for each dataset.

Results: Fig. 1a shows the mean within-subject CoV. In both WM (not shown) and GM, the original and third data-sets achieved the lowest CoVs (>0.5%) and (>3%) respectively compared to the second dataset. Fig. 1b shows the kurtosis tensor residuals calculated for each DWI image (averaged across all brain voxels). Two DWI images (encircled) have high residuals in the three datasets with the second dataset having the highest.

Conclusion: The ability of DKI to precisely quantify different tissue type has a direct correlation with the maximum

b-values used to acquire the underlying DWI data. Most importantly, our analyses show that the precision (i.e. CoV) and the goodness of fit of the third dataset is comparable to the original dataset. In contrast, the more common acquisition strategy (i.e., second dataset) is characterized by higher inter-scan variability and higher fitting residuals. These findings suggest that it is possible to achieve similar DKI precision as in three shells data with only two shells leading to shorter acquisition times and therefore, increased utility in a clinical setting.

References: [1]. Jensen, J. et al., *Magn. Reson. Med.* **53**, 1432–1440 (2005). [2]. Shahim, P., et al., *Sci. Rep.* **7**, (2017). [3]. Glasser, M. F. et al., *NeuroImage* **80**, 105–124 (2013).

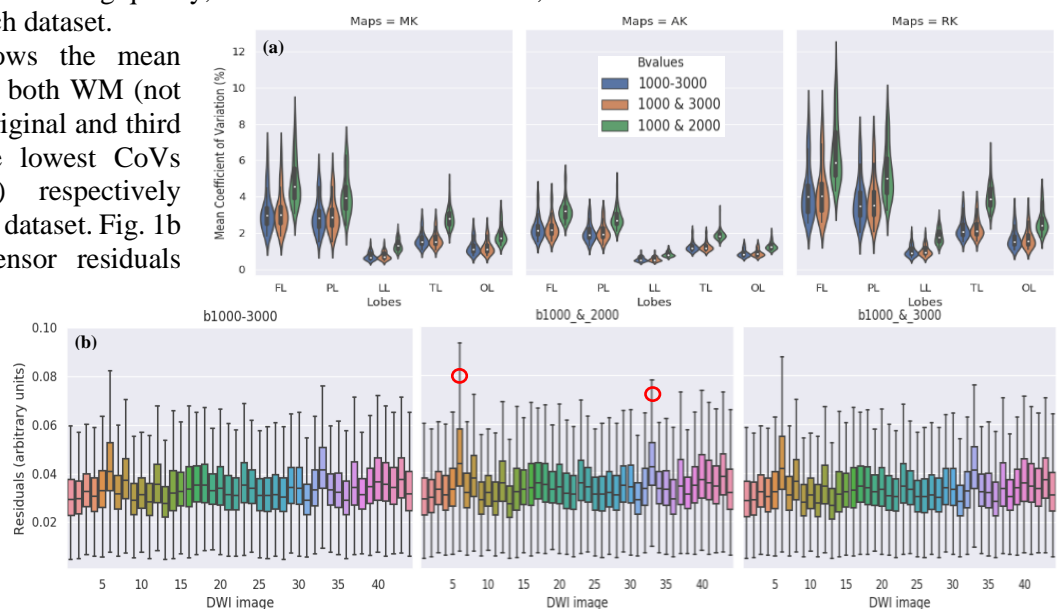


Fig 1. Mean within-subject CoV within the grey-matter (FL-Frontal Lobe, PL-Parietal Lobe, LL-Limbic Lobe, TL-Temporal Lobe and OL-Occipital Lobe) for MK-mean, AK-axial and RK-radial kurtosis (a). Residuals from DKI fitting for each DWI averaged across all brain voxels (b).

Endocannabinoid Metabolism in Posttraumatic Stress Disorder: Results from a Neuroimaging Study with the Novel Fatty Acid Amide Hydrolase Probe, [C-11] CURB

Erin Gaudette^{1,2,5}, Sarah Watling^{1,2,5}, Jerry Warsh¹⁻⁵, Tina McCluskey^{1,2}, Junchao Tong^{1,2}, Sylvain Houle¹⁻³, Pablo Rusjan^{1,2,4,5}, Shawn G. Rhind⁷, Richard Bazinet⁶, Rachel F. Tyndale^{2,3,4}, J. Don Richardson^{8,9}, Matt N. Hill¹⁰, Rakesh Jetly¹¹, Stephen Kish¹⁻⁵, Isabelle Boileau^{1-3,5}

¹Research Imaging Centre and ²Campbell Mental Health Research Institute, Centre for Addiction and Mental Health, Toronto, Ontario, Canada

³Department of Psychiatry, ⁴Pharmacology and Toxicology and ⁵Institute of Medical Sciences,

⁶Department of Nutritional Sciences, University of Toronto, Toronto, Ontario, Canada

⁷Defense Research and Development Canada, Toronto Research Centre, Toronto, Ontario, Canada

⁸Parkwood Operational Stress Injury Clinic, London, Ontario, Canada

⁹Department of Psychiatry, University of Western Ontario, London, Ontario, Canada

¹⁰Hotchkiss Brain Institute, University of Calgary, Calgary, Alberta, Canada

¹¹Directorate of Mental Health, Canadian Forces Health Services, Ottawa, ON, Canada.

Background: Preclinical studies suggest that levels of Fatty Acid Amide Hydrolase (FAAH)—an enzyme involved in signal regulation of the endocannabinoid system—may be elevated in post-traumatic stress disorder (PTSD). However, the status of the endocannabinoid system *in vivo* in PTSD patients remains unclear. Here we tested the hypothesis that brain levels of FAAH are increased in PTSD.

Methods: Healthy volunteers (n=29) and individuals with PTSD (n=15) completed a dynamic positron emission tomography scan using a 3D high resolution research tomograph (HRRT) brain tomograph (CPS/Siemens, Knoxville, TN, USA) following injection of the FAAH probe [C-11]CURB and an MRI scan (3T MR-750 scanner, General Electric, Milwaukee, WI, USA) to structurally guide region of interest (ROI) based analysis. Using a two-tissue compartment model with irreversible binding to the second compartment, the composite parameter λk_3 was used to quantify FAAH levels in each region of interest. PTSD participants completed the PTSD Symptom Scale (PSS) and the PTSD Checklist (PCL) to assess symptomatology and were genotyped for a FAAH polymorphism (rs324420) that affects [C-11]CURB binding (λk_3). Repeated measures ANOVA with FAAH genotype as a covariate was used to evaluate group differences in [C-11]CURB λk_3 across 11 cortical and subcortical brain ROIs. Pearson correlations were used to assess associations between symptom clusters and regional [C-11]CURB λk_3 in people with PTSD.

Results: We find no evidence for elevated [C-11]CURB λk_3 (-6.85%; p=0.275) in PTSD. We further find no evidence that symptom clusters and overall PSS and PCL scores are correlated with λk_3 (p's > 0.123).

Conclusion: These preliminary *in vivo* data do not support the preclinical finding of elevated brain FAAH in PTSD, but do not rule out FAAH as a therapeutic target in PTSD. This finding, if confirmed in a larger sample, may indicate that results from animal models do not translate to humans. Given that FAAH inhibitors have been proposed in this condition, further research should be done to confirm the status of FAAH in PTSD.

Investigating brain monoamine oxidase B status in alcohol use disorder with the positron emission tomography (PET) tracer [C-11]SL25.1188

Jennifer Truong^{1,5}, Laura M. Best^{1,5}, Tina McCluskey¹⁻², Junchao Tong^{1,2,4}, Pablo M. Rusjan^{1,2,5,6}, Jeffrey H. Meyer^{1,2,4,6}, Bernard Le Foll^{1,2,4,6}, Christian S. Hendershot^{2,4}, Dafna S. Rubin-Kahana^{3,4}, Jerry Warsh^{1,2,4,6}, Sylvain Houle^{1,2,4}, Stephen J. Kish^{1,2,4,6}, Isabelle Boileau^{1,2,4,6}

¹Research Imaging Centre and ²Campbell Mental Health Research Institute, and ³Translational Addiction Research Laboratory Centre for Addiction and Mental Health, Toronto, Ontario, Canada ⁴Department of Psychiatry, ⁵Pharmacology and Toxicology and ⁶Institute of Medical Sciences, University of Toronto, Toronto, Ontario, Canada

BACKGROUND: Alcohol use disorder (AUD) relapse rates are high and new therapeutic targets are required. MAO-B is an enzyme, partly found in astrocytes, that degrades monoamine neurotransmitters such as dopamine linked to addiction pathology. Based on limited post-mortem brain data, our objective was to establish whether MAO-B levels, as inferred from binding of a positron emission tomography (PET) radiotracer, [C-11]SL25.1188, will be above-normal in living brain in AUD.

METHODS: We examined [C-11]SL25.1188 total distribution volume (VT) in brains of treatment-seeking AUD participants (n=10) during early abstinence (2.7±2.6 days; mean±SD) and in age and gender-matched non-smoking controls (n=17). VT was measured in ten brain regions of interest (ROI) using a two-tissue compartment model. A RM-ANOVA (ROI X group) was conducted to measure statistical significance.

RESULTS: AUD was associated with modestly lower global brain [C-11]SL25.1188 VT (-17%; F(1,25)=5.04; p=0.03). However, the reduction was largely restricted to five (of ten) AUD subjects who were smokers (-36%; F(1,20)=24.9; p=0.00). There were no differences between non-smoking AUD and controls (+0.8%; F(1,20)=0.00, p=0.95). Pearson correlations between [C-11]SL25.1188 VT and a measure of withdrawal symptoms (CIWA) were significant in most brain regions (r = -0.65 – 0.88, 10 of 12 brain areas, p<0.05).

CONCLUSION: Our preliminary data suggests that brain levels of MAO-B might be normal in AUD in early abstinence. In line with earlier studies of cigarette smoking individuals using 1st generation MAO-B probes, ([C-11]L-deprenyl-D2) our data also suggest that brain MAO-B concentrations might be moderately to markedly decreased in tobacco smokers with AUD. Given that MAO-B metabolizes behaviourally important monoamines, our early finding suggest possibility that low brain MAO-B could influence behaviour in AUD smokers. Future recruitment of smoking controls may provide better insight into this potential therapeutic target in alcohol users. Supported by U.S. NIH NIAAA 026680.

Investigating Fatty Acid Amide Hydrolase Levels in Social Anxiety Disorder: A positron emission tomography (PET) study using [C-11]CURB

Mashal Ahmed^{1,6}, Rachel F. Tyndale³⁻⁵, Dafna S. Rubin-Kahana^{2,5}, Bernard Le Foll¹⁻⁶, Zafiris J. Daskalakis^{1,3-6}, Isabelle Boileau^{1,3,5-6,*}, Stefan Kloiber^{1,3,5-6,*}

¹Research Imaging Centre, ²Translational Addiction Research Laboratory, ³Campbell Family Mental Health Research Institute, Centre for Addiction and Mental Health, Toronto, Canada

⁴Department of Pharmacology and Toxicology, ⁵Department of Psychiatry, and ⁶Institute of Medical Science, University of Toronto, Toronto, Canada

*Supervising Authors: Isabelle Boileau, Stefan Kloiber

Introduction: Social anxiety disorder (SAD) is one of the most common psychiatric disorders worldwide. Preclinical studies suggest that anxiety-spectrum disorders may be associated with up-regulated activity of fatty acid amide hydrolase (FAAH), a major catabolic enzyme of the endocannabinoid system. However, there are no clinical in-vivo studies investigating FAAH status in SAD. This study aims to determine whether whole brain FAAH levels are elevated in individuals with SAD compared to healthy controls (HC) using positron emission tomography (PET) imaging with the FAAH radioligand, [C-11]CURB.

Methods: Ten participants with SAD completed one PET imaging scan with [C-11]CURB. A proton density-weighted magnetic resonance imaging (MRI) scan was acquired for brain region of interest (ROI) placement. [C-11]CURB λk_3 ($\lambda=K_1/k_2$), an index of brain FAAH levels, was calculated using an irreversible two-tissue compartment model. λk_3 was investigated in whole brain and 12 ROIs using a repeated-measures ANCOVA, controlling for FAAH genetic variability (rs324420 C>A). Severity of social anxiety was assessed using the Liebowitz Social Anxiety Scale (LSAS).

Results: Individuals with SAD (n=10; females=70%; age 26.10±6 years) demonstrated 2.95% elevated whole brain [C-11]CURB λk_3 (F(1,41)=4.42, p=0.04) compared to HC (n=34; females=59%; age 28.59±9 years). Pairwise comparisons showed that [C-11]CURB λk_3 in the SAD group was elevated in 4 of 12 ROIs (p<0.05). Moreover, a positive correlation of [C-11]CURB λk_3 and total LSAS score was detected in 9 of 12 ROIs (p<0.05).

Conclusion: In line with our hypothesis, our preliminary findings suggest that whole brain FAAH levels are elevated in individuals with SAD. Further analysis with a larger sample in our ongoing study is needed to consolidate these findings. This study may provide insight into the neurobiological mechanisms in SAD and inform development of FAAH-targeted interventions.

Comparative Radiosyntheses of [¹⁸F]FPEB for PET Imaging of mGluR5: Preliminary Imaging Studies in a Transgenic Mouse Model of Alzheimer's disease.

Cassia Varlow,^{a,b} Emily Murrell,^a Nickeisha A. Stephenson,^{a,c} and Neil Vasdev^{a,b,d*}

^aAzieli Centre for Neuro-Radiochemistry, Brain Health Imaging Centre, Centre for Addiction and Mental Health; ^bInstitute of Medical Science, University of Toronto; ^cDepartment of Chemistry, The University of West Indies at MONA, Jamaica; ^dDepartment of Psychiatry, University of Toronto.

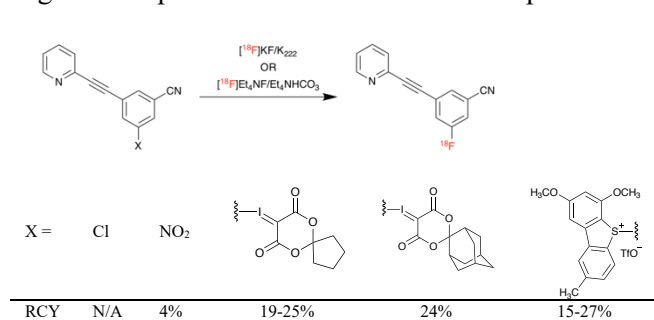
*neil.vasdev@utoronto.ca

Objectives: Metabotropic glutamate receptor subtype 5 (mGluR5) receptors are involved in regulation of the glutamatergic system, neurotransmitter release and memory processes. 3-[¹⁸F]fluoro-5-[(pyridin-3-yl)ethynyl] benzonitrile ([¹⁸F]FPEB) is a radiopharmaceutical selective for mGluR5, used in clinical positron emission tomography (PET) research to measure changes in regional distribution of this receptor.¹ Our objectives were to: 1) synthesize [¹⁸F]FPEB through the available precursors in the literature, and validate the optimum methodology for submission to Health Canada for human use at our site and 2) to investigate changes in mGluR5 uptake by preclinical PET imaging in a transgenic mouse model of Alzheimer's disease (AD) vs. controls.²⁻⁶

Methods: [¹⁸F]FPEB was prepared by a nucleophilic aromatic substitution reaction on an automated radiosynthesis unit (GE TRACERlabTM FX2N). Radiofluorination was conducted on precursors with varying leaving groups, to address the low radiochemical yield (RCY) that arises from labelling non-activated arenes. The different leaving groups included Cl, NO₂, spirocyclic iodonium ylide (SCIDY) with cyclopentyl (SPI5) and adamantyl (SPIAd) auxiliaries and a sulfonium salt precursor (Scheme 1). Preliminary PET/CT imaging studies were conducted in B6C3-Tg(APP^{swe},PSEN1^{de9})85Dbo/J (APP/PS1) mice, and data were compared with age-matched wild-type (WT) B6C3F1/J control mice (Fig. 1).

Results: The Cl precursor had negligible radiochemical yield (RCY) by manual synthesis and was not translated for automated synthesis. The NO₂ precursor produced [¹⁸F]FPEB in a 4% RCY as isolated, after HPLC purification and formulation. Both SCIDY precursor yields were similar, SPI5 produced [¹⁸F]FPEB with RCYs ranging from 19-25% and SPIAd with a 24% RCY. The sulfonium salt precursor produced [¹⁸F]FPEB ranging from 15-27% RCY. Preliminary PET imaging data with [¹⁸F]FPEB shows an increased brain uptake in the transgenic model of AD vs. the age-matched controls (10 month data shown in Figure 1).

Conclusions: [¹⁸F]FPEB was prepared through nucleophilic aromatic substitution with [¹⁸F]fluoride using 5 precursors. The SCIDY chemistry and the sulfonium salt precursor resulted in similar yields. Ultimately, the SPI5-auxiliary with the SCIDY precursor was chosen for further validation and translation for human use. Preliminary PET/CT imaging studies in a transgenic mouse model of AD demonstrated a functional link between [¹⁸F]FPEB brain uptake reflective of mGluR5 expression and AD progression. Increased uptake in APP/PS1 mouse models of AD compared with controls is consistent with increased radiotracer binding observed in patients with early mild cognitive impairment.³ Further studies to explore mGluR5 as an early biomarker for AD are underway.



Scheme 1. Radiofluorination of [¹⁸F]FPEB via 5 different precursors.

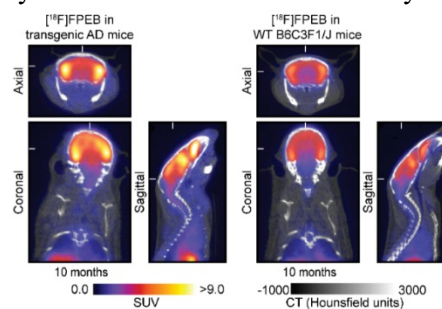


Fig. 1. PET/CT images of [¹⁸F]FPEB in APP/PS1 (transgenic) mice and aged-matched WT B6C3F1/J (control) mice, n= 3 / group at 10 months.

References:

- Sullivan, J. M.; Lim, K.; Labaree, D.; Lin, S.-f.; McCarthy, T. J.; Seibyl, J. P.; Tamagnan, G.; Huang, Y.; Carson, R. E.; Ding, Y.-S.; Morris, E. D. *Journal of Cerebral Blood Flow & Metabolism* 2012, 33 (4), 532-541.
- Rotstein, B. H.; Stephenson, N. A.; Vasdev, N.; Liang, S. H. *Nature Communications* 2014, 5 (1), 4365.
- Liang, S. H.; Yokell, D. L.; Jackson, R. N.; Rice, P. A.; Callahan, R.; Johnson, K. A.; Alagille, D.; Tamagnan, G.; Collier, T. L.; Vasdev, N. *MedChemComm* 2014, 5 (4), 432-435.
- Liang, S. H.; Wang, L.; Stephenson, N. A.; Rotstein, B. H.; Vasdev, N. *Nature Protocols* 2019, 14 (5), 1530-1545.
- Gendron, T.; Sander, K.; Cybulska, K.; Benhamou, L.; Sin, P. K. B.; Khan, A.; Wood, M.; Porter, M. J.; Årstad, E. *Journal of the American Chemical Society* 2018, 140 (35), 11125-11132.
- Stephenson, N. A.; Holland, J. P.; Kassenbrock, A.; Yokell, D. L.; Livni, E.; Liang, S. H.; Vasdev, N. *Journal of Nuclear Medicine* 2015, 56 (3), 489-492.

Evaluating Anesthetic Protocols for Non-Human Primate Functional Neuroimaging

Megha Verma(1), Spencer Arbuckle(2), Ravi Menon(3), Andrew Pruszyński(4)

(1)MSc Neuroscience Candidate at the University of Western Ontario (2) PhD Neuroscience Candidate at the University of Western Ontario (3) Centre for Metabolic Mapping at the University of Western Ontario (4) Department of Physiology and Pharmacology at the University of Western Ontario, London, Ontario, Canada

Introduction

Functional magnetic resonance imaging (fMRI) is a powerful, non-invasive technique that can be used to measure a proxy of neural activity *in vivo*. Compared to more invasive techniques such as spike recordings, the great strength of fMRI is the high spatial coverage (4). This is particularly valuable in exploratory experiments that focus on how the brain reorganizes itself after perturbation, such as a stroke or peripheral nerve injury. Non-human primates (NHPs) are the ideal models for such studies because of their similarities to humans.

However, fMRI is very sensitive to motion, and thus anesthetic sedation is commonly used in NHP neuroimaging studies. These anesthetic protocols vary considerably, and it is unclear which protocol best preserves brain activity while safely causing loss of consciousness in the animal. This is an issue because task-based fMRI activity is often undetectable under current anesthetic procedures (1) even though neural activity is still apparent in anesthetized task-based electroencephalography (EEG) (2). There is also evidence that resting state networks change as well (3). In order to take advantage of both fMRI and NHP models, an appropriate anaesthetic protocol must be developed that best approximates the awake brain. In this project, I systematically compared three of the most commonly used anesthetic protocols in the same animals, focusing on how the protocols altered the activity evoked by visual and tactile stimulation.

Methods

We used 7T fMRI (Centre for Metabolic Mapping, Western University) to measure the evoked blood-oxygen level-dependent (BOLD) signal in two rhesus macaques (*Macaca mulatta*) during a visual and tactile stimulation. The stimulation was presented in a block-design. For tactile stimulation, we stimulated the glabrous skin of the NHP's right hand, and expected significant activity increases in the primary sensory cortex (S1). For visual stimulation we presented a high contrast, moving visual stimulus on a screen mounted in front of the NHP in the scanner. We expected significant activity increases during visual stimulation in the medial temporal area (MT). During these scans, the NHPs were anesthetized via one of three protocols: (1) Isoflurane gas alone (2) Isoflurane + Fentanyl (3) Propofol + Fentanyl. Finally, we also acquired resting state scans in the same NHPs under each anesthetic protocol as a positive control to ensure that the anesthetic level was not high enough to ablate brain activity in the animal.

Results

In each anesthetic protocol, resting state networks were observed that match resting state networks that have been previously reported in anesthetized macaques. However, the effects of these protocols on responses evoked by stimulation differed. Under isoflurane alone (protocol 1), we observed no significant activity evoked in S1 during tactile stimulation, nor in MT during visual stimulation. Under fentanyl alone (protocol 2), visual stimulation elicited significant activity in area MT but somatosensory stimulation did not elicit any activity in S1. During sedation with both propofol and fentanyl (protocol 3), the visual stimulus did not elicit significant activity, however, somatosensory stimulation did elicit robust activity in S1.

Conclusions

We conclude that different anesthetic agents and protocols may be better suited to preserve activity from different sensory modalities. Despite the ability to detect significant BOLD activity from some sensory modalities, it is clear that anesthetic sedation significantly attenuates sensory-evoked responses across the cortex, corroborating the thalamic attenuation theory.

References

1. Hutchinson M et al. 2014 Human Brain Mapping 35(12)
2. Leopold DA, Logothetis NK et al. 2002 Exp Brain Res 143(3):359-72
3. Liu JV, Silva AC et al. 2013 Neuroimage 78:186-195
4. Logothetis NK. 2008 Nature Reviews 453(7197)
5. Watson KK, Platt ML. 2012 J Neurodevelopmental Disorders 4:21
6. Zhao F, Hu X et al. 2008 Neuroimage 39:248-260
7. Kaufman MJ et al. Exp Clin Pharmacol. 2013 21(4): 323-331
8. Murnane KS & Howell LL. J. of Neurosci. Methods. 2010 191:11-20

PET Imaging Extra-Striatal D2 Receptors in Parkinson's Disease with Rapid Eye Movement Sleep Behaviour Disorder

Mikael Valli^{1,2,3}, Sang Soo Cho^{1,2}, Yuko Koshimori¹, Maria Diez-Cirarda^{1,2}, Alexander Mihaescu^{1,2,3}, & Antonio P. Strafella^{1,2,3,4}

1. Research Imaging Centre, Campbell Family Mental Health Research Institute, Centre for Addiction and Mental Health, University of Toronto, Ontario, Canada.
2. Division of Brain, Imaging and Behaviour – Systems Neuroscience, Krembil Research Institute, UHN, University of Toronto, Ontario, Canada.
3. Institute of Medical Science, University of Toronto, Ontario, Canada.
4. Morton and Gloria Shulman Movement Disorder Unit & E.J. Safra Parkinson Disease Program, Neurology Division, Dept. of Medicine, Toronto Western Hospital, UHN, University of Toronto, Ontario, Canada.

Disclosures: All authors declare none.

Introduction: Rapid eye movement sleep behaviour disorder (RBD) is a common condition found in 50% of Parkinson's disease (PD) patients (Chung et al. 2017). Molecular imaging evidence shows that PD with RBD (PD-RBD+) has a distinct striatal dopamine phenotype compared to PD without RBD (PD-RBD-) where PD-RBD+ show lower dopamine transporter activity within the caudate and putamen (Chung et al. 2017; Arnaldi et al. 2016). However, the characterization of the extra-striatal dopamine within the mesocortical and mesolimbic pathways remains unknown. Therefore, we aim to elucidate this with PET imaging in PD patients with and without RBD, while having healthy older adults as controls (HC).

Methods: A total of 45 participants were recruited and participated in the imaging study: 15 were PD-RBD+ (mean age = 68.1 ± 6.48 years; 10 males), 15 were PD-RBD- (mean age = 70.7 ± 5.67 years; 8 males) and 15 were HC (mean age = 67.1 ± 5.14 years; 3 males). Each participant underwent a single PET scan with [¹¹C]FLB 457 to detect the D2 receptors within the extra-striatal regions of interest (ROI), including the prefrontal and temporal areas. They also underwent a single MRI scan to rule out structural lesions and to provide anatomical reference for the parametric PET image analysis. [¹¹C]FLB 457 retention was expressed as the non-displaceable binding potential (BP_{ND}) using the simplified reference tissue model 2 with the cerebellum as a reference region (Wu & Carson 2002; Sandiego et al. 2015). Analysis of variance was used to compare the BP_{ND} between the three groups for each ROI. Post hoc independent sample *t* tests were used to test for differences between conditions and were corrected for multiple comparisons using false discovery rate.

Results: The main effect of group condition on [¹¹C]FLB 457 binding was tested and revealed significance within the superior temporal region on the right [F(2, 42)=3.98, *p*=0.026] and left [F(2, 42)=4.29, *p*=0.02] hemisphere; and left uncus para-hippocampus [F(2, 42)=4.43, *p*=0.018]. Specifically, we found that PD-RBD- binding was lower than HC in the superior temporal region in both right (*p*=0.039) and left (*p*=0.021) hemispheres. However, the PD-RBD+ binding was found to be lower relative to HC (*p*=0.045) on the right side only, and slightly higher than PD-RBD-, but this did not reach significance. For the left uncus para-hippocampus, both PD-RBD+ (*p*=0.027) and PD-RBD- (*p*=0.027) binding was lower than HC, but PD-RBD+ was slightly higher than PD-RBD-, which did not reach significance.

Conclusions: Our results implicate that relative to HC, PD-RBD+ has lower levels of D2 receptor availability within the left uncus para-hippocampus, a region involved in the limbic system, which influences sleep; and the right superior temporal region. Results imply that extra-striatal dopaminergic system may play a role in contributing to the RBD in PD patients but validation with a larger sample size is needed. Results also suggest that other underlying physiology within extra-striatal regions may be taking a larger role in contributing to RBD in PD such as the cholinergic system (Kotagal et al., 2012).

Regularization of Continuous-Wave Hyperspectral Near Infrared Spectroscopy with Spatially-Resolved Measurements Improves Accuracy

Naomi Abayomi¹, Mamadou Diop^{1,2*}

¹Department of Medical Biophysics, University of Western Ontario, London, Ontario, Canada

²Imaging Division, Lawson Health Research Institute, London, Ontario, Canada

Introduction: Near infrared spectroscopy (NIRS) is a promising tool for monitoring cerebral hemodynamics in neonates. Continuous-wave hyperspectral near infrared spectroscopy (CW-*h*NIRS) is a portable and inexpensive subtype of NIRS that uses spectral derivatives methods to reliably quantify tissue deoxyhemoglobin (Hb) and water content [1]. However, accurate estimation of oxyhemoglobin (HbO₂) and tissue scattering from CW-*h*NIRS remains a challenge. We hypothesize that adding Tikhonov regularization to spatially-resolved CW-*h*NIRS will improve the accuracy of the recovered scattering amplitude (Alpha), scattering power (Beta), and HbO₂. The aim of this study was to test this hypothesis by conducting *in silico* experiments and applying a novel fitting algorithm that incorporates Tikhonov regularization into the spectral derivatives fitting.

Methods: Simulations were conducted with NIRFAST, a software package for modeling near infrared light transport in tissue [5]. An MRI image of an infant head was segmented into cerebral tissue, scalp and skull (i.e., extracerebral layer; ECL), and cerebral spinal fluid layer (CSF). Further, 3-layer slab models with various top-layer thickness, but with a fixed scalp to skull thickness ratio of 5:8, were generated. We then placed one emission source and four detectors (at 3, 3.3, 3.6 and 3.9 cm from the source) on the top surface of each model and simulated light propagation in the medium. This spatially-resolved CW-*h*NIRS data were used to estimate the effective attenuation coefficient (μ_{eff}) of the medium. More specifically, for every wavelength, we computed the slope of the attenuation with respect to the source-detector distance (r) and fit this to extract the (μ_{eff}) which was then used to regularize the fitting step where the concentration of HbO₂ and scattering parameters are estimated [6].

Results: Fig. 1 displays the difference between the scattering parameters and chromophore concentrations used in the simulations and the values recovered with the classic spectral derivative (CSD) and the new regularized spectral derivative (RSD) approach for our segmented MRI head model. The largest discrepancy was recorded for the oxyhemoglobin concentration with a mean error of $25.8\% \pm 4.2\%$ for the CSD and $3.6\% \pm 2.1\%$ for the RSD method. When evaluating the effects of increased extracerebral thickness, the RSD and CSD methods estimated the scatter power (Beta) with an error of $2.7\% \pm 1.9\%$ and $37.7\% \pm 34\%$ respectively, when applied to a slab with 3mm upper layer thickness (results not shown).

Conclusion: Adding Tikhonov regularization to spectral derivatives analysis of CW-*h*NIRS data improves the recovery of the scattering parameters and the chromophore concentrations. Interestingly, when comparing the new method to the traditional fitting approach, the error introduced by increased skull thickness is reduced with regularization. However, accuracy declines for both methods when the thickness of the skull increases, which is likely due to the use of a homogeneous analytical model in the fitting. Future work will implement a 2-layer analytical model in the fitting and validate this novel algorithm in tissue mimicking phantoms and an animal model of neonate.

References: [1] M. Kewin et al. *Biomed Opt Express*. 10(9) (2019). [2] M. Diop et al. *Biomed. Opt. Express* **6**, (2015).[3] Z. Kováčová et al. *SPIE 11074*, Vol. VII of *Diffuse Optical Spectroscopy and Imaging 110740P* (2019).[4] L. Yang et al. “in *SPIE 11074*, Vol. VII of *Diffuse Optical Spectroscopy and Imaging 110740A* (2019).[5] H. Dehghani et al. *Commun Numer Methods Eng.* **25**(6) (2008).[6] M. Diop et al. *J Biomed Opt* **19**(5), (2014).

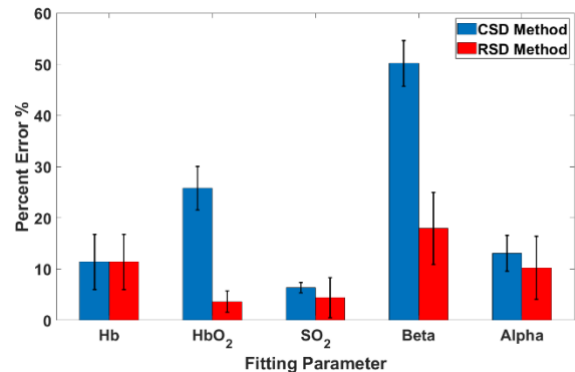


Fig. 1. Percent Error (%) of the CSD Method and the RSD Method for the Segmented Infant Head showing the distribution across 8 different SO₂ values (40-80%).

Relationships between Dynamic functional connectivity patterns and dopaminergic therapy in Parkinson's disease

M. Díez-Cirarda^{1,2,3}, I. Gabilondo³, N. Ibarretxe-Bilbao⁴, J.C. Gomez-Esteban³, J. Kim^{1,2}, O. Lucas-Jimenez⁴, R. del Pino³, J. Peña⁴, N Ojeda⁴, M. Acera³, A. Mihaescu^{1,2}, M. Valli^{1,2}, A. Cabrera-Zubizarreta⁵, M. Gómez-Beldarrain⁶, and A.P Strafella^{1,2}

- 1- Research Imaging Centre, Centre for Addiction and Mental Health, University of Toronto, Toronto (Canada)
- 2- Division of Brain, Imaging and Behaviour – Systems Neuroscience, Krembil Research Institute, University Health Network, University of Toronto, Toronto (Canada)
- 3- Neurodegenerative Diseases Group, BioCruces Health Research Institute, Barakaldo, Bilbao (Spain).
- 4- Department of Methods and Experimental Psychology, University of Deusto, Bilbao (Spain).
- 5- OSATEK, MR Unit, Hospital of Galdakao, Galdakao, Bilbao, (Spain)
- 6- Neurology Service, Hospital of Galdakao, Galdakao, Bilbao (Spain)

Disclosures: All authors declare none.

Introduction

Static brain functional connectivity in Parkinson's disease (PD) has shown relationships with levodopa daily dose (LEDD). However, to date, no study has evaluated the relationship between temporal properties of dynamic connectivity and LEDD in PD patients. The main objective of the present study was to evaluate the relationships between dynamic functional connectivity and LEDD in PD.

Methods

One hundred and eight PD patients and 63 age-matched healthy controls (HC) were recruited. Resting-state functional MRI (axial orientation; TR = 2000/2100ms; Matrix size = 64×64/ 80×79; Slice thickness = 5/3 mm; Volumes = 240/214; Acquisition time = 8'04"/7'40") and T1-weighted MRI (TR = 6.7/7.4 ms; Flip angle 8°/9°; Matrix size = 256×256/228×218; Slice thickness = 0.9/1.1 mm) were also acquired. Dynamic FC analyses were performed in GIFT toolbox, and dynamic indexes were also analyzed: *fractional time window*, *mean dwell time*, and *state transitions*. Multivariate analyses of covariance were performed to test differences between groups and partial correlations were performed to test relationships between LEDD and dynamic indexes.

Results

Two dynamic connectivity States were identified. A first state (State I) showed stronger within-network connectivity and a second state (State II) showed stronger connectivity between-networks (mostly between somatomotor, and visual networks). PD patients showed dynamic FC alterations in *fractional time window* in State I and II ($p = .017$) and reduced *mean dwell time* in State I ($p = .009$) compared to HC. In addition, PD patients showed increased *state transitions* compared to HC ($p = .012$). LEDD significantly correlated with *fractional time window* ($p = .011$) and *state transitions* ($p = .032$).

Conclusions

Results showed that LEDD has significant effect on time-varying connectivity patterns in PD patients, showing that the higher LEDD the greater time spent in the between-network connected state and lesser time spent in within-network connected state.

Changes in blood oxygen level dependent (BOLD) signal to smoking cues in the insula, anterior cingulate gyrus and inferior frontal gyrus are negatively associated with baseline smoking consumption: preliminary findings from a smoking cessation RCT.

Zhang, H^{1,2}, Lobaugh, N.^{3,4}, Chavez, S^{3,5}, Zawertailo, L.^{1,2}

1. Nicotine Dependence Service, Addictions Program, Centre for Addiction and Mental Health, Toronto, Canada.
2. Department of Pharmacology and Toxicology, Faculty of Medicine, University of Toronto, Canada
3. Research Imaging Centre, Campbell Family Mental Health Research Institute, Centre for Addiction and Mental Health, Toronto, Canada.
4. Department of Neurology, Faculty of Medicine, University of Toronto.
5. Department of Psychiatry, Faculty of Medicine, University of Toronto.

Introduction: Smoking is the leading cause of preventable death world-wide. Relapse rates are high, with many smokers unable to remain abstinent following treatment with first-line pharmacotherapies. Smoking-related environmental stimuli can elicit smoking urges and cravings, which is associated with compulsive smoking and relapse. As such, functional brain activation to smoking cues has shown potential as a biomarker of nicotine dependence severity. The objective of this analysis was to explore the relationship between cigarettes smoked per day and functional brain activation during smoking related cues at baseline in five bilateral regions of interest: the insula, anterior cingulate gyrus, posterior cingulate gyrus, middle frontal gyrus and inferior frontal gyrus.

Methods: Participants were recruited as part of an on-going clinical trial for smoking cessation. Participants underwent an MRI scan under nicotine satiety (within 2 hours of last cigarette, carbon monoxide confirmed). During the scan, participants viewed smoking images and content matched neutral images. Scans were completed using the GE scanner with EPI sequences @ 2650 TE; 49 slices @ 3 mm isotropic. Blood oxygen level dependent (BOLD) signal was collected during smoking cues. Data was corrected for motion and B0 distortions, prior to temporal autocorrelation in univariate linear modeling (FEAT; FMRIB FSL). Average percent change in BOLD signal during smoking cues was extracted (feat-query; FMRIB FSL). BOLD signal change was correlated with cigarettes smoked per day using Pearson's correlation.

Results: To date, 20 participants have been recruited (14M, 6F), average age: 34.4 ± 5.3 and average cigarettes per day (CPD): $14.5 (\pm 4.2)$. CPD was negatively correlated with % BOLD signal change when viewing smoking cues in the insula ($r = -0.65$; $p = 0.002$), inferior frontal gyrus ($r = -0.65$; $p = 0.002$) and anterior cingulate gyrus ($r = -0.46$ $p = 0.04$) whereby heavier smokers had decreased BOLD signal change, whilst those that were lighter smokers had increased BOLD signal change in the aforementioned areas. A similar negative correlation was seen for the posterior cingulate cortex and middle frontal gyrus, however, these were not statistically significant ($p = 0.1$ and $p = 0.2$ respectively).

Conclusions: Preliminary analysis shows increased cigarette consumption to be negatively associated with activation changes in regions of the brain involved in behavior regulation, attention and sensory processing. There were distinct activation patterns in heavier smokers compared to lighter smokers, a potentially useful marker for future predictions of smoking cessation. Future work will prioritize longitudinal neural correlate trends following smoking cessation treatment.

Towards identifying reliable short-ranged, U-shaped structural connectivity

Jason Kai^{1,2}, Ali R. Khan^{1,2}

¹Dept. Of Medical Biophysics, ²Robarts Research Institute, Western University, London, ON, Canada

Introduction: Diffusion MRI (dMRI), together with tractography techniques, enable non-invasive investigation of the brain's structural pathways¹. While the brain's long-range connections have been studied, less is known about the short-range, U-shaped pathways, which comprise the brain's superficial white matter joining together nearby regions of the brain. Quantitative differences have been observed between healthy and patient populations in previously studied connections and by studying the short-ranged pathways, additional insight may be gained and compliment existing knowledge to help diagnose neurological or psychiatric disorders. One challenge complicating the investigation of short-ranged connections is the differences in local folding patterns across individuals. These differences could result in different spatial arrangements of the U-shaped connectivity. In this work, we determine reliably identified U-shaped connectivity across healthy individuals through clustering and analyzing corresponding spatial and quantitative features.

Methods: Preprocessed dMRI data (n=100) from the Human Connectome Project^{2,3} was used to create a population template. Additional subjects (n=15) were utilized to assess reliability of U-shaped connections. Data was acquired on a custom Siemens Skyra 3T scanner at 1.25mm isotropic resolution, b-values=1000, 2000, 3000s/mm² (90 diffusion-encoding directions each). Multiple dMRI sessions (n=15) of a single subject from the MyConnectome Project⁴ were also used to explore U-shaped connectivity. Data was acquired on a separate Siemens Skyra 3T scanner at 1.74x1.74x1.7 mm³ resolution, b-values=1000, 2000 s/mm² (30 directions each). Preprocessing was performed using in-house pipelines and whole-brain tractography was generated before applying a filter to identify U-shaped streamlines. Candidate pathways were identified by comparing streamline length and endpoint distances. Remaining streamlines were clustered to identify distinct pathways. Euclidean distances between pathway centroids, streamline count, intraclass correlation (ICC) for fractional anisotropy and coefficient of variation (CV) of streamline counts were computed to assess reliability of identified pathways.

Results: Computed Euclidean distances and streamline counts enabled identification of non-reliable pathways. ICC in candidate pathways were all above 0.80 indicating great reliability. Computed CVs (figure 1A) were employed to identify and apply a threshold to extract reliably identified pathways (figure 1B).

Conclusions: Using a clustering tool together with spatial and quantitative characteristics, 125 reliable U-shaped tracts are identified between two datasets. Such analysis may aid further studies to better understand short-range connectivity in healthy and patient populations. Future work includes further assessment of the biophysical properties of these connections and their relation to cortical measurements, and to explore changes to these pathways in patient populations.

References:

- [1] Sotiropoulos and Zalesky. (2017). *NMR Biomed.* [3] Van Essen *et al.* (2013). *NeuroImage*
 [2] Glasser *et al.* (2013). *NeuroImage* [4] Poldrack *et al.* (2015). *Nat Commun.*

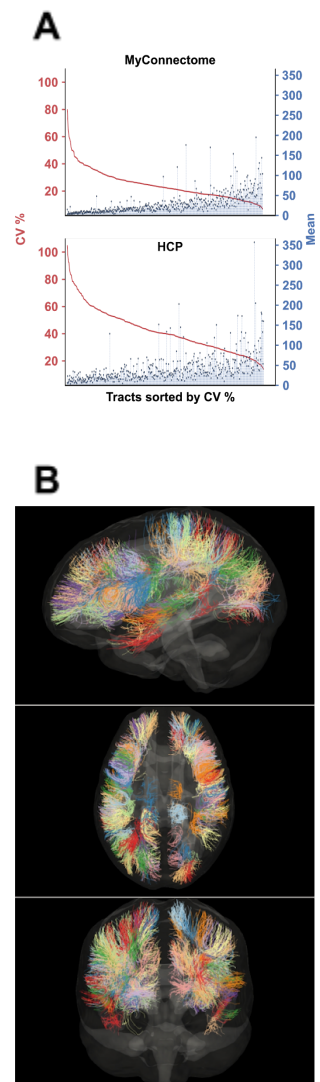


Figure 1. (A) All identified clusters sorted by CV %. (B) Identified candidate tracts following thresholding in three axial (top), sagittal (middle), and coronal (bottom) views.

MRI to investigate neurological complications in patients with TTP and the implementation of quantitative myelin water imaging by mcDESPOT

JG Hamilton¹, MT Jurkiewicz^{2,3}, JD Thiessen^{1,2}, SHS Huang^{1,2,3,4}

¹Department of Medical Biophysics, Western University, London, Ontario, Canada

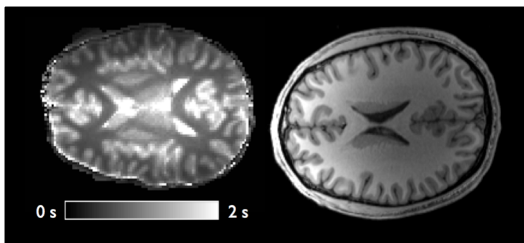
²Lawson Health Research Institute, London, Ontario, Canada

³Department of Medicine, Schulich School of Medicine & Dentistry, London, Ontario, Canada

⁴The Lilibeth Caberto Kidney Clinical Research Unit, London, Ontario, Canada

Introduction: Thrombotic thrombocytopenic purpura (TTP) is a rare, life-threatening blood disorder characterized by insufficient activity in a protein called ADAMTS13 which functions to prevent blood clotting. This results in spontaneous blood clotting throughout the microvasculature and other symptoms include kidney failure and neurological changes such as confusion and a higher likelihood of having a stroke or a seizure. Despite treatments which restore hemostasis, these neurological changes persist. The objective of this study is to observe brain changes over time in patients with TTP by using a comprehensive magnetic resonance imaging (MRI) protocol. A specific aim is to implement quantitative myelin water imaging to measure brain white matter.

Methods: Individuals with diagnosis of TTP are eligible for this observational study if they are ≥ 18 years and have had no signs or symptoms of microvascular injury for at least 30 days. The 65-minute 3T MRI (Siemens mMR Biograph) includes 20 minutes for high-resolution qualitative acquisitions (including T1-, T2-, susceptibility- and diffusion-weighted images) [1] and 45 minutes for quantitative acquisitions, featuring mcDESPOT (multi-component driven equilibrium single pulse observation of T1 and T2) for myelin water matter imaging [2]. 7 patients were scanned after the protocol was validated in 3 volunteers. Interpretation of the qualitative MRI images was done by a neuroradiologist and mcDESPOT to generate quantitative maps (T1, T2, and myelin water) was done by QUIT (Quantitative Imaging Tools) [3].



Example of quantitative map in comparison to equivalent slice in standard clinical qualitative acquisition.
Left: T1 map **Right:** T1-weighted

Results: Five patients exhibit multiple non-specific spots or white matter hyperintensities, two exhibit infarcts, and one exhibits a blood clot. In the mcDESPOT, quantitative T1 (shown in figure) and T2 maps were reproducible and provided accurate relaxation times by tissue. Myelin water maps were generated but require further processing steps including co-registration of T2-weighted volumes.

Conclusions: Current results are preliminary as the necessary comparisons to age-matched healthy controls are forthcoming. These outlined regions will be analyzed by mcDESPOT to quantify the white matter. We will test the hypothesis that white matter decreases over time in comparison with controls using Student's t-test. Patients will continue to be recruited and follow-up scans will be at 6 and 12 months. Controls will undergo the same imaging protocol. To our knowledge, this is the first study of its kind and we hope to better understand these neurological changes in order to improve the quality of life of individuals who experience TTP.

References: [1] Leiva-Salinas et al, 2010 *Neuroimaging Clinics of North America* [2] Deoni et al, 2008 *Magnetic Resonance in Medicine* [3] Wood, 2018 *Journal of Open Source Software*

Assessing Functional Complexity and Structural Connectivity in mTBI Patients

Nicholas Simard¹, M. D. Noseworthy²

¹McMaster University, Electrical and Computer Engineering, Hamilton, Canada, ²McMaster University, School of Biomedical Engineering, Hamilton, Canada

Introduction: There are upwards of 1.7 million people each year affected by a mild traumatic brain injury (mTBI)¹. Victims are left with poor diagnosis and a robust technique is required to identify severity and brain regions affected by an MTBI. The goal of this research was to investigate individuals who have suffered an mTBI using diffusion tensor imaging (DTI) to assess structural integrity and resting state MRI (rsMRI) to identify functional abnormalities through complexity analysis.

Methods: mTBI patients (M/F age 35 to 55) having experienced an mTBI within 2 years were recruited. Healthy control subjects were sourced from data repositories (ICBM, PPMI, etc). A GE MR750 Discovery 3T MRI scanner and 32-channel RF receiver coil were used for scanning mTBI patients. Axial DTI was acquired using a dual echo EPI sequence (TE/TR=87/8800ms, 122x122 matrix, 2mm thickness, FOV=244mm). Tract-Based Spatial Statistics (TBSS) was used for analysis and parameters Fractional anisotropy (FA), Mean Diffusivity (MD), Radial Diffusivity (RD), and Axial Diffusivity (AD) were examined. Resting state data was also acquired using an EPI sequence (TE/TR=35/2000ms, 64x64 matrix, 3mm thickness, FOV=22cm). A MATLAB processing pipeline was used for functional complexity analysis². Voxel wise statistics were performed and commonly registered ROIs were segmented using the JHI Atlas (*results shown in Figures 1. and 2*). Group statistics were not performed as a Z- transform approach was used to identify subject-specific abnormalities³. The healthy control database included at least n=25 for each age and sex.

Brain Region	FD Z-Score
GM Amygdala centromedial group Left	-1.783973
GM Amygdala centromedial group Right	-2.241955
GM Amygdala laterobasal group Left	-1.814279
GM Amygdala laterobasal group Right	-2.127023
GM Amygdala superficial group Left	-1.731538
GM Amygdala superficial group Right	-2.28871
GM Anterior intra-parietal sulcus hiP1 Left	-3.051084
GM Anterior intra-parietal sulcus hiP1 Right	-2.74604
GM Anterior intra-parietal sulcus hiP2 Left	-2.744676
GM Anterior intra-parietal sulcus hiP2 Right	-2.422258
GM Anterior intra-parietal sulcus hiP3 Left	-2.139609
GM Anterior intra-parietal sulcus hiP3 Right	-1.565178
GM Broca's area BA44 Left	-0.851212
GM Broca's area BA44 Right	-1.535705
GM Broca's area BA45 Left	-0.627478
GM Broca's area BA45 Right	-1.244673

Figure 1. rsMRI complexity Z-score results shown with mildly injured areas in orange ($1.65 < Z < 2$), severely injured areas in red ($2 < Z < 3$) and extremely injured areas in maroon ($Z > 4$).

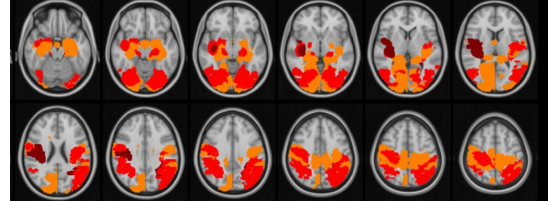


Figure 2. Transverse view of rsMRI results. Injured areas correspond to the calculated Z-scores

Results: In all DTI and rsMRI parameters, control data Z scores were below 1.65 ($p < 0.05$). Structurally, injured individuals yielded at least 4 brain regions with Z scores above 1.65 ($p < 0.05$) in at least one DTI parameter. Functionally, injured individuals yielded at least 6 brain regions with Z scores above 1.65 ($p < 0.05$). In some cases, reduced functional complexity was observed in the right or left brain, showing localized areas of injury.

Conclusions: Deficits in both structural and functional connectivity were clearly noted within individuals who have recently suffered an mTBI. Case by case analysis reinforces that group statistics should not be employed as all patients had a different clinical presentation due to heterogeneity of injury types. More information on the injury should be collected to identify whether type of injury correlates with specific regional deficits.

References: [1] Faul M. (2010). Traumatic Brain Injury in the United States. Centers for Disease Control

[2] Mandelbrot. "Self-affine fractals and fractal dimension." *Physica scripta*

[3] Mayer AR. (2018). An evaluation of Z-transform algorithms for identifying subject-specific abnormalities in neuroimaging data

Advanced Near-Infrared Spectroscopy for Improved Sensitivity to Cerebral Oxygenation in Adults

David Jonathan Fulop Cohen¹ and Mamadou Diop^{1,2,3*}

¹Department of Medical Biophysics, Western University, London, Ontario, N6A 5C1, Canada

²School of Biomedical Engineering, Western University, London, Ontario, N6A 5C1, Canada

³Imaging Program, Lawson Health Research Institute, London, Ontario, N6A 4V2, Canada

*mdiop@uwo.ca

Intro: Time-resolved (TR) Near-infrared Spectroscopy (NIRS) allows for the detection of changes in adult cerebral oxygen saturation (S_cO_2) [PMID: 21054120]. However, the accuracy of current methods decreases with S_cO_2 – when accuracy is most needed – due to small number of wavelengths used. Accuracy can be improved by using a large number of wavelengths (i.e. hyperspectral TR-NIRS). Importantly, recent advancements in TR technology has led to the development of time-gated detectors that provide exceptional sensitivity to deep tissue by only detecting late arriving photons [PMID: 28906462], which are more sensitive to the deep tissue changes [PMID: 24156081]. This advancement, in combination with the advent of supercontinuum TR lasers, makes it possible to envision the development of late-photon hyperspectral NIRS (Lp-*h*NIRS). We hypothesize that Lp-*h*NIRS would have higher sensitivity to changes in deep tissues and would provide more accurate estimates of cerebral oxygenation in adults than methods using few wavelengths (i.e., multispectral TR-NIRS). This hypothesis was tested using Monte-Carlo simulations of Lp-*h*NIRS and multispectral TR-NIRS in the adult human head.

Methods: A 3D MRI image of an adult head was segmented into four tissue types consisting of the skin, skull, cerebrospinal fluid, and brain. Monte-Carlo simulations of light propagation [PMID: 19997242] in the head model were conducted for each wavelength between 650 nm and 950 nm. The light source was placed on the right temple and a detector was positioned 2 cm anteriorly from the source. Typical optical properties were assigned to each tissue type using published literature values [PMID: 23666068]. The scalp and brain absorption coefficients were computed on a per wavelength basis using the method described in Diop *et al.* 2015 [PMID: 26504641], and skin and brain oxygenation were varied from 50% to 70% in 10% increments. The simulations were used to estimate the absorption coefficient of the brain at all wavelengths. The absorption coefficients were subsequently used to estimate the concentrations of water, oxyhemoglobin, and deoxyhemoglobin in the brain. For the multispectral TR-NIRS method, four wavelengths (680 nm, 750 nm, 800 nm, and 830 nm) were used to recover the S_cO_2 using the method outlined in Gagnon *et al.* 2008 [PMID: 19021399].

Results: Fig. 1 shows the heatmaps of the recovered S_cO_2 using both the Lp-*h*NIRS method (Fig. 1A) and the multispectral TR-NIRS method (Fig. 1B). While both methods show a high dependence on inputted S_cO_2 , the Lp-*h*NIRS method has greater accuracy in the lower S_cO_2 range (50% and 60%) than the multiwavelength TR-NIRS method. The recovered S_cO_2 using the Lp-*h*NIRS method had a maximum difference from the inputted S_cO_2 of ~5%, while the multispectral TR-NIRS method showed a peak difference of ~13%. At normal S_cO_2 (70%), the two methods provided similar results.

Conclusion: This study suggests that Lp-*h*NIRS can provide more accurate estimate of cerebral oxygen saturation than the more widely used multispectral TR-NIRS method, especially in the lower range of cerebral oxygenation. Future work will include conducting simulations on a wider range of brain/scalp oxygenations to further assess the robustness of the method, as well as validation in tissue mimicking phantoms and animal models of the adult head.

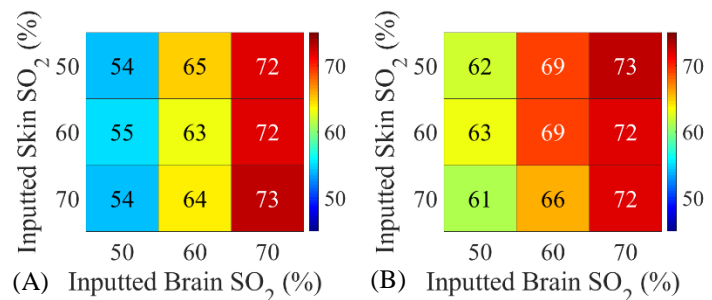


Figure 1: (A) Heatmap displaying the recovered S_cO_2 for each brain/scalp pair using the Lp-*h*NIRS method. (B) A heatmap displaying the recovered S_cO_2 for each brain/scalp pair using the multispectral TR-NIRS method.

Connective Morphology for Efficient Skull-stripping of Head CT Images

Kevin J. Chung,^{1,2} Bijoy K. Menon,² Wu Qiu²

¹Department of Mechanical and Manufacturing Engineering, University of Calgary, Calgary, Alberta, Canada

²Department of Clinical Neurosciences, University of Calgary, Calgary, Alberta, Canada

Introduction: Skull-stripping, or brain extraction, is an important pre-processing step for head computed tomography (CT) images in which extraneous features such as tissue and bone are removed from the image to isolate the brain. This step is required for the automatic assessment of Alberta Stroke Program Early CT (ASPECT) score, hematoma volume in intracranial hemorrhage patients, and automatic calculation of blood flow maps from CT perfusion studies. While there are extensively validated skull-stripping tools available for magnetic resonance images, the same algorithms do not easily translate onto CT. We propose a computationally efficient method of skull-stripping head CT images using morphology and connectivity.

Methods: Forty non-contrast CT (NCCT) and ten CT angiography (CTA) images of patients presenting with acute stroke were acquired from a local clinical database. A binary mask was generated by thresholding image voxels between 0 and 90 Hounsfield units (HU) for NCCT and 0 and 300 HU for CTA. Connections between brain tissue and extraneous structures in this mask were removed using morphological erosion and connected-component analysis that identified a central region of the brain. A morphological dilation restored the eroded brain voxels and gaps were filled using a binary hole-filling algorithm. Our skull-stripping algorithm was compared to manual delineations of the brain using quantitative metrics such as the Dice similarity coefficient (DSC), which measured spatial overlap, the Pearson coefficient (r) for brain volume correlation, and Bland-Altman analysis for volume agreement.

Results: Mean DSC and volume correlation were excellent ($DSC > 0.950$; $r > 0.950$, $p < 0.001$) for the entire NCCT and CTA dataset but brain volume was systematically underestimated up to 50 ml. Computational time largely depended on the number of axial slices but was under 3 s for NCCT (~32 5-mm thick slices) and 20 s for larger CTA (~250 0.625-mm thin slices) images.

Conclusion: By leveraging the connectivity and morphology of the brain, an accurate brain mask could be delineated efficiently for skull-stripping of head CT images. The use of standard image processing functions allows this algorithm to be easily reproducible and serve as a reliable pre-processing step in future studies.

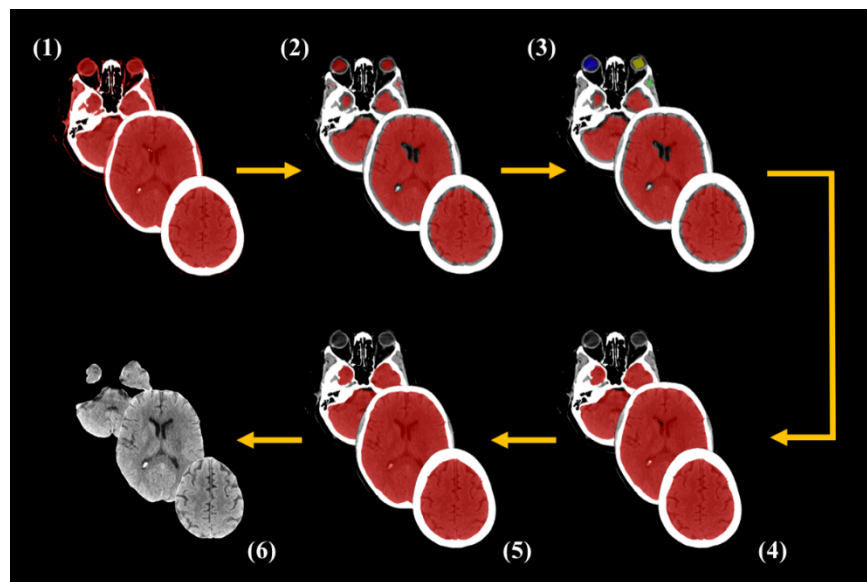


Figure. Image processing pipeline for skull-stripping head CT images. (1) binary thresholding; (2) morphological erosion; (3) connected-component analysis; (4) morphological dilation; (5) binary hole-filling; (6) brain extraction

Title: Pilot testing of neuromelanin as a biomarker of late-life depression

Authors: Navona Calarco, Breno Diniz, Yuliya Nikolova

Affiliations: Centre for Addiction and Mental Health (CAMH)

INTRODUCTION. Neuromelanin (NM) is a dark pigment evident in the substantia nigra (SN) and locus coeruleus (LC). NM accumulates over the lifespan, and is generally considered to have neuroprotective properties in late life. NM-derived metrics have proven an objective marker of neuronal loss in several neurodegenerative illnesses, including Parkinson's disease. In this pilot analysis, we sought to test the utility of NM as a biomarker in late-life depression (LLD). We used neuromelanin-sensitive MRI (NM-MRI) to characterize the SN and LC, and investigated associations with depressive symptoms and neurocognition, in LLD and age-matched healthy controls (HC).

METHODS. This pilot analysis includes data from 31 participants (16 LLD, 15 HC, ages 60-82). Scans were acquired on a Siemens 3T Prisma with a 64-channel head coil. The NM-MRI sequence was a 2D gradient echo sequence with an explicit magnetization transfer (MT) preparation pulse placed prior to the excitation pulse. Images were acquired with the following parameters: TR/TE=389/2.9ms, 512x512 acquisition matrix, FOV=124.8x200mm, voxel size=.4x.4x.3mm³, slice thickness=3mm, FA=40° (MT FA=300°, RF offset=1200), 15 contiguous slices, and 4 measurements. We segmented the SN and LC via a semi-automated reference ROI thresholding method. Specifically, for the SN, a trained rater identified voxels from a subset found to have a signal intensity 4 or more standard deviations greater than a reference region. The LC was localized based on anatomical landmarks, and assumed to be comprised of all voxels with a signal intensity 3 or more standard deviations greater than a reference region. For both the SN and LC, we calculated volume as the product of the number of ROI voxels and voxel size, and contrast-to-noise ratio (CNR) as $(\text{mean signal of ROI} - \text{mean signal of reference ROI}) / \text{standard deviation of signal of reference ROI}$.

RESULTS. No scans had to be discarded due to motion artifacts. Moreover, our semi-automated segmentation technique produced SN and LC structures topographically consistent with known anatomy, and volume and CNR in both structures approximated a normal distribution, an important proof-of-principle for NM imaging in the LLD population. Average CNR, but not volume, was suggestive of population differences (LLD>HC) of medium-to-large effect size in both the SN ($d=.66$) and LC ($d=.60$), though neither reached statistical significance ($p=0.076$ and $p=0.106$, respectively). When examining raw data distributions as part of an exploratory analysis, we observed that SN volume appeared to increase with age in LLD ($r=.375$) but not HC, and CNR decreased with age in both LLD ($r=-.482$) and HC ($r=-.531$). We also observed that SN volume in LLD appeared to be positively associated with higher neurocognition scores ($r=.404$), whereas HC showed a negative association ($r=-.602$). Finally, in LLD, depression severity showed a strong association with CNR in the SN ($r=.558$) and a moderate association with CNR in the LC ($r=.261$).

CONCLUSION. Here, we demonstrated the ability to simultaneously image the SN and LC in an older healthy and psychiatric population. Preliminary analyses suggest that, with adequate sample size, we may be able to differentiate groups on the basis of CNR in the SN and LC. Moreover, volume in the SN, and CNR in the SN and LC, may provide useful indices of neurocognition and depression severity in LLD, respectively. We will increase sample size and acquire longitudinal data to further probe the utility of NM as a biomarker of LLD.

Macromolecular Pool Fraction (MPF) Maps in Minimal Scan Time Using a Modified Fast SPGR Sequence and a Calibrated Synthetic MT Reference Image

Kim Desmond¹, Tobias C Wood², and Sofia Chavez^{1,3}

¹CAMH, Toronto, ON, Canada, ²King's College, London, United Kingdom, ³University of Toronto, ON, Canada

Introduction

The macromolecular pool fraction (MPF) has been shown to correlate with myelin¹. MPF maps can be generated efficiently from T1, B1 and B0 maps and the collection of two additional volumes: a reference with no MT pulse (MT_0) and an MT-weighted volume (MT_Δ) acquired at an optimal frequency offset, Δ^2 . Further time efficiency was proposed by using the T1 and B1 maps to create a synthetic MT_0 , $synMT_0^3$. In the original work, T1 maps were generated using a variable-flip-angle method from two images that were acquired with the same sequence (spoiled-gradient echo, SPGR) and resolution as MT_Δ . Restrictions on TR for MT-prepared scans makes matching scans across MT and T1 mapping acquisitions not optimal. Recently, we showed that $synMT$ can be created using a T1 mapping method relying on fastSPGR (FSPGR) scans if a calibration procedure is used to account for systematic differences across sequences⁴. The calibration was found to be subject-independent and thus the scaling factor, f , was determined a priori and applied on subsequent $synMT$. However, discrepancies in bandwidth across sequences led to inaccuracies in $synMPF_0$ in regions of large susceptibility gradients ($\Delta\chi$). In this work, we optimize T1 and B1 mapping acquisitions to reduce scan time for $synMT$ generation and we match sequences to reduce inconsistencies in regions of large $\Delta\chi$.

Method

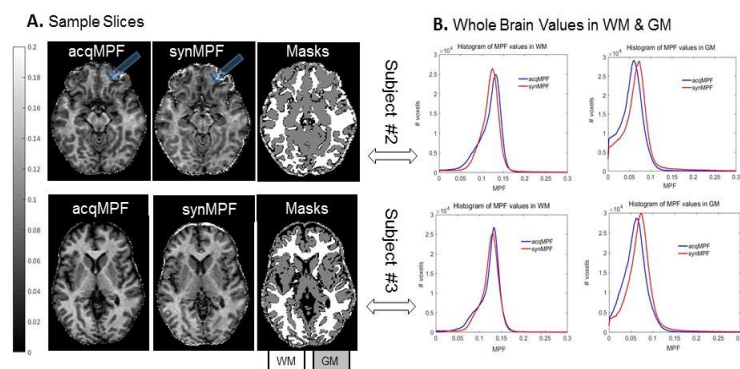
Simulations are used to study the effect of T1 and B1 inaccuracies on MPF maps computed using the acquired MT (acqMPF) and calibrated $synMT$ ($synMPF$). Scan time for $synMPF$ mapping is reduced by acquiring lower resolution T1 maps and an efficient 2D-B1 mapping implementation of the double-angle-method (DAM). The modified FSPGR sequence with in-plane acceleration allows for a large reduction in scan time for MT_Δ .

Four volunteers (37 ± 10 yrs) were scanned on a 3T scanner (GE Healthcare) according to the institutional REB. MT_0 and MT_Δ were acquired using the modified FSPGR sequence; calibrated B1 and T1 maps were obtained using calibrated DAM⁵ and VFA⁶ methods, respectively. Image processing was done using FSL (FMRIB software library) and MATLAB. The scaling factor for $synMT_0$ calibration was found as per Ref.4 for each subject, then averaged to yield the scaling factor applied to all $synMT_0$. MPF maps were computed using

acquired and calibrated synthetic MT_0 ,

yielding acqMPF and $synMPF$, respectively.

Results: Simulations predict that B1 errors lead to more severe discrepancies in $synMPF$ and acqMPF errors than T1 errors. In all cases, errors are more pronounced for GM values than WM values. The figure shows acqMPF and $synMPF$ and values in WM and GM, for two subjects. The $synMPF$ is well-matched to acqMPF in WM (<1.5% difference) which is our primary focus. In GM, $synMPF$ is biased towards an overestimation relative to acqMPF (18%-32%). This is due to (i) the smaller GM



MPF values and (ii) larger acqMPF and $synMPF$ discrepancies for GM T1 and MPF values (predicted by simulations). **Discussion:** We showed that the proposed optimized MPF acquisitions yield fast $synMPF$ estimates (32% less scan time than acqMPF). Results for $synMPF$ are very well matched to acqMPF in WM and overestimated in GM. Matching sequences for MT_Δ and $synMT_0$ improved $synMPF$ estimates, especially in regions of large $\Delta\chi$. Future work aims to improve GM $synMPF$ values by testing other B1 mapping methods.

References: 1. Khodanovich MY, et al. Scientific reports; 7, 2017. 2. Yarnykh VL. Magn Reson Med, 2011. 3. Yarnykh VL. Magn Reson Med; 75 (5), 2016. 4. Chavez S, et al. Proc. ISMRM. p 4001, 2019. 5. Chavez SE. Proc. ISMRM. p 2269, 2018. 6. Chavez SE. Proc. ISMRM. p 537, 2018.

Undersampled 3D Hyperpolarized ^{13}C Imaging of the Human Brain: a Retrospective Analysis

Clara M. Fleisig¹, Benjamin J. Geraghty^{2,3}, Casey Y. Lee^{2,3}, Albert P. Chen⁴, William J. Perks⁵, Hany Soliman⁶ and Charles H. Cunningham^{3,2}

¹The Foundation for Student Science and Technology, Ottawa, Ontario, Canada, ²Department of Medical Biophysics, University of Toronto, Toronto, Ontario, Canada, ³Physical Sciences, Sunnybrook Research Institute, Toronto, Ontario, Canada, ⁴GE Healthcare, Toronto, Ontario, Canada ⁵Pharmacy, Sunnybrook Health Sciences Centre, Toronto, ON, Canada, ⁶Radiation Oncology, Sunnybrook Health Sciences Centre, Toronto, ON, Canada

Introduction Hyperpolarized (HP) $[1-^{13}\text{C}]$ pyruvate MRI holds tremendous potential for non-invasive study of neurophysiological metabolism¹. Rapid encoding strategies are needed to obtain time-resolved, volumetric coverage of the injected substrate and its downstream metabolites i.e. lactate, bicarbonate, and for applications requiring large fields-of-view (FOV), the size of the imaging matrix can limit the achievable temporal resolution. Acceleration methods such as parallel imaging or compressed sensing can be leveraged to further reduce acquisition time. This study uses data from the brains of 18 human participants that were imaged with HP $[1-^{13}\text{C}]$ pyruvate to investigate the feasibility of acceleration via pseudo-random undersampling.

Methods

Written informed consent was obtained from 15 healthy volunteers and 3 patients with brain metastases. A 20-gauge intravenous catheter was inserted into the subjects' forearms prior to being positioned supine and head-first in a GE MR750 3.0T MRI scanner (GE

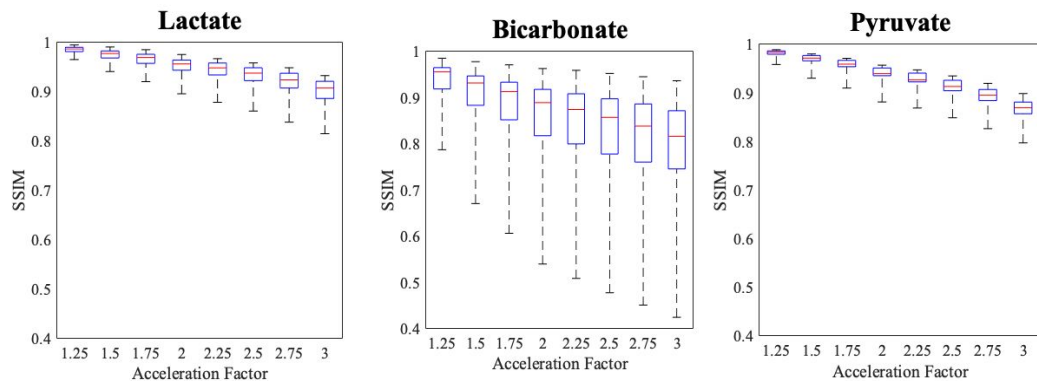


Fig 1. The similarity between the original image and the retrospectively undersampled image was measured using Structural Similarity Index (SSIM) as a metric. The average SSIM of 18 subjects across 100 trials at each acceleration was compared separately for lactate, bicarbonate and pyruvate metabolic brain EPIs. In the diagram, the red lines represent the mean, the upper and lower limits of the box that surrounds the red line represent the upper and lower quartiles, and the ends of the dotted line represent the upper and lower extremes of the SSIM values at a given acceleration.

Healthcare, Waukesha, WI). A home-made birdcage ^{13}C head coil placed over the subject's head was used to acquire ^{13}C -signals following the injection of HP $[1-^{13}\text{C}]$ pyruvate. The ^{13}C signal was acquired with spectral-spatial excitation² of lactate/bicarbonate/pyruvate resonances (sequentially) followed by a 3D dual-echo EPI (DE-EPI) readout³. Retrospective undersampling was performed at 8 different acceleration factors, each using 100 different sampling masks. Masks were generated to simulate a "pseudo-random raster" k-space trajectory⁴. Images were reconstructed using an annihilating filter-based low-rank Hankel matrix algorithm⁵. Reconstruction fidelity was quantified with structural similarity index⁶ (SSIM).

Results The SSIM comparing the original and undersampled images was obtained for each of the reconstructions. As the acceleration factors increased, the image fidelity decreased. Although most SSIMs of the same metabolite and acceleration factor were within a relatively small range, outliers could fall well below. This suggests that image quality will occasionally be poor using this undersampling technique. The SSIM of bicarbonate images had a notably lower fidelity than those of the lactate and pyruvate images, potentially attributable to the typically low SNR of bicarbonate brain images produced with injected HP ^{13}C . Treating an SSIM of 0.9 to indicate acceptable image quality, then the maximum allowable acceleration factors for pyruvate, lactate and bicarbonate images were 2.25, 2 and 1.25 respectively.

Conclusion Pseudo-random undersampling can allow for modest reductions in the acquisition times of 3D HP ^{13}C MRI. Extending undersampling into the temporal dimension may allow for further acceleration.

References 1) Lee CY, et al. *NeuroImage*. 2019. 2) Cunningham CH, et al. *J. Magn. Res.* 2008. 3) Geraghty BJ, et al. *Magn. Res. Med.* 2018. 4) Geraghty BJ, et al. *Magn. Res. Med.* 2017. 5) Lee D, et al. *Magn. Res. Med.* 2016 6) Wang Z, et al. *IEEE Trans. Image Proc.* 2004

Brain Structure Volume Analysis after Accelerated MR Imaging

Wallace Loos^{1,2}, Roberto Souza^{1,2}, R. Marc Lebel^{1,3}, and Richard Frayne^{1,2}

¹Radiology and Clinical Neuroscience, Hotchkiss Brain Institute, University of Calgary; ²Seaman Family MR Research Centre, Foothills Medical Centre; and ³General Electric Healthcare, Calgary, AB, Canada

Introduction: Deep-cascade networks have been proposed to reconstruct under-sampled magnetic resonance (MR) images. Under sampling decreases the amount of acquired data and is commonly used to speed up the MR image acquisition. However, a major drawback of deep-cascade networks is the blurring introduced into the images from under sampling of high k-space frequencies. Blurring can potentially compromise the quality of the segmentation of brain structures and consequently affect morphological analyses. In this work, we investigate the impact of a deep-cascade network on brain structure segmentation. We use information from previous scans on the same subject and speed-up factors $R = 10\times$, $15\times$, and $20\times$.

Material and Methods: Seventy-four (74) volumetric T1-weighted volumetric images collected on normal subjects at 3 T were used [43 volumes (11,008 slices) were used for training; 18 volumes (4,608 slices), for validation; and 12 volumes (3,328 slices), for testing]. Poisson-disc sampling was used to retrospectively under sample k-space by 90%, 94%, and 95% (corresponding to $R = 10\times$, $15\times$, and $20\times$). Reference images were computed using the inverse of the Fourier transform on the fully sampled k-space data (used only to evaluate the quality of the reconstruction). A deep-cascade network based on the WW-net [1] was trained from scratch over 50 epochs. The network, consisted of four U-nets and consistency layers, was used to initially reconstruct the under sampled data. Linear registration then was used to align the WW-net reconstructed images with images from the previous scan. A second network (single U-net), operating on the registered images, was used to enhance the reconstructed image (trained on the follow-up sampled as reference). The volume of three commonly reported brain structures (whole brain, cortex, and white matter) were estimated using Freesurfer. The error between the reference volume and the MR image reconstruction under different accelerations, with and without the enhancement from the second network, were calculated. A two-way ANOVA test (factors: brain region, reconstruction method) and paired t -tests was used with $p < 0.05$ as the threshold for statistical significance. Mean \pm standard deviation values were reported.

Results and Discussion: The enhanced reconstruction approaches decreased image blurring resulting in reduced error compared to the reference (Figure 1). Across all regions and acceleration factors, the average volume error with enhancement ($0.05\% \pm 6.58\%$) was smaller than the error with no enhancement ($-0.07\% \pm 9.27\%$). Significant variations by brain region ($p < 0.001$, ANOVA) were observed but not by reconstruction method ($p = 0.951$). A significant ($p < 0.001$) region-reconstruction interaction was also observed. The whole brain volume between enhanced and non-enhanced method was not significant ($p = 0.785$, paired t -test), but was statistically different for the cortex and white matter volume ($p < 0.007$).

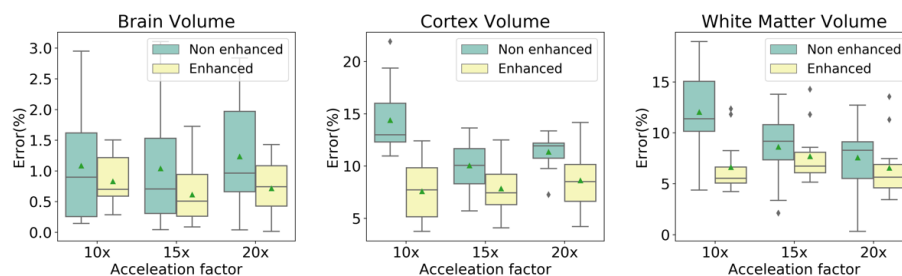


Fig. 1: Box plot of error on regional volume (non-enhanced and enhanced reconstructed images) compared to the reference volume for the whole brain, cortex, and white matter volume; and for different under-sampling factors ($R = 10\times$, $15\times$, and $20\times$).

Conclusions: The use of information from previous scans (enhanced method) decreased image blurring, improved brain segmentation and decreased error in whole brain volume estimation. Statistically significant differences, however, were found between measured cortex and white matter volumes.

[1] Souza, R., Frayne, R. A Hybrid Frequency-domain/Image-domain DeepNetwork for Magnetic Resonance Image Reconstruction, arXiv preprint arXiv:1810.12473, 2018.

Validation of a Preclinical Lipopolysaccharide Model of Neuroinflammation using the TSPO PET Radiotracer [¹⁸F]FEPPA

Vidya Narayanaswami, Junchao Tong, Christin Schifani, Peter Bloomfield, Michael Harkness, Armando Garcia, Kenneth Dahl and Neil Vasdev*

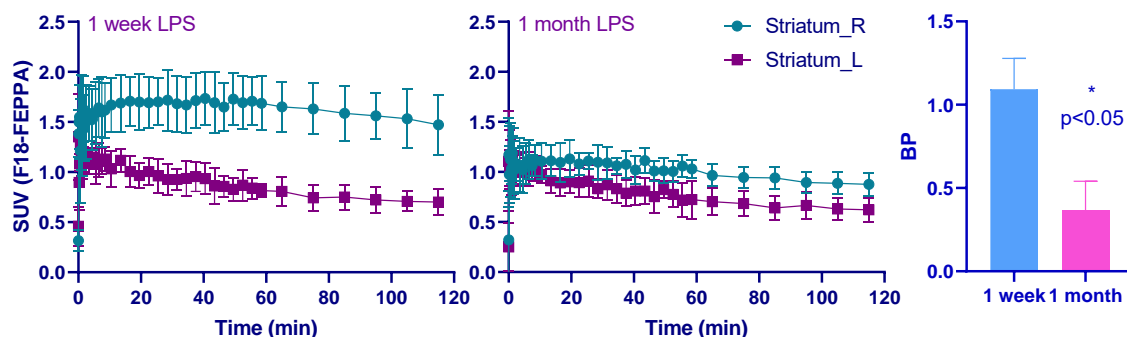
Azrieli Centre for Neuro-Radiochemistry, Brain Health Imaging Centre, Centre for Addiction and Mental Health, Toronto, ON

Introduction: Neuroinflammation is a dynamic and multicellular process that constitutes a viable target for the development of both diagnostics and therapeutics for psychiatric and neurodegenerative diseases. Positron emission tomography (PET) radiotracer development for neuroinflammation represents an active area of research with several emerging targets and radiotracers under various preclinical stages and clinical studies underway (Naryanaswami & Vasdev, et al, 2018). The most studied imaging biomarker of neuroinflammation is the translocator protein (TSPO). Our Centre developed and translated a second-generation TSPO radiotracer, [¹⁸F]FEPPA as a biomarker for neuroinflammation in clinical research. The goal of the current study is to apply this radiotracer to characterize a lipopolysaccharide (LPS) rodent model of neuroinflammation and extend this paradigm for evaluation of alternate PET biomarkers of neuroinflammation, including monoamine oxidase B (MAO-B) using [¹¹C]deprenyl or [¹¹C]SL25.1188, a putative biomarker of astrocyte activation.

Methods: An acute rat model of neuroinflammation was developed by injecting adult male Sprague Dawley rats (n=4) with LPS (50 µg/4 µL; flow rate of 0.5 µL/min) in the right striatum. Longitudinal multi-tracer PET/MR studies (Mediso nanoScan PET/MR 3T) were acquired at 1 and 4 weeks following the LPS injection. Dynamic PET images were reconstructed using a 2D-filtered back projection algorithm and regional brain time activity curves (TACs) were extracted using a stereotaxic MRI atlas (Schwarz et al, 2006) implemented in PMOD (v4.004). Standardized uptake values (SUV) were calculated by normalizing regional radioactivity for injected dose and body weight of the animal. Tracer binding potentials (BP) for the right striatum were estimated using simplified reference tissue model with the left striatum as the reference tissue.

Results: TACs extracted from the PET data demonstrated significantly increased [¹⁸F]FEPPA uptake in the right striatum compared to the left side with a peak BP of 1.1 at 1 week after LPS injection. The uptake in the LPS injected side decreased gradually over time as highlighted by a BP of 0.37 1-month post LPS injection. In contrast, a trend toward increased [¹¹C]deprenyl uptake was not observed until 2-4 week time point.

Conclusions: The LPS rat model of neuroinflammation may serve as a preliminary screening tool for benchmarking newly developed tracers targeted towards distinct neuroinflammatory mechanisms that develop at different time following the insult. Further studies are underway to extend this preclinical paradigm to alternate PET biomarkers including the MAO-B tracers [¹¹C]SL25.1188 and [¹¹C]deprenyl, to study astrocyte activation.



Novel Radiosynthesis of [¹¹C]Bexarotene for PET Imaging of Retinoid X Receptors in the Brain

Ian R. Duffy,^a Kenneth Dahl,^a and Neil Vasdev^{a,b,*}

^aAzrieli Centre for Neuro-Radiochemistry, Brain Health Imaging Centre, Centre for Addiction and Mental Health; ^bDepartment of Psychiatry, University of Toronto, Toronto, ON. *E-mail: neil.vasdev@utoronto.ca; Tel: +1-416-535-8501 ext. 30988.

Introduction: Carbon-11 (99.8% β⁺, *t*_{1/2} = 20.3 min) is a valuable radionuclide for molecular imaging with positron emission tomography (PET). While ¹¹C-methylation is by far the most prominent method employed for radiopharmaceutical production, novel synthetic methodologies that incorporate [¹¹C]CO₂ into radiotracers of interest for the preparation of ¹¹C-amides and ¹¹C-carboxylic acids are avidly sought.¹ Conversion of aryl boronic esters to [¹¹C]carboxylic acids has previously been achieved by copper(I)-mediated [¹¹C]CO₂ fixation² and our laboratory translated the first ¹¹C-carboxylic acid, [¹¹C]bexarotene, a retinoid X receptor (RXR) agonist, for preclinical use with this methodology.³ The use of aryl boronic esters however, have since afforded low yields (<1%) for the radiosynthesis of next-generation RXR agonists⁴ and has generally not been widely adopted. Motivated by the search for higher yielding and broadly applicable ¹¹C-carboxylation methods, we present in this work a novel copper(I)-mediated ¹¹C-carboxylation strategy employing organostannane precursors.

Methods: No carrier added [¹¹C]CO₂ was produced using a MC17 cyclotron (Scanditronix) by the ¹⁴N(p,α)¹¹C reaction and a gaseous target of N₂ (+ 0.5 % O₂). An oven-dried vial was charged with the appropriate copper(I) salt, followed by the sequential addition of solvent, base and organostannane. [¹¹C]CO₂ was then transferred to the solution using (*ca.* 10 mL/min) gaseous He. The reaction vessel was then sealed, and the solution heated to the desired temperature for five minutes, before being acidified with aqueous formic acid solution. The radiochemical identity and purity of the labelled products were then quantified using radioHPLC.

Results: The preparation of [¹¹C]benzoic acid was optimized as a model substrate with the following reaction conditions: temperature: 100 °C; time: 5 minutes; DMF (600 μL); [PhSnBu₃] = 0.1 M; [copper (I) thiophene-2-carboxylate] = 9.4 mM; and [*N,N,N',N'*-tetramethylethylenediamine] = 1.3 M. Evaluation of the substrate scope with several aryl- and heteroarylstannanes were next carried out: decay-corrected radiochemical yields (RCYs) of *ca.* 30–70% were obtained with arylstannanes (PhSnBu₃ and its corresponding *p*Me, *p*MeO and *p*CF₃ substituted derivatives). Formation of ¹¹C-carboxylic acids bearing 3-pyridyl, and 2-pyrazyl groups were successfully generated with RCYs between 32–34%, while transfer of electron-rich heteroarenes 2-furyl and 2-thienyl were generally lower (<3%). The method was successfully applied to the radiosynthesis of [¹¹C]bexarotene (Figure 1),³ wherein isolated formulations containing 155 mCi of activity, molar activities of up to *A*_m = 1700 mCi/μmol, and radiochemical purities >99% were obtained, corresponding to a decay corrected RCY of 32 ± 5% (n = 3).

Conclusion: A novel copper(I)-mediated carboxylation methodology for the preparation of aryl carboxylic acids has been developed. We envisage this method be broadly useful for the radiosynthesis of ¹¹C-carboxylic acids including RXR derivatives as well as other biologically active small molecules that have been radiolabeled for PET imaging.

References:

1. Rotstein, B. H.; Liang, S. H.; Placzek, M. S.; Hooker, J. M.; Gee, A. D.; Dolle, F.; Wilson, A. A.; Vasdev, N. *Chem Soc Rev.* **2016**, *45*, 4708.
2. Riss, P. J.; Lu, S.; Telu, S.; Aigbirhio, F. I.; Pike, V. W. *Angew Chem Int Ed.* **2012**, *51*, 2698.
3. Rotstein, B. H.; Hooker, J. M.; Woo, J.; Collier, T. L.; Brady, T. J.; Liang, S. H.; Vasdev, N. *ACS Med Chem Lett.* **2014**, *5*, 668.
4. Shibahara, O.; Watanabe, M.; Yamada, S.; Akehi, M.; Sasaki, T.; Akahoshi, A.; Hanada, T.; Hirano, H.; Nakatani, S.; Nishioka, H.; Takeuchi, Y.; Kabuta, H. *J Med Chem.* **2017**, *60*, 7139.

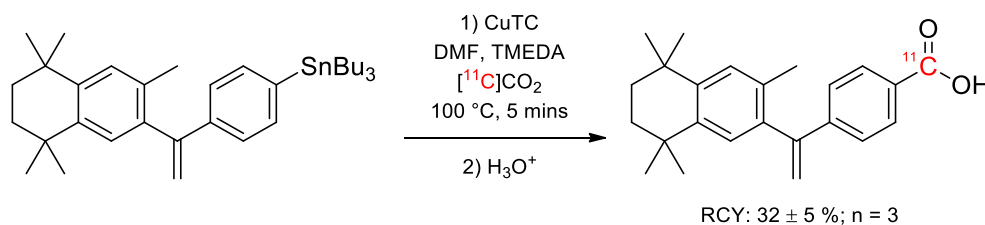
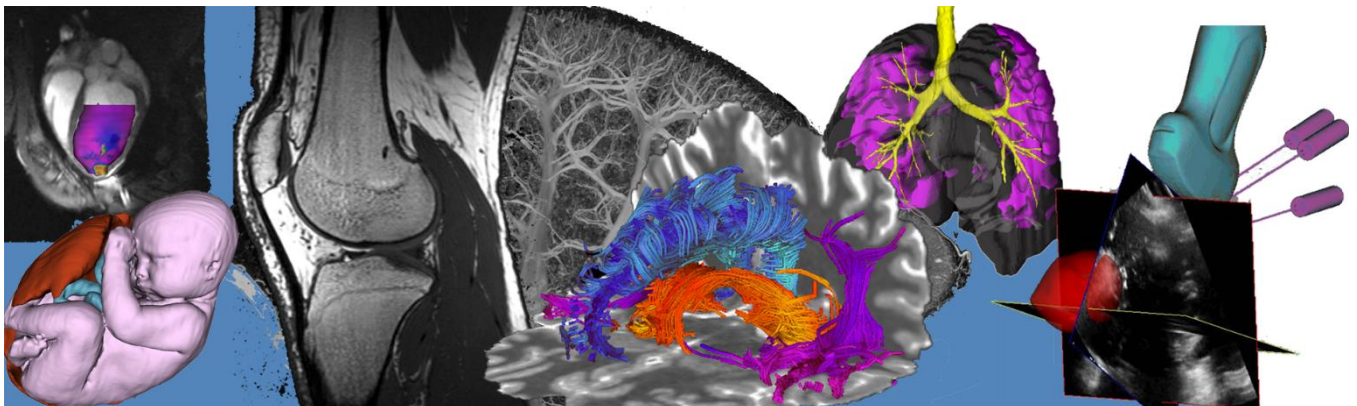


Figure 1: Novel radiosynthesis of [¹¹C]bexarotene

Poster Presentation Abstracts

Session 7: Musculoskeletal Imaging and Technology



Development of scaphoid kinematics using four-dimensional computed tomography

Sydney M. Robinson¹, Nina Suh^{2,3}, Emily A. Lalone^{1,2}

1: Department of Biomedical Engineering, Western University, 2: Roth McFarlane Hand and Upper Limb Centre, 3: Department of Surgery, Schulich School of Medicine and Dentistry, Western University

Introduction:

The scaphoid relies heavily on surrounding ligamentous structure for support to coordinate normal carpal kinematic behavior. In particular, traumatic injury of the scapholunate ligament (SLL) is known to lead to long-term degenerative arthritis, referred to as scapholunate advanced collapse (SLAC). Current diagnostic tools for SLL injuries are limited to radiographs and clinical examinations, which are unable to detect subtle bony movement abnormalities; in particular, the latter relies heavily on clinician experience and thus, is subjective. The radiographic imaging methods are unable to detect dynamic instabilities, which are early markers of scaphoid instabilities, but their detection could lead to earlier diagnosis and surgical intervention. However, four-dimensional computed tomography (4DCT) can capture abnormal bony movements and allows for quantification of carpal kinematics in real time. The purpose of this study was to use 4DCT as a method of measuring scaphoid kinematics, specifically the translation of its centroid during radio-ulnar deviation in a clinical setting.

Methods:

A participant with no history of wrist pain or injury was recruited from a tertiary care academic centre. The participant underwent unilateral imaging of the wrist using a 4DCT scanner while performing three cycles of radio-ulnar deviation (8 seconds each) beginning in radial deviation. Models of the scaphoid and radius were made in Materialise Mimics 22.0 for three frames of interest: maximum radial and ulnar deviation; and neutral, the position in which the long axis of the third metacarpal and that of the radius were parallel. The bones were registered using Python and transformation matrices were used using Matlab to describe the position of the centroid of the scaphoid in each kinematic frame relative to the position of the radius in the static frame.

Results:

Figure 1 shows the radius and scaphoid in the static frame, with points marking the centroid of the scaphoid in three kinematic frames: maximum radial deviation (red), maximum ulnar deviation (blue), and neutral (green). The scaphoid radially deviated $[-0.715, 7.67, -0.0647]$ mm and ulnarly deviated $[-19.5, -5.05, -0.655]$ mm from the neutral position in terms of the $[x, y, z]$ axes. The scaphoid translated further in ulnar deviation and the greatest magnitudes of translation were in the x - and y -axes for both radial and ulnar deviation.

Conclusion:

Previous studies have examined scaphoid translation and rotation in cadaveric model and have shown that the magnitude of displacement increases as the severity of injury increases. Otherwise, little has been done to quantify the kinematics of the scaphoid to better understand its mechanism of motion, especially in a clinical setting. These preliminary results show that 4DCT can be used to analyze scaphoid motion in vivo in a clinical setting. The results of this research, once completed, provides novel insight into the motion of carpal bones and how that motion changes in the presence of a scapholunate tear.

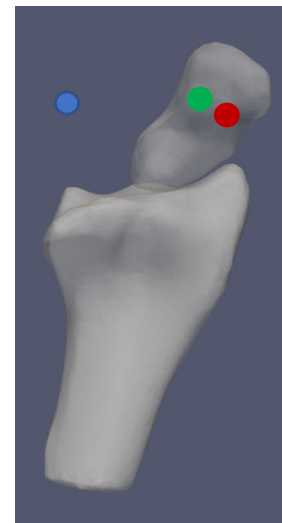


Figure 1: Radius and scaphoid in the static frame, with points marking the centroid of the scaphoid in three kinematic frames: maximum radial deviation (red), maximum ulnar deviation (blue), and neutral (green).

Four-Dimensional Computed Tomography Scans Allow Dynamic Visualization and Measurement of Scapulothoracic Joint Kinematics

Baraa Daher¹, George S. Athwal², Emily Lalone¹

¹Western University, London, ON, Canada, ²Roth McFarlane Hand and Upper Limb Center, St. Joseph's Health Care, London, ON, Canada

Introduction: The shoulder is the most mobile joint in the human body. Yet, measuring shoulder kinematics is challenging due to complex anatomy and functional complexity. The scapulothoracic joint of the shoulder describes the articulation of the concave anterior surface of the scapula as it slides over the convex surface of the thorax. Literature surrounding the characterization of this joint is limited and controversial. Some studies have considered this joint to be 'fictitious' or modelled it as 'fixed' in kinematic analysis. One of the many challenges faced when characterizing scapulothoracic motion is the difficulty in detecting/palpating anatomical landmarks and the limited use of static 3-dimensional (3D) imaging to measure complex motion. Therefore, the objective of this study is to use 4-dimensional computed tomography (4DCT) scanning to quantitatively evaluate scapular translation during active internal/external rotation.

Methods: A single healthy participant with no previous history of shoulder injuries was recruited for this study and underwent dynamic 4DCT imaging of their shoulder joint while positioned lying on their side with their elbow flexed at 90° using a GE Revolution CT Scanner. CT scans during active rotation were performed for eight seconds (producing 25 frames of images). The participant started with the shoulder adducted and internally rotated with palm flat on their abdomen (i.e. first frame). The participant was then instructed to move their hand from their abdomen, around the thorax, to rest the dorsum of the hand on their back (i.e. last frame). This is called internal rotation with arm behind back. Neutral CT frame obtained from the scan (i.e. frame 13), along with the first and last frames of dynamic motion, were used to reconstruct 3D models of the scapula and spine. The neutral scapula surface was matched with the scapula of the two frames using a surface based registration algorithm (ICP). Landmarks were placed on the trigonum, superior angle and third thoracic (T3) vertebrae of the spine as shown in Figure 1. Translations of the trigonum relative to the neutral position of T3 (medial/lateral) and the superior angle relative to its neutral position (posterior/anterior) were calculated using a MATLAB algorithm.

Results: Translation of the scapula was measured for first and last frame relative to the neutral frame. In the first frame, the trigonum moved 21mm laterally with respect to the T3, and the superior angle moved 19mm inferiorly with respect to its neutral position. In the last frame, the trigonum moved 19mm medially with respect to the T3, and the superior angle moved 17mm superiorly with respect to its neutral position.

Conclusion: The scapulothoracic joint is a mobile joint that contributes to the motion of the shoulder. Preliminary results suggest that the scapula translates with respect to the spine and glides across the thorax during shoulder motion and is not fixed. Figure 2 shows the neutral scapula (grey) and how the landmarks moved in the first and last kinematic frame (purple and blue). The technique of using 4DCT scans and a surface based registration algorithm can be used to better understand and measure the scapulothoracic joint kinematics in six degrees of freedom. Future work will develop a coordinate system and will model and measure joint translation and rotation over the full range of motion.

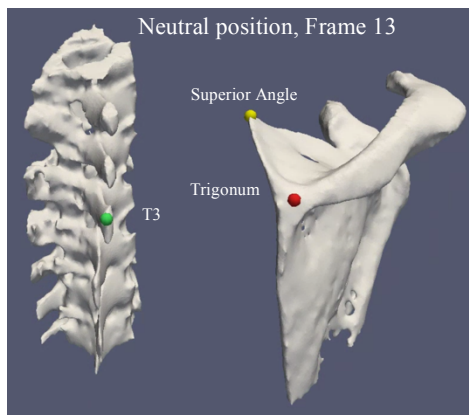


Figure 1: Landmarks used to quantify scapular translation during active internal/external rotation.

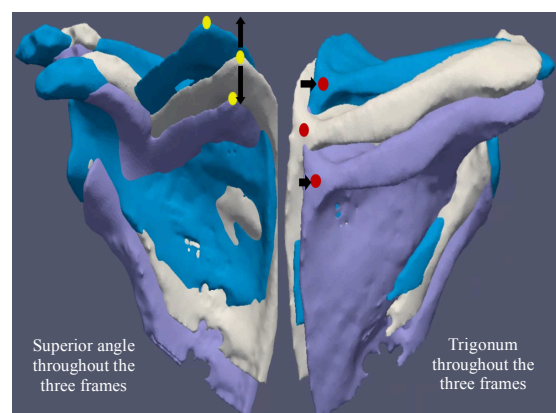


Figure 2: Scapular translation over the three frames

Deep Learning of Automatic Image Segmentation for TKR in Radiostereometric Analysis

Xunhua Yuan, Yingli Lu, Terry Peters and David Holdsworth

Medical Imaging Lab, Robarts Research Institute

Western University, London, Ontario, Canada

Introduction: Radiostereometric Analysis (RSA) is a clinical tool that has been used in orthopaedics for many years¹. It uses two radiographic views to detect 3D skeletal movements. Although it has high measurement accuracy, its application has been limited to use in research centers. One reason for this is that RSA is time consuming, as measurements are all completed manually. Developing a real time, automatic procedure would help to promote the use of RSA clinically and routinely. Stimulated by the recent successes of deep learning in medical imaging, we performed this pilot study, where we applied a deep learning model to make automatic RSA measurements.

Methods: A small X-ray dataset was created based on 100 manually segmented 2D images of total knee replacements (TKR) from Anterior-Posterior, Lateral and oblique views. A region of interest (ROI) on the image was cropped to focus on the anatomy of interest. The images were randomized to either a training, validation, or inference dataset, with the fraction of images in each dataset being 70%, 15%, and 15%, respectively. The input images and their corresponding segmentation maps are trained by U-Net² on the NiftyNet platform³. The loss function is a combination of dice and cross entropy⁴. Since training samples are small, data augmentation was applied with random spatial scaling and axes flipping. The study was performed on a PC workstation (CPU: Intel i7-7800x 3.5 GHz, GPU: Nvidia GTX Titan Xp, RAM: 64GB).

Results: The whole training and validation tasks took approximately 3 hours with 10000 iterations. At the inference stage, the segmentation was about 0.6 seconds per image. Overall, the segmentation accuracy of our approach achieved a Dice metric of 0.962 ± 0.046 .

Conclusion: This pilot study shows that the development of a new RSA procedure with automatic segmentation using deep learning is achievable and promising. To the best of our knowledge, this is the first-time deep learning has been used in RSA. Future works will be focusing on obtaining a large dataset to improve the segmentation accuracy, and extending our study from the knee joint to the other joints, such as the hip, shoulder, etc.

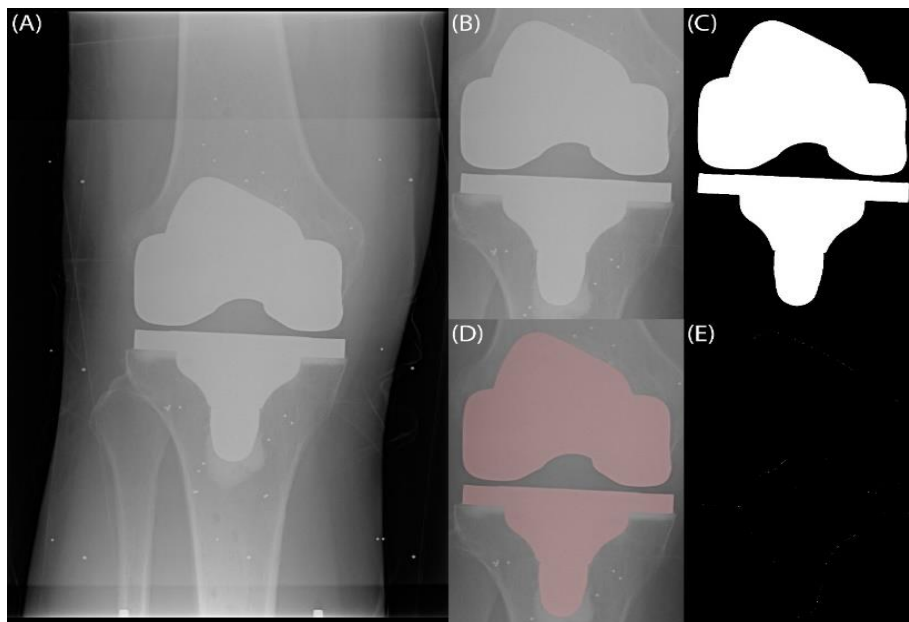


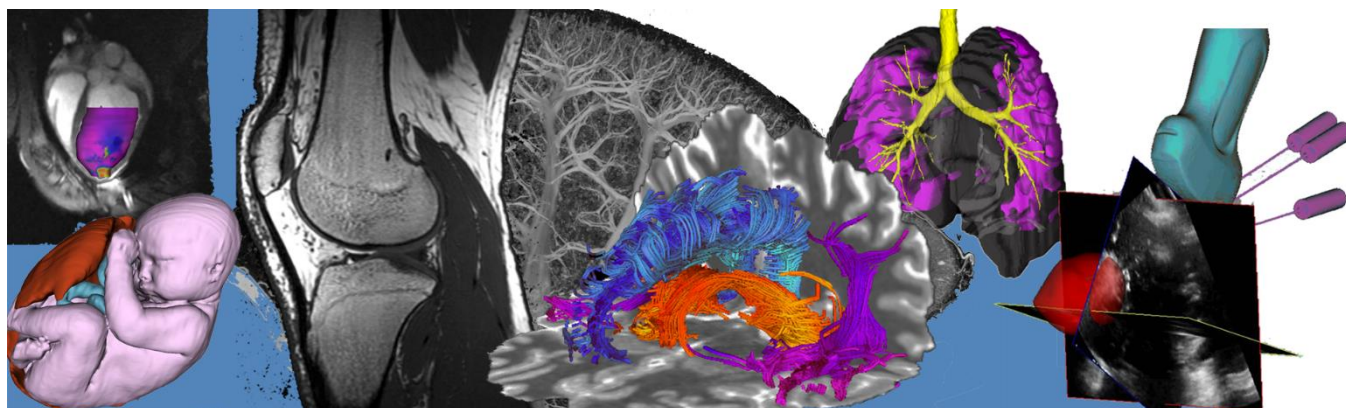
Figure 1

- (A) Original image
- (B) Cropped image
- (C) Manual measure
- (D) Auto-measure overlaid on the cropped image.
- (E) Difference of the auto-measure vs manual measure.

Reference: ¹Acta Orthop Scand Suppl. 1989. ²<https://arxiv.org/pdf/1505.04597.pdf>. ³Comput Methods Programs Biomed. 2018 May; 158:113-122. ⁴<https://arxiv.org/pdf/1809.10486.pdf>.

Poster Presentation Abstracts

Session 8: Cardiovascular and Vascular Imaging



Stroke thrombus RBC content and etiology prediction using R_2^* and susceptibility values *ex vivo* at 3TSpencer D. Christiansen,^{1,2} Junmin Liu,¹ Michael B. Boffa,³ and Maria Drangova^{1,2}¹Robarts Research Institute, ²Dept. of Medical Biophysics, ³Dept. of Biochemistry
Western University, London, Ontario, Canada

Introduction: Stroke is a devastating disease and the 3rd leading cause of death in Canada.¹ Stroke thrombus red blood cell (RBC) content has been shown to be associated with multiple valuable clinical parameters including stroke etiology² and response to tissue plasminogen activator³ and endovascular therapies (EVT).⁴ Histological examination is the standard method for determining RBC content, but can only be performed after a patient has been treated, and the thrombus retrieved, with EVT. MR imaging provides the opportunity to estimate thrombus RBC content non-invasively from measured imaging values; a previous study quantitatively predicted RBC content of blood clots *in vitro* using the ratio of R_2^* and quantitative susceptibility mapping (QSM) values.⁵ This study evaluates the application of R_2^* and QSM for prediction of RBC content as well as etiology differentiation (cardioembolism (CE) vs. large artery atherosclerosis (LAA)) in retrieved human stroke thrombi *ex vivo*.

Methods: Thrombus collection- 109 thrombi retrieved from EVT procedures completed at University Hospital on 65 acute ischemic stroke patients were collected between Feb 2016 and Nov 2017. Retrieved thrombi were kept in a plastic jar and scanned between 0.5 to 106 hours after retrieval, then fixed in formalin for histological examination. Stroke etiology was determined by hospital neurologists as part of standard care.

Imaging- Thrombi were scanned at 3T with a 32-channel receive head-coil using a custom dual echo-train 3D gradient echo sequence (TE1/ Δ TE/TE5 = 3.20/1.46/9.04 ms, TE6/ Δ TE'/TE10 = 16.75/7.15/45.35 ms, TR: 47.6 ms, resolution: 0.94x0.94x1 mm³, matrix: 192x192x32, BW: 142.86 kHz, flip angle: 10°, scan time = 4 min 58 sec). A co-registered steady-state free precession (SSFP) scan with identical resolution was also acquired.

Image post-processing- Channel-combined complex data were processed using the non-iterative B0-NICE⁶ and MEDI QSM⁷ algorithms to calculate R_2^* and QSM maps, respectively.

Histology- Eleven thrombi scanned within 6 hours of retrieval were selected for preliminary analysis (etiology: 5 CE, 4 LAA, 2 dissection). Histological sections (5- μ m thick) were stained with hematoxylin & eosin (H&E) to identify RBC, fibrin and white blood cell (WBC) content.

Analysis- Thrombi were segmented on the SSFP images and derived ROIs were used to calculate mean R_2^* and QSM values, which were used to predict RBC content following the equations defined in [5]. Corrections for partial volume and orientation effects were applied.⁸ H&E slides were analyzed using ImageJ to quantify RBC content.

Results: R_2^* , QSM and histology slices of a representative thrombus are shown in Fig. 1; qualitative correspondence is apparent between bright regions on R_2^* and QSM maps and RBC-rich regions in the histology slice. An example histology image at high magnification is shown next to its segmentation output in Fig. 2. A Bland-Altman plot showing the difference between MR-derived prediction and histological RBC content in all thrombi is shown in Fig. 3A; mean bias and absolute difference were -10.0% and 25.5%, respectively. For perspective, the published mean difference in RBC content between CE and LAA thrombi is ~15%.² Notably, this difference between CE and LAA thrombi was replicated in both the histological and MR predictions of RBC content in this study (14.0 and 15.3%, respectively; Fig. 3B).

Conclusions: In this preliminary study, 11 thrombi were analyzed and their histological RBC content was compared against an MR imaging derived prediction. Absolute prediction accuracy was low, but the difference between CE and LAA RBC content matched previous publications, suggesting predictions may still be prognostic of etiology as a relative score. Analysis of additional retrieved thrombi is required to solidify these conclusions, and is ongoing.

References: [1] statcan.gc.ca [2] Sporns PB et al. Stroke 2017. [3] Choi MH et al. Stroke 2018. [4] Hashimoto T et al. Stroke 2016. [5] Christiansen SD et al. J NeuroIntervent Surg 2019. [6] Liu J et al. Magn Reson Med 2015. [7] Liu J et al. NeuroImaging 2012. [8] Li J et al. Magn Reson Med 2012.

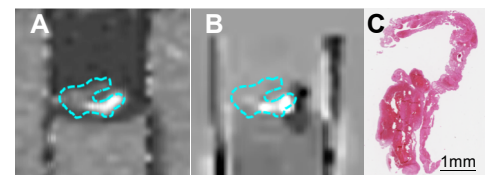


Fig. 1: (A) R_2^* , (B) QSM and (C) histology slice of a representative thrombus (cyan).

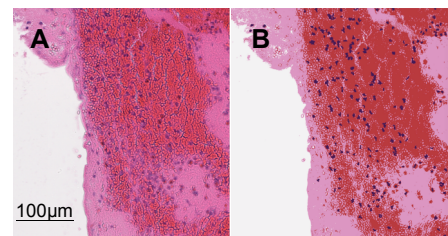


Fig. 2: Representative thrombus (A) H&E section and (B) segmentation output at 20x magnification (red: RBC, pink: fibrin, blue/black: WBC).

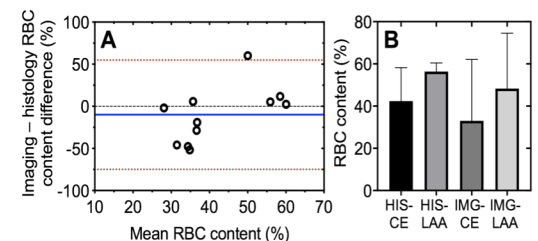


Fig. 3: (A) Bland-Altman plot of histological assessment and MR prediction of thrombus RBC content (blue: mean bias, red: 95% agreement). (B) Mean histology (HIS) and imaging prediction (IMG) of RBC content in CE and LAA thrombi.

Processing phase data from qT1 scans for the production of SWI-like vasculature maps: preliminary dataVishaal Sumra^{1,3} and Sofia Chavez^{1,2,3}¹Research Imaging Centre – MRI, Centre for Addiction and Mental Health, Toronto, ON, Canada²Department of Psychiatry, University of Toronto, Toronto, ON, Canada³Institute of Medical Science, University of Toronto, Toronto, ON, Canada**Introduction**

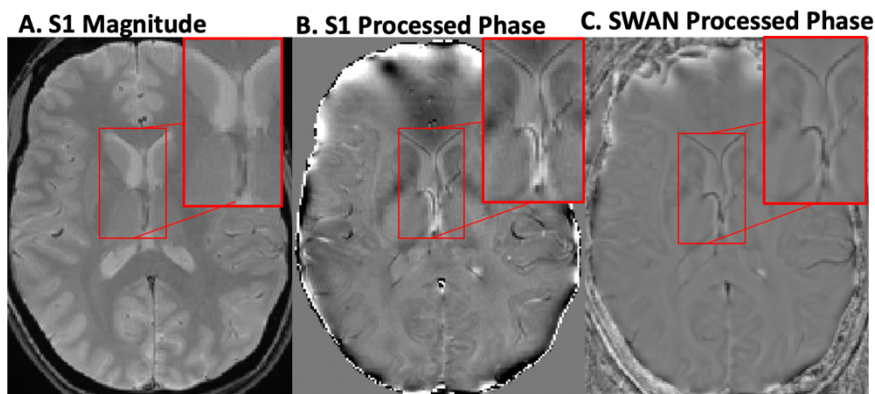
Quantitative T1 (qT1) maps can aid in the interpretation of volumetric studies that rely on the more arbitrary T1-weighted contrast¹. These maps can be created using magnitude information from a spoiled-gradient-echo (SPGR) sequence². Brain vasculature is commonly depicted in susceptibility weighted images (SWI), which rely on phase-based contrast induced by local changes in the magnetic susceptibility associated with the level of deoxyhemoglobin in venous blood³. Recently, an acquisition has been designed such that qT1 and SWI data can be acquired using the phase and magnitude from the same set of scans⁴. We aim to (i) use phase information from our standard qT1 mapping scans with an elongated echo time (TE), to produce SWI-like phase-contrast images of vasculature, and (ii) estimate blood T1 by examining highly vascularized areas on qT1 maps.

Methods

Two healthy volunteers were scanned in a 3T MRI scanner (MR750, GE Healthcare) according to the institutional REB. Data was acquired using our standard 3D qT1 mapping protocol⁵ (which includes B1 mapping scans) and a reference SWI was acquired according to scanner specifications (stock SWAN protocol, $0.5 \times 0.5 \times 2$ mm³, TE= 22.9 ms). Phase and magnitude were acquired for the two SPGR scans (1mm³) for qT1 mapping (proton density weighted, S1, and T1-weighted, S2) with an elongated echo time (TE = 11.6 ms). Images were co-registered and resampled using tools from FSL (FMRIB Software Library). Phase processing was done with MATLAB (The MathWorks, Inc., MA). Phase maps from S1 were resampled to ($1 \times 1 \times 2$ mm³) and high-pass filtered similar to SWI data³. Average T1 value in the identified vasculature was compared to literature values of blood T1⁶.

Results

Processed phase maps (Fig.1B) revealed vasculature that was not visible on the magnitude images (Fig.1A). The vasculature was confirmed through comparisons with SWAN images (Fig.1C). qT1 maps were in the same space and thus this allowed for simple extraction of blood T1 measurements. Within highly vascularized ROIs, voxels with phase less than -0.15 radians were found to correspond well to blood vessels. Using this phase thresholding within a cortical ROI of approximately ($66 \times 27 \times 10$ mm³) resulted in a mean qT1 of 1611 ms ($\sigma = 333$ ms), similar to reference values for blood T1 (approx. 1600 ms)⁶.

**Conclusions**

These preliminary results indicate that current qT1 maps are affected by the presence of blood due to the inconspicuous vasculature. Our novel approach enables the extraction of blood contributions to tissue T1 measurements. Our future research aims to investigate the confounding effects of vasculature on qT1 and volumetric studies through a caffeine-based manipulation of cerebral blood flow.

References

1. Lorio S, et al. Hum Brain Mapp; 37, 2016
2. Chavez S, Stanisiz GJ. NMR in Biomed; 25, 2012
3. Haacke EM, et al. AJNR Am J Neuroradiol; 30, 2009
4. Chen Y, et al. Magn Reson Imaging; 46, 2018
5. Chavez S. Proc. ISMRM. p 537, 2018
6. Lu H, et al. Magn Reson Med; 52, 2004

Assessing Myocardial Perfusion After Cardiac Irradiation Using Dynamic Contrast Enhanced Hybrid PET/MRI

O. W. Chau^{1,2}, O. El-Sherif³, M. Mouawad^{1,2}, G. Wisenberg^{1,4}, F. Prato^{1,4}, S. Gaede^{1,2,4}

¹Western University, London, ON, ²London Regional Cancer Program, London, ON, ³Mayo Clinic, Rochester, MN, ⁴Lawson Health Research Institute, London, ON

INTRODUCTION: Using hybrid PET/MR imaging, cardiac abnormalities, myocardium inflammation and coronary artery disease can be simultaneously assessed noninvasively with both imaging modalities in one single session. N-13 ammonia is a PET tracer which has 10 mins half-life suitable for rest and stress perfusion imaging. In the same imaging session, F-18 FDG PET tracer can be used for detecting inflammation but will significantly increase the total imaging time. Dynamic contrast enhanced MR (DCE-MR) can also be used for perfusion imaging and can be acquired simultaneously with the FDG-PET. However, a direct comparison between DCE-MR and N-13 Ammonia PET for measuring radiation-induced changes to myocardial blood flow (MBF) has not been reported. A previous canine study done in our lab demonstrated that hybrid PET/MRI can detect an increase in MBF with N-13 PET and was associated with a global inflammatory response after a low radiation dose exposure.¹ A new investigation was retrospectively performed on the DCE-MR perfusion data simultaneously acquired using a dual bolus gadolinium contrast injection technique. To accurately quantify the MBF parameters to assess myocardial condition, different curve fitting techniques for the tissue curves had to be evaluated. By comparing the similarity of MBF between the two imaging modalities, we can optimize the PET/MRI protocol for radiation treatment response imaging. Information gained from this study can be used to correlate with the administered radiation quantity to the degree and extent of injury. This will assist in treatment strategies designed to minimize cardiac damage and improve treatment outcomes of cancer patients receiving incidental cardiac dose.

PURPOSE: To determine the optimal curve fitting method for the Toft's model to accurately quantify and detect radiation-induced changes in myocardial blood flow (MBF) parameter, Ktrans, measured with dual bolus Gd-DTPA based Dynamic Contrast Enhanced (DCE)-MRI.

METHODS: Five canines received simultaneous N-13 Ammonia PET and dual bolus Gd-DTPA DCE-MR imaging at baseline, 1-week, 1, 3, 6, and 12-months after external beam irradiation targeted at the left anterior descending artery. Rest and adenosine-induced stress scans were conducted utilizing a fast gradient echo sequence on a Siemens 3T hybrid PET/MR scanner. The myocardium was contoured on the DCE-MRI dataset following a 17-segment-model. Since $MBF = K_{trans}/E$, where E is the extraction fraction, the left ventricle was selected as the arterial input function (AIF). The myocardial tissue curves were fitted in MATLAB using Toft's model for both dual bolus and separate bolus techniques. Ktrans from blood plasma to extracellular/extravascular space was then calculated. N-13 Ammonia PET defined MBF was also calculated using 1-compartment model in FlowQuant (Ottawa Heart Institute, Canada). Paired t-tests were used to compare MBF between DCE-MRI and N-13 PET for each curve fitting technique.

RESULTS: Statistical significance was observed between MBF obtained by separate bolus DCE-MR curve fitting technique and N-13 PET ($p < 0.05$) in all artery supplied regions under both rest and stress conditions. This indicated an AIF signal saturation effect. However, MBF obtained by the dual bolus DCE-MR technique was not statistically different than N-13 PET defined MBF ($p > 0.05$). Also, DCE-MR Ktrans rest and stress data trended differently after the 1-month timepoint.

CONCLUSION: Dual bolus curve fitting using Toft's model to determine myocardial Ktrans was necessary to accurately compute MBF with GD-DTPA MR imaging. However, we were not able to observe the same post- irradiation trends when comparing rest to stress MBF with both N13-PET and DCE-MR imaging.

1. El-Sherif O, et al, Am. J. Physiol. Heart. Circ. Physiol., 2019; 316(3):586-595

Evaluation of left atrial fibrosis in canines following irregular cardiac pacing using 3D late gadolinium enhanced CMR images

Farrag, Nadia A.¹, Thornhill, Rebecca^{2,1}, Prato, Frank S.³ & Ukwatta, Eranga^{4,1}

¹Department of Systems & Computer Engineering, Carleton University, Ottawa, ON, K1S 5B6

²Department of Radiology, University of Ottawa, Ottawa, ON, K1Y 4W7

³Department of Medical Imaging and Medical Biophysics, University of Western Ontario, London, ON, N6A 4V2

⁴School of Engineering, University of Guelph, Guelph, ON, N1G 2W1

Introduction: Atrial fibrillation (AF), the most common form of cardiac arrhythmia, is characterized by rapid and irregular beating of the atria and is associated with the presence of atrial myocardial fibrosis (MF). While the association between AF and MF is known, the causality of AF versus MF is yet to be fully understood. Atrial MF may promote persistent AF, however, MF may also be a consequence of a prior fibrillation process; and studies supporting the causality of both sides have been reported (Platonov, 2017). In this work, we aim to address this controversy in a canine model of AF, where MF burden is evaluated by 3D late gadolinium enhancement (LGE) cardiac magnetic resonance (CMR) imaging before and after pacing.

Methods: Twelve (12) canines (10 experimental, 2 control subjects) were imaged at 3T using 3D IR-FLASH LGE-CMR at baseline (i.e. before pacing) to establish a reference level of MF. Following baseline imaging, canines underwent surgery to insert a pacing device to induce AF over the course of 4 – 6 weeks. The pacing device was removed such that further 3D LGE-CMR imaging could be performed in-vivo. Following in-vivo imaging, canines were sacrificed such that 3D LGE-CMR imaging could be performed in-situ. Finally, the hearts were surgically extracted, such that ex-vivo LGE-CMR and histology imaging could be performed. Image processing of 3D LGE-CMR acquisitions were performed at baseline, in-vivo, and in-situ time points. The atrial chamber was manually segmented using 3D Slicer software. To generate LA myocardium segmentations, dilation and Boolean remove algorithms were applied using the Cardiac MRI Toolkit (Scientific Computing and Imaging Institute, University of Utah, 2019). To quantify MF, the LA wall voxel intensity was first normalized by dividing each voxel in the LA by the mean intensity of the left atrial blood pool. Atrial MF was quantified using an image intensity ratio (IIR) threshold $> \text{mean IIR} + 2 \text{ IIR standard deviations}$, and MF volumes were computed by multiplying the sum of the scar voxels by the voxel dimensions. To assess the evolution of LA enhancement, a landmark-based registration was performed to account for motion differences across different time points using the following landmarks: ascending and descending aorta, aortic arch, left and right pulmonary arteries, inferior/superior left and right pulmonary veins, left atrial/ventricular septum, LA appendage, left anterior descending artery, and aortic valve.

Results: Among the two control subjects, minimal evolution of atrial enhancement was observed over baseline and in-vivo time points (average computed enhancement volumes 4.68 mm^3 and 20.7 mm^3 , respectively). Among the experimental group, LA enhancement was observed across all time points for all subjects (average enhancement volume at baseline = 65.32 mm^3). Prominent LA enhancement was observed post-arrhythmia at the in-vivo time point in 8/10 canines (average enhancement volume of 256.25 mm^3).

Conclusions: 3D LGE-CMR imaging adequately demonstrates MF in the left atria of canines. MF is observed in canines before and after the occurrence of AF, however, fibrotic tissue increases significantly after AF is induced by irregular pacing. Further studies are required to better establish the relationship and causality of AF with MF.



Reconstructed 3D myocardial (white) and MF (green) volumes at baseline, in-vivo and in-situ time points of an experimental canine. MF is observed post-arrhythmia, increasing progressively across in-vivo and in-situ imaging.

Microstructural changes in the penumbra of cerebral small vessel disease lesions

K. Walker¹, J. Ramirez^{1,2}, H. Akhavein¹, M. F. Holmes¹, C. J. M. Scott^{1,2}, H. Haddad², P. McLaughlin², B. Levine², D. Kwan², M. Montero-Odasso², E. Finger², A. Lang², C. Tartaglia², J. Mandzia², B. J. MacIntosh^{1,2}, M. Freedman², S. Strother², M. Masellis^{1,2}, S. Symons², R. Bartha², R. H. Swartz^{1,2}, S. E. Black^{*1,2}, M. Goubran^{*1,2}

¹Hurwitz Brain Sciences Program, Sunnybrook Research Institute, ²ONDRI, *co-senior authors

Introduction: Previous studies report a spectrum of white matter injury in the penumbra (peri-lesional zone) surrounding white matter hyperintensities (WMH) in Alzheimer's disease (AD) patients [1] and older adults [2], as seen by diffusion tensor imaging (DTI). This has not yet been examined in lacunar infarcts or MRI-visible enlarged perivascular spaces (PVS) observed in cerebral small vessel disease (CSVD). Additionally, it is not known whether diffusion MRI metrics within the penumbra of vascular lesions are associated with cognitive performance.

Methods: 132 individuals were recruited from the cerebrovascular disease with and without cognitive impairment (CVD ± CI) cohort of the multi-site Ontario Neurodegenerative Disease Research Initiative (ONDRI) study. Lacunes, PVS and WMH were segmented using the SABRE-LE pipeline [2]. Their penumbra was created using a probability score map by adding lesion volume in the image around every non-lesional voxel and dividing by the radial distance in relation to that voxel. The probability map was then thresholded into peri-lesional Layers 1, 2 and normal appearing white matter (NAWM) based on the probability score across all non-lesional voxels. Diffusion data was corrected for bias-field inhomogeneities, eddy currents, and distortions. Tensor fitting was performed to obtain maps of fractional anisotropy (FA) and mean diffusivity (MD). Mean FA and MD were then extracted from the lesions, penumbra layers and NAWM of PVS, lacunes and WMH (both periventricular and deep). A linear model was fit to each subject's diffusion metrics to compute a gradient (slope) across layers from lesion to penumbra layer 2. Linear regressions were performed to assess associations with cognition accounting for age, sex and education.

Results: An analysis of covariance of FA and MD in the penumbra of periventricular lacunes (pLACN), deep lacunes (dLACN) and PVS revealed significant differences across layers ($p < 0.0001$). FA was lower in Layer 1 than in Layer 2 and NAWM ($p < 0.0001$) and MD higher in Layer 1 than in Layer 2 and NAWM in both PVS, lacunes and WMH ($p < 0.0001$).

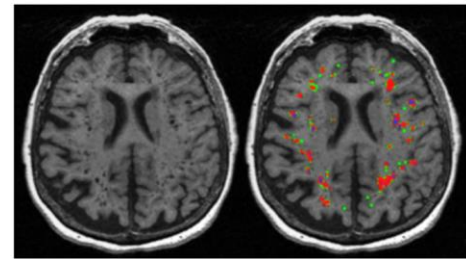


Figure 1. PVS penumbra (peri-lesional zone) segmentation showing lesion (blue) and peri-lesional Layer 1 (red), and Layer 2 (green).

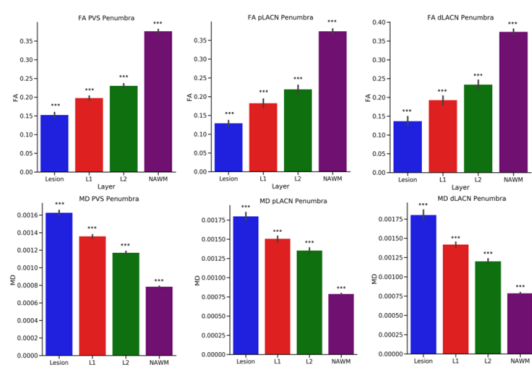


Figure 2. FA and MD in lesion, penumbra layers and NAWM of PVS, pLACN and dLACN ($p < 0.001$)

vascular lesions demarcated by structural MRI for lacunes and PVS. Furthermore, the pWMH changes appear to have clinical implications, as this was associated with processing speed. Future analyses will investigate the relationships between diffusion metrics in the penumbra of PVS with sleep measures, and those of lacunes with measures of stroke severity.

References: [1] Maillard P et al. Stroke. 45(6):1721-6 (2014) [2] Maniega et al. Frontiers in Neurology. 10:784 (2019) [3] Rameriz J et al. J Vis Exp. (86), e50887 (2014) [4] Vazzana R et al. J Am Geriatr Soc. 58(4): 719-723 (2010)

The gradient (slope) of FA and MD from periventricular WMH (pWMH) were associated with processing speed ($p < 0.001$, $p < 0.01$) as measured by the trails making test [3]. We observed a trending association between dWMH FA gradient with stroke volume ($p=0.07$). These associations were not observed when investigating diffusion gradients based on lesions and NAWM alone, without incorporating diffusion metrics from penumbra layers.

Conclusions: FA and MD were significantly altered in both layers within the penumbra of lacunes and PVS

compared to NAWM. These findings suggest that there are alterations in the white matter that extend beyond the

Carotid plaque progression prediction by U-Net

Qiong Liu,¹ Ran Zhou,¹ Melanie Jonnalagadda,² M. Reza Azarpazhooh,³ Samineh Hashemi,³ J. David Spence,^{3,4} Aaron Fenster⁴

¹Biomedical Engineering, Huazhong University of Science and Technology, Wuhan, Hubei, China;

²Medical Sciences, Western university, London, Ontario, Canada;

³Stroke Prevention and Atherosclerosis Research Centre, Robarts Research Institute, Western University, London, Ontario, Canada

⁴Robarts Research Institute, Western University, London, Ontario, Canada;

Introduction: Stroke is a serious neurological problem globally and is the third leading cause of death among North American adults¹. About 85% of strokes are ischemic, most being due to blockage of a cerebral artery by an athero-thrombotic embolus (consisting of either an embolus of a clump of platelet aggregates, or a fragment of plaque). Atherosclerosis at the carotid bifurcation is a major cause for the generation of thrombosis and subsequent cerebral emboli leading to stroke. Analyzing carotid plaque progression helps to identify patients at risk of stroke, helps to evaluate treatment effect, and requires a non-invasive imaging method. The clinical application of high-resolution ultrasound (US) imaging has been shown that it can be used for the visualization of carotid atherosclerotic plaques and monitoring changes in the area of the plaques at different timepoints.² The plaque area is quantified by delineating plaques in the US image, but manual segmentation of plaque boundaries is time-consuming, experience-based, and variable. Computer-aided segmentation is becoming more popular to solve this problem. In this project, we introduced a deep-learning method (U-Net) to segment carotid plaques from carotid US images automatically, and evaluated the progression of each plaque over time.

Methods: In this study, 180 patients from the Stroke Prevention Clinic and the Premature Atherosclerosis Clinic at the University Hospital, London were enrolled. 1162 plaques in US images with manual segmentation results were used as the training dataset. Regions-of-interest (ROIs) (width and height ratio=3:4) containing plaques were used for training (157 patients; 638 plaques) and testing (23 patients; 524 plaques). After the network was trained, model weights were saved for testing. The test results were compared with manual segmentation in terms of Dice coefficient, sensitivity, specificity, and accuracy.

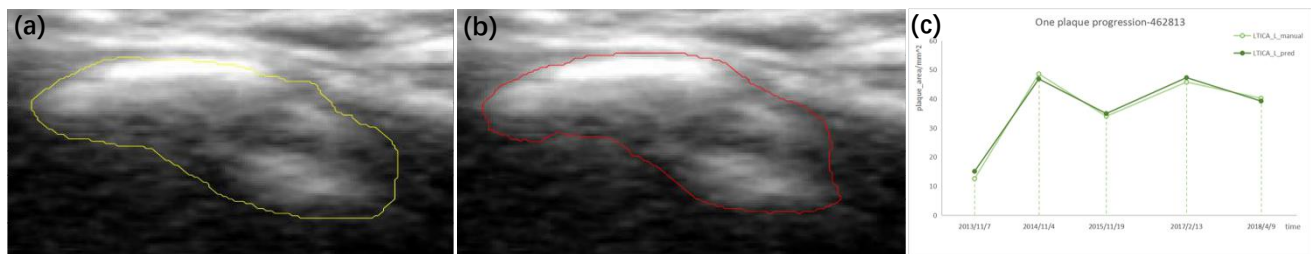


Figure 1. (a) Manual segmentation(yellow); (b) U-Net predicted segmentation (red); (c)Example carotid plaque progression

Results: The predicted plaque area showed a strong correlation with manual segmented plaque area, with a correlation coefficient of 0.923. The largest error was less than 5 mm². The average DICE was 86.47%. The average sensitivity, specificity, and accuracy were 89.44%, 95.60%, and 94.42% respectively. The average individual plaque segmentation time was 8.3±3.1 ms.

Conclusions: We used U-Net to segment carotid plaques in longitudinal carotid US images obtained at different timepoints. The high values of the testing results suggest that our automated and fast segmentation approach may be used clinically to monitor patients' carotid plaques and help to assess risk for stroke. Monitoring plaque progression automatically may have a significant clinical value for assessing atherosclerosis progression.

1. Thom T, Haase N, et al. Heart disease and stroke statistics - 2006 update - a report from the American heart association statistics committee and stroke statistics subcommittee. *Circulation*. 2006;113:E85-E151.
2. Spence JD, Rundek T. *Toward clinical applications of carotid ultrasound: Intima-media thickness, plaque area, and three-dimensional phenotypes ultrasound and carotid bifurcation atherosclerosis*. Springer London; 2011.

Acknowledgement: We acknowledge funding from CIHR for the computing infrastructure.

Comparison of Cartesian and radial phase contrast MRI for fetal blood flow measurement

Datta Singh Goolaub^{1,2}, Jiawei Xu³, Eric Schrauben², Liqun Sun³, Davide Marini³, Mike Seed³, Christopher K. Macgowan^{1,2}

¹Medical Biophysics, University of Toronto, Toronto. ²Translational Medicine, The Hospital for Sick Children, Toronto. ³Labatt Family Heart Centre, The Hospital for Sick Children, Toronto, Ontario, Canada.

Background

Phase contrast cardiovascular magnetic resonance (PC-CMR) is a standard clinical tool for managing fetal pathologies such as congenital heart disease (CHD) and growth restriction [1], [2]. Determining the optimal therapy needs accurate blood flow quantification. One challenge with fetal MRI is that fetal motion cannot be predicted or controlled, and motion compensation techniques are required to reduce motion corruption in the resulting flow quantifications. Feasibility of fetal through-plane PC-CMR using Cartesian sampling has been shown previously [3]. However, such measurements lack motion correction. The purpose of this study is to compare through-plane fetal flow measurements using Cartesian sampling with retrospectively motion corrected radial PC-CMR.

Methods

17 pregnancies (6 healthy, 4 small-for-gestational age and 7 with CHD) were imaged with informed consent. Cartesian and radial PC-CMR were performed on great fetal vessels. Scan parameters are in Table 1. Cartesian and motion-corrected radial reconstructions follow [4] and [5], respectively. Two reviewers graded the quality of the reconstructions on a scale of 0 to 4 and drew ROIs on the target vessels. The peak and mean flow values obtained from the two sampling techniques were compared using linear regression, Bland-Altman analysis and paired t-test (significance level of 5%).

Results

Example Cartesian and radial reconstructions are shown in Figure 1. The Cartesian image is corrupted by ghosting from maternal breathing while the corresponding radial image has more conspicuous vessels. A Wilcoxon signed rank test indicated that there was significant difference between Cartesian and radial scores ($p < 0.05$). Linear regressions for the peak and mean flows between the two techniques were (slope=0.95, $r^2=0.80$) and (slope=0.81, $r^2=0.67$) respectively. Bland-Altman analysis results (bias, limit-of-agreement) for the peak and mean Cartesian and radial flows were (-23.4mL/min per kg, [-214.5 167.8] mL/min per kg) and (-0.24mL/min per kg, [-76.2 75.8] mL/min per kg) respectively. The differences for the flow measurements were significant ($p < 0.05$) for vessels with a low Cartesian score of 0 or 1.

Conclusions

Repeating fetal Cartesian PC-CMR at the expense of increased imaging time and maternal discomfort does not always yield accurate reconstructions. The quality of the radial images was better. Radial PC scans allow for retrospective data rejection for bulk fetal motion and motion compensation for in-plane motions allowing for the measurement to be performed once.

References

[1] M. Y. Zhu *et al.* *AJOG*. 214(3) 367.e1:367.e17, 2016 [2] P. Porayette *et al.* *Prenat. Diagn.* 36(3) 274:281, 2016 [3] M. Seed *et al.* *JCMR*. 14(1) 79, 2012 [4] Prsa Milan *et al.* *Circ Cardiovasc.* 7(4), 663:670, 2014 [5] D. S. Goolaub *et al.* *JCMR*. 20(1), 77, 2018

Table 1. In-vivo acquisition parameters for Cartesian and Radial PC-CMR.

	Sequence	
	Cartesian PC-CMR	Radial PC-CMR
Scan Time (s)	22	17
Slices	1	1
Voxel size (mm ³)	1.3×1.3×5.0	1.3×1.3×5.0
TR/TE (ms)	6.8/3.0	5.8/3.4
Flip Angle (°)	20	20
Averages	1	1
Acceleration Factor (R)	2 (GRAPPA)	R ≥ 3
Views-per-segment	3	-
Encode vel. (cm/s)	100-150	100-150
Base Resolution	192 × 192	192×192 (1500 spokes per encode)

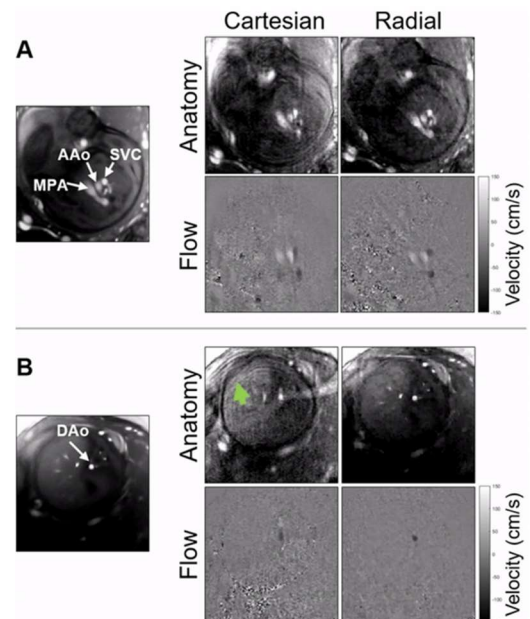


Figure 1: Fetal PC-CMR reconstructions for the superior vena cava (A) and descending aorta (B). The labels for the different vessels are shown on the right static images. The green arrow shows ghosting in the Cartesian reconstruction. A/DAo - ascending/descending aorta; SVC - superior vena cava; MPA - main pulmonary artery.

Co-registered cardiac ex vivo DT images and histological images for fibrosis quantification

Peter Lin^{1,2}, Anne L. Martel^{1,2}, Susan Camilleri-Newbigging³, Mihaela Pop^{1,2}

¹Medical Biophysics, University of Toronto; ²Sunnybrook Research Institute -Toronto; ³Lunenfeld Institute - Toronto, CA

Introduction: Scar-related sustained ventricular tachycardia (VT) is a major cause of sudden cardiac death [1]. Clinically, the chronic scar and VT substrate (harboured by heterogeneous fibrosis located at the scar periphery) are identified using contrast-enhanced MRI methods. The VT substrate has an intermediate MR signal intensity between healthy (H) tissue and infarct core (IC), and is named gray zone (GZ) [2]. However, these MR images do not provide myocardial anisotropy information, which is critical in evaluating tissue remodelling. In contrast, fractional anisotropy (FA) is a scalar metric calculated from diffusion tensor (DT) MR that describes the degree of diffusivity of water molecules in tissue [3], and could help us understand abnormal structure-function interaction in scarred hearts. Here we present a novel image analysis pipeline to study subtle characteristics of heterogeneous fibrosis in a pre-clinical pig model of chronic infarction, using histologically-validated FA maps.

METHODS: Myocardial infarction was generated in n=10 pigs and allowed to heal for 6 weeks. *Ex vivo* DT images of explanted hearts (fixed in formalin) were acquired using a 1.5T GE Sigma Excite scanner with the following MR parameters: TE=35ms, TR=700ms, b value=0 s/mm² for unweighted images, b=500 s/mm² for the 7 diffusion gradients, and 0.6×0.6×1.2 mm in-plane image resolution as in [2]. From each heart, one representative 4 mm thick slab was cut in short-axis orientation (matching one DT image and including H, IC and GZ tissues), stained with collagen-sensitive stain (Picrosirius Red) and digitally scanned. Histology images and FA maps were then overlaid in the open source software *Sedeen Viewer* [4,5] for manual affine registration using anatomical landmarks. Once registered, 3×3 MR pixel regions of interest (ROIs) were selected on the histology image for stain quantification in each zone (H, IC, GZ). We employed the *Stain Analysis* plugin in *Sedeen* to quantify tissue with a positive stain for collagen and to derive “% collagen” area per each ROI. Using our previous collagen-density grading system [2], this plugin was used to classify each tissue category as: either H (<20% collagen), GZ (20-70% collagen) or IC (>70% collagen). Lastly, once classified, the same ROI was imposed onto a FA map for calculation of mean FA per ROI using *DSI Studio* software (Labsolver, 2018) [6].

RESULTS: Figure 1 shows the workflow for quantitative analysis of co-registered FA maps and corresponding histology images, as exemplified in one heart slice. The bottom-right image illustrates an analyzed ROI showing pixels with a positive stain for collagen (red). The bottom-left image shows the corresponding ROI on the FA map as a gray-scale display of FA values between [0-1] across the image, where brighter areas (i.e., H zones) had higher anisotropy values than darker areas (i.e., IC). Figure 2 shows the resulting mean FA for the 3 zones categorized based on % collagen density: H (0.52 ± 0.12), GZ (0.43 ± 0.13) and IC (0.29 ± 0.17). We observed a significant difference in FA values between all 3 zones (one-way ANOVA, $p < 0.05$). Our results suggest that GZ has an altered anisotropy which can substantially contribute to a disturbed electrical wave propagation (i.e., reduced conduction velocity in GZ) and the genesis of dangerous scar-related VT.

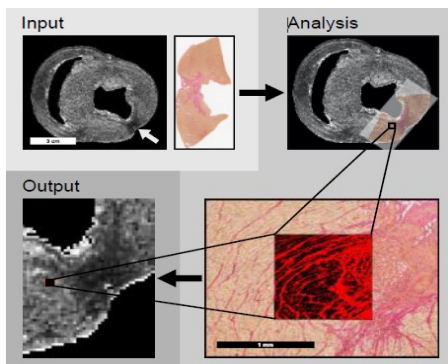
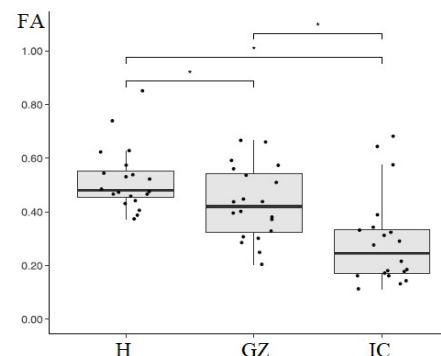


Figure 1 (left): Example of a co-registered histology digital image and the FA map for quantitative collagen analysis. Note: the white arrow points to the infarct scar.

Figure 2 (right): Results from the FA analysis. Mean FA values in the healthy, gray zone and infarct core myocardium illustrated using Tukey boxplot (* indicates a statistically significant difference, $p < 0.05$).

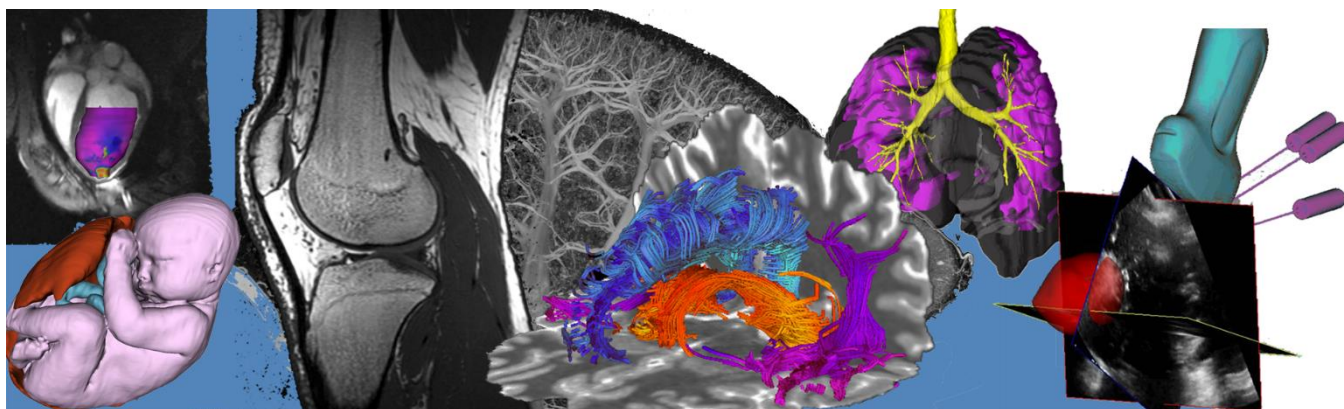


CONCLUSION: We successfully developed a robust image processing pipeline using co-registered DTI and histologically-classified ROIs, which allowed us to demonstrate that DTI-derived FA decreases significantly with the increase of collagenous fibrosis from H to GZ to IC, in agreement with histopathological findings. Future work will focus on using the pipeline to analyze structural features of fibrosis using *in vivo* MR images.

REFERENCES: [1] Stevenson W and John RM, *Circulation* 2011; [2] Pop M et al, *Phys Med Biol* 2013; [3] Wu E et al, *Mag Res Med* 2007 [4] <https://pathcore.com/sedeen/>; [5] Martel AL et al, *Cancer Research*, 2017; [6] <http://dsi-studio.labsolver.org>.

Poster Presentation Abstracts

Session 9: Instrumentation and Technology Development



Proposed Torsional Spring Calibration in Torque Measurement Method Described in ASTM F2213-17

X Ding¹, WB Handler¹, D Gignac¹, BA Chronik¹

¹ The xMR Labs, Physics and Astronomy, University of Western Ontario, Canada

INTRODUCTION: Amongst the safety concerns of commercial medical devices in the MR environment is static field induced torque. Similar to a compass needle aligning with Earth's magnetic field, long slender devices may align with the static field of an MR scanner. There are several internationally recognized test standards that regulate medical devices in the MR environment and the standard on induced torque, ASTM F2213-17, outlines five test methods^{1,2}. Three are pass/fail criteria and two are quantitative measurements. The 'Torsional Spring Method' is one such quantitative method and relies on a platform suspended by nylon threads under an adjustable tension capable of rotating with induced torque. The method outlined in ASTM F2213-17 states the induced torque, τ , to be the product of the torsional spring constant, k , and angular deflection, $\Delta\theta$ ^{1,2}. To effectively use this method, the spring needs to be calibrated to quantify k . In addition, due to the $\Delta\theta_{\max} = 25^\circ$ limit, the springs need to be adjusted an appropriate k . The latest version of the standard does not include a method for calibration or quantifying k values of the torsional springs, which is necessary for its use and calculating the torque.

METHODS: The following outlines a proposed method for calibrating the torsional springs by using standard masses and relies on a constructed apparatus (**Fig. 1**). Around the holding platform, there needs to be a groove so that a thread can be wound. The thread is connected to a weight holder into which, well-known pre-defined standard masses can be placed, the use of which eliminates the need for yet another measurement. The thread is then placed over a low-friction pulley so that the τ applied from the weight of the mass creates a $\Delta\theta$ in the holding platform. The τ from the mass is the product of the platform radius and the weight of the mass used, $\tau = mgr$, which in turn can be used to quantify k from the measured $\Delta\theta$ because $\tau = k\Delta\theta$ so therefore, $k\Delta\theta = mgr$. With

a desired k , the $\Delta\theta$ that would occur from the mass used is calculated and the platform-spring system is adjusted until the approximate angular position is achieved. Once the desired k has been calibrated, the ASTM published procedure can be performed for τ measurements.

RESULTS: The calibration and accuracy of $k = 0.3, 0.9, 1.5,$ and 2.1 mNm were calculated. These values were used to propagate the absolute and relative instrument uncertainties of the torsional spring method (**Fig. 2**).

CONCLUSIONS: The $\Delta\theta_{\max} = 25^\circ$ is restrictive of the the torsional spring method. Even more cumbersome, information on the type of springs used and how k is quantified are absent from the current standard. The proposed calibration schema for the springs allows the apparatus to be dynamically calibrated for the necessary range of torque measurements. Appropriate use depends upon choosing the right k which depends on the torque being measured. For small torques a large k results in a large error, so k would need to be reduced. Therefore, the torsional spring method, in spite of present limitations, can be used for a variety of devices by the calibration of the springs and it would be even better if the ability to calibrate the springs was built into apparatus. This work proposes such a method to enhance the utility of an internationally recognized test standard.

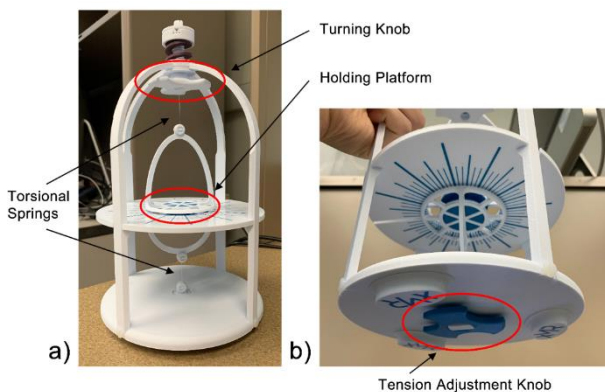
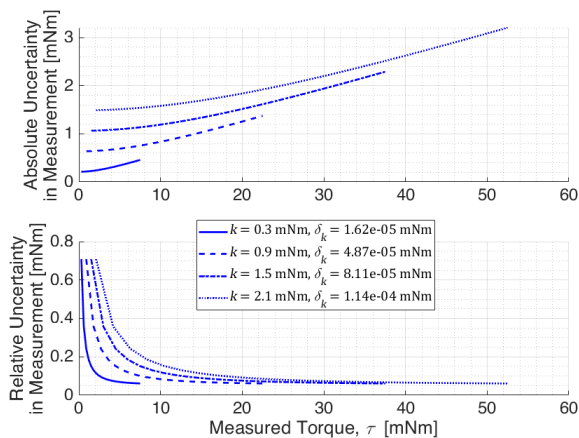


Fig. 1: a) Front and b) bottom views of a torsional spring apparatus based on ASTM specifications.



(top) and relative (bottom) uncertainties were propagated for the full range of measurable torques from 1° to 25° .

[1] Woods, T. O. (2007) *J Magn Reson Imaging*, 26, 1186–1189

[2] ASTM F2213-17 (2017)

Robust Retrospective Eddy Current Correction for Diffusion MRI

Jake J Valsamis, Corey A Baron

Centre for Functional and Metabolic Mapping, The University of Western Ontario

Robarts Research Institute, The University of Western Ontario

Department of Medical Biophysics, The University of Western Ontario

Introduction. Diffusion Magnetic Resonance Imaging (dMRI) has become an extremely powerful diagnostic tool for a variety of medical conditions ranging from ischemic stroke to liver cirrhosis [1,2].

Diffusion MRI uses large magnetic field gradients to sensitize the MRI signal to the diffusion of water. The application of large gradients generate transient eddy currents (ECs) in nearby conductive components of the MRI. These ECs generate their own magnetic fields that lead to distortions and blurring in dMRI images. Eddy currents consist of a spatially invariant term (B_0) and linear field gradient terms (G_x , G_y , and G_z), each of which can be described by the magnetic field gradient $G_{\text{eddy}} = A \exp\{-t/\tau\}$ [3]. Quantification of EC properties provides information into how the k-space trajectory was altered during acquisition, yielding the potential to retrospectively correct the erroneous trajectory to remove distortions from the data. The current gold standard for EC correction, FSL eddy, assumes that EC decay times are infinitely long, leading to simple affine distortions that are easy to detect and correct [4]. However, some advanced forms of dMRI, such as oscillating gradient dMRI, induce large ECs that decay over time. In this case, FSL's simplifying assumptions do not accurately reflect the experimental conditions, and considerable artefacts remain. Accordingly, we have recently developed a new approach to determine the decay time constants and amplitudes of the ECs from the data itself.

Methods. Pairs of images were synthetically generated assuming ECs with opposite polarity, which can be realized experimentally using opposite polarity diffusion gradients. This leads to distortions along opposite directions defined by EC terms with the same τ but opposite amplitude. Our method uses an optimization technique to find the EC parameters that minimizes the difference between each pair of corrected images (FIG 1).

Results. Since distortions were synthetically applied to dMRI data, the amplitude and τ of each EC term is known. FIG 2 displays the amplitude and τ that our method was able to recover for twenty sets of randomly generated EC distortions.

Conclusion. In contrast to FSL eddy, our method's capacity to find the amplitude and τ for each EC term provides a basis for correction regardless of how the EC decays. The synthetic application of ECs with the same magnitude but opposite direction as the initial distortions recovers the actual k-space trajectory, allowing image correction (FIG 1). This work has demonstrated the efficacy of our method using simulated data, and next steps will be to investigate its correction performance in actual EC corrupted oscillating gradient dMRI data.

References. [1] Feibach J, et al. (2002) *AHA*, 33:2206-2210. [2] Patel J, et al. (2010) *MRM*, 31:589-600. [3] Jezzard P, et al. (1998) *MRM*, 39:801-812.

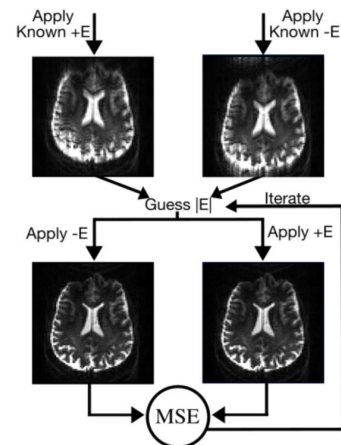


FIG 1: Eddy current (E) correction workflow, where MSE is the mean squared error between each image.

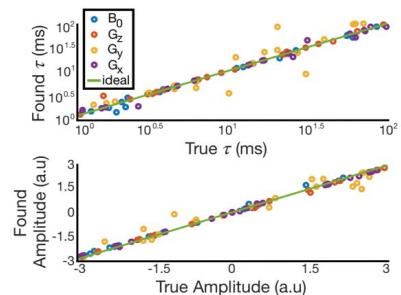


FIG 2: The recovered amplitude and tau of each eddy current term for 20 pairs of distorted images.

Test-Retest Reproducibility of *in vivo* Cortical GABA and Glx Measurements with MEGA-PRESSPeter Truong¹, Napapon Sailasuta^{1,2}, and Sofia Chavez^{1,2}¹Research Imaging Centre – MRI, Centre for Addiction and Mental Health, Toronto, ON, Canada²Department of Psychiatry, University of Toronto, Toronto, ON, Canada**Introduction**

Higher-numbered phased-array coils can provide significant increases in SNR, particularly in regions closer to the coil¹. Although magnetic resonance spectroscopy (MRS) is expected to benefit from increased SNR, field homogeneity is also an important factor, particularly for J-edited techniques such as MEGA-PRESS². In this study, we wish to assess the benefit of going from an 8-channel to 32-channel head coil for two cortical regions-of-interest (ROIs) which are expected to be most influenced by coil choice. In particular, we want to quantify the reproducibility of the MEGA-PRESS method for GABA+ and Glx (Glu+Gln) measurements in the Anterior Cingulate Cortex (ACC) and Left-Dorsolateral Prefrontal Cortex (Lt-DLPFC).

Methods

Scanning: Seven healthy participants (36±14 yrs; 4F, 3M) were recruited. All participants were scanned using a 3T GE MR750 scanner (GE Healthcare), first using the 32-channel head coil (Nova Medical), 32HC, followed by the 8-channel coil (GE Healthcare), 8HC. Two consecutive (test/retest) MEGA-PRESS GABA+ scans in the ACC and Lt-DLPFC (Fig.1) (TE/TR = 68 ms/1500 ms, 192 averages, 24 cc, 5:12 scan time) were performed with each coil.

Processing: MRS voxel-image co-registration was performed using Gannet3.0³ and SPM12 (www.fil.ion.ucl.ac.uk/spm/). The MRS voxel overlap between the two coils was calculated using FSL5.0-tools (FMRIB software library). IDL-based program XsOs-NMR⁴ were used to fit the GABA+, Glx, and water peaks of the difference spectra. The editing-OFF spectra were parsed and combined using an in-house script, which was then analyzed using LCMoel⁵. Reproducibility was computed as the percentage difference (relative to the average) between the test/retest measurements: %Diff.

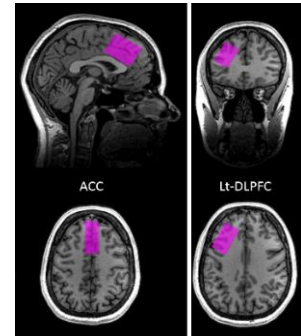


Fig.1 -Voxel placements

Results

MRS voxels were placed consistently across coils (average overlap >86%). There were no significant differences in tissue composition for all subjects ($p < 0.00001$). SNR gains were not as big as expected (3%-10%), particularly in the ACC, and slight increases in line width were observed with the 32HC. In general, 32HC MEGA-PRESS data (both GABA+ and Glx) had a lower %Diff compared to 8HC if the subjects did not move during the scans and if the %Diff was not already low (%Diff < 10%) in the 8HC (Fig.2). Water-scaled Glx results from LCMoel were reproducible (%Diff < 10%) in both coils in the ACC, but inconsistent in the Lt-DLPFC. From the difference spectra, Glx reproducibility was consistently low for the 32HC in both regions.

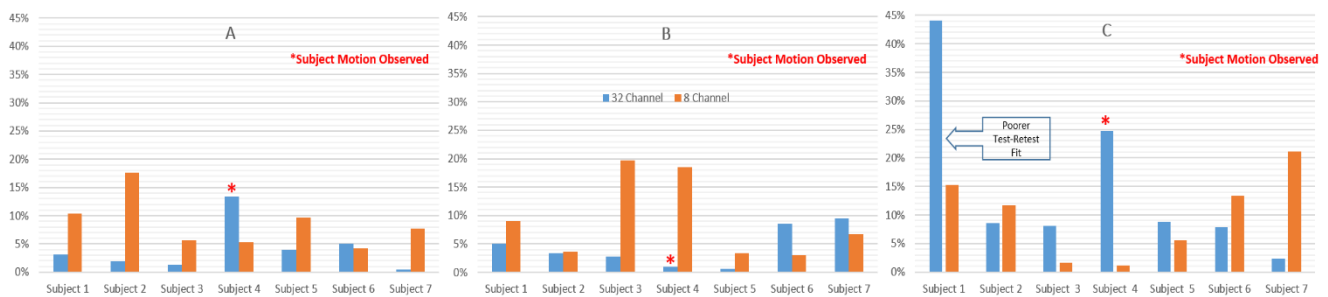


Fig.2 %Diff for 32HC and 8HC data in the Lt-DLPFC. **A.** GABA+/H₂O and **B.** Glx/H₂O processed from difference spectra with XsOs-NMR, and **C.** Glx water scaled data from editing-OFF spectra processed by LCMoel

Conclusions

The reproducibility of GABA+ and Glx measurements were improved when the 32HC was used instead of the 8HC although the extent of the benefit of using the 32HC varied with ROI. The results of the editing-OFF spectra analyzed through LCMoel generally were less reproducible compared to the difference spectrum fits, which were contrasting to van Veenendaal⁶.

References 1. Gruber B., et al. JMRI. 2018. 2. Mullins P.G., et al. Neuroimage 2014. 3. Edden R.A.E., et al JMRI 2014. 4. Shungu D.C., et al. NMR Biomed 2016. 5. Provencher S.W, NMR Biomed 2001. 6. van Veenendaal T.M., et al. MRI 2018

Measuring electric fields induced by an X-axis gradient coil in a tissue-mimicking ASTM phantom

Arjama Halder^{1,3}, Ali Attaran¹, Jack Hendriks^{1,2}, WB Handler^{1,2}, BA Chronik^{1,2,3}

¹The xMR Labs, ²Physics and Astronomy, ³Medical Biophysics, Western University, Canada.

INTRODUCTION: The electromagnetic interactions between implantable medical devices and various sub systems of MR scanners lead to potential hazards that can cause patient to have limited, to no access to an MRI¹. The ISO/TS 10974:2018¹ mentions one such potential cause of worry to be the electric fields resulting from the interaction between the MR scanner pulsed gradient fields and AIMDs (Active Implantable Medical Devices). Most of the studies performed to address device compatibility with the MR scanner that focuses on this issue, concentrates on designing different test platforms that mimics the dB/dt fields produced by gradients or developing test methods that allow electric field measurements without the need of generating dB/dt fields². Here we propose the use of an ultra-low frequency (frequency range of kHz) electric field probe to measure the actual variation of the electric field in a saline filled ASTM (American Society for Testing and Materials) phantom as a representation of a tissue-mimicking environment within a high-performance asymmetric head gradient coil outside of the scanner.

METHOD: To perform these measurements the ASTM phantom was filled with saline up to the height of 9 cm (conductivity of saline = 0.47 S/m) and placed within a gradient coil as shown in figure 1. For this set of measurement, only the X-Axis of the gradient coil was used, with the a sinusoidal current of 126 A at a frequency of 1 kHz. The ultra-low frequency electric field probe was held and moved by a robotic arm which allowed precise measurements at locations near the head region of the phantom. The probe was constructed using a 2 cm short dipole antenna followed by a 2-stage instrumentation amplifier and a differential amplifier that provided differential amplification and removed common-mode voltage respectively. This probe had a differential input impedance of $0.8||2$ (G $\Omega||\mu$ F), while the designed amplifier had a gain of 100 and a cut-off frequency of 31 kHz. Data was collected via a connection to an oscilloscope with a termination impedance of 1 M Ω using an RG58 cable. To remove the extrinsic influences in the measurements the saline solution was grounded.

RESULTS: Figure 1 show the measured and simulated results along a line $y = 0$ on 2 different yz plane that are about 3 cm off in either direction from the center of the phantom with the probe oriented in the z direction.

DISCUSSION: The experimental results show a considerable agreement with the simulated behaviour (performed using the quasi-static solver in Sim4Life, Zurich Med tech.) of the electric field given the sensitivity of the field measured. Future measurements will build upon this to explore the full extent of the phantom and the other gradient axes. Measurements will also be performed with an AIMD within the phantom. The results achieved from this study show possible commercial use of such a probe for conducting gradient induced electric field measurements in AIMDs within a scanner or a test platform.

CONCLUSION: ISO/TS 10974:2018 considers gradient induced extrinsic electric fields to a potential cause of worry for patients with AIMDs. The standard proposes radiated gradient immunity test to account for these effects. This research provides a supplementary test method that allows direct measurement of the variation in electric field using an ultra-low frequency electric field probe within an X-Axis gradient coil.

REFERNCES: 1. International Organization for Standardization. Assessment of the safety of magnetic resonance imaging for patients with an active implantable medical device. ISO/TS 10974. 2018;4. 2. Xin X, Chen XL, Sison S. A MRI Gradient Induced Electric Field Exposure System for Active Implanted Medical Devices. ISMRM. 2019; Abstract # 1440.

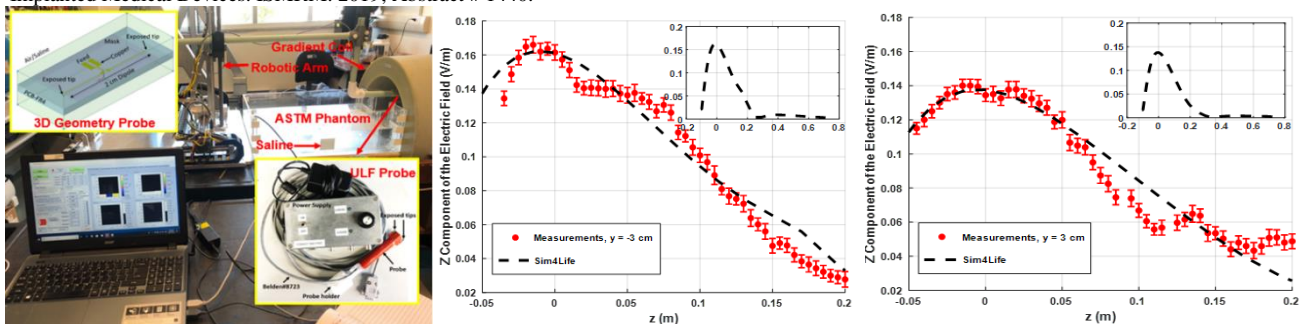


Fig. 1. The left plot shows the experimental setup. The middle and the right plot compares the measured with the simulated electric field along a line $y = 0$ on 2 different yz plane with the probe orientated in the z direction. The first yz plane is located 3 cm away in the negative direction from the center of the phantom. The second yz plane is located 3 cm away in the position direction from the center of the phantom. It can be seen from these plots that the peak point for the middle plot is higher than right plot suggesting an asymmetric electric field behavior within the phantom. The subplots in both cases show the overall simulated behavior of the field as a function of location.

Validation of commercially available quasi-static solvers in SEMCAD and Sim4life that simulates electromagnetic interactions between implantable devices and gradient coils in an MRI to assist device testing

Arjama Halder^{1,3}, Ali Attaran¹, Jack Hendriks^{1,2}, WB Handler^{1,2}, BA Chronik^{1,2,3}

¹The xMR Labs, ²Physics and Astronomy, ³Medical Biophysics, Western University, Canada.

INTRODUCTION: SEMCAD and Sim4Life are commercially used for device testing purposes, however, there are no validation studies performed that suggest the behavior predicted by these solvers are correct or consistent across different versions. The electromagnetic interaction between active implantable medical devices (AIMDs) and gradient coils, something that can be studied using these solvers, is a cause of concern as suggested in the ISO/TS 10974:2018¹, making it necessary to validate these solvers. Such a validation study will ensure that the behavior predicted by the solvers are accurate, allowing device testing companies to correctly identify the class of devices that require physical testing, which will effectively reduce operating expense and test time.

METHOD: For the purpose of this abstract a cylindrical phantom made up of acrylic material with a thickness of 1.33 cm, inner diameter of 22.8 cm and length of 30.9 cm was filled with saline (conductivity of saline = 0.47 S/m) up to the height of 10 cm and placed within a dB/dt exposure coil (essentially a Helmholtz pair) as shown in figure 1. The current applied to this exposure coil was sinusoidal in nature with a peak value of 80 A. Simulation studies were performed using low frequency magneto quasi-static solvers available in Sim4Life and SEMCAD. The vector potential generated within the dB/dt exposure coil was calculated using the Biot-Savart law in the

quasi-static regime. The solver used the curl of the vector potential to calculate the magnetic field and computed the electric field using tricubic interpolation. This electric field was perturbed due to the presence of a conducting phantom within the coil, as will be the case in the presence of any AIMD. This simulation study was validated with measurements performed using an ultra-low frequency electric field and a dB/dt probe that were constructed in the lab. The calibration factor associated with the electric and dB/dt probe are 2.64 (V/m)/V and 50 (T/s)/V respectively. Data from the probes were collected using an oscilloscope as the recording device, to determine the peak electric field and dB/dt at each location inside the phantom. To remove extrinsic influences on voltage changes observed in the measurements, the saline solution was grounded.

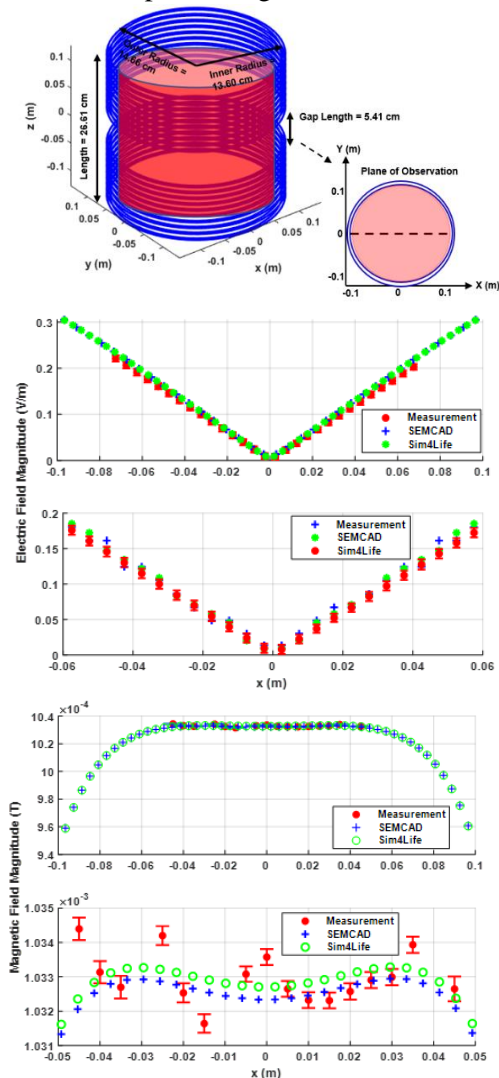
RESULTS: Figure 1 compares the measured with the simulated results of the electric and magnetic fields along the line $y = 0$ on the xy plane at the center of the coil.

DISCUSSION: Figure 1 suggests there is a strong agreement between the measurements performed and the simulated behavior for both electric and magnetic fields within the coil. The average percentage error for the electric and magnetic field experienced between simulation platforms and measurements is less than 10%. This allows us to conclude that these solvers can correctly map the electromagnetic environment within a gradient coil, thus providing a method to study the interactions between gradient coils and AIMDs.

CONCLUSION: This abstract aims to provide a validation study which suggest that these low-frequency quasi-static solvers available in Sim4Life and SEMCAD allow us to accurately simulate the electromagnetic interactions.

REFERENCES: 1. International Organization for Standardization. Assessment of the safety of magnetic resonance imaging for patients with an active implantable medical device. ISO/TS 10974. 2018;4.

Fig.1. (Top) shows the schematic of the experimental setup. (Middle) shows the electric field and (Bottom) shows the magnetic field measured and simulated results along the line $y = 0$ on the xy plane at the center of the coil.



An increased homogeneity design method for delta relaxation enhanced magnetic resonance systems

Matthew A. McCready¹, William B. Handler¹, Blaine A. Chronik¹

¹The xMR Labs, Department of Physics and Astronomy, Western University, London ON, Canada

INTRODUCTION: Delta relaxation enhanced magnetic resonance (dreMR) is a promising field-cycling based contrast-enhanced MRI method for quantitative molecular imaging. DreMR uses a B_0 insert magnet to shift the magnitude of the main magnetic field of an MRI as a pulse preparation phase of the pulse sequence. Using “activatable” MR probes —contrast agents which have strong longitudinal relaxivity (r_1) field dependence when bound, images can be subtracted to create images based upon bound agent only, with signal proportional to concentration of agent.¹ Many contrast agents such as *vivoTrax* and *Feraheme*, and activatable probes such as *Ablavar* experience higher field dependence at 0.5T than standard clinical field strengths (1.5T, 3T). This means that if imaging is done at a lower field strength, specifically at 0.5T, a dreMR insert can be developed with a high contrast resulting from a small field shift, decreasing the amount of current and number of windings required. To explore possible dreMR inserts for a new MR system at 0.5 T, a novel approach has been taken to improve upon previous designs by using the boundary element method (BEM)² to correct for field inhomogeneity in the dreMR system, resulting in a dreMR coil with greatly improved homogeneity to previous designs (which were approximately 5%).³

METHODS: Our approach begins by choosing the number of radial and axial windings (NR , NZ) of the outer solenoid required to bring us close to the desired field shift (ΔB_0). A mesh of regular triangles is created in a meshing program to use as a surface on which current can flow to correct the homogeneity. This surface is located just inside the solenoid radially and is intended to be constructed from finer wire than the hollow, water cooled solenoid, and be cooled by its proximity. In MATLAB, the wire pattern of the solenoid is used to calculate the field at random points (P) on a spherical surface with radius 75% that of the coil’s inner radius using Biot-Savart’s Law. Differences between the field at P and the field at the isocenter of the solenoid were then used as field targets for the BEM, to create a current density on the mesh that would negate these differences and thus homogenize the dreMR field. As a preliminary study of the design space, the diameter of spherical volume (DSV) with field inhomogeneity below 1% was found for each coil design by changing the number of windings radially and axially. Designs were evaluated based on their ΔB_0 and $DSV < 1\%$.

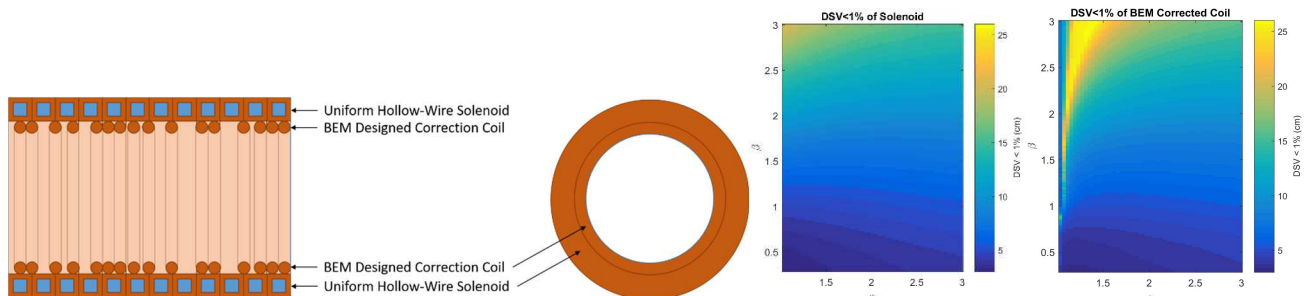


Figure 1 (Left). Cross sections of dreMR coil in YZ (left) and XY (right) planes. **Figure 2 (Right).** $DSV < 1\%$ for solenoid without (left) and with (right) correction coil for varying Fabry parameters α , β .

RESULTS: A grid search of solenoid windings showed that as the total number of windings (N) increased, ΔB_0 and $DSV < 1\%$ increased. While coils with many windings could be designed with strong ΔB_0 and high homogeneity, the weight and space requirements of such coils become strong limiting factors. Going forward the space available for a dreMR system and heating considerations will constrain designs, but it is important to note that the homogeneity in the imaging region of a field shifting coil can be greatly improved using the addition of a field correction layer.

CONCLUSION: Here we have outlined a new method for the development of homogenous field shifting dreMR insert coils, using the BEM to correct the field of a standard solenoid. It has been seen through simulation that such coils, if used in a 0.5T field strength MRI system, may produce significant signal from active MR probes and contrast agents for a small field shift, and thus greatly benefit from improved homogeneity.

REFERENCES: [1] Alford J, Rutt B, Scholl T, et al. 2009;61(4):796–802. [2] Harris, C. T. (2013). Electronic Thesis and Dissertation Repository. 1422. <https://ir.lib.uwo.ca/etd/1422>. [3] Harris C, Handler W, Araya Y, et al. *Magnetic Resonance in Medicine*. 2013;72(4):1182–1190. [4] Montgomery DB. *Solenoid Magnet Design: The Magnetic and Mechanical Aspects of Resistive and Superconducting Systems*. New York: Wiley; 1969.

Parametric Design of Focussed Collimator for Real-Time Intra-Operative Gamma Detection

Sydney Wilson^{1,2}, Hristo N. Nikolov³, Rob Stodilka^{4,5}, David W. Holdsworth^{1,2,6}

¹School of Biomedical Engineering, Western University, ²Faculty of Engineering, Western University, ³Robarts Research Institute, Western University, ⁴Department of Medical Imaging, London Health Science Centre, ⁵Department of Medical Imaging, Schulich School of Medicine and Dentistry, Western University, ⁶Department of Surgery, Western University, London, Ontario, Canada

Introduction: There has been a long-standing need to improve the standard of care for breast cancer patients, which includes novel techniques to identify tumour margins [1] and accurately localize sentinel lymph nodes (SLN) for biopsy [2]. Advancements to radiation-emitting labels have made it possible to specifically identify cancerous cells [3] and map drainage patterns surrounding a tumour to the SLN [2]. It is possible to fabricate complex objects with current techniques in 3D metal printing, which is ideal for designing a focussed gamma collimator (FGC) with high geometric efficiency that could accurately detect gamma radiation from a small region of interest during surgery.

Methods: The proposed FGC design is modular consisting of a focussed collimator insert and an exterior ring to house the insert and gamma counting electronics. Computer-aided design (CAD) for the FGC insert was completed using an open source design software (Blender 2.79 with Sverchok addon). A parametric node tree was created for a convergent close-packed hexagonal collimator insert. The parametric tree allowed for easy modifications to the design through various user inputs: hexagon radius, septal thickness, collimator height, top/bottom outer radius of insert, and focal length. To maximize collimator efficiency, the septal walls were tapered in proportion to the scaling factor of the focal point. Limitations of the manufacturing process dictated that septal thickness had to be a minimum of 160 μm . The compact collimator insert was designed to have a height of 20 mm, a focal point 35 mm below the collimator face, and a truncated conical shape with a base radius of 13.45 mm and a top radius of 8.55 mm. Two different hexagonal diameters were manufactured in order to perform collimator resolution and efficiency tests. Hexagonal radii of 1.155 mm and 1.833 mm were chosen, consistent with a design constraint of a grid ratio of at least 10. The exterior ring was designed in TurboCAD to hold the collimator insert and create a visual guide for the focal point of the gamma probe. All components of the FGC were 3D printed using laser powder-bed fusion of a cobalt-chrome alloy (AM400, Renishaw plc).

Results: The parametric and modular FGC allowed for collimators with varying parameters to be quickly redesigned and inserted into the existing exterior ring mechanism. The FGC was designed to have geometry which was optimal for manufacturing through 3D metal printing. The geometric transmission efficiency, defined as the fraction of open area to total surface area of collimator face, was calculated to be 72% and 80% for the 1.155 mm and 1.833 mm hexagonal radii, respectively.

Conclusions: Parametric design and fabrication of a highly focussed gamma collimator with large geometric transmission efficiency, approximately double that of existing gamma collimators, was possible through 3D metal printing. Future work will focus on 3D metal printing of the FGC insert in metals with higher attenuation coefficients (eg. tungsten) to improve the collimation specificity for typical high energy intra-operative gamma emitters such as Technetium-99m. The proposed FGC is unique in that it can collect gamma rays at a specified focal point below the collimator surface, allowing the compact FGC to be integrated with ultrasound imaging to provide a complete real-time intraoperative image guidance system for tumour resection and SLN identification.

References: 1. D. Dumitru *et al.*, "Novel techniques for intraoperative assessment of margin involvement," *Ecancermedicalscience*, vol. 12, p. 795, 2018.
2. S. Usmani *et al.*, "Evaluation of the Gamma Probe Guided SLNB and the Blue Dye Technique in the Management of Breast Cancer," 2009.
3. J. F. Valliant, "A Bridge Not Too Far: Linking Disciplines Through Molecular Imaging Probes," *J. Nucl. Med.*, vol. 51, no. 8, p. 1258-1268, 2010.

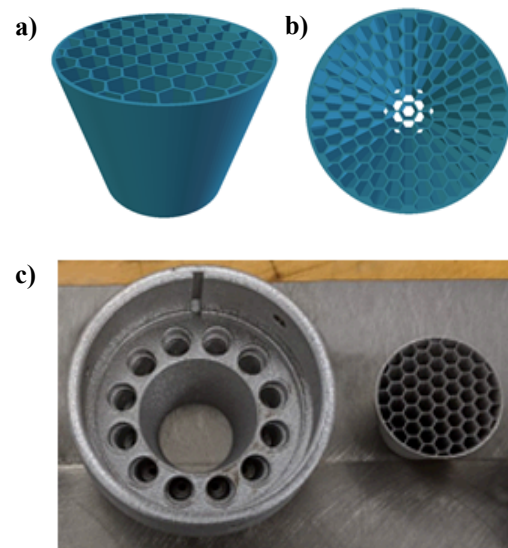


Fig. 1: (a) CAD model of FGC insert with a hexagonal radius of 1.833 mm. (b) Top view of FGC insert with hexagonal radius of 1.155 mm. (c) 3D metal printed cobalt-chrome exterior ring (left) and close packed hexagonal FGC insert with 1.833 mm hexagonal radius (right).

Transurethral light delivery for photoacoustic imaging of porphyrin contrast agent in prostate mimicking phantoms

Nidhi Singh^{1,2}, Yohannes Soenjaya², C. Felipe Roa^{1,2}, Gang Zheng^{1,3}, Brian C. Wilson^{1,3}, F. Stuart Foster^{1,2}, Christine E.M. Demore^{1,2}

¹Medical Biophysics, University of Toronto, Toronto, Ontario, Canada, ²Sunnybrook Health Sciences Centre, Toronto, Ontario, Canada, ³University Health Network, Toronto, Ontario, Canada

Background, Motivation and Objective

Prostate cancer (PCa) in most cases, is a multifocal disease but several studies have suggested that the largest, or ‘Index Lesion’ predominantly determines the natural history of disease. Photothermal Therapy (PTT), a focal therapy that selectively ablates index lesions in prostate while sparing majority of the prostate gland, delicate neurovascular bundles and urinary sphincter, offers an effective alternative to radical prostatectomy. However, these treatment approaches need accurate index lesion delineation and real-time image guidance. We are investigating photoacoustic (PA) imaging combined with a transrectal micro-ultrasound (micro-US) as a means of achieving both high optical contrast and high spatial resolution for guiding focal therapies in the prostate. Prior work indicated deeper illumination is required to obtain useful PA images of the prostate. The PA image can also be enhanced with improved imaging depth and by using PA contrast agents, for example organic porphyrin-lipid porphyrin (PS) nanoparticles that have enhanced uptake in tumours [1]. Here we introduce and evaluate a transurethral (TU) illumination system combined with PS contrast agents for improved PA imaging depth in tissue mimicking phantoms.

Methods and Materials

Fiber design and imaging system: A side-fire TU light delivery is designed to deliver light through the urethra into the prostate. A 1.5 mm core multimode optical fiber is flat cleaved and polished. A 3 mm X 3 mm right angled prism is used to divert the light sideways at an angle of 90°. Light beam from a tunable Nd:YAG laser (Vevo LAZR, VisualSonics, Toronto, ON, Canada) is coupled into optical fiber with a coupling efficiency of ~70%. The LASER pulses with 5mJ per pulse energy generated a fluence of 160 mJ/cm² at 2 mm from the surface of the fiber tip. A 256-element, 20 MHz linear array transducer is used to receive the acoustic signals and to display beamformed PA images at a frame rate of 5 fps.

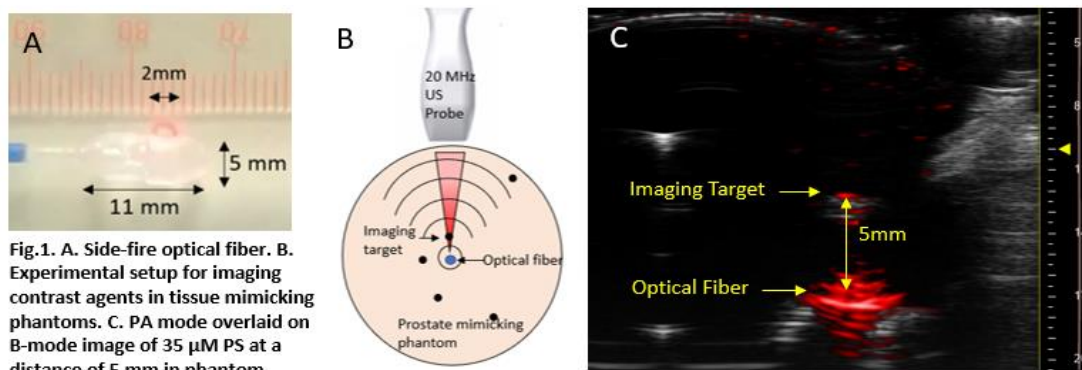
Phantom Studies: Tissue mimicking phantom is made from PVC-Plastisol. The optical fiber is placed in the central lumen and polyurethane (PUR) tubes are inserted at an incremental distance from the central lumen in the range from 3 mm to 15 mm. 350 μM stock solution of parent porphyrins (p-PS) is diluted to varying concentrations in the range (35 μM to 135 μM) with PBS and injected in the tubes.

Results/Discussion

PA and B-mode images localized PS contrast to all PUR tubes for contrast agent concentration > 135 μM. We were able to detect 35 μM concentration of PS at 10 mm but SNR at lower concentrations needs more investigation and optimization of the phantom. These results are promising for TU illumination of the prostate and future translation to imaging PS nanoparticles in tumours to delineate lesions for focal therapy.

References

- [1] C. S. Jin *et al.*, “Nanoparticle-Enabled Selective Destruction of Prostate Tumor Using MRI-Guided Focal Photothermal Therapy; Nanoparticle-Enabled Selective Destruction of Prostate Tumor Using MRI-Guided Focal Photothermal Therapy.”



Micro-CT Derivation of the Relationship Between Visceral Adipose Tissue and Whole-Body Adipose Tissue in Rats and Mice

Joseph U. Umoh,¹ A. Burke,² E. Turley,² C. Norley,¹ S.I. Pollmann,¹ J. Dunmore-Buyze,¹
T. Appleton,³ M. Drangova,^{1,4} M. Huff,² and D.W. Holdsworth^{1,4}

Ontario Pre-Clinical Imaging Consortium

¹Preclinical Imaging Research Centre, Robarts Research Institute, ²Depts. of Medicine and Biochemistry,

³Depts of Physiology and Pharmacology, ⁴Depts. of Medical Biophysics and Surgery,

Western University, London, ON, Canada

Introduction: Adipose tissue stores energy and provides insulation for some organs. However, the accumulation of excess visceral adipose tissue is linked to different risks of obesity or diabetes. Research interest in adipose tissue is growing not only because investigators are seeking solutions to the problem of obesity but also because of the realization that adipose tissue in human is a potential reservoir of adult stem cells¹, which could be used in tissue repair and engineering. Clinical research in adipose tissue often begins in rat and mouse models. In this study, the mass of visceral adipose tissue (VAT) in the abdominal cavity and whole-body adipose tissue (WAT) were measured from micro-CT scans in rats and mice. While WAT measurement is easily automated, VAT quantification requires manual segmentation and is time consuming. Our objective is to derive an empirical relationship between VAT and WAT in both rat and mouse models, which will enable VAT to be easily estimated from WAT in these animals.

Methods: Fifty rats and 80 mice (male and female) were used in this study. The animals were imaged using a *GE Locus Ultra* micro-CT scanner, with the same scan protocol and reconstruction parameters: x-ray tube voltage 80 kV, tube current 55 mA, 1000 projections, exposure time 16 s, and 154 μm 3D image voxels. Using the 3D micro-CT images, the abdominal cavity was segmented out for each animal. Lower (-380 HU) and upper (-30 HU) image threshold values of the adipose tissue were determined from the histogram plots of the whole animal image values. A software utility was written to compute volume and mass of the adipose tissue. Volume was calculated using pixel values between the two thresholds; and mass was calculated by multiplying the volume by a pre-determined density (0.90 g cm^{-3}) for adipose tissue.² Using the image of the whole-body, the program computed the mass of WAT for each animal. Similarly, using the segmented image of the abdominal cavity, the program computed the mass of VAT (Fig. 1). Linear regression analysis was performed between VAT and WAT to determine their relationship.

Results: Linear regression analysis between VAT (V) and WAT (W) showed (Fig. 2) that the two quantities could be expressed as $V = aW - b$, where a and b are constants. For rats (subscript r), $a_r = 0.43 \pm 0.01$ (std error) and $b_r = 8.96 \pm 1.19$ and for mice (subscript m), $a_m = 0.35 \pm 0.01$ (std error) and $b_m = 0.71 \pm 0.10$. For both rats and mice $R^2 = 0.97$ and $p < 0.0001$. The root-mean-square error between the model and observations was 3.1 g for rats and 0.2 g for mice.

Conclusions: This study has derived a functional relationship between the mass of visceral adipose tissue and that of the whole-body adipose tissue in both rats and mice. Knowing the mass of a whole-body adipose tissue (which is more readily computed using threshold segmentation), this relationship could be used to predict the mass of visceral adipose tissue.

References: [1] Zuk *et al.* *Mol. Biology of the Cell* 2002; 13: 4279-4295.
[2] Granton, P., Norley, C., Umoh, J., Turley, E., Frier, B., Noble, E., and Holdsworth, W. *J. Appl Physiol* 2010; 109: 1162-1169.

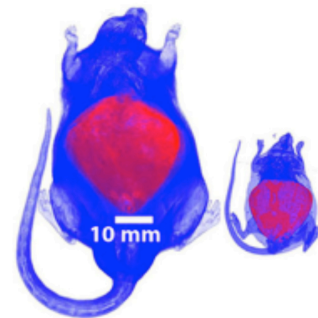


Figure 1: Micro-CT image-rendering of a whole-body (face-up) rat (left) and a mouse (right) showing the mass of visceral adipose tissue (red) and the rest of the adipose tissue (blue).

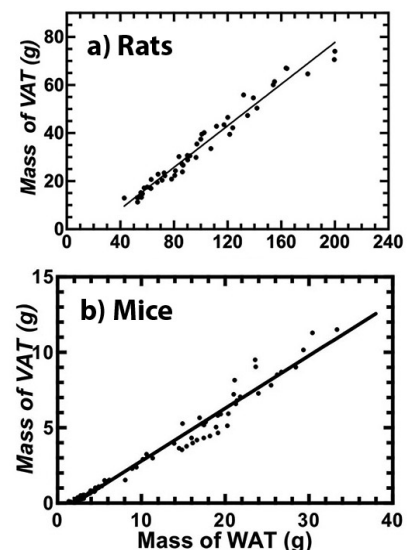


Figure 2: Plot of the mass of the whole-body adipose tissue (WAT) against the mass of the visceral adipose tissue (VAT) showing the linear regression line for (a) rats and (b) mice.

Fabrication of anthropomorphic maxillofacial and forearm phantoms from patient scans using 3-dimensional printing technology for medical imaging and dosimetry

Sawyer Badiuk^{1,2} M.Sc., David Sasaki² M.Sc. MCCPM, Daniel Rickey^{1,2} Ph.D. MCCPM.

Department of ¹Physics & Astronomy University of Manitoba, ²CancerCare Manitoba, Winnipeg MB.

Introduction: To provide quality patient care it is ideal to use anthropomorphic phantoms for imaging evaluation, training and dosimetry. However, these phantoms are quite costly. Consequently, they also often lack diversity in patient type and represent an average patient. Three-dimensional (3D) printing excels at producing models of complex objects such as spines and have been used to produce phantoms. However, the radiographic properties, e.g., computed tomography (CT) number of body tissues, are not well reproduced. 3D-printing materials, epoxy resin and polyurethane rubbers were evaluated and modified by adding high- or low-density additives to generate radiographic properties that mimicked various body tissues. The results were then applied to fabricate anthropomorphic imaging phantoms from patient CT scans that simulate body tissues for training and dosimetry.

Methods: Samples printed using stereolithography (SLA) printer technology were evaluated to establish CT numbers simulating various body tissues. Commercial resins (FormLabs, Somerville, MA) were subsequently modified by adding calcium carbonate (CaCO_3) and strontium carbonate (SrCO_3) powders or glass bubbles to alter the radiographic properties as needed. Epoxy resin and polyurethane rubbers were modified in a similar fashion for use as adhesives and fillers. A maxillofacial phantom was designed that included the patient's anatomy from the cervical spine (C4 vertebrae) to midway through the orbits and contains a cavity in the approximate anatomical location of the trachea for insertion of an ion chamber for dose measurements. A forearm phantom was designed that extends from mid-forearm to midway through the wrist. Both phantoms were examined with planar x-ray and CT (including dual energy CT), with the maxillofacial phantom undergoing additional cone-beam CT and panoramic imaging used in dentistry.

Results: Commercially available resins were found to have a CT number near 100 HU. Adding CaCO_3 and SrCO_3 powders to the resin raised the CT number to 1900 HU, while adding glass bubbles decreased the CT number to 15 HU. Phantoms contained simulated muscle printed with a resin containing glass bubbles (60 HU), bones printed with resin containing CaCO_3 and SrCO_3 powders (1200 & 1500 HU) and intervertebral discs and skin printed with a commercial resin (100 HU). 3D printed bones were filled with polyurethane rubber with a CT number of 40 HU was modified by adding either glass bubbles to simulate bone marrow (-60 HU) or CaCO_3 to simulate trabecula (200 HU). Phantoms were assembled with epoxy resin modified by adding glass bubbles for both construction and as a cartilaginous material. Glass bubbles were added to polyurethane rubber to simulate soft tissue that was used as a filler material between the various printed parts.

Conclusion: SLA printing technology offers a tremendous capacity to generate anthropomorphic phantoms with materials that mimic the radiographic properties of body tissues. Imaging showed good contrast and that the printed structures depict the anatomy, were free of defects and had suitable alignment. However, soft tissues showed small air bubbles in both x-ray and CT images. Dental images acquired of the maxillofacial phantom exhibited that the phantom was oriented properly, contained sufficient anatomy, showed good contrast between tissues and fit a 6cc ion chamber securely. This study demonstrated that a maxillofacial phantom mimicking anatomy and radiographical properties of a patient can be constructed using 3D printing technologies. Furthermore the designed phantom models, material modification method and assembly process can be easily applied to generate phantoms that better represent diverse patient types (different size, anatomy, chamber cavities) with materials that simulate the radiographical properties of tissues.



Figure 1. Maxillofacial phantom: Assembled internal 3D printed parts including mandible, spine (C1-C4 vertebrae with intervertebral discs) and maxilla. (A) Planar x-ray image acquired at 80kV. (B) Sagittal CBCT image with 6cc ion chamber inserted. (C). Forearm phantom: 3D printed forearm muscle printed with white resin modified by adding glass bubbles. (D) Planar x-ray image acquired at 60kV. (E)

Title: Gadolinium Detection in Liver & Kidney Phantoms Using X-Ray Fluorescence

Authors: Mélodie Cyr, McMaster University; David Chettle, McMaster University & Fiona McNeill, McMaster University

Author Affiliations: Radiation Sciences Graduate Programs, Department of Physics and Astronomy, McMaster University

Introduction:

Gadolinium (Gd) is commonly used in contrast agents to improve magnetic resonance imaging. Gd based contrast agents (GBCAs) help distinguish between healthy and diseased tissue, improving tumour imaging. GBCAs were thought to be stable and clear from the body through excretion after administration. However, they have been found to dissociate and remain in organs such as the liver, kidneys, and bone (Lord, M, 2019). The minimum detection limit (MDL) of Gd in bone has been found to be 0.87ppm. This study is to find the MDL of Gd in liver and kidney to optimize the detection system previously used for bone eventually to use it in a portable clinical setting (Lord, M, 2019).

Methods:

A non-invasive K x-ray fluorescence (K-XRF) detection system utilizing a clover-leaf detector formation to improve the detection limit is the detection method used. The detection system was altered to detect Gd in the liver and kidney of a human body. In these studies, a cadmium-109 (Cd-109) source with a relatively low activity of 0.78GBq irradiated a human body water phantom as well as liver phantoms with Gd concentrations ranging from 0-100ppm. The Gd used was standard for ICP in 2% nitric acid. The MDL was calculated from 5-hour measurements, which were used to predict the MDL for a stronger source, a more realistic measurement time of 30 minutes and associated dead time. Liver phantom measurements with varying overlaying tissue thicknesses from 6mm-26mm were investigated. An MDL was determined for overlaying tissue thickness with the 6mm phantom data. The water phantom contributed to dead time, therefore dead time was investigated at several distances with measurement times of 10 minutes and varying distances from 5mm-45mm.

Results:

At present, the K-XRF detection system can detect the Gd in the liver phantoms. The MDL for the cloverleaf system for liver in a water phantom is 7.5ppm. The MDL variation with tissue overlay is still being determined. Currently, the detection of Gd is by using an invasive method involving surgery. This detection is non-invasive and is able to detect low concentrations of Gd in the liver phantom. Several changes were made to the Gd peak analysis calculation. Gd emits two $K\alpha$ x-rays, $K\alpha_1$ is 42.996 keV and $K\alpha_2$ is 42.308 keV. A t-test was used to analyze the significance of the variation of the ratio of the amplitudes of the two peaks with depth. The t-test was not significant; therefore the peak amplitude ratio does not vary significantly with depth, within the 6mm to 26mm range investigated, and they can be tied together in the analysis and essentially analyzed as one Gd peak.

Conclusion:

This detection system can measure Gd in liver phantoms and has low MDL's, confirming that it has potential usefulness. Future work will focus on measuring kidney phantoms with varying Gd concentrations and varying overlaying tissue thicknesses. Eventually, these experimental results could be compared with simulations using Monte Carlo methods.

Miniature C-Arm Simulator Using Wireless Accelerometer Based Tracking

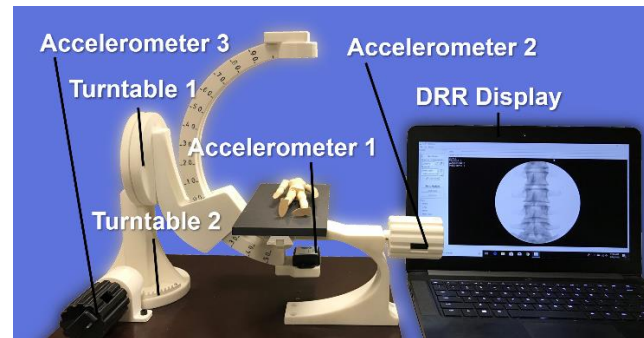
D.R.Allen, J.Moore, A. Joschko, C. Clarke, T.Peters, E.C.S.Chen

Robarts Research Institute, School of Biomedical Engineering, Western University

Purpose: The C-Arm has enabled minimally-invasive procedures to be performed under real-time image guidance. These procedures require extensive training on how to manipulate the C-Arm in order to produce the desired images. Standard training requires physical access to a C-Arm and exposes the trainee to prolonged radiation [1]. To provide a hands-on radiation-free means of training, we propose a miniature C-Arm simulator using wireless accelerometer-based tracking.

Methods: The C-Arm model was 3D-printed and fixed with wireless Bluetooth® Inertial Measurement Units (IMU's) to track the orientation of the C-Arm head (3 Degrees of Freedom (DoF)) and position of the table (1 DoF). The Digitally Reconstructed Radiographs (DRRs) were generated in real-time using a 1-dimensional transfer function and the tracked orientation of the C-Arm head. A user study was conducted in order to evaluate the efficacy of the simulator as a training tool. 20 medical residents (10 control, 10 experimental) were recruited. Both groups performed the same C-Arm placement evaluation task but the experimental group was given 5 minutes of training using the real-time DRR functionality of the system.

Figure 1: System overview



Results: Qualitative analysis shows that the system is capable of generating realistic real-time DRRs based on the tracked position of the C-Arm source. The results from the user study are shown in Table 1. Results from a 5-pt Likert scale questionnaire filled out by each participant indicated general positive feedback of the system with the mean score for each question being 4.0 or higher.

Table 1: User study results

Group	Angular Error (degrees)	Translational Error (mm)	Time (min)
Control	6.49 ± 10.88	16.64 ± 12.66	8.89
Experimental	5.43 ± 8.61	12.78 ± 8.03	9.59

Conclusions: We developed a C-Arm simulator system consisting of a miniature 3D-printed C-Arm, wireless Bluetooth® IMUs, and software capable of generating real-time DRRs. Results from a user study show promising potential for the use of our system as a C-Arm placement training tool. Future work includes incorporating an interface to simulate needle-guided interventions using web-cam-based needle tracking to provide low cost end-to-end training for interventional spinal procedures.

References: [1] Bott, O.J., Dresing, K., Wagner, M., Raab, B.W., Teistler, M.: Informatics in radiology use of a C-arm fluoroscopy simulator to support training in intraoperative radiography. *Radiographics* 31 (3) (2011)

Toward Generalizable Semantic Medical Image Segmentation

Fraser Raney¹, Richard K. G. Do³, and Amber L. Simpson^{1,2}

¹School of Computing, Queen's University

²Department of Biomedical and Molecular Sciences, Queen's University

³Department of Radiology, Memorial Sloan Kettering Cancer Center

Introduction: Semantic segmentation is the process of annotating regions of interest in medical images without the need for human input. This research focuses on creating a generalizable semantic segmentation network that generalizes to new labels of different anatomies without modifying the network explicitly. The goal of this research is to evaluate a state-of-the-art implementation of a semantic segmentation network on an open-source dataset and improve Dice scores with our own generalizable model.

Methods: We used imaging data from the Medical Segmentation Decathlon (MSD) [1], a crowdsourced challenge aimed at developing and benchmarking generalizable medical image segmentation. The MSD data contains both CT scan and MRI images collected from ten different anatomies (liver, spleen, pancreas, etc), which were segmented by expert radiologists. Each dataset was split into training and test sets for validation. The 2018 MSD winner, nnUNet [2], which had the highest per task, per region, Dice scores across all tasks, was implemented to establish a baseline. The 3dfullres U-Net from nnUNet's ensemble networks was used for training with five-fold cross-validation on five MSD sets: liver (n=201), spleen (n=61), and pancreas (n=420) training datasets using NVIDIA's Apex library for PyTorch (NVIDIA RTX 2080Ti GPU).

Results: Our results for five MSD tasks are listed in Table 1, which demonstrate that a network that generalizes to new labels is possible. We are currently working to evaluate improvements to the network and to test on all MSD anatomies.

ROI	Liver	Liver Tumour	Spleen	Pancreas	Pancreas Tumour
3D U-Net	0.96	0.85	0.97	0.82	0.51

Table 1: Mean Dice scores for the 3dfullres U-Net from nnUNet's ensemble networks. All experiments were run on five-fold cross validation.

Conclusions: We are able to reproduce state-of-the-art Dice scores using in-house resources. Our data supports that we will be able to ablate design choices from nnUNet to determine what contributed to its success as well as experiment with other design choices such as Liu et al's anisotropic hybrid model [4]. Our future work will implement the third-place winner from NVIDIA (NVDLMED) [3], a variational auto-encoder model, both for comparison and as an additional baseline and train both networks on the other MSD anatomies. A tool for fast and accurate image segmentation is critical to the use of quantitative imaging in clinical practice.

References:

- [1] Simpson, A.L., Antonelli, M., Bakas, S., Bilello, M., Farahani, K., van Ginneken, B., Kopp-Schneider, A., Landman, B.A., Litjens, G., Menze, B. and Ronneberger, O. (2019). A large annotated medical image dataset for the development and evaluation of segmentation algorithms. arXiv preprint arXiv:1902.09063.
- [2] Isensee, F., Petersen, J., Klein, A., Zimmerer, D., Jaeger, P.F., Kohl, S., Wasserthal, J., Koehler, G., Norajitra, T., Wirkert, S. and Maier-Hein, K.H. (2018). nnU-net: Self-adapting framework for u-net-based medical image segmentation. arXiv preprint arXiv:1809.10486.
- [3] Myronenko, A. (2018, September). 3D MRI brain tumor segmentation using autoencoder regularization. In International MICCAI Brainlesion Workshop (pp. 311-320). Springer, Cham.
- [4] Liu, S., Xu, D., Zhou, S.K., Pauly, O., Grbic, S., Mertelmeier, T., Wicklein, J., Jerebko, A., Cai, W. and Comaniciu, D. (2018, September). 3d anisotropic hybrid network: Transferring convolutional features from 2d images to 3d anisotropic volumes. In International Conference on Medical Image Computing and Computer-Assisted Intervention (pp. 851-858). Springer, Cham.

Development of endoscopic micro-ultrasound transducers for intraluminal imaging

C.F. Roa¹, J. Yin², A. Boyes², E. Chérin², N. Singh¹, F.S. Foster^{1,2}, C.E.M. Démoré^{1,2}

¹Department of Medical Biophysics, University of Toronto, Toronto

²Sunnybrook Research Institute, Sunnybrook Health Sciences Centre, Toronto

Introduction

Improving survival rates of diseases like esophageal cancer (EC) strongly depends on early detection of tumors, especially when minimally invasive therapy is advisable and has positive outcomes. Current techniques to detect small malignant lesions in patients at risk of EC are limited in terms of specificity and ability to assess invasion depth. Endoscopic micro-ultrasound (micro-US) and photoacoustic imaging (PAI) have the potential to give useful diagnostic information, including the visualization of changes in microvasculature, or upregulated molecular biomarkers such as epidermal growth factor receptor (EGFR) when combined with targeted contrast agents. We present ongoing work to develop a high frequency US mini-probe for *in vivo* human intraluminal imaging.

Methods

We present the design for a micro-US array packaged in an endoscopic form factor. The device considers space for future addition of optical fibres for photoacoustic imaging. Fabrication approaches for defining array elements in PZT piezoceramic plates and electrode tracks on polyimide flexible substrate for cabling are discussed. An excimer laser was used to separate individual elements in the piezoelectric ceramic. A novel photolithography process incorporating laser machining was used to pattern conductive traces on a flexible polyimide substrate without damaging the polymer; this forms the cabling connection to the 25- μm -wide elements of the array. Cr-Au sputtering followed by laser machining was used to connect element electrodes to copper traces on the flexible cabling. Electrical impedance, pulse-echo response and acoustic pressures were measured.

Results and Conclusions

A prototype transducer array operating at 32 MHz center frequency with 32 elements has been fabricated and characterized. Flexible circuit cabling with 60 μm pitch tracks for 3 mm length was achieved with the patterning method developed. Electrical connections with metal vapor deposition on a loaded epoxy matrix could be reproduced reliably and are suitable for a < 6 mm diameter housing. Electrical and acoustic characterization results show expected performance. Extension to a 64-element array with improvements in design, e.g. matching layers, to optimize performance is needed for *in vivo* imaging.

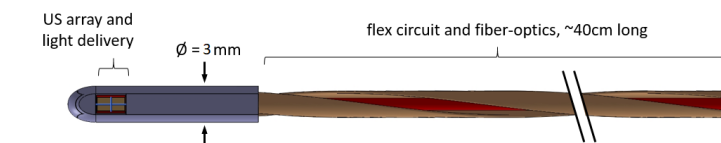


Figure 1. Miniature endoscopic probe integrating micro-US and PAI.

MRI Room Placement: The effect of an elevator operation on local magnetic environment

Diego F. Martinez, Kieffer J. Davieau, Eric J. Lessard, William B. Handler, Blaine A. Chronik

The xMR Labs, Department of Physics and Astronomy, Western University, London ON, Canada

INTRODUCTION: Developments in modern MR systems are allowing for more widely accessible systems that blur the lines of the typical “4 zone” MR room approach. This simplification can reduce costs associated with the set up of systems but comes at the expense of placing these sensitive systems nearer to objects which cause field distortions, potentially introducing challenges for applications which require high field stability. Of concern are the sources of field disturbance whose distortions are dynamic and cannot simply be resolved with shimming. Studies to date on the magnetic fields generated by this class of objects focus more on applications for localization based on these distortions and their analysis is based on data collected using magnetometers with low precision [1]. In this paper, the field distortions due to typical elevators were investigated to gain insight into the potential effects on main magnetic fields of moving metal objects near an MR scanner.

METHODS: Field information was collected using a 3-axis fluxgate probe with calibration range 0-100 μT (Metrolab THM1186). The sampling rate of the probe was set to 100 points per second, and a 50-point rolling average was performed to reduce the noise in the measurements. Two elevators (Elevator A and Elevator B) were used in this study, and the testing was conducted in the hallways the elevators were connected to. A time series was acquired while the elevator was taken to each floor in order, producing a record of the field changes relative to the initiation of data collection. This process was repeated for all the accessible floors for both elevators. The analysis of magnetic field time series was conducted in Python, with the maximum field change determined at each of the sampling locations. The maximum field change as a function of distance was fitted to a $1/r^3$ function to match a gross approximation of the elevators as magnetic dipoles [2].

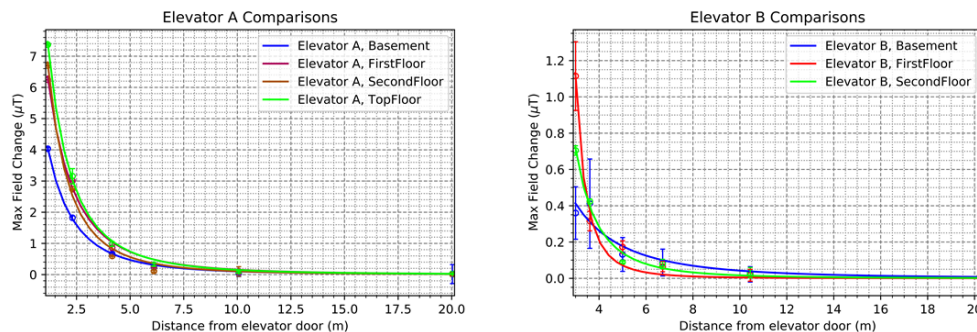


Figure 1: Graph displaying the maximum field change in a) elevator A and b) elevator B compared to the distance from the elevator door. The data follows an inverse cubic relationship in all cases, as can be seen in figure a) where the shape remains consistent throughout the entire length.

RESULTS: Figure 1 shows the collected data points for maximum field change as the distance from elevator door varies, with a $1/r^3$ fit matching the behaviour of a magnetic dipole to each.

DISCUSSION: The expected fit showing the $1/r^3$ behaviour was verified, suggesting that in terms of modelling and predicting the effects that a system could be exposed to, a magnetic dipole approximation is appropriate. The limitations of this are evidently displayed in Figure 1 where the spread of the 50 point average leads to large error bars, particularly near the elevator door in B. Thus, it is recommended that for any modelling, the nearest predictions using a dipole approximation occur past 5m from the elevator door. In general, the effect on field was in the order of 1000 nT at ~5 m, 100 nT at ~10 m, and 10 nT at ~20 m. Typically, it is only the field oriented in the axis of the magnet that will affect imaging, and the current through the superconducting coils will flow to compensate for a changing magnetic flux. These factors represent a reduction in the effect of the distorting field of about an order of magnitude, with further work to be done quantifying these relationships. To expand the work, other elements which can contribute to magnetic distortions can be quantified in order to present a full picture of how the main magnetic field is affected.

Modern approaches to field stability normally attempt to measure and compensate for or prevent distortion, such as using passive superconducting coils and passive steel room shielding. Developing guidelines for MR placement that account for some of these other factors could help to simplify the siting of an MR system.

REFERENCES: [1] Shu, Y., Bo, C., Shen, G., Zhao, C., Li, L., & Zhao, F. (2015). Magical: Indoor localization using pervasive magnetic field and opportunistic WiFi sensing. *IEEE Journal on Selected Areas in Communications*, 33(7), 1443-1457. [2] Jackson, J. D. (1999). *Classical electrodynamics*.

Quench Dynamics Across Multiple Field Strengths

Diego F. Martinez, William B. Handler, Blaine A. Chronik

The xMR Labs, Department of Physics and Astronomy, Western University, London ON, Canada

INTRODUCTION: Development of cryogen-free MR systems has allowed for the main field to be quickly and easily varied without helium boil-off, leading to unexplored applications. Additionally, with modifications, standard high field MR systems can be run at lower field strengths to take advantage of reduced susceptibility artefacts while still maintaining state-of-the-art MR components¹. To ensure system safety, methods for eliminating the main field (quenching) need to adapt to variable current in the magnet.

Generally, a quench is initiated by heating the magnet above critical temperature where the wire becomes non-superconducting and allowing the system to then propagate the expansion of the non-superconducting region while protecting from damaging the rest of the MR components. The critical temperature of each coil in the magnet is affected by the field the system is set at, and this affects the amount of energy required to heat the windings above the superconducting threshold temperature. Passive quench protection circuits must be designed to operate at the lowest current the magnet is expected to be run at, as it is a priority to ensure the magnet itself is not damaged by the heating which occurs in the magnet coils during this process². In this paper, we delve into quench propagation behaviours of a prototype cryogen-free magnet and show results from a preliminary study on the change in the static field during an emergency quench at a variety of fields and model the behaviour of these quenches.

METHODS: The quench dynamics were investigated using a calibrated magnetic field probe placed at the isocenter inside the bore of a cryogen-free superconducting magnet designed to operate at a maximum field of 0.5T at 101A. The field probe voltage output and the voltage of the quench circuit were recorded with an NI DAQ system, using a LabVIEW program, with data collection occurring until recorded field had settled to less than 5 Gauss for general public safety. Ten quenches were conducted with current varying between 10A and 101A (maximum current). The analysis of the quench was done using MATLAB and Python to optimize a fit using a plateaued difference of exponentials to model the behaviours of the main field coils and the shielding coils. The model of the quench was used to test the predicted settling time (time until the field measured reached 5 Gauss).

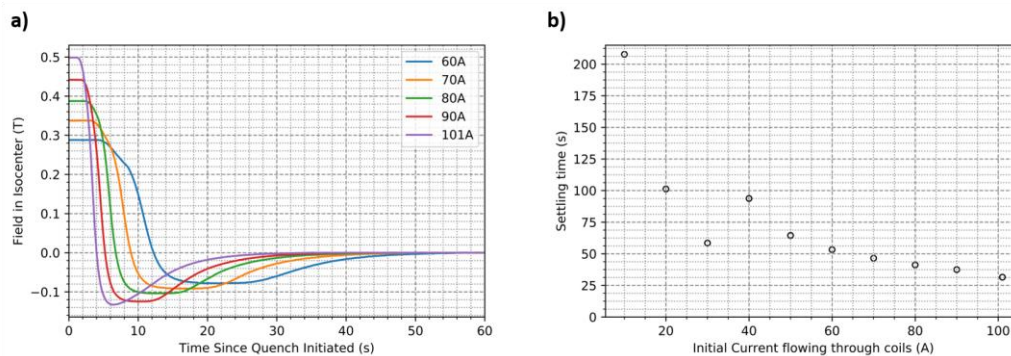


Figure 1: **a)** Set of field measurements for quenches, with the initial field in the bore of the magnet determined by current flowing through coils. **b)** Graph of settling time required for the field in the central axis to reach the 5 gauss level.

RESULTS: The field dynamics for a set of quenches from 60A to 101A is shown in **Figure 1a**, In **Figure 1b**, the settling time to the 5 Gauss level is shown as a function of the initial current through the coils.

DISCUSSION: **Figure 1b** shows that the time taken to quench the system increases as the starting field is reduced, rather unexpectedly. This behaviour is proposed to be due to the increase in critical temperature as the field falls at the location of the superconductor. It can also be seen from **Figure 1a** that magnetic field flips from the initial orientation and is likely due to the shield coils being the last to quench. Below 40A, the quench occurs as a single step, simply settling to zero and not reversing field direction. The two regimes of behaviour can be seen with the entire system quenching in one step at lower current, and at higher currents the shield coils being the last coils to quench causing the settling time to take longer at 40A and 50A than at 30A.

CONCLUSION: In order to improve the settling time in this magnet, the quench circuit could be amended to deposit more heat and the heating elements on the shields and primary coils could be better balanced to make the quench simultaneous.

REFERENCES: [1] Campbell-Washburn, A. E., Ramasawmy, et al. (2019). Opportunities in interventional and diagnostic imaging by using high-performance low-field-strength MRI. *Radiology*, 293(2), 384-393. [2] Seeber B (Ed.). (1998). *Handbook of applied superconductivity* (Vol. 2). CRC press.

Designing a high-pass 21 MHz RF birdcage coil for testing of medical implants

Colin J. Metrow¹, Kieffer J. Davieau^{1,2}, James E. Pardy¹, Blaine A. Chronik^{1,2}

¹The xMR Labs, Department of Physics and Astronomy, Western University, ON, Canada

²Department of Biophysics, Western University, London, ON, Canada

INTRODUCTION: Recently, head-only cryogen free MRI machines have been developed and are beginning to be used in clinical settings at a lower field strength of 0.5 T. It is well known that specific absorption rates (SAR) values can increase dramatically in the tissue surrounding a medical implant depending on the device's material and geometry.¹ This makes it necessary to test the effects of RF exposure, at a lower frequency of 21 MHz, on the heating of tissues surrounding implantable medical devices in order to determine the safety of these machines. This project aims to design and simulate a 21 MHz head sized RF exposure platform to test the safety of medical implants. A high pass birdcage coil configuration was chosen for the RF exposure system. Birdcage coils are the most commonly used RF transmit coils used in clinical MRI today due to their high field homogeneity ease of construction². Birdcage coils are most often composed of two conducting rings connected by a series of rungs as shown in Fig. 1 (a). A high-pass design was chosen instead of a low pass configuration since they are the most common type of design in clinical scanners.

METHODS: The coil was designed as a layout and a schematic using Advanced Design Systems (ADS, Keysight Technologies). It is tuned by varying the main, isolation, matching, and tuning capacitors, as shown in Fig. 1 (b). The calculated capacitances provide an estimation of what to use once the coil is eventually constructed. An EM cosimulation was performed in ADS to tune the coil in order to maximize the strength of the produced magnetic field. The coil was designed at a diameter of 30.1 cm and length 36.7cm. A conductor width of 8 mm was used for the end rings and 6 mm for the rungs, with the conductors simulated as copper with a thickness of 210 microns. The coil has 16 rungs, typical for head-only RF transmit coils. In addition, a copper shield with a radius of 39.7cm outside the coil was incorporated into the simulation.

RESULTS: The coil was tuned to a resonant frequency of 21.28 MHz. The S parameters were minimized so that the power from the ports is transferred into the coil and not into back into the ports Fig. 1 (c). A simulation in ADS found that a main capacitance of roughly 1000 pF produces resonance in the coil. Each of the 16 capacitances in the ring are within 10% of the main capacitance Fig. 1 (b). This is necessary to produce a homogenous field².

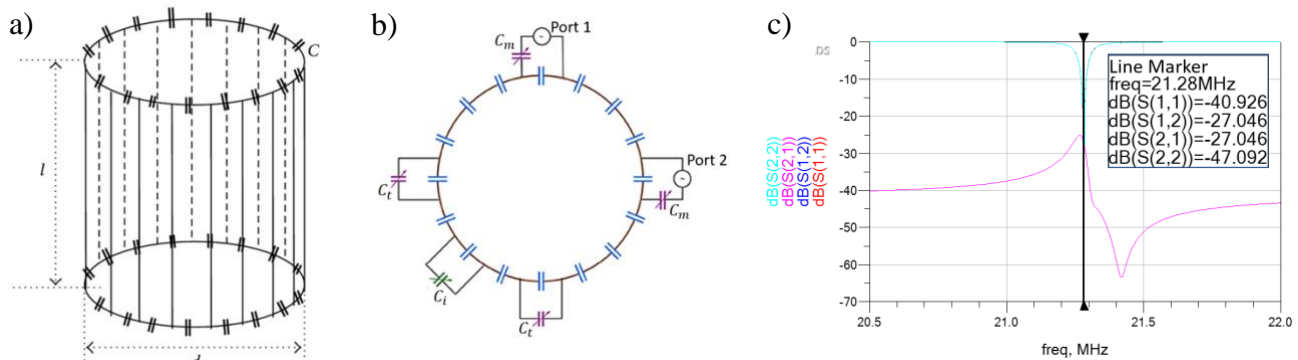


Figure 1: a) High pass birdcage coil configuration with 16 rungs. b) Tuning capacitors (C_t), matching capacitors (C_m), and isolation capacitors (C_i) are used to tune the coil to resonance. c): The coil is tuned to minimize the S-parameter reflection coefficients and maximize the strength of the magnetic field.

CONCLUSION: As the prevalence of head-only MRI machines continues to grow, it is important to know exactly which devices are safe to enter a machine. At a time when medical implants are increasingly common it is necessary to have a variety of RF exposure platforms with which devices can be tested.

References:

- [1] Yeung CJ, Susil RC, Atalar E. RF safety of wires in interventional MRI: using a safety index. *Magn Reson Med* 2002;47:187–193. [2] Hayes EC, Edelstein WA, Schenck JF et al. An efficient highly homogeneous radiofrequency coil for whole-body NMR imaging at 1.5 T. *J Magn Reson* 1985; 63:622-828. [3] R Ansoorge, M Graves. Radio frequency transmission and reception. Morgan and Claypool Publishers. 2016. Chapter 3. Page 4. [4] J. Mispelter, M. Lupu, A Briguet. NMR Probheads for Biophysical and Biomedical Experiments. London, UK: Imperial Collage Press, 2006.

Cost-effective micro-CT scanner for remote archaeological sites

Santiago F Cobos,^{1,6} Jay T Stock,^{2,6} Andrew J Nelson,^{2,3,6} and David W Holdsworth,^{1,4,5,6}

¹Department of Medical Biophysics, ²Department of Anthropology, ³Department of Chemistry, ⁴Robarts Research Institute, ⁵Department of Surgery, ⁶Bone and Joint Institute, Western University, London, Ontario, Canada

Introduction: Archeological analysis of bony samples can be enhanced by high-resolution 3D digital data.^{1,2} In this context, micro-computed tomography (micro-CT) is key when evaluating the micromorphological structure (i.e., trabeculae) and the atomic number of any associated inclusions or infiltrations (i.e., sand or soil).¹ However, micro-CT scanning remains under-utilized because the removal of samples from the archeological sites might be culturally insensitive or impractical, due to high-cost or risk in transport.² Recent advancements in data acquisition and data processing allow the generation of high-resolution (i.e., < 150 μm) CT images of large samples using low-cost and portable imaging hardware. Here we describe the implementation of a cost-effective and portable micro-CT prototype system and its performance when imaging two bony archeological samples.

Methods: Two bony samples, one hemi-mandible and one femoral-head (Fig. 1a), were imaged using our portable micro-CT system (Fig. 1b) and a commercially available industrial scanner (XT H 225, Nikon Metrology). The portable scanner consisted of a rotary table (PSR300, IntelLiDrives, Inc) that was coupled to a 350x423 mm flat-panel detector (DRX-Plus 3543, Carestream Health) using standard laboratory equipment. Visual inspection was enough to ensure that the detector was positioned as orthogonal as possible to the top of the rotary table. The x-ray unit (Proteus XR/a, GE Medical Systems, 80kVp, 0.5mAs) was placed 732 mm away from the detector with the central ray pointing to the central pixel. The samples were wrapped with Styrofoam and placed inside a polycarbonate cylinder. The cylinder included three 0.94 mm metal markers distributed along its length. The metal markers were used to calibrate the scanner geometry and to correct non-idealities in the custom setup.³ 215 projection images were used to reconstruct the samples using a Parker-weighted FDK algorithm. The volumes for the portable scanner were reconstructed at 102 μm isometric voxels. Images, generated by the custom scanner, were co-registered and qualitatively compared to the images acquired using the commercial scanner (105 kVp, 105mA, 1800 views, 57.5 μm isometric voxels).

Results: The hardware required for the portable scanner, which was purchased for a fraction of the cost of the commercial system (i.e., < \$100,000 CAD), was easy to transport and mount. The portable scanner successfully generated micro-CT reconstructions for both archeological samples. The 102 μm voxels allowed for visualization of small morphological details such as trabecular bone (Fig. 1c-d) and dental fractures (Fig. 1e). Scanning time was 50 minutes per specimen, which is practical for this application since specimens do not move. Line profiles across co-registered regions of the scans showed geometrical agreement between systems (Fig. 1f). High density inclusions were also easily visualized and segmented (Fig. 1e).

Conclusions: Portable imaging hardware can be used to generate micro-CT reconstructions of archeological samples. Most of the archaeologically relevant details (i.e., trabecular bone, fracture lines, and inclusions) were shown by both the proposed and commercially available systems. Although the commercial micro-CT scanner generated sharper images (i.e., higher spatial resolution), the custom micro-CT scanner showed to be a cost-effective solution. The system should have to be used within a radiation-safe room or in the field using an array of sensors to establish a radiation-safe perimeter. Portable micro-CT systems might contribute to the technical and ethical improvements of archeological analysis in remote communities in the future.

References: 1. X. Villagran et al., "Virtual micromorphology: The application of micro-CT scanning for the identification of termite mounds in archaeological sediments," *J. of Archaeological Science* 24, 785-795 (2019) 2. YC. Hirst et al., "Standardisation in 3D Geometric Morphometrics: Ethics, Ownership, and Methods," *Archaeologies* 14.2, 272-298 (2018) 3. R. Fahrig et al., "Three-dimensional computed tomographic reconstruction using a C-arm mounted XR11: Image-based correction of gantry motion nonidealities," *Medical Physics* 27.1, 30-38 (2000)

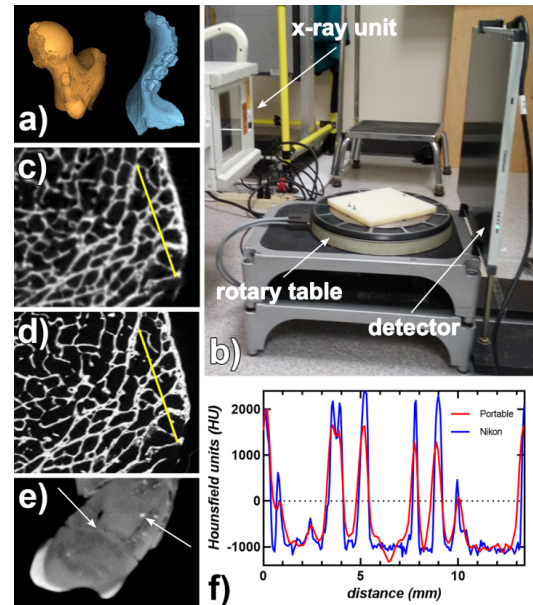


Fig. 1: a) renderings of samples - femur head and hemi-mandible. b) Portable micro-CT scanner setup. c) Trabecular bone (portable scanner, 102 μm voxel-size). d) Trabecular bone (Nikon micro-CT, 57.5 μm voxel-size). e) Mandibular molar showing fracture lines and high-density inclusions (portable micro-CT). f) Profile-line (yellow solid in c and d) showing geometrical agreement between co-registered volumes from the portable (red-line) and Nikon (blue-line) systems.

Creation and Validation of the Quantitative Imaging for Personalized Medicine Artificial Intelligence Development and Collaboration Environment

B. Driscoll¹, T Patel^{1,2}, J. Lee^{1,2}, T Tadic², S. Sajja¹, D. Shah¹, T. Shek¹, L. Brzozowski¹, I. Yeung^{2,3} & J. Publicover¹

(1) Techna Institute, University Health Network, Toronto, Canada

(2) Radiation Medicine Program, Princess Margaret Cancer Center, Toronto, Canada

(3) Dept Radiation Oncology, University of Toronto, Toronto

Purpose

The evolution of deep learning (DL) algorithms combined with increasing computing power have driven the development of artificial intelligence (AI) in radiology. By applying DL to large volume clinical imaging data sets there is an opportunity for identification of imaging biomarkers that can identify disease sooner or predict response more accurately leading to improved decision support and medical image interpretation.

Since 2012 the Quantitative Imaging for Personalized Cancer Medicine (QIPCM) program has provided a central repository for imaging data and analysis tools to ease the management of multi-centre clinical trials. The QIPCM collaboration environment adheres to privacy and security regulations and allows the data sponsor to provide or revoke access as needed. Leveraging this framework, QIPCM has recently developed an AI development and collaboration environment in which academic researchers, industry and startups interested in pursuing AI-related research can work together towards a common goal of improving patient outcomes.

Methods

The QIPCM platform provides a supportive framework for the development, testing and validation of algorithms designed to solve problems in the domain of medical imaging using machine learning techniques. Large size datasets can be ingested into the QIPCM platform along with other accompanying information such as labels and contours using the recently adopted radiomics support tool MIRA. Developed at Princess Margaret Hospital, MIRA is a suite of software tools to simplify processes in radiation oncology and medical imaging studies through a pipeline which integrates different software such as RT planning, radiomics feature extraction and other similar software.

Results

The QIPCM platform currently serves 34 active clinical trials spanning 32 sites globally. The image store currently holds over 19.5 million images more than from 17,000 imaging studies. The addition of MIRA to the QIPCM infrastructure has provided the ability to rapidly retrieve data from multiple clinical systems and process them with Radiomic feature extraction tools such as PyRadiomics and send the resulting feature sets to the connected HPC4Health cluster for DL analysis. This framework has been used successfully for 3 trials to date spanning over 200 patients.

Conclusions

The QIPCM AI Development and Collaboration Environment has shown success already and should continue to grow. Future steps are to add the elements of the system to QIPCMs robust regulatory framework and validate it with larger volume data sets to make it even more appealing to collaborators from both academia and industry.

Developing an Analysis Pipeline for Hyperion™ Imaging System Data

Sindhura Thirumal¹, Amoon Jamzad¹, Tiziana Cotecchini¹, Charles Hindmarch¹, Parvin Mousavi¹

¹Queen's University

Introduction

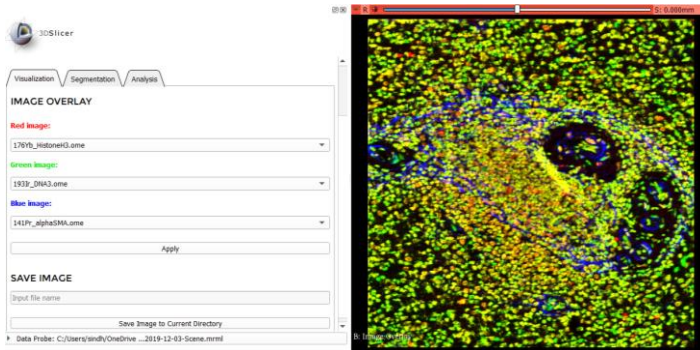
The Hyperion™ Imaging System is an Imaging Mass Cytometry (IMC) technology that is capable of high-throughput imaging of cells and proteins [1]. It is able to provide highly multiplexed, deep profiling of the tissues and their microenvironments at a subcellular resolution. The current methods of analysis are fairly preliminary and require the use of multiple different software to complete the tasks of visualization, segmentation, and analysis. The major drawback of having to use multiple software is the extra time it takes to learn and be comfortable with the different user interfaces. Additionally, it requires unnecessary exportation of data in order to move between software. The purpose of this research is to develop a platform to perform all data pre-processing, analyses, and visualization via the open source 3D Slicer environment [2]. A future application is establishing whether a certain immune signature in bladder cancer tissue, as analyzed through the platform, reflects the response to treatment, or even prognosis.

Method

We are using 3D Slicer's environment – a software built for medical image processing – to implement the full analysis pipeline of Hyperion data [2]. The requirements are that the developed module has to be capable of visualizing several images individually as well as an overlay of multiple channels at a time. Then, since the tissue is stained with Iridium that binds to DNA, the nucleus of each cell must be accurately located and segmented into individual cells. Finally, the resulting cell mask can be used for various statistical analyses.

Results

Our module in Slicer is split into 3 parts: Visualization, Segmentation, and Analysis. *Visualization*: Our module is capable of transparently overlaying up to 3 channels at a time, as well as saving the resulting overlaid image for further use (Fig 1).



Segmentation: Our module will segment the nucleus channel to create a nucleus, cell, and cytoplasm mask for the given region of interest. *Analysis*: Using the cell mask, we can analyze the cell data using various statistical plots as well as export the statistics for use in external applications.

Fig 1. User interface of the Visualization tab of Slicer module, showing an overlay of 3 channels.

Conclusion and Future Work

With this Slicer module, the user is able to perform all processing, visualization, and analysis functions on mass cytometry data within one environment. Additionally, the platform is available through an open source environment, enabling collaboration and exchange between multiple groups. This is an improvement on the current data analysis pipeline, which requires the use of various software tools to perform individual tasks and to exchange data results from one software to the next. In the future, we plan to perform user studies using the platform to evaluate efficiency. In addition, the application of the module for quantification of immune response in bladder cancer is an active application of the platform.

[1] Chang, Q., Ornatsky, O. I., Siddiqui, I., Loboda, A., Baranov, V. I., & Hedley, D. W. (2017). Imaging mass cytometry. *Cytometry part A*, 91(2), 160-169.

[2] Fedorov A., Beichel R., Kalpathy-Cramer J., Finet J., Fillion-Robin J-C., Pujol S., Bauer C., Jennings D., Fennessy F., Sonka M., Buatti J., Aylward S.R., Miller J.V., Pieper S., Kikinis R. 3D Slicer as an Image Computing Platform for the Quantitative Imaging Network. *Magnetic Resonance Imaging*. 2012 Nov;30(9):1323-41. PMID: 22770690.

Novel Functional Imaging Method to Determine Capillary Network Geometry and *in vivo* Capillary Hemoglobin Concentration in Skeletal Muscle

J. Christie¹, L. Mawdsley¹, I. Kong¹, A. Doornekamp¹, J. Baek¹, G. Fraser², C.G. Ellis¹, and R. Sove¹

¹Department of Medical Biophysics, University of Western Ontario, London, Ontario, Canada

²Department of BioMedical Sciences, Memorial University of Newfoundland, St. John's, NL, Canada

Introduction: The ability to study and quantify structural and hemodynamic changes in the microcirculation can help us better understand the regulation of oxygen delivery to surrounding tissue. In diseases such as sepsis and diabetes, microvascular dysfunction and dysregulation can be detected before the onset of clinical symptoms; the ability to measure and compare changes in microvascular blood flow in the microvascular bed is invaluable. Investigating how different hemodynamic parameters and microvascular structures change with time can help elucidate the progression of these diseases [1,2]. Quantification of the concentration of hemoglobin is an important hemodynamic parameter in determining impairment in local tissue functionality. Hematocrit and mean corpuscular hemoglobin concentration (MCHC) are other potential indicators of the state of the microvasculature. The aim of this study was to develop a tool to visualize hemodynamic information, such as hemoglobin concentration and hematocrit, within the microvascular network *in vivo*. Additionally, we aimed to facilitate the reconstruction of the 3D microvascular network using the path length through the capillaries in the z direction (L) all obtained using intravital video microscopy (IVVM).

Methods: Images taken from an *in vivo* preparation of a rat *extensor digitorum longus* muscle were obtained from 60 second captures from an IVVM protocol [3]. Custom MATLAB software was then developed to calculate the optical density (OD) for each pixel, using the Beer-Lambert law. The Beer-Lambert law states that hemoglobin concentration can be determined if path length and optical density are known. Capillaries were delineated using a combination of a Sum of Absolute Difference (SAD) image and an OD_{max} image which were created using masks based on red blood cell (RBC) flow. An OD ratio was subsequently used to calculate the L of each capillary. The network geometry was reconstructed using the calculated Ls. The ODs and Ls were then used to find hemoglobin concentration, MCHC, and hematocrit of the capillaries in the field of view (FOV). The method was compared to a phantom of capillaries in a FOV at known hematocrits and hemoglobin values.

Results: Six capillary networks were analyzed, and functional images were generated of hemoglobin concentration, MCHC, and hematocrit. *Figure 1* shows functional images displaying the hemoglobin concentration and MCHC in the FOV of one of the six analyzed networks. *Figure 2* shows a section of a capillary network that was reconstructed using the calculated Ls. The edges of the reconstructed capillary are smooth and rounded, and the reconstructed vessel recovers capillary intersections and bifurcations. The algorithm was tested with the phantom and the values matched known phantom values within 0.0025% and 1.49% of the hemoglobin and hematocrit values respectively.

Conclusions: This method provides a novel approach for calculating *in vivo* RBC path length in the z direction, hematocrit and hemoglobin concentration as well as characterizing the geometry of the microvascular network from *in vivo* images of RBC flow. This method of calculating Ls can only be used for vessels where RBCs fill the vessel lumen. The functional images generated for each of these parameters allows for easy visualization of the microcirculatory hemodynamic parameters. This methodology can be a useful tool for studying both physiological and pathological states of the microcirculation *in vivo*.

References: [1] D. E. McMillan., 2012 [2] A. Tyagi et. al., 2009 [3] G.M. Fraser et. al., 2012

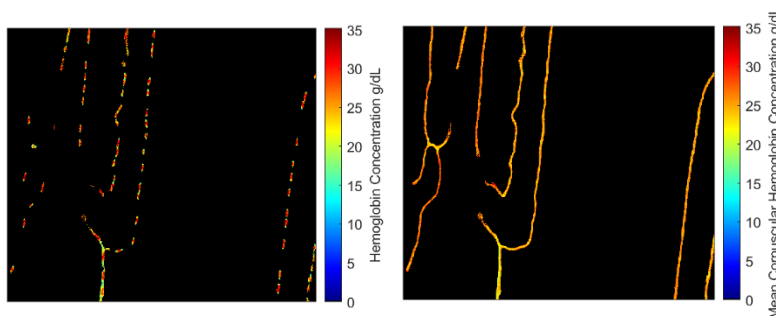


Figure 1. Functional images showing the Hemoglobin concentration, mean corpuscular hemoglobin concentration at 20x magnification

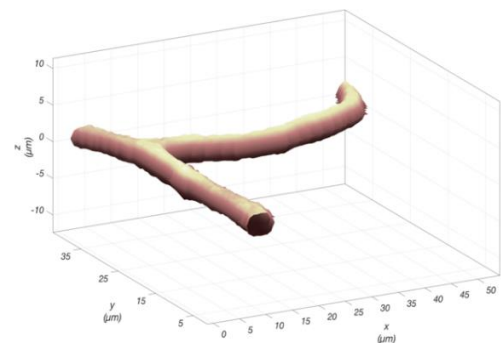


Figure 2. Reconstructed 3D Geometry of a capillary network section at 20x magnification

Design and 3D Printing of Wireless Load Cells for Biomedical Applications

William D Anderson¹, Sydney Wilson¹, David W Holdsworth^{1,2,3,4}

¹School of Biomedical Engineering, ²Robarts Research Institute, ³Department of Medical Biophysics,

⁴Department of Surgery, Schulich School of Medicine and Dentistry, Western University, London, Canada

Introduction: Load data is an integral part of many biomedical applications as it provides quantitative information about the forces acting on structures. Load is a valuable outcome measure in many clinical and research studies, as well as commercial devices. Previously described advancements in automotive pressure sensor technology have enabled an alternative method of monitoring real-time load and strain data [1]. To be effective, the sensor package must be embedded within a deformable enclosure designed to transduce compression, tension, flexure, or torque forces. The objective of this study is to develop customizable, 3D printed load cells capable of measuring a range of compressive loads for use in biomedical applications. The custom load cells developed in this study could be used to measure orthopaedic loads within joint replacements, intervertebral disc replacements, and spinal fusion cages.

Methods: A deformable compression enclosure was produced by generating a two-component rectangular structure with four internal cantilever beams. In subsequent designs, the width of the beams was increased from 2 mm to 4 mm at 0.5 mm increments to generate structures that required more force to deform. The height of the beams was held constant. When under compression, the load was evenly distributed to the unfixed end of each beam using a flat surfaced lid component. The fixed end of the beam acts as a hard stop to prevent deformation greater than 500 microns, preventing damage to our sensor package. The two-component enclosure was imported into Abaqus to determine the theoretical load capacity of the package when fabricated using two different materials, polylactic acid (PLA) and Ti-6Al-4V. The elastic modulus of PLA and Ti-6Al-4V was 3 GPa and 114 GPa, respectively. Linear static analysis with tetrahedral elements was used to model the enclosure (Fig. 1a). Load was evenly applied over the entire proximal surface of the lid component. Theoretical and experimental load capacity was defined as the load that was required to compress the lid until it reached the hard stop. To determine the experimental load capacity of the enclosures, the packages were 3D printed in PLA and subjected to compressive deformation applied by an Instron 3343. Compressive deformation was applied at a rate of 500 microns/min using a 3D printed indenter.

Results: The theoretical load capacity of the enclosure when fabricated in PLA ranged from approximately 5 to 12 N (Fig. 1b) and the experimental load capacity followed a similar linear trend. The sensitivity of the PLA experimental load capacity vs wall width plot was approximately 3 N/mm. The average percent error between the theoretical and experimental PLA load capacity was 2.62%. The theoretical load capacity of the Ti-6Al-4V enclosure (as predicted by finite-element modeling) ranged from 210 to 460 N.

Conclusion: The results of this study show that custom load cell enclosures can be 3D printed to measure specific load values by altering the design of internal features and the materials used in fabrication. In combination with our load sensor, a retasked tire pressure sensor, we will be able to develop a range of wireless telemetric load cells with varying load capacity. Future enclosures could be designed to transduce tension, flexure, and torsion forces.

References: [1] W. D. Anderson, S. Wilson, D. W. Holdsworth, "Wireless telemetry load sensor for orthopaedic applications," In Proc. Imaging Network Ontario Symposium, 2019, pp. 160

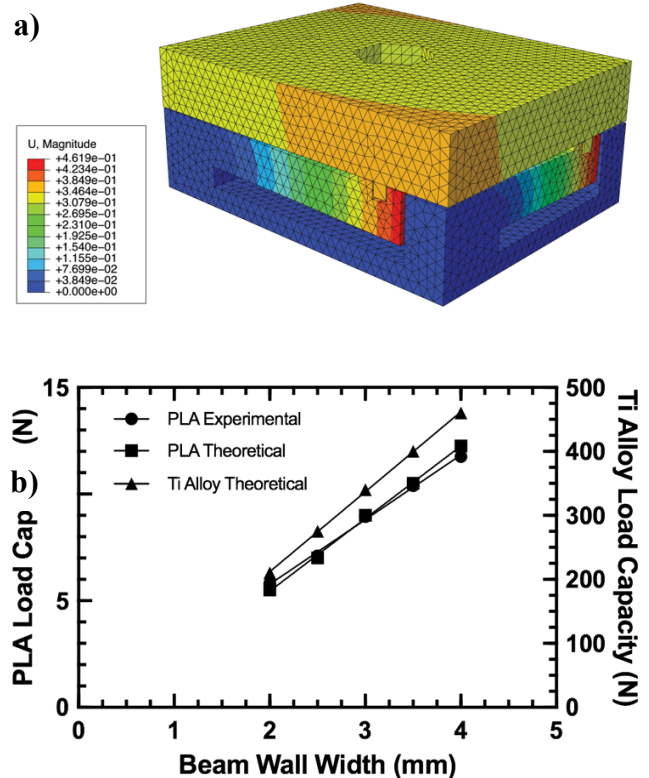


Fig. 1: (a) FEA of two-component compression enclosure. (b) Results of FEA and compression testing, PLA/Ti Alloy load capacity vs. beam wall width

Modelling Static Field Induced Torque on Simplified Medical Devices

X Ding¹, WB Handler¹, BA Chronik¹

¹ The xMR Labs, Physics and Astronomy, University of Western Ontario, Canada

INTRODUCTION: The most recent test standard published by ASTM International for assessing the MR compatibility of medical devices, specifically static field induced torque, outlined five experimental test methods as an update to the previous edition with only one method^{1,2}. As of Dec 2019, there is not an internationally recognized method for assessing torque by computational means. In the development of systematic and efficient testing of medical device safety, numerical methods based on the finite element method (FEM) are a possible tool that could be used to model the torque induced on devices placed in the static field environment of an MR scanner. The torque induced on stainless-steel (SS) grades 304 and 316 cylindrical rods were measured and compared to the results from a torque simulation created in COMSOL (COMSOL Inc., Sweden), an FEM solver.

METHODS: Sixteen rods (SS304 and 306, $d = 0.64$ and 1.27 cm, and $l = 3, 5, 7,$ and 9 cm) were measured on a 3 T scanner using the *Pulley Method* from ASTM F2213-17. Measured values were compared with simulated values obtained from COMSOL. A cubic simulation domain was created into which, cylinders of dimensions matching the machined SS rods were placed. The magnetic susceptibility, χ , defined the properties of the cylinders while all other domains were defined as air. A 3 T external field was applied, and the ASTM experimental procedure was simulated. All objects were discretized with tetrahedra with dV being the size of each element. Two physics solvers, *Magnetic Fields, No Current* and *PDE Coefficient*, were used to solve for \mathbf{B} and $\nabla\mathbf{B}$ respectively. The peak torque experienced by each simulated cylinder was found by summing the torque on each individual element at a distance, \mathbf{r} , from the center of the cylinder given that $\boldsymbol{\tau} = \mathbf{F} \times \mathbf{r}$ and $\mathbf{F} = \frac{\chi dV}{\mu_0(1+\chi)} (\mathbf{B} \cdot \nabla)\mathbf{B}$.

RESULTS: The experimentally measured and simulated torques of each rod was tabulated with the percentage difference calculated using measured values as truth (Fig. 1).

CONCLUSIONS: The experimental and numerical torque peaks appear to increase linearly with length of the rod. The percent difference between the experimental and numerical values were less than 5%. The susceptibilities calculated all lie in the range expected for the stainless-steel materials often reported as between 1000 to 20000

ppm with SS316 more precisely known to be between 3520 to 6700 ppm. It is important to note that this method still requires validation using a material with a known magnetic susceptibility. However, internally the simulation is seen to be self-consistent and given this self-consistency, FEM models would provide an effective tool in efficiently and systematically assessing medical devices. With further validation, the application of numerical methods to device testing could minimize the number of measurements required. Rather than testing every configuration within a group of devices, conservative limits can be established on the group as a whole via laboratory measurements on the computationally identified worst case. Although this study just the preliminary step, further studies on models with greater geometric complexity may reveal FEM to be an effective tool in assessing the MR compatibility, in regard to static field induced torque, of whole product lines of medical devices.

	Length	Tests [mNm]	Sims [mNm]	% diff
SS316 $d = 1.27$ cm $\chi = 5026 \pm 34$ ppm	3 cm	0.133 ± 0.018	0.134	0.752
	5 cm	0.307 ± 0.018	0.301	1.954
	7 cm	0.444 ± 0.019	0.452	1.802
	9 cm	0.614 ± 0.021	0.612	0.326
SS304 $d = 1.27$ cm $\chi = 12246 \pm 207$ ppm	3 cm	0.772 ± 0.016	0.789	2.202
	5 cm	1.710 ± 0.027	1.788	4.561
	7 cm	2.787 ± 0.040	2.677	3.947
	9 cm	3.728 ± 0.052	3.643	2.280
SS316 $d = 0.64$ cm $\chi = 5501 \pm 79$ ppm	3 cm	0.052 ± 0.002	0.053	1.923
	5 cm	0.105 ± 0.004	0.103	1.905
	7 cm	0.145 ± 0.005	0.141	2.759
	9 cm	0.168 ± 0.006	0.175	4.167
SS304 $d = 0.64$ cm $\chi = 12542 \pm 128$ ppm	3 cm	0.272 ± 0.008	0.274	0.735
	5 cm	0.515 ± 0.012	0.538	4.466
	7 cm	0.739 ± 0.016	0.732	0.947
	9 cm	0.936 ± 0.018	0.912	2.564

Fig. 1: The simulated torques were compared to measurement by percent difference and gives a sense of the numerical accuracy.

[1] ASTM F2213-17 (2017) [2] Woods, T. O. (2007) *J Magn Reson Imaging*, 26, 1186–1189 [3] Nyenhuis, J. A. et al. (2005) *IEEE T Device Mat Re*, 5(3), 467–480 [4] Schenck, J. F. (1996). *J Med Phys*, 23(6), 815–850.

Synthesis of novel MRI phantoms for the enhanced imaging of intraplaque hemorrhage

Matteo Bomben¹, Amanda Ricketts¹, Alan Moody², Naomi Matsuura^{1,2}

(1)Institute of Biomaterials and Biomedical Engineering; (2)Department of Medical Imaging, University of Toronto

Introduction

15-20% of strokes are attributable to the rupture of atherosclerotic plaques in the carotid artery. Plaque rupture is strongly correlated to the presence of intraplaque hemorrhage (IPH) sites in the core of these plaques. As such, Moody et al. have developed a technique that uses a T1-weighted gradient echo sequence to detect IPH and thus identify those at risk of stroke. However, such a method cannot be approved for clinical use until its efficacy is first proven through multi-centre imaging studies. Such studies require a novel set of MRI phantoms that would allow for images of IPH-positive plaques taken across multiple scanning platforms to be standardized. As such, the objective of this research was to synthesize two novel phantoms that would facilitate multi-centre IPH imaging: one that models IPH sites and another that mimics vessel wall thickening during atherosclerosis

Methods

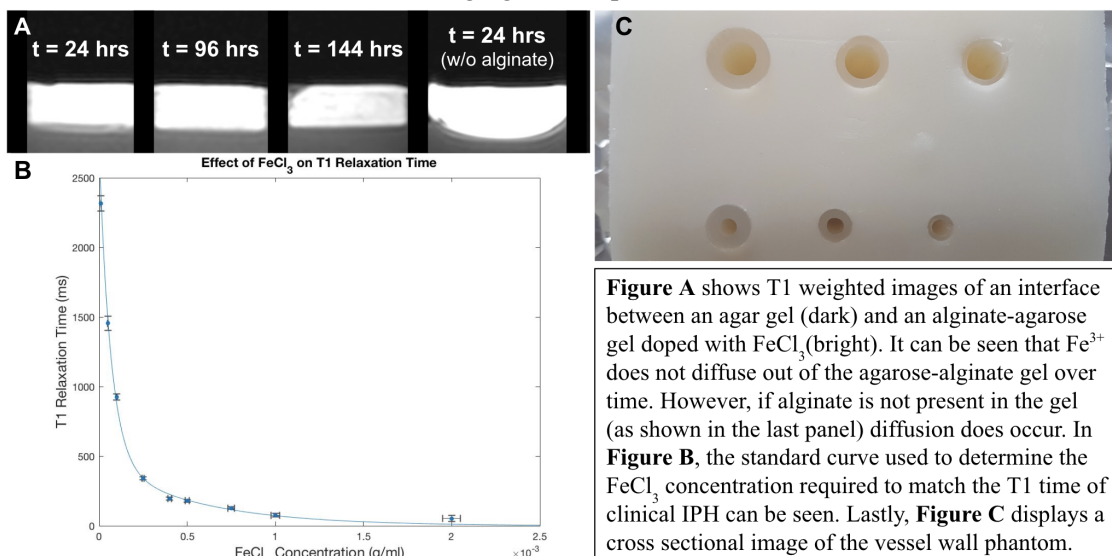
A material that mimics the imaging properties of IPH was created by adding FeCl_3 to a 0.15%-alginate, 1.5%-agarose gel. IPH possesses a short T1 relaxation time due to the high concentration of methemoglobin-bound ferric iron in hemorrhaged blood. This was mimicked in the phantom through the addition of FeCl_3 with a standard curve being used to determine the FeCl_3 concentration required to match the T1 time of clinical IPH. Furthermore, the inclusion of alginate in the gel formula provided Fe^{3+} ions with an anionic polymer chain to bind to and ensured that these ions did not diffuse out of the mock IPH sites. The final phantom consisted of 1-8 mm diameter cylinders that were filled with the IPH gel. To create the 2nd phantom, vessel wall models were cast out of 2% agar gel using 3D printed moulds. Specifically, vessels with wall thicknesses between 1-3 mm were made and then embedded in a lard-paraffin wax mixture which simulated the fatty tissue around the carotid.

Results

It was found that a gel with an FeCl_3 concentration of 0.25 mg/ml had a T1 relaxation time of 341 ms and thus best matched that of clinical IPH. Furthermore, tests showed that the addition of alginate to the IPH phantom gel prevents Fe^{3+} diffusion and thus leads to the preservation of IPH site shape/size over at least 6 days. Also, the final IPH site phantom was imaged with the aforementioned T1-weighted sequence and was found to mimic IPH site appearance. Lastly, images of cross sectional slices of the vessel wall phantom demonstrated that the fabrication technique used produced the desired array of vessel walls with varying thicknesses.

Conclusions

The IPH phantom produced in this study possess a T1 relaxation time similar to that of clinical IPH and also resists the long-term shape-altering effects of Fe^{3+} diffusion. As such, it, in combination with a vessel wall phantom that mimics a range of carotid geometries, represents a strong first step on the path to develop a set of phantoms that will facilitate the multi-centre imaging of IPH-positive atherosclerosis.



The X-Mode Gradient: Improved Performance for Select Applications

EJ Lessard^{1,2}, WB Handler², BA Chronik^{1,2}

¹Department of Medical Biophysics, ²The xMR Labs, Department of Physics and Astronomy, Western University, Canada.

INTRODUCTION: Previously, we have proposed the development and use of an actively shielded gradient coil with cut-outs to accommodate the patient's shoulder for use in a head-only MRI system, allowing imaging below the brain and into the cervical spine.¹ This setup would allow imaging of both the brain and cervical spine regions with only limited patient translational movement. Unfortunately, the presence of cut-outs in the conducting surfaces next to the patient's shoulders leads to an imbalance in the performance between gradient axes, specifically, the X-gradient has a larger degradation in performance compared to a full cylinder than is observed for the Y-gradient. We hypothesize that by rotating the transverse axes by $\pi/4$ we will have an improvement in the previously X-gradient performance and a decrease in the previously Y-gradient performance allowing a better-balanced gradient coil configuration.

METHODS: Triangular element meshes were created using COMSOL Multiphysics (COMSOL, Burlington, MA) and composed of a primary surface (length = 0.76 m, radius = ~ 0.22 m), a shield surface (length = 1.00 m, radius = 0.26 m) and a bore surface (length = 1.00 m, radius = 0.325 m). The cut-out size was held constant with a height (Y-direction) of 0.15 m and a length (Z-direction) of 0.21 m. The boundary element method (BEM)² was implemented using custom built MATLAB (Mathworks, Natick, MA) software. To employ the BEM, a set of discrete field targets were chosen as a 0.20 m diameter sphere situated at the isocentre. The field targets were a linear field gradient rotated by $\pi/4$. We denote the rotated reference frame directions as d_1 and d_2 . **Figure 1** shows an illustration of gradient directions. For our design algorithm we set the target efficiency to 0.125 mT/m/A while the minimum wire spacing for the gradients were chosen as 3.5 mm to accommodate realistic manufacturing capabilities.

RESULTS: Examples of the transverse gradients are shown in **Figure 2** along with simulated magnetic field maps, normalized per unit current.

CONCLUSIONS: As shown in **Table 1** the rotation of the gradient axes allows the X- and Y-gradients to obtain similar performance to each-other while achieving electromagnetic properties acceptable for imaging and a large imaging region defined by a DSV₃₀ of approximately 0.28 m for each axis. One important future direction is to shift the imaging region further towards the

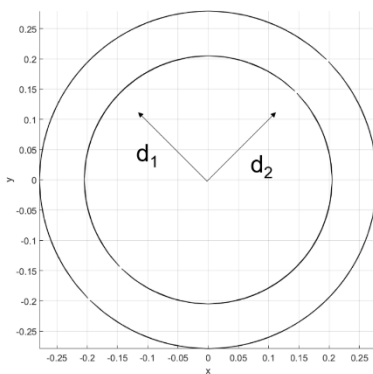


Figure 1: Rotated Gradient Frame

patient end allowing direct comparison of previous work and the potential to improve cervical spine imaging while still allowing

	d_1 Gradient	d_2 Gradient
Efficiency [$\text{mT m}^{-1} \text{A}^{-1}$]	0.125	0.125
Resistance [$\text{m}\Omega$]	96	102
Inductance [μH]	352	360
Min Wire Spacing [mm]	3.6	4.8
DSV ₃₀ [m]	0.28	0.28

Table 1: DSV₃₀ = Diameter of Spherical Volume with Deviation < 30%

performance of the transverse axes. To date this is the first theoretical demonstration of the feasibility of rotating the gradient axes to design a shoulder cut-out gradient coil.

REFERENCES:

1. Lessard EJ et al. Proc. Intl. Soc. Mag. Reason. Med. 27 (2019) Abstract #1481
2. Poole M, and Bowtell R., Concepts Magn. Reason., 31B(3): 162-175 (2007)

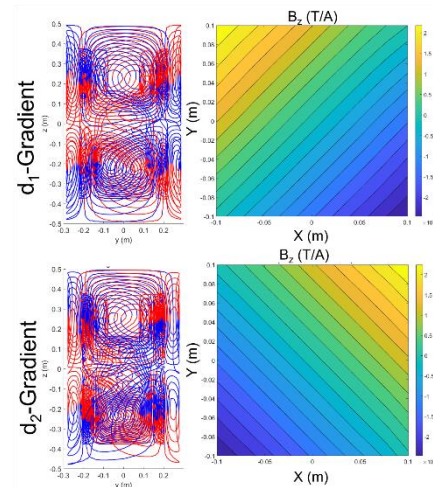


Figure 2: Gradient Wire Patterns and Field Maps at 1 A current

imaging of the brain.

Ultimately, we have performed a preliminary design study to explore the effect of rotating the gradient axes on performance in an actively shielded shoulder cut-out gradient coil. This proof-of-concept study demonstrates the feasibility of designing a gradient coil with shoulder cut-outs that well balances the

Multi-Echo Spin Echo MRI Signal Modulation Based on Slice Profiles

Layale Bazzi¹, Mark Armstrong¹, Dan Xiao¹

¹Physics Department, University of Windsor, ON, Canada

Introduction: Multi-Echo Spin Echo (MESE) MRI experiment acquires multiple images with different T_2 weighting. Signal evolution at various echo times is acquired for each image voxel and analyzed to extract the spatially resolved MR T_2 relaxation times. Quantitative T_2 measurements provide insight into microscopic information not available in conventional T_2 -weighted imaging methods. However, the voxel-wise signal modulation deviates from the ideal exponential decay, due to non-ideal slice profiles. It is important to quantify the slice profile influence to improve the accuracy of spatially resolved T_2 measurements. Bloch equation simulations were employed to model the signal decay curve for various slice profiles in the MESE sequence.

Methods: Bloch equation simulations were programmed on Python ver. 3.7 on the Spyder IDE ver. 4 beta. All codes were written in-house using the NumPy and SciPy libraries. Simulations were performed for $T_1 = 100$ ms, $T_2 = 50$ ms, 30 echoes (ETL) with an echo spacing of 5 ms. A rectangular radiofrequency (RF) pulse, a Gaussian pulse, and sinc pulses with 1 and 5 lobes were investigated. For each decay signal simulation, the excitation and refocusing RF pulses were of identical shape and duration. Local field inhomogeneities were modelled with a Lorentzian distribution. The four RF pulses had identical FWHM in the excitation slice profiles.

Results: The decay signals corresponding to different RF pulses are shown in Figure 1. In (a), the excitation and refocusing slice profiles significantly deviated from ideal, resulting in strong interference of different coherence pathways. The signal amplitude is substantially reduced. The Gaussian pulse (b) removed the side lobes in the slice profile. The second echo signal is higher than the first echo signal due to the stimulated echo. In (c) and (d), the sinc pulses increased the first echo amplitude. As the RF pulse approached the ideal multi-lobe sinc shape, the slice profile approached a more uniform rectangular shape, producing smoother decay curves. Fitting the simulated decays to a single-exponential decay returned T_2 values of (a) 59, (b) 61, (c) 55 and (d) 52 ms. Performing an identical simulation with a T_2 of 5 ms resulted in estimation errors of 50% - 100%.

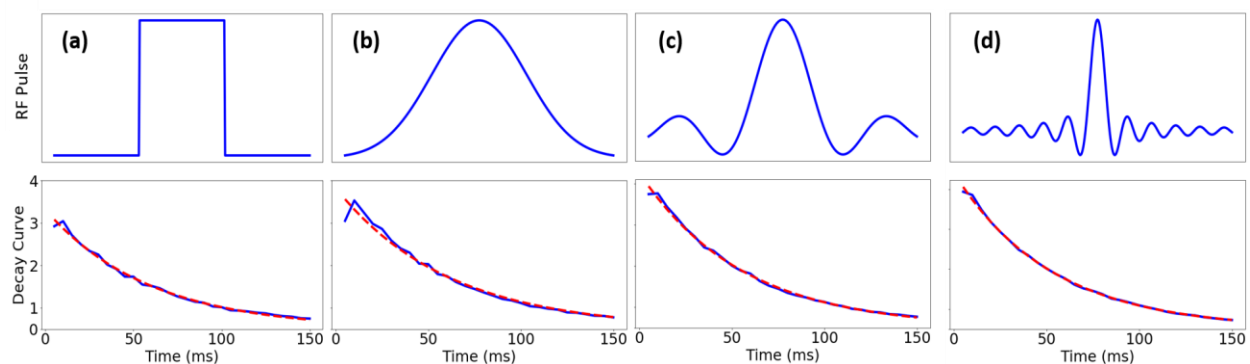


Figure 1: RF pulse shapes (top row) and the corresponding simulated decay signals (— bottom row) and single-exponential fittings (---). (a) rectangular, (b) Gaussian, (c) 1-lobe sinc, (d) 5-lobe sinc.

Conclusions: The RF pulse shape largely affects the decay signal, which should be considered in extracting the voxel-wise T_2 relaxation times. Otherwise, large errors are expected in the result of exponential fitting. Simulating the decay signal and matching the experimental result with simulation will provide a more accurate T_2 estimation.

Quantification of T1 and T2* Relaxation Times of Fetal Fat and Fetal Muscles at 1.5 T

Simran Sethi¹, Stephanie A. Giza¹, Mary-Ellen ET. Empey¹, Barbra de Vrijer^{2,3}, Charles A. McKenzie^{1,3}

¹Medical Biophysics, Western University, ²Obstetrics & Gynaecology, Western University, ³Division of Maternal, Fetal and Newborn Health, Children's Health Research Institute, London, ON, Canada

Introduction: Magnetic resonance imaging (MRI) is a powerful tool that can be used to visualize fetal anatomy as well as identify pathology¹⁻³. Experience with fetal MRI is limited, particularly regarding the knowledge of fetal MR T1 and T2* relaxation parameters. Although conventional T1- and T2*-weighted fetal images provide sufficient tissue contrast, signal intensity can only be interpreted qualitatively because it is affected by intrinsic contrast mechanisms, which in turn are influenced by both MR hardware and software⁴. Consequently, comparison of fetal images, as well as interpreting physiological properties based on signal values can prove to be challenging. Therefore, the purpose of this study is to quantify T1 and T2* relaxation times of fetal tissues as a function of gestational age (GA) as these relaxation times have physical meanings.

Methods: Consenting women with singleton pregnancies, and a GA between 28 and 38 weeks were imaged in a wide-bore (70 cm diameter), 1.5 T MRI. Two 3D water-fat chemical shift encoded MRI volumes were acquired axial to the maternal abdomen during two separate maternal breath holds (IDEAL-IQ: TE: 4.3-4.6 ms, Echo Train Length: 6, Flip Angle: 6° or 20°, TR: 9.3-9.8 ms, acquisition time: 12-28s). 3D Slicer (v4.10.2-2019-5-55)⁷ was used to segment the whole volume of fetal adipose tissue (AT) compartments and fetal muscles. AT segmentations were done on the fat-only images while the muscle segmentations were done on the water-only images. Mean lipid T1 of the AT compartments and mean water T1 of the muscle were calculated using DESPOT1⁸. T2* values were quantified by transferring the T1 segmentations onto R2* maps and calculating the mean T2* of the volume. A sum-of-squared F-test was performed to see if the slope of T1 and T2* as a function of GA for each tissue was significantly different from zero ($\alpha = 0.05$).

Results: Nineteen women (GA: 28-27 weeks) participated in the study. Acquisitions from eight women were excluded due to insufficient tissue contrast ($n = 3$) and complicated pregnancies ($n = 5$). IDEAL-IQ acquisitions were repeated for three participants due to fetal motion and no participant was excluded due to significant fetal motion. Only the slope of lipid T1 of lower legs AT, the T2* of all fetal AT except the cheeks, and the T2* of all the muscles except the thighs and paravertebral were significantly different from zero, indicating the values are changing during the investigated gestational period (Figure 1).

Conclusion: This study showed that the lipid T1 of lower legs, the T2* of all fetal compartments except the cheeks, and the T2* of all fetal muscles except the thighs and paravertebral were found to change as a function of GA between 28- and 38-weeks gestation.

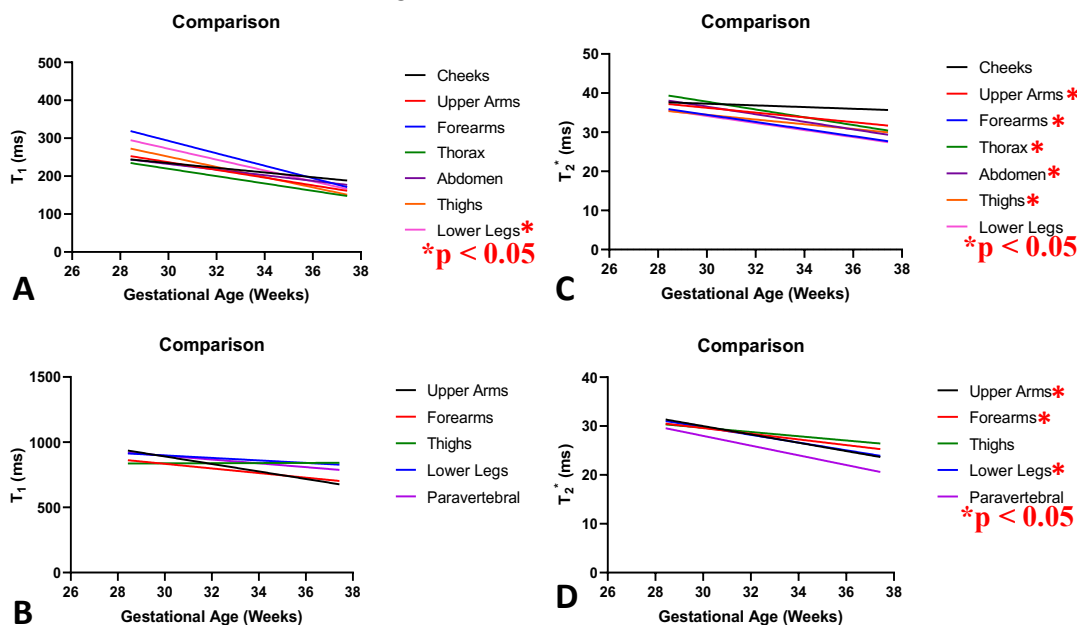


Figure 1. Lipid T1 of fetal adipose tissue compartments (A), water T1 of fetal muscles (B), T2* of fetal adipose tissue compartments (C), and T2* of fetal muscles (D) are plotted as a function of

References: (1) Frates MC, *et al.* Radiology 2004. (2) Levine D, *et al.* Top Magn Reson Imaging 2001. (3) Stecco A, *et al.* Radiol Med 2007. (4) Cheng HLM, *et al.* J Magn Reson Imaging 2012. (5) Fedorov A, *et al.* Magn Reson Imaging 2012. (6) Deoni SC, *et al.* Magn Reson Med 2003.

The study of RF Induced Heating on Orthopedic Implant at 63.87 MHz

Saghar Batebi, Dereck Gignac, William B Handler, and Blaine Alexander Chronik

The xMR Labs, Physics and Astronomy, Western University, London, ON, Canada, Department of Medical Biophysics, Western University, London, ON, Canada

INTRODUCTION

In the presence of medical implants in magnetic resonance imaging systems, the RF induced heating in the tissue might be increased due to the coupling of the electric field induced in the body with the conductive device which can cause tissue damage. Numerical simulation is an essential tool for MRI safety testing of medical devices with different configurations to identify the worst case[1], which is time-consuming and costly if done on a real MRI machine. In this work, using electromagnetic finite difference time domain analysis, we studied the peak spatial averaged specific absorption rate (PsSAR, which is maximum average SAR within a constant-mass cubes of tissue) and temperature rise in the vicinity of the orthopedic implants for 1.5 T using plane wave exposure to find the “worst-cases”.

METHODS

The simulations were performed in Sim4life[2]. To ensure the implants are exposed to almost homogeneous excitation, two plane wave box sources with opposite propagation and magnetic field directions with electric fields aligned with the rod of the implants are applied. The implants were modeled as perfect electrical conductors, placed in the center of rectangular box sources of dimension 300*300*400 cm and gel dimension of 400*400*500 cm, density of 1001, Electric conductivity of 0.47 s/m and relative permittivity of 78. The EM excitation signal set to Harmonic at frequency 63.87 MHz, such that the SAR value at the center of Gel without any device be 10 w/kg. The thermal simulation was performed in Sim4Life, using the results of the EM simulation as the source of heat, to evaluate the location of max temperature and temperature pattern in each device. The orthopedic implants, used in this study consisted of a metallic rod with the length of 150 mm and different number of screws 4,5 and 7 with the length of 18, 65 and 105 mm.

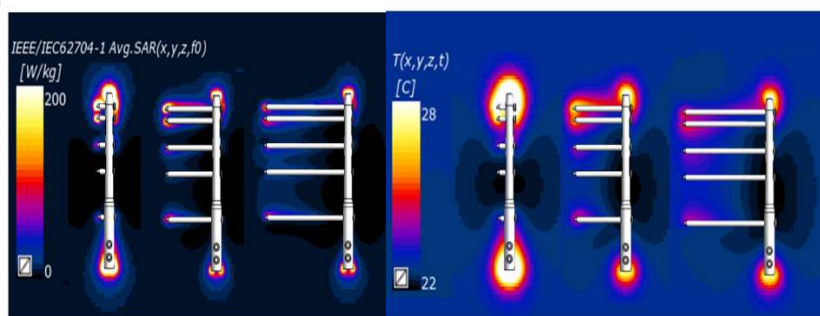
RESULTS

The temperature before exposing the RF radiation is 22°C. The thermal simulations were performed for 360 s exposure. The 0.1 g PsSAR and temperature rise for 63.87 MHz are listed in the bellow Table. The 0.1 g PsSAR and temperature pattern of implants with the rod length of 150 mm and 7 screws with the length of 18, 65 and 105 mm in YZ plane are shown in the bellow Figure.

CONCLUSION

From the result it could be seen that the temperature rise is related to the length of rods and the length of screws and the maximum temperature rise locations are close to both ends of the rods or at the screws tip. This study demonstrates the importance of modeling to evaluate the interaction of RF radiation with different medical implants during MRI imaging, and can help to guide the simulation parameter space and more complicated simulations.

Rod length (mm)	Screw length (mm)	#screws	0.1g PsSAR (w/kg)	Peak Temp (°C)
No device	No device	No device	24.4001	23.6936
150	18	4	588.256	37.6747
150	18	5	589.016	37.6956
150	18	7	565.356	37.1011
150	65	4	384.008	29.1391
150	65	5	384.461	29.1776
150	65	7	253.283	28.6756
150	105	4	236.534	28.3591
150	105	5	237.039	28.3646
150	105	7	229.45	28.1917



REFERENCES

- [1] J. Kabil, L. Belguerras, S. Trattnig, C. Pasquier, J. Felblinger, and A. Missoffe, “A Review of Numerical Simulation and Analytical Modeling for Medical Devices Safety in MRI,” *Yearb. Med. Inform.*, no. 1, pp. 152–158, Nov. 2016.
- [2] <https://zmt.swiss/sim4life/>.

Imaging Network Ontario (ImNO) Code of Conduct

All attendees, speakers, sponsors and volunteers at ImNO are required to agree with the following code of conduct. Organisers will enforce this code throughout the event. We expect cooperation from all participants to help ensure a safe environment for everybody.

Need Help?

If you are being harassed, notice that someone else is being harassed, or have any other concerns, speak to ImNO staff or send an email to ombudsperson@ImNO.ca or chair@ImNO.ca.

Overview

Imaging Network Ontario is committed to providing a harassment-free conference experience for everyone, regardless of gender, gender identity and expression, age, sexual orientation, disability, physical appearance, body size, race, ethnicity, religion (or lack thereof), or technology choices. We do not tolerate harassment of conference participants in any form. Use of sexualised language and imagery that does not convey a scientific message is not appropriate. We expect participants and sponsors to follow these rules for the duration of the conference in any conference venue, including talks, workshops, parties, Twitter and other online media. Conference participants violating these rules may be sanctioned or expelled from the conference without a refund at the discretion of the conference organisers.

Details

All attendees, speakers, sponsors and volunteers at ImNO are subject to the anti-harassment policy.

Harassment includes offensive verbal comments related to gender, gender identity and expression, age, sexual orientation, disability, physical appearance, body size, race, ethnicity, religion, technology choices, sexual images in public spaces, deliberate intimidation, stalking, following, harassing photography or recording, sustained disruption of talks or other events, inappropriate physical contact, and unwelcome sexual attention. Use of images, activities, uniforms/costumes or other materials that create a sexualised environment will not be tolerated.

Anyone asked to stop any harassing behavior is expected to comply immediately.

If anyone engages in harassing behavior, the conference organisers may take any action they deem appropriate, including warning the offender or expulsion from the conference **with no refund**.

If you are being harassed, notice that someone else is being harassed, or have any other concerns, please contact a member of conference staff immediately. Conference staff can be identified as they'll be wearing clearly marked badges saying "ImNO staff". You can also send an email to the ImNO ombudsperson, Dr. Maria Drangova, at ombudsperson@ImNO.ca or the ImNO 2020 Chair, Dr. Amber Simpson, at chair@ImNO.ca.

Conference staff will be happy to help participants contact hotel/venue security or local law enforcement, provide escorts, or otherwise assist those experiencing harassment to feel safe for the duration of the conference. We value your attendance.

We expect everyone to follow these rules for the duration of the conference within and outside conference venues, including but not limited to conference-related talks, workshops, and social events involving ImNO attendees, and in all conference related communications, including social media.

Author Index

Name	Presentation	Page
Abayomi, Naomi S	Poster 6-12	149
Abolmaesumi, Purang	Oral 3-4	36
Acera, Marian	Poster 6-13	150
Adamo, Sabrina	Poster 6-2	139
Addy, Nii Okai	Oral 5-5	51
Ahmed, Mashal	Poster 6-8	145
Ahn, Joshua	Poster 3-5	112
Akbari, Alireza	Poster 4-8	123
Akhavein, Hassan	Poster 8-5	172
Alfano, Ryan M	Oral 1-5	23
Al-Khishman, Nassir U.N.	Oral 6-4	56
Allen, Daniel	Poster 9-12	188
Alonzo-Proulx, Olivier	Oral 3-6	38
Amalou, amel	Oral 3-4	36
Anderson, William	Poster 9-22	198
Appleton, Tom	Oral 7-1	59
	Poster 9-9	185
Arbuckle, Spencer	Poster 6-10	147
Arezza, Nico J J	Oral 9-4	76
	Oral 10-4	82
Armstrong, Mark	Poster 1-14	99
	Poster 9-26	202
Aslam, Danesh	Oral 2-2	27
Asselin, Mark	Oral 5-4	50
	Poster 4-1	116
	Poster 5-7	131
Athwal, George	Poster 7-2	165
Attaran, Ali	Poster 9-4	180
	Poster 9-5	181
Au, Ryan	Oral 2-3	28
	Poster 2-5	105
Azarpazhooh, Reza	Poster 8-6	173
Babichev, Yael	Oral 4-2	41
Badiuk, Sawyer	Poster 9-10	186
Baek, Jason	Poster 9-21	197
Bainbridge, Daniel	Oral 8-4	69
Balachandran, Vinood	Poster 4-5	120
Baranova, Katherina	Oral 3-3	35
Barker, Kevin	Poster 5-10	134

Name	Presentation	Page
Baron, Corey	Oral 9-3	75
	Oral 9-4	76
	Oral 9-5	77
	Oral 10-2	80
	Oral 10-3	81
	Oral 10-4	82
	Poster 9-2	178
Baronette, Rudy	Oral 7-3	61
Barr, Colton A	Oral 5-4	50
Barry, Jennifer	Oral 8-1	66
	Oral 8-2	67
	Oral 8-3	68
Bartha, Robert	Oral 6-2	54
	Poster 6-2	139
	Poster 8-5	172
Bartlett, Jason	Oral 2-2	27
Basharat, Fateen	Poster 2-3	103
Bassman, Jared	Poster 4-5	120
Batch, Karen	Poster 3-2	109
Batebi, Saghar	Poster 5-9	133
	Poster 9-28	204
Battie, Michele	Poster 3-5	112
Bauman, Glenn	Oral 1-5	23
	Oral 3-2	34
Bauza, Xavier	Oral 2-2	27
Bax, Jeffrey	Oral 4-3	42
	Poster 5-10	134
Bazinet, Richard	Poster 6-6	143
Bazzi, Layale	Poster 9-26	202
Beach, Tyson	Poster 5-3	127
Berman, David	Poster 4-4	119
Bernards, Nicholas	Poster 1-1	86
Best, Laura M.	Poster 6-7	144
Biernaski, Heather	Oral 8-5	70
Black, Sandra	Poster 6-2	139
	Poster 8-5	172
Bloomfield, Peter	Poster 6-24	161
Boffa, Michael	Poster 8-1	168

Name	Presentation	Page
Boileau, Isabelle	Oral 6-1	53
	Poster 6-3	140
	Poster 6-6	143
	Poster 6-7	144
	Poster 6-8	145
Bomben, Matteo	Poster 9-24	200
Borsos, Kevin B	Oral 10-2	80
Boyes, Aaron	Poster 9-14	190
Boyle, Amanda	Oral 1-4	22
Brenkel, Megan	Poster 5-3	127
Brown, Arthur	Oral 10-4	82
Brzozowski, Luke	Poster 9-19	195
Buchler, Ariel	Poster 1-10	95
Burke, Amy	Poster 9-9	185
Butler, John	Oral 1-5	23
	Oral 8-5	70
Cabrera, Alberto	Poster 6-13	150
Calarco, Navona	Poster 6-20	157
Calvert, Nicholas D.	Poster 1-12	97
Camilleri-Newbigging, Susan	Poster 8-8	175
Camire, Daenis	Oral 4-4	43
Carnahan, Patrick	Oral 8-4	69
Carvalho, Marco Antônio Garcia	Poster 6-4	141
Cecchini, Matthew	Oral 3-3	35
Chakraborty, Jayasree	Poster 4-5	120
Chau, Oi Wai	Poster 8-3	170
Chavez, Sofia	Poster 6-14	151
	Poster 6-21	158
	Poster 8-2	169
	Poster 9-3	179
Chen, Albert	Poster 6-22	159
Chen, Brian	Oral 4-4	43
Chen, Elvis C. S.	Oral 4-1	40
	Oral 8-4	69
	Poster 5-11	135
	Poster 9-12	188
Chen, Tan	Oral 4-5	44
Chen, Yuanxin	Oral 1-3	21
Cherin, Emmanuel	Poster 9-14	190
Chettle, David	Poster 9-11	187
Cheung, Alison	Poster 1-4	89

Name	Presentation	Page
Chin, Joseph	Oral 1-5	23
	Oral 3-2	34
	Poster 3-7	114
Cho, Jessica	Poster 3-2	109
Cho, Sang Soo	Oral 6-5	57
	Poster 6-11	148
Chou, Yuting	Poster 4-5	120
Choueib, Saleh	Poster 5-4	128
Choyke, Peter	Oral 3-4	36
Christiansen, Spencer	Poster 8-1	168
Christie, Jaryd R	Poster 9-21	197
Chronik, Blaine	Oral 9-2	74
	Poster 5-9	133
	Poster 9-1	177
	Poster 9-4	180
	Poster 9-5	181
	Poster 9-6	182
	Poster 9-15	191
	Poster 9-16	192
	Poster 9-17	193
	Poster 9-23	199
	Poster 9-25	201
	Poster 9-28	204
Chu Kwan, William	Oral 7-5	63
Chung, Kevin J	Oral 8-6	71
	Poster 6-19	156
Clarke, Collin	Poster 9-12	188
Cleland, Theo S	Oral 3-6	38
Clement, Allison J	Poster 4-6	121
Cobos, Santiago F	Oral 7-3	61
	Oral 7-6	64
	Poster 9-18	194
Cohen, David J F	Poster 6-18	155
Connolly, Laura	Oral 5-3	49
	Poster 5-7	131
	Poster 4-1	116
Cook, Moses P	Oral 8-1	66
Cotechini, Tiziana	Poster 9-20	196
Cottrell, Tricia	Poster 4-5	120
Couch, Marcus	Oral 2-4	29

Name	Presentation	Page
Coxson, Harvey O	Oral 2-2	27
	Oral 2-3	28
	Poster 2-6	106
	Poster 2-1	101
Crawford, Eric	Oral 4-5	44
Cronin, Alicia	Oral 6-2	54
Cunningham, Charles H	Poster 6-22	159
Curpen, Belinda	Poster 3-6	113
Cyr, Melodie	Poster 9-11	187
Daher, Baraa	Poster 7-2	165
Dahl, Kenneth	Poster 6-24	161
	Poster 6-25	162
Daly, Michael J	Poster 5-1	125
Dammak, Salma	Oral 3-3	35
Daoud, Rebecca	Oral 10-1	79
Daskalakis, Jeff	Poster 6-8	145
Davieau, Kieffer J	Oral 9-2	74
	Poster 5-9	133
	Poster 9-15	191
	Poster 9-17	193
de Bruyn, John	Poster 1-13	98
de Vrijer, Barbra	Poster 9-27	203
Delpino, Rocio	Poster 6-13	150
Demore, Christine	Poster 9-8	184
	Poster 9-14	190
Desmond, Kim	Poster 6-21	158
Detombe, Sarah	Oral 6-2	54
Dhanvantari, Savita	Oral 8-5	70
	Poster 1-7	92
Dharmakumar, Rohan	Oral 8-5	70
Diez-Cirarda, Maria	Oral 6-5	57
	Poster 6-11	148
	Poster 6-13	150
Dima, Robert	Oral 7-1	59
Ding, Xiao Fan	Poster 9-1	177
	Poster 9-23	199
Diop, Mamadou	Poster 6-12	149
	Poster 6-18	155
Dixon, S. Jeffrey	Poster 1-13	98
Do, Richard	Poster 3-2	109
	Poster 4-5	120
	Poster 9-13	189

Name	Presentation	Page
Doornekamp, Ande	Poster 9-21	197
Dourthe, Benjamin	Poster 5-3	127
Dowlatshahi, Dariush	Poster 6-2	139
Downes, Michelle	Poster 3-7	114
Doyle-Pettypiece, Pat	Oral 6-2	54
Drake, James	Oral 7-5	63
Drangova, Maria	Oral 7-6	64
	Poster 8-1	168
	Poster 9-9	185
Driscoll, Brandon	Poster 9-19	195
D'Souza, David	Oral 3-1	33
Duan, Qingling	Poster 3-4	111
	Poster 4-5	120
Duarte, Kauê T N	Poster 6-4	141
Dubois, Veronica	Poster 1-6	91
Dubovan, Paul I	Oral 9-3	75
Dueck, Andrew	Oral 5-1	47
Duffy, Ian R	Poster 6-25	162
Duggal, Neil	Oral 6-2	54
Dunmore-Buyze, Joy	Poster 9-9	185
Eagleson, Roy	Poster 5-6	130
Eddy, Rachel L	Oral 2-6	31
	Poster 2-4	104
Elbatarny, Lydia	Poster 4-7	122
El-Deeb, Omar	Oral 9-5	77
Ellis, Christopher	Poster 9-21	197
El-Sherif, Omar	Poster 8-3	170
Empey, Mary-Ellen	Poster 9-27	203
Erb, Jason	Oral 4-4	43
Escartin, Terenz R	Oral 8-3	68
Eu, Donovan	Poster 5-1	125
Faber, Cornelius	Poster 1-14	99
Farber, Gedaliah	Poster 1-10	95
Farrag, Nadia A	Poster 8-4	171
Fenster, Aaron	Oral 3-1	33
	Oral 4-3	42
	Oral 4-6	45
	Oral 7-1	59
	Poster 5-10	134
	Poster 8-6	173
Fernando, Ann	Poster 1-9	94

Name	Presentation	Page
Fichtinger, Gabor	Oral 4-4	43
	Oral 5-2	48
	Oral 5-3	49
	Oral 5-4	50
	Poster 4-1	116
	Poster 4-3	118
	Poster 4-7	122
	Poster 5-2	126
	Poster 5-4	128
	Poster 5-7	131
	Poster 5-8	132
	Poster 5-12	136
	Filippov, Mihail	Poster 5-8
Finger, Elizabeth	Poster 8-5	172
Finkelstein, Joel	Oral 4-5	44
Fleisig, Clara	Poster 6-22	159
Fleisig, Jacqueline	Poster 5-1	125
Fliss, Jordan D	Oral 2-1	26
Foltz, Warren	Oral 4-2	41
	Oral 7-5	63
Fortin, Maryse	Poster 3-5	112
Foster, Paula	Oral 1-2	20
	Poster 1-3	88
	Poster 1-6	91
	Poster 1-11	96
	Poster 1-12	97
Foster, Stuart	Poster 9-8	184
	Poster 9-14	190
Fox, Matthew	Oral 6-4	56
	Poster 1-7	92
	Poster 2-2	102
Fradin, Cecile	Oral 1-6	24
Fraser, Graham	Poster 9-21	197
Frayne, Richard	Poster 6-4	141
	Poster 6-23	160
Freedman, Morris	Poster 8-5	172
Fukuda, Hitoshi	Poster 5-5	129
Gabilondo, Inigo	Poster 6-13	150
Gaed, Mena	Oral 1-5	23
Gaede, Stewart	Poster 4-2	117
	Poster 8-3	170
Gangai, Natalie	Poster 3-2	109

Name	Presentation	Page
Gao, Fuqiang	Poster 6-2	139
Garcia, Armando	Poster 6-24	161
Gardi, Lori	Oral 4-3	42
	Poster 5-10	134
Gariepy, Jean	Poster 1-9	94
Garvin, Gregory	Poster 5-6	130
Gaudette, Erin V	Oral 6-1	53
	Poster 6-6	143
Gazit, Lior	Poster 3-2	109
Genkin, Daniel	Oral 2-2	27
Geraghty, Benjamin	Poster 6-22	159
Gerolami, Justin	Oral 9-1	73
Gerstle, J. Ted	Oral 4-2	41
Ghugre, Nilesh	Oral 8-1	66
	Oral 8-2	67
Gignac, Dereck	Poster 9-1	177
	Poster 9-28	204
Gilbank, Ashley	Poster 5-1	125
Gill, Talwinder	Oral 6-1	53
Gillies, Derek J	Oral 3-1	33
	Oral 4-6	45
	Oral 7-1	59
	Poster 5-10	134
Ginty, Fiona	Poster 1-4	89
Giza, Stephanie A	Poster 9-27	203
Gladdy, Rebecca	Oral 4-2	41
Gobbi, David	Poster 6-4	141
Goertz, David	Poster 1-2	87
Goldhawk, Donna	Oral 1-6	24
Golia Pernicka, Jennifer S.	Poster 3-4	111
Gomez Beldarrain, MariaAngeles	Poster 6-13	150
Gomez-Esteban, Juan Carlos	Poster 6-13	150
Gomez-Lemus, Jose	Oral 1-5	23
	Oral 3-2	34
Gonen, Mithat	Poster 4-5	120
Goolaub, Datta Singh	Poster 8-7	174
Gormley, William	Oral 5-4	50
Goubran, Maged	Poster 6-2	139
	Poster 8-5	172
Grebenisan, Andrew	Poster 3-3	110
Green, Duncan GJ	Poster 6-3	140
Gregor, Alexander	Poster 1-1	86

Name	Presentation	Page
Groves, Leah	Oral 4-1	40
Gyackov, Igor	Oral 3-1	33
	Oral 4-6	45
Haast, Roy AM	Poster 6-5	142
Hachinski, Vladimir	Oral 6-4	56
Haddad, Seyyed M. H.	Poster 8-5	172
Halder, Arjama	Poster 9-4	180
	Poster 9-5	181
Hamilton, Amanda	Oral 1-2	20
	Poster 1-3	88
	Poster 1-11	96
Hamilton, Jeffrey G	Poster 6-16	153
Han, Wenchao	Oral 3-2	34
	Poster 3-7	114
Handler, William	Poster 5-9	133
	Poster 9-1	177
	Poster 9-4	180
	Poster 9-5	181
	Poster 9-6	182
	Poster 9-15	191
	Poster 9-16	192
	Poster 9-23	199
	Poster 9-25	201
Poster 9-28	204	
Hardisty, Michael	Oral 4-5	44
	Poster 5-3	127
	Poster 4-6	121
Harkness, Michael	Poster 6-24	161
Harvey, Jennifer	Oral 3-6	38
Hashemi, Samineh	Poster 8-6	173
Hassan, Saqeeb	Oral 5-5	51
Hawco, Colin	Oral 10-5	83
Hechtman, Jaclyn F.	Poster 3-4	111
Hemachandra, Dimuthu	Poster 6-1	138
Hendershot, Christian S.	Poster 6-7	144
Hendriks, Jack	Poster 9-4	180
	Poster 9-5	181
Hicks, Justin	Oral 8-5	70
	Poster 1-7	92
Hill, Matt N	Poster 6-3	140
	Poster 6-6	143
Hindmarch, Charles	Poster 9-20	196

Name	Presentation	Page
Hisey, Rebecca	Oral 4-4	43
Hocking, David	Poster 5-6	130
Hogg, James C	Oral 2-3	28
	Oral 2-2	27
	Poster 2-1	101
	Poster 2-6	106
	Oral 7-3	61
	Oral 7-6	64
Holdsworth, David W	Poster 1-5	90
	Poster 1-13	98
	Poster 7-3	166
	Poster 9-7	183
	Poster 9-9	185
	Poster 9-18	194
	Poster 9-22	198
Holmes, Melissa	Poster 6-2	139
	Poster 8-5	172
Hong, Gregory	Oral 7-6	64
Hou, Jinqiang	Oral 8-5	70
Houle, Sylvain	Oral 6-1	53
	Poster 6-3	140
	Poster 6-6	143
	Poster 6-7	144
Howes, Daniel	Oral 4-4	43
Hrinivich, W. Thomas	Oral 4-6	45
Huang, Laurie	Oral 3-2	34
Huang, Susan	Poster 6-16	153
Huff, Murray	Poster 9-9	185
Hutchison, Michael	Oral 6-1	53
Ibarretxe-Bilbao, Naroa	Poster 6-13	150
Innis, Robert	Oral 1-4	22
Irish, Jonathan	Poster 5-1	125
Izard, Jason	Poster 3-3	110
Jaeger, Melanie	Poster 5-4	128
Jaffray, David	Poster 5-1	125
Jamaspishvili, Tamara	Poster 4-4	119

Name	Presentation	Page
Jamzad, Amoon	Oral 3-4	36
	Oral 5-3	49
	Oral 9-1	73
	Poster 4-1	116
	Poster 4-3	118
	Poster 4-4	119
	Poster 5-2	126
	Poster 5-7	131
	Poster 9-20	196
Janssen, Natasja	Oral 5-3	49
	Poster 5-2	126
	Poster 5-4	128
Javed, Ahsan	Oral 8-2	67
Jetly, Rakesh	Oral 6-1	53
	Poster 6-6	143
Jonnalagadda, Melanie	Poster 8-6	173
Joschko, Abigayel	Poster 9-12	188
Jurkiewicz, Michael	Poster 6-16	153
Kai, Jason	Poster 6-15	152
Kakani, Nirmal	Poster 5-10	134
Kalsi-Ryan, Sukhvinder	Oral 6-2	54
Kasa, Loxlan W.	Poster 6-5	142
Kasuya, Hidetoshi	Poster 5-5	129
Kaufmann, Martin	Oral 5-3	49
	Poster 4-1	116
	Poster 4-4	119
	Poster 5-2	126
Kelly, John	Poster 1-6	91
	Poster 1-7	92
Keunen, Ben	Oral 4-2	41
	Oral 7-5	63
Khan, Ali R.	Oral 9-5	77
	Oral 10-3	81
	Oral 10-4	82
	Poster 6-1	138
	Poster 6-5	142
	Poster 6-15	152
Khazae, Tina	Oral 7-6	64
	Poster 1-5	90
Kim, Jinhee	Oral 6-5	57
	Poster 6-3	140
	Poster 6-13	150

Name	Presentation	Page
Kirby, Alexia	Poster 1-8	93
Kirby, Miranda	Oral 2-2	27
	Oral 2-3	28
	Poster 2-1	101
	Poster 2-5	105
	Poster 2-6	106
Kish, Stephen	Oral 6-1	53
	Poster 6-3	140
	Poster 6-6	143
	Poster 6-7	144
Kloiber, Stefan	Poster 6-8	145
Knight, Ashley C	Oral 6-3	55
Knipping, Danielle	Oral 2-6	31
Kong, Isaac	Poster 9-21	197
Koo, Meghan	Oral 2-3	28
	Poster 2-5	105
Koshirmori, Yuko	Oral 6-5	57
	Poster 6-11	148
Koszalka, Maura	Poster 4-5	120
Krahn, Philippa	Oral 8-3	68
Krasnichuk, Chris	Oral 4-2	41
Krishna Jeyaraj, Satheesh	Oral 3-5	37
	Poster 3-1	108
Krishnan, Sri	Oral 2-2	27
Kuehn, Tristan K	Oral 9-5	77
	Oral 10-3	81
	Oral 10-4	82
	Poster 3-6	113
Kuling, Grey C	Poster 3-6	113
Kwak, Jin Tae	Oral 3-4	36
Kwan, Donna	Poster 6-2	139
	Poster 8-5	172
Kwan, Keith	Oral 3-3	35
Laflamme, Michael	Oral 8-1	66
Laframboise, Jacob R	Oral 5-2	48
Lalone, Emily	Oral 7-2	60
	Poster 7-1	164
	Poster 7-2	165
	Poster 6-2	139
Lang, Anthony	Poster 6-2	139
	Poster 8-5	172
Lanius, Ruth	Oral 6-1	53
Larsen, Melissa	Oral 8-2	67
	Oral 8-3	68

Name	Presentation	Page
Lasso, Andras	Oral 5-4	50
	Poster 5-7	131
Lawrence Dewar, Jane	Poster 6-2	139
Le Foll, Bernard	Poster 6-7	144
	Poster 6-8	145
Lebel, Marc	Poster 6-23	160
Lee, Casey Y	Poster 6-22	159
Lee, Jenny	Poster 9-19	195
Lee, Ting	Oral 7-2	60
	Oral 8-6	71
	Poster 4-2	117
Lessard, Eric J	Poster 9-15	191
	Poster 9-25	201
Levine, Brian	Poster 8-5	172
Levit, Alexander	Oral 6-4	56
Li, Daniel	Oral 2-1	26
Li, Natalie	Oral 4-1	40
Li, Si Jia	Oral 9-1	73
Licskai, Chris	Oral 2-6	31
Lin, Peter	Oral 8-3	68
	Poster 8-8	175
Lindenmaier, Andras	Oral 2-1	26
Lindenmaier, Tamas	Oral 2-6	31
Liu, Junmin	Poster 8-1	168
Liu, Kela	Poster 1-4	89
Liu, Qiong	Poster 8-6	173
Lo, Benjamin W.Y.	Poster 5-5	129
Lobaugh, Nancy	Poster 6-3	140
	Poster 6-14	151
Loos, Wallace S	Poster 6-23	160
Lorusso, Daniel	Poster 1-13	98
Lownie, Stephen	Poster 5-5	129
Lu, Yingli	Poster 7-3	166
Lucas-Jimenez, Olaia	Poster 6-13	150
Lui, Victor	Poster 2-5	105
Lui, Wai Tai	Oral 2-3	28
Lupton, Kaelan	Poster 3-2	109
Luyt, Leonard	Oral 8-5	70
MacDonald, Penny	Poster 6-1	138
Macgowan, Christopher K	Poster 8-7	174
MacIntosh, Bradley	Poster 8-5	172

Name	Presentation	Page
MacNeil, Jonathan	Oral 2-5	30
	Poster 2-4	104
Mainprize, James	Oral 3-6	38
Makela, Ashley	Oral 1-2	20
	Poster 1-11	96
Mandzia, Jennifer	Poster 8-5	172
Marini, Davide	Poster 8-7	174
Mark Hirsch, Steven	Poster 5-3	127
Marras, Connie	Poster 6-2	139
Martel, Anne	Poster 1-4	89
	Poster 3-6	113
	Poster 8-8	175
Martinez, Diego F	Poster 9-15	191
	Poster 9-16	192
Martinez, Francisco M	Poster 4-8	123
	Poster 1-7	92
Masellis, Mario	Poster 6-2	139
	Poster 8-5	172
Matheson, Alexander M	Poster 2-4	104
	Poster 1-1	86
Matsuura, Naomi	Poster 1-2	87
	Poster 9-24	200
	Poster 9-21	197
Mawdsley, Laura	Poster 9-21	197
McCluskey, Tina	Oral 6-1	53
	Poster 6-3	140
	Poster 6-6	143
	Poster 6-7	144
McCormack, David	Oral 2-5	30
	Oral 2-6	31
	Poster 2-2	102
McCready, Matthew A	Poster 9-6	182
McGarry, Ciara	Poster 5-4	128
McGrath, Sean F	Poster 1-1	86
McIntosh, Marrisona	Oral 2-6	31
	Poster 2-4	104
McIntyre, Caitlin	Poster 3-4	111
	Poster 4-5	120
McKay, Doug	Oral 5-3	49
	Poster 5-2	126
McKenzie, Charles	Poster 9-27	203
McLaughlin, Paula	Poster 8-5	172
McLeod, Jonathan	Poster 5-5	129

Name	Presentation	Page
McNeill, Fiona	Poster 9-11	187
Mehrtash, Alireza	Oral 3-4	36
Melo, Kierstin P	Poster 1-11	96
Menard, Alexandre	Poster 3-3	110
Menon, Bijoy	Oral 8-6	71
	Poster 6-19	156
Menon, Ravi	Poster 6-10	147
Metrow, Colin	Oral 9-2	74
	Poster 9-17	193
Meyer, Jeffrey H.	Oral 6-1	53
	Poster 6-7	144
Mihaescu, Alexander	Oral 6-5	57
	Poster 6-11	148
	Poster 6-13	150
Moehring, Amanda	Oral 9-5	77
Mojiri Forooshani, Parisa	Poster 6-2	139
Montero-Odasso, Manuel	Poster 8-5	172
Moody, Alan	Poster 6-2	139
	Poster 9-24	200
Moore, John	Oral 8-4	69
	Poster 5-11	135
	Poster 9-12	188
Morse, Nicole	Poster 4-4	119
Moslemi, Amir	Poster 2-6	106
Motooka, Yamato	Poster 1-1	86
Mouawad, Matthew	Poster 8-3	170
Mousavi, Parvin	Oral 3-4	36
	Oral 5-3	49
	Oral 9-1	73
	Poster 3-3	110
	Poster 4-1	116
	Poster 4-3	118
	Poster 4-4	119
	Poster 5-2	126
	Poster 5-7	131
	Poster 9-20	196
Moussa, Madeleine	Oral 1-5	23
	Oral 3-2	34
Mu, Yanyu	Poster 5-6	130
Munch, Maxime	Poster 1-10	95
Munidasa, Samal	Oral 2-4	29
Murrell, Emily	Poster 6-9	146

Name	Presentation	Page
Mushtaha, Farah N	Oral 9-5	77
	Oral 10-3	81
	Oral 10-4	82
Narayanaswami, Vidya	Poster 6-24	161
Nayak, Krishna	Oral 8-2	67
Nazeri, Arash	Oral 10-5	83
Nelson, Andrew	Poster 9-18	194
Ng, Matthew	Oral 8-3	68
Ngugama, Malaika	Poster 3-4	111
Nguyen, Huy	Poster 3-2	109
Nicol, Christopher	Poster 4-1	116
	Poster 4-3	118
	Poster 5-7	131
Nikolov, Hristo N	Poster 1-5	90
	Poster 1-13	98
	Poster 9-7	183
Nikolova, Yuliya	Poster 6-20	157
Nisar, Hareem	Poster 5-11	135
Norley, Chris	Poster 1-5	90
	Poster 9-9	185
Noseworthy, Michael	Poster 6-17	154
Ntiri, Emmanuel Edward	Poster 6-2	139
Nyström, Nivin N	Oral 1-1	19
	Poster 1-7	92
Ogrodnik, Natalia	Oral 7-4	62
Ohashi, Pam	Poster 1-4	89
Ojeda, Natalia	Poster 6-13	150
O'Reilly, Meaghan	Oral 7-4	62
Orlando, Nathan	Oral 3-1	33
Orr, Christine	Poster 4-3	118
Ouriadov, Alexei V	Poster 2-2	102
Ozzoude, Miracle	Poster 6-2	139
Palma, David	Oral 3-3	35
Panoyan, MaryAnne	Poster 4-5	120
Papernick, Sam	Oral 7-1	59
Parasram, Tristhal	Oral 10-1	79
Parry, James	Oral 9-2	74
	Poster 9-17	193
Park, Claire K	Oral 4-3	42

Name	Presentation	Page
Parraga, Grace	Oral 2-5	30
	Oral 2-6	31
	Poster 2-2	102
	Poster 2-4	104
Patel, Jaykumar	Oral 5-5	51
Patel, Tirth	Poster 9-19	195
Patterson, Lindsey	Poster 5-4	128
Pautler, Stephen	Oral 1-5	23
	Oral 3-2	34
	Poster 3-7	114
Pavlosky, William	Oral 1-5	23
Pellow, Carly	Poster 1-2	87
Pena, Javier	Poster 6-13	150
Perks, William	Poster 6-22	159
Peters, Terence M	Oral 4-1	40
	Oral 8-4	69
	Poster 3-5	112
	Poster 5-5	129
	Poster 5-6	130
	Poster 5-11	135
	Poster 6-5	142
	Poster 7-3	166
Poster 9-12	188	
Pichardo, Samuel	Oral 4-2	41
Pickering, Geoffrey	Poster 1-13	98
Pieper, Steve	Oral 5-4	50
Pigeau, Grace	Poster 4-7	122
	Poster 5-12	136
Pike, Victor	Oral 1-4	22
Pinto, Peter	Oral 3-4	36
Piorkowska, Karolina	Oral 4-2	41
	Oral 7-5	63
Poepping, Tamie	Poster 1-13	98
Pollmann, Steven I	Oral 7-3	61
	Poster 1-5	90
	Poster 9-9	185
Pop, Mihaela	Oral 8-3	68
	Poster 8-8	175
Prato, Frank	Oral 1-6	24
	Oral 8-5	70
	Poster 8-3	170
	Poster 8-4	171

Name	Presentation	Page
Pruszynski, Andrew	Poster 6-10	147
Publicover, Julia	Poster 9-19	195
Qi, Qi	Oral 6-4	56
Qi, Xiuling	Oral 8-1	66
	Oral 8-3	68
Qiang, Beiping	Oral 8-1	66
Qiu, Wu	Poster 6-19	156
Quinto, John	Oral 8-3	68
Rachinsky, Irina	Oral 1-5	23
Rahman, Naila M	Oral 10-4	82
Ramanan, Venkat	Oral 8-3	68
Ramirez, Joel	Poster 6-2	139
	Poster 8-5	172
Raney, Fraser	Poster 9-13	189
Ranota, Puneet K	Oral 7-2	60
Ratjen, Felix	Oral 2-4	29
Rayment, Jonathan	Oral 2-4	29
Ren, Kevin	Poster 4-4	119
Rhind, Shawn G.	Oral 6-1	53
	Poster 6-6	143
Richardson, Don	Oral 6-1	53
	Poster 6-6	143
Ricketts, Amanda	Poster 9-24	200
Rickey, Daniel	Poster 9-10	186
Rivaz, Hassan	Poster 3-5	112
Roa, Felipe	Poster 9-8	184
	Poster 9-14	190
Robertson, Faith	Oral 5-4	50
Robinson, Sydney M	Poster 7-1	164
Rodgers, Jessica R	Oral 4-6	45
Romagnoli, Cesare	Oral 3-1	33
Romagnuolo, Rocco	Oral 8-1	66
Ronald, John	Oral 1-1	19
	Oral 1-3	21
	Poster 1-6	91
	Poster 1-7	92
Roseborough, Austyn	Oral 6-4	56
Rotstein, Benjamin	Poster 1-10	95
Roy, Trisha	Oral 5-1	47
Rubin-Kahana, Dafna S.	Poster 6-7	144
	Poster 6-8	145

Name	Presentation	Page
Rubino, Rachel	Poster 4-1	116
	Poster 4-3	118
	Poster 5-7	131
Rudan, John	Oral 5-3	49
	Poster 4-1	116
	Poster 4-3	118
	Poster 5-2	126
Rusjan, Pablo	Poster 6-6	143
	Poster 6-7	144
Sacoransky, Ethan	Poster 1-13	98
Sadanand, Siddharth	Oral 2-1	26
Sailasuta, Napapon	Poster 9-3	179
Sainsbury, Ben	Poster 5-8	132
Sajja, Shailaja	Poster 9-19	195
Santilli, Alice ML	Poster 5-2	126
	Oral 5-3	49
Santyr, Giles	Oral 2-1	26
	Oral 2-4	29
Sasaki, David	Poster 9-10	186
Satkunarajah, Janani	Oral 7-4	62
Satler Diniz, Breno	Poster 6-20	157
Saumur, Tyler	Poster 5-3	127
Schieda, Nicola	Oral 3-5	37
	Poster 3-1	108
Schifani, Christin	Oral 10-5	83
	Poster 6-24	161
Scholl, Timothy J	Oral 1-1	19
	Poster 1-7	92
	Poster 4-8	123
Schonwille, Abigael	Poster 4-7	122
	Poster 5-12	136
Schrauben, Eric	Poster 8-7	174
Scott, Christopher	Poster 6-2	139
	Poster 8-5	172
Sedghi, Alireza	Oral 3-4	36
	Poster 3-3	110
	Poster 4-1	116
	Poster 4-4	119
Seed, Michael	Poster 8-7	174
Sehl, Olivia C	Oral 1-2	20
	Poster 1-3	88
Sethi, Simran	Poster 9-27	203

Name	Presentation	Page
Sewani, Alykhan	Oral 5-1	47
Shah, Duoaud	Poster 9-19	195
Shalaby, Nourhan	Poster 1-7	92
Sharma, Maksym	Oral 2-5	30
Shek, Tina	Poster 9-19	195
Shen, Yu-Jack	Poster 1-1	86
Shuhendler, Adam	Poster 1-8	93
	Poster 1-12	97
Siddiqui, Maryam	Oral 4-2	41
Siemens, Robert	Poster 3-3	110
Simard, Nicholas	Poster 6-17	154
Simpson, Amber	Poster 3-2	109
	Poster 3-4	111
	Poster 4-5	120
	Poster 9-13	189
Singh, Nidhi	Poster 9-8	184
	Poster 9-14	190
Singh, Sheldon	Oral 8-3	68
Smith, Paige	Oral 7-4	62
Soenjaya, Yohannes	Poster 9-8	184
Soliman, Hany	Poster 6-22	159
Soon, Kayla	Poster 1-13	98
Souza, Roberto	Poster 6-23	160
Sove, Richard	Poster 9-21	197
Speechley, Mark	Oral 6-2	54
Spence, David	Poster 8-6	173
Srouji, Rami	Poster 3-4	111
Stephenson, Nickeisha	Poster 6-9	146
Stirrat, Elaine	Oral 2-1	26
Stock, Jay	Poster 9-18	194
Stodilka, Rob	Poster 9-7	183
Stone, Simone	Poster 1-4	89
Strafella, Antonio	Oral 6-5	57
	Poster 6-3	140
	Poster 6-11	148
	Poster 6-13	150
Strother, Stephen	Poster 6-2	139
	Poster 8-5	172
Suchý, Mojmír	Poster 1-8	93
	Poster 1-12	97
Suh, Nina	Oral 7-2	60
	Poster 7-1	164

Name	Presentation	Page
Sullivan, Rebecca	Oral 8-5	70
Sumra, Vishaal	Poster 8-2	169
Sun, Liqun	Poster 8-7	174
Sun, Qin	Oral 1-6	24
Sun, Simon	Poster 3-2	109
Sunderland, Kyle	Oral 5-2	48
	Poster 5-8	132
	Poster 5-12	136
Surry, Kathleen	Oral 4-6	45
Swartz, Rick	Poster 6-2	139
	Poster 8-5	172
Sykes, Jane	Oral 8-5	70
Symons, Sean	Poster 6-2	139
	Poster 8-5	172
Tadic, Tony	Poster 9-19	195
Tan, Wan-Cheng	Oral 2-2	27
	Oral 2-3	28
	Poster 2-1	101
	Poster 2-6	106
Tanguay, Jesse	Poster 2-3	103
Tardif, Jean-Claude	Poster 6-2	139
Tartaglia, Carmela	Poster 8-5	172
Tavallaei, Ali	Oral 5-1	47
Teeter, Matthew	Oral 7-3	61
Tessier, David	Poster 5-10	134
Thiessen, Jonathan	Oral 1-5	23
	Oral 6-4	56
	Oral 8-5	70
	Poster 1-7	92
	Poster 6-16	153
Thirumal, Sindhura	Poster 9-20	196
Thompson, R. Terry	Oral 1-6	24
Thornhill, Rebecca	Poster 8-4	171
Tong, Junchao	Oral 1-4	22
	Oral 6-1	53
	Poster 6-3	140
	Poster 6-6	143
	Poster 6-7	144
	Poster 6-24	161
Truong, Jennifer	Poster 6-7	144
Truong, Peter	Poster 9-3	179
Turkbey, Ismail Baris	Oral 3-4	36

Name	Presentation	Page
Turley, Eva	Poster 9-9	185
Tyndale, Rachel	Poster 6-3	140
	Poster 6-6	143
	Poster 6-8	145
Ukwatta, Eranga	Oral 3-5	37
	Poster 3-1	108
	Poster 8-4	171
Umoh, Joseph U.	Poster 9-9	185
Ungi, Tamas	Oral 4-4	43
	Oral 5-2	48
	Poster 4-1	116
	Poster 4-7	122
	Poster 5-2	126
	Poster 5-4	128
	Poster 5-7	131
	Poster 5-8	132
	Poster 5-12	136
Valli, Mikaeel	Oral 6-5	57
	Poster 6-11	148
	Poster 6-13	150
Valsamis, Jake J	Poster 9-2	178
Van Asseldonk, Brandon	Oral 5-1	47
van der Kwast, Theodorus	Poster 3-7	114
Vanderbeck, Kaitlin	Oral 5-3	49
	Poster 5-2	126
Varlow, Cassis	Oral 6-3	55
	Poster 6-9	146
Varma, Sonal	Poster 4-3	118
Vasdev, Neil	Oral 1-4	22
	Oral 6-1	53
	Oral 6-3	55
	Poster 6-9	146
	Poster 6-24	161
	Poster 6-25	162
Vassallo, Reid	Poster 5-5	129
Verma, Megha	Poster 6-10	147
Villalobos, Dalila	Poster 4-3	118
Virdee, Sukhraj	Poster 2-1	101
Voineskos, Aristotle	Oral 10-5	83
Walker, Kirstin A	Poster 8-5	172
Walker, Matthew	Oral 7-5	63

Name	Presentation	Page
Wang, Ami	Oral 5-3	49
	Poster 5-2	126
Wang, Ben X.	Poster 1-4	89
Wang, Dan	Poster 1-4	89
Wang, Jenny	Poster 4-4	119
Wang, TianDuo	Oral 1-3	21
Wang, Xin Yue	Poster 4-8	123
Wang, Zhan Tao (Peter)	Poster 5-6	130
Ward, Aaron	Oral 1-5	23
	Oral 3-2	34
	Oral 3-3	35
	Poster 3-7	114
Warsh, Jerry	Oral 6-1	53
	Poster 6-6	143
	Poster 6-7	144
Waspe, Adam	Oral 4-2	41
	Oral 7-5	63
Wasserstein, David	Poster 5-3	127
Watling, Sarah	Oral 6-1	53
	Poster 6-6	143
Wej, Alice	Poster 4-5	120
Westcott, Andrew	Oral 2-5	30
Westwood, Duncan	Poster 6-3	140
Weyers, Jill	Oral 8-1	66
	Oral 8-2	67
Whitehead, Shawn	Oral 6-4	56
Whyne, Cari	Poster 4-6	121
	Poster 5-3	127
Wilson, Brian C	Poster 9-8	184
	Poster 5-1	125
Wilson, Sydney	Poster 9-7	183
	Poster 9-22	198
Wisenberg, Gerald	Oral 8-5	70
	Poster 8-3	170
Wood, Bradford J	Oral 3-4	36
Wood, Tobias	Poster 6-21	158
Woodward, Elise	Poster 2-2	102
Wright, Graham	Oral 5-1	47
	Oral 5-5	51
	Oral 8-1	66
	Oral 8-2	67
	Oral 8-3	68

Name	Presentation	Page
Wu, Catherine O	Poster 5-8	132
Wu, Victoria	Poster 4-7	122
	Poster 5-12	136
Wunker, Claire	Oral 4-2	41
Xia, Wenyao	Poster 3-5	112
Xiang, Yun	Poster 1-1	86
	Poster 1-2	87
Xiao, Dan	Oral 10-1	79
	Poster 1-14	99
	Poster 9-26	202
Xiao, Yiming	Poster 3-5	112
	Poster 5-5	129
Xu, Jiawei	Poster 8-7	174
Xu, Sheng	Oral 3-4	36
Yaeger, Rona	Poster 3-4	111
Yaffe, Martin	Oral 3-6	38
	Poster 1-4	89
	Poster 4-1	116
Yam, Scott	Poster 4-3	118
	Poster 5-7	131
Yamashita, Cory	Oral 2-6	31
Yasufuku, Kazuhiro	Poster 1-1	86
Yates, Lauren	Poster 5-7	131
Yeung, Ivan	Poster 9-19	195
Yi Mi Ren, Kevin	Poster 5-2	126
Yin, Jianhua	Poster 9-14	190
Young, Heather M	Poster 4-2	117
Yu, Lihai	Oral 8-5	70
Yu, Liu	Oral 1-6	24
Yu, Yue (Cindy)	Oral 8-3	68
Yuan, Xunhua	Oral 7-3	61
	Poster 7-3	166
Zabihollahy, Fatemeh	Oral 3-5	37
	Poster 3-1	108
Zabjek, Karl	Poster 5-3	127
Zanette, Brandon	Oral 2-1	26
Zawertailo, Laurie	Poster 6-14	151
Zevin, Boris	Oral 5-2	48
Zhang, Helena	Poster 6-14	151
Zhang, Yukun	Oral 4-5	44

Name	Presentation	Page
Zheng, Gang	Poster 9-8	184
Zhou, James J	Oral 5-1	47
Zhou, Ran	Poster 8-6	173
Zou, Yiran	Poster 1-1	86
	Poster 1-2	87
Zulkernine, Farhana	Poster 3-2	109

The Scientific and Organizing Committee for the ImNO 2020 Annual Symposium would like to thank you for participating and acknowledge our supporting consortia.

We invite you to attend the 19th ImNO Annual Symposium in March 2021 in Toronto, Ontario.

